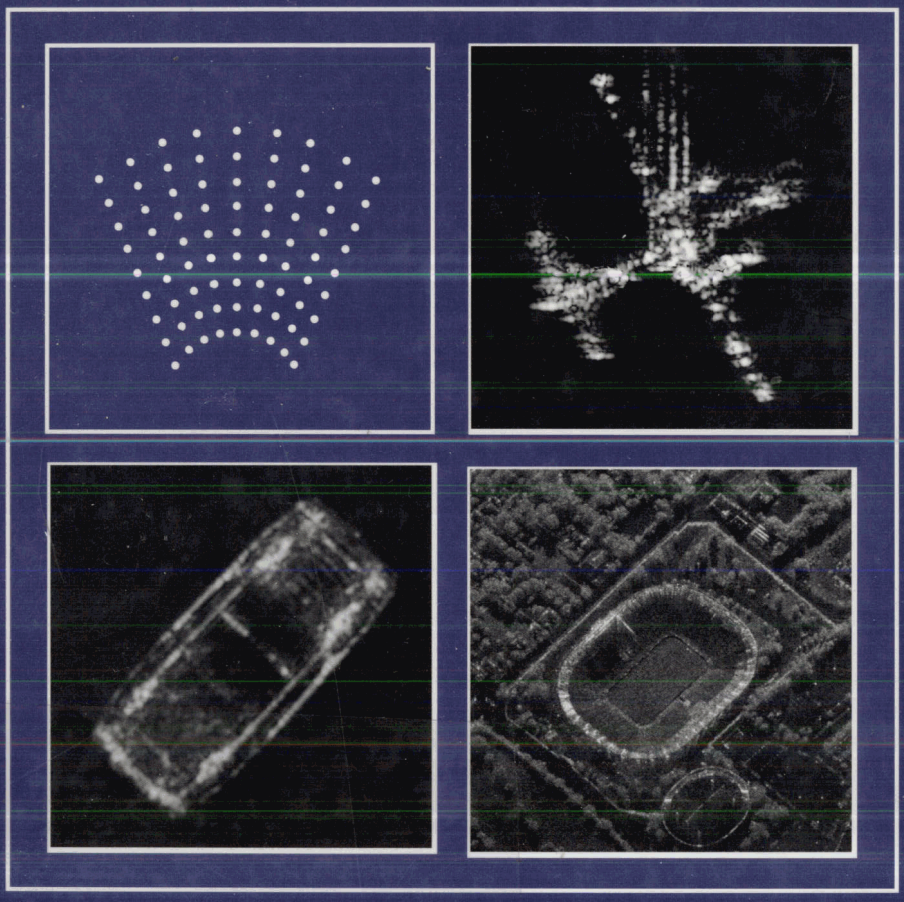
Spotlight Synthetic Aperture Radar

Signal Processing Algorithms



Walter G. Carrara
Ron S. Goodman
Ronald M. Majewski

Spotlight Synthetic Aperture Radar

Signal Processing Algorithms

The Artech House Remote Sensing Library

Fawwaz T. Ulaby, Series Editor

Handbook of Radar Scattering Statistics for Terrain, F. T. Ulaby and M. C. Dobson

Introduction to Electromagnetic Wave Propagation, P. Rohan

Microwave Radiometric Systems: Design and Analysis, N. Skou

Microwave Remote Sensing, Volume I: Fundamentals and Radiometry, F. T. Ulaby, R. K. Moore, and A. K. Fung

Microwave Remote Sensing, Volume II: Radar Remote Sensing and Surface Scattering and Emission Theory, F. T. Ulaby, R. K. Moore, and A. K. Fung

Microwave Remote Sensing, Volume III: From Theory to Applications, F. T. Ulaby, R. K. Moore, and A. K. Fung

Microwave Scattering and Emission Models and Their Applications, Adrian K. Fung

Radar Polarimetry for Geoscience Applications, F. T. Ulaby and C. Elachi, editors

Radar Scattering Statistics for Terrain: Software and User's Manual, F. T. Ulaby and M. C. Dobson

Spotlight Synthetic Aperture Radar: Signal Processing Algorithms, Walter G. Carrara, Ron S. Goodman, and Ronald M. Majewski

For further information on these and other Artech House titles, contact:

Artech House
685 Canton Street
Norwood, MA 01602
617-769-9750
Fax: 617-762-9230
Telex: 951-659
email: artech@world.std.com

Artech House
Portland House, Stag Place
London SW1E 5XA England
+44 (0) 71-973-8077
Fax: +44 (0) 71-630-0166
Telex: 951-659
email: artech@world.std.com

Spotlight Synthetic Aperture Radar
Signal Processing Algorithms

Walter G. Carrara
Ron S. Goodman
Ronald M. Majewski

Artech House
Boston • London

Library of Congress Cataloging-in-Publication Data
Carrara, Walter G.
Spotlight synthetic aperture radar: signal processing algorithms / Walter G. Carrara, Ron S. Goodman, Ronald M. Majewski.
Includes bibliographical references and index.
ISBN 0-89006-728-7
1. Synthetic aperture radar. 2. Signal processing. 3. Algorithms. I. Goodman, Ron S. II. Majewski, Ronald M. III. Title.
TK6592.S95C37 1995 95-19078
621.3848–dc20 CIP

British Library Cataloguing in Publication Data
Carrara, Walter G.
Spotlight Synthetic Aperture Radar: Signal Processing Algorithms
I. Title
621.3827

ISBN 0-89006-728-7

© 1995 ARTECH HOUSE, INC.
685 Canton Street
Norwood, MA 02062

All rights reserved. Printed and bound in the United States of America. No part of this book may be reproduced or utilized in any form or by any means, electronic or mechanical, including photocopying, recording, or by any information storage and retrieval system, without permission in writing from the publisher.

International Standard Book Number: 0-89006-728-7
Library of Congress Catalog Card Number: 95-19078

10 9 8 7 6 5 4 3 2

To my wife Carol
WGC

To Myong, Kyle, and Ryan
RSG

To my wife Mary, and to my parents Ron & Nancy and Ray & Marge
RMM

Contents

Preface	**xiii**
Chapter 1 Introduction	**1**
1.1 SYNTHETIC APERTURE RADAR	2
1.2 SAR MODES	4
1.3 SPOTLIGHT MODE ATTRIBUTES	5
1.4 EARLY SAR DEVELOPMENT	5
1.4.1 Spotlight Mode and Polar Format	6
1.4.2 The Move to Digital Processing	7
1.5 SPOTLIGHT SAR TODAY	9
REFERENCES	9
Chapter 2 Synthetic Aperture Radar Fundamentals	**13**
2.1 SAR SYSTEM OVERVIEW	13
2.1.1 System Operation	14
2.1.2 SAR Sensor	15
2.1.3 Motion Sensor	19
2.1.4 Image Formation Processor	20
2.1.5 Image Processor	20
2.1.6 Image Exploitation Segment	21
2.2 IMAGING CONSIDERATIONS	21
2.3 PULSE COMPRESSION AND RANGE RESOLUTION	26
2.3.1 Short Pulse	27
2.3.2 Linear FM Waveform	27
2.3.3 Stepped-Frequency Waveform	30
2.4 SYNTHETIC APERTURE CONCEPT AND AZIMUTH RESOLUTION	31
2.4.1 Real Beam Radar and SAR	31
2.4.2 Synthetic Aperture Interval	38
2.4.3 Beam Compression Ratio	41
2.4.4 Azimuth Chirp Rate and Doppler Bandwidth of Received Signal	42
2.4.5 Spotlight Scene Bandwidth after Azimuth Dechirp	43
2.5 SAR COHERENCE REQUIREMENTS	46
2.5.1 Propagation Effects on Phase Coherence	46
2.5.2 Source Coherence in SAR	47
2.5.3 Motion Effects on Phase Coherence	48
2.6 SIGNAL PHASE EQUATION	56
2.6.1 Spotlight Data Collection Geometry	57
2.6.2 Transmitted Signal—Linear FM Chirp	61
2.6.3 Received Signal	63
2.6.4 Demodulated Signal	65
2.6.5 Sampled Signal	69
2.6.6 Fine Motion Compensation	70
2.6.7 Components of Signal Phase Equation	71
2.7 INVERSE SAR	72
2.7.1 ISAR Geometry	73
2.7.2 ISAR Analytical Model	75
2.8 SAR SENSOR PARAMETRIC DESIGN EXAMPLE	76
2.9 SUMMARY	78
REFERENCES	78

Chapter 3 Spotlight SAR and Polar Format Algorithm **81**
3.1 SCOPE OF PROCESSING TASK 81
3.1.1 Signal Processing Requirements 82
3.1.2 Challenges in Spotlight Data Processing 84
3.2 REVIEW OF IMAGE FORMATION ALGORITHMS 88
3.2.1 Algorithm Survey 88
3.2.2 Limitation of Rectangular Format 90
3.3 POLAR FORMAT ALGORITHM 95
3.3.1 Algorithm Overview 95
3.3.2 Signal History Model 97
3.3.3 Polar Format Transformation 99
3.3.4 Focus Target Plane Concept 107
3.3.5 Selection of Image Display Plane 109
3.4 SAR IMAGING GEOMETRY 111
3.4.1 Geometry Models 111
3.4.2 Relative Motion 113
3.4.3 Differential Range 116
3.4.4 Approximation for Differential Range 117
3.5 TAYLOR SERIES EXPANSION PROCEDURE 119
3.5.1 Taylor Series Coefficients 119
3.5.2 Calculation Procedures 122
3.6 BASIC IMAGING TERMS IN THE SIGNAL EQUATION 126
3.6.1 Phase of Image Pixels 127
3.6.2 Basic Imaging Relationship 128
3.7 RANGE CURVATURE 132
3.8 NONPLANAR MOTION AND THREE-DIMENSIONAL SCENE 137
3.9 MOTION MEASUREMENT ERRORS 140
3.9.1 Scene Center Displacements 142
3.9.2 Geometric Distortion 143
3.9.3 Quadratic Phase Error 143
3.10 RESIDUAL VIDEO PHASE 143
3.11 ADDITIONAL ERROR SOURCES 147
3.12 RELATIONSHIP BETWEEN TARGET AND IMAGE COORDINATES 148
3.12.1 Individual Contributors 148
3.12.2 Correction for Range Curvature Image Distortion 150
3.13 IMAGE FOCUS ERROR SUMMARY 152
3.14 SUMMARY 153
REFERENCES 154
Chapter 4 Digital Polar Format Processing **157**
4.1 SAMPLING RATE CONVERSION 158
4.1.1 Upsampling 158
4.1.2 Downsampling 163
4.1.3 Resampling 163
4.2 POLYPHASE FILTERS 166
4.2.1 A Resampling Example 166
4.2.2 Use of Polyphase Filters 168
4.2.3 Filtering Mechanics 171
4.3 DIGITAL POLAR FORMAT RELATIONSHIPS 175
4.4 DIGITAL POLAR INTERPOLATION 180
4.4.1 Range Interpolation 181
4.4.2 Azimuth Interpolation 187

4.5 IMAGE SCALE FACTORS 189
4.6 SIGNAL HISTORY PROJECTIONS 191
4.6.1 Collection Surface to Focus Target Plane 191
4.6.2 Focus Target Plane to Image Display Plane 191
4.7 STABILIZED SCENE POLAR INTERPOLATION 192
4.7.1 Example with Line-of-Sight Polar Interpolation 193
4.7.2 Example with Stabilized Scene Polar Interpolation 193
4.7.3 Considerations in Stabilized Scene Polar Interpolation 195
4.8 SUBPATCH PROCESSING 198
4.9 SUMMARY 200
REFERENCES 200

Chapter 5 Phase Errors **203**
5.1 CLASSIFICATION OF PHASE ERRORS 204
5.1.1 Low-Frequency Phase Errors 206
5.1.2 High-Frequency Phase Errors 212
5.2 MANAGEMENT OF PHASE ERRORS 220
5.3 MAGNITUDE OF PHASE ERRORS 223
5.3.1 Errors in Position and Motion Measurement 225
5.3.2 Range Curvature 233
5.3.3 Residual Video Phase 233
5.3.4 Nonplanar Motion 235
5.3.5 Other Error Sources 235
5.4 REQUIREMENTS ON A PRACTICAL SAR MOTION SENSOR 236
5.5 MOVING TARGET EFFECTS 238
5.6 SUMMARY 242
REFERENCES 243

Chapter 6 Autofocus Techniques **245**
6.1 MAPDRIFT 246
6.1.1 Overview 246
6.1.2 Analytical Development 249
6.1.3 Implementation 252
6.2 MULTIPLE APERTURE MAPDRIFT 252
6.2.1 Overview 254
6.2.2 Analytical Development 254
6.2.3 Implementation 258
6.3 PHASE DIFFERENCE 260
6.3.1 Overview 262
6.3.2 Analytical Development 262
6.3.3 Implementation 264
6.4 PHASE GRADIENT AUTOFOCUS 264
6.4.1 Overview 265
6.4.2 Analytical Development 265
6.4.3 Implementation 268
6.5 PROMINENT POINT PROCESSING 268
6.5.1 Single Prominent Point Processing Algorithm 270
6.5.2 Multiple PPP Algorithm 274
6.5.3 Selection of Prominent Points 281
6.6 SPACE-VARIANT REFOCUS 282
6.7 SUMMARY 285
REFERENCES 287

Chapter 7 Processor Design Examples **289**
7.1 THE COMMON UNIX SAR PROCESSOR 289
7.1.1 DCS System Overview 289
7.1.2 Processor Overview 292
7.1.3 Signal Processor Software Architecture 294
7.2 THE GROUND-TO-AIR IMAGING RADAR PROCESSOR 297
7.2.1 GAIR System Overview 297
7.2.2 Processor Overview 302
7.2.3 Preprocessing Segment 304
7.2.4 Interactive Segment 308
7.2.5 Image Formation Segment 310
7.2.6 Image Exploitation Segment 313
7.3 SUMMARY 313
REFERENCES 314
Chapter 8 SAR System Performance **315**
8.1 IMAGE QUALITY METRICS 316
8.2 SYSTEM PERFORMANCE BUDGET 317
8.3 REQUIREMENTS RELATING TO SYSTEM IMPULSE RESPONSE 320
8.3.1 Resolution 323
8.3.2 Peak Sidelobes 329
8.3.3 Integrated Sidelobe Ratio 330
8.4 REQUIREMENTS ON SYSTEM NOISE 330
8.4.1 Multiplicative Noise 332
8.4.2 Additive Noise 333
8.4.3 Contrast Ratio 335
8.5 GEOMETRIC DISTORTION 339
8.6 SECONDARY IMAGE QUALITY METRICS 342
8.7 TEST SITES FOR IMAGE QUALITY VERIFICATION 345
8.7.1 Elements of the Test Site 345
8.7.2 Measurement of System Noise Parameters 349
8.7.3 Example Test Site 351
8.8 SUMMARY 355
REFERENCES 356
Chapter 9 Spotlight Processing Applications **357**
9.1 SPOTLIGHT PROCESSING OF STRIPMAP SAR DATA 357
9.1.1 Mode Differences 357
9.1.2 Stripmap-to-Spotlight Conversion Process 358
9.1.3 Image Example 361
9.2 FORWARD-LOOK SAR 361
9.2.1 Geometry Model 362
9.2.2 Image Attributes 363
9.2.3 Image Examples 367
9.3 INTERFEROMETRIC SAR 367
9.3.1 Nature of SAR Interferometry 369
9.3.2 Interferometry Model 370
9.3.3 Processing Requirements 374
9.3.4 Height Measurement Error 375
9.3.5 Absolute Height Information 377
9.3.6 Orthorectification 379
9.3.7 Image Examples 380
9.3.8 Other Approaches to Height Measurement 383

9.4 VIBRATING TARGET DETECTION 386
9.4.1 Data Collection Model 387
9.4.2 Effect of Vibration 389
9.4.3 Smearing of Paired Echoes 390
9.4.4 Phase Adjustment to Focus Paired Echoes 392
9.4.5 Vibration Detection Process 394
9.4.6 Simulated Examples with Vibrating Targets 396
9.5 SUMMARY 399
REFERENCES 399

Chapter 10 Range Migration Algorithm **401**
10.1 SIGNAL MODEL 402
10.2 ALGORITHM OVERVIEW 407
10.2.1 Along-Track Fourier Transform 409
10.2.2 Matched Filtering 413
10.2.3 Stolt Interpolation 416
10.2.4 Two-Dimensional Inverse Fourier Transform 420
10.3 ANALYTICAL DEVELOPMENT 420
10.3.1 Principle of Stationary Phase 423
10.3.2 Along-Track Fourier Transform Analysis 425
10.3.3 Matched Filtering Analysis 427
10.3.4 Stolt Interpolation Analysis 427
10.4 ASPECTS OF RANGE MIGRATION PROCESSING 428
10.4.1 Along-Track Sampling Requirements 428
10.4.2 Processing Squinted Data 429
10.4.3 Space-Variant Impulse Response 431
10.4.4 Approximation for Stolt Interpolation 432
10.4.5 Relation between Range Migration and Polar Format Algorithms 433
10.5 APPLICATIONS OF RANGE MIGRATION PROCESSING 435
10.5.1 L-Band SAR 436
10.5.2 Ultra-Wideband SAR for FOPEN 437
10.6 SUMMARY 438
REFERENCES 439

Chapter 11 Chirp Scaling Algorithm **443**
11.1 SIGNAL MODEL WITHOUT DECHIRP-ON-RECEIVE 443
11.2 ALGORITHM OVERVIEW 447
11.2.1 Azimuth Fourier Transform 447
11.2.2 Chirp Scaling Operation 449
11.2.3 Range Compression 452
11.2.4 Two-Dimensional Phase Compensation 455
11.2.5 Azimuth Inverse Fourier Transform 455
11.3 ANALYTICAL DEVELOPMENT 456
11.3.1 Azimuth Fourier Transform 456
11.3.2 Chirp Scaling Operation 461
11.3.3 Range Fourier Transform 461
11.3.4 Two-Dimensional Matched Filtering 463
11.3.5 Range Inverse Fourier Transform 464
11.3.6 Two-Dimensional Phase Compensation 464
11.3.7 Azimuth Inverse Fourier Transform 464
11.4 ALGORITHM LIMITATIONS 465
11.5 ALGORITHM APPLICATIONS 468

11.6 SUMMARY 470
REFERENCES 471

Chapter 12 Comparison of Image Formation Algorithms **473**
12.1 IMAGE FORMATION ALGORITHM MODELS 474
12.1.1 Polar Format Algorithm 474
12.1.2 Range Migration Algorithm 476
12.1.3 Chirp Scaling Algorithm 476
12.2 COMPUTATIONAL COMPLEXITY 479
12.3 ADDITIONAL ASPECTS OF ALGORITHM PERFORMANCE 482
12.3.1 Polar Format Algorithm 482
12.3.2 Range Migration Algorithm 484
12.3.3 Chirp Scaling Algorithm 484
12.4 SUMMARY 485
REFERENCES 486

Appendix A Fast Algorithm for Digital Quadrature Demodulation **487**
REFERENCES 493

Appendix B Tomographic Processing of Spotlight Data **495**
B.1 TOMOGRAPHIC RECONSTRUCTION 495
B.2 ALGORITHM ATTRIBUTES 497
REFERENCES 498

Appendix C Removal of Residual Video Phase **501**
C.1 PRESENCE OF RVP 501
C.2 COMPENSATION WITH A FREQUENCY-DEPENDENT DELAY 502
C.3 UTILITY OF RVP COMPENSATION 505

Appendix D Sidelobe Control in SAR Imagery **507**
D.1 FINITE APERTURES 507
D.2 COMMON WEIGHTING FUNCTIONS 512
D.3 SPATIALLY VARIANT APODIZATION 515
D.4 SUMMARY 526
REFERENCES 529

Appendix E Description of SAR Images **531**
E.1 DATA COLLECTION SYSTEM 531
E.2 GROUND-TO-AIR IMAGING RADAR 531
E.3 ROTATING PLATFORM FACILITY 533
E.4 P-3/SAR SYSTEM 534
E.5 SIMULATED IMAGES 535
REFERENCES 536

Acronyms **537**

Symbols **541**

Index **549**

Preface

This book began with a determination to present SAR concepts and signal processing techniques unique to *spotlight mode* and the *polar format algorithm*. The existing database of technical articles and books on SAR would serve as a background and starting point, allowing the text to concentrate on practical procedures and advanced analyses in the implementation and evaluation of spotlight SAR image formation processing. As often happens, the fleshing out of the details changed and enlarged the scope of the presentation. The authors believe that the final product, with its broader scope, provides detailed insight into spotlight mode, its applications, and its processing algorithms.

Early writing activity quickly reminded the authors that spotlight and stripmap SAR modes have more similarities than differences. Thus, an introductory chapter on spotlight SAR fundamentals soon became a chapter on SAR fundamentals. Early reviewer comments led to a hesitancy to present subtle SAR relationships with simply a final result and a list of references to guide the reader. In fact, a number of detailed relationships involving a long derivation have no readily available references. Thus, a single equation describing SAR azimuth resolution grew into a three-page explanation, while a chapter on spotlight SAR signal characteristics and the polar format algorithm grew from 60 to over 200 equations. As the research activities of the authors expanded into new algorithms during this writing, the book's concentration on the polar format algorithm with a brief summary of alternative algorithms evolved to include individual chapters on the *range migration algorithm* and the *chirp scaling algorithm* with an appendix on the *tomographic back-projection algorithm.*

We believe the reader will find this level of detail coupled with depth and scope to be a valuable resource. We base this belief, in part, on the fact that the authors, while writing this book, have referred to it frequently during their daily professional activities.

The primary basis for this book is more than three decades of pioneering activities in synthetic aperture radar by the Environmental Research Institute of Michigan (ERIM) and its predecessor, the Willow Run Laboratories of the University of Michigan. The book also draws on contributions to the SAR field by numerous other individuals and organizations.

The focus of this book is the digital formation of spotlight SAR imagery. The goal is to transfer to the reader a working knowledge of spotlight SAR processing techniques in an understandable and practical manner, using real-world examples to reinforce theoretical aspects whenever possible. This book is not a mathematical development of SAR theory. Rather, it describes the topic in a practical, hands-on fashion. The authors assume a familiarity with basic radar system concepts and with digital signal processing techniques. The text includes introductory material to acclimate the reader to SAR concepts and to considerations specific to the processing of spotlight SAR data.

Chapter 1 provides introductory definitions of and applications for spotlight and stripmap SAR; it outlines the history of SAR leading to digital processing of spotlight mode data in a polar format. After a review of basic SAR concepts and requirements in Chapter 2, this book covers the polar format algorithm to process spotlight mode SAR data in Chapters 3 and 4. The book evaluates the sources and effects of phase errors in SAR data in Chapter 5, autofocus solutions in the image formation processor in Chapter 6, and image quality specification and assessment in Chapter 8. It provides image formation processor design examples from two fine-resolution SAR systems in Chapter 7, and describes a variety of imaging applications in Chapter 9. It also presents and analyzes two alternative algorithms, the range migration algorithm in Chapter 10 and the chirp scaling algorithm in Chapter 11, with a comparison of these three algorithms in Chapter 12. The book contains five appendices with Appendices D and E being of particular interest. Appendix D discusses sidelobe control in SAR imagery and Appendix E summarizes the parameters of each SAR image in the book and provides a brief description of the radar systems that produced the images.

One aspect of this book that did not change from the beginning is its widespread use of actual SAR images to reinforce the text. Where better to begin using SAR images than on the cover? The four blocks on the cover collage, beginning at top left and moving clockwise, are a cartoon display of radar data samples stored in wavenumber (polar) space; an inverse SAR image of an in-flight Convair-580 aircraft obtained from a ground-based radar system; a spotlight SAR image of the University of Michigan football stadium obtained from an airborne SAR system; and an image of an automobile obtained from a rotating platform inverse SAR facility.

We are indebted to many ERIM staff members, not only for strong reviews of various chapters of this book, but principally for contributions to the technical environment and achievements on which this book draws. We give special recognition to Linda E. Brown and Brian P. Williams who participated in the early organizational stages of this book project, contributed to the technical content in several areas, and provided a detailed review of many chapters.

With respect to critical technical review, we particularly acknowledge the efforts of Elmer L. Johansen, Norman E. McIver, and Jack M. Miller, each a long-term member of the ERIM technical staff who is now retired. We also express gratitude to T. Patrick Bidigare, David A. Carrara, and J. Morris Swiger for significant technical reviews. The contributions of these individuals truly improved the quality of the final manuscript.

Having combined three decades of research in synthetic aperture radar and a memorable two-year writing experience into one SAR book, the authors offer this summary of the subject: "In SAR, ***motion is the solution and the problem.***" A more comprehensive discussion of SAR from a signal processing algorithm perspective begins in Chapter 1.

Chapter 1
Introduction

The word *radar* is an acronym based on the phrase "radio detection and ranging." Radar is an important sensor technology because it provides an all-weather, day/night capability to not only detect and locate objects, but to generate a spatial, visual representation (that is, an image) of the radar reflectivity of an illuminated scene. A radar has day/night capability because it supplies its own illumination. A radar has all-weather capability because radio waves propagate through clouds and rain with only limited attenuation. Of particular interest in this book is the extension of this capability to the imaging of terrain and cultural features.

A radar system consists of a transmitter, a receiver, an antenna (including a pointing or steering mechanism), and a signal processing and display unit. A radar system emits a sequence of bursts, or pulses, of radio waves at regularly spaced intervals in time. The emitted pulses propagate outward to illuminate the area within the antenna beam. An illuminated object absorbs a fraction of the incident energy and scatters the remainder. The part of the scattered energy reflected back to the radar antenna is the received signal.

Radio waves propagate at the speed of light. The time delay between transmission of a pulse and the return of a reflection from an object provides a measure of the two-way distance, or twice the *range*, between the radar and the object. The delay is the two-way distance divided by the speed of light. Accuracy in the measurement of this time delay directly impacts the ability to determine an object's range position.

A radar system employs a directional antenna that radiates energy within a narrow beam in a known direction. The energy reflected back to the antenna by an object varies as a function of antenna pointing. In a conventional radar, this variation is the basis for determining the angular position of the object. Antenna beamwidth and accuracy in the measurement of antenna-pointing directly impact the ability to determine angular position. By combining range and angular information, it is possible to construct a three-dimensional map of the position and radar reflectivity of objects in the volume scanned by the radar beam.

Closely related to position measurement is spatial resolution. An imaging radar system must distinguish between single and multiple scatterers located in close proximity. Resolution is, nominally, the minimum distance needed between adjacent scatterers to separate them in the image. Fine resolution provides the capability to image a complex object or scene as a number of separate scattering centers. This type of image provides detailed information to detect, characterize, and identify specific objects of interest.

Because of the importance of object identification in military applications, much development effort has been directed at improving radar resolution.

An imaging radar typically provides a two-dimensional representation of scatterers in the illuminated volume with no resolution or positioning of scatterers in the third dimension. Generally, we speak of radar resolution in the range and cross-range or azimuth directions. Range resolution is inversely proportional to the bandwidth of the transmitted signal. A wider bandwidth means finer range resolution.

In a conventional aperture radar, resolution in the azimuth direction improves as the azimuth antenna beamwidth becomes smaller. Antenna beamwidth becomes smaller as the antenna aperture size or radar frequency increases. A larger antenna aperture or a higher radar frequency corresponds to a narrower beamwidth. Practical constraints on both antenna size and transmitted frequency limit the azimuth resolution that a conventional aperture radar can achieve.

1.1 SYNTHETIC APERTURE RADAR

In June 1951, Carl Wiley of the Goodyear Aircraft Corporation proposed an alternative means for improving azimuth resolution [1, 2]. Wiley's work indicated that a pulse-to-pulse comparison of the signals collected by a moving radar could produce finer azimuth resolution than the real antenna beamwidth provides. The concept was called *synthetic aperture radar* (SAR) to signify that a signal synthesis accomplished what would otherwise require a larger antenna aperture. This synthesis involves the proper summation of the signals produced by transmitting and receiving from a sequence of locations. A practical means for moving through these locations is to mount a SAR sensor on a moving platform, such as an aircraft.

The synthetic aperture concept offers improvement in azimuth resolution only. However, most SAR system designs achieve comparable resolution in both range and azimuth. The ability to improve azimuth resolution provides the incentive to increase radar signal bandwidth and thereby improve range resolution.

A SAR image is a two-dimensional mapping of received signal energy. The intensity assigned to individual pixels is the computed energy in the signal received from the corresponding location within the illuminated scene. A separate computation is necessary for each of the many pixels that form an image. Figure 1.1 presents an example of a SAR image. This image is a 940×940 pixel array representing a scene that is approximately 630×630 m. The image resolution is 1 m in both the horizontal (range) and vertical (azimuth) directions. Near range is on the left side, indicating that the radar illuminates the scene from the left side. The brighter areas in the scene indicate scatterers with higher radar reflectivity.

With its fine two-dimensional resolution capability and the possibility of day/night operation in all weather, SAR has evolved to satisfy a variety of applications for both civilian and military users. These applications center on target imaging and terrain mapping. A target is a specific object of interest that the radar illuminates. The typical target is man-made and consists of multiple scattering centers. Terrain consists of objects



Figure 1.1 X-band spotlight SAR image.

that cover large areas, such as fields, forests, lakes, rivers, and roads. In some applications, such as crop or forest condition assessment, the terrain itself is the target. In other applications, such as locating military vehicles on a battlefield, the terrain is undesired background noise. Military SAR applications include intelligence gathering, battlefield reconnaissance, and weapons guidance. Civilian applications include topographic mapping, oil spill monitoring, sea ice characterization and tracking, agricultural classification and assessment, land use monitoring, and planetary or celestial investigations.

Many excellent historical papers [1, 2], tutorial or review articles [3-6], and books [7-10] on SAR are available to the reader. Among the earlier published papers are [11-13]. Early papers relating to optical processing of SAR data include [14, 15]. A sampling of papers on digital signal processing of SAR data includes [16-19]. Reference [20] provides a comprehensive discussion of spotlight mode.

1.2 SAR MODES

Figure 1.2 illustrates the three common SAR imaging modes: spotlight, stripmap, and scan. During a *spotlight mode* data collection, the sensor steers its antenna beam to continuously illuminate the terrain patch being imaged. In the *stripmap mode*, antenna pointing is fixed relative to the flight line. The result is a moving antenna footprint that sweeps along a strip of terrain parallel to the path of motion. The stripmap mode involves either a broadside imaging geometry, which Figure 1.2 illustrates, or a squinted imaging geometry. In the squinted stripmap mode, the antenna is pointed forward or behind the normal to the flight line. In the *scan mode*, the sensor steers the antenna beam to illuminate a strip of terrain at any angle to the path of motion. The scan mode is a versatile operating mode that encompasses both the spotlight and stripmap modes as special cases.

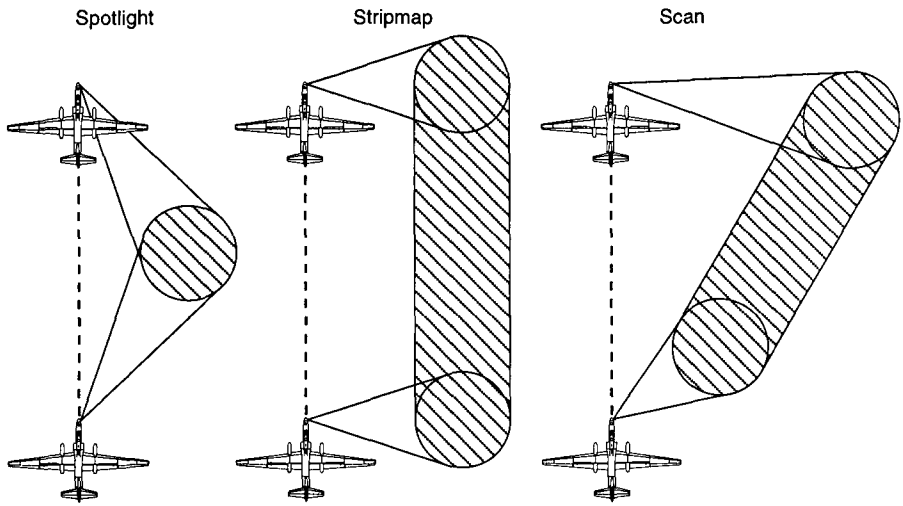


Figure 1.2 Synthetic aperture radar modes.

Because scan mode involves additional operational and processing complexity, spotlight and stripmap modes are the most common SAR modes. The spotlight mode is a practical choice when the mission objective is to collect fine-resolution data from one or more localized areas. The stripmap mode is most efficient when used for coarse-resolution mapping of large regions.

A fourth operating mode called inverse SAR (ISAR) produces radar signal data similar to that of spotlight mode SAR. However, the ISAR mode is different in that data collection is accomplished with the radar stationary and the target moving. The signals are similar because it is the *relative* position and motion between the sensor and the scene being imaged that is important. Since the signals are similar, the processing required to produce an image is similar also.

1.3 SPOTLIGHT MODE ATTRIBUTES

Three attributes distinguish spotlight and stripmap modes. First, spotlight mode offers finer azimuth resolution than that achievable in stripmap mode using the same physical antenna. Second, spotlight imagery provides the possibility of imaging a scene at multiple viewing angles during a single pass. Third, spotlight mode allows efficient imaging of multiple smaller scenes whereas stripmap mode naturally images a long strip of terrain.

SAR azimuth resolution improves with the length of the synthetic aperture. In stripmap mode, antenna pointing is fixed relative to the flight line; azimuth antenna beamwidth limits the available synthetic aperture length because it determines the transit distance over which the sensor illuminates each scatterer. Spotlight mode avoids this limitation on synthetic aperture length by steering the antenna illumination pattern to illuminate the scene for a long period. Consequently, antenna beamwidth does not limit azimuth resolution in spotlight mode.

A SAR sensor usually travels a long distance relative to the synthetic aperture length required to achieve the desired azimuth resolution. Stripmap mode naturally uses the full transit distance to image a long strip of terrain. Spotlight mode can use the transit distance in excess of the synthetic aperture length to generate additional images of a single scene or to image multiple scenes. The first choice involves imaging a scene from multiple viewing angles. This choice is valuable because most targets exhibit scattering properties that vary strongly with angle of observation. The ability to exploit imagery at multiple viewing angles greatly improves the potential for target detection and identification. The second choice involves imaging a variety of small scenes along the flight path. A combination of these choices provides spotlight mode with a useful operational flexibility.

1.4 EARLY SAR DEVELOPMENT

In early 1953, a group from the University of Illinois experimentally demonstrated stripmap SAR [2]. The resulting image was of a seven-mile-long swath along the coast of Key West, Florida. The image formation process that the group employed was able to produce an image well-focused in azimuth over only a small range interval.

In the summer of 1953, the U.S. Army opened a short study at the University of Michigan called Project Wolverine [11]. Study participants included the University of Illinois, the University of Michigan, Goodyear Aircraft Corporation, Philco, General Electric, and Varian [21]. The task was to recommend research and development programs to improve battlefield surveillance techniques. One result of this study was to assign the task of building a new optical SAR processor to a team at the University of Michigan's Willow Run Laboratories. This processor was to accept wideband radar signals and generate imagery that was focused at all range intervals. Over the next four years, the Willow Run group built an X-band radar and an optical processor based on a helium-neon laser light source. In August 1957, the completed system produced the first fully focused stripmap SAR image. (Willow Run Laboratories eventually became the Environmental Research Institute of Michigan, ERIM.)

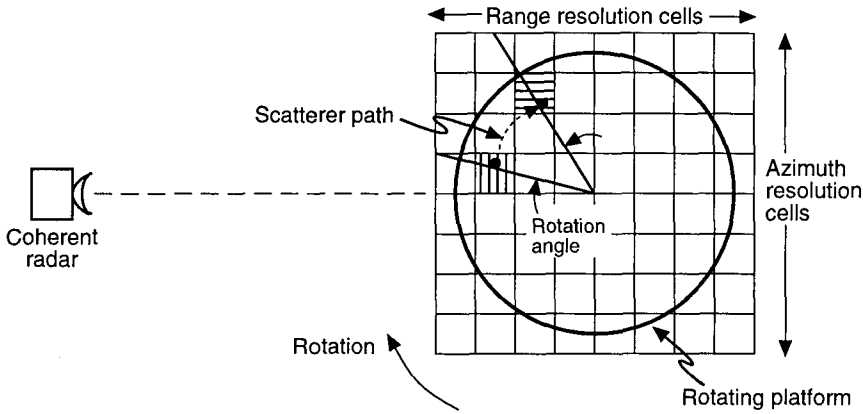


Figure 1.3 Scatterer motion through resolution cells.

1.4.1 Spotlight Mode and Polar Format

In the early 1960s, the Willow Run Laboratories began research to develop techniques for fine-resolution imaging of rotating objects using radar. This assignment was the result of an Air Force-sponsored study concerned with the identification of spaceborne objects [21]. To support the goal of imaging objects rotating in space, initial experiments utilized a rotating platform illuminated by a stationary, ground-based coherent radar. The platform size of about 7 m in diameter limited the imaged scene size. Operating in an ISAR mode, this radar imaging system collected data which helped to refine processing techniques for SAR image formation. Later experiments using an airborne SAR sensor involved the imaging of large areas of terrain.

The principal difficulty hampering early efforts to image scenes at fine resolution was target smearing caused by scatterer motion through resolution cells [22]. Figure 1.3 uses a rotating platform ISAR geometry to illustrate the motion that causes this problem. During the scene rotation required to achieve azimuth resolution, an individual scatterer changes its locations in range and azimuth relative to the radar sensor. In this illustration, the scatterer moves from the horizontally shaded resolution cell at the start of rotation to the vertically shaded resolution cell by the end of rotation. Smearing is more serious when attempting finer resolution because the motion becomes larger and the resolution cell size becomes smaller.

During these early studies, engineers collected and processed SAR data using analog optical processing techniques [14]. The SAR data required formatting and photographic recording to produce the appropriate input to the optical processor. Initially, data was stored in a rectangular format, as Figure 1.4(a) suggests. In the rectangular format, the processor stores successive radar pulses side by side and parallel to each other.

In 1969, scientists discovered that recording the data in a polar format greatly alleviated the problem of motion through resolution cells. This discovery opened the way for

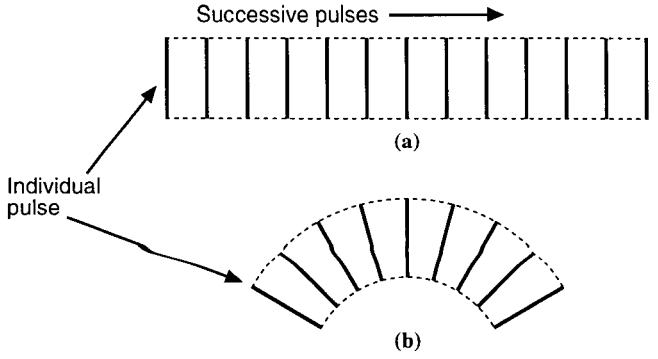


Figure 1.4 Spotlight SAR data storage formats: **(a)** Rectangular format; **(b)** Polar format.

the generation of fine-resolution spotlight imagery. In polar format, the processor stores successive pulses along radial lines, as Figure 1.4(b) suggests. An internal Willow Run Laboratories memorandum dated 24 November 1970 provided the first documentation of polar format recording for SAR image formation. Figure 1.5 is a photograph included in that memorandum; this figure compares rectangular and polar format signal histories from a single point scatterer.

Dr. Jack Walker provided the first open publication of this work in his dissertation at the University of Michigan [23]. Later, the *IEEE Aerospace and Electronic Systems Transactions* published this same material [24]. The polar storage technique is applicable to various wave phenomena as well as to SAR signal processing [25].

1.4.2 The Move to Digital Processing

Analog optical processing was, of necessity, the approach when SAR image formation processing techniques were initially developed. The digital computers of that era were inadequate to handle the quantity of data and the required computational loads. Typically, a single image may require hundreds of megabytes of data. In addition, SAR image formation requires computationally complex calculations as high as 1000 floating point operations per image pixel. This requirement amounts to one billion calculations to generate a single 1000×1000-pixel image. In contrast, a single spherical lens can perform the two-dimensional Fourier transform (a major component of SAR image formation) in a virtually instantaneous operation.

Optical processing requires a recording device to store the radar signal data on photographic film. Figure 1.6 is a diagram of the basic rectangular format film recorder used in early SAR systems. The radar signal returned from successive transmitted pulses modulates the intensity of a line-scan cathode-ray tube (CRT). The lens images the CRT sweep onto the moving strip of film. A separate operation positions the developed film at the front focal plane of a spherical lens. A source of collimated, monochromatic, coherent light illuminates the film and the image appears at the rear focal plane of the lens.

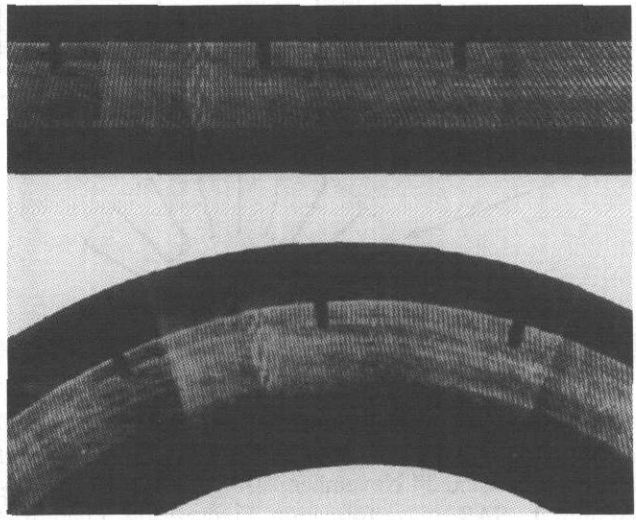


Figure 1.5 Rectangular and polar format signal histories.

To record data in a polar format as in the early rotating platform ISAR system, a rotating, disk-mounted sheet of film replaces the translating film strip in Figure 1.6. This recording method was adequate for the small scene sizes of the rotating platform.

In the late 1970s, digital computers matured enough for use in SAR image formation processing. A now-declassified paper given at the 25th Annual Tri-Service Radar Symposium (September 1979) outlined an early digital polar format processor [26]. It used a Floating Point Systems AP-120B programmable vector processor hosted by a DEC PDP 11/45 general-purpose minicomputer.

In a digital SAR processor, a fast Fourier transform (FFT) is an essential step. However, the spotlight SAR data is inherently in polar coordinates as Figure 1.4(b) indicates. To perform an efficient FFT, the digital processor must resample or interpolate the polar formatted signal data onto a rectangular grid. We call this step polar-to-rectangular interpolation, or polar interpolation. Polar interpolation remains central to digital polar format processing; Chapter 4 discusses this topic in detail.

SAR image formation using a general-purpose computer occurs at a slow rate. The time required to form an image is often much greater than the data collection time. However, real-time SAR image formation systems, in which the processing keeps pace with the data collection, are common today. Such processors employ high-performance and/or specialized computing elements to achieve the necessary computational rate.

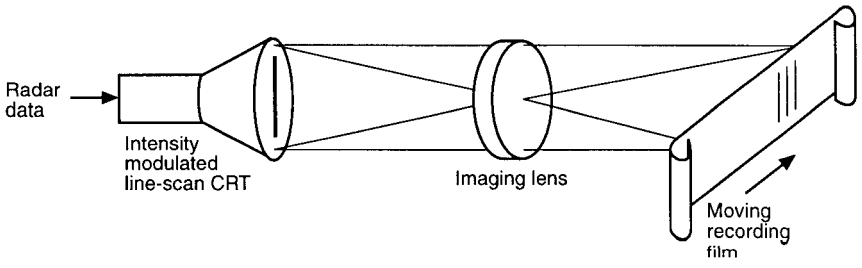


Figure 1.6 A rectangular format film recorder.

1.5 SPOTLIGHT SAR TODAY

Spotlight mode SAR has progressed beyond the experimental phase of the 1960s and testbed stages of development in the 1970s and 1980s; a number of active operational systems now use this mode. The ERIM data collection system (DCS) is an example of a SAR testbed with a fine-resolution spotlight imaging mode and a polar format digital processor [27]. Section 7.1 discusses this system. Another SAR system with a spotlight imaging mode is the advanced detection technology sensor (ADTS) radar at The Lincoln Laboratory [28]. This system includes a fine-resolution mode with a full polarimetric capability; it transmits and receives both horizontal and vertical polarizations.

An example of a fielded reconnaissance system employing a fine-resolution spotlight imaging mode and digital image formation is the Hughes ASARS-2 that flies aboard the U.S. TR1 aircraft [29]. ASARS stands for advanced synthetic aperture radar system.

A current development thrust is the deployment of SAR systems in either stripmap or spotlight mode in unmanned aerial vehicle (UAV) platforms. Such a deployment requires a lightweight sensor and desires a real-time processor [30]. Another active area is low-frequency SAR for foliage and ground penetration [31, 32]. A low-frequency SAR system utilizes signals down to a few hundred megahertz to improve penetration capability; its design typically involves a high percent bandwidth waveform to achieve adequate range resolution. Additional thrusts include interferometric SAR (Section 9.3) to obtain three-dimensional scene information, automatic target recognition (ATR) [33, 34] to ease the information overload on the users of SAR imagery, and sensor fusion [35] to combine information from a variety of sensors to assist image exploitation.

REFERENCES

[1] Wiley, C.A., "Synthetic Aperture Radars," *IEEE Transactions on Aerospace and Electronic Systems*, Vol. AES-21, No. 3, May 1985, pp. 440-443.

[2] Sherwin, C.W., J.P. Ruina, and R.D. Rawcliffe, "Some Early Developments in Synthetic Aperture Radar Systems," *IRE Transactions on Military Electronics*, Vol. MIL-6, No. 2, April 1962, pp. 111-115.

[3] Mensa, D.L., "Radar Imaging," *International Journal of Imaging Systems and Technology*, Vol. 4, 1992, pp. 148-163.

[4] Munson, D.C., "A Signal Processing View of Strip-Mapping Synthetic Aperture Radar," *IEEE Transactions on Acoustics, Speech, and Signal Processing*, Vol. 37, No. 12, December 1989, pp. 2131-2147.

[5] Tomiyasu, K., "Tutorial Review of Synthetic Aperture Radar (SAR) with Applications to Imaging of the Ocean Surface," *Proceedings of the IEEE*, Vol. 66, No. 5, May 1978, pp. 563-583.

[6] Raney, R.K., "Processing Synthetic Aperture Radar Data," *International Journal of Remote Sensing*, Vol. 3, No. 3, 1982, pp. 243-257.

[7] Curlander, J.C., and R.N. McDonough, *Synthetic Aperture Radar: Systems and Processing*, New York, Wiley, 1991.

[8] Hovanessian, S.A., *Introduction to Synthetic Array and Imaging Radars*, Norwood, MA, Artech House, 1980.

[9] Mensa, D.L., *High Resolution Radar Imaging*, Norwood, MA, Artech House, 1981.

[10] Wehner, D.R., *High Resolution Radar*, Norwood, MA, Artech House, 1987.

[11] Cutrona, L.J., W.E. Vivian, E.N. Leith, and G.O. Hall, "A High-Resolution Radar Combat-Surveillance System," *IRE Transactions on Military Electronics*, Vol. MIL-5, No. 2, April 1961, pp. 127-131.

[12] Brown, W.M., "Synthetic Aperture Radar," *IEEE Transactions on Aerospace and Electronic Systems*, Vol. AES-3, No. 2, March 1967, pp. 217-229.

[13] Brown, W.M., and L.J. Porcello, "An Introduction to Synthetic Aperture Radar," *IEEE Spectrum*, September 1969, pp. 52-62.

[14] Cutrona, L.J., E.N. Leith, L.J Porcello, and W.E. Vivian, "On the Application of Coherent Optical Processing Techniques to Synthetic Aperture Radar," *Proceedings of the IEEE*, Vol. 5, No. 8, August 1966, pp. 1026-1032.

[15] Kozma, A., E.N. Leith, and N.G. Massey, "Tilted-Plane Optical Processor," *Applied Optics*, Vol. 11, No. 8, August 1972, pp. 1766-1777.

[16] Kirk, J.C., Jr., "Discussion of Digital Processing in Synthetic Aperture Radar," *IEEE Transactions on Aerospace and Electronic Systems*, Vol. AES-11, No. 3, May 1975, pp. 326-337.

[17] Ausherman, D.A., "SAR Digital Image-Formation Processing," *Proceedings of the SPIE*, Vol. 528, Digital Image Processing, Los Angeles, CA, January 1985.

[18] Barber, B.C., "Theory of Digital Imaging from Orbital Synthetic Aperture Radar," *International Journal of Remote Sensing*, Vol. 6, No. 7, 1985, pp. 1009-1057.

[19] Ausherman, D.A., "Digital versus Optical Techniques in SAR Data Processing," *Optical Engineering*, Vol. 19, No. 2, March/April 1980, pp. 157-167.

[20] Munson, D.C., J. D. O'Brien, and W. K. Jenkins, "A Tomographic Formulation of Spotlight-Mode Synthetic Aperture Radar," *Proceedings of the IEEE*, Vol. 71, No. 8, August 1983, pp. 917-925.

[21] Ausherman, D.A., A. Kozma, J.L. Walker, H.M. Jones, and E.C. Poggio, "Developments in Radar Imaging," *IEEE Transactions on Aerospace and Electronic Systems*, Vol. AES-20, No. 4, July 1984, pp. 363-400.

[22] Brown, W.M., and R.J. Fredericks, "Range-Doppler Imaging with Motion through Resolution Cells," *IEEE Transactions on Aerospace and Electronic Systems*, Vol. AES-5, No. 1, January 1969, pp. 98-102.

[23] Walker, J.L., "Range-Doppler Imaging of Rotating Objects," PhD dissertation, University of Michigan, 1974.

[24] Walker, J.L, "Range-Doppler Imaging of Rotating Objects," *IEEE Transactions on Aerospace and Electronic Systems*, Vol. AES-16, No. 1, January 1980, pp. 23-52.

[25] United States Patent No. 4,191,957, J.L. Walker and W.G. Carrara, "Method of Processing Radar Data from a Rotating Scene Using a Polar Recording Format," 4 March 1980.

[26] Ausherman, D.A., and R.S. Powers, "Digital Image-Formation Processing of Spotlight SAR Data," *25th Annual Tri-Service Radar Symposium*, September 1979.

[27] DiMango, M., W. Hanna, and L. Andersen, "The Data Collection System (DCS) Airborne Platform," *First International Airborne Remote Sensing Conference and Exhibition*, Strasbourg, France, September 1994.

[28] Novak, L.M., M.C. Burl, R.D. Chaney, and G.J. Owirka, "Optimal Processing of Polarimetric Synthetic-Aperture Radar Imagery," *The Lincoln Laboratory Journal*, MIT, Vol. 3, No. 2, 1990, pp. 273-290.

[29] Blake, B., Editor, *Jane's Radar and Electronic Warfare Systems*, Fifth Edition, Coulsdon, Surrey, England, 1993-1994, p. 252.

[30] "Tier 2 UAV Revealed," *Aviation Week and Space Technology*, 7 February 1994, p. 23.

[31] Sheen, D.R., T.B. Lewis, S.C. Wei, and D. Kletzli, Jr., "Imaging of Buried and Foliage-Obscured Objects with an Ultrawide Bandwidth Polarimetric SAR," *Proceedings of the SPIE*, Vol. 1942, Orlando, FL, 1992, pp. 12-20.

[32] Gustavsson, A., P.O. Frölind, H. Hellsten, T. Jonsson, B. Larsson, and G. Stenström, "The Airborne VHF SAR System CARABAS," *IGARSS '93*, Tokyo, Japan, 1993, pp. 558-562.

[33] Sherman, J., C. Swonger, L. Clark, and M. LaHart, "Automated Target Recognition Systems" in *The Infrared and Electro-Optical Systems Handbook: Volume 8, Emerging Systems Technologies*, Robinson, S., J. Accetta, and D. Shumaker, editors, Bellingham, Washington, The International Society for Optical Engineering (SPIE), 1993, pp. 345-402.

[34] Dudgeon, D.E., and R.T. Lacoss, "An Overview of Automatic Target Recognition," *The Lincoln Laboratory Journal*, Vol. 6, No. 1, Spring 1993, pp. 3-10.

[35] Waltz, E.L., and J. Llinas, *Multisensor Data Fusion*, Norwood, MA, Artech House, 1990.

Chapter 2
Synthetic Aperture Radar Fundamentals

Chapter 2 reviews SAR system concepts and develops the basic equations describing spotlight mode SAR data. Much of this material applies to all SAR modes, although the modes do vary in choice of reference function, application of motion compensation, and use of specific image formation algorithms. The similarity among the three SAR modes becomes evident in Section 9.1, where we present a procedure to process data collected in stripmap or scan mode with a spotlight mode algorithm. However, the primary subject of this book is digital processing of spotlight mode SAR data.

This chapter reviews the basic building blocks of a SAR system, SAR imaging concepts, and the basis for range and azimuth resolution. It discusses critical SAR coherence requirements with emphasis on motion compensation, models SAR image formation analytically, and illustrates an example SAR system design.

This chapter develops SAR image formation from the perspective of the *signal phase equation.* The signal phase equation is an analytical model of the radar signal. It begins with generation of the initial waveform and continues with the signal's progression through the radar hardware and processor software. This equation provides a functional guide to the understanding, design, and validation of a SAR system. It provides concrete direction on requirements for and development of an appropriate image formation algorithm. The signal phase equation perspective progresses through the image formation processor to an output image as discussed in Chapter 3.

In a basic SAR system, the platform carrying the sensor provides the motion between the radar and the scene being imaged. In inverse synthetic aperture radar (ISAR) imaging, target movement provides this motion. In practice, ISAR often involves sensor motion as well as target motion. The material in this chapter encompasses both SAR and ISAR.

2.1 SAR SYSTEM OVERVIEW

A top-level view of a basic SAR system includes five blocks (Figure 2.1). The *SAR sensor* and the *motion sensor* constitute the real-time data collection resources. These resources provide radar signal data (backscattered from the illuminated scene) and auxiliary data describing SAR platform motion. The *image formation processor* (IFP) utilizes these two data streams to deliver SAR imagery to the *image processor* and subsequently to the *image exploitation segment.* The latter three blocks may also operate in real time.

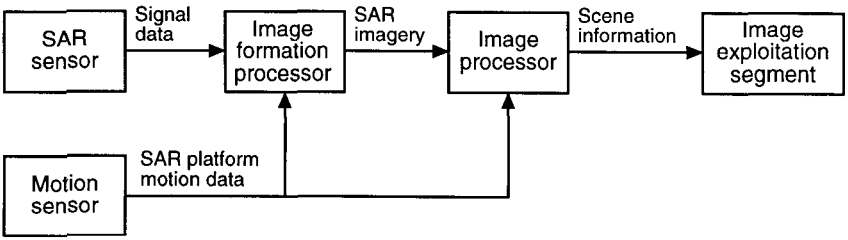


Figure 2.1 SAR system overview.

Section 2.1.1 discusses system operation and explains the need for each subsystem block in Figure 2.1. Subsequent sections summarize the function of each subsystem and indicate the scope of coverage of each within this book. The following discussion applies equally to SAR and ISAR systems.

2.1.1 System Operation

A SAR generates and transmits a series of coded pulses at regular time intervals as the radar platform moves along its path. The ideal path is a straight line traversed at constant velocity. In a practical environment, variations from this ideal are inevitable. Measured changes in along-track velocity present no real difficulty. Small vertical and horizontal displacements from this ideal trajectory are acceptable if measured accurately. Larger, deliberate variations from the ideal path, such as those by a SAR system engaging in a high acceleration "pop-up" maneuver to avoid detection, present a challenge to image formation; this challenge is a nonplanar motion effect (Section 3.3.4). To accumulate the signals necessary to generate one fine-resolution image, the SAR sensor transmits pulses to interrogate the scene over an angular interval inversely proportional to the required azimuth resolution. This interval is the *coherent aperture time* in the time domain, the *synthetic aperture length* in the spatial domain, or the *azimuth processing aperture* in the IFP. The illuminated scene reflects a fraction of the energy from each transmitted pulse back toward the radar sensor. The SAR receives and accepts the return signals within a selected time delay interval after pulse transmission; this interval is the *range gate*. The range gate corresponds to the range interval being imaged.

In SAR imaging, the creation of a fine-resolution image from a sequence of received signals requires the following steps:

1. Generate, transmit, and receive a wide bandwidth coded signal with a deterministic phase relationship from pulse to pulse;
2. Measure and compensate for the relative translational and rotational motions between the radar antenna phase center (APC) and the scene or target;
3. Format the data based on radar system parameters and data collection geometry;
4. Compress the data in range and azimuth to achieve the desired resolution.

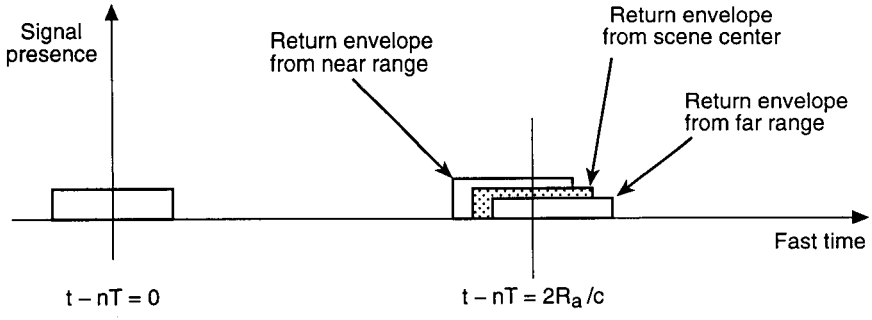
The first two steps are necessary to maintain phase coherence from pulse to pulse during the required coherent aperture time (Section 2.5). Signal processing using the polar format algorithm is generally the norm for imaging scenes of moderate size and fine resolution at X-band and K-bands. As the scene size increases and resolution improves, algorithms other than polar format become interesting, particularly at lower radar frequencies. Lower frequencies require a larger azimuth angular interval and a higher percent bandwidth (that is, ratio of transmitted bandwidth to maximum transmitted frequency) to maintain fine resolution. With proper execution of the first three steps, a direct, two-dimensional fast Fourier transform (FFT) of the signal history data accomplishes data compression.

The SAR receiver typically decodes the signals in range and removes the carrier frequency in the process of initial onboard motion compensation. It digitizes the signals and stores the digital data for later ground processing. Data linking of the signal data to the ground or real-time onboard processing are also possibilities. In the stripmap mode, the angular interval over which the sensor collects data from each scatterer in the scene cannot exceed the azimuth beamwidth of the antenna. During a spotlight mode data collection, the angular interval over which the sensor collects data from each scatterer may greatly exceed the azimuth beamwidth of the antenna. This possibility exists because a signal derived from the motion sensor steers the antenna beam to continuously illuminate the fixed scene being imaged. In this case, the data collection time may include an angular interval many times larger than the azimuth beamwidth.

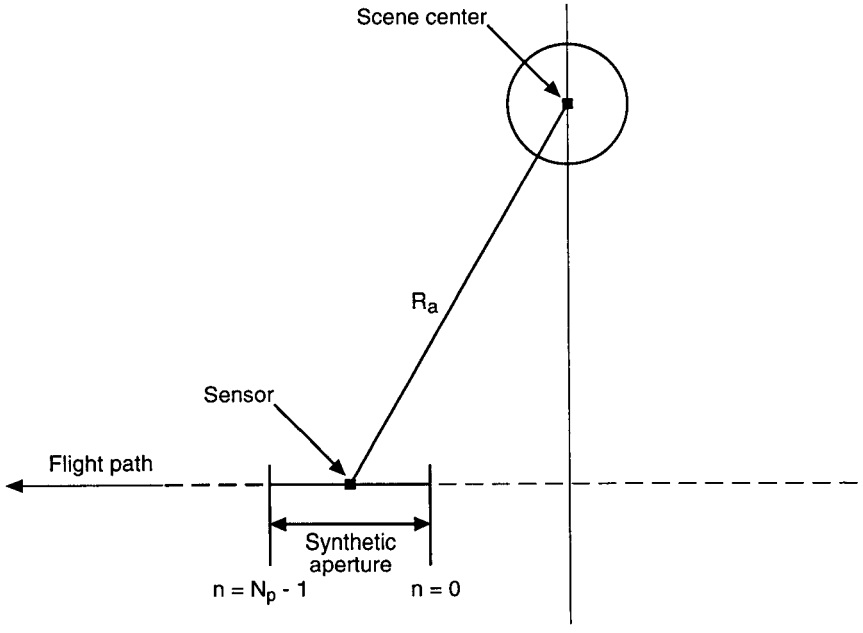
The time interval T between successively transmitted pulses is the *pulse repetition interval* or *interpulse time*. SAR operation often maintains a constant interpulse time leading to a constant *pulse repetition frequency* (PRF); the PRF is the reciprocal of T. Time within a signal received from a specific transmitted pulse and referenced to the time of pulse generation is *fast time* designated $\hat{t} = t - nT$ using the pulse number n as a counter. Pulse number varies from $n = 0$ for the first pulse in the coherent aperture time to $n = N_p - 1$ for the last pulse. Each pulse corresponds to a unique SAR sensor along-track position which, in turn, relates to azimuth aspect viewing angle. The two-dimensional coordinates (Figure 2.2) of the SAR data collection are fast time and antenna location. In Figure 2.2, R_a is the distance between the radar and scene center. Sometimes it is appropriate to use pulse number or azimuth angle as the second coordinate. Often, this second coordinate is imprecisely referred to as *slow time*. This two dimensionality of basically a one-dimensional temporal signal consisting of a sequence of N_p pulses in time leads to the need to distinguish among various categories of motion in SAR system activity. This area involves motion between and during SAR pulse transmissions (Section 2.5.3.5).

2.1.2 SAR Sensor

The term *SAR sensor* encompasses all electronics required to generate, transmit, and receive SAR signals. It includes the radar antenna and a data link, recording device, or physical interface to convey collected signals to the IFP. Typically, an airborne platform carries the SAR sensor, although an unmanned aerial vehicle (UAV) or a space vehicle is an acceptable platform as well. An ISAR sensor may be stationary or moving while it images a moving target.



(a)



(b)

Figure 2.2 SAR signal coordinates: (**a**) Fast time ($t - nT$); (**b**) Azimuth antenna location (pulse number).

Figure 2.3 depicts the basic components in a SAR sensor which generate, collect, and begin to process the signals into imagery. A numerical key in this figure identifies intermediate signals at various stages in the process and relates these signals to the analysis beginning in Section 2.6. Table 2.1 displays this key and references relevant equations in Section 2.6. A practical system also incorporates frequency conversion and both low-pass and bandpass filtering stages to generate and maintain the desired signals. A stable reference clock provides the timing and coherent phase reference for all signals in the radar.

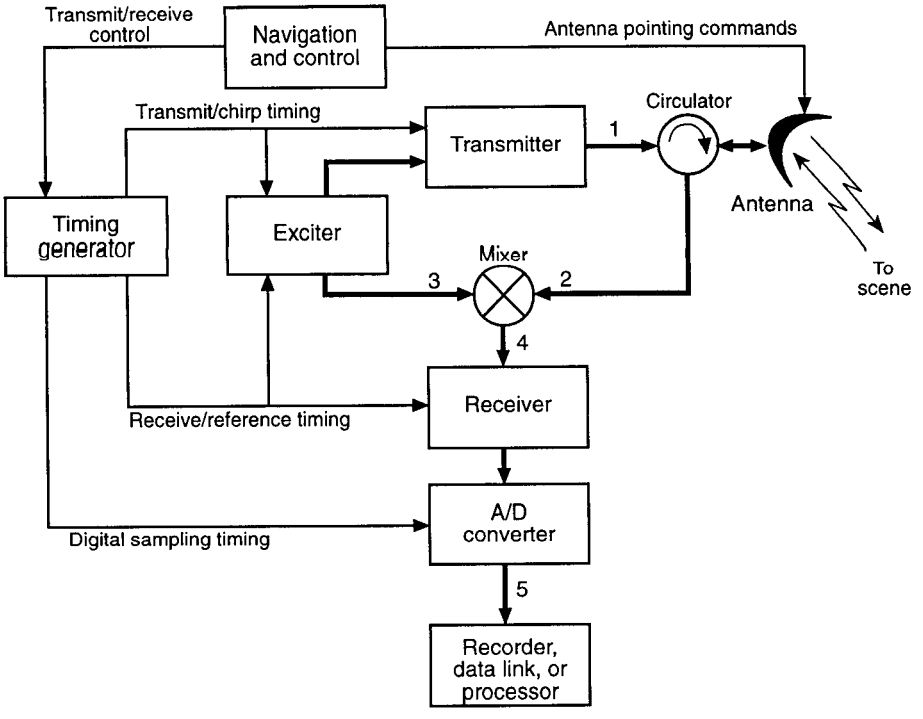


Figure 2.3 SAR sensor.

Table 2.1
Numerical Key for Use with Figure 2.3

Point Number	*Name*	*Symbol*	*Equation*
1	Transmitted signal	$s_x(n, t)$	(2.47)
2	Received signal	$s_r(n, t)$	(2.49)
3	Reference signal	$s_{ref}(n, t)$	(2.55)
4	Signal at IF	$s_{if}(n, \hat{t})$	(2.56)
5	Digitized signal	$s_d(n, k)$	(2.63)

The transmitter in a modern SAR system generates a wide-bandwidth signal via digital-to-analog (D/A) conversion of a sampled waveform stored in memory [1]. The transmitter bandpass filters this digitally synthesized signal, mixes the resulting analog signal up to radio frequency (RF), amplifies it, and sends it to the transmit antenna.

A receiver accepts the backscattered signal within a selected range gate from the receive antenna, provides low noise RF amplification, and mixes the amplified RF signal with a digitally generated and filtered reference signal; this reference signal removes the RF carrier and, if desirable, the transmit signal modulation. Following video amplification, an analog-to-digital (A/D) converter produces the digitized signal for a data storage medium. A presummer/buffer may follow the A/D converter to reduce data storage requirements or aid data transmission. A presummer reduces the azimuth bandwidth and downsamples the data in azimuth using a digital, low-pass filter. Presumming is feasible only if the PRF is higher than necessary to adequately sample the data in azimuth. A speed buffer is useful when it is necessary to slow down the real-time (A/D) data rate to record or transmit the data. It operates by briefly storing the samples that correspond to a single presummed pulse; it reads out these samples at a slower rate, but before it receives data from the next presummed pulse. By stretching out the pulses in time, the speed buffer effectively reduces instantaneous data rate at the cost of increasing duty cycle following the buffer. Buffering does not reduce the number of samples.

The sampling rate must satisfy the Nyquist criterion in both range and azimuth. In range, the A/D sampling rate must exceed the signal bandwidth when using I (in-phase) and Q (quadrature) channels. In azimuth, the PRF is the sampling rate. Without dechirp in azimuth, the PRF must exceed the Doppler bandwidth corresponding to somewhat more than the antenna mainlobe width (Section 2.4.5). When the sampling rate in either dimension exceeds Nyquist, downsampling can reduce the size of the data arrays and the subsequent processing load.

The PRF is a factor also in range and azimuth ambiguities. Azimuth ambiguities occur when the radar PRF does not adequately sample the Doppler frequency of returned signals; the problem signals typically originate from scatterers illuminated by the edges of the mainlobe or by the sidelobes of the azimuth antenna pattern. Range ambiguities occur when signals originating from illumination by a previous pulse reach the receiver during a range gate associated with the current pulse. An antenna pattern with low sidelobes is the primary defense to limit energy from range and azimuth PRF ambiguous regions [2, 3].

While X-band is a popular choice for the SAR carrier frequency, VHF (400 MHz) through K_a-band (35 GHz) SAR imaging systems are increasingly common. Many diverse considerations influence frequency selection. These factors include resolution, power, and coherence requirements; propagation factors including weather and ground or foliage penetration; target signature effects; and stealth or low probability of intercept (LPI) considerations.

The radar sensor in Figure 2.3 utilizes the same physical antenna to both transmit and receive signals. A ferrite multi-port circulator directs the outgoing signal to the antenna and directs the returned signal to the receiver [4]. This configuration is a *monostatic* SAR. In contrast, a *bistatic* system has separately located transmit and receive antennas, typically mounted on two different aircraft [5, 6]. Monostatic SAR is the principal configuration for most operational systems today; it is the primary subject of this book.

2.1.3 Motion Sensor

Returning to Figure 2.1, a motion sensor is a vital subsystem in most high-performance SAR imaging systems. The motion sensor provides data to estimate both short-term and long-term changes in the position of the SAR antenna. Short-term refers to cyclical motions with a period less than a synthetic aperture time, and long-term refers to motions with a period greater than the aperture time. A motion sensor is unnecessary in a satellite-based SAR system because of the satellite's deterministic motion and low vibration environment.

A modern SAR system accomplishes precise measurement of APC motion using a motion sensing system that consists of an inertial measurement unit (IMU) and a global positioning system (GPS) navigator. The inertial navigation system (INS) is present primarily for aircraft navigation, although either the INS or the IMU may provide auxiliary radar functions such as aligning the flight pass to the desired line, setting the range gate, and pointing the radar antenna. Figure 2.4 shows an example of a sensor combination that utilizes a cockpit-mounted INS for aircraft navigation with an IMU located above a steerable antenna, together with a GPS receiver for APC motion measurement. Generally, the APC position estimate is the result of calculating the vectors from the GPS antenna to the IMU and from the IMU to the APC. The IMU, with GPS updates, provides measurements of low-frequency (long-term) components of motion. The IMU responds to and provides measurements of high-frequency (short-term) components of motion. The IMU also provides dynamic attitude (angular) information.

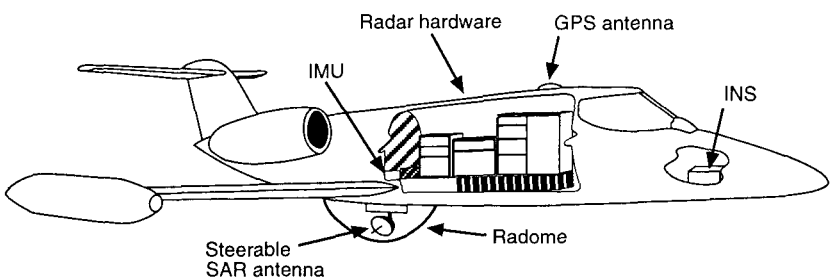


Figure 2.4 Motion measurement sensor layout.

The SAR uses motion sensor outputs in real time to point the antenna beam, to adjust the radar range gate, and to specify the reference signal in the receiver. The use of this reference signal removes certain effects of nonideal motions from collected SAR signal data. The IFP utilizes these motion sensor outputs to calculate the refined antenna position estimates needed to remove the residual effects of nonideal motions. These motion compensation procedures are critically important to successful SAR imaging (Section 2.5). Chapter 5 presents requirements on motion measurement accuracy and the effects of measurement inaccuracy on image quality.

2.1.4 Image Formation Processor

The term *image formation processor* (IFP) encompasses the hardware and software elements which perform the data formatting and processing operations necessary to produce an image from SAR signal and motion data. These operations include:

- Auxiliary data processing;
- Compensation for nonideal waveform generator and propagation effects;
- Azimuth filtering (to limit azimuth scene size) and presumming;
- Range deskew;
- Motion compensation operations;
- Range filtering (to limit range scene size);
- Signal interpolation and decimation (data formatting);
- Aperture weighting for image sidelobe control;
- Two-dimensional Fourier transform (compression);
- Autofocus;
- Amplitude correction and radiometric calibration;
- Geometric distortion correction (interpolation).

Auxiliary data processing involves conversion of motion sensor data to useful SAR signal correction parameters. A number of IFP operations involve small pulse-to-pulse phase and frequency adjustments to refine the motion compensation function and to compensate for other deterministic effects. Other operations involve filtering to downsample or presum the data in azimuth and to interpolate or decimate the data in both dimensions; these steps reduce the subsequent processing load and perform necessary data formatting. In some situations, it may be desirable to upsample the data. Final operations involve aperture weighting and a two-dimensional Fourier transform with optional autofocus and distortion corrections to recover a two-dimensional image of the radar reflectivity of the illuminated scene. Typically, the processor performs autofocus in azimuth in conjunction with the azimuth Fourier transform.

The digital signal processing algorithms which achieve these operations are the emphasis of this book. Chapter 3 includes an extensive discussion of the need for these operations while Chapter 4 presents procedures for digital implementation.

2.1.5 Image Processor

The term *image processor* encompasses image enhancement, feature extraction, registration with other SAR images or with other sensor data (sensor fusion), automatic target detection (ATD), and automatic target recognition (ATR). Image processing may also include a variety of multichannel processing operations in SAR systems having multiple transmit/receive configurations. Examples of multichannel processing are terrain height extraction from a dual-channel interferometric SAR system (Section 9.3), moving target detection using multiple along-track antennas, and image comparison using images with various configurations of transmit/receive polarization.

Certain image processing applications, such as the precise registration of a SAR image to earth coordinates, require knowledge of absolute sensor position during data collection. Hence, geodetic position and motion history data, as well as imagery, may be an important input to the image processor.

While this book emphasizes algorithms for image formation processing, it does discuss several interesting image processing applications including interferometric SAR and vibrating target detection in Chapter 9 and image enhancement via sidelobe reduction in Appendix D. Both ATR [7, 8] and sensor fusion [9] are active areas of development in the SAR community today.

2.1.6 Image Exploitation Segment

The *image exploitation segment* involves the extraction and use of information about the imaged scene to address a diversity of SAR applications. Image exploitation naturally includes the end user of the SAR system output products. Missions may include terrain mapping and imaging of targets; they involve military, commercial, and civilian users. Applications include intelligence gathering, battlefield reconnaissance, weapons guidance, vehicle identification, topographic mapping, oil spill monitoring, sea ice characterization and tracking, agricultural classification and assessment, land use monitoring, mapmaking, and planetary investigations.

Scene information for exploitation may be as complicated as enhanced multichannel imagery presented to a human interpreter; or it may be as simple as a list of prioritized coordinates for a precision strike application. The division between the image processor and the exploitation segment is not always clear. One common division is the boundary between computer-automated processing of digital imagery and some action that the user takes based on scene information resulting from such processing.

2.2 IMAGING CONSIDERATIONS

A processor requires three kinds of information to construct an image from sensor signals. First, it needs *positioning* information to locate the source of the returns in two (or three) dimensions. Second, it needs spatial or angular *resolution* to differentiate among returns from separate scatterers or scene areas. Finally, it needs the *intensity* of the signal associated with each scatterer or scene area in the target field. The signal intensity characterizes a quantity which varies over the scene to provide a spatial image. In the case of radar, this quantity is either the radar cross-section of individual scatterers or the radar backscatter coefficient of distributed scatterers.

Simple optical imaging systems use angle/angle discrimination to position received signals in the field of view (independent of distance from the sensor). In Figure 2.5, the angles α_1 and α_2 are representative of two angles that an optical imaging system could use to position the scatterer P_1. The optical imaging system assigns all scatterers on the line L_1 to the same position in its image.

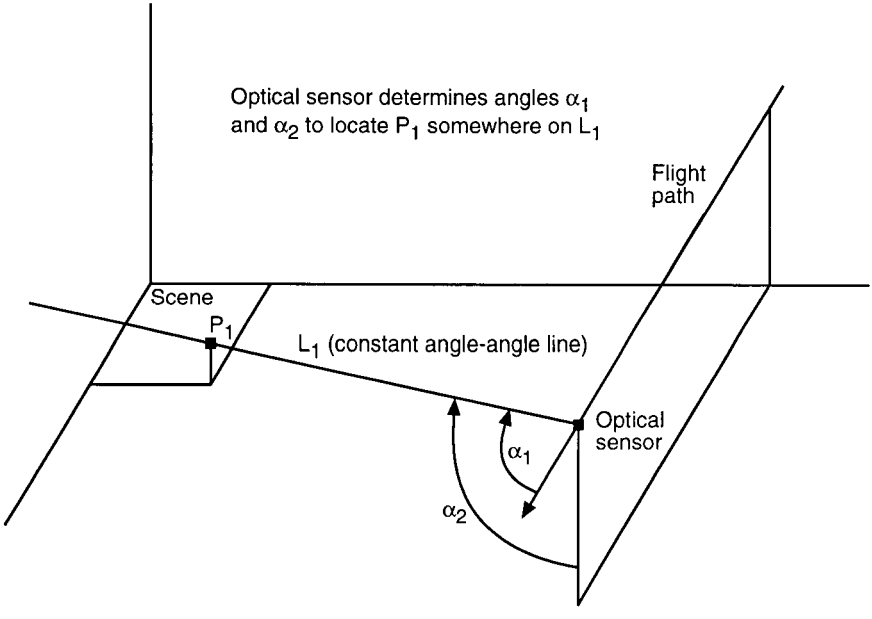


Figure 2.5 Optical angle-angle positioning of scatterer P_1.

A SAR system, on the other hand, measures range (distance) from the APC and angle from the antenna velocity vector $\boldsymbol{V_a}$ in order to position received signals. This angle is the *Doppler cone angle*. Figure 2.6 illustrates target positioning by a SAR system. The SAR sensor determines range R_t to scatterer P_1 by measuring the time delay between transmission and reception of the signal which P_1 reflects back to the radar. The SAR determines Doppler cone angle α_d by observing the change in range over the observation interval. It is common to refer to the time rate of change in range as *range rate*. A specific scatterer is at a 90-deg cone angle when its range rate is zero. The SAR system obtains two-dimensional positioning and resolution in distance (range) and cone angle. The radar positions all returns from scatterers on the circle C_1 with center at P_2 and radius $R_t \sin(\alpha_d)$ in the same location in the conventional SAR image. Point P_2 is the intersection with the flight path of a plane through P_1 with normal parallel to the flight path. Circle C_1 is the intersection of a constant-range sphere of radius R_t centered at the APC and a constant Doppler conical surface with apex at the APC and half cone angle α_d relative to the APC velocity vector. This circle is an iso-range-Doppler circle. It lies in a plane normal to the antenna velocity vector.

This positioning of returns received by a pulse-Doppler radar corresponds to a two-dimensional projection of the scene radar cross-section (RCS) onto a range/cone angle grid. The magnitude of the resulting image pixel is the coherent (complex) summation of contributions from all returns originating from scatterers on the corresponding iso-range-Doppler circle.

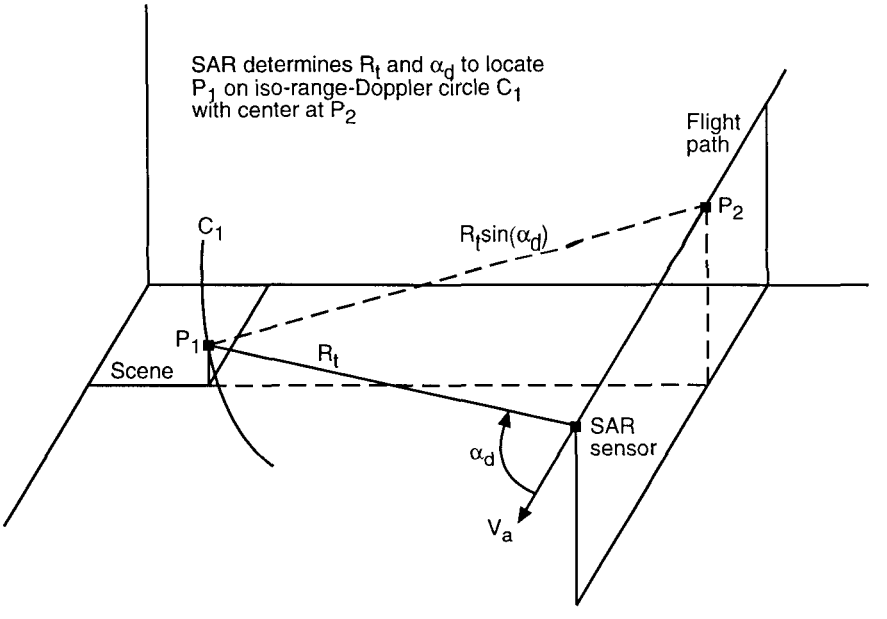


Figure 2.6 SAR range-Doppler positioning of scatterer P_1.

The instantaneous range rate $\dot{R}_t$ is a measure of the angle of the radar return signal with respect to the antenna velocity vector. Range rate is the component of the sensor velocity vector away from the scatterer. It is equal to the sensor velocity V_a times the negative of the cosine of the Doppler cone angle α_d in the form $\dot{R}_t = -V_a \cos(\alpha_d)$. Figure 2.7 suggests this result whether the range between the sensor and the scene is decreasing (closing) or increasing (opening). Radar systems in general, and SAR systems in particular, simply measure range to a target from a large number of different antenna locations. That is, the only quantity a radar really measures directly is range itself as a function of time; processing of these measurements provides target position in angle relative to the sensor velocity vector and target range relative to the APC. The SAR does not directly measure the rate of change of range, the Doppler cone angle, or any other angle.

Figure 2.8(a) shows a SAR sensor flying at a constant velocity parallel to a nominal ground plane *XY*. Spheres of constant range intersect the ground plane as circles centered on the SAR nadir point as Figure 2.8(b) suggests. For equal range intervals corresponding to the system range resolution, the circles are widely spaced near the nadir point and approach a spacing equal to range resolution at far range. Cones of constant Doppler cone angle intersect this plane as hyperbolas as Figure 2.8(c) suggests. Iso-Doppler lines at equal range rate intervals are most closely spaced near the *Y* axis, itself an iso-Doppler line. Figure 2.8(d) shows an overlay of these two sets of contours. Near the *Y* axis, the

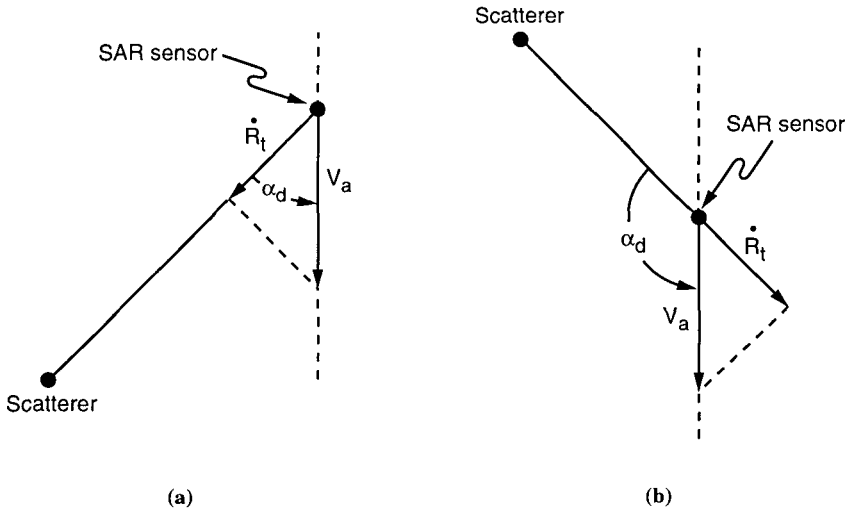


Figure 2.7 Range rate $\dot{R}_t$ between scatterer and antenna: **(a)** Range closing; **(b)** Range opening.

contours form a nominally orthogonal grid, indicative of the ability of range-Doppler discrimination to separate ground scatterer returns by position on this two-dimensional grid. This situation represents *broadside* imaging (at a 90-deg Doppler cone angle) with the antenna pointed orthogonally to the flight path. Near the sensor nadir line (parallel to the X axis), the two sets of contour lines are nominally parallel, suggesting the inability of range-Doppler discrimination to position ground scatterer returns in two dimensions. This situation represents a *forward-look* SAR imaging geometry; it is of interest for an ability to position scatterer returns in height (Section 9.2).

Although the emphasis here is two-dimensional imaging, three-dimensional SAR imaging is also possible. The mechanism for positioning and resolving scatterers in the third dimension is an interferometric technique that uses a second antenna during a data collection pass (or a second collection pass on a similar nearby flight path with the single antenna); the relative phase between the two resulting complex images yields information in the third dimension (Section 9.3). This third dimension, which the interferometer provides, is the angle of the return relative to the baseline vector joining the two antenna phase centers; it is available via radar interferometric techniques analogous to optical interferometry. Figure 2.9 illustrates this discrimination in the third dimension. The interferometric SAR locates the scatterer P_1 at the intersection of the two iso-range-Doppler circles C_1 and C_2. While a single antenna is adequate to determine the cone angle α_d in this diagram, the second antenna must also be present to determine the vertical angle α_2 identified in this figure. Section 9.3 discusses an interferometric SAR system and presents fine-resolution imagery examples.

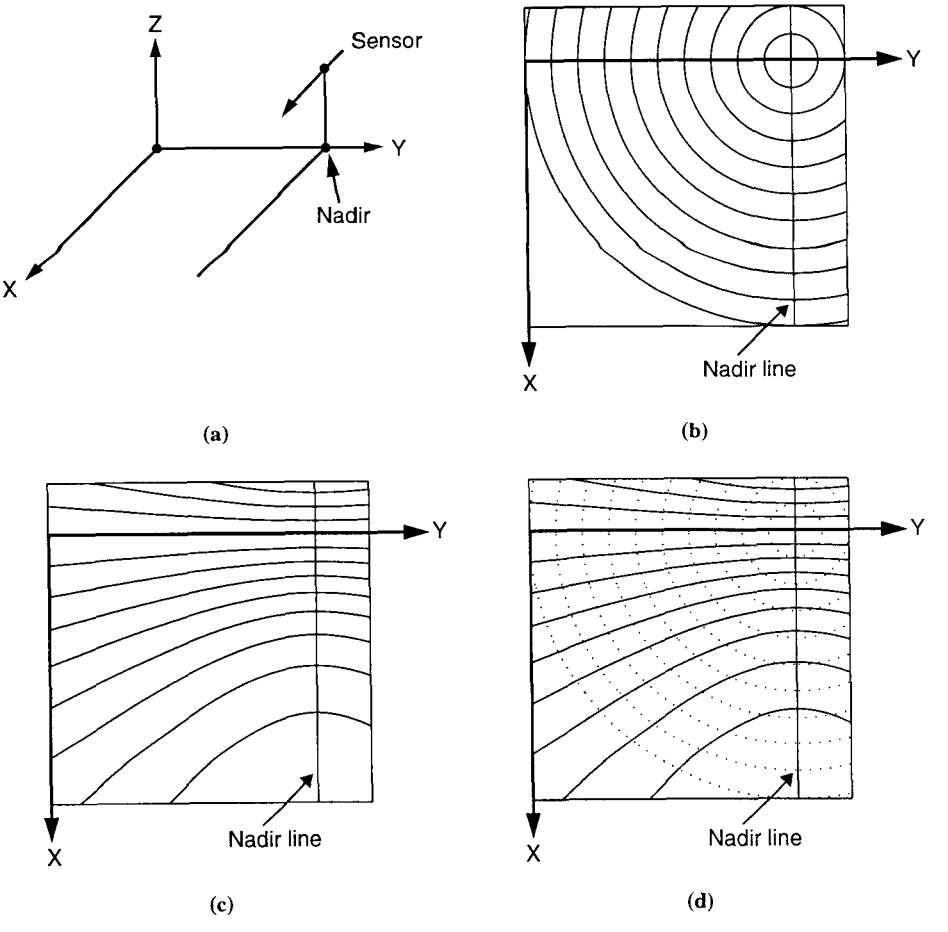


Figure 2.8 Range and Doppler cone angle contours in the ground plane: **(a)** Collection geometry; **(b)** Circles of constant range in the *XY* plane; **(c)** Hyperbolas of constant Doppler cone angle in the *XY* plane; **(d)** Combination of constant range circles and constant Doppler hyperbolas.

Imaging a rigid scene rotating about a fixed scene center by a stationary radar is analogous to spotlight imaging of a stationary scene by a moving radar sensor. The rotational component of relative motion between the radar APC and the scatterers is similar in the two cases. The analogy considers the fixed radar to be traveling in a circle about the scene, now held stationary. The imaging system positions each target relative to scene center based on the differences in range and Doppler cone angle characteristics between the target's backscattered signal and that of a target at scene center.

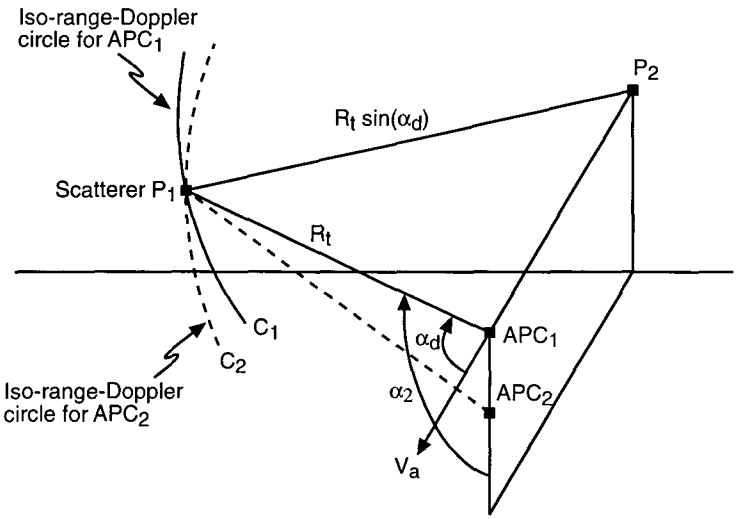


Figure 2.9 Interferometric SAR imaging coordinates.

In each case, image resolution is the precision to which the IFP is able to compute these coordinates. In the range dimension, the transmitted bandwidth of the radar determines the theoretical resolution. In the Doppler cone angle dimension, the center frequency and the angular interval over which the radar observes the scene during the coherent processing aperture determine resolution. That is, the angular interval selected for processing determines the Doppler (azimuth) resolution. Section 2.3 and Section 2.4 discuss and quantify range resolution and azimuth resolution, respectively.

2.3 PULSE COMPRESSION AND RANGE RESOLUTION

A radar system can transmit and receive energy continuously and simultaneously or it can transmit a short burst and wait to receive the reflected echoes before transmitting again. Modern SAR and ISAR systems are pulsed radars. They transmit and receive at a PRF which may be constant or may vary over time. Varying the PRF with changes in sensor velocity allows the system to maintain a constant spatial distance between pulses.

A pulsed radar signal may be a short, single-frequency pulse or a longer waveform with either amplitude or phase modulation. The modulation or coding may be analog with continuous modulation within the pulse. Alternatively, the modulation may consist of discrete steps in phase or frequency at fixed intervals within the pulse. Analog linear frequency modulation (FM) of a constant amplitude pulse is the choice of many SAR systems today. Discrete phase and frequency codes are useful in special situations such as RCS measurement facilities and LPI applications. Phase codes may be binary codes with only 0 and π rad phase levels or more general polyphase codes. Binary codes include Barker codes and pseudo-random phase codes [10].

The following three sections discuss the single-frequency pulse, the analog linear FM waveform, and the stepped-frequency waveform. The stepped-frequency waveform represents a discrete implementation of the analog linear FM waveform.

2.3.1 Short Pulse

The time delay between transmission and reception of a radar pulse indicates the range from the antenna to a scattering center. Thus, the radar system's ability to distinguish small changes in time delay determines its range resolution capability. In the presence of noise, the accuracy to which time delay can be measured is related to the width of the transmitted pulse; the radar system can distinguish the return echoes from two adjacent targets, and thereby resolve them, when the echoes are separated in time delay by the pulse width. That is, range resolution ρ_r is

$$\rho_r = cT_p/2 \tag{2.1}$$

where c is the speed of light and T_p is the pulse length. With a single-frequency waveform, a short pulse means fine range resolution.

2.3.2 Linear FM Waveform

While a shorter pulse improves range resolution, eventually it becomes difficult to maintain a satisfactory average power level; this difficulty arises due to practical limits on peak power. Here, *average power* refers to power averaged over the interpulse time T while *peak power* refers to power averaged over the pulse length T_p. Modern radar and communication systems overcome this difficulty by transmitting long, phase-coded pulses which can be compressed with signal processing operations after reception. The linear FM waveform is the popular choice as an analog phase code for fine-resolution SAR systems; its popularity is due largely to the ease in signal generation and processing. A common name for this waveform is *chirp* because an audio signal of rising (or falling) frequency over time is similar to a bird's chirp. The treatment of SAR throughout this book will assume the use of the linear FM waveform. The attributes and characteristics of linear FM signals are well documented in two early references [11, 12] and later in [10]. The linear FM chirp signal is not unique to SAR applications. Conventional radars may also employ chirp waveforms and pulse compression techniques.

The linear FM waveform exists over a pulse length T_p. Its frequency is a linear function of time, varying at a rate γ referred to as the *chirp rate*. Correspondingly, its phase is a quadratic function of time. The instantaneous frequency is then $f_c + \gamma(t - nT)$ where f_c is the center frequency and $t = nT$ signifies the center of pulse n. The bandwidth B of the pulse is γT_p. From signal theory, a pulse of bandwidth B can be compressed to a time duration of approximately $1/B$. From (2.1), this time duration corresponds to a

spatial resolution in the range dimension of

$$\rho_r = \frac{cK_r}{2B} \tag{2.2}$$

This result includes K_r as an excess bandwidth factor to compensate for the mainlobe broadening introduced by the aperture weighting function (Appendix D) used for sidelobe control and by any low-frequency phase errors present in the signal (Chapter 5). Bandwidths on the order of hundreds of megahertz are practical today, suggesting theoretical range resolutions finer than 1 m. In modern SAR and ISAR imaging systems, range resolutions approaching the theoretical limits are attainable.

The range compression factor is the ratio of the pulse's length before time compression (T_p) to its length after compression ($1/B$). This pulse compression ratio (PCR) is

$$\text{PCR} = T_p B = \gamma T_p^2 \tag{2.3}$$

The PCR is equal to the time-bandwidth product of the transmitted pulse and represents the improvement in resolution that pulse compression offers, assuming K_r in (2.2) is unity. An uncoded pulse has bandwidth $1/T_p$ and therefore a compression ratio of unity. Compression ratios greater than 10^5 are practical today using phase coded pulses such as the linear FM chirp waveform.

An advantage of the linear FM waveform in signal processing is the ability to reduce the analog signal bandwidth when receiving linear FM pulses from scatterers over a small range swath size. This reduction eases the speed requirement for the A/D converter and the size requirement for digital memory. The bandwidth reduction procedure is to mix the returned analog signal with a replica of the transmitted waveform delayed by the two-way time delay from the APC to the center of the range swath. This process is referred to as *range dechirping* or *deramping* of the FM signal. Radars that use this process are *dechirp-on-receive* systems.

Figure 2.10 illustrates the timing relationships among the transmitted linear FM signal, the received signals from the desired scene range extent, and the reference signal which accomplishes the dechirp function. The reference signal coincides with, but extends beyond, the return from scene center. The top part of Figure 2.10 shows the signals as received before range dechirp. The vertical coordinate corresponds to the instantaneous transmit frequency centered at frequency f_c. The transmit signal bandwidth is B over the pulse time T_p. The horizontal coordinate is time, showing the time interval corresponding to transmission of the first pulse ($n = 0$) and the returns from scatterers at near, center, and far ranges. As depicted, the returns over a range extent Δr occupy different time intervals indicating the natural variation in time delay as a function of range.

The lower part of Figure 2.10 shows the signals after the range dechirp operation by the mixer in Figure 2.3. After dechirp, the signal returned by each scatterer has a frequency related to its time delay relative to the dechirp signal. We refer to the bandwidth of the dechirped signal as the intermediate frequency (IF) bandwidth to distinguish it from

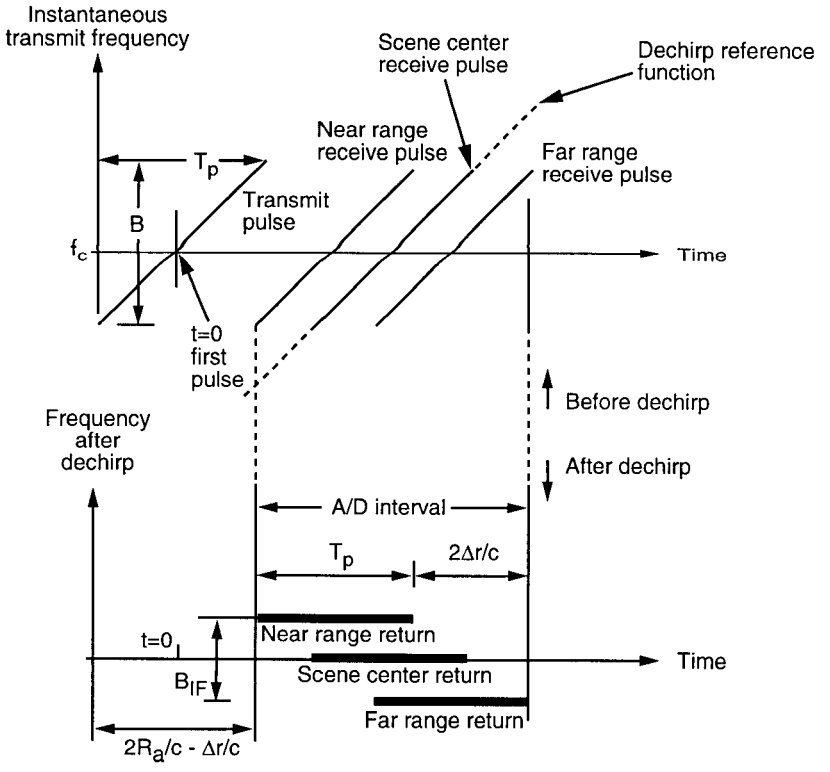


Figure 2.10 Timing relationships and range swath for range dechirp procedure.

the RF bandwidth B of the transmitted signal. The desired range swath size Δr and the chirp rate γ determine the IF bandwidth B_{IF}. In Figure 2.10, the time $2\Delta r/c$ between the end of the returns from near range and those from far range is the two-way time delay associated with the range swath Δr. The frequency of the signal from each scatterer is equal to the chirp rate multiplied by the time delay between it and the reference function. On this basis, the IF bandwidth is equal to the range swath size times the chirp rate. The IF bandwidth becomes

$$B_{IF} = \frac{2\gamma\Delta r}{c} \tag{2.4}$$

for all resolution bins within the range swath, Δr. This bandwidth requires an A/D sampling rate of at least $2B_{IF}$ if sampled in real-valued form and at least B_{IF} if sampled in complex-valued form with quadrature channels. In practice, the A/D rate is increased by 10 to 20 percent to accommodate receiver analog filter effects. The ratio of B_{IF} to B

indicates the reduction in required A/D sample rate possible with range dechirp. Using $B = \gamma T_p$, this ratio becomes

$$\frac{B_{IF}}{B} = \frac{2\Delta r}{cT_p} \tag{2.5}$$

This ratio is generally less than unity in a fine-resolution spotlight imaging mode. In the stripmap mode, the range swath is typically larger while the range resolution is coarser; this situation often makes it unwise to employ dechirp-on-receive since the dechirped bandwidth can exceed that of the transmitted signal.

As Figure 2.10 suggests, sampling is necessary over a time interval T_S given by

$$T_S = T_p + \frac{2\Delta r}{c} \tag{2.6}$$

to accommodate the pulse duration time plus the range swath time interval $T_s = 2\Delta r/c$. The sampling begins at t_b given by

$$t_b = \frac{2R_a}{c} - \frac{\Delta r}{c} - \frac{T_p}{2} \tag{2.7}$$

where R_a is the distance from the APC to scene center. The first term in t_b is the two-way time delay to scene center, the second term accounts for the half of the (two-way) range swath closer than scene center, and the third term reflects the fact that time is referenced to the center of the pulse while the sampling must begin at the start of the pulse.

The situation in Figure 2.10, in which the signal from a near range scatterer occurs earlier in time than the signal from a far range scatterer, is called *range skew.* This condition impacts SAR imagery with an effect commonly denoted as *residual video phase.* Section 3.10 and Appendix C discuss residual video phase, its consequences, and possible compensations.

In this development of the dechirp-on-receive procedure, the returns from near range naturally occur at a higher IF frequency than the returns from far range (Figure 2.10). In practice, a specific receiver implementation is likely to invert the IF spectrum so that near-range returns appear at lower IF frequency than far-range returns.

The development of (2.6) and (2.7) represents one strategy in selecting the interval to sample the received signal. A second approach disregards the range skew and samples the signal only over the time interval associated with the return from scene center.

2.3.3 Stepped-Frequency Waveform

The stepped-frequency waveform is a discrete implementation of the linear FM waveform [13-15]. Rather than transmit a wide bandwidth signal as a single pulse at each sensor location, the stepped-frequency system constructs its wide bandwidth signal at each sensor location over a group of pulses. On the first pulse within the group, the system transmits a narrow-band signal, sets the range gate, receives the return, and digitizes it into a single

complex value. The transmitter increases, or steps, the transmit frequency by a constant increment on each subsequent pulse. After stepping the transmit frequency over the required bandwidth, the transmitter resets to the initial frequency and repeats the procedure from the next sensor position. The group of received pulses from each sensor position corresponds to the returns from a single FM waveform pulse; each sensor position corresponds to a transmitted pulse in a SAR system on an airborne platform. In practice, it is acceptable for the sensor position to be changing continuously within each group of pulses as well as between groups. As with any SAR waveform, sensor position relative to the scene varies either by platform rotation in an ISAR facility illuminating a rotating platform or by actual sensor motion in the case of a SAR system on a moving platform.

Ground-based ISAR systems use this waveform widely because of the simplicity of its design and implementation. A prime example here is the radar target scatter site (RAT SCAT) radar cross-section facility [16, 17].

2.4 SYNTHETIC APERTURE CONCEPT AND AZIMUTH RESOLUTION

The signal processing technique that SAR employs to achieve fine azimuth resolution is the feature that distinguishes SAR from other imaging radars [18]. This technique is similar to the signal processing in the range channel which compresses a long, linear FM-coded pulse to yield the range resolution of a short pulse. Synthetic aperture processing in azimuth exploits the linear FM modulation that the (approximately) quadratic variation in range to a scatterer introduces as the sensor passes. The processor is able to compress this modulated azimuth signal to generate the resolution associated with a narrow beamwidth from a wide beamwidth antenna. Table 2.2 summarizes the equations that characterize the synthetic aperture concept. The derivations that follow include definitions of the symbols in this table.

It is instructive to begin a discussion of the synthetic aperture concept by looking at the differences between a real beam and a synthetic aperture beam. Then, the development of expressions for the azimuth chirp rate, the beam compression ratio, and Doppler bandwidth of the azimuth signal shows the similarities between pulse compression in range and SAR beam compression in azimuth.

2.4.1 Real Beam Radar and SAR

A real beam radar determines the angular position of a scatterer by the pointing angle of the antenna illumination pattern at a specific time. The real beam radar resolves two scatterers if the angular separation between them is greater than one beamwidth; this radar cannot distinguish (in angle) among returns from scatterers illuminated at the same time. The real beam scans physically in angle, interrogating successive resolution cells in a sequential manner.

Table 2.2
Synthetic Aperture Equations

Quantity	*Relationship*	*Equation Reference*
Azimuth resolution	$\rho_a \approx \frac{\lambda_c K_a}{2\Delta\theta}$	(2.20)
Synthetic aperture length	$L \approx \frac{R_a \Delta\theta}{\sin(\alpha_{dc})}$	(2.21)
Synthetic aperture time	$T_a = \frac{L}{V_a} \approx \frac{R_a \Delta\theta}{V_a \sin(\alpha_{dc})}$	(2.22)
Azimuth chirp rate	$\gamma_a = \frac{2V_a^2 \sin^2(\alpha_{dc})}{\lambda_c R_a}$	(2.30)
Doppler bandwidth of single scatterer (chirped)	$B_d \approx \frac{2V_a \Delta\theta \sin(\alpha_{dc})}{\lambda_c}$	(2.28)
Doppler bandwidth of full scene (dechirped)	$B_a \approx \frac{2V_a W_a \sin(\alpha_{dc})}{\lambda_c R_a}$	(2.32)

In a real aperture radar, an unweighted antenna of length D illuminates a scene with a half-power one-way beamwidth β_a approximated by

$$\beta_a \approx 0.89\frac{\lambda_c}{D} \tag{2.8}$$

where λ_c is the center wavelength. This beamwidth times the range R_t to a target area suggests a spatial (azimuth) resolution of

$$\rho_a \approx 0.89\frac{\lambda_c R_t}{D} \tag{2.9}$$

for the real antenna, as Figure 2.11 suggests. The pointing angle α relative to a reference line and the beamwidth of the antenna illumination pattern combine to determine the location and resolution, respectively.

A SAR synthesizes a long antenna aperture by a coherent summation of phase-adjusted complex data samples (pulses). The SAR collects these samples along a path length L while illuminating the scene with a wide antenna beamwidth. This distance L is the *synthetic aperture length*. With a real antenna aperture size, D, this beamwidth is given by (2.8). The synthetic aperture length is much larger than the real antenna aperture.

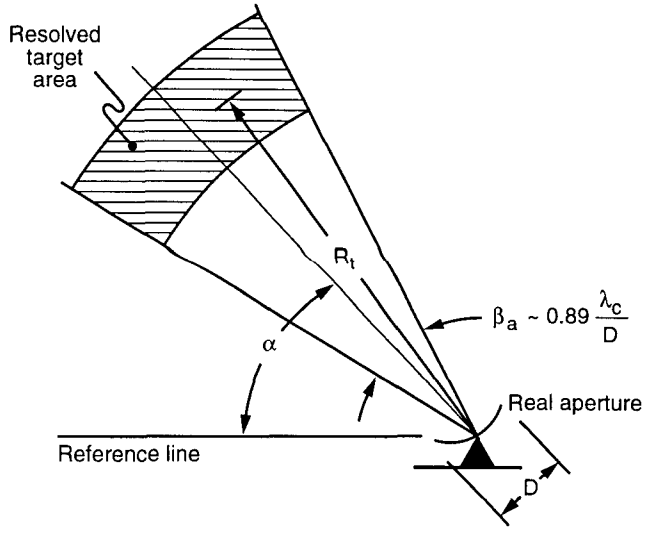


Figure 2.11 Azimuth resolution using a real aperture.

Aided by appropriate phase adjustments before coherent summation in the data processor, the large synthetic aperture generates an effective beamwidth that is much smaller than the real antenna beamwidth. In a sense, the synthetic beam scans, not physically as in the case of the real antenna, but analytically in the processor. The processor accomplishes this scan by applying different linear phase functions across the synthetic aperture length after appropriate (nominally quadratic) phase adjustments. The Fourier transform kernel provides these linear phase functions to interrogate the signal in successive azimuth resolution cells.

For $R_t >> L$, azimuth resolution for an unweighted synthetic aperture of length L is

$$\rho_a \approx \frac{\lambda_c K_a R_t}{2L \sin(\alpha_{dc})} \tag{2.10}$$

where α_{dc} is the Doppler cone angle which identifies the direction toward the scene relative to the direction of the array. The factor K_a represents a generalized mainlobe-broadening factor introduced by aperture weighting in the processor to control sidelobes of the system impulse response and by residual amplitude and phase errors. Figure 2.12 suggests this result. The synthetic array consists of the transmission and reception of radar pulses from a series of positions along the real antenna trajectory. The real antenna beam is pointed at an angle α_{dc} relative to its velocity vector.

An intuitive understanding of the size of the synthetic beamwidth begins with the returns to each array position properly adjusted in phase to point in the direction α_{dc}. Returns originating from a scatterer at the angle α_{dc} relative to the array add in phase to

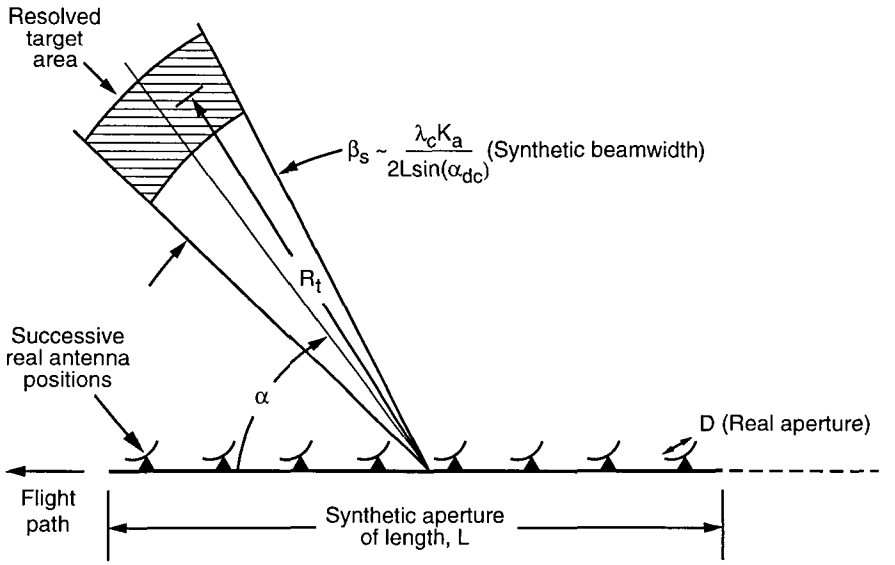


Figure 2.12 Azimuth resolution using a synthetic aperture.

produce a strong return. The angular variation from α_{dc} at which the backscattered signals to all array sample positions cancel each other suggests the size of the synthetic beamwidth. This angle represents an estimate of one-half the angular beamwidth between the first nulls of the synthetic antenna pattern. To estimate this angle, it is helpful to pair off the array of samples across the entire aperture length and determine the angle from α_{dc} at which the backscattered signals to each pair of samples cancel. As Figure 2.13 suggests, each pair of elements is separated by $L/2$. The SAR transmits and receives the data from each synthetic antenna element (SAR pulse) individually; later, the processor coherently sums the individual returns with proper phasing.

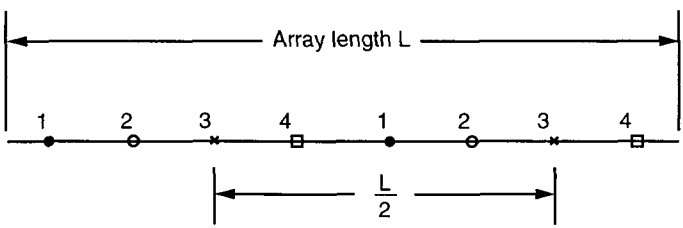


Figure 2.13 Four pairs of elements (each with $L/2$ separation) over an eight-sample synthetic aperture array.

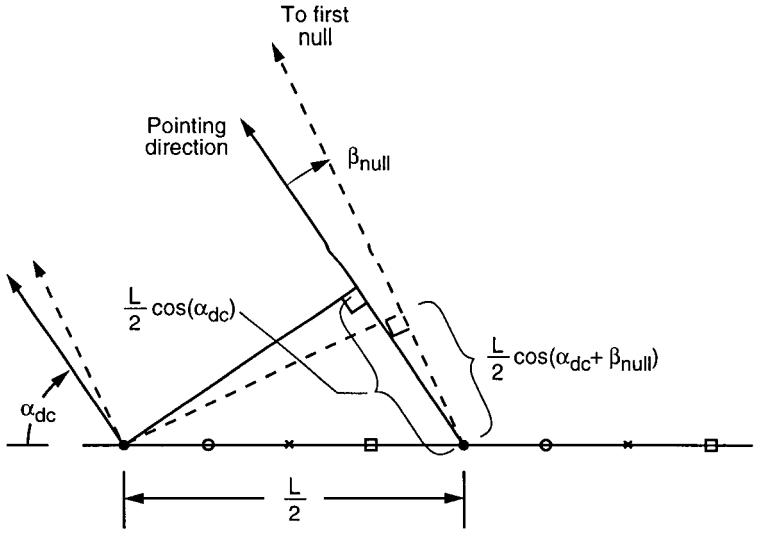


Figure 2.14 Calculation of synthetic aperture beamwidth.

From Figure 2.14, β_{null} is the angular distance off the pointing direction at which the first null in the synthesized antenna pattern occurs. An estimate for β_{null} is the angle for which the change in distances from the target to the center element and to the end element (and to each of the other pairs of elements) is $\lambda_c/4$. This change causes the two-way paths to change by $\lambda_c/2$; the signals received from scatterers in the far field by the two elements in each pair are out of phase and cancel. This cancellation implies the existence of a null in the pattern at this angle. The first null occurs at an angle β_{null} off the pointing direction where the change in the two-way path difference ΔP to a target is $\lambda_c/2$. This path difference is

$$\Delta P = 2\left[\frac{L}{2}\cos(\alpha_{dc} + \beta_{null}) - \frac{L}{2}\cos(\alpha_{dc})\right] \tag{2.11}$$

as Figure 2.14 suggests. Equating the magnitude of ΔP to $\lambda_c/2$, an approximation for β_{null} is

$$\sin(\beta_{null}) \approx \frac{\lambda_c}{2L\sin(\alpha_{dc})} \tag{2.12}$$

An additional small-angle approximation yields

$$\beta_{null} \approx \frac{\lambda_c}{2L\sin(\alpha_{dc})} \tag{2.13}$$

A measure of the half-power azimuth synthetic beamwidth β_s is $K_a\beta_{null}$, or $K_a/2$ times the null-to-null beamwidth of $2\beta_{null}$. Therefore, the expression for the half-power azimuth beamwidth which the coherent summation operation of the SAR synthesizes is

$$\beta_s \approx \frac{\lambda_c K_a}{2L\sin(\alpha_{dc})} \tag{2.14}$$

This beamwidth times the range R_t to a target area establishes azimuth resolution as (2.10).

This synthetic beamwidth perspective is most appropriate when $R_t >> L$. A useful adjustment to (2.14) and (2.10) as the size of L approaches R_t is to divide each result by $\cos(\Delta\theta/2)$ where the angular interval $\Delta\theta$ represents the angle through which the target is viewed during the coherent processing aperture. This factor indicates a broadening of the synthetic aperture beamwidth for wide angle synthetic apertures. In this case, the adjusted version of (2.14) becomes

$$\beta_s \approx \frac{\lambda_c K_a}{2L\sin(\alpha_{dc})\cos\left(\frac{\Delta\theta}{2}\right)} \tag{2.15}$$

The rationale for this adjustment is that it leads to results consistent with an analysis of signal Doppler bandwidth to establish azimuth resolution (Section 2.4.4). Using (2.15), the adjusted version of (2.10) as the size of L approaches R_t is

$$\rho_a \approx \frac{\lambda_c K_a R_t}{2L\sin(\alpha_{dc})\cos\left(\frac{\Delta\theta}{2}\right)} \tag{2.16}$$

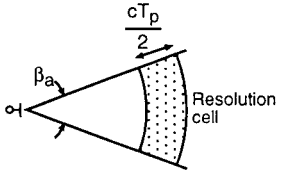
Two observations regarding (2.16) are significant. First, for a *fixed* synthetic aperture length, azimuth resolution is range-dependent just as it is for a real antenna with a fixed antenna size. Second, azimuth resolution is a factor of two smaller for the synthetic aperture than it is for the real aperture for equal synthetic antenna and real antenna sizes. This difference arises because a synthetic array element receives a return signal only from its own transmitted signal before coherent summation of the contributions from all elements, whereas a real antenna element receives return signals from transmissions by each element in the array. In the synthetic array, the two-way path difference determines the phase difference between pairs of elements before coherent summation over all elements. In the case of the real beam, it is the one-way path difference that matters initially when an element coherent sums the returns from all elements in the array. In the second summation over all elements, it is the one-way path difference that matters again [14].

In SAR then, the synthetic azimuth beamwidth provides an azimuth resolution much narrower or finer than the real antenna beamwidth. That is, the processor is able to

separate the signals from scatterers within the real beamwidth although the radar illuminates the scatterers simultaneously. A mathematical development of the beamwidths for real and synthetic apertures is available in a number of references such as [14, 15].

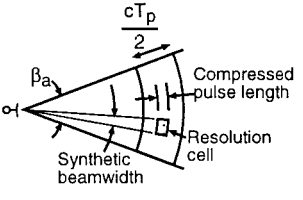
Figure 2.15 summarizes the comparison between a simple short pulse radar and a SAR using pulse compression in terms of range and azimuth positioning and resolution. Basically, the simple radar illuminates a single resolution cell at one time while the SAR illuminates many resolution cells simultaneously but separates the returns from each resolution cell by pulse compression and beam compression techniques. Of course, it is natural for a real beam radar to utilize pulse compression techniques in range; thus, the key difference here is in azimuth resolution.

Simple Radar—illuminates a single resolution cell at one time



	Position Determined by	*Resolution Determined by*
Range	Time delay	Pulse length
Azimuth	Vehicle along-track position (translating antenna)	Antenna beamwidth
	Antenna pointing angle (rotating antenna)	Antenna beamwidth

SAR—illuminates many resolution cells at the same time but separates returns from each one



	Position Determined by	*Resolution Determined by*
Range	Time delay	Compressed pulse length
Azimuth	Vehicle along-track position (stripmap)	Synthetic aperture beamwidth
	Synthetic antenna pointing angle (spotlight)	Synthetic aperture beamwidth

Figure 2.15 Simple radar and SAR comparison of positioning and resolution.

2.4.2 Synthetic Aperture Interval

Stripmap mode operation produces a moving synthetic aperture such that all scatterers at a given distance from the flight line generate signal histories over the same azimuth pointing angle and angular interval. Thus, targets at all azimuth (along-track) positions have identical signal histories except for a shift in time (or along-track) location. The real antenna beamwidth in azimuth limits this angular interval to $\beta_a = 0.89\lambda_c/D$; in this way, the maximum synthetic aperture length is limited to $R_t\beta_a/\sin(\alpha_{dc})$ by the illumination pattern duration on a target at range R_t. Figure 2.16(a) shows the case of broadside imaging with $\alpha_{dc} = 90$ deg. In a stripmap mode collection squinted at the angle α_{dc} from the velocity vector, the synthetic aperture length is

$$L = \frac{0.89\lambda_c R_t}{D\sin(\alpha_{dc})} \tag{2.17}$$

Using this expression in (2.10) with $K_a = 0.89$, the finest azimuth resolution available in a stripmap collection is $D/2$, independent of range. In this case, azimuth resolution is independent of range because the synthetic aperture length increases with range.

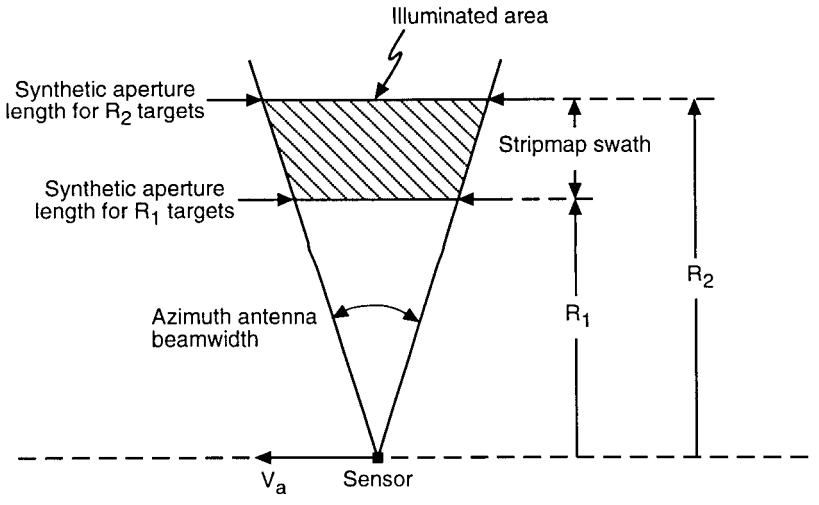
A spotlight mode collection uses a single synthetic aperture that is common to all scatterers in the scene. Thus, the angular interval over which the spotlight mode illuminates a particular scatterer and collects data varies with the range and azimuth positions of the scatterer. Figure 2.16(b) suggests the dependence on range position. The variation in angular interval with azimuth position of the scatterer is particularly relevant in comparing the polar format algorithm to the range migration and chirp scaling algorithms in Chapters 10 and 11, respectively.

Figure 2.17 illustrates a simple spotlight data collection geometry at a nominal slant range R_a and sensor velocity V_a. An approximation for the angular interval $\Delta\theta$, representing the angle through which the target at scene center is viewed during the coherent processing aperture, is available as

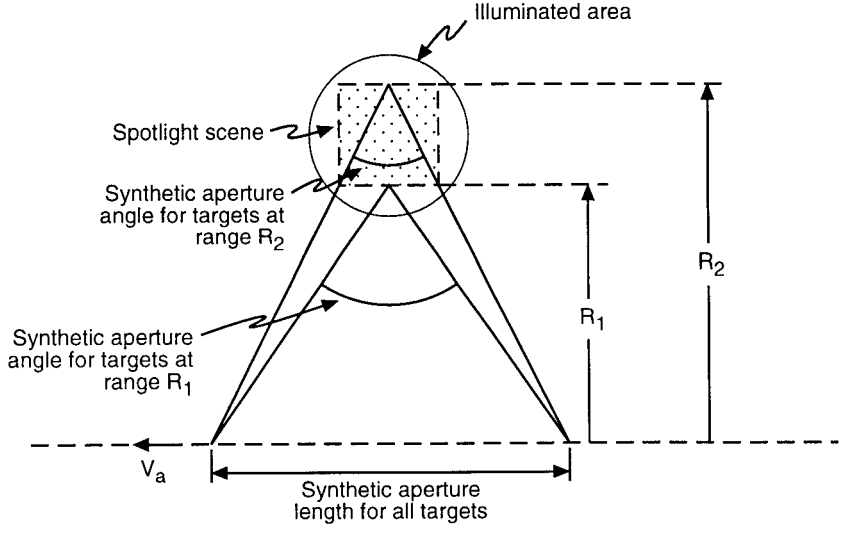
$$R_a\tan\left(\frac{\Delta\theta}{2}\right) \approx \frac{L}{2}\sin(\alpha_{dc}) \tag{2.18}$$

It is common to approximate L/R_t in (2.10) by L/R_a although, in fact, this quantity varies as a function of target position in the scene. With this approximation, use of (2.18) in (2.10) leads to the common expression for resolution in the azimuth dimension [19, 20]. This expression for azimuth resolution is

$$\rho_a \approx \frac{\lambda_c K_a}{4\sin\left(\frac{\Delta\theta}{2}\right)} \tag{2.19}$$



(a)



(b)

Figure 2.16 Synthetic aperture comparison: **(a)** Variable aperture length in stripmap mode; **(b)** Variable aperture angle in spotlight mode.

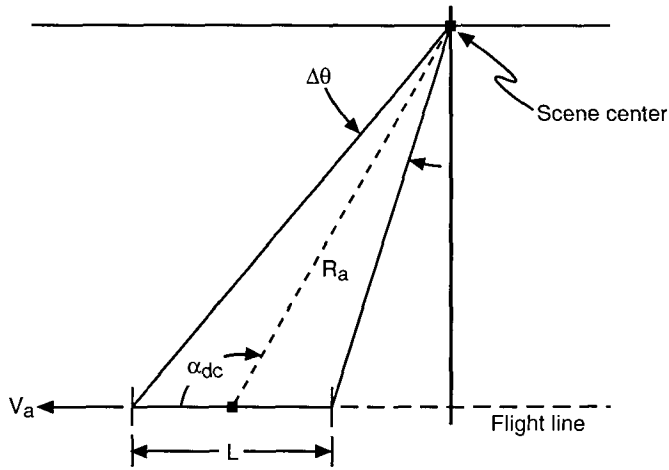


Figure 2.17 Spotlight synthetic aperture interval.

which, with an additional small-angle approximation, becomes

$$\rho_a \approx \frac{\lambda_c K_a}{2\Delta\theta} \tag{2.20}$$

Here K_a represents a generalized mainlobe-broadening factor introduced by aperture weighting in the processor to control sidelobes of the system impulse response and by residual amplitude and phase errors. As an example, a specification to achieve 1-m azimuth resolution with an X-band (10 GHz) system using a unity aperture weighting factor requires approximately 1 deg of target rotation.

In terms of $\Delta\theta$, the synthetic aperture length is

$$L \approx \frac{\lambda_c R_a K_a}{2\rho_a \sin(\alpha_{dc})} \approx \frac{R_a \Delta\theta}{\sin(\alpha_{dc})} \tag{2.21}$$

It is the distance over which the sensor transmits, receives, and processes signal pulses to synthesize one narrow illumination beam for fine azimuth resolution.

In a modern SAR imaging system employing a high-precision motion sensor, azimuth resolution approaching the theoretical limit is attainable. In some ISAR systems, precise motion data sometimes is not available; in such a case, cross-range resolution may be several times coarser than the theoretical limit or it may be unpredictable.

The collection geometry, sensor velocity, and required azimuth resolution determine the required synthetic aperture time T_a and corresponding aperture length L. For sensor

velocity V_a and slant range R_a, the synthetic aperture time is

$$T_a = \frac{L}{V_a} \approx \frac{R_a \Delta\theta}{V_a \sin(\alpha_{dc})} \tag{2.22}$$

Here α_{dc} is the Doppler cone angle between the antenna velocity vector and the radar line of sight to scene center evaluated at the center of the azimuth processing aperture.

The synthetic aperture technique provides two benefits unique to the spotlight mode. First, azimuth beamwidth does not limit azimuth resolution in spotlight mode since the real antenna beamwidth in azimuth does not limit the synthetic aperture length; in stripmap mode, the real antenna beamwidth limits azimuth resolution to $D/2$. Second, because it is possible to employ a narrow real beamwidth, the spotlight mode can operate with high antenna gain when needed to improve signal levels relative to noise. Relative to stripmap operation, spotlight mode can acquire a finer-resolution, stronger signal from the scene at the cost of a reduced scene size or area imaging rate.

2.4.3 Beam Compression Ratio

The beam compression ratio (BCR) is the ratio of the real azimuth half-power beamwidth β_a required to illuminate the scene to the synthetic aperture half-power beamwidth β_s. Another name for BCR is azimuth compression ratio. In spotlight mode, the required real beamwidth is

$$\beta_a = \frac{W_a}{R_a} \tag{2.23}$$

where W_a is the azimuth size of the scene. The synthetic beamwidth associated with the synthetic aperture length L is

$$\beta_s = \frac{\lambda_c K_a}{2L \sin(\alpha_{dc})} \tag{2.24}$$

The BCR is

$$\text{BCR} = \frac{W_a / R_a}{\lambda_c K_a / 2L \sin(\alpha_{dc})} = \frac{W_a}{\rho_a} \tag{2.25}$$

using (2.21) to arrive at the final expression for BCR. Post-collection processing compresses the real azimuth beamwidth to a much narrower beamwidth. This compression improves the azimuth resolution from $W_a = R_a \beta_a$ (the fully illuminated scene) to ρ_a.

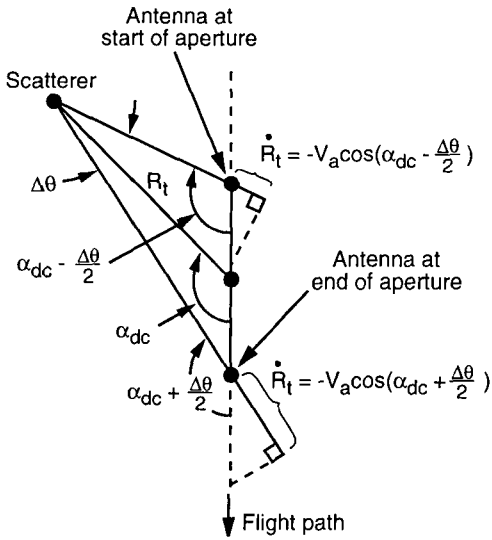


Figure 2.18 Geometry to depict variation in scatterer range rate.

2.4.4 Azimuth Chirp Rate and Doppler Bandwidth of Received Signal

The instantaneous Doppler frequency of a signal returned from a specific scatterer in the illuminated scene is minus twice the scatterer's range rate divided by the wavelength of the signal. While the Doppler frequency does vary with wavelength within the chirp pulse, use of the center wavelength λ_c is adequate in this development. The Doppler frequency f_d represents the time rate of change from pulse to pulse of the backscattered signal's phase at a fixed time delay from the time of pulse transmission. Referring to Figure 2.18, the scatterer's range rate is minus the antenna velocity times the cosine of the Doppler cone angle.

At the start of the synthetic aperture, where $\alpha_d = \alpha_{dc} - \Delta\theta/2$, the Doppler frequency f_{d1} is

$$f_{d1} = \frac{2V_a\cos\left(\alpha_{dc} - \frac{\Delta\theta}{2}\right)}{\lambda_c} \tag{2.26}$$

At the end of the synthetic aperture, where $\alpha_d = \alpha_{dc} + \Delta\theta/2$, the Doppler frequency f_{d2} is

$$f_{d2} = \frac{2V_a\cos\left(\alpha_{dc} + \frac{\Delta\theta}{2}\right)}{\lambda_c} \tag{2.27}$$

Thus, the Doppler bandwidth B_d, of the signal received from a point scatterer over the cone angle interval, $\Delta\theta$, is approximately

$$B_d \approx \frac{4V_a \sin\left(\frac{\Delta\theta}{2}\right)\sin(\alpha_{dc})}{\lambda_c} = \frac{V_a K_a \sin(\alpha_{dc})}{\rho_a} \tag{2.28}$$

The signal exists on the Doppler offset or carrier frequency f_{do} where

$$f_{do} = \frac{2V_a \cos(\alpha_{dc})}{\lambda_c} \tag{2.29}$$

The expression for the nominal azimuth chirp rate γ_a is the Doppler bandwidth B_d divided by the synthetic aperture time T_a. This division yields

$$\gamma_a = \frac{2V_a^2 \sin^2(\alpha_{dc})}{\lambda_c R_a} \tag{2.30}$$

This quantity represents the nominally linear FM rate at which the azimuth signal changes frequency as the sensor illuminates a scatterer over a small cone angle interval.

The Doppler bandwidth from (2.28) suggests an alternative perspective on azimuth resolution for the synthetic aperture technique. A bandwidth B_d leads to a time resolution of $\Delta t = 1/B_d$ in target along-track location relative to the antenna location. Relating changes in antenna location and time by $\Delta X = V_a \Delta t$, azimuth resolution ρ_a is given by $K_a \Delta X \sin(\alpha_{dc})$, which yields

$$\rho_a \approx K_a [V_a \Delta t] \sin(\alpha_{dc}) = \frac{K_a V_a \sin(\alpha_{dc})}{B_d} = \frac{\lambda_c K_a}{4\sin\left(\frac{\Delta\theta}{2}\right)} \tag{2.31}$$

in agreement with (2.19).

2.4.5 Spotlight Scene Bandwidth after Azimuth Dechirp

In spotlight mode, it is common practice to remove the azimuth chirp characteristic from the received signals by mixing them with a reference phase function equal to the azimuth chirp phase of a hypothetical scatterer at scene center. This process of *azimuth dechirping* converts the signal from each scatterer into a nominally constant frequency in terms of pulse-to-pulse phase change. After azimuth dechirping, the bandwidth B_a of the composite signal received from all resolution cells within an azimuth size W_a is the azimuth chirp rate γ_a multiplied by the time, $t_w = W_a / V_a \sin(\alpha_{dc})$, to traverse the azimuth scene

extent. The result is

$$B_a \approx \frac{2V_a W_a \sin(\alpha_{dc})}{\lambda_c R_a} \tag{2.32}$$

This result is also available by use of W_a/R_a, the angle subtended by the scene as viewed from the antenna, for $\Delta\theta$ in (2.28). This approach again yields B_a as the composite signal bandwidth of all scatterers in the spotlight scene.

This composite signal exists for the time T_a from (2.22) to yield an azimuth time-bandwidth product TB_a after dechirp of

$$TB_a = \frac{2W_a \Delta\theta}{\lambda_c} = \frac{K_a W_a}{\rho_a} \tag{2.33}$$

TB_a is a measure of the number of complex samples required to preserve the information in the signal. It exceeds the beam compression ratio in (2.25) by the factor K_a. This difference occurs because the BCR relates to the actual azimuth resolution improvement while TB_a relates to the ideal resolution, ρ_a/K_a.

To store this data at bandwidth B_a for time T_a over the spotlight synthetic aperture would require $B_a T_a$ complex samples. This quantity is the TB_a from (2.33). Since samples are associated with pulses in this case, these data characteristics would require a PRF after presumming equal to or greater than B_a. At this PRF, the corresponding spacing S_a between samples along the antenna trajectory is equal to V_a/B_a. Using (2.32), this quantity becomes

$$S_a \approx \frac{\lambda_c R_a}{2W_a \sin(\alpha_{dc})} \approx \frac{\lambda_c}{2\beta_a \sin(\alpha_{dc})} \tag{2.34}$$

where the second approximation assumes that the azimuth scene size W_a fills the azimuth antenna beamwidth β_a. This equation indicates that the minimum sample spacing is independent of azimuth resolution in the spotlight mode.

The requirement of $B_a T_a$ complex samples is significantly less than the azimuth time bandwidth product associated with each individual scatterer before azimuth dechirp whenever the angular extent of the scene is small relative to angular interval required for the azimuth resolution. Actually, spotlight data without azimuth dechirp requires a bandwidth larger than B_d, roughly the sum of B_d and B_a. While targets at various azimuth locations have this same Doppler bandwidth, they have different Doppler center frequencies because the cone angle to each scatterer at the center of the coherent processing aperture varies with the scatterer's azimuth position. This means that the Doppler frequency intervals of scatterers at different azimuth positions do not completely overlap. The result is that angular extent of the scene in azimuth plus the cone angle interval $\Delta\theta$ is the relevant angle to use in (2.28) to determine the full Doppler bandwidth from an extended scene without azimuth dechirp. This consideration is one reason to employ

azimuth dechirp in spotlight mode. Another reason is that the polar format algorithm requires it. On the other hand, the range migration and chirp scaling algorithms require azimuth data with the chirp present. Stripmap mode naturally preserves the azimuth chirp.

In spotlight mode with azimuth dechirp, the presumming would typically involve two steps. The first step is a presum in the receiver after A/D conversion. This step eases the data transmission or storage requirements. The second step is a presum in the processor to achieve the minimum allowable azimuth sample rate required by the desired scene size. Because the available data often greatly exceeds the desired scene size, low-pass filtering and downsampling (decimating) in one or both directions are useful to reduce the processing load in later processing operations.

In stripmap mode, the azimuth antenna beamwidth β_a is the appropriate angle to use in (2.28) to calculate the composite signal bandwidth (including all scatterers in the strip). The signal from each scatterer has the same Doppler frequency interval B_d which equals $2V_a\beta_a \sin(\alpha_{dc})/\lambda_c$. These data characteristics require a sample rate (PRF after any azimuth presumming) equal to or greater than B_d. To store this data at bandwidth B_d for time T_a requires B_dT_a complex samples. At this PRF, the corresponding spacing S_a between samples along the antenna trajectory is equal to V_a/B_a. This value equals the result in (2.34) for spotlight mode. In this case, however, the minimum sample space is directly related to azimuth resolution since β_a determines azimuth resolution. The minimum spacing between samples corresponds to $\rho_a/K_a \sin(\alpha_{dc})$ in the stripmap mode.

A consideration of (2.22) and (2.32) provides insight on azimuth resolution from the viewpoint of the frequency domain, analogous to time domain presentation in (2.31). From (2.32), a change ΔW in W_a corresponds to a change ΔB in B_a according to

$$\Delta W = \frac{\lambda_c R_a \Delta B}{2V_a \sin(\alpha_{dc})} \tag{2.35}$$

From (2.22), the minimum detectable change in B_a is roughly the reciprocal of the observation time T_a or

$$\Delta B = \frac{V_a \sin(\alpha_{dc})}{R_a \Delta\theta} \tag{2.36}$$

Inserting (2.36) into (2.35) and including the mainlobe-broadening factor K_a yields a change in W of

$$\Delta W = \frac{\lambda_c K_a}{2\Delta\theta} \tag{2.37}$$

which is ρ_a, in agreement with (2.20) and (2.31).

2.5 SAR COHERENCE REQUIREMENTS

A normal SAR data collection involves sampling the amplitude and phase of a function that is the Fourier transform of a two-dimensional projection of the target field reflectivity. This statement applies equally to SAR imaging of stationary targets from a moving platform and to ISAR imaging of moving targets from either a moving platform or a stationary ground-based radar. The capability to measure the proper relative phase of this Fourier transform at each sample point requires phase coherence within each pulse. It also requires phase coherence from pulse to pulse over the collection time needed for azimuth resolution.

Motion compensation is only one aspect of SAR coherence [21, 22]. In fact, three specific factors impact the phase coherence of the two-dimensional SAR signal and introduce phase effects that influence the processing complexity and the resulting image quality. These factors are:

1. Propagation, including weather and foliage effects;
2. Source coherence for transmitted and reference signals;
3. Extraneous antenna motion and the adequacy of motion compensation.

Typical SAR applications achieve coherence in fast time by the proper generation and management of the transmitted waveform. Phase nonlinearity in the frequency-modulated pulse results in phase errors in the range dimension of the range-Doppler imaging operation. A loss in coherence from pulse to pulse results in azimuth phase errors. Chapter 5 includes a general discourse on sources, categories, and effects of phase errors on SAR imagery.

2.5.1 Propagation Effects on Phase Coherence

A fine-resolution SAR imaging system employs a wide-bandwidth pulse for range (time delay) resolution and a narrow synthetic antenna beamwidth for azimuth (angular) resolution. Two propagation effects that impact phase coherence with respect to such a system are a frequency-dependent index of refraction and a variation in the integrated refractive index as a function of pulse number.

A frequency-dependent index of refraction, including waveguide dispersion, induces phase errors in the range dimension of the signal history. The magnitude of this dispersive propagation effect varies with such parameters as medium properties, path length, radar center frequency, and transmitted bandwidth. A deterministic focus adjustment in range will remove any predictable component of this phase error whereas a range refocus procedure in the signal processing chain is a possibility for any unpredictable component. While the troposphere is essentially nondispersive, the ionosphere is dispersive. Imaging from space may encounter significant ionospheric dispersive effects at lower frequencies. Ionospheric dispersion has little impact at higher frequencies [23-25].

A variation in the integrated refractive index between the radar antenna and scatterers during the synthetic aperture interval introduces azimuth phase errors in the signal history. Spatial inhomogeneity in the refractive index of the medium is a source of this variation [26, 27]. The magnitude of this phase effect varies with radar center frequency, azimuth resolution, and characteristics of the propagation medium including weather conditions and the presence of intervening foliage. The IFP can compensate for any space-invariant component of this phase effect whereas any space-variant component is not easy to compensate. A space-invariant component is the same for all scatterers; a space-variant component varies across the scene.

2.5.2 Source Coherence in SAR

A SAR system employing a wideband coherent signal with linear frequency modulation over the required bandwidth must either know, measure, or self-reference the relative starting phase and frequency of each pulse at a precise time. Typically, the use of an extremely stable reference clock to generate all RF and IF frequencies provides this coherence. Additionally, in azimuth, the SAR system utilizes the same stable reference clock to derive the PRF clock. Measurement of the relative starting phase and frequency of each pulse requires a reference oscillator that is coherent over the shorter of either the two-way pulse transit (delay) time or the azimuth aperture time. If the reference oscillator is coherent over the two-way transit time, the procedure is to mix the return signal with a reference signal consisting of a continuation of the transmitted signal. This self-referencing procedure cancels the unknown starting phase and frequency. Rather than continue the transmitted signal, it is normal in this situation to generate a separate reference signal at the appropriate time using the coherent reference oscillator to maintain phase coherence with the original transmitted signal. If the reference signal is coherent over the full aperture time, then it provides a known phase and frequency reference for each transmitted pulse within one aperture time.

In the absence of the required reference oscillator, it is possible to self-reference the transmitted waveform by mixing the return signal with a delayed version of the transmitted signal. The delayed version may be the signal from a reference reflector at an appropriate range, from a prominent point within the target field, or from a delay line. Use of a target prominent point to produce the reference signal is an especially powerful technique, where feasible, because this procedure also neutralizes, to a large extent, the majority of any deleterious propagation and motion measurement effects.

A transmitted pulse with linear frequency modulation can provide the required phase coherence over the transmitted bandwidth in SAR fast time. However, deviations from the quadratic phase variation associated with linear frequency modulation can reduce phase coherence and cause difficulties, especially if these deviations vary from pulse to pulse. To assure phase coherence from pulse to pulse (in the azimuth domain), it is necessary to neutralize the effects of any random uncertainty in the starting phase and frequency of each pulse.

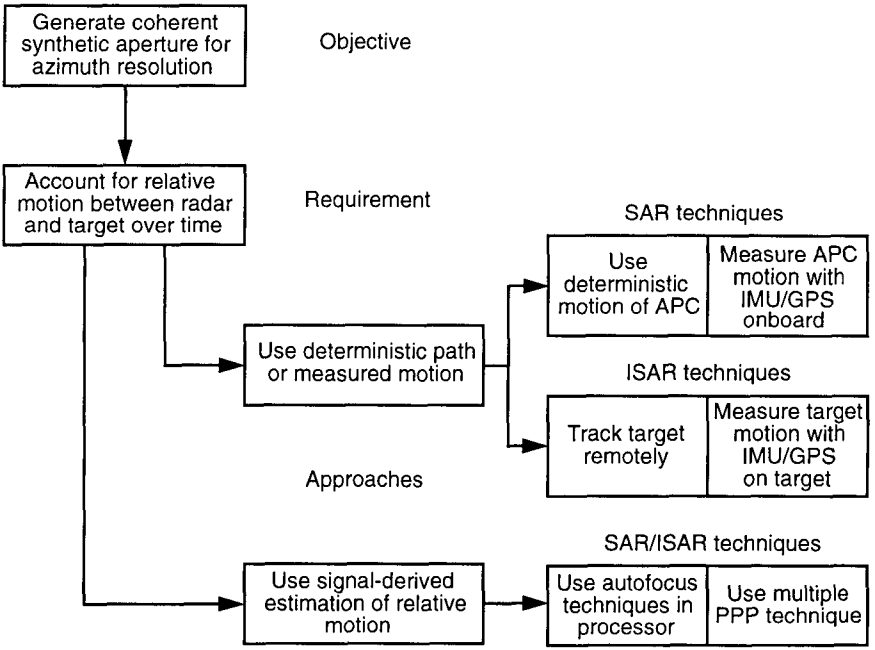


Figure 2.19 Means to achieve azimuth coherence.

A master oscillator with adequate phase stability over the *two-way delay time* to the target field would be able to remove the pulse-to-pulse phase and frequency uncertainty resulting from the random starting phase of each pulse. A master oscillator with phase stability over the *azimuth aperture time* would control the starting phase and frequency of each pulse completely, introducing no pulse-to-pulse phase uncertainty. In practice, however, the master oscillator is short of ideal and residual phase noise is always present.

2.5.3 Motion Effects on Phase Coherence

The APC position naturally affects the pulse-to-pulse phase coherence over the synthetic aperture. The APC position history includes both planned changes in, and unplanned perturbations of, the antenna location. Extraneous APC motions create phase effects in the SAR signal history that the processor must cancel in order to maintain phase coherence and achieve good image quality.

To use the synthetic aperture concept for generating fine azimuth resolution in radar imagery, the SAR system must account for the distance from the target to the radar APC at the transmission time of each radar pulse. It may choose either one or a combination of procedures to account for this distance. Figure 2.19 summarizes the possibilities, differentiating between SAR and ISAR applications.

To account for the distance from the target to the radar, the first possibility is either to measure relative position and motion or to know the relative motion in cases where that motion follows a deterministic path. Such an approach applies to both SAR and ISAR. For airborne SAR, an inertial measurement unit (IMU) and possibly a global positioning system (GPS) receiver are onboard the SAR platform; for spaceborne SAR and railborne SAR (for example, Rail SAR [28]), knowledge of position by various means or a deterministic path is the solution without the need for explicit, *in situ*, measurements. For an ISAR system, either the target carries an IMU/GPS motion measurement system or the system tracks the target via ground-based sensors able to measure both range and attitude as a function of time. In the case of an ISAR rotating platform imaging facility, the path is deterministic in that the range to scene center is constant; however, the rotation rate may require monitoring if it varies.

The second option is to obtain the needed information from the received radar signals themselves. This approach involves measuring the effects of the motion (for example, phase errors) without explicitly measuring the associated motions. In some methods, these measurements can yield estimates of the associated motions. This second option includes various autofocus techniques (Chapter 6) and prominent point processing (PPP). PPP with a single point (Section 6.5.1) is an autofocus technique whereas PPP with multiple prominent points (Section 6.5.2) is an interactive focusing technique, with the potential to accomplish more than estimation of space-invariant phase errors. Autofocus techniques and PPP with a multiple-point algorithm are applicable to either SAR or ISAR. In SAR, these techniques may replace motion measurement entirely or they may simply be an adjunct to actual motion measurements.

2.5.3.1 Motion Compensation Procedures

The synthetic aperture concept requires the radar system to interrogate the scene being imaged over a Doppler cone angular interval that is adequate to achieve the desired azimuth resolution. At the same time, accurate measurement of and adequate compensation for translational and angular relative motion between the APC and the scene during the interrogation time is a major practical challenge in fine-resolution SAR imaging.

The minimum objective for motion compensation is to reduce motion-induced phase effects to a level that an autofocus algorithm can accommodate. The magnitude of residual phase errors will be a function of the quality of motion measurement, magnitude and characteristics of the motion being measured, and adequacy of the algorithm for converting sensed motion into APC location. Chapter 5 characterizes and discusses the effects of the resulting phase errors when motion compensation is imperfect.

For spotlight SAR and ISAR, the ideal APC relative motion is circular motion in a plane containing scene center at a constant angular velocity and constant radius about scene center. With this ideal movement, spotlight mode operation requires no motion compensation at all. In rotating platform imaging, this movement is analogous to locating the SAR antenna in a plane containing scene center and orthogonal to the axis of rotation.

APC movement along a straight path at constant forward velocity is ideal for stripmap SAR and acceptable for spotlight mode. For such motion, stripmap mode operation requires no compensation; the processor simply stores the return pulses side by side with the same time delay from transmit time and with the same separation between pulses. On the other hand, spotlight mode operation typically requires motion compensation in the IFP to:

- Modify the frequency and starting phase of each return pulse so that a return from scene center has constant phase;
- Vary the time delay from transmit time to the first range sample to accommodate the changing range to scene center;
- Vary the sample spacing in azimuth in response to the aspect angle change from the radar to scene center.

Depending on resolution, scene size, and motion characteristics, the omission of some of these compensations may be acceptable in a particular application.

In reality, the antenna position generally does not follow a straight line or a circular path. Instead, the antenna generally proceeds with short-term fluctuations in three dimensions about the desired path. This extraneous motion creates additional phase effects in the SAR signal history for which compensation is necessary in order to maintain acceptable image quality. The SAR system handles these variations with the same three steps just outlined and one additional step in which the adjustments follow the actual APC path. The fourth step is to vary the sample spacing in the range dimension for each pulse in response to changes in grazing angle (defined in Section 2.6.1) to scene center.

This last item is a reference to compensation for nonplanar motion of the radar line-of-sight (LOS) vector to scene center. Such motion causes an azimuth phase effect that varies with target height (Section 3.3.4).

2.5.3.2 Types of Relative Motion

Motion effects in synthetic aperture radar involve three types of relative motion between the radar sensor and the target. These three types of motion are:

1. LOS translational motion which changes the distance between the target and the sensor without affecting the angular orientation between them;
2. Rotational motion which changes the angular orientation between the target and the sensor without affecting the distance between them;
3. Motion of individual targets in SAR applications or nonrigid-body motion (vibration or bending) of an ISAR target.

LOS translational motion does not contribute to the SAR imaging process. This motion introduces primarily space-invariant phase effects in the SAR signal history. If not removed by deterministic motion compensation procedures, these effects are amenable to quadratic and higher order focus techniques in the IFP. Rotational (attitude) motion of the

sensor platform contributes to this LOS translational motion through the lever arm from the center of rotation to the radar antenna. To avoid degradation in image quality, the processor also must compensate for mechanical vibrations and bending motion within the platform structure carrying the antenna to the extent that such motions affect line-of-sight APC position.

The rotational motion between the sensor and the target is important for two reasons. First, the appropriate component of rotational motion provides the basis for azimuth resolution in SAR. Second, the image formation algorithm must also compensate for the component of rotational motion which causes nonplanar motion of the radar LOS vector.

The motion of individual targets in SAR imaging applications generally receives no compensation and results in various forms of image degradation. In the case of ISAR, target rotational motions (roll, pitch, and yaw) are particularly important because they greatly impact relative motion between the target and the radar. A small rotation of the ISAR target can have the equivalent effect of a severe maneuver in an airborne radar scenario. Nonrigid-body (vibration or bending) motion of the target in ISAR applications causes space-variant image degradation, which the processor cannot ordinarily remove.

Related to rotational (attitude) motion of the SAR sensor platform, high-frequency variations (jitter) in the antenna pointing direction and slower mispointing of the illumination pattern introduce amplitude effects (as opposed to phase effects) in the SAR signal history. Amplitude modulation of SAR signals impacts image quality in the areas of signal-to-background ratio, image contrast ratio, shape of the system impulse response, and image intensity uniformity (Chapter 8).

2.5.3.3 Importance of Motion Characteristics

Uncompensated relative motion degrades image quality. The tolerable magnitude of uncompensated motion increases with radar center wavelength because the phase error associated with an uncompensated distance varies inversely with wavelength. At a given wavelength, the tolerable uncompensated distance is relatively independent of azimuth resolution because any associated low-frequency phase errors have a similar impact on the system impulse response regardless of the aperture size. Likewise, random high-frequency phase errors, which affect the sidelobes of the impulse response, have a similar impact whether the aperture is 1 sec long or 10 sec long. Resolution can be a factor when the associated aperture time changes the phase error between low-frequency and high-frequency categories.

Although resolution does not impact the tolerable magnitude of uncompensated motion over an aperture, it does naturally impact the allowable velocity or acceleration measurement error since the resulting motion error increases with aperture time. Section 5.3 quantifies requirements on motion measurement accuracy as a function of image quality impact.

An important factor in motion compensation is the period of cyclical motion relative to the azimuth aperture time. Aperture times are typically on the order of 1 to 20 sec when imaging stationary targets at fine resolution from a moving platform at X-band and

K_u-band operating wavelengths. The tolerable magnitude of uncompensated antenna motion is smaller for short-period (high-frequency) motion relative to the aperture time than for motion with a period longer than the aperture time. For example, a high-frequency RMS phase error of only 10 deg may have a significant impact on image quality, whereas a low-frequency phase error of up to 60 deg is hardly noticed. For aperture times of 1 to 20 sec, undesirable low-frequency and high-frequency motions are likely for both an airborne SAR platform and a moving ISAR target. Mechanical vibration of the platform, antenna bending, and target motion at the rate of a few hertz would be in the high-frequency range, to which the radar signal is more sensitive.

It is useful to separate antenna motions into constant velocity and constant acceleration components over the aperture interval, wideband random motion characterized by power spectral densities for three acceleration components (cross-track, along-track, and vertical), and discrete single-frequency motions. This type of separation is necessary to evaluate motion compensation requirements and subsystem phase error allocations for a fine-resolution SAR imaging system.

In addition, three aspects of wideband random motion deserve consideration. These aspects are:

1. Gust-induced acceleration representing translational motion for a rigid-body platform;
2. Vibration-induced acceleration representing nonrigid-body motion (including bending) between the APC and the platform inertial measurement sensor;
3. Platform angular rotation (roll, pitch, and yaw) causing translational motion of the APC relative to the inertial sensor because of the lever arm distance between the antenna and the inertial sensor.

Each of these aspects requires different measurement and compensation procedures. A SAR system routinely measures rigid-body translational motion and provides appropriate compensation signals in the receiver and in the IFP. Vibration compensation is difficult because it requires motion sensors with high-frequency measurement capability on or near the physical antenna. For this reason, it is particularly important to evaluate whether or not the vibrational motion requires compensation. If compensation is unnecessary, platform-based inertial sensor measurements using global positioning system (GPS) [29, 30] initialization and updating may satisfy the measurement requirements. Rotational motion of the antenna about the inertial sensor location generates additional translational motions of the APC that require a lever arm compensation algorithm.

2.5.3.4 Measurement of APC Motion

To be adequate for SAR motion compensation, a measurement of APC motion requires a position history with accuracy over both the short and the long terms. Long-term accuracy involves components of the APC velocity and acceleration vectors averaged over the synthetic aperture time. Short-term accuracy involves short-period (high-frequency) motion relative to the aperture time.

The direct approach to determine APC location is to process data from an inertial sensor suite (accelerometers and gyroscopes) located on the SAR platform. The SAR platform has six degrees-of-freedom (DOF) with different power spectra characteristics for three acceleration components (cross-track, along-track, and vertical) and three angular spectra (roll, pitch, and yaw). The inertial sensor suite measures the six DOF translational and rotational motion of the platform at the location of its attachment to the platform. Ideally, this location is near and rigidly connected to the SAR antenna. Precise reconstruction of the APC position requires calculation of the lever arm distance between the motion sensing elements and the APC as well as proper combination of the attitude (and lever arm) data with the translational motion data. Depending on the antenna gimbal design, the lever arm distance from the motion sensor to the APC might be a dynamic one; calculation of this distance will include translational and rotational corrections based on the aircraft attitude, the lever arm distances, and the antenna pointing angles.

Figure 2.20 suggests a procedure to reduce the six DOF motion measurements to a single vector position history of the APC. This procedure involves two paths. The first path involves double integration of the translational acceleration measurements (three-axis velocity changes) from the inertial sensors with the proper initial conditions (bias estimates) to calculate the position history of the inertial sensor suite. The second path involves use of gyro measurements of rotational motion of the inertial sensor suite (three-axis angle changes) to provide data for the lever arm correction. The lever arm correction data supplements the position history of the sensor suite to account for the added motion at the APC location. It is usual to filter the motion data to eliminate higher-frequency components not typical of the radar platform. These components likely originate from measurement error or from vibration local to the measurement sensors, neither of which reflects APC motion. The final step is to resolve the calculated APC position into the correct coordinate frame. The radar system uses this calculation of APC position to compute the phase correction to apply to the received signal and to determine proper formatting of the signal data (Section 2.5.3.1).

A modern SAR sensor accomplishes precision measurement of APC motion using a motion sensing system consisting of some combination of an inertial navigation system (INS), an inertial measurement unit (IMU), and a global positioning system (GPS) navigator (Figure 2.4). The INS and IMU are precision inertial measurement devices using three orthogonal accelerometers to measure accelerations and three orthogonal gyroscopes to measure angular rates. The GPS provides an estimate of absolute position of a GPS receiver unit based on simultaneous measurements of the one-way transit times of RF signals from four satellites out of a constellation of 24 GPS satellites to the receiver unit [30].

An INS uses a gyro-stabilized locally level platform with software to calculate aircraft position and attitude from the accelerometer and gyroscope output data. Most early and some current SAR motion compensation systems relied on an INS as the motion sensor. Historically, the use of an INS as a SAR motion sensor involved the adaptation of existing navigation hardware to the SAR motion compensation problem. Modified navigation sensors are often poorly adapted to the motion compensation task since navigation is

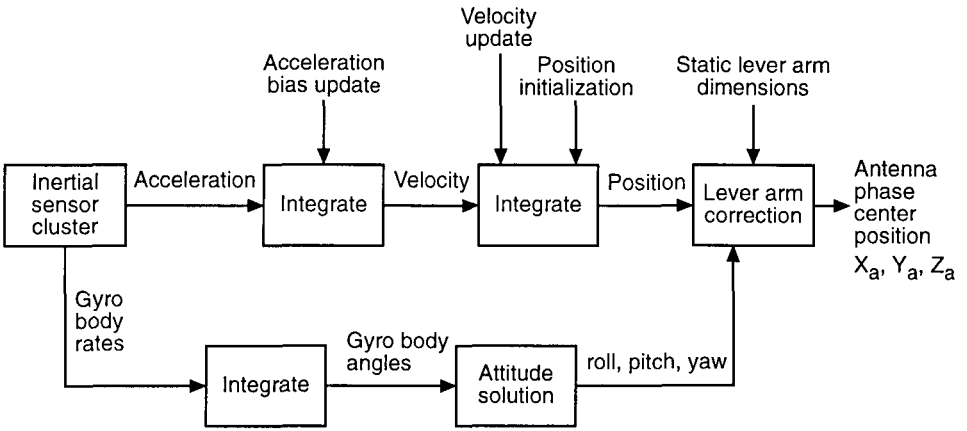


Figure 2.20 Motion computation procedure.

strictly concerned with accumulated errors, and motion compensation stresses different aspects of INS design than those needed in navigation applications. Also, proximity of the sensor package to the APC is an important factor to minimize errors; however, INS systems are typically too large or heavy to mount on or near the antenna. Using an INS, position estimation includes a lever arm correction to account for the separation between the INS and APC. When the lever arm length is relatively long (perhaps a few meters), lever-arm flexure and limited short-term accuracy of the INS attitude solution may degrade image quality. If compensated for the drift inherent in its data, the INS provides an acceptable estimate of absolute position (for navigation, antenna pointing and setting the radar range gate) and reasonable low-frequency velocity and attitude rate information for motion compensation. The INS is limited in its ability to provide high-frequency position information for motion compensation.

The long lever arm length associated with INS usage indicates the value of a strapdown IMU sensor located on the antenna and aligned to a locally level reference [31]. Like an INS, an IMU uses three orthogonal accelerometers to measure accelerations and three orthogonal gyroscopes to measure angular rates. However, the IMU processes and utilizes the available data more fully to produce the high-frequency information required in SAR motion compensation.

The development of ring-laser and fiber optics gyros of sufficient precision, coupled with the availability of the GPS for velocity update and an enhanced real-time processing capability, has made a lightweight strapdown IMU the current instrument of choice. These devices are small and light enough to mount close to the antenna. This placement helps to ensure a rigid structure between the IMU and the antenna. With this arrangement, the IMU is able to sense and measure structural vibration and other local high-frequency motion to provide a precise history of the APC position during a SAR data collection. The selection of an IMU over an INS improves high-frequency performance and reliability of the

motion sensor at a cost of a greater computational burden. A stand-alone IMU system provides superior performance in measuring high-frequency motion. With GPS updates, an IMU measures absolute position and low-frequency components of APC motion well. Because its close proximity to the APC results in a short lever arm, an IMU provides adequate attitude information for lever arm correction.

GPS navigators typically provide accurate absolute position information and accurate measurements of low-frequency position and velocity variations below 1 Hz. (A low sampling rate limits the frequency response.) An important GPS attribute is its consistency. The GPS position and velocity accuracies do not change over time; that is, the GPS navigation solution does not drift. While lacking the short-term accuracy and sampling rates to be a primary motion compensation sensor for most SAR applications, the GPS is an ideal resource to provide initial conditions and updates to the primary sensor. In particular, the GPS is valuable because INS velocity bias (typically 1 to 2 km/h) causes an INS-only position estimate to drift over time. A position estimate based on IMU measurements has a similar difficulty. Since its navigation solution does not drift, the GPS is a valuable resource to provide periodic position updates to correct the drift in an INS or IMU estimate of APC position history. Attitude (angular) information is not available from a single GPS antenna. Multiple GPS antennas and receivers (for instance, on the wingtips and tail) might provide useful attitude information.

The use of two (or more) GPS receivers together with differential data processing techniques [32] can dramatically improve the precision of GPS-derived position and velocity data. These techniques can reduce absolute position accuracy from roughly 100 m to less than 1 m and velocity accuracy from 1.0 m/s to 0.01 m/s. While the first GPS receiver is mounted on the moving SAR platform, the second GPS receiver is located on the ground in the vicinity of the data collection. (For use in any real-time applications, differential data processing requires a datalink between the ground and the data collection platform.)

2.5.3.5 Categories of Motion in SAR

In discussing the effects on SAR imagery induced by motion, it is instructive to distinguish among three categories of measured antenna motion during a SAR data collection. These categories are:

1. Motion occurring between successive transmitted pulses;
2. Motion occurring during transmission and reception of a pulse;
3. Motion occurring in the interval between transmission and reception of a pulse.

While each motion category is discussed here, Section 2.6 concentrates on the first category in the derivation of a SAR signal phase equation. Uncompensated target motion in an otherwise stationary scene is a somewhat different aspect of motion in SAR imaging. Section 5.5 discusses the consequences of imaging a moving target.

The objective of a SAR data collection is to sample the returned signal field along a trajectory in target space. In principle, the SAR system may accomplish the necessary sampling by holding the platform (antenna) stationary at one sample location while transmitting a pulse and receiving a reflected signal, and then moving to the next sampling location to transmit and receive the next pulse. In fact, ground-based measurement facilities often operate in this fashion [16]. This procedure involves motion only in the first category listed above and is sufficient to develop the desired SAR phase history. The second and third motion categories are unavoidable, and generally undesirable, consequences of a SAR sensor being carried by a continuously moving platform. Fortunately, these latter categories generally cause only small effects that are negligible in many applications.

Typically, when considering the effects of target and antenna motion on radar signals, it is reasonable to assume that all motion occurs while the radar signals are in free space or between pulses. In such a case, the only effect of the motion on the signal is a time delay with no other changes in the amplitude or phase character of the signal. If $s(t)$ is transmitted, then $s(t - \tau)$ is received, where τ is a constant for a given pulse. This perspective involves motion in the first category only.

In fact, however, the antenna may be moving in the LOS direction while transmitting or receiving a signal and a target may be moving in the LOS direction while reflecting a signal. In these cases, the phase and amplitude character of the signal is changed in a more complicated way than a constant time delay. Historically, this effect is referred to as the Doppler-variant character of waveforms, or Doppler distortion [33-35].

Antenna motion during transmission and reception of a pulse causes pulse distortion and is analogous to the familiar Doppler frequency shift associated with sound waves, such as the changing pitch of a horn from a passing automobile or train. Typically, the phase effect of motion during a pulse is small, but this effect can become significant as pulse lengths increase and motions become faster.

The third category is antenna motion between the times of pulse transmission and reflected signal reception. This motion contributes a bistatic radar effect, analogous to transmitting and receiving data with spatially separate antennas. While generally small, the bistatic effect complicates data formatting and processing when the processor must take it into account, as in the case of a fast-moving platform imaging at a long standoff range. Signal processing for a dual-platform bistatic SAR imaging system must, of course, also account for this effect.

2.6 SIGNAL PHASE EQUATION

In SAR signal history data, signal phase is more important than magnitude. For this reason, SAR system analysis often concentrates on the phase of the signal backscattered from a single, idealized point scatterer at an arbitrary location within an imaged scene. This procedure is *point target analysis*. While the actual transmitted pulse and received radar signals are real quantities, it is acceptable and convenient to use the complex exponential form to represent these signals.

Point target analysis models all signal phase contributions arising from signal generation, transmission, and reception. The model encompasses demodulation, real-time motion compensation, presumming, and digitization. It continues into the IFP to include fine motion compensation and data formatting. As a whole, this model becomes the SAR *signal phase equation.* This equation is essential to the design and validation of a SAR system. It provides concrete direction on the requirements for the IFP. To obtain the signal phase equation, it is useful to develop an analytic form of the SAR signal at successive stages in the SAR system (numbered 1 through 5 in Figure 2.3) by tracing the signal backscattered from a single scatterer (a point target) through these stages.

First, this procedure establishes a coordinate system and geometry model for SAR data collection. This geometry model and the associated signal phase equation are useful throughout all phases of spotlight radar system analysis in this book. Section 3.1 uses this geometry and the signal phase equation to motivate the need for proper formatting of SAR signal history data to compensate for undesirable signal attributes inherent in the imaging procedure. Chapter 3 uses the signal phase equation to calculate geometric distortions and residual defocus effects present in the data with use of the polar formatting algorithm. Section 9.3 uses this model to show how target height extraction is possible with the use of SAR interferometry. The model also serves as the starting point for development of the range migration algorithm and the chirp scaling algorithm for image formation in Chapters 10 and 11, respectively.

2.6.1 Spotlight Data Collection Geometry

The spotlight data collection model begins with an orthogonal XYZ coordinate system with origin at the center of the scene being imaged. The XY plane is the *focus target plane*; the IFP selects parameters to optimally focus scatterers located in this plane. Normally, the nominal ground plane is chosen as this focus target plane, although a different choice is acceptable.

The data collection model considers a SAR sensor installed in a moving platform. The sensor travels a relatively linear path, nominally in the positive X direction. In spotlight mode, it illuminates a fixed area of terrain about the selected scene center. This model assumes monostatic operation in which a single sensor both transmits and receives. It does not encompass the bistatic case with separate platforms for transmit and receive subsystems. Figure 2.21 illustrates the monostatic data collection geometry. The IFP converts the geometric information it needs into this coordinate system.

Over time, the SAR community has established a nomenclature for this data collection geometry and for subsequent processing and image geometries. The following definitions of these terms correspond to the data collection model in Figure 2.21.

The *antenna phase center* (APC) is a point from which the energy transmitted by the SAR antenna appears to originate based on its far-field phase curvature and on which energy collected by the SAR antenna focuses. The APC serves as the best geometric reference point for the collected signal history data. The geometric location of the APC at the center of the processing aperture is the *aperture reference point* (ARP).

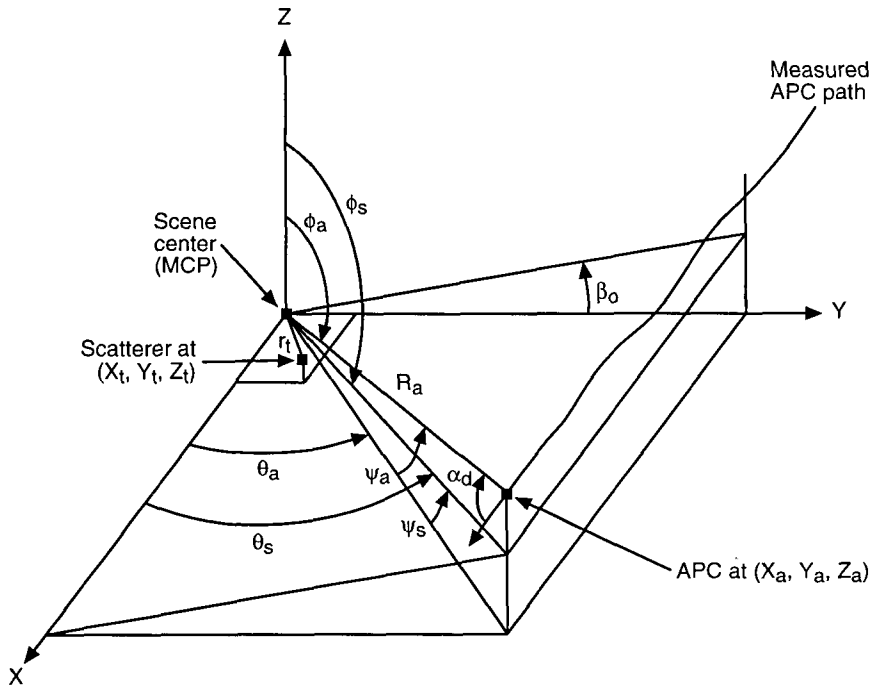


Figure 2.21 Data collection geometry.

The *scene center* is the point that will be the center of the resulting image. The scene center is also the motion compensation point (MCP) or the central reference point. The SAR motion sensor must accurately derive the position history of the APC with respect to the MCP to synthesize the long antenna needed to achieve fine azimuth resolution.

The *target location vector*, $\boldsymbol{r}_t = (X_t, Y_t, Z_t)$, is the vector from scene center to a scatterer at (X_t, Y_t, Z_t). Its magnitude r_t is

$$r_t = \sqrt{X_t^2 + Y_t^2 + Z_t^2} \tag{2.38}$$

The *slant range vector*, $\boldsymbol{R}_a = (X_a, Y_a, Z_a)$, is the measured LOS vector from scene center to the APC. Its magnitude R_a, denoted *slant range*, is

$$R_a = \sqrt{X_a^2 + Y_a^2 + Z_a^2} \tag{2.39}$$

where (X_a, Y_a, Z_a) represents the measured position of the APC. The APC position varies with time. The *data collection surface* is the surface traced by the slant range vector during data collection. Section 3.8 shows that, when the slant range vector traces out a nonplanar surface, available motion compensation algorithms compensate optimally only for scatterers in the selected focus plane.

In general, the slant range vector and its components represent the measured values used for motion compensation and data formatting in the IFP. Similarly, the angles defined below based on these measurements are measured values also. This designation as measured values generalizes the model to include the possibility of error in measurement of APC motion. In the absence of any such error, these measured values equal the actual values.

The instantaneous SAR *slant plane* is the plane containing the instantaneous APC velocity vector and the instantaneous slant range vector. The slant plane varies over time since the data collection generally occurs on a three-dimensional surface, not on a two-dimensional plane. For this reason, the SAR slant plane is not a particularly useful concept.

The *image display plane* (IDP) is the plane onto which the IFP projects or positions scatterers in the three-dimensional scene. This projection proceeds, first, from the scatterer location to the instantaneous slant plane at the aperture center along an iso-range-Doppler circle. From this point, the projection continues to the IDP along a line orthogonal to the instantaneous slant plane (Section 8.5). A reasonable fit to the nominal data collection surface is a common choice for the IDP. The focus plane is also a logical choice which more closely preserves target shape and size relationships as an aid to image interpretation. The model under development here selects an IDP to include the X axis since the sensor travels nominally in the positive X direction. The angle β_o between the IDP and the XY plane specifies the IDP. Figure 2.22 depicts an example of the focus plane and an IDP selected in this way. The angle β_o between the IDP and the XY plane is the *slope angle* for the IDP. Figure 2.22 also displays the data collection surface.

The instantaneous *grazing angle* is the angle ψ_a between the instantaneous slant range vector and the XY plane. This angle is available from

$$\sin(\psi_a) = \frac{Z_a}{R_a} \tag{2.40}$$

The grazing angle of an image refers to the grazing angle ψ_{ac} defined at the ARP for that image.

The instantaneous *incidence angle* is the angle ϕ_a between the Z axis and the instantaneous slant range vector. This angle is available from

$$\cos(\phi_a) = \frac{Z_a}{R_a} \tag{2.41}$$

The incidence angle of an image refers to the incidence angle ϕ_{ac} defined at the ARP for that image.

The instantaneous *Doppler cone angle* (*cone angle,* for short) is the angle α_d measured between the instantaneous APC velocity vector and the instantaneous slant range vector. The cone angle α_{dc} of an image refers to the cone angle at the ARP for that

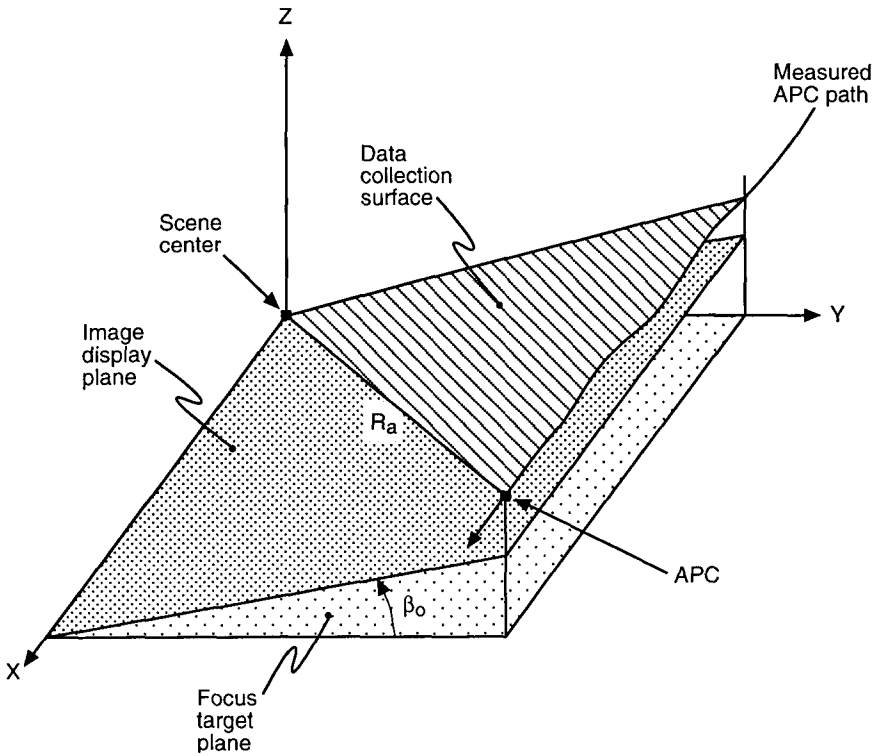


Figure 2.22 SAR collection planes.

image. The case $\alpha_{dc} = 90$ deg defines a *broadside* image or a *broadside* data collection. The locus of points at a given instantaneous cone angle forms the surface of a cone with apex at the APC. This surface is an iso-Doppler surface because all scatterers on this surface have the same Doppler frequency. We choose to apply the convention of positive Doppler cone angle for right-looking imaging situations and negative cone angle for left-looking imaging situations. This distinction is needed to proceed with the processing operations in an unambiguous manner. Since the sensor travels nominally in the positive X direction, the current model deals with a right-looking geometry with cone angle on the interval $[0, \pi]$.

The instantaneous *squint angle* is the angle in the XY plane between the X axis and the vertical (Z) projection of the slant range vector onto the XY plane. This angle is available from

$$\cot(\theta_a) = \frac{X_a}{Y_a} \tag{2.42}$$

The squint angle of an image refers to the squint angle θ_{ac} defined at the ARP for that image.

The instantaneous *display squint angle* is the angle between the X axis and the vertical projection of the slant range vector onto the IDP. This angle is available from

$$\cot(\theta_s) = \frac{X_a \cos(\beta_o)}{Y_a} \tag{2.43}$$

The display squint angle of an image refers to the display squint angle θ_{sc} defined at the ARP for that image.

The instantaneous *display grazing angle* is the angle between the vertical projections of the slant range vector onto the IDP and the XY plane. This angle is available from

$$\sin(\psi_s) = \frac{Y_a \cos(\theta_s) \tan(\beta_o)}{X_a} \tag{2.44}$$

The display grazing angle of an image refers to the display grazing angle ψ_{sc} defined at the ARP for that image.

The instantaneous display *incidence angle* is the angle ϕ_s between the Z axis and the vertical projection of the instantaneous slant range vector onto the IDP. This angle is available from

$$\cos(\phi_s) = \frac{Y_a \cos(\theta_s) \tan(\beta_o)}{X_a} \tag{2.45}$$

It is the complement of the instantaneous display grazing angle. The display incidence angle of an image refers to the incidence angle ϕ_{sc} defined at the ARP for that image.

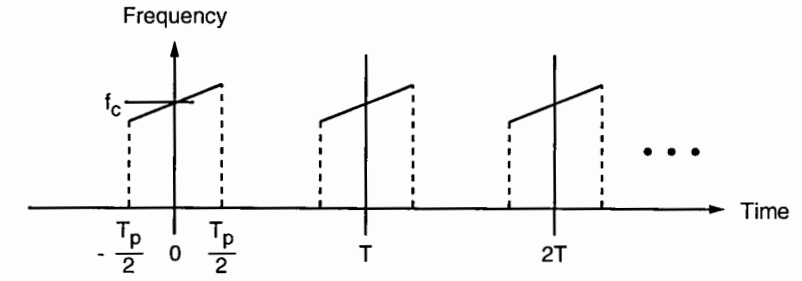
These angles and other quantities are illustrated in Figure 2.21 and Figure 2.22. The ground terrain and associated targets being imaged are in or near the XY plane. Data collection in spotlight mode requires a single pass with the SAR antenna pointed continuously at the scene being imaged.

2.6.2 Transmitted Signal—Linear FM Chirp

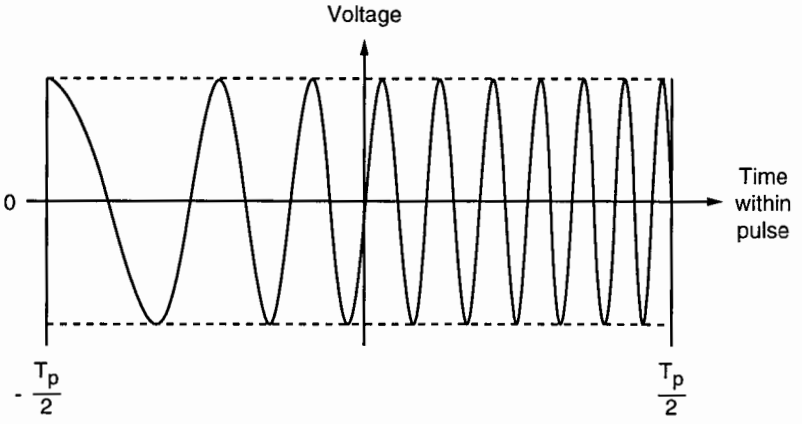
This section derives the signal that the SAR system generates and transmits. The radar transmits pulses using a linear FM chirp signal with chirp rate γ, interpulse period T, and center frequency f_c. These pulses exit the transmitter with a signal $s_t(n,t)$ of the form

$$s_t(n,t) = A(t) \cos\left[2\pi f_c t + \pi\gamma(t - nT)^2\right] \tag{2.46}$$

Here, the quantity n is pulse number with $n = 0$ representing the first transmitted pulse. The expression $t - nT$ represents fast time, that is, time within a signal received from a



(a)



(b)

Figure 2.23 Linear FM pulse train: **(a)** Pulse sequence; **(b)** Waveform.

specific transmitted pulse and referenced to the time of pulse generation. Figure 2.23 illustrates this pulse train and waveform.

It is convenient to select a rectangular pulse shape of amplitude A_o for $A(t)$ and to use the complex exponential form to represent this real signal. Defining $\hat{t} = t - nT$, the transmitted signal (point 1 in Figure 2.3) becomes

$$s_x(n,t) = A_o \text{rect}\left(\frac{\hat{t}}{T_p}\right) e^{j\left[2\pi f_c t + \pi\gamma\hat{t}^2\right]} \tag{2.47}$$

where T_p is the transmitted pulse length. The definition of the *rect*( ) function in (2.47) is

$$\text{rect}(u) = \begin{cases} 1, & |u| \le \frac{1}{2} \\ 0, & |u| > \frac{1}{2} \end{cases} \tag{2.48}$$

The expression for the transmitted signal in (2.47) does not incorporate the effects of the transmit amplifier and waveguide dispersion on the signal. It does not include the time delay for the signal to reach the antenna. Subsequent analysis suppresses the amplitude A_o of the transmitted signal. These effects do not contribute to the understanding of the SAR signal and image formation techniques.

2.6.3 Received Signal

This section develops an equation for the signal phase received by a SAR system from a single scatterer at scene coordinates (X_t, Y_t, Z_t). This development assumes an ideal point scatterer of radar cross-section $\sigma_t(X_t, Y_t, Z_t)$ with amplitude and phase characteristics which do not vary with frequency and aspect angle. This assumption is realistic for many scatterers over the limited RF bandwidth and small interval of coherent aspect angle required in SAR imaging. For simplicity, this model ignores antenna gain, amplitude effects of propagation on the signal, and any additional time delays due to atmospheric effects. The signal (point 2 in Figure 2.3) received from a single point target at (X_t, Y_t, Z_t) at pulse n is

$$s_r(n, t) = a_t \operatorname{rect}\left(\frac{\hat{t} - t_d}{T_p}\right) e^{j2\pi f_c (t - t_d)} e^{j\pi\gamma(\hat{t} - t_d)^2} \tag{2.49}$$

where $a_t = \sqrt{\sigma_t}$ and t_d is the total time delay from the transmit antenna to the target and back to the receive antenna. It is appropriate to view the received signal as a two-dimensional signal in the coordinates n and $\hat{t}$. Because the received signal (voltage) is proportional to the square root of σ_t, the quantity a_t is appropriate in the signal equations here.

The derivation of (2.49) ignores any attenuation due to the two-way propagation of transmitted energy to the scene and back to the radar. In fact, the amplitude of the received signal will be a function of many factors including the amplitude of the transmitted signal, distance to the target, and gain of the antenna, in addition to the RCS of the target. Normally the radar will illuminate a complex scene consisting of numerous individual scatterers and the received signal will equal the coherent sum of all returns over the receive data window.

In general, the quantity t_d includes the three categories of relative motion described in Section 2.5.3.5. That is, it includes motion between successive transmitted pulses, motion during transmission and reception of a pulse, and motion between transmission and reception of a pulse. An accurate expression for t_d that incorporates these features depends on fast time, the rate of change of R_t, and on R_t itself. In fact, relative motion during and between pulse transmission and reception does occur; principally, it introduces a space-invariant defocus effect and small distortion effects. If necessary, it is possible to remove this defocus with a reasonable effort because the defocus is space-invariant.

Although these additional effects can become significant as pulse lengths increase and relative motion between the APC and the target becomes faster, typically they are small.

Because these additional effects are usually not significant, it is common practice to make the simplifying assumption that the sensor is stationary during pulse transmission and reception while moving in discrete increments between pulses. We will make this assumption throughout this analysis. In this situation, an adequate approximation for t_d is

$$t_d \approx \frac{2R_t}{c} \tag{2.50}$$

In this expression, R_t is the distance from the actual location of the APC to the point target at the time, $t = nT$ for pulse n. Using this result, (2.49) becomes

$$s_r(n,t) = a_t \,\mathrm{rect}\left(\frac{\hat{t} - 2R_t/c}{T_p}\right) e^{j2\pi f_c\left(t-\frac{2R_t}{c}\right)} e^{j\pi\gamma\left(\hat{t}-\frac{2R_t}{c}\right)^2} \tag{2.51}$$

The distance $R_t(n)$ varies from pulse to pulse. An exact expression for this quantity is

$$R_t = \sqrt{(X_a + X_e - X_t)^2 + (Y_a + Y_e - Y_t)^2 + (Z_a + Z_e - Z_t)^2} \tag{2.52}$$

The slant range vector $\boldsymbol{R_a} = (X_a, Y_a, Z_a)$ of magnitude R_a represents the measured, time-varying APC position during the data collection. The vector $\boldsymbol{R_e} = (X_e, Y_e, Z_e)$ represents any error in motion measurement. Figure 2.24 illustrates these quantities. For most purposes, this model assumes the altitude Z_a and the coordinate Y_a of the APC are constant at Z_{ac} and Y_{ac}, respectively. Similarly, the model assumes the along-track X_a location varies linearly with pulse number as $X_{ac} + V_{xa}(n - n_c)T$ as a result of the constant along-track velocity V_{xa}. Here, n_c represents the pulse transmitted with the sensor located at the aperture reference point (ARP) with coordinates (X_{ac}, Y_{ac}, Z_{ac}). The ARP is the center of the azimuth processing aperture. In some instances, a more general expression for measured antenna position variations over time is useful. In these cases, the model allows a general quadratic maneuver with nonzero X, Y, and Z components of the measured position vector $\boldsymbol{P_a} = (X_{ac}, Y_{ac}, Z_{ac})$, the measured velocity vector $\boldsymbol{V_a} = (V_{xa}, V_{ya}, V_{za})$, and the measured acceleration vector $\boldsymbol{A_a} = (A_{xa}, A_{ya}, A_{za})$ at aperture center. The slant range vector in the form

$$\boldsymbol{R_a} = \boldsymbol{P_a} + \boldsymbol{V_a} n_\Delta T + 0.5\boldsymbol{A_a}(n_\Delta T)^2 \tag{2.53}$$

represents low-frequency variations in measured position from pulse to pulse over the coherent aperture time centered at pulse n_c, for convenience defining $n_\Delta = n - n_c$. The vectors $\boldsymbol{P_a}$, $\boldsymbol{V_a}$, and $\boldsymbol{A_a}$ represent measured position, velocity, and acceleration, respectively, at pulse n_c.

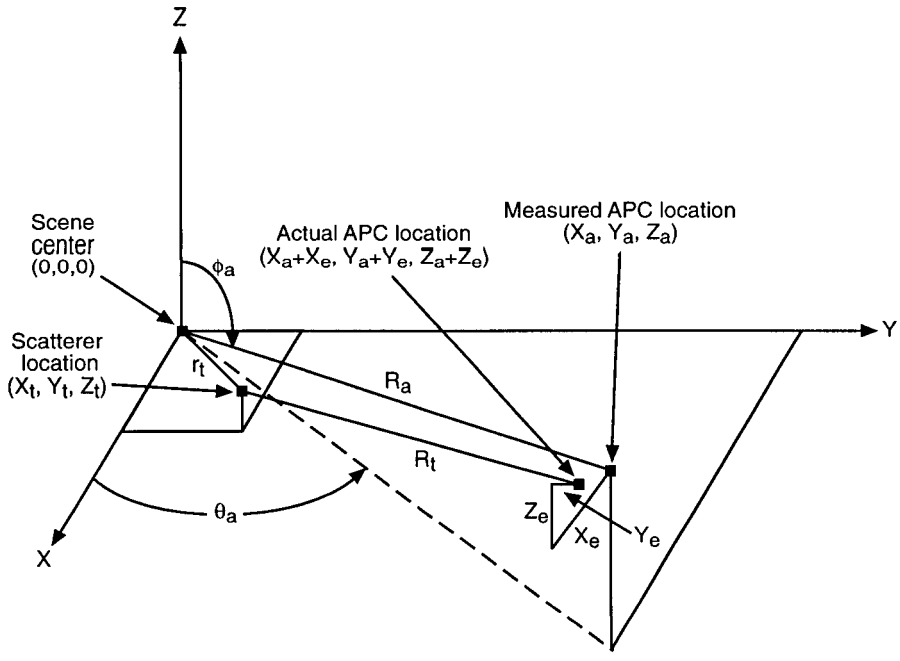


Figure 2.24 Measured and actual locations and distances in the data collection geometry.

Except to evaluate the effects of errors in motion measurement, the model assumes that X_e, Y_e, and Z_e are identically zero. To evaluate the effects of errors in motion measurement, the model requires an expression for variations in motion measurement error over time. In these cases,

$$\boldsymbol{R}_e = \boldsymbol{P}_e + \boldsymbol{V}_e n_\Delta T + 0.5\boldsymbol{A}_e (n_\Delta T)^2 \tag{2.54}$$

represents low-frequency variations in measurement error from pulse to pulse over the coherent aperture centered at pulse n_c. Vectors $\boldsymbol{P}_e = (X_{ec}, Y_{ec}, Z_{ec})$, $\boldsymbol{V}_e = (V_{xe}, V_{ye}, V_{ze})$, and $\boldsymbol{A}_e = (A_{xe}, A_{ye}, A_{ze})$ represent position, velocity, and acceleration measurement errors at pulse n_c, respectively.

2.6.4 Demodulated Signal

The last analog signal conditioning step before sampling the received signal is demodulation. It is common at this point in fine-resolution spotlight mode operation to dechirp the signal in range as a part of this demodulation. A spotlight mode system, occasionally, and stripmap or scan mode systems, often, will not perform this dechirp. We choose to include the dechirp operation in the model development here. This operation usually involves a

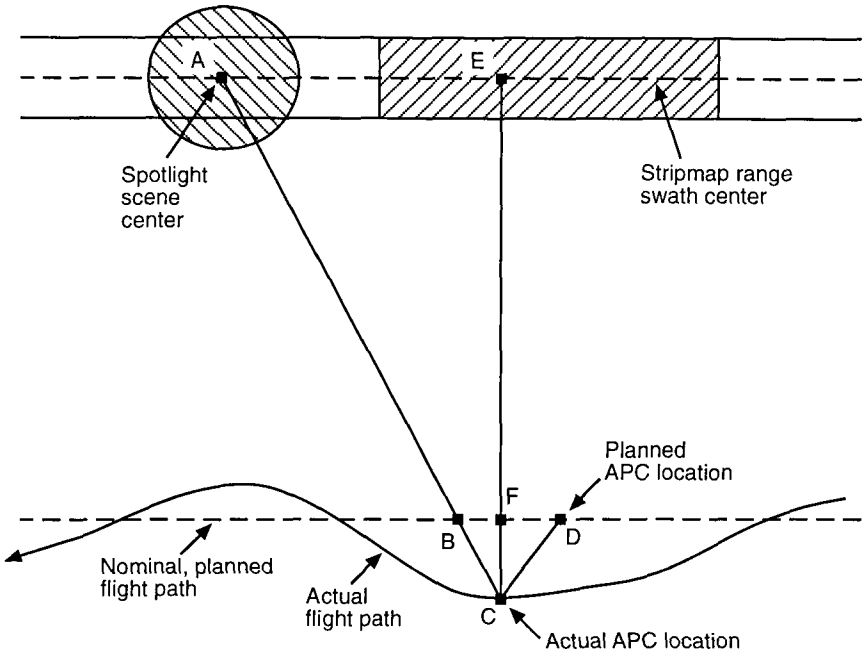


Figure 2.25 Motion compensation comparison.

multistage frequency conversion and filtering. The radar demodulates the received signal by mixing it with a replica of the transmitted waveform (point 3 in Figure 2.3) delayed by a time $2R_o/c$. It is common to employ this dechirp-on-receive procedure in wide-bandwidth (fine-resolution) systems to reduce the required A/D sample rate and the digital buffer speed and size requirements.

At this point in the model, we also have the opportunity to select and apply a motion compensation strategy. The choice of motion compensation involves a choice between spotlight mode and stripmap mode.

Stripmap and spotlight modes differ in selection of a motion compensation signal, method of its introduction, and its effect. Figure 2.25 illustrates this difference. The signal returned from a single transmitted pulse contains reflected signals from each scatterer in the illuminated scene. Spotlight compensates each pulse exactly for the scatterer at scene center to convert this scatterer's signal to a constant phase, ideal with respect to measured antenna motions. In Figure 2.25, the spotlight mode compensates for the distance AC and treats the data as if it came from point B in subsequent processing. Scatterers away from scene center suffer some image degradation even when the system applies a motion compensation that is perfect for scene center. This degradation occurs because the LOS component of any motion deviation varies slightly as a function of angle to the target. This target-location-dependent effect is usually small and generally not of consequence even in

modern fine-resolution systems operating at higher frequencies (for example, L-band, X-band, and K-band). Other factors typically place an upper bound on scene size before this motion effect becomes significant.

In broadside stripmap mode, on the other hand, compensation occurs for the component of motion deviation normal to the nominal flight path for every position (pulse) along the synthetic aperture. Stripmap mode compensates for the distance CF in Figure 2.25 and treats the data in subsequent processing as if it came from point F. This procedure does not provide motion compensation perfectly for any scatterer. Rather it compensates exactly for each scatterer for the pulse when a particular scatterer is broadside; it compensates only approximately for pulses from all other angles to the scatterer. The result is that the azimuth impulse response is invariant with azimuth scatterer location (unlike spotlight) but is never perfect in the presence of sensor motion deviations.

This difference in motion compensation strategy is a serious consideration when generating a stripmap image over large azimuth angles of tens of degrees. Such a situation is necessary for low-frequency (for example, VHF) SAR systems at fine resolution, the direction of current research and system development for ground and foliage penetration applications [36].

We choose to proceed with the spotlight model here and provide a motion compensation signal during demodulation aimed at stabilizing the signal received from scene center. The radar incorporates a real-time motion compensation operation by mixing the received signal $s_r(n, t)$ of (2.51) with a reference function $s_{ref}(n, t)$ to produce the intermediate frequency (IF) signal $s_{if}(n, t)$. The reference signal (point 3 in Figure 2.3) is

$$s_{ref}(n, t) = e^{j\left[2\pi f_c\left(t - \frac{2R_o}{c}\right) + \pi\gamma\left(\hat{t} - \frac{2R_o}{c}\right)^2\right]} \tag{2.55}$$

Again, the model does not include the effects of any receiver waveguide dispersion on the signal nor any receiver filter and waveguide time delays.

The reference range $R_o(n)$ is designed to track the measured slant range $R_a(n)$ from the APC to the scene center. The slant range changes significantly as the radar moves along its path. Spotlight SAR systems often use a range-tracking technique in real time to provide a coarsely quantized version of R_a to use as a reference range R_o. Accuracy requirements on R_o are not severe. Accuracy must be sufficient to keep the scene area within the recorded range swath. This approach reduces the collected range bandwidth without requiring extremely accurate real-time motion measurement. Fine motion compensation and signal formatting procedures in the IFP take care of the differences between R_a and R_o.

Since R_o tracks the nominally quadratic variation in R_a, the mixing operation accomplishes a dechirp in azimuth as well as in range. The IF signal (point 4 in Figure 2.3) that results from mixing (2.51) with (2.55) is

$$s_{if}(n, \hat{t}) = a_t \,\mathrm{rect}\left(\frac{\hat{t} - 2R_t/c}{T_p}\right) e^{-j\frac{4\pi(f_c + \gamma\hat{t})}{c}(R_t - R_o)} e^{j\frac{4\pi\gamma}{c^2}(R_t^2 - R_o^2)} \tag{2.56}$$

It is convenient to write this equation in the form

$$s_{if}(n,\hat{t}) = a_t \,\mathrm{rect}\left(\frac{\hat{t}-2R_t/c}{T_p}\right) e^{-j\frac{4\pi\gamma}{c}\left(\frac{f_c}{\gamma}+\hat{t}-\frac{2R_o}{c}\right)(R_t-R_o)} e^{j\frac{4\pi\gamma}{c^2}(R_t-R_o)^2} \tag{2.57}$$

After this real-time motion compensation, it is desirable that the signal corresponding to a target at scene center have zero range frequency and zero Doppler frequency. The quantized approximation to R_a is sufficiently accurate to make the range frequency approximately zero, typically to within a frequency corresponding to a few meters of range. Often, however, R_o is not a sufficiently accurate estimate of R_a to make the azimuth frequency zero; that is, it does not accomplish Doppler signal stabilization.

To analyze this situation in azimuth, it is useful to rewrite the dechirp reference range R_o using

$$R_o = R_a + R_q \tag{2.58}$$

where R_a is the measured range from the antenna to scene center, R_o is the real-time and quantized estimate of R_a used in real-time compensation, and R_q is the estimation and quantization error. In practice, R_q is a small distance, typically less than a few meters. The radar uses R_o in (2.55) as the demodulation signal whereas R_a is the ideal value to use. The difference between using these two values is the phase

$$\Phi_{rmc}(n,\hat{t}) = \frac{4\pi\gamma}{c}\left(\frac{f_c}{\gamma}+\hat{t}-\frac{2R_o}{c}\right)R_q + \frac{4\pi\gamma}{c^2}R_q^2 \tag{2.59}$$

This phase represents the residual motion compensation provided by the IFP and equals the phase of the signal returned by a scatterer at scene center after demodulation in the receiver. Thus, (2.59) equals the phase in (2.57) with $R_t = R_a$. With nonzero R_q, the range frequency of scene center is nonzero as indicated by the coefficient of the $\hat{t}$ term. This frequency is small, however, compared to that of targets at the near-range or far-range edges of the scene. The azimuth frequency of scene center depends on the variations in both R_q and R_a over the azimuth aperture interval. These variations can lead to severe phase effects in the azimuth signal. The fine motion compensation operation in the IFP removes the residual range frequency and azimuth phase from the signal returned by a scatterer located at scene center.

A SAR system that uses the dechirp-on-receive approach to accomplish bandwidth reduction is initiating the signal processing, normally associated with the IFP, in the receiver. First, this procedure reduces the remaining signal compression operation in range to a fast-time Fourier transform and, second, it performs an approximation to the motion compensation operation.

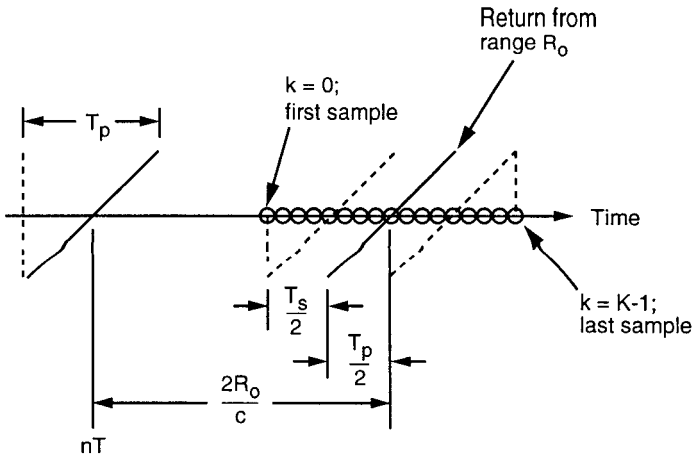


Figure 2.26 Timing diagram for A/D samples.

2.6.5 Sampled Signal

A traditional SAR system necessarily accomplishes the preceding steps in real time using analog RF techniques to achieve the demodulated IF signal. With the advent of extremely high speed digital components, the IF signal is amenable to A/D conversion, bringing subsequent operations into the digital realm. Following the sampling of the demodulated signal by the A/D converter at the appropriate sampling rate, the final step in motion compensation involves complex digital-multiply operations. The model assumes that A/D sampling begins at the same time as the dechirp starts. Time delays in filters potentially require adjustments to motion compensation and data formatting operations; these complications in the processing algorithm are beyond the scope of this discussion.

The A/D converter samples the video signal at the times $t_s(n, k)$ where

$$t_s(n,k) = \frac{k}{F_s} + nT + \frac{2R_o}{c} - \frac{T_p}{2} - \frac{T_s}{2} \tag{2.60}$$

This equation represents the time of sample k of K samples in pulse number n of N_p pulses. The quantity F_s is the A/D sampling frequency and T_s is the time interval associated with the range window Δr. The form of T_s is

$$T_s = \frac{2\Delta r}{c} \tag{2.61}$$

Figure 2.26 illustrates the timing in (2.60) with $k = 0$ and $k = K - 1$ representing the first and last samples, respectively, in pulse n. From the time corresponding to the return of the center of the pulse from the quantized reference range R_o, the A/D trigger for the first

sample steps back by $T_p/2$ to the start of the pulse and back $T_s/2$ to the start of the range window. The total sampling time is $T_S = T_s + T_p$.

The phase of the signal from a hypothetical scatterer at scene coordinates (X_t, Y_t, Z_t) for sample (n, k) in two-dimensional sample space is available by using t_s from (2.60) for t (that is, for $\hat{t} + nT$) in (2.57). The result is

$$\Phi_1(n,k) = -\frac{4\pi\gamma}{c}\left(\frac{f_c}{\gamma} + \frac{k}{F_s} - \frac{T_p}{2} - \frac{T_s}{2}\right)(R_t - R_o) + \frac{4\pi\gamma}{c^2}(R_t - R_o)^2 \tag{2.62}$$

The model assumes transmission of N_p pulses where N_p is an even number. The slow time variable n associated with pulse number takes on integer values between 0 and $N_p - 1$. The first chirp starts at time $t = -T_p/2$ and ends at $t = T_p/2$ with subsequent chirps centered at $t = nT$. The fast time variable k takes on integer values between 0 and $K-1$. The two-dimensional, digitized signal (point 5 in Figure 2.3) becomes

$$s_d(n,k) = a_t \sum_{n=0}^{N_p-1}\left[\sum_{k=0}^{K-1} e^{j\Phi_1(n,k)}\right] \tag{2.63}$$

to encompass K samples per pulse over N_p pulses.

2.6.6 Fine Motion Compensation

Fine motion compensation and signal formatting procedures in the IFP take care of differences between R_a and R_o including quantized dechirp delay times and post-collection refinements in estimates of R_a. It is possible also to tailor the recompensation signal to account for other peculiarities of the radar design such as filter time delays and quantized delay time to start of A/D sampling.

The first signal processor step to complete the compensation for measured APC motion is to multiply the demodulated and sampled receive signal by a unity amplitude, sampled signal with phase equal to the negative of (2.59). This fine motion compensation signal corresponds to the conjugate of the expected signal from a point scatterer located at scene center. The measured slant range from the instantaneous APC to scene center R_a and the quantized dechirp time delay R_o provide the quantities needed to generate the motion compensation signal. The result of this stabilization step is the digitized signal

$$s_o(n,k) = a_t \sum_{n=0}^{N_p-1}\left[\sum_{k=0}^{K-1} e^{j\Phi(n,k)}\right] \tag{2.64}$$

with phase

$$\Phi(n,k) = -\frac{4\pi\gamma}{c}\left(\frac{f_c}{\gamma} + \frac{k}{F_s} + \frac{2R_o}{c} - \frac{2R_a}{c} - \frac{T_s}{2} - \frac{T_p}{2}\right)(R_t - R_a) + \frac{4\pi\gamma}{c^2}(R_t - R_a)^2 \tag{2.65}$$

This final signal stabilization step maintains the return from scene center at constant phase regardless of antenna motion as long as no error in motion measurement exists. This space-invariant motion compensation is generally adequate within a spotlight scene. This procedure completes the first step of the motion compensation described in four steps in Section 2.5.3.1. Chapter 3 describes the procedures for the remaining three steps. The IFP accomplishes compensation for the *relative* rotational motion of other targets through resolution cells by using the polar format algorithm. It compensates for changes in the range gate during the coherent aperture by adjusting the polar format.

For reference, the counterpart to (2.64) in analog form before A/D sampling is

$$s_o(n,\hat{t}) = a_t \sum_{n=0}^{N_p-1} \left[\text{rect}\left(\frac{\hat{t} - 2R_t/c}{T_p} \right) e^{j\Phi(n,\hat{t})} \right] \tag{2.66}$$

with

$$\Phi(n,\hat{t}) = -\frac{4\pi\gamma}{c}\left(\frac{f_c}{\gamma} + \hat{t} - \frac{2R_a}{c} \right)(R_t - R_a) + \frac{4\pi\gamma}{c^2}(R_t - R_a)^2 \tag{2.67}$$

As a reminder, in the general case which allows error in motion measurement, R_a is the distance between scene center and the *measured* APC location and R_t is the distance between the target and the *actual* location of the APC.

2.6.7 Components of Signal Phase Equation

Table 2.3 identifies the individual components of the sampled signal phase given by (2.65) and its analog equivalent (2.67). The *Doppler frequency term* (involving f_c) is responsible for positioning scattering centers in azimuth and for achieving azimuth resolution. Over a small azimuth processing aperture, the quantity $R_t - R_a$ varies in an approximately linear fashion. Thus, the Doppler frequency term has approximately a linear phase variation (constant frequency) over the aperture. The slope of this linear phase determines the location of the scatterer's impulse response in the azimuth Fourier transform domain, corresponding to the azimuth image domain. The processing aperture size determines the duration of the azimuth signal which, together with transmitted frequency, in turn determines azimuth resolution. Since $R_t - R_a$ is only approximately linear, the phase of the Doppler frequency term is not precisely linear in the azimuth dimension. It is the goal of the SAR image formation processing algorithm to linearize this phase for all scatterers within the imaged scene. Chapter 3 discusses these issues in more detail and describes the polar format algorithm as one approach for improving the phase linearity of the Doppler frequency term.

Similarly, the *range frequency term* of the signal phase equation is responsible for positioning scattering centers in range and achieving range resolution. This term involves the fast-time variable k/F_s in the sampled signal and $\hat{t}$ in the analog representation of the

signal. For a single pulse, a scatterer at a distance R_t from the APC has a range frequency of $-2\gamma(R_t - R_a)/c$. This frequency is proportional to the scatterer's LOS distance from scene center $R_t - R_a$. A Fourier transform of the pulse compresses the scatterer's response and correctly positions it within the imaged range swath. From Section 2.3.2, transmitted bandwidth B governs achievable range resolution. This bandwidth is the product of the radar chirp rate γ and the pulse duration T_a.

The *residual video phase* (RVP) term contains the square of $R_t - R_a$. This phase term is an unwanted artifact arising from the range dechirping process. It does not contribute positively to geometric positioning or resolution of scattering centers in either range or azimuth. On the contrary, if sufficiently large, the presence of this phase can introduce geometric distortion and degradation of the azimuth impulse response. Typically, RVP is small and the image formation procedure can safely ignore it without a serious impact on image quality. Appendix C presents a procedure for removing RVP from collected signal history data, if necessary.

Table 2.3
Components of Signal Phase Equation

Component Name	*Expression in Sampled Signal Phase Equation*	*Expression in Analog Signal Phase Equation*
Doppler frequency term	$-\frac{4\pi\gamma}{c}\left(\frac{f_c}{\gamma}\right)(R_t - R_a)$	$-\frac{4\pi\gamma}{c}\left(\frac{f_c}{\gamma}\right)(R_t - R_a)$
Range frequency term	$-\frac{4\pi\gamma}{c}\left(\frac{k}{F_s} + \frac{2R_o}{c} - \frac{2R_a}{c} - \frac{T_s}{2} - \frac{T_p}{2}\right)(R_t - R_a)$	$-\frac{4\pi\gamma}{c}\left(\hat{t} - \frac{2R_a}{c}\right)(R_t - R_a)$
Residual video phase	$\frac{4\pi\gamma}{c^2}(R_t - R_a)^2$	$\frac{4\pi\gamma}{c^2}(R_t - R_a)^2$

2.7 INVERSE SAR

Inverse SAR (ISAR) imaging, in its narrowest sense, refers to the use of target motion alone to generate a synthetic aperture for azimuth resolution. In practice, ISAR often includes antenna platform motion. ISAR applications include rotating platform (turntable) imaging facilities, imaging of maneuvering aircraft or ground-moving vehicles from either stationary ground-based radars or maneuvering SAR platforms, and ground-based imaging of planets and earth satellites.

ISAR may also encompass imaging a ground-moving target or a surface ship during an airborne SAR data collection. Without any special processing operations to account for the rotational motion of a moving target, this data collection represents a conventional SAR operation with the complication of space-variant, uncompensated motion of any moving targets. If the processor attempts to take into account the target's rotation in

formatting the data and in calculating the aspect angle interval for azimuth resolution, then this combination of data collection and image formation represents an ISAR operation.

2.7.1 ISAR Geometry

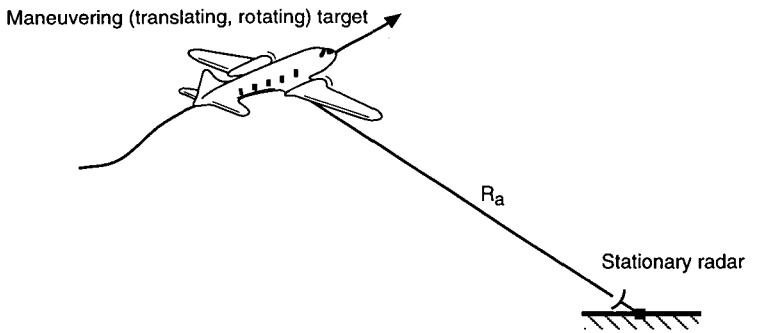
Figure 2.27(a) illustrates the ISAR concept and geometry. It shows a stationary radar sensor illuminating a passing airborne target. The target's velocity and attitude changes (roll, pitch, and yaw) each contribute to the angular interval over which the radar sensor collects data from the target. It is common to model an ISAR data collection and process ISAR data by treating it as an equivalent maneuvering SAR illuminating a stationary target. Figure 2.27(b) illustrates this perspective. The actual target motions determine the equivalent maneuvering SAR flight path for this ISAR data collection from a stationary target perspective. Section 2.7.2 examines this perspective in detail.

In ISAR imaging, the orientation of the iso-range-Doppler circles depends on the direction of the target's rotation vector relative to the radar during the processing interval. These circles direct the projection of the target's reflectivity distribution onto a two-dimensional image space. The target's rotation vector is likely to vary with time because ground-moving targets, aircraft in flight, and ships move with changing direction and velocity and with time-varying components of roll, pitch, and yaw. Thus, the orientation of the iso-range-Doppler circles likely will vary from interval to interval, providing a variety of views of the target.

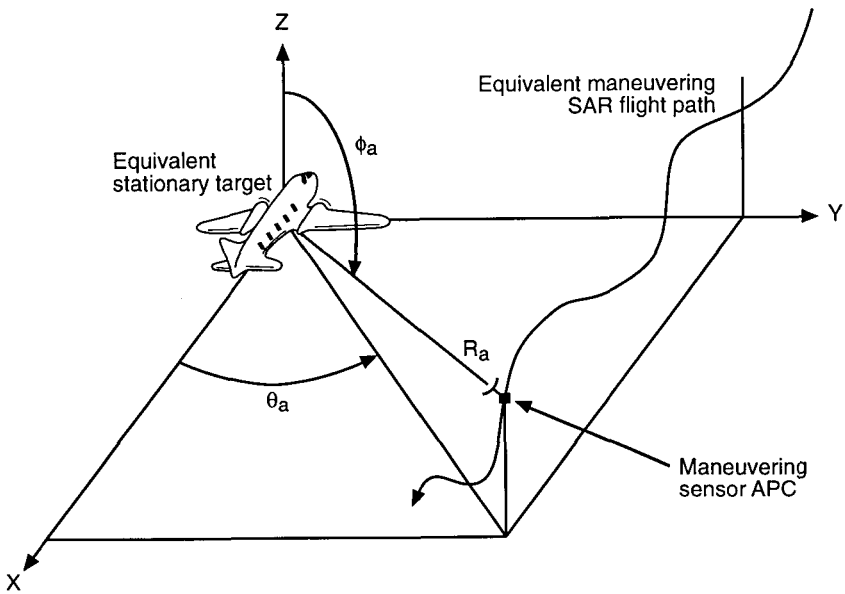
Rotating platform imaging is uncomplicated because the target motion is precisely known and of a constant rotation rate about a fixed axis. A rotating platform facility is useful for signature analysis and as an RCS measurement range. Space-object imaging (SOI), including imaging of planets from a fixed ground-based radar, is a challenging application of ISAR. Another realistic and relevant application of ISAR is airborne imaging of ships at sea utilizing the target's pitch and roll motions to generate the synthetic aperture. Somewhat more challenging are the imaging of airborne targets from any ground or airborne platform and of ground-moving targets from airborne platforms. These latter situations are made difficult either by competing clutter environments or by unpredictable broadband target rotational and translational motions. The target's motion will not be suitable for imaging at all times.

Differences between conventional SAR and ISAR data collection and processing occur primarily in the azimuth direction. In range, compression of a wide-bandwidth transmitted radar signal to achieve fine resolution is identical in both situations. In azimuth, SAR and ISAR differ in the methods they use to achieve and the methodology they use to estimate (or measure) pulse-to-pulse relative translational and rotational motion of the target. They also differ in the means they use to implement any compensation of the data required by the relative motions. In conventional SAR imaging, an inertial sensor usually measures this information during the data collection.

Image formation for an ISAR system may utilize an interactive, signature-based processing technique known as prominent point processing (Section 6.5). The idea is to isolate the signal from a prominent point in the target field for use as a reference signal,



(a)



(b)

Figure 2.27 ISAR concept and geometry perspective: (**a**) Moving target; (**b**) Maneuvering sensor.

thereby cancelling space-invariant phase errors which are common to all targets. This cancellation will include motion-induced phase effects and other space-invariant phase error sources. Use of this single prominent point does not provide the information needed to address space-variant phase errors related to target rotation. Additional prominent points may be used to reduce or remove these space-variant errors. This hands-off approach to motion measurement and compensation is discussed in Section 6.5.

The single prominent point implementation relies on external data (for example, flight plan, onboard INS, or ground tracker data) to estimate variations in aspect angle and the total change in aspect angle between target and radar over the azimuth processing time. Unestimated variations in angular rate will cause image defocus whereas an error in estimating the total angular change will cause an error in azimuth scale factor resulting in scatterer location error.

In ISAR applications without measurements of target motion or with inadequate motion measurement accuracy, targets without a significant clutter background are particularly conducive to motion estimation and compensation based on the radar signals returned from the target. In these cases, target-tracking via auxiliary data (for example, the nominal velocity and heading of a passing aircraft) can be adequate for collecting and storing the data to initiate motion estimation and compensation in the processor.

2.7.2 ISAR Analytical Model

The ISAR geometry of Figure 2.27(b) presents an ISAR data collection as an equivalent maneuvering SAR illuminating a stationary target. An analytic model of this viewpoint must first establish expressions for the equivalent SAR maneuver quantities R_a, θ_a, and ϕ_a in terms of the translational and rotational components of ISAR target motion. Target attitude variations (roll, pitch, and yaw) are likely to be dominant contributors to θ_a and ϕ_a variations. Only target translational motion affects R_a. After transfer of target motion to equivalent SAR antenna motion, the SAR analytical model also provides an ISAR analytical model.

Because only relative motion is important here, it is acceptable to reverse the motion from a stationary radar and moving target to a stationary target and moving radar. With this reversal in perspective, all data collection and image planes, all angles and all geometric definitions are the same and apply equally to SAR and ISAR modeling. On this basis, the signal phase equation for ISAR at various stages in the radar follows (2.47) through (2.63). Significant differences in the magnitudes of various terms exist, depending on the type and accuracy of the measurement of relative motion between the APC and the ISAR target. In particular, the motion estimation and quantization error, R_q in (2.58), may be unusually large, leading to large variations in scene center phase as (2.59) indicates. In addition, the values for R_q may not be available with any reasonable accuracy from auxiliary sensors; in this case, fine motion compensation as described in Section 2.6.6 will not be straightforward. Rather, as Section 2.5.3 discusses and Figure 2.19 suggests, signal-derived motion compensation techniques will be necessary. Chapter 6 presents these autofocus and multiple PPP techniques.

Section 7.2 describes a processor design that provides a good example of an ISAR application without a clutter background. Section 4.7 shows a series of images from a rotating platform ISAR system described briefly in Appendix E.

2.8 SAR SENSOR PARAMETRIC DESIGN EXAMPLE

We use three tables to illustrate an example X-band SAR sensor parametric design. Design parameters include the categories of basic radar hardware parameters in Table 2.4, system performance (image quality) parameters in Table 2.5, and collection geometry and platform parameters in Table 2.6. These design parameters are consistent with each other and compatible with a ground-imaging SAR radar system with fine resolution (1 m in azimuth by 1 m in range). The parametric design supports both spotlight and stripmap operation. Section 2.3 and Section 2.4 define and explain the significance of these design parameters. Chapter 8 discusses the system performance parameters. Numerous examples of imagery consistent with such a design are contained within this book. A SAR system design typically requires that the next pulse not be transmitted until the desired backscatter signal is received from the current pulse. The design in these tables satisfies this requirement. Such a requirement does not apply to a long-range SAR system, which, because of the long two-way time delay to scene center, may have multiple pulses in transit at one time.

Table 2.4
Example Radar Hardware Parameters

Parameter	*Description*	*Value*
f_c	Center frequency	10 GHz
λ_c	Center wavelength	0.03 m
B	RF bandwidth	185 MHz
PRF	Pulse repetition frequency	1000 Hz
γ	FM chirp rate	4.8 MHz/μs
T_p	Transmitted pulse length	38.5 μs
β_a	Azimuth beamwidth	5.25 deg
β_e	Elevation beamwidth	6.25 deg
G	Antenna gain	29 dB
F_s	A/D complex sample rate	45 MHz
K	Complex samples per pulse	2048
N_p	Pulses per synthetic aperture	1950
PCR	Pulse compression ratio	7120

Table 2.5
Example System Performance Parameters

Parameter	*Description*	*Value*
ρ_r	Range resolution	1 m
ρ_a	Azimuth resolution	1 m
ISLR	Integrated sidelobe ratio	−21 dB
K_r	Mainlobe-broadening factor in range	1.23
K_a	Mainlobe-broadening factor in azimuth	1.30
	Aperture weighting function (Taylor)	−35 dB; $\bar{n} = 5$
β_s	Azimuth synthetic beamwidth	0.0057 deg
BCR	Beam compression ratio	916
MNR	Multiplicative noise ratio	−18 dB
σ_n	Additive noise coefficient	−35 dB

Table 2.6
Example Collection Geometry and Platform Parameters

Parameter	*Description*	*Value*
H	Altitude	5000 m
V_a	Forward velocity	100 m/s
R_a	Slant range	10,000 m
θ_{ac}	Squint angle	90 deg
Δr	Range scene size (slant plane)	1050 m
W_a	Azimuth scene size	916 m
T_a	Synthetic aperture time	1.95 sec
L	Synthetic aperture length	195 m
γ_a	Azimuth chirp rate	66.66 Hz/s
$\Delta\theta$	Coherent integration angle	1.12 deg
B_a	Azimuth bandwidth after dechirp	610 Hz
TB_a	Azimuth time bandwidth product	1190
B_d	Doppler bandwidth of a single scatterer before azimuth dechirp	130 Hz
B_{IF}	Range bandwidth after dechirp	33.62 MHz

In this design, it is normal for the BCR to equal the ratio of azimuth scene swath to azimuth resolution while the azimuth time bandwidth product TB_a exceeds this ratio by the azimuth mainlobe-broadening factor K_a. This difference occurs because the BCR relates to the actual azimuth resolution improvement while TB_a relates to the basic resolution, ρ_a/K_a. Similarly, in range the PCR exceeds the ratio of pulse length T_p to time delay $2\rho_r/c$ associated with a range resolution cell by the range broadening factor K_r. The K samples per pulse result from sampling at a rate F_s over the sum of the pulse length T_p plus the time delay $2\Delta r/c$ associated with the range scene size Δr. Dechirping the signal in range has reduced the bandwidth from B = 185 MHz to B_{IF} = 33.62 MHz. Dechirping the signal in azimuth has decreased the azimuth bandwidth from B_d plus B_a, which is 740 Hz, to B_a, which is 610 Hz.

Using β_s for β_a in (2.8), the real aperture length necessary to achieve ρ_a = 1 m is 268 m. This value is less than twice the synthetic aperture length L in this design by the ratio $0.89/K_a$, reflecting the effect of azimuth mainlobe-broadening in the synthetic aperture design.

2.9 SUMMARY

The heart of a SAR is the radar sensor which generates, transmits, and receives a carefully constructed radar signal. The digital IFP formulates this signal into a digital image representation of the scene radar reflectivity. To function optimally in forming the azimuth synthetic aperture, the radar sensor requires a motion sensor to track radar sensor position. This sensor combination, together with high-bandwidth pulse coding, allows the SAR system to receive signals simultaneously from millions of resolution cells and still differentiate each signal to decipher the location and radar reflectivity of each cell.

The signal equation is a formalism to substantiate this functionality. This formalism offers a mathematical model of all signal phase contributions arising from signal generation, transmission, and reception. This procedure includes demodulation, real-time motion compensation, presumming, and digitization. It continues into the IFP to include fine motion compensation and data formatting. An understanding of the signal equation is essential to design and validate a SAR system. It motivates the selection of an image formation algorithm and indicates the requirements for the IFP. It is this signal phase equation which proceeds from this chapter into Chapter 3 and succeeding chapters to motivate and illustrate digital signal processing algorithms for spotlight mode synthetic aperture radar.

REFERENCES

[1] Gallaway, W.D., K.F. Luckscheiter, E.H. Cowen, and J.W. Wilhelm, "A Direct Digitally Synthesized Exciter Achieving Near Theoretical Performance for an Operational SAR System," *IEEE National Radar Conference*, Ann Arbor, MI, 20-21 April, 1988, pp. 22-27.

[2] Bayma, R.W., and P.A. McInnes, "Aperture Size and Ambiguity Constraints for a Synthetic Aperture Radar," *1975 IEEE International Radar Conference Record*, 1975, pp. 499-504.

[3] Li, F.K., and W.T.K. Johnson, "Ambiguities in Spaceborne Synthetic Aperture Radar Systems," *IEEE Transactions on Aerospace and Electronic Systems*, Vol. AES-19, No. 3, May 1983, pp. 389-396.

[4] Kefalas, G.P., and J.C. Wiltse, *Radar Handbook*, M.I. Skolnik, Editor, Chapter 8, "Transmission Lines, Components, and Devices," New York, McGraw Hill, 1970.

[5] Willis, N.J., *Bistatic Radar*, Norwood, MA, Artech House, 1991.

[6] Lee, P.K., and T.F. Coffey, "Space-Based Bistatic Radar: Opportunity for Future Tactical Air Surveillance," *IEEE International Radar Conference*, Arlington, VA, 1985, pp. 322-329.

[7] Bhanu, B., "Automatic Target Recognition: State of the Art Survey," *IEEE Transactions on Aerospace and Electronic Systems*, Vol. AES-22, No. 4, July 1986, pp. 364-379.

[8] Dudgeon, D.E., and R.T. Lacoss, "An Overview of Automatic Target Recognition," *The Lincoln Laboratory Journal*, Vol. 6, No. 1, Spring 1993, pp. 3-10.

[9] Waltz, E.L., and J. Llinas, *Multisensor Data Fusion*, Norwood, MA, Artech House, 1990.

[10] Cook, C.E., and M. Bernfeld, *Radar Signals, An Introduction to Theory and Applications*, Orlando, FL, Academic Press, Inc., 1967.

[11] Cook, C.E., "Pulse Compression—Key to More Efficient Radar Transmission," *Proceedings of the IRE*, Vol. 48, No. 3, March 1960, pp. 310-316.

[12] Klauder, J.R., A.C. Price, S. Darlington, and W.J. Albersheim, "The Theory and Design of Chirp Radars," *The Bell System Technical Journal*, Vol. 39, No. 4, July 1960, pp. 745-808.

[13] Sheer, J.A., and J.L. Kurtz, editors, *Coherent Radar System Performance Estimation*, Norwood, MA, Artech House, 1993.

[14] Mensa, D.L., "Radar Imaging," *International Journal of Imaging Systems and Technology*, Vol. 4, 1992, pp. 148-163.

[15] Wehner, D.R., *High Resolution Radar*, Norwood, MA, Artech House, 1987.

[16] Marlow, H.C., D.C. Watson, C.H. Van Hoozer, and C.C. Freeny, "The RAT SCAT Cross-Section Facility," *Proceedings of the IEEE*, August 1965, pp. 946-954.

[17] Knott, E.F., J.F. Shaeffer, and M.T. Tuley, "Outdoor RCS Ranges," Chapter 12 in *Radar Cross Section*, 2nd ed., Norwood, MA, Artech House, 1993.

[18] L.J. Cutrona, "A Comparison of Techniques for Achieving Fine Azimuth Resolution," *IRE Transactions on Military Electronics*, Vol. MIL-6, No. 2, April 1962, pp. 119-121.

[19] Brown, W.M., "Synthetic Aperture Radar," *IEEE Transactions on Aerospace and Electronic Systems*, Vol. AES-3, No. 2, March 1967, pp. 217-229.

[20] Brown, W.M., and Porcello, L.J., "An Introduction to Synthetic Aperture Radar," *IEEE Spectrum*, September 1969, pp. 52-62.

[21] Mims, J.H., and J.L. Farrell, "Synthetic Aperture Imaging with Maneuvers," *IEEE Transactions on Aerospace and Electronic Systems*, Vol. AES-8, No. 4, July 1972, pp. 410-418.

[22] Kirk, J.C., Jr., "Motion Compensation for Synthetic Aperture Radar," *IEEE Transactions on Aerospace and Electronic Systems*, Vol. AES-11, No. 3, May 1975, pp. 338-348.

[23] Quegan, S., and J. Lamont, "Ionospheric and Tropospheric Effects on Synthetic Aperture Radar Performance," *International Journal of Remote Sensing*, Vol. 7, No. 4, 1986, pp. 525-539.

[24] Brown, W.D., and D.C. Ghiglia, "Some Methods for Reducing Propagation-Induced Phase Errors in Coherent Imaging Systems, Part 1, Formalism," *Journal of the Optical Society of America*, Vol. 5, No. 6, June 1988, pp. 942-957.

[25] Ghiglia, D.C., and W.D. Brown, "Some Methods for Reducing Propagation-Induced Phase Errors in Coherent Imaging Systems, Part II, Numerical Results," *Journal of the Optical Society of America*, Vol. 5, No. 6, June 1988, pp. 924-941.

[26] Porcello, L.J., "Turbulence-Induced Phase Errors in Synthetic-Aperture Radar Systems," *IEEE Transactions on Aerospace and Electronic Systems*, Vol. AES-6, No. 5, September 1970, pp. 636-644.

[27] Fante, R.L., "Turbulence-Induced Distortion of Synthetic Aperture Radar Images," *IEEE Transactions on Geoscience and Remote Sensing*, Vol. 32, No. 4, July 1994, pp. 958-961.

[28] Sheen, D., T.B. Lewis, S.C. Wei, and D. Kletzli, Jr., "Imaging of Buried and Foliage-Obscured Objects with an Ultrawide Bandwidth Polarimetric SAR," *SPIE Proceedings: Underground and Obscured Object Imaging and Detection*, Vol. 1942, pp. 12-20.

[29] Milliken, R.J. and C.J. Zoller, "Principle of Operation of NAVSTAR and System Characteristics," *Navigation: Journal of the Institute of Navigation*, Vol. 25, No. 2, Summer 1978, pp. 95-106.

[30] Parkinson, B.W., "History and Operation of NAVSTAR, the Global Positioning System," *IEEE Transactions on Aerospace and Navigational Electronic Systems*, Vol. AES-30, No. 4, October 1994, pp. 1145-1161.

[31] Farrell, J.L., "Strapdown Inertial Navigation System Requirements Imposed by Synthetic Aperture Radar," *Journal of Guidance, Control, and Dynamics*, Vol. 8, No. 4, July-August 1985, pp. 433- 439.

[32] Brod, L.E., W.H. Dunlevy, and R.F. Rawson, "Synthetic Aperture Radar Exploitation of GPS," *Proceedings of the Institute of Navigation (ION)*, GPS-93 Conference, Salt Lake, September 1993.

[33] Thor, R.C., "A Large Time-Bandwidth Product Pulse Compression Technique," *IRE Transactions on Military Electronics*, Vol MIL-6, April 1962, pp. 169-173.

[34] Kelly, E.J., and R.P. Wishner, "Matched Filter Theory for High-Velocity Accelerating Targets," *IEEE Transactions on Military Electronics*, Volume MIL-9, January 1965, pp. 56-69.

[35] Kroszczynski, J., "Pulse Compression by Means of Linear Period Modulation," *Proceedings of the IEEE*, Vol. 57, No. 7, July 1969, pp. 1260-1266.

[36] Goodman, R., S. Tummala, and W. Carrara, "Issues in Ultra-Wideband, Widebeam SAR Image Formation," *Record of the 1995 IEEE International Radar Conference*, Washington, DC, May 1995, pp. 479-485.

Chapter 3
Spotlight SAR and Polar Format Algorithm

The signal phase equation of Chapter 2 describes spotlight SAR operation and the resulting signal data after motion compensation. A simplistic spotlight mode processor stores data received from successive transmitted pulses in a parallel, side-by-side (rectangular) format and limits the processing aperture size to avoid smearing or defocus of the image. This approach, common in the earliest development of spotlight mode, is a carryover from stripmap mode procedures. It limits resolution over a given scene size, not by transmitted bandwidth and angular processing aperture as (2.2) and (2.20) suggest, but by inadequate compensation for undesired phase effects inherent in the SAR signal data. This situation changed beginning in 1969 with the development of the polar format approach to spotlight data processing.

This chapter characterizes and quantifies several challenges an image formation algorithm must solve in order to achieve high image quality when processing fine resolution spotlight mode SAR data. With analysis and quantitative examples, it illustrates aspects of the signal phase equation to which a successful image formation algorithm must respond. Coverage includes motion through resolution cells (and range curvature), interaction between nonplanar motion (NPM) and a three-dimensional scene, presence of a residual video phase (RVP) term, and the effects of motion measurement errors.

The scope of this chapter includes the basis for the polar format algorithm (PFA). It demonstrates the utility and limitations of this algorithm in addressing the challenges to spotlight SAR image formation. Chapter 4 covers the digital implementation of the PFA.

3.1 SCOPE OF PROCESSING TASK

A SAR sensor illuminates a target area with a series of linear frequency modulation (FM) pulses. It receives energy scattered back to its antenna from a multitude of scatterers in the illuminated area and constructs a signal history. We model the signal history for a single point scatterer as a two-dimensional linear FM signal. From (2.51), this signal history is

$$s_r(n,t) = a_t \text{rect}\left(\frac{\hat{t} - 2R_t/c}{T_p}\right) e^{j2\pi f_c\left(t-\frac{2R_t}{c}\right)} e^{j\pi\gamma\left(\hat{t}-\frac{2R_t}{c}\right)^2} \tag{3.1}$$

Here, f_c is the center frequency, n is the pulse number, γ is the FM chirp rate, T_p is the pulse length, c is the velocity of microwave propagation, and R_t is the distance between the antenna phase center (APC) and a specific scatterer of radar cross-section σ_t. The received signal amplitude, a voltage, is proportional to $a_t = \sqrt{\sigma_t}$. The expression $\hat{t} = t - nT$ represents fast time, that is, time within a signal received from a specific transmitted pulse and referenced to the time of individual pulse generation. Here, T is the interpulse period. The range chirp, indicated by the presence of $\hat{t}^2$ in the second exponential term, arises from the linear FM transmitted waveform. The azimuth chirp, indicated by R_t in the first exponential term, results from the nearly quadratic variation in range as the radar platform passes by the scatterer. In this model, the spotlight radar sensor removes the chirp characteristic of the signal in real time in both range and azimuth by the use of analog electronic reference signals within the radar hardware. Equation (2.55) illustrates this reference signal for the two-dimensional "dechirp" procedure as

$$s_{ref}(n,t) = e^{j\left[2\pi f_c\left(t-\frac{2R_o}{c}\right)+\pi\gamma\left(\hat{t}-\frac{2R_o}{c}\right)^2\right]} \tag{3.2}$$

This approach is common in the sensor execution of fine-resolution spotlight mode.

Ideally, $R_o = R_o(nT)$ is the exact range from the APC to the selected scene center at each pulse transmission time. In practice, the value of R_o that the receiver uses in real time varies from this desired value. Hardware-imposed limitations on real-time motion measurements, quantization constraints on the value used, and motion measurement error contribute to this variation. The task of the SAR processor is to compress the signal from each scatterer to a satisfactory output signature (point impulse response) representative of the location and radar cross-section (RCS) characteristic of the scatterer. After A/D conversion, this process includes additional motion compensation and appropriate storage (formatting) of the data collected over the full coherent processing interval. Finally, the processor compresses the data from a scatterer to the desired point impulse response via a two-dimensional FFT operation.

The SAR image formation processor (IFP) is responsible for numerous operations to convert the signal history into an image. Section 2.1.4 outlines these operations; the following section provides some insight into these requirements.

3.1.1 Signal Processing Requirements

Signal processing requirements can be viewed from the following perspective. The spotlight sensor, in real time, approximately stabilizes scene center before delivery of the signal history of the entire scene to the IFP. Here, *stabilize* means that the sensor adjusts the two-dimensional signal equation representing a scatterer to a constant frequency signal. This constant frequency is zero for a scatterer at scene center. A constant frequency (and amplitude) signal will compress via the Fourier transform to a focused impulse response, which represents an ideal image of a point scatterer. This compression is the goal, not only for scene center, but for all scatterers within the scene.

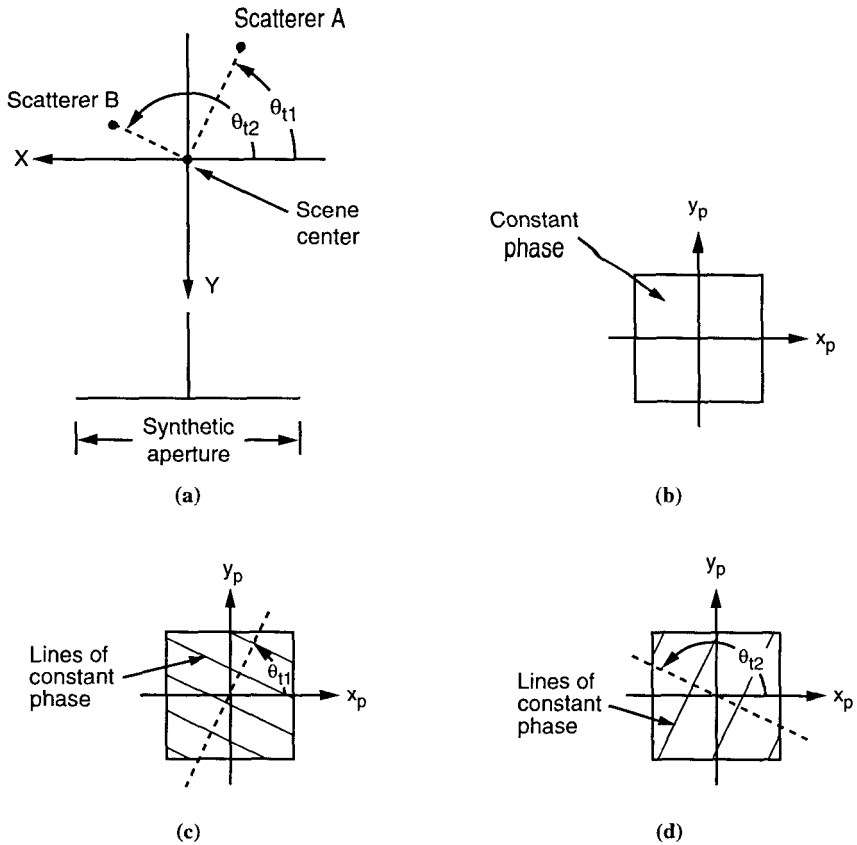


Figure 3.1 Ideal signal representing three point scatterers: **(a)** Scene geometry; **(b)** Scene center scatterer; **(c)** Scatterer A away from scene center; **(d)** Scatterer B near scene center.

In a fully compensated two-dimensional SAR signal history, the signal from each scatterer is a two-dimensional constant frequency signal with amplitude proportional to the square root of scatterer RCS. Figure 3.1 illustrates this ideal signal by showing lines of constant phase in signal history or processor space (x_p, y_p) for signals from various scatterer locations. In processor space, x_p is associated with the azimuth dimension and y_p is associated with the range dimension. First, Figure 3.1(a) indicates the data collection geometry and a simple scene consisting of three point scatterers. The remaining panels of the figure indicate the signals for the three scatterers identified in the scene. The frequency of each scatterer's two-dimensional signal is proportional to scatterer distance from scene center; the orientation of the constant phase lines of each signal mirrors scatterer angular position. The scatterer at scene center has constant phase (zero frequency) over the full processor space, while the other two scatterers have spacing and orientation of constant

phase lines which reflect scatterer location relative to scene center and radar line-of-sight (LOS). The system impulse response is the two-dimensional Fourier transform of the aperture shape and amplitude weighting that supports the data.

As explained in Section 2.6.4, the typical SAR sensor only approximately stabilizes scene center during data collection. Given adequate motion measurement information, it is a straightforward operation for the IFP to precisely stabilize scene center. However, the IFP must stabilize all scatterers in the scene, not only scene center. Scene-wide stabilization is not a simple task. This requirement to achieve scene-wide stabilization is the real challenge in the design of an image formation processing algorithm for spotlight data. Since the early origins of spotlight SAR mode in the late 1960s, the SAR community has developed a number of increasingly sophisticated algorithms to address this requirement.

3.1.2 Challenges in Spotlight Data Processing

SAR locates a scatterer by its range and by its range rate (similarly, cone angle or Doppler frequency). In spotlight mode SAR, scene center stabilization establishes a single location in the scene as the reference range and the reference range rate from which to locate all other scatterers. This location, or scene center, is also referred to as the motion compensation point (MCP) or the central reference point. Processing of spotlight data is a challenge largely because the differential range and differential range rate to each scatterer vary over the coherent aperture time required for azimuth resolution. It is common to refer to this effect as scatterer motion through (range and Doppler) resolution cells [1]. Figure 3.2 illustrates these variations in differential range and differential range rate qualitatively for a simple case. Figure 3.2(a) indicates the geometry with respect to a target that is offset in azimuth relative to scene center. Figure 3.2(b) shows the variation in differential range over the synthetic aperture (solid line) and over a lengthy flyby (dashed line). Figure 3.2(c) shows the variation in differential range rate over the synthetic aperture (solid line) and over a lengthy flyby (dashed line). The differential range to the target goes through zero when the sensor is halfway between the target and aperture center, suggesting appropriately that the target belongs near the same range as scene center. However, the variation in differential range over the aperture is indicative of motion through range resolution cells. The differential range rate is nonzero at aperture center, correctly suggesting that the target is offset in azimuth from scene center; however, the variation over the aperture is indicative of motion through azimuth resolution cells. At the extremes of the flyby, the differential range approaches X_t and the differential range rate approaches zero as the LOS nears the direction of the X axis.

Similarly, Figure 3.3(a) indicates the geometry with respect to a target that is offset in range relative to scene center. Figure 3.3(b) shows the variation in differential range over the synthetic aperture (solid line) and over a lengthy flyby (dashed line). Figure 3.3(c) shows the variation in differential range rate over the synthetic aperture (solid line) and over a lengthy flyby (dashed line). The differential range rate goes through zero at aperture center, suggesting appropriately that the target belongs at zero azimuth; however, the variation over the aperture is indicative of motion through azimuth resolution cells.

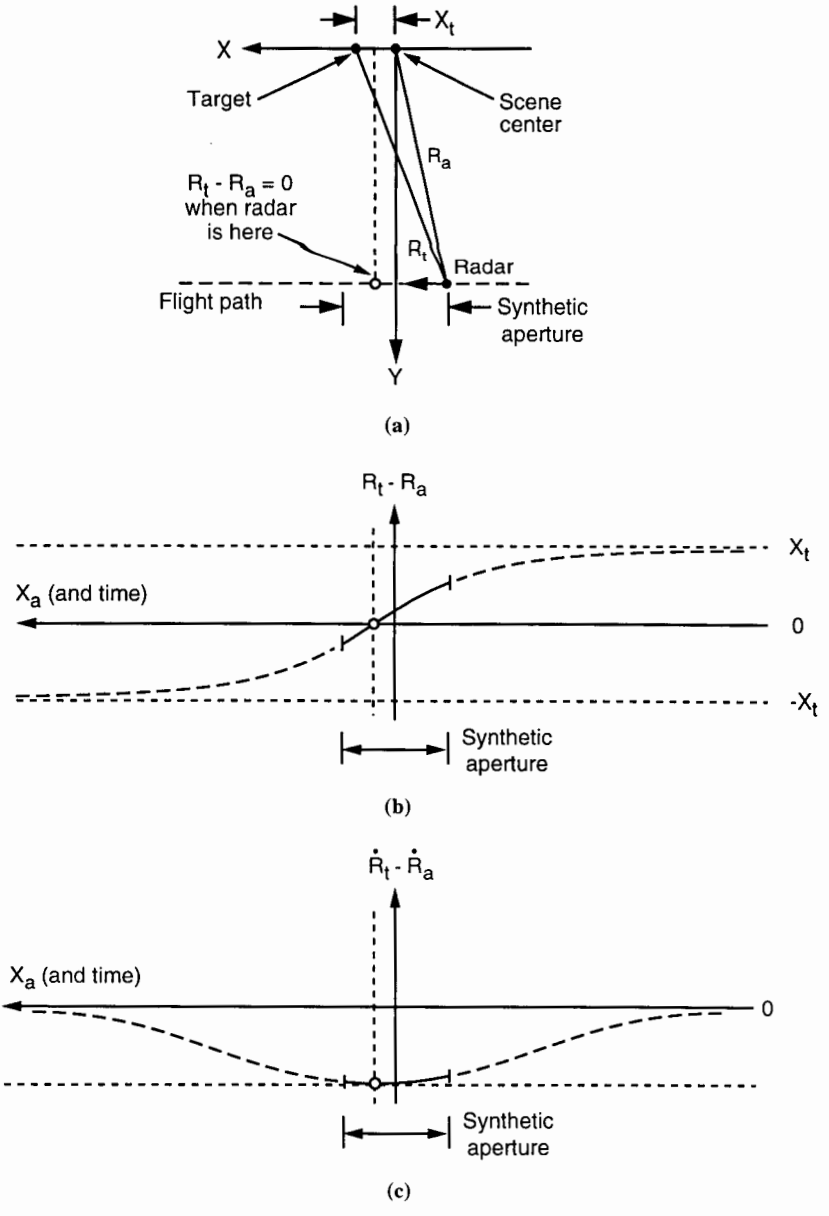


Figure 3.2 Scatterer displaced in azimuth: **(a)** Data collection geometry; **(b)** Variation in differential range; **(c)** Variation in differential range rate.

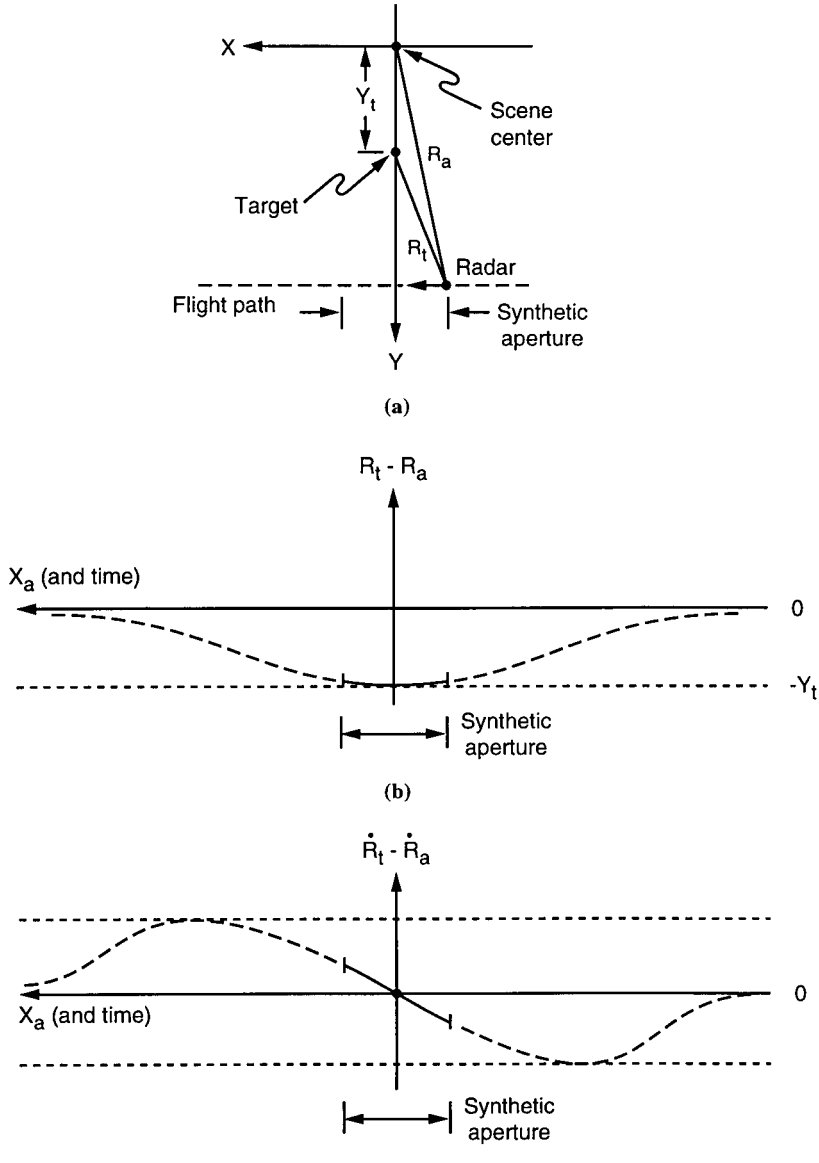


Figure 3.3 Scatterer displaced in range: **(a)** Data collection geometry; **(b)** Variation in differential range; **(c)** Variation in differential range rate.

The differential range is nonzero and relatively constant at aperture center ($X = 0$), correctly suggesting that the target is offset in range from scene center; however, the slight variation over the aperture is indicative of some motion through range resolution cells. At the extremes of the flyby, both the differential range and the differential range rate approach zero as the radar LOS nears the direction of the X axis.

As resolution becomes finer, the severity of this problem increases for two reasons. First, finer resolution means that a smaller movement will cause a scatterer to "change resolution cells." Second, finer azimuth resolution requires a longer coherent aperture angular interval and therefore greater movement by each scatterer.

Use of the PFA partially compensates for motion through resolution cells (MTRC). After polar format, the residual MTRC is a space-variant effect referred to as *range curvature*. The range migration algorithm (Chapter 10) is able to completely remove MTRC including the range curvature effect.

Two additional challenges in processing fine-resolution SAR data are (1) APC motion, which results in a nonplanar data collection surface, and (2) residual video phase, identified as the last term in (2.67). These two concerns, like MTRC and range curvature, are systemic to SAR data delivered to an IFP; each of the available algorithms has a similar difficulty with them. A final challenge is to minimize the impact of errors in motion measurement on the quality of the SAR image [2]. The PFA, with its natural resampling in both range and azimuth coordinates, readily adapts to the additional signal processing needed to address these challenges. Other IFP algorithms require additional operations to accommodate such processing.

Table 3.1 summarizes these challenges in spotlight image formation processing and indicates the location of analysis regarding the requirements and consequences associated with each factor. The completeness with which the selected IFP algorithm addresses each of these concerns impacts image quality in many areas.

Table 3.1
Challenges in Spotlight Image Formation

Challenge	*Location of Analysis*
Measured planar motion	Section 2.6; Section 3.4
MTRC	Section 3.2.2
Range curvature	Section 3.7
Measured nonplanar motion	Section 3.3.4; Section 3.8
RVP	Section 3.10
Motion measurement errors	Section 3.9

3.2 REVIEW OF IMAGE FORMATION ALGORITHMS

Table 3.2 provides a listing of five processing algorithms applicable to spotlight image formation processing and indicates the section in which serious discussion of each algorithm begins. These algorithms are listed in terms of increasing ability to manage MTRC. This listing proceeds from rectangular format (as in the original stripmap mode) through polar format to range migration processing with the chirp scaling implementation seen as a computationally efficient, often applicable approximation to the more accurate migration technique. The rectangular format and the polar format originated as optical signal processing techniques before the popular application of digital signal processing to spotlight SAR image formation [3]. The tomographic back projection algorithm (Appendix B) has its origins in the field of medical imaging, in particular, computer-aided tomography. The range migration algorithm (RMA) and chirp scaling algorithm (CSA) are relatively new arrivals on the SAR scene; Chapters 10 and 11 discuss them in detail while Chapter 12 compares them to polar format.

Table 3.2
Algorithms for Spotlight Image Formation

Algorithm	*Comments*
Rectangular format (Section 3.2.1)	Does not compensate for MTRC
Polar format (Section 3.3)	Partially compensates for MTRC (residual range curvature remains)
Chirp scaling (Chapter 11)	Compensates for MTRC including much of range curvature
Tomographic back projection (Appendix B)	Compensates fully for MTRC in its most complete implementation
Range migration (Chapter 10)	Compensates fully for MTRC

3.2.1 Algorithm Survey

The first approach to spotlight image formation (after motion compensation to scene center) is to store a limited aperture of data in a rectangular format and perform a two-dimensional Fourier transform to compress the data. This approach follows naturally from stripmap mode techniques. It places data received from successive transmitted pulses in a parallel, side-by-side (rectangular) format as Figure 3.4(a) suggests. This process achieves a two-dimensional image indicative of the RCS and the spatial distribution of scatterers in the illuminated scene. It fails, however, as the scene becomes larger and the resolution requirement becomes finer. This failure arises because the range to scatterers and the range rate of scatterers vary over the coherent aperture time. When this range movement exceeds a range resolution cell or the range rate variation exceeds that associated with an azimuth resolution cell, the rectangular format algorithm fails. The further a target is from the

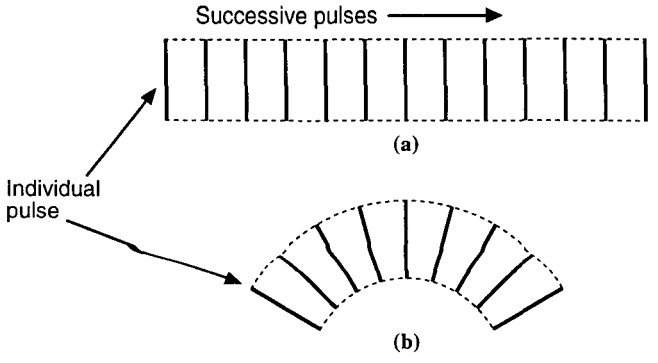


Figure 3.4 Two possible geometries for SAR data storage: **(a)** Rectangular format; **(b)** Polar format.

scene center the greater the MTRC. The maximum focused scene size for fine-resolution imaging is surprisingly small (Section 3.2.2). The rectangular format algorithm does not attempt to compensate for MTRC but, instead, tolerates it as a limit on aperture size and resolution relative to scene size.

In early SAR applications, matched filter processing [4, 5] of stripmap mode data in rectangular format was able to proceed without specific compensation for MTRC. This approach was possible only because the data corresponded to relatively coarse azimuth resolution (which limited the required angular aperture intervals) and to relatively coarse range resolution. Together, these attributes limited the amount of motion present while allowing more motion before resolution cells were traversed. As azimuth and range resolutions improved, stripmap matched filter processing evolved to compensate for MTRC for targets at the center of the range swath. With this compensation, and still at coarse resolutions relative to what is common with spotlight mode today, a stripmap image focused over a large swath (measured in kilometers) was possible. The possible range swath in this case exceeded that possible in spotlight mode with rectangular format using similar radar parameters. The reason for this difference is that the stripmap implementation compensated exactly for swath center target motion (and adequately for the motion of other targets), while the spotlight implementation did not. In many stripmap mode collections, the difference in target motion across the swath is sufficiently small that compensation of targets at swath center is adequate to compensate all targets. Spotlight mode with the PFA, for instance, has the advantage that it compensates MTRC for targets at all locations rather than only at swath center.

A successful image formation algorithm must compensate for scatterer motion through both range and azimuth resolution cells to image large spotlight scenes. To achieve both fine range and fine azimuth resolution simultaneously over a reasonably large scene, one technique is to break the scene down into many small pieces of limited size. The implementation of this approach is inefficient and faces the need to recombine or mosaic the subimages in an acceptable manner. Fortunately, additional algorithms are available to deal effectively with MTRC when imaging larger scenes.

Research initiated in 1969 showed that compensation for target MTRC is possible by storing the demodulated signal return in a polar format rather than in the conventional rectangular shape borrowed from stripmap processing [3]. The polar format approach places data received from successive transmitted pulses in an annular shape related to the transmitted RF frequency and the changing angular relationship between the sensor and the scene being imaged as Figure 3.4(b) suggests. The algorithm begins with motion compensation to a single scatterer at scene center. This process completely removes the effect of MTRC from the scene center scatterer and partially removes it from other scatterers. Following motion compensation, the polar storage format removes most of the remaining effect of MTRC from all scatterers, leaving a residual effect referred to as *range curvature* in discussions of the PFA. Finally, a two-dimensional Fourier transform produces the SAR image. A detailed discussion of this algorithm begins in Section 3.3. We discuss digital procedures to implement the PFA in Chapter 4 and show various imagery examples throughout the book.

The polar format technique does not solve all IFP challenges in processing spotlight mode data. Analysis of some PFA limitations begins in Section 3.7 while Chapters 10 and 11 introduce two recent wavenumber algorithms to address one of these limitations. These new algorithms, the RMA and the CSA, are similar to the polar format approach in that they require active motion compensation. They differ from polar format primarily in their ability to more fully accommodate MTRC including its residual range curvature aspects. The three algorithms also differ in the amount and complexity of signal filtering that each requires for implementation. Chapter 12 compares the recent algorithms to the PFA.

Terminology regarding range curvature differs somewhat in the literature describing stripmap mode. Discussions of stripmap mode divide MTRC into two parts called *range walk* and *range curvature*. Range walk is the linear component of scatterer migration or MTRC, relevant particularly to a squinted stripmap collection geometry (that is, at other than a 90-deg Doppler cone angle). In stripmap discussions, range curvature is the remaining (nominally quadratic) component of this motion. In stripmap nomenclature, range curvature is related to the reality of curved wavefronts emanating from the antenna in the far field. This additional terminology and the stripmap description of range curvature are not relevant to the PFA discussions that follow. They are relevant to the RMA and the CSA, which use the stripmap terminology.

3.2.2 Limitation of Rectangular Format

Rectangular format becomes inadequate when system parameters and performance requirements dictate that MTRC must be acknowledged and compensated in order to maintain image quality. Heuristically, this point is reached when the change in differential range to any scatterer over the required coherent aperture interval approaches the size of a resolution cell. Not surprisingly, it is difficult to assign a scatterer to a location when the scatterer is changing positions during the observation period.

Differential range is the quantity $R_t - R_a$ and is identified by the symbol R_Δ. The range to scene center R_a becomes a reference range in the process of motion compensation

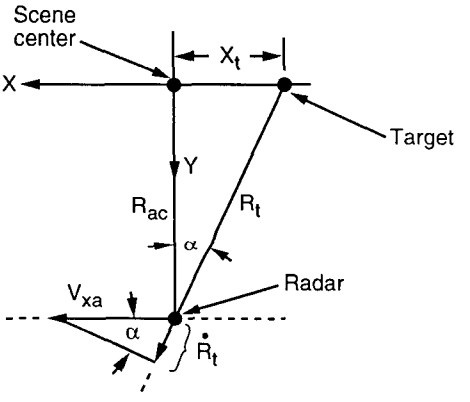


Figure 3.5 Range rate from the perspective of a broadside airborne collection.

to stabilize scene center. The change in differential range is roughly the time rate-of-change of differential range times the coherent aperture time, T_a. The differential range rate is $\dot{R}_t - \dot{R}_a$, identified by the symbol $\dot{R}_\Delta$. Here, $\dot{R}_t$ and $\dot{R}_a$ are the time rates-of-change of R_t and R_a, respectively.

To indicate the point at which rectangular format becomes inadequate, it is convenient to examine the simple case of a spotlight data collection at a 90-deg Doppler cone angle (broadside) with SAR sensor motion defined by a constant along-track velocity V_{xa}. Figure 3.5 illustrates this geometry. As Section 3.4.3 will show, the differential range rate for this case simplifies to

$$\dot{R}_\Delta = -\frac{X_t V_{xa}}{R_t} \tag{3.3}$$

Also, a geometrical basis for (3.3) is available from Figure 3.5. Because the antenna velocity vector is perpendicular to the vector $\boldsymbol{R_a}$ from the antenna to scene center, $\dot{R}_a$ is nominally zero and $\dot{R}_\Delta$ then equals $\dot{R}_t$. From Figure 3.5, $\dot{R}_t$ is nominally the component of the antenna velocity toward the target, that is, $V_{xa}\sin(\alpha)$ with α representing the angle between the antenna LOS to scene center and LOS to the scatterer at X_t. Making the substitution $-X_t/R_t$ for $\sin(\alpha)$ yields (3.3).

The differential range change ΔR over a time interval T_a is the differential range rate times the aperture time. Using (3.3) in the case of broadside imaging, the differential range change is

$$\Delta R = \dot{R}_\Delta T_a = -\left(\frac{X_t V_{xa}}{R_t}\right) T_a = -X_t\left(\frac{\lambda_c K_a}{2\rho_a}\right) \tag{3.4}$$

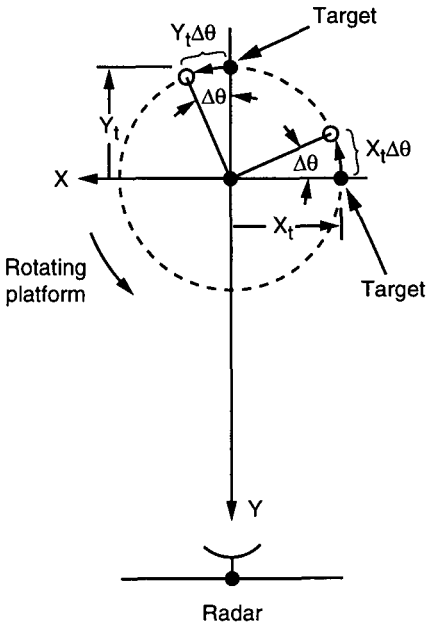


Figure 3.6 MTRC from rotating platform collection perspective.

We use (2.10) with $L = V_{xa}T_a$ to obtain the second equality. Here, K_a is the azimuth aperture mainlobe-broadening factor.

It is desirable to limit this change in range to the range resolution ρ_r. This limit yields a constraint on resolution relative to azimuth scatterer location X_t (representing one-half the allowable scene extent in azimuth) in the form

$$\rho_a\rho_r > \frac{\lambda_c K_a |X_t|}{2} \tag{3.5}$$

Phase error analysis indicates that this constraint holds the associated phase error to a tolerable level of $\pi/2$ rad [6]. A similar analysis of motion in azimuth during the coherent aperture produces the constraint

$$\rho_a^2 > \frac{\lambda_c K_a |Y_t|}{2} \tag{3.6}$$

where Y_t represents the scatterer location in range [6, 7].

Figure 3.6 suggests these results from the perspective of a rotating platform collection in a spotlight mode. In this situation, scene center is naturally stabilized since it experiences no motion in range or azimuth. From this perspective, the motion through range resolution cells is approximately $X_t\Delta\theta$, the target distance from scene center times

the angular scene rotation, $\Delta\theta$. Using (2.20) in this expression for range motion and constraining it to be less than ρ_r yields (3.5). The motion through azimuth resolution cells is approximately $Y_t\Delta\theta$; using (2.20) in this expression for azimuth motion and constraining it to be less than ρ_a yields (3.6).

Assuming equal range and azimuth resolutions of ρ_o and a scene of radius r_o, a general limitation to avoid significant MTRC is

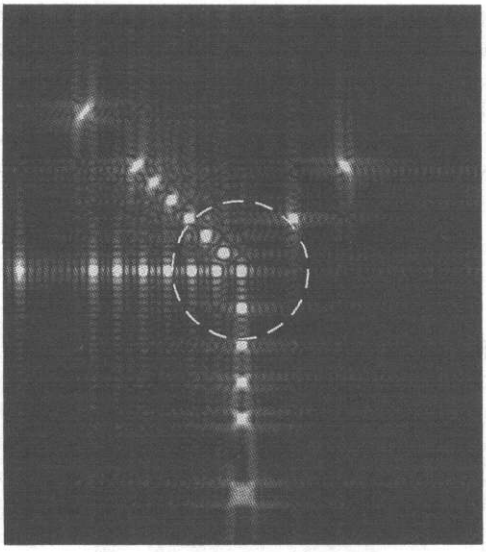
$$r_o < \frac{2\rho_o^2}{\lambda_c K_a} \tag{3.7}$$

Table 3.3 illustrates this relationship between allowable scene size and resolution for typical radar wavelengths and resolutions; it examines the ability to image a scene with a 1200-m radius at a slant range of 10 km with $K_a = 1.3$. The allowable scene size decreases rapidly with finer resolution. To image a scene exceeding the allowable scene size, the IFP algorithm must provide compensation for MTRC. Otherwise, the image area outside of the radius given by (3.7) and Table 3.3 will suffer serious degradation. For example, at 10 GHz (X-band) frequency and 1-m resolution, noticeable degradation occurs beyond about a 51-m radius.

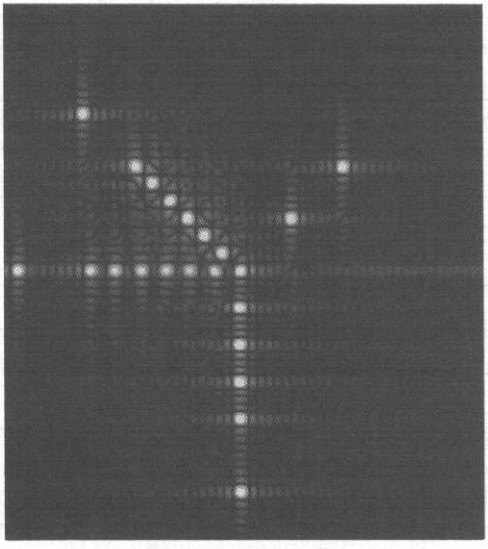
Table 3.3
Rectangular Format Limit on Scene Radius (m) as a Function of Resolution and Wavelength

	Wavelength (Frequency)			
Resolution	*0.01 m (30 GHz)*	*0.03 m (10 GHz)*	*0.2 m (1.5 GHz)*	*0.6 m (500 MHz)*
10 m	Full size	Full size	769	256
3 m	Full size	462	90	23
1 m	154	51	8	Too small
0.3 m	14	5	Too small	Too small
0.15 m	3	1	Too small	Too small

The image in Figure 3.7(a) results from using a rectangular format on a simulated signal history associated with a rotating platform ISAR facility operating at X-band. Near range is to the left in this image. The simulated data contains adequate RF bandwidth and azimuth angular interval to provide 0.15-m resolution in each dimension with uniform weighting ($K_a = 0.89$). The resulting image indicates the degradation in resolution which necessitates polar format. The target at scene center realizes full resolution. The circle overlaid on this image indicates the scene radius limitation of 1.68 m which (3.7) suggests. Each major line of scatterers extends out to a radius of 5 m. The horizontal line of scatterers at zero azimuth and increasing ranges from scene center is affected by a range-dependent azimuth quadratic defocus; the scatterers are smeared in azimuth only



(a)



(b)

Figure 3.7 Simulated images of a rotating platform scene: **(a)** Using rectangular format; **(b)** Using polar format.

with severity proportional to range distance from scene center. The vertical line of scatterers at zero range and increasing azimuth distance from scene center is affected by azimuth-dependent cross-product (range times azimuth) quadratic defocus; the scatterers are smeared in both range and azimuth with severity proportional to azimuth distance from scene center [6]. Scatterers on the diagonal line are affected by a mixture of each effect. The image from the same data using polar format is well-focused at all distances from scene center as seen in Figure 3.7(b).

3.3 POLAR FORMAT ALGORITHM

The spotlight mode provides the opportunity to collect SAR data over a wide azimuth angular interval (independent of antenna azimuth beamwidth) with the potential for extremely fine azimuth resolution. Without compensation, target MTRC prevents the realization of fine resolution over a reasonable scene size, limited by (3.7). The PFA is valuable because it compensates adequately for MTRC over a scene size much larger than (3.7) indicates. The residual MTRC that PFA does not compensate is range curvature; we discuss and quantify the effects of range curvature in Section 3.7. As an example, at X-band and a 10-km range, the use of polar format extends the allowable scene radius at 1-m resolution from about 50 m to about 900 m.

The PFA does not require use of a linear FM waveform; it applies also to systems that transmit alternate waveforms [6]. The current analysis assumes and is specific to a linear FM waveform for convenience and because fine-resolution SAR systems commonly use this waveform. While the PFA does require use of the range dechirp procedure with the linear FM waveform, it need not employ dechirp-on-receive; dechirp in the digital processor after A/D conversion is an acceptable alternative.

3.3.1 Algorithm Overview

Figure 3.8 indicates the basic components of a SAR system and the data transfers among them. The digital recorder is unnecessary in real-time operation. Functions of the preprocessor may include real-to-complex data conversion and presumming in azimuth. Auxiliary data processing involves conversion of motion sensor data to a position history of the APC. This processed motion data provides parameters to the IFP for motion compensation.

Figure 3.9 provides a block diagram of a SAR image formation procedure which incorporates the PFA. Working in the context of the SAR system, this procedure encompasses the IFP operations necessary to produce an image from collected SAR signal and motion data. Section 2.1.4 outlines these operations. It is important to realize that the basic polar formatting operation itself is simply a modification in the data storage format. In effect, the polar formatting operation means recording successive pulses not side-by-side as in Figure 3.4(a) but in an annular geometry as in Figure 3.4(b). It involves no intrinsic phase or frequency adjustments to the motion-compensated data.

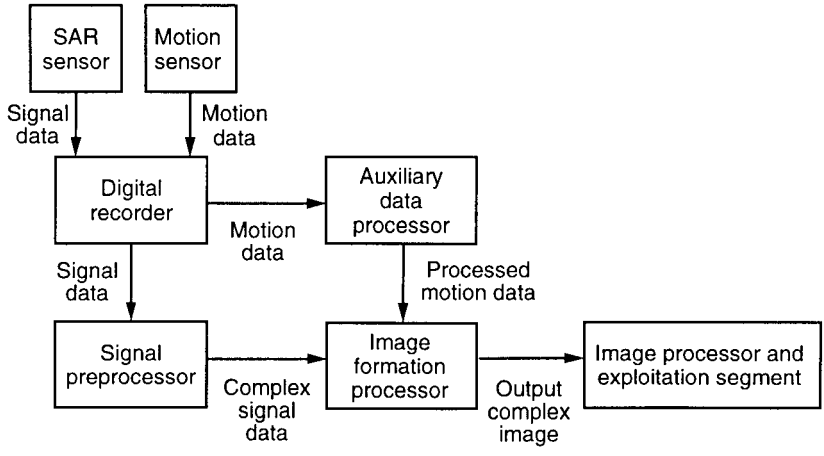


Figure 3.8 Basic components of a SAR system.

Examination of an extreme imaging geometry is useful to illustrate the presence of MTRC in SAR data. Figure 3.10(a) shows such a geometry consisting of three point scatterers spread over a 200-m range extent in the illuminated scene. In this example, the synthetic aperture length is 200 m; the SAR system collects N_p pulses over this interval. At aperture center, the range to scene center is R_{ac} = 1000 m. Figure 3.10(b) shows the result of compressing the signals from successive pulses in range for scatterers at near, mid, and far range. The three scatterers experience changes in distance to the antenna (range) of 5.539, 4.988, and 4.536 m, respectively, over the 200-m synthetic aperture length. Scene center motion compensation removes range curvature and MTRC completely for the scene center scatterer. Range compression after motion compensation yields *residual* curvature for each of the three scatterers as shown in Figure 3.10(c). The straight horizontal line (a single range bin or range resolution cell) for scene center indicates the complete removal of all motion for this scatterer. The scatterer at near range still experiences 0.551 m of range change while the scatterer at far range experiences 0.452 m of range change. The process of polar formatting the scene-center-stabilized data reduces the spatial frequency of the signals from pulses at the ends of the synthetic aperture, thereby reducing the residual curvature. The situation after the polar formatting operation is shown in Figure 3.10(d). The mid-range scatterer is unaffected by the reformatting while the near-range and far-range scatterers now experience similar residual motion of only 0.05 m over the aperture time. This residual motion, or range curvature, is a function of scatterer location in range and azimuth relative to scene center.

The key to the polar format approach involves the storage of the signal data from successive pulses along adjacent radial lines instead of in a rectangular format (Figure 3.4). Placement of the data within each pulse along a radial line is proportional to the instantaneous frequency of the transmitted signal. The angle of the radial line used for a specific pulse rotates in synchronism with the effective rotation of the scene. A rigorous presentation of this data formatting requirement begins in Section 3.3.3.

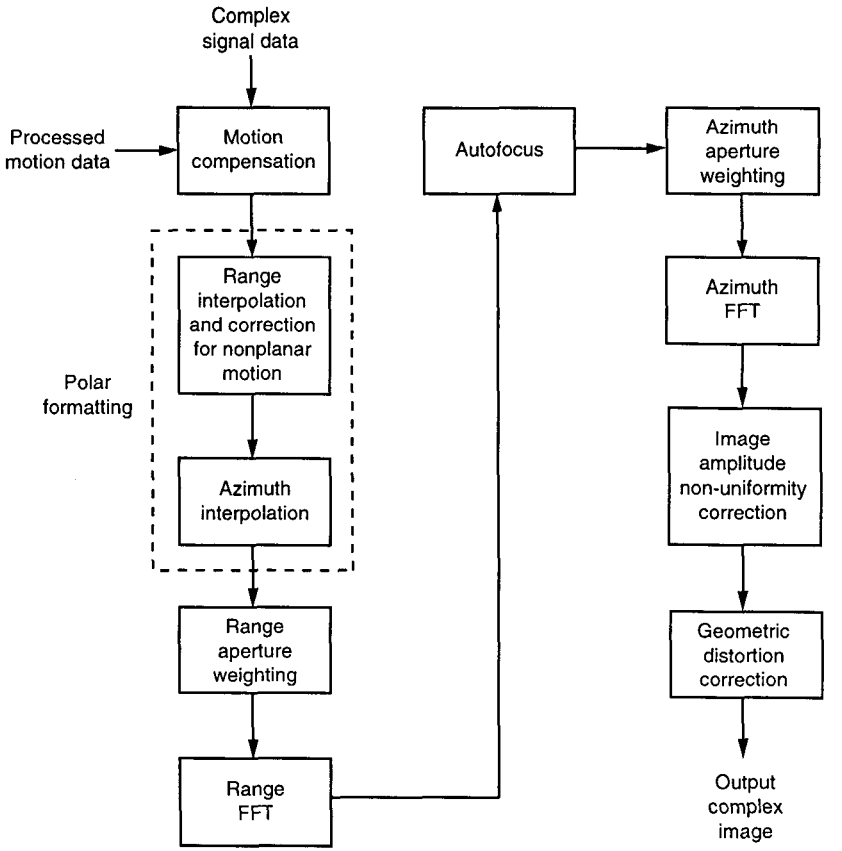


Figure 3.9 Image formation procedure using the PFA.

Figure 3.11 illustrates the phase of the signal from a single point scatterer before and after polar formatting. The curved and nonparallel fringes in Figure 3.11(a) before the polar format operation are indicative of the changing differential range and range rate over the processing aperture. After completion of the polar format interpolation and except for any residual range curvature, the fringes in Figure 3.11(b) are uniform and straight; a two-dimensional Fourier transform of the data array produces a focused image of the point scatterer.

3.3.2 Signal History Model

The signal history delivered to the polar formatting procedure after fine motion compensation is pulsed in time and sampled within each pulse. In analysis, however, it is convenient

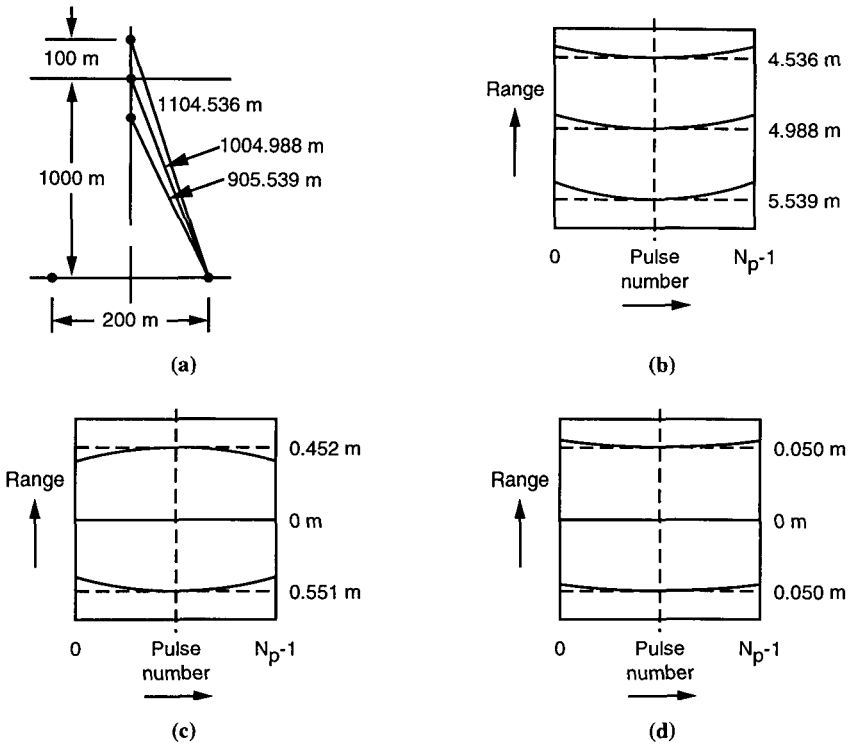


Figure 3.10 Scatterers in range-compressed domain after motion compensation to scene center: **(a)** Data collection geometry; **(b)** Result after range compression without motion compensation; **(c)** Result after motion compensation; **(d)** Result after polar formatting operation.

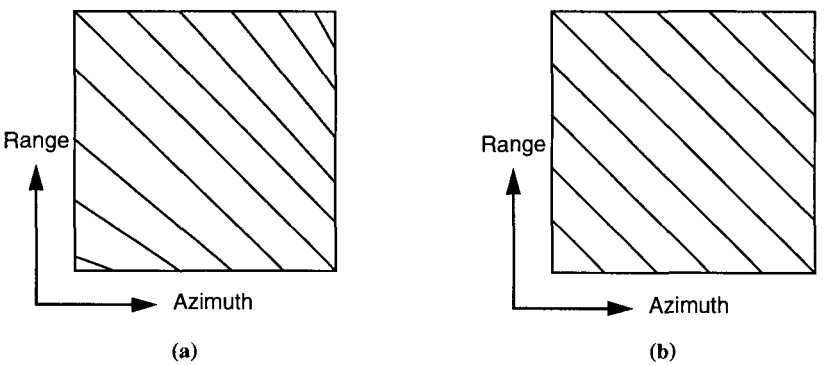


Figure 3.11 Lines of constant phase in the signal history of a point scatterer: **(a)** Before polar formatting; **(b)** After polar formatting.

to maintain the continuous variable $\hat{t} = t - nT$ within each pulse rather than acknowledge the sampling in fast time. Based on (2.66), a synthetic aperture of data returned by a scatterer of radar cross-section σ_t is

$$s_o(n,\hat{t}) = a_t \sum_{n=0}^{N_p-1} \text{rect}\left(\frac{\hat{t} - 2R_t/c}{T_p}\right) e^{j\Phi(n,\hat{t})} \tag{3.8}$$

with $a_t = \sqrt{\sigma_t}$. Its phase is

$$\Phi(n,\hat{t}) = -\frac{4\pi\gamma}{c}\left(\frac{f_c}{\gamma} + \hat{t} - \frac{2R_a}{c}\right)R_\Delta + \frac{4\pi\gamma}{c^2}(R_\Delta^2) \tag{3.9}$$

based on (2.67) with

$$R_\Delta = R_t - R_a \tag{3.10}$$

Here, n is an index corresponding to pulse number. The expression $\hat{t} = t - nT$ represents fast time or time within a signal received from a specific transmitted pulse and referenced to the time of pulse generation, γ is the linear FM rate, f_c is the transmitted center frequency, T is the pulse repetition interval, T_p is the time duration of the transmitted pulse, R_t is the distance between the APC and the scatterer, and R_a is the distance between the APC and scene center. This signal represents two-dimensional data in the coordinates, n and $\hat{t}$. The radar signals are dechirped in range by the SAR system implementation and dechirped in azimuth as a part of the motion compensation operation.

3.3.3 Polar Format Transformation

While the SAR sensor traverses a path in physical space transmitting a wideband pulsed signal, the received SAR signals (with appropriate spotlight mode compensations and adjustments) provide samples of the three-dimensional Fourier transform of the radar reflectivity of the illuminated scene. For a linear FM transmit waveform, an appropriate processing procedure is to dechirp the received SAR signals in range and apply the usual spotlight mode motion compensation operations. In this case, these operations include azimuth dechirp (or scene center stabilization). Because of the unique properties of chirp signals, dechirp in range effectively transforms the data from the range-time domain to the range-frequency domain. Similarly, motion compensation to a point transforms data from the azimuth-time (or space) collection domain to the azimuth-frequency domain. The PFA effectively operates in the two-dimensional spatial-frequency or wavenumber domain. Despite this fact, it is common practice to visualize the dechirped signal history in a time domain (that is, the fast-time and slow-time representation).

The extrapolation from data collection geometry to wavenumber space is made via the wavenumber vector $\boldsymbol{K}$ defined by

$$\boldsymbol{K} = \frac{4\pi f}{c}\hat{\boldsymbol{R}}_a \tag{3.11}$$

where $\hat{\boldsymbol{R}}_a$ is a unit vector along the instantaneous slant range vector $\boldsymbol{R}_a$; f represents the instantaneous frequency of the transmitted pulse and extends over the transmitted bandwidth [8]. Both the azimuth angle θ_a and the incidence angle ϕ_a in the physical $\hat{\boldsymbol{R}}_a$ space are identical, respectively, to the azimuth angle θ_p and the incidence angle ϕ_p in the wavenumber $\boldsymbol{K}$ space. A three-dimensional Fourier transform relationship exists between wavenumber $\boldsymbol{K}$ space (with spatial-frequency Cartesian coordinates K_x, K_y and K_z to locate a $\boldsymbol{K}$ vector) and physical target space (with spatial Cartesian coordinates X, Y, and Z to locate a scatterer position vector). Figure 3.12 illustrates these two geometry models.

In this section, we offer a simple mathematical rationale to demonstrate this Fourier transform relationship. This three-dimensional viewpoint serves as an introduction to a more rigorous analytical development of the two-dimensional PFA that begins in Section 3.4. For reference, Table 3.4 summarizes some of the abbreviations for angles and trigonometry functions we use throughout the analyses in this chapter. Note that θ_a and ϕ_a vary with pulse number n; however, we usually suppress this dependency for convenience and write θ_a for $\theta_a(n)$ and ϕ_a for $\phi_a(n)$.

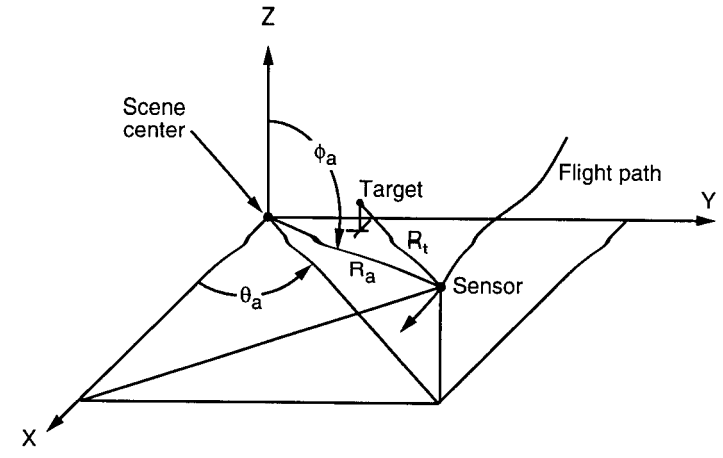
Table 3.4
List of Trigonometry Abbreviations

Quantity	*Abbreviation*	*Meaning*
$\sin(\theta_a)$	$S_{\theta a}$	Sine of the instantaneous squint angle θ_a
$\sin(\theta_{ac})$	$S_{\theta c}$	Sine of the aperture center squint angle θ_{ac}
$\cos(\theta_a)$	$C_{\theta a}$	Cosine of the instantaneous squint angle θ_a
$\cos(\theta_{ac})$	$C_{\theta c}$	Cosine of the aperture center squint angle θ_{ac}
$\sin(\phi_a)$	$S_{\phi a}$	Sine of the instantaneous incidence angle ϕ_a
$\sin(\phi_{ac})$	$S_{\phi c}$	Sine of the aperture center incidence angle ϕ_{ac}

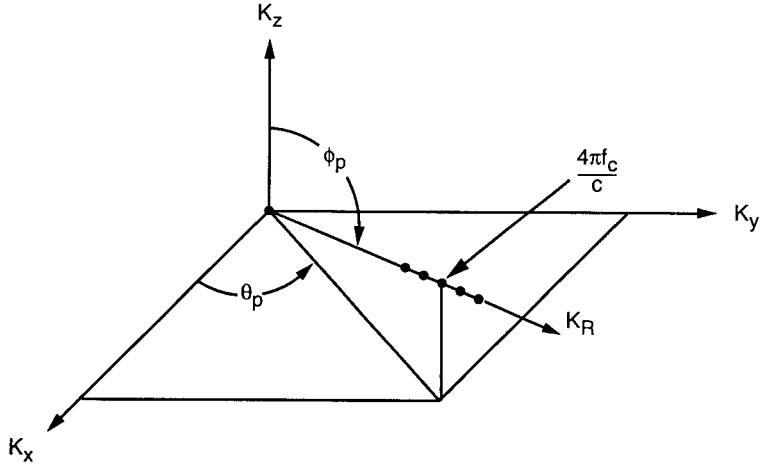
This initial discussion begins with (3.9) and makes two simplifications. It disregards the final term in (3.9), known as residual video phase (RVP), since it is a small effect. It approximates R_Δ in (3.9) by

$$R_\Delta \approx -\frac{(\boldsymbol{R}_a \bullet \boldsymbol{r}_t)}{R_a} = -S_{\phi a}\left[X_t C_{\theta a} + Y_t S_{\theta a} + Z_t \cot(\phi_a)\right] \tag{3.12}$$

where the scatterer position vector $\boldsymbol{r}_t = (X_t, Y_t, Z_t)$ of magnitude r_t defines a scatterer location relative to scene center. This approximation for R_Δ is adequate for $r_t << R_a$.



(a)



(b)

Figure 3.12 Data geometry: **(a)** Location of sensor (sample) in data collection space; **(b)** Corresponding line of data samples in wavenumber or spatial-frequency processor space.

Later analysis will again include and analyze RVP and additional smaller terms in R_Δ. With these two simplifications, an approximate form for the phase of the radar signal representing a scatterer at (X_t, Y_t, Z_t) becomes

$$\Phi(n, \hat{t}) \approx \frac{4\pi\gamma}{c}\left(\frac{f_c}{\gamma} + \hat{t} - \frac{2R_a}{c}\right) S_{\phi a}\left[X_t C_{\theta a} + Y_t S_{\theta a} + Z_t \cot(\phi_a)\right] \tag{3.13}$$

Inspection of (3.13) indicates that the transformations

$$K_R(n,\hat{t}) = \frac{4\pi\gamma}{c}\left(\frac{f_c}{\gamma}+\hat{t}-\frac{2R_a}{c}\right) \tag{3.14}$$

$$\theta_p(n) = \theta_a \tag{3.15}$$

and

$$\phi_p(n) = \phi_a \tag{3.16}$$

convert this signal phase to a desirable Fourier transform kernel. With these transformations, the signal phase becomes

$$\Phi(n,\hat{t}) \approx K_R(X_tC_{\theta a}S_{\phi a}+Y_tS_{\theta a}S_{\phi a}+Z_tC_{\phi a}) \tag{3.17}$$

or

$$\Phi(n,\hat{t}) \approx X_tK_x+Y_tK_y+Z_tK_z \tag{3.18}$$

with K_x, K_y, and K_z being rectangular signal coordinates associated with the spherical coordinates K_R, θ_p, and ϕ_p. The scatterer coordinates along the X, Y, and Z axes are coded in frequency along the K_x, K_y, and K_z axes, respectively. Since X_t, Y_t, and Z_t are in units of distance, it is natural that K_x, K_y, and K_z are in units of radians per unit distance in the spatial-frequency domain. Variations in R_a do not affect the sample locations or spacing in $\boldsymbol{K}$ space; rather, θ_a and ϕ_a in physical space affect the angular location in $\boldsymbol{K}$ space while the instantaneous frequency affects the radial location K_R. Figure 3.12 illustrates these geometric relationships. This model indicates a three-dimensional Fourier transform relationship between the three-dimensional scene RCS in physical space and the collected data field formatted in a three-dimensional spherical $\boldsymbol{K}$ space. In principle, a three-dimensional Fourier transform of this data yields a three-dimensional image of the scene RCS with resolution in each scene dimension. The shape and fill (three-dimensional support) of the $\boldsymbol{K}$ space data determines the resolution in each dimension. This presentation is compatible with the wavenumber domain analysis associated with range migration and chirp scaling algorithms in Chapters 10 and 11. In fact, these three algorithms are closely related.

In practice, two-dimensional data storage and signal processing implementations are desirable. Projection of the $\boldsymbol{K}$ vector onto the K_xK_y plane results in a reasonable two-dimensional data storage format to use when the scene is nominally in the XY plane; this procedure selects the normal ground plane as the focus target plane (FTP) and as the image display plane (IDP). A square area on the ground will appear nominally as a square

in this IDP. This projection uses the transformations

$$K_p(n,\hat{t}) = K_R S_{\phi a} = \frac{4\pi\gamma}{c}\left(\frac{f_c}{\gamma} + \hat{t} - \frac{2R_a}{c}\right) S_{\phi a} \tag{3.19}$$

and

$$\theta_p(n) = \theta_a \tag{3.20}$$

Figure 3.13 illustrates this projection that stores all data in the $K_x K_y$ plane. The presence of the term $S_{\phi a}$ in K_p establishes the XY plane as the FTP (Section 3.3.4) while the use of θ_a as θ_p establishes the XY plane as the IDP (Section 3.3.5). Here, ϕ_a is the incidence angle and θ_a is the squint angle associated with the data collection. The origin of the (x_p, y_p) coordinate system in Figure 3.13(b) is $(K_p, \theta_p) = (K_c, \theta_{ac})$. This location is the center of the data window being processed. The data represents samples of the Fourier transform of the scene over an area of frequency significantly offset from the origin which is zero spatial frequency. This factor, however, does not inhibit the generation of high-quality imagery as long as the phase of the complex reflectivity of the scene is highly random over space [9].

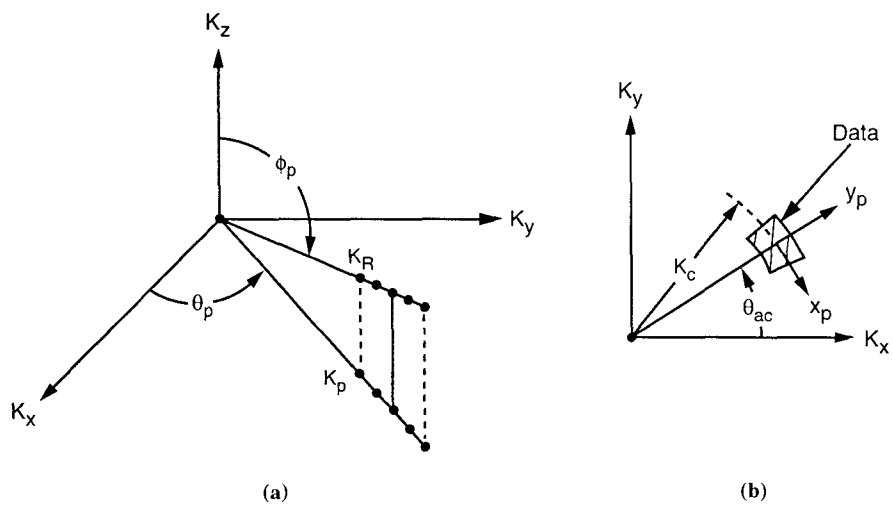


Figure 3.13 SAR data in wavenumber space projected onto $K_x K_y$ plane: **(a)** Projection of a single data pulse; **(b)** Synthetic aperture of SAR signal data after projection.

With the transformations of (3.19) and (3.20), the signal phase from (3.13) becomes

$$\Phi(n,\hat{t}) \approx X_t K_x + Y_t K_y + Z_t K_p \cot(\phi_a) \tag{3.21}$$

Now K_x and K_y are rectangular signal coordinates associated with the polar coordinates

K_p and θ_p. Again, the scatterer X_t and Y_t coordinates are coded in frequency along the K_x and K_y axes. The polar format angle θ_p and the distances R_t and R_a vary with n, the pulse number; thus, θ_p is constant within a pulse but varies linearly with the measured angle θ_a from pulse to pulse. In turn, θ_a is a variable based on sensor location in the data collection geometry. The signal returned from a scatterer at location (X_t, Y_t, Z_t) at pulse n is stored in processor space along the line $\theta_p = \theta_a(n)$.

From (3.19) and (3.20), we see that the two-dimensional polar format approach records each pulse's return (samples) at an angle in the spatial-frequency domain related to the relative rotation angle θ_a of the scene and at a radial position proportional to the instantaneous transmitted frequency, $f_c + \gamma\hat{t}$. The relationship between radial position and instantaneous transmitted frequency is evident by rewriting (3.19) in the form

$$K_p = K_c \frac{S_{\phi a}}{S_{\phi c} f_c}\left[f_c + \gamma\left(\hat{t} - \frac{2R_a}{c}\right)\right] \tag{3.22}$$

with

$$K_c = \frac{4\pi f_c}{c} S_{\phi c} \tag{3.23}$$

where $S_{\phi a} = \sin(\phi_a)$ and $S_{\phi c} = \sin(\phi_{ac})$. Here K_c corresponds to the polar radius in $K_x K_y$ space for storing the signal returning at $\hat{t} = 2R_{ac}/c$ and $n = n_c$. Here, n_c represents the pulse transmitted from the APC location at aperture center and R_{ac} is the value of R_a at aperture center. K_c is the projection of $\boldsymbol{K}(n_c, 2R_{ac}/c)$ from (3.11) onto the $K_x K_y$ plane. The complete signal history, including the RVP term and the full expression for R_Δ, is given by

$$s_o(n, \hat{t}) = a_t \sum_{n=0}^{N_p - 1} \text{rect}\left(\frac{\hat{t} - 2R_t/c}{T_p}\right) e^{j\Phi(n, \hat{t})} \tag{3.24}$$

with phase

$$\Phi(n, \hat{t}) = -K_p\left(\frac{R_\Delta}{S_{\phi a}}\right) + \frac{4\pi\gamma}{c^2} R_\Delta^2 \tag{3.25}$$

and

$$R_\Delta = R_t - R_a \tag{3.26}$$

While $\theta_p(n)$ does not appear explicitly in these equations, it is implicit in both R_Δ and $S_{\phi a}$. We define the change in θ_p over the N_p pulses making up the processing aperture by the quantity $\Delta\theta_p$. From (2.64), the two-dimensional sampled counterpart to (3.24) after A/D sampling is

$$s_o(n, k) = a_t \sum_{n=0}^{N_p - 1} \left[\sum_{k=0}^{K-1} e^{j\Phi(n, k)}\right] \tag{3.27}$$

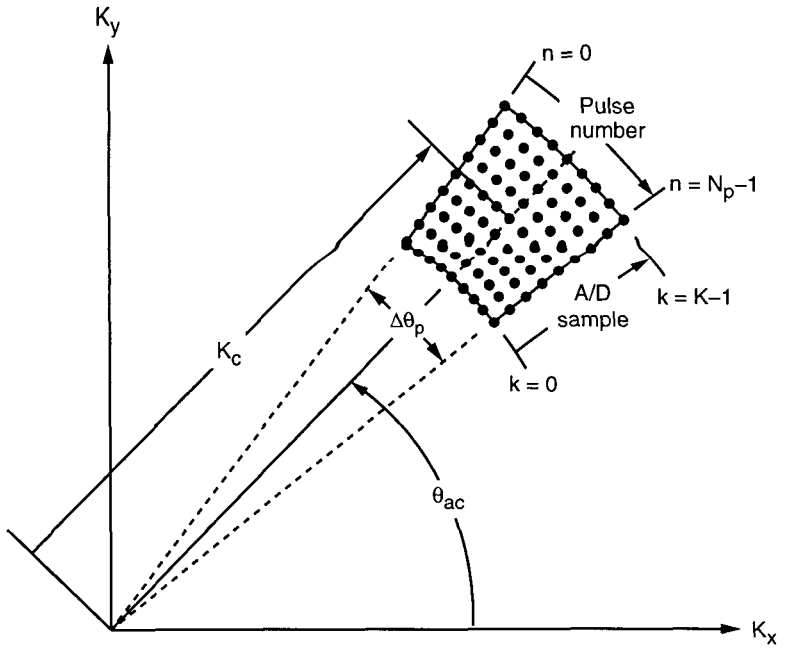


Figure 3.14 Sampled data geometry in K_xK_y plane.

with phase

$$\Phi(n,k) = -K_p\left(\frac{R_\Delta}{S_{\phi a}}\right) + \frac{4\pi\gamma}{c^2}(R_\Delta^2) \tag{3.28}$$

The sampled signal data encompasses K samples per pulse over N_p pulses. Figure 3.14 illustrates the location of this two-dimensional array of samples in K_xK_y space.

This projection in frequency space to the K_xK_y plane increases the radial (range) frequency in this space associated with each ground scatterer (nominally in the XY plane). This factor effectively reverses a reduction in image ground range scale by $S_{\phi a}$; the initial reduction is associated with the shorter differences among ground scatterers in distance from the APC relative to the differences in ground-range distance. The net result is that distance among scatterers in the image correctly represents ground distance rather than a shorter distance based on differences in differential range to the APC.

Somewhat aside, a number of choices for the along-track variable are possible. These choices include sampled time nT (or pulse number n), since the data is sampled in real time at intervals of T by the radar pulse train; along-track position X_a of the APC at each pulse transmission time; and display squint angle θ_s or its polar format counterpart θ_p. Each viewpoint is valid; convenience, simplification of analysis, and ease in conceptual understanding are factors that guide the selection at various stages of system analysis.

The IFP receives data with samples in K_p and θ_p from the radar sensor after A/D conversion. The collection of N_p pulses from $0 \le nT < T_a$ in sampled time makes up the two-dimensional signal in processor space during this processing interval. Here, T_a is the time required to collect a coherent processing aperture yielding the desired azimuth resolution. The processor resamples the data in a rectangular grid in x_p and y_p coordinates (Chapter 4). However, it is convenient in this mathematical development to treat the signal history (3.25) as a continuous signal in either (K_p, θ_p) coordinates or (x_p, y_p) coordinates.

The phase effects in $\Phi_p(x_p, y_p)$ determine the location, phase, and width of the mainlobe (resolution). These effects also impact the sidelobe characteristics of the system impulse response in image space. The first term of (3.25) encompasses the imaging term, range curvature, motion measurement errors, and NPM effects. Motion measurement errors are included in R_t within R_Δ. The second term in (3.25) is the RVP effect. RVP is often small and not a concern in practice. Information in Section 5.3 helps to quantify the distortion and quadratic phase error associated with RVP. For situations in which RVP is significant, a preprocessing operation is available to remove this phase effect completely (Appendix C).

It is instructive to determine the size of the data support in K_xK_y space for the simple case in which the APC follows a straight line parallel to the X axis. A small-angle approximation for the extent Δx of the data in x_p is

$$\Delta x \approx K_c \Delta\theta_p = \frac{4\pi \sin(\phi_{ao})\,\Delta\theta}{\lambda_c S_{\phi c}} \tag{3.29}$$

This result uses the relationship between the angular interval $\Delta\theta$ in the slant plane required for azimuth resolution and the corresponding change $\Delta\theta_p$ in θ_p in K_xK_y space in the form

$$\Delta\theta_p \approx \frac{\sin(\phi_{ao})\,\Delta\theta}{S_{\phi c}^2} \tag{3.30}$$

available from a consideration of the geometry. Here ϕ_{ao} is the angle between the XY plane and the plane formed by the antenna trajectory (parallel to the X axis in this simple case) and the X axis. The expression $\tan(\phi_{ao}) = Y_{ac}/Z_{ac}$ defines this angle. In terms of azimuth resolution, Δx becomes

$$\Delta x \approx \frac{2\pi K_a \sin(\phi_{ao})}{\rho_a S_{\phi c}} \tag{3.31}$$

For a transmitted bandwidth $B = \gamma T_p$, it is clear from (3.19) that the extent of the data in y_p is

$$\Delta y \approx \frac{4\pi B S_{\phi c}}{c} = \frac{2\pi K_r S_{\phi c}}{\rho_r} \tag{3.32}$$

Together, (3.31) and (3.32) provide useful bounds for the two-dimensional signal support after polar formatting in the $K_x K_y$ plane.

Building on the introduction to polar formatting in this section, the following sections proceed with the full development of the PFA including a detailed analytical model, Taylor series expansion procedures, basic imaging relationships, and error analyses. Chapter 4 completes this presentation with a discussion of procedures to implement the PFA in a digital processing environment.

3.3.4 Focus Target Plane Concept

The motion compensation described in Section 2.6 accommodates two-dimensional motion. It compensates for motions within a data collection plane defined by the sensor's nominal forward velocity vector and a selected MCP at or near the scene center. It corrects for variations in the range between the APC and the MCP and handles angular changes in the data collection plane. This two-dimensional approach is adequate for a spotlight radar with a nominally straight-line flight path.

A third dimension of motion occurs when a maneuvering vehicle, for instance, carries the radar antenna out of the nominal data collection plane during a coherent processing aperture. This third dimension of motion causes additional, undesired phase effects in the radar signal histories because it changes the relative ranges to scatterers even with no change in range or angle to scene center in the nominal data collection plane. Nonplanar motion arises from movement orthogonal to the nominal data collection plane. Figure 3.15 indicates the source of this undesired phase when the data collection surface becomes nonplanar. The mechanism is the changing grazing angle within the coherent aperture time, which results in a differing target range rate over the aperture time without any change in the range or angle in the nominal data collection plane. Therefore, this motion indicates no change in the normal two-dimensional motion compensation procedures. But range does change to other scatterers in the scene. Figure 3.15(a) indicates an example of NPM. If the motion were planar, the sensor would be at position A_0 at the center of the aperture; instead it is at A_1, a variation α in angle out of the plane. As Figure 3.15(b) suggests, this variation in angle leads to a change in range relative to scene center of $r_1 - r_0$ for the scatterer in the figure. This range change varies with W_t, which is the scatterer distance out of the slant plane. It causes a phase effect in the SAR signal which would not be present had the flight path remained planar. As the angle α varies over the synthetic aperture interval, a varying phase effect is added to the signal that represents the scatterer. Simple trigonometry from Figure 3.15(b) shows that

$$r_1 - r_0 \approx \alpha W_t \tag{3.33}$$

and therefore the phase effect is approximately

$$\Delta\Phi \approx \frac{4\pi}{\lambda_c}\alpha W_t \tag{3.34}$$

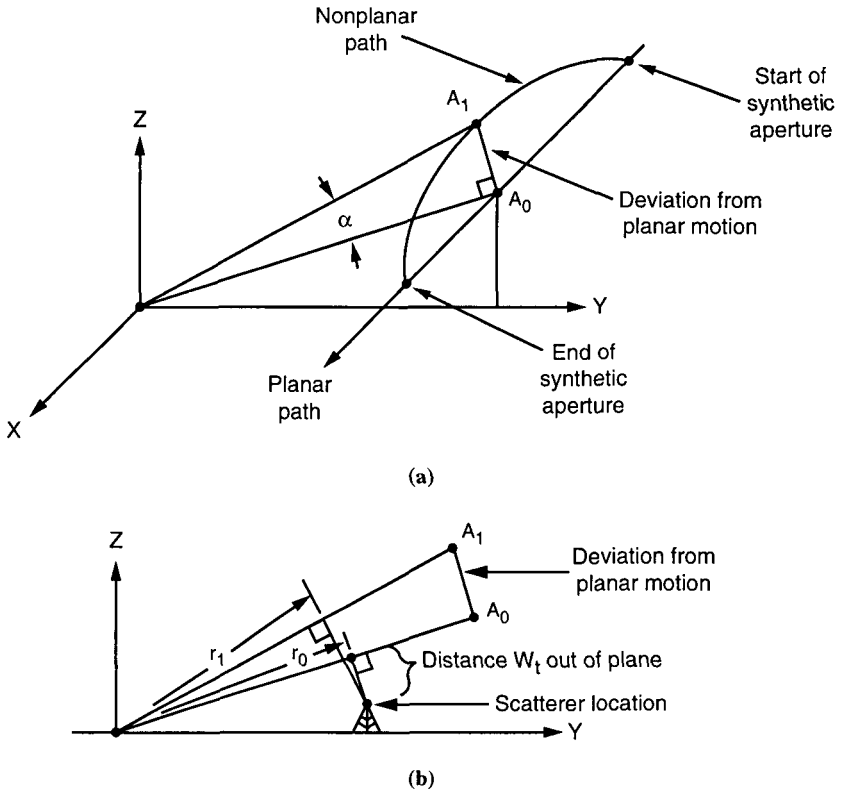


Figure 3.15 Source of NPM phase effect: **(a)** Example of nonplanar flight path; **(b)** Range change $r_1 - r_0$ caused by NPM.

The NPM then leads to a phase effect and possible image degradation which varies with scatterer distance out of the slant plane. This situation is a serious concern because most scatterers are near the nominal ground plane and far out of the slant plane. Without appropriate compensation by the IFP algorithm, NPM would severely impact the image quality of these scatterers.

In spotlight mode imaging, an algorithm enhancement is available to compensate for measured motions in three dimensions. This technique is equally applicable to the PFA and to other spotlight processing algorithms. In three-dimensional motion compensation, three surfaces are involved. The first is the data collection surface defined as the three-dimensional surface swept out by the radar LOS vector. The second is the FTP for which the three-dimensional motion compensation is optimized. The third is an independent IDP, selected to accommodate the needs of the image interpreter, an automatic target recognition (ATR) algorithm, or other user. The squint angle used to determine the rotation of data

in the polar format transformation is measured in the IDP; this angle is the display squint angle defined by (2.43). The choice of IDP impacts the character but not the quality of the data and output imagery.

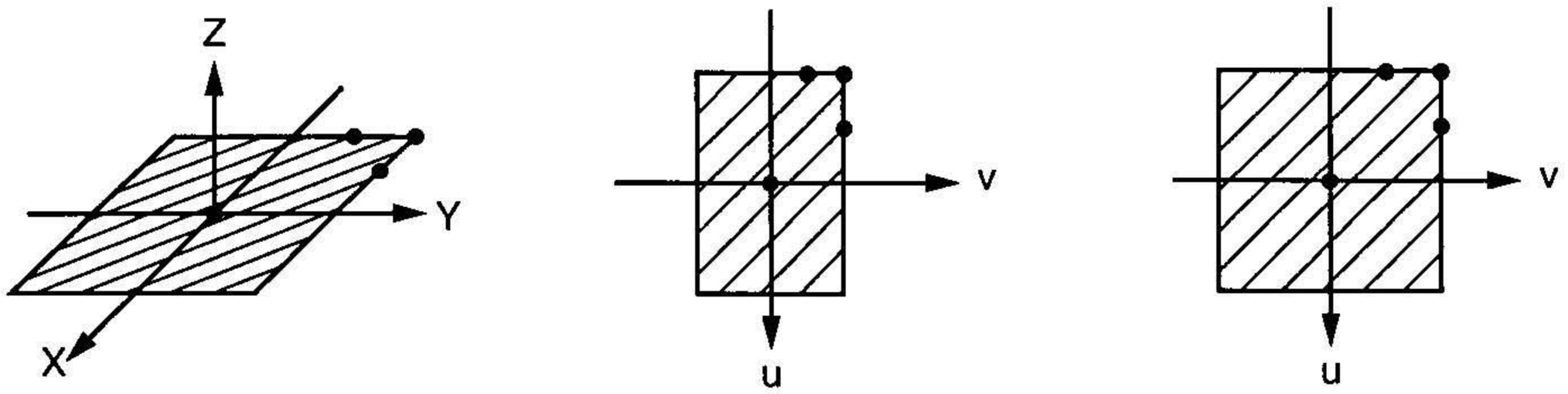
A generalization of the PFA (Section 3.3.5) naturally provides this third dimension of motion compensation. The compensation for nonplanar motions of the APC involves a projection of the signal history onto the FTP. The procedure projects the collected SAR data from a three-dimensional data collection surface perpendicular to and onto the two-dimensional FTP. This three-dimensional motion compensation technique, however, is sufficient only for scatterers in one specific plane, the selected FTP. Typically, the local ground plane is chosen to be this compensation plane. However, it is acceptable to make another choice such as the side of a hill or the surface of a large complex target if *a priori* knowledge of its geometry is available.

Imaging a three-dimensional scene from a three-dimensional data collection surface leads to a defocusing of scatterers out of the FTP. The amount of defocus increases linearly with scatterer distance out of the FTP. For a particular data collection, we refer to the distance above and below the FTP for which scatterers are adequately focused as the height-of-focus (HOF). The HOF can be small during aircraft maneuvers out of a nominal slant plane; this limitation poses a serious difficulty in fine-resolution imaging during aggressive maneuvers by the SAR platform. When the platform accelerates out of a nominal slant plane, scatterers out of the FTP experience a phase error in azimuth. In a constant acceleration maneuver, the magnitude of the primarily quadratic phase error increases linearly with scatterer height out of the compensation plane and quadratically with the reciprocal of resolution. Section 3.8 analyzes and quantifies this limitation.

In a sense, this three-dimensional motion compensation technique is not really a correction for NPM but a change in FTP from the nominal slant plane to another preferred plane containing the scene of interest. This viewpoint arises from the observation that the nominal slant plane becomes the FTP by default if the data projection aspect of the polar formatting operation is omitted.

3.3.5 Selection of Image Display Plane

In the presence of a nonplanar data collection surface, the processing algorithm compensates for the effects of NPM best for scatterers in the FTP. When mapping terrain, it is natural to select a nominal terrain plane as the FTP since the majority of scatterers will be near the nominal terrain plane. This selection provides the best chance to have a focused image of the terrain. Selection of the IDP is more flexible; this selection impacts the geometric presentation of the image but does not affect image quality in any other way. Two choices for the IDP are common and reasonable. Sometimes, the nominal slant plane is the choice, usually to accommodate the customs of the end user. In this case, the imagery is foreshortened relative to its ground plane view. That is, a square area on the ground (in the FTP) will appear with a nominally parallelogram outline in this IDP. The second common choice for the IDP is the FTP. In this case, a square ground area (in the FTP) will remain square in the image. Figure 3.16 provides sketches to illustrate these geometry effects.



(a) (b) (c)

Figure 3.16 Impact of IDP choice on the image display geometry: **(a)** Square ground patch in the *XY* plane; **(b)** Nominal slant plane as the IDP; **(c)** *XY* plane as the IDP.

The form of the polar format transformation, such as that in (3.19) and (3.20), determines the choice of IDP. In fact, (3.19) and (3.20) select the *XY* plane (in this case the FTP) to be the IDP also. The form of the polar format transformations to select a more general IDP defined by the *X* axis and the angle β_o in Figure 2.21 is

$$K_p(n,\hat{t}) = K_c\left(\frac{\gamma}{f_c}\right)\frac{S_{\phi a}\sin(\phi_{sc})}{S_{\phi c}\sin(\phi_s)}\left(\frac{f_c}{\gamma}+\hat{t}-\frac{2R_a}{c}\right) \tag{3.35}$$

and

$$\theta_p = \theta_s(nT) \tag{3.36}$$

with

$$K_c = \frac{4\pi f_c}{c}\frac{S_{\phi c}}{\sin(\phi_{sc})} \tag{3.37}$$

This form for K_p is more general than (3.14) because it allows for an IDP other than the FTP. The quantities K_p and K_c are in units of radians per unit distance in wavenumber space. The presence of the term $S_{\phi a}$ in K_p establishes *XY* as the FTP (Section 3.3.4) while $\sin(\phi_s)$ in K_p and θ_s in θ_p establish the IDP. Here, ϕ_a is the incidence angle, ϕ_s is the display incidence angle with value ϕ_{sc} at aperture center, and θ_s is the display squint angle with value θ_{sc} at aperture center. The location $(K_p, \theta_p) = (K_c, \theta_{sc})$ is the center of the data window to process in this case.

Viewed in this alternative, general two-dimensional polar format, the phase history for a single scatterer from (3.9) would vary with K_p according to

$$\Phi_p(n,\hat{t}) = -K_p\frac{\sin(\phi_s)}{\sin(\phi_{sc})}\left(\frac{R_\Delta}{S_{\phi a}}\right)+\frac{4\pi\gamma}{c^2}R_\Delta^2 \tag{3.38}$$

While included here for completeness and as a reference, this generalized formulation does not aid the development of the principles and characteristics of the PFA. For simplicity and clarity of presentation, all analyses after this subsection utilize (3.19) and (3.20) to present the XY plane as both the FTP and the IDP. Analyses allowing a more general IDP would proceed in a similar fashion but require additional terms that obscure key relationships. When the IDP is the FTP, it follows that $\phi_s = 90$ deg, $\psi_s = 0$, $\theta_s = \theta_a$, and $\beta_o = 0$ in Figure 2.21.

3.4 SAR IMAGING GEOMETRY

A complete analysis of the PFA begins with a presentation of three geometry models. These models include the data collection geometry, data format geometry, and image geometry. The data collection geometry specifies the APC location relative to the imaged scene as a function of time. The data format geometry specifies the relationship between the sampled time signal (K samples on each of N_p pulses) output by the radar receiver and the way in which these samples are arranged in two-dimensional processor space. The image geometry indicates the two-dimensional image display space. Although each of these geometries varies with time based on the relative motion between the APC and the scene being imaged, time is a dummy parameter in many respects. The path (locus) in space of the APC relative to the scene is more relevant than the timing of the data collection movement along this path.

3.4.1 Geometry Models

Figure 3.17 illustrates these three geometry models. This development follows the choice of the FTP as the IDP. The data collection geometry begins with an orthogonal XYZ coordinate system with origin at the center of the scene being imaged. The scatterer position vector $\boldsymbol{r}_t = (X_t, Y_t, Z_t)$ defines a scatterer location relative to this scene center. The XY plane is the selected FTP with respect to compensation for nonplanar antenna motion (Section 3.3.4). Initially, no constraint with respect to the target and sensor geometry or relative motion is placed on the angular orientation of the orthogonal X and Y axes in the XY plane. The data collection model in Figure 3.17(a) is basically the data collection geometry presented in Figure 2.21 with the IDP selected to coincide with the FTP; both planes are the XY plane.

The definitions of geometric quantities and symbols used in Section 2.6 are valid here. The squint angle θ_a between the X axis and the vertical projection of the slant range vector onto the XY plane has value θ_{ac} at aperture center. The Doppler cone angle α_d between the antenna velocity vector and the slant range vector to scene center has value α_{dc} at aperture center. The incidence angle ϕ_a at aperture center is ϕ_{ac}.

For clarification, Figure 3.17(b) shows the projection of the slant range vector onto the XY plane at aperture center. An xy coordinate system based on θ_{ac} is defined in which x relates to azimuth and y relates to (negative) range. Figure 3.17(c) presents the data

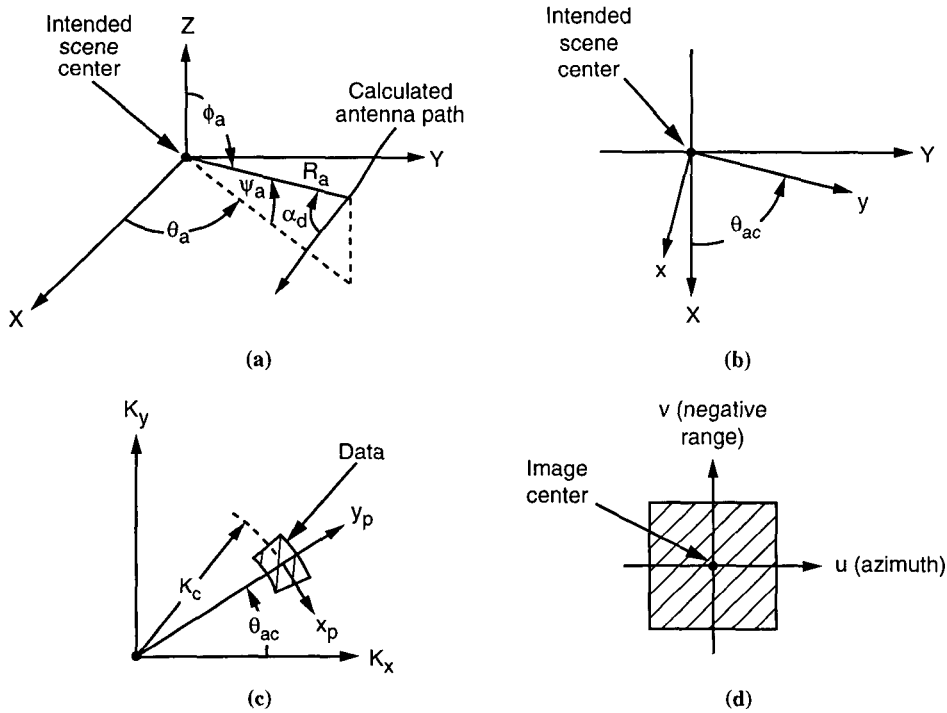


Figure 3.17 Geometry models with FTP as IDP: **(a)** Data collection; **(b)** Data collection (*XY* plane view); **(c)** Data format; **(d)** Image.

format geometry in coordinates K_x and K_y; data format space is a spatial-frequency or wavenumber domain. The data formatting operation uses a polar transformation described in (3.35) and (3.36) to compensate for MTRC, to reduce the effects of NPM, and to establish the *XY* plane as the IDP. The image geometry in Figure 3.17(d) consists of azimuth and (negative) range coordinates (*u, v*) in the IDP where *u* corresponds to *x* and *v* corresponds to *y* in the data collection space.

For reference and for completeness, Figure 3.18 presents the data collection and data format geometry models to include the possibility of a FTP different from the IDP. These generalized models do not aid the development of the principles and characteristics of the PFA. For simplicity, all future discussions below utilize (3.22) through (3.25) and the geometry models in Figure 3.17, which present the *XY* plane as both the focus plane and the IDP.

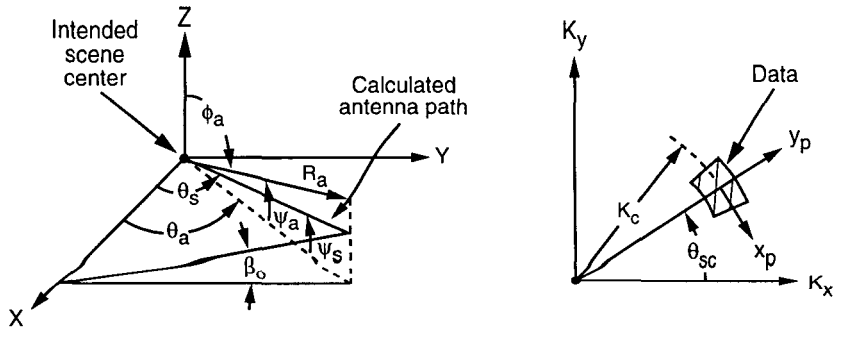


Figure 3.18 Geometry models with IDP different from FTP: **(a)** Data collection; **(b)** Data format.

3.4.2 Relative Motion

It is natural that each of the three components of antenna velocity (V_{xa}, V_{ya}, V_{za}) at aperture center in the XYZ coordinate system can be nonzero. However, we lose no generality by rotating the X and Y axes about the Z axis such that V_{ya} (the Y component of sensor velocity at aperture center) becomes zero for each specific data processing aperture. Eventually it will be convenient to assume this rotation in some cases to simplify the analysis and its interpretation.

We will broaden the model to include the case of a second-order maneuver by allowing each of the components of the velocity and acceleration vectors to be nonzero. It is important to include accelerations in this model in order to illustrate the complications to image formation processing introduced by NPM of the SAR sensor. Values of measured position vector $\boldsymbol{P_a} = (X_{ac}, Y_{ac}, Z_{ac})$, velocity vector $\boldsymbol{V_a} = (V_{xa}, V_{ya}, V_{za})$, and acceleration vector $\boldsymbol{A_a} = (A_{xa}, A_{ya}, A_{za})$ at aperture center (that is, at $t = 0$) define the quadratic maneuver. Thus, $\boldsymbol{P_a}$ is the midaperture location of the sensor. Because each component of these vectors is the value at aperture center, all components are constant over the synthetic aperture being modeled. Figure 3.19 illustrates a quadratic maneuver in the Z direction.

Based on (2.53), a continuous time expression for the radar slant range vector $\boldsymbol{R_a} = (X_a, Y_a, Z_a)$ incorporating the position, velocity, and acceleration vectors is

$$\boldsymbol{R_a} = \boldsymbol{P_a} + \boldsymbol{V_a}t + 0.5\boldsymbol{A_a}t^2 \tag{3.39}$$

The length of the vector $\boldsymbol{R_a}$ is R_a.

It is straightforward to derive an exact expression relating time to sensor motion. The procedure begins with the equation for instantaneous squint angle from (2.42) in the form

$$\cot(\theta_a) = \frac{X_{ac} + V_{xa}t + 0.5A_{xa}t^2}{Y_{ac} + V_{ya}t + 0.5A_{ya}t^2} \tag{3.40}$$

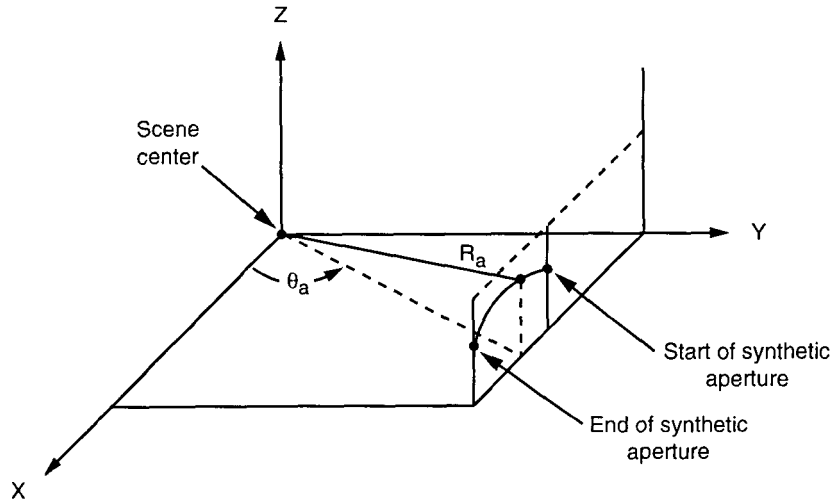


Figure 3.19 Example of a quadratic maneuver.

Solving this equation for t yields the relationship

$$t = \frac{Y_{ac}\Delta c}{V}\left[\frac{2}{F}\right] \tag{3.41}$$

where

$$\Delta c = C_{\theta a} - \cot(\theta_{ac})\, S_{\theta a} \tag{3.42}$$

$$V = V_{xa}S_{\theta a} - V_{ya}C_{\theta a} \tag{3.43}$$

$$F = 1 + \sqrt{1 + \frac{2Y_{ac}A\Delta c}{V^2}} \tag{3.44}$$

and

$$A = A_{xa}S_{\theta a} - A_{ya}C_{\theta a} \tag{3.45}$$

Here, $S_{\theta a}$ is $\sin(\theta_a)$ and $C_{\theta a}$ is $\cos(\theta_a)$. Also, V and A represent the components of antenna velocity and acceleration, respectively, which change the angle θ_a.

Additionally, it is straightforward to show that the values at aperture center of the first two derivatives of time with respect to θ_a are

$$\left.\frac{dt}{d\theta_a}\right|_c = -\frac{Y_{ac}/S_{\theta c}}{V_{xa}S_{\theta c} - V_{ya}C_{\theta c}} \tag{3.46}$$

and

$$\left.\frac{d^2t}{d\theta_a^2}\right|_c = \frac{2Y_{ac}/S_{\theta c}}{(V_{xa}S_{\theta c}-V_{ya}C_{\theta c})^2}\left[V_{xa}C_{\theta c}+V_{ya}S_{\theta c}-\frac{Y_{ac}(A_{xa}S_{\theta c}-A_{ya}C_{\theta c})}{2(V_{xa}S_{\theta c}-V_{ya}C_{\theta c})S_{\theta c}}\right] \tag{3.47}$$

Here, $S_{\theta c}$ is $\sin(\theta_{ac})$ and $C_{\theta c}$ is $\cos(\theta_{ac})$ with θ_{ac} being the value of θ_a at aperture center.

For the case in which all the measured accelerations are zero, (3.41) simplifies to

$$t = \frac{Y_{ac}\Delta c}{V} \tag{3.48}$$

since $F = 2$ in this situation. Also, for the case in which all the measured accelerations and V_{ya} are zero, (3.46) simplifies to

$$\left.\frac{dt}{d\theta_a}\right|_c = -\frac{Y_{ac}}{V_{xa}S_{\theta c}^2} \tag{3.49}$$

and (3.47) simplifies to

$$\left.\frac{d^2t}{d\theta_a^2}\right|_c = \frac{2Y_{ac}C_{\theta c}}{V_{xa}S_{\theta c}^3} \tag{3.50}$$

These two simple relationships will prove useful later when we perform a Taylor series expansion of the signal phase in situations that assume this simple collection geometry.

Similarly, to evaluate the effects of errors in motion measurement, continuous time expressions for variations in motion measurement error over time are desirable. Motion measurement error is the difference between the measured and the actual positions of the radar APC; this error naturally varies with time over the synthetic aperture interval. From (2.54), the vector $\boldsymbol{R}_e = (X_e, Y_e, Z_e)$, with

$$\boldsymbol{R}_e = \boldsymbol{P}_e + \boldsymbol{V}_e t + 0.5\boldsymbol{A}_e t^2 \tag{3.51}$$

represents low-frequency variation in measurement error from pulse to pulse over the synthetic aperture time centered at $t = 0$. The vectors $\boldsymbol{P}_e = (X_{ec}, Y_{ec}, Z_{ec})$, $\boldsymbol{V}_e = (V_{xe}, V_{ye}, V_{ze})$, and $\boldsymbol{A}_e = (A_{xe}, A_{ye}, A_{ze})$ represent position, velocity, and acceleration measurement error vectors, respectively, at $t = 0$. Because each component of these vectors is the value at aperture center, all components are constant over the synthetic aperture being modeled.

Figure 3.20 illustrates the relationships among the position vectors in this model. Here, $\boldsymbol{r}_t$ is the scatterer position vector $\boldsymbol{r}_t = (X_t, Y_t, Z_t)$ relative to scene center. Its magnitude is r_t. The quantity R_t is the distance between the APC and the scatterer.

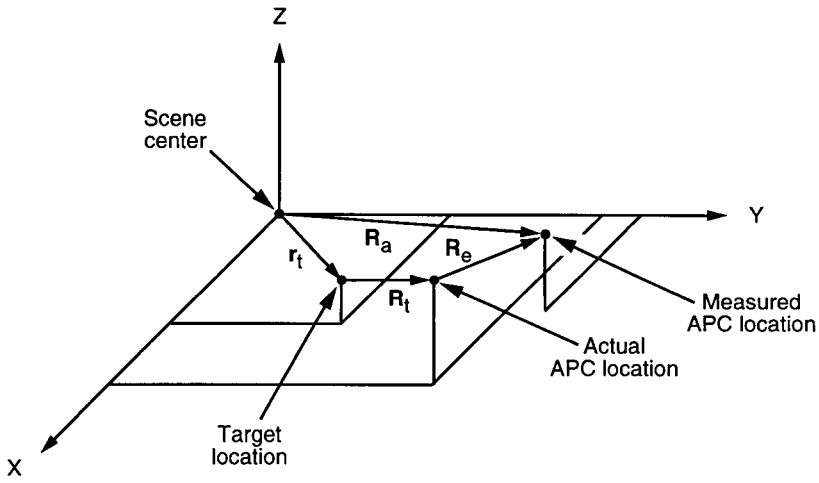


Figure 3.20 Relationships among data collection position vectors.

3.4.3 Differential Range

The designation, R_Δ, represents $R_t - R_a$, the differential range. It is not surprising that the differential range is a dominant factor in the signal history in (3.24). The distance R_a is deterministic; it is a known quantity which the radar system provides to the signal processor. It is the estimate by the radar system (aided by its motion sensor) of the distance between the APC and a desired scene center. This distance provides the time reference relative to which the radar measures the propagation time (the time delay, R_t/c), from the APC to a scatterer in the scene. This relative time delay (and associated relative differential range, R_Δ) is the basic quantity which the SAR measures at (nominally) the time of transmission of each pulse. The Cartesian form for differential range is

$$R_\Delta = \sqrt{(X_a + X_e - X_t)^2 + (Y_a + Y_e - Y_t)^2 + (Z_a + Z_e - Z_t)^2} - \sqrt{X_a^2 + Y_a^2 + Z_a^2} \qquad (3.52)$$

The first square-root term in this equation is an expression for R_t. This expression includes motion measurement error because R_t represents the *actual* distance from the sensor to a scatterer. Because the scatterer may be anywhere in the scene, this expression also includes scatterer coordinates. The second square-root term in (3.52) represents R_a. This term does not include motion measurement error because R_a represents the *measured* distance from the sensor to scene center. The radar receiver and the IFP use the quantity R_a to provide motion compensation to the received signals.

Direct differentiation of (3.52) with respect to time yields the differential range rate $\dot{R}_\Delta$, evaluated at aperture center as

$$\dot{R}_{\Delta c} = \left[-\frac{\boldsymbol{r}_t \bullet (\boldsymbol{V}_a + \boldsymbol{V}_e)}{R_t} + \frac{\boldsymbol{P}_e \bullet (\boldsymbol{V}_a + \boldsymbol{V}_e)}{R_t} - \frac{(\boldsymbol{P}_a \bullet \boldsymbol{V}_a) R_\Delta}{R_{ac} R_t} + \frac{(\boldsymbol{P}_a \bullet \boldsymbol{V}_e)}{R_t} \right]_c \tag{3.53}$$

The subscript c notation indicates evaluation at aperture center. A simplification of (3.53) by setting $\boldsymbol{P}_e = 0$, $\boldsymbol{V}_e = 0$, $V_{ya} = 0$, $V_{za} = 0$, $Y_{ac} = 0$, and $Z_{ac} = 0$ yields the relationship of (3.3) in Section 3.2.2.

For future reference, direct differentiation of (3.52) yields the second derivative of R_Δ with respect to time, evaluated at aperture center, as

$$\ddot{R}_{\Delta c} = \left[\frac{B_1}{R_t} - \frac{B_2^2}{R_t^3} + \frac{(\boldsymbol{P}_a \bullet \boldsymbol{V}_a)^2}{R_{ac}^3} - \frac{R_\Delta B_3}{R_t R_{ac}} \right]_c \tag{3.54}$$

where

$$B_1 = \boldsymbol{P}_e \bullet \boldsymbol{A}_a - \boldsymbol{r}_t \bullet \boldsymbol{A}_a + 2(\boldsymbol{V}_e \bullet \boldsymbol{V}_a) + |\boldsymbol{V}_e|^2 + \boldsymbol{P}_e \bullet \boldsymbol{A}_e - \boldsymbol{r}_t \bullet \boldsymbol{A}_e + \boldsymbol{P}_a \bullet \boldsymbol{A}_e \tag{3.55}$$

$$B_2 = \boldsymbol{P}_a \bullet \boldsymbol{V}_a - \boldsymbol{r}_t \bullet \boldsymbol{V}_a + \boldsymbol{P}_a \bullet \boldsymbol{V}_e + \boldsymbol{P}_e \bullet \boldsymbol{V}_a - \boldsymbol{r}_t \bullet \boldsymbol{V}_e + \boldsymbol{P}_e \bullet \boldsymbol{V}_e \tag{3.56}$$

and

$$B_3 = (\boldsymbol{P}_a \bullet \boldsymbol{A}_a) + |\boldsymbol{V}_a|^2 \tag{3.57}$$

3.4.4 Approximation for Differential Range

Equation (3.52) provides an exact expression for differential range. A useful approximation for this quantity, available by Taylor series expansion for the common case in which $|R_\Delta| << R_a$, is

$$R_\Delta \approx -\frac{(\boldsymbol{R}_a \bullet \boldsymbol{r}_t)}{R_a} + M_e + R_c \tag{3.58}$$

where M_e (for motion measurement error) is

$$M_e = \frac{(\boldsymbol{R}_a \bullet \boldsymbol{R}_e)}{R_a} - \frac{(\boldsymbol{r}_t \bullet \boldsymbol{R}_e)}{R_a} + \frac{(\boldsymbol{R}_a \bullet \boldsymbol{r}_t)(\boldsymbol{R}_e \bullet \boldsymbol{R}_a)}{R_a^3} \tag{3.59}$$

and R_c (for range curvature) is

$$R_c = \frac{r_t^2}{2R_a} - \frac{(\boldsymbol{R}_a \bullet \boldsymbol{r}_t)^2}{2R_a^3} \tag{3.60}$$

Here $\boldsymbol{R}_e$ is the motion measurement error vector, $\boldsymbol{r}_t$ is the scatterer position vector, and $\boldsymbol{R}_a$ is the slant range vector of length R_a as illustrated in Figure 3.20. As a reminder, R_t is the distance between the APC and the scatterer.

The first term on the right in (3.58) provides both the basic imaging expression and the effects of a nonplanar data collection surface introduced by the measured acceleration vector, $\boldsymbol{A}_a = (A_{xa}, A_{ya}, A_{za})$. The M_e term comprises the effects of motion measurement error identified by the vector $\boldsymbol{R}_e = (X_e, Y_e, Z_e)$. The R_c term represents the effect of range curvature. Range curvature involves terms that are quadratic and higher order in the scatterer location vector $\boldsymbol{r}_t = (X_t, Y_t, Z_t)$; only the quadratic terms are significant enough to include here.

Equation (3.53) provides an exact expression for differential range rate evaluated at aperture center. A useful approximation for the differential range rate, proceeding from a differentiation of (3.58), is

$$\dot{R}_\Delta \approx -\frac{\boldsymbol{r}_t \bullet \boldsymbol{V}_a}{R_a} + \frac{(\boldsymbol{P}_a \bullet \boldsymbol{V}_a)\,(\boldsymbol{R}_a \bullet \boldsymbol{r}_t)}{R_a^3} + \dot{M}_{e1} + \dot{M}_{e2} + \dot{R}_c \tag{3.61}$$

with

$$\dot{M}_{e1} = -\frac{\boldsymbol{r}_t \bullet \boldsymbol{V}_e}{R_a} + \frac{\boldsymbol{P}_e \bullet \boldsymbol{V}_a}{R_a} + \frac{(\boldsymbol{P}_a \bullet \boldsymbol{V}_e)}{R_a} \tag{3.62}$$

$$\dot{M}_{e2} = -\frac{(\boldsymbol{R}_a \bullet \boldsymbol{R}_e)\,(\boldsymbol{R}_a \bullet \boldsymbol{V}_a)}{R_a^3} + \frac{(\boldsymbol{R}_a \bullet \boldsymbol{r}_t)\,(\boldsymbol{R}_a \bullet \boldsymbol{V}_e)}{R_a^3} \tag{3.63}$$

and

$$\dot{R}_c = -\frac{r_t^2\,(\boldsymbol{V}_a \bullet \boldsymbol{R}_a)}{2R_a^3} + \frac{3\,(\boldsymbol{R}_a \bullet \boldsymbol{r}_t)^2\,(\boldsymbol{V}_a \bullet \boldsymbol{R}_a)}{2R_a^5} - \frac{(\boldsymbol{R}_a \bullet \boldsymbol{r}_t)\,(\boldsymbol{V}_a \bullet \boldsymbol{r}_t)}{R_a^3} \tag{3.64}$$

With regard to position measurement error, only the displacement effects are included in this expression since the space-variant (image distortion) effects are not large and serve only to complicate the analysis.

The key to analysis of the characteristics of the signal phase in (3.25) is to have expressions for R_Δ and $S_{\phi a}$ in terms of the polar coordinate, θ_p. It is necessary to evaluate these quantities and their derivatives with respect to θ_p at aperture center in order to complete a two-dimensional Taylor series expansion of the signal phase. Equation (3.52)

relates R_Δ and time, and the equation

$$S_{\phi a} = \frac{\sqrt{X_a^2 + Y_a^2}}{R_a} \tag{3.65}$$

relates $S_{\phi a}$ and time. Equations (3.20) and (3.41) provide the connection between time and θ_p. Taylor series expansion provides a means to separate a phase error function into components with which we associate specific effects on the image.

3.5 TAYLOR SERIES EXPANSION PROCEDURE

We have an expression for the complete radar signal history $s_o(n, \hat{t})$ in (3.8) and an expression for its phase $\Phi_p(n, \hat{t})$ after polar formatting in (3.25). Ideally, the polar-formatted signal from a point scatterer is a constant frequency signal with linear phase across the two-dimensional signal history. In reality, the signal deviates from linear phase. This deviation is due largely to motion measurement errors and algorithm approximations. The Taylor series expansion is a tool to analyze these variations from the ideal signal by separating them into components with identifiable effects on the SAR imagery.

A two-dimensional Taylor series expansion of the signal phase, centered about the location $(x_p, y_p) = (0, 0)$, separates the signal phase into:

- A constant (affecting image pixel phase);
- A linear term (affecting image location, geometric fidelity, and distortion);
- A quadratic term (affecting image focusing and image pixel phase);
- Higher order terms.

The following presentation will formulate the mechanics to do this expansion in rectangular coordinates (x_p, y_p) using, however, the derivatives in polar coordinates of the function being expanded. While it may seem natural to use rectangular coordinates throughout this expansion, advantages in simplicity and understanding are available by proceeding in this mixture of rectangular and polar domains.[1]

3.5.1 Taylor Series Coefficients

The Taylor series expansion of a function $f_1(x_p, y_p) = f(K_p, \theta_p)$ about $(x_p, y_p) = (0, 0)$, or identically about $(K_p, \theta_p) = (K_c, \theta_{ac})$, is

$$f_1(x_p, y_p) = a_0 + a_1 x_p + a_2 y_p + a_{11} x_p^2 + a_{12} x_p y_p + a_{22} y_p^2 + \text{higher order terms} \tag{3.66}$$

1. The authors first became aware of the advantages of this approach through unpublished analyses and discussions with J. Craig Dwyer of the Environmental Research Institute of Michigan (ERIM). Section 3.5 draws heavily from Mr. Dwyer's early ideas.

where the higher order (including cubic) terms are acknowledged but not emphasized here because they generally are small. Here, x_p and y_p are the processor space coordinates, centered at aperture center and associated with azimuth and (negative) range, respectively. Figure 3.17(c) illustrates these coordinates. The constant phase term a_0 affects the phase of the Fourier transform of a nominally linear phase function; this term is of interest primarily in applications that exploit the coherent nature of SAR imagery, such as interferometry. The linear phase terms a_1 and a_2 relate to scatterer positioning in the image. The quadratic terms relate to image focus.

Based on a two-dimensional Fourier transform with kernel $-j\,(ux_p + vy_p)$ of a signal with phase $f_1(x_p, y_p)$, image coordinates u_i and v_i corresponding to a scatterer at (X_t, Y_t, Z_t) are related to the coefficients a_1 and a_2 by

$$u_i = a_1 \tag{3.67}$$

and

$$v_i = a_2 \tag{3.68}$$

where u_i corresponds to x (azimuth) and v_i corresponds to y (decreasing range) in the data collection space. Here, a_1 and a_2 are functions of scatterer coordinates X_t, Y_t, and Z_t or equally x_t, y_t, and z_t with

$$x_t = X_t S_{\theta c} - Y_t C_{\theta c} \tag{3.69}$$

$$y_t = X_t C_{\theta c} + Y_t S_{\theta c} \tag{3.70}$$

$$z_t = Z_t \tag{3.71}$$

Figure 3.17(b) illustrates the relationship between these scatterer coordinates.

It is helpful to write the image coordinates u_i and v_i in a format to emphasize the relationship between scatterer position and image position. This format is

$$u_i = m_x\,[x_t + P_x Z_t + L_x + l_x\,(X_t, Y_t, Z_t)\,] \tag{3.72}$$

$$v_i = m_y\,[y_t + P_y Z_t + L_y + l_y\,(X_t, Y_t, Z_t)\,] \tag{3.73}$$

where m_x and m_y are image scaling or magnification factors, P_x and P_y are geometry factors relating to the projection of scatterers onto the IDP, L_x and L_y are image displacements caused by space-invariant phase effects, and l_x and l_y are image distortions caused by space-variant phase effects.

A discussion of dimensions is useful here. If the dimensions of u_i and v_i are *samples* and those of x_i and y_i are *meters*, then m_x and m_y have dimensions of *samples/meter* or equally *pixels/meter*. Based on Figure 3.17, the scaling factors appear to be positive since the y coordinate points in the direction of decreasing range in the FTP and the v coordinate points in the direction of decreasing range in the image domain. However, factors and

procedures in the IFP affect both the magnitude and the sign of these scaling factors (Section 4.5). The linear coefficients (a_1 and a_2) of the Taylor series expansion provide expressions for the remaining factors in (3.72) and (3.73).

The quadratic coefficients (a_{11}, a_{12}, and a_{22}) of the Taylor series expansion are expressions for the quadratic phase error (QPE) coefficients present in the data. The magnitude of the quadratic phase error from zero-to-peak is available by replacing x_p and y_p in the expansion terms by their respective values at aperture extremes. From (3.31) and (3.32), these extreme values are available for the simple case in which the APC follows a straight line parallel to the X axis. Related to range and azimuth resolutions, these extreme values are

$$\left.\frac{x_p}{K_c}\right|_{\max} = \frac{\Delta x}{2K_c} = \frac{\lambda_c K_a \sin(\phi_{ao})}{4\rho_a S_{\phi c}^2} \tag{3.74}$$

and

$$\left.\frac{y_p}{K_c}\right|_{\max} = \frac{\Delta y}{2K_c} = \frac{\lambda_c K_r}{4\rho_r} \tag{3.75}$$

In sizing QPE, it is reasonable to simplify (3.74) by using $\sin(\phi_{ao}) \approx S_{\phi c}$ without serious error.

The expressions for the Taylor series expansion coefficients in (3.66) are

$$a_0 = [f]_c \tag{3.76}$$

$$a_1 = -\frac{1}{K_c}\left[\frac{df}{d\theta_p}\right]_c \tag{3.77}$$

$$a_2 = \left[\frac{df}{dK_p}\right]_c \tag{3.78}$$

$$a_{11} = \frac{1}{2K_c^2}\left[\frac{d^2 f}{d\theta_p^2}\right]_c + \frac{1}{2K_c}\left[\frac{df}{dK_p}\right]_c \tag{3.79}$$

$$a_{12} = \frac{1}{K_c^2}\left[\frac{df}{d\theta_p}\right]_c - \frac{1}{K_c}\left[\frac{d^2 f}{dK_p d\theta_p}\right]_c \tag{3.80}$$

$$a_{22} = \frac{1}{2}\left[\frac{d^2 f}{dK_p^2}\right]_c \tag{3.81}$$

All derivatives in these coefficients are evaluated at aperture center as indicated by the subscript c notation; thus they are constants.

3.5.2 Calculation Procedures

The derivative chain rule relationships given by

$$\frac{\partial}{\partial \theta_p} = \frac{dt}{d\theta_p}\frac{\partial}{\partial t} \tag{3.82}$$

and

$$\frac{\partial^2}{\partial \theta_p^2} = \frac{d^2 t}{d\theta_p^2}\frac{\partial}{\partial t} + \left(\frac{dt}{d\theta_p}\right)^2 \frac{\partial^2}{\partial t^2} \tag{3.83}$$

are useful to obtain the derivatives with respect to $\theta_p(t)$ in terms of time derivatives. This procedure is useful because the geometry parameters are readily available as functions of time.

The signal equation (3.25) to be expanded consists of two terms. The first term encompasses the imaging term, range curvature, motion measurement errors and NPM effects. This term is given by

$$g_1 = -K_p \frac{R_\Delta}{S_{\phi a}} \tag{3.84}$$

It has the form

$$g_1 = -K_p g_\theta \tag{3.85}$$

with $g_\theta = g_\theta(\theta_p)$, a function of θ_p. Here, $g_\theta = R_\Delta / S_{\phi a}$. For g_1, the coefficients of the Taylor series expansion become

$$a_0 = -\frac{4\pi}{\lambda_c} R_{\Delta c} \tag{3.86}$$

$$a_1 = \left[\frac{dg_\theta}{d\theta_p}\right]_c = \left[\frac{dt}{d\theta_p}\right]_c \dot{g}_{\theta c} \tag{3.87}$$

$$a_2 = -g_{\theta c} \tag{3.88}$$

$$a_{11} = -\frac{1}{2K_c}\left[\frac{d^2 g_\theta}{d\theta_p^2}\right]_c - \frac{1}{2K_c} g_{\theta c} = -\frac{1}{2K_c}\left[\frac{d^2 t}{d\theta_p^2}\right]_c \dot{g}_{\theta c} - \frac{1}{2K_c}\left[\frac{dt}{d\theta_p}\right]_c^2 \ddot{g}_{\theta c} - \frac{1}{2K_c} g_{\theta c} \tag{3.89}$$

$$a_{12} = 0 \tag{3.90}$$

$$a_{22} = 0 \tag{3.91}$$

after making use of the chain rule relationships. Here, the dots refer to first and second time derivatives while the addition of a subscript c indicates that the derivative is evaluated at aperture center. Without further analysis, it is clear that the effects included in the first term introduce QPE in azimuth only since a_{11} is the only nonzero quadratic coefficient.

The two derivatives of g_θ with respect to time are complicated by the presence of the variable $S_{\phi a}$ as well as the variable R_Δ. The general expressions for these derivatives evaluated at aperture center are

$$\dot{g}_{\theta c} = \frac{\dot{R}_{\Delta c}}{S_{\phi c}} - \frac{R_{\Delta c}\dot{S}_{\phi ac}}{S_{\phi c}^2} \tag{3.92}$$

and

$$\ddot{g}_{\theta c} = \frac{1}{S_{\phi c}}\left[\ddot{R}_{\Delta c} - \frac{2\dot{R}_{\Delta c}\dot{S}_{\phi ac}}{S_{\phi c}} - \frac{R_{\Delta c}\ddot{S}_{\phi ac}}{S_{\phi c}} + 2R_{\Delta c}\frac{\dot{S}_{\phi ac}^2}{S_{\phi c}^2}\right] \tag{3.93}$$

Again, the dots refer to first and second time derivatives; the subscript c on derivative expressions indicates the value at aperture center. Direct differentiation of $S_{\phi a}$ from (3.65) yields

$$\dot{S}_{\phi a} = \frac{V_{xa}C_{\theta a} + V_{ya}S_{\theta a}}{R_a} - \frac{S_{\phi a}}{R_a}\left[\frac{\boldsymbol{R}_a \bullet \boldsymbol{V}_a}{R_a}\right] \tag{3.94}$$

The second term from the signal equation is the RVP effect. This term is given by

$$g_2 = \frac{4\pi\gamma}{c^2}R_\Delta^2 \tag{3.95}$$

It is independent of K_p; thus, all derivatives with respect to K_p are zero. On this basis, the constant and linear coefficients of a Taylor series expansion representing g_2 are

$$a_0 = g_{2c} \tag{3.96}$$

$$a_1 = -\frac{1}{K_c}\left[\frac{dt}{d\theta_p}\right]_c \dot{g}_{2c} \tag{3.97}$$

and

$$a_2 = 0 \tag{3.98}$$

The quadratic coefficients are

$$a_{11} = \frac{1}{2K_c^2}\left[\frac{d^2t}{d\theta_p^2}\right]_c \dot{g}_{2c} + \frac{1}{2K_c^2}\left[\frac{dt}{d\theta_p}\right]_c^2 \ddot{g}_{2c} \tag{3.99}$$

$$a_{12} = \frac{1}{K_c^2}\left[\frac{dt}{d\theta_p}\right]_c \dot{g}_{2c} = -\frac{a_1}{K_c} \tag{3.100}$$

and

$$a_{22} = 0 \tag{3.101}$$

The g_2 term causes distortion in azimuth only since a_2 is zero and causes no QPE directly in range since a_{22} is zero. The expressions for the remaining coefficients are simplified with the removal of the terms containing derivatives with respect to K_p.

The two derivatives of g_2 with respect to time come easily since the only variable in g_2 is R_Δ. The results are

$$\dot{g}_{2c} = \frac{8\pi\gamma}{c^2} R_{\Delta c}\dot{R}_{\Delta c} \tag{3.102}$$

and

$$\ddot{g}_{2c} = \frac{8\pi\gamma}{c^2}\left(R_{\Delta c}\ddot{R}_{\Delta c} + \dot{R}_{\Delta c}^2\right) \tag{3.103}$$

All quantities are values at the center of the processing aperture as indicated by the c subscript.

Table 3.5 identifies the derivatives to be evaluated at aperture center for each of the two terms (main term and RVP term). This table also identifies the equations presented earlier which provide the needed derivatives.

The time derivatives $\dot{R}_\Delta$ and $\ddot{R}_\Delta$ of the differential range R_Δ are available using (3.53) and (3.54). The time derivatives of $S_{\phi a}$ may be derived using (3.65). Some simplification and approximation in these quantities is needed to reach and interpret useful results.

Both g_1 and g_2 involve R_Δ. Equation (3.52) provides an exact expression for this quantity. A useful approximation for this differential range, available by Taylor series expansion for the common case $|R_\Delta| << R_a$, is presented in (3.58). Use of (3.58) in g_1 provides the basic imaging expression, the effects of a nonplanar data collection surface, the effects of motion measurement error, and the effects of range curvature. Use of (3.58) in g_2 provides the effects of RVP.

Expressions are needed for the time rate of change of the differential range and for the second derivative of the differential range with respect to time. Exact expressions for these quantities are available from (3.53) and (3.54). In some instances, approximations to these expressions are more useful. For the time rate of change of the differential range, (3.61) provides a useful, approximate expression.

Table 3.5
Derivatives Required for Taylor Series Expansion

Derivative	*Main Term* g_1 (3.84)	*RVP Term* g_2 (3.95)
$\frac{dt}{d\theta_p}$	Needed; (3.46)	Needed; (3.46)
$\frac{d^2 t}{d\theta_p^2}$	Needed; (3.47)	Needed; (3.47)
$\left(\frac{dt}{d\theta_p}\right)^2$	Needed; (3.46)	Needed; (3.46)
$\dot{g}$	Needed; (3.92)	Needed; (3.102)
$\ddot{g}$	Needed; (3.93)	Needed; (3.103)
$\frac{\partial g}{\partial K_p}$	Needed; simple	Zero
$\frac{\partial^2 g}{\partial \theta_p \partial K_p}$	Not needed	Zero
$\frac{\partial^2 g}{\partial K_p^2}$	Zero	Zero

The signal history model that we develop here is general in two respects. First, it maintains a general quadratic maneuver by the SAR platform with all components of velocity vector $\boldsymbol{V_a}$ and acceleration vector $\boldsymbol{A_a}$ possibly nonzero. Second, it allows all the imaging and error effects to be present simultaneously. This generality leads to cross-product effects among the various imaging terms and error sources; such effects are generally small and of little use, but greatly complicate the analysis and confuse an understanding of the basic ideas. For instance, the presence of a nonzero antenna acceleration vector is important only in the analysis of NPM; similarly, there is no need for antenna motion in any but the X direction to analyze and understand range curvature and RVP effects. On this basis, it is appropriate to make various simplifications to the model on a case-by-case basis to apply to the analysis of each effect. Table 3.6 and Table 3.7 provide summary charts of these simplifications to use in subsequent analyses. With respect to measured velocity and measured acceleration, Table 3.6 entries indicate which motion components we include in the analysis of each phase term. With respect to distortion, displacement, and QPE, Table 3.7 indicates which phase effects we consider in the analysis of each phase term.

Table 3.6
Motion Assumptions for Analysis of Phase Terms

Motion Quantity	*Basic Imaging Term*	*Range Curvature*	*NPM*	*Motion Errors*	*RVP*
Measured velocity	All components	V_{xa} only	All components	All components	V_{xa} only
Measured acceleration	All components	None	All components	None	None

Table 3.7
Phase Effects in Analysis of Phase Terms

Phase Effect	*Basic Imaging Term*	*Range Curvature*	*NPM*	*Motion Errors*	*RVP*
Distortion	Not applicable	Considered	Considered	Yes—except position error	Considered
Displacement	Not applicable	Not applicable	Not applicable	Considered	Not applicable
Space-variant QPE	Not applicable	Considered	Considered	Not considered	Considered
Space-invariant QPE	Not applicable	Not applicable	Not applicable	Considered	Not applicable

3.6 BASIC IMAGING TERMS IN THE SIGNAL EQUATION

The Taylor series expansion yields essential information about the behavior of the SAR image inherent in the signal equation. This information includes undesirable effects not addressed specifically by the PFA. The PFA does not completely eliminate the problem of MTRC; range curvature remains. In addition to range curvature, the presence of RVP, the use of single-point motion compensation (while the required compensation for a particular deviation from the desired antenna path varies slightly with scatterer angular location), and other effects combine to limit the size of the scene that the PFA can handle without significant degradation in image quality at the edges of the scene.

Only the range curvature effect is a specific polar format limitation, that is, a problem because of a unique polar format inadequacy. The other effects discussed throughout this chapter and specifically in this section are problems for all available algorithms for processing spotlight SAR data. These same problems are present in various forms also in stripmap data and its associated signal processing algorithms.

The Taylor series expansion of the SAR signal identifies a constant phase effect that contributes to image pixel phase; linear phase effects that determine image location; geometric fidelity and distortion; and quadratic phase effects that impact image focusing and image pixel phase. These linear and quadratic effects are discussed separately for each of the primary sources: range curvature, nonplanar data collection surface, APC motion measurement errors, and RVP.

This section concentrates on the basic imaging terms in the signal equation to indicate the phase of image pixels and the ideal geometric relationship between three-dimensional scatterer coordinates and two-dimensional image coordinates.

3.6.1 Phase of Image Pixels

Traditional uses for SAR imagery involve a display of the magnitude of the image reflectivity—the phase is discarded when the complex image is magnitude detected. The phase of an image pixel representing a single scatterer is deterministic; however, the phase of an image pixel representing multiple scatterers (in the same resolution cell) is made up of both a deterministic part and a nondeterministic, statistical part. For this reason, pixel phase in a single SAR image is generally not useful. Pixel phase is important in SAR interferometry applications (Section 9.3) which employ two SAR images of the same area, obtained under special conditions to ensure that the random, nondeterministic part of the phase is nearly identical in the two images.

This section presents a mathematical description of the expected phase of an image pixel representing a single scatterer. This deterministic phase is due to the two-way propagation path between the antenna and the scatterer. This expected phase is given by the term a_o in the Taylor series expansion of the signal phase.

Evaluation of $\Phi_p(x_p, y_p)$ in (3.25) at $(x_p, y_p) = (0, 0)$ yields the phase Φ_{po} related to this scatterer point. The result is

$$\Phi_{po} = \Phi_p(0, 0) = -\frac{4\pi}{\lambda_c} R_{\Delta c} + \frac{4\pi\gamma}{c^2} R_{\Delta c}^2 \tag{3.104}$$

This quantity represents an approximation to the deterministic contribution to the image phase of the scatterer at (X_t, Y_t, Z_t) where $R_{\Delta c}$ is the value of R_Δ at the center of the processing time. It is significant to note that Φ_{po} depends on antenna location only at $nT = 0$, the center of the azimuth coherent processing time. This result also indicates that the procedures on a single coherent aperture of data to establish a FTP (here XY) and to select a reference or IDP (here defined by X and β_o) do not affect the phase of individual image pixels. In particular, changing the IDP will not change the relative phase of individual image pixels.

This result assumes that Φ_{po} alone is responsible for the deterministic phase of the image pixel; in fact, higher order coefficients of the Taylor series expansion also impact image phase in a small way. In particular, a quadratic phase term across the signal history

slightly affects the image phase; the presence of a quadratic phase weighting across an aperture changes the mainlobe phase of the Fourier transform of the aperture up to about 45 deg for an uncorrected quadratic phase of a few cycles [10]. This effect is particularly relevant when the size of the quadratic phase varies with scatterer location. Both the RVP term and terms from NPM effects may introduce such space-variant quadratic phase effects. NPM effects naturally will depend on antenna position over the entire coherent aperture. In the presence of significant NPM, these effects require evaluation in applications for which image phase is important. In any case, these NPM effects are small for scatterers near the FTP.

Interferometric analysis requires an expression for the relative phase between corresponding pixels in two images generated from two antennas separated from each other primarily in the Y direction (ΔY). In practice, limited separation in the X direction (ΔX) and Z direction (ΔZ), related to antenna placement and aircraft attitude, also are present. The required expression depends on the geometry between the scatterer and the two antennas at the time corresponding to the center of the processing aperture. Section 9.3 addresses these issues of relative image pixel phase between two images collected with similar data collection geometries.

3.6.2 Basic Imaging Relationship

The use of the first term of the differential range from (3.58) in g_1 of (3.84) provides the desirable part of the signal history which relates scatterer location and RCS to image pixel number and amplitude. The first term of (3.58) is

$$(R_\Delta)_{\text{basic}} = -\frac{(\boldsymbol{R}_a \bullet \boldsymbol{r}_t)}{R_a} = -S_{\phi a}\left[X_t C_{\theta a} + Y_t S_{\theta a} + Z_t \cot(\phi_a)\right] \tag{3.105}$$

We can write this expression in the form

$$(R_\Delta)_{\text{basic}} = -S_{\phi a}\left\{X_t C_{\theta a} + \left[Y_t + Z_t \frac{\cot(\phi_{ac})}{S_{\theta c}}\right] S_{\theta a}\right\} + \mathrm{N}_{pm} \tag{3.106}$$

The term N_{pm} (for nonplanar motion) is

$$\mathrm{N}_{pm} = -Z_t S_{\phi a} S_{\theta a}\left[\frac{\cot(\phi_a)}{S_{\theta a}} - \frac{\cot(\phi_{ac})}{S_{\theta c}}\right] \tag{3.107}$$

This term represents the effects of the nonplanar data collection surface. Section 3.8 addresses this term.

The remaining expression in (3.106), when inserted in g_1, is the basic imaging term; it provides the desired Fourier transform kernel that represents the signal from each

scatterer in the scene by a two-dimensional, constant-frequency complex sinusoid. We insert the expression in (3.106) without the NPM term into g_1 to provide

$$(g_1)_{\text{imaging}} = \left[X_t C_{\theta a} + Y_t S_{\theta a} + Z_t \left(S_{\theta a} \frac{\cot(\phi_{ac})}{S_{\theta c}} \right) \right] K_p \tag{3.108}$$

which becomes

$$(g_1)_{\text{imaging}} = X_t K_x + \left[Y_t + Z_t \frac{\cot(\phi_{ac})}{S_{\theta c}} \right] K_y \tag{3.109}$$

This signal equation is a two-dimensional sinusoid in K_x and K_y processor coordinates. While it may be obvious that the coefficients of K_x and K_y in this expression represent the projected location of the elevated scatterer in X and Y, it is instructive to proceed with the formality of the Taylor series expansion in x_p and y_p processor coordinates. In these coordinates, the expression in (3.109) becomes

$$(g_1)_{\text{imaging}} = \left[x_t - Z_t \frac{\cot(\phi_{ac})\, C_{\theta c}}{S_{\theta c}} \right] x_p + \left[y_t + Z_t \cot(\phi_{ac}) \right] y_p + \phi_c \tag{3.110}$$

where

$$\phi_c = \frac{4\pi S_{\phi c}}{\lambda_c} \left[y_t + Z_t \cot(\phi_{ac}) \right] \tag{3.111}$$

This result uses (3.69) and (3.70) and the relationships

$$K_x = K_c C_{\theta c} + x_p S_{\theta a} + y_p C_{\theta a} \tag{3.112}$$

and

$$K_y = K_c S_{\theta c} - x_p C_{\theta a} + y_p S_{\theta a} \tag{3.113}$$

which reflect the processor space geometry seen in Figure 3.17(c). The term ϕ_c relates only to the image phase since it is independent of processor space coordinates. It is the largest contributor to Φ_{po} in (3.104). The processing requirement to convert this basic imaging term into a two-dimensional impulse response representing the image of the associated scatterer projected onto the XY image display plane is simply a two-dimensional FFT in x_p and y_p.

Inspection of (3.110) indicates that the Taylor series coefficients associated with this imaging term are

$$a_{0b} = \phi_c \tag{3.114}$$

$$a_{1b} = x_t - Z_t \frac{\cot(\phi_{ac})\, C_{\theta c}}{S_{\theta c}} \tag{3.115}$$

and

$$a_{2b} = y_t + Z_t \cot(\phi_{ac}) \tag{3.116}$$

From (3.67) and (3.68), the basic image position is

$$u_{ib} = a_{1b} = x_t - Z_t \frac{\cot(\phi_{ac})\, C_{\theta c}}{S_{\theta c}} \tag{3.117}$$

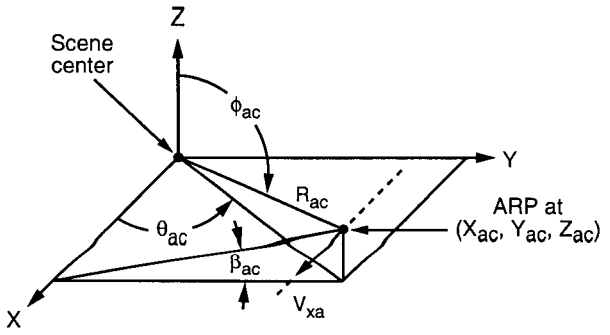
and

$$v_{ib} = a_{2b} = y_t + Z_t \cot(\phi_{ac}) \tag{3.118}$$

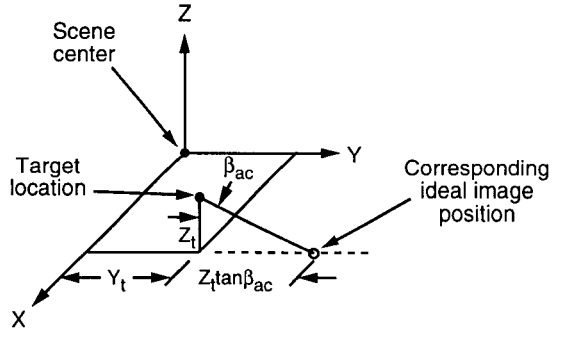
which, at this point, suggests unity scale factors in (3.72) and (3.73), that is, 1 unit distance per output image sample. The coefficients of the Z_t terms in these two equations contribute to P_x and P_y in (3.72) and (3.73).

To illustrate this mapping, Figure 3.21(a) indicates the data collection geometry at aperture center with the antenna at the aperture reference point (ARP). The expression $\tan(\beta_{ac}) = Z_{ac}/Y_{ac}$ defines the angle β_{ac} in the diagram. Figure 3.21(b) illustrates the mapping of an elevated scatterer location as reflected in (3.110). Figure 3.21(c) presents a ground plane view of the projection indicated by the bracketed coefficients of x_p and y_p in (3.111). The coefficients of Z_t within these brackets are contributions to P_x and P_y in (3.72) and (3.73). Scatterers in the XY plane, for which $Z_t = 0$, are ideally imaged in the corresponding position in the image. This perspective views the positioning or projection of any scatterer with a nonzero Z_t coordinate as an acceptable projection, not geometric distortion. We consider the distinctions among ideal positioning, projection based on scatterer height, image displacement, and image distortion in Section 8.5.

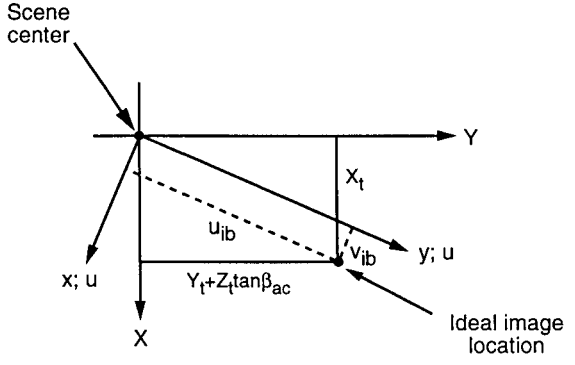
These results and the projections shown in Figure 3.21 indicate that the so-called range layover for elevated scatterers is in the Y_t, or cross-track direction, not in the y_t, or range direction. Elevated scatterers are moved, not in range, but in cross-track regardless of the spotlight squint angle, θ_{ac}. This result illustrates the fact that circles of constant range-Doppler (that is, the locus of all points at a fixed range and Doppler cone angle) are



(a)



(b)



(c)

Figure 3.21 Projection onto IDP: **(a)** Data collection geometry; **(b)** Three-dimensional view of projection; **(c)** Ground plane view of projection.

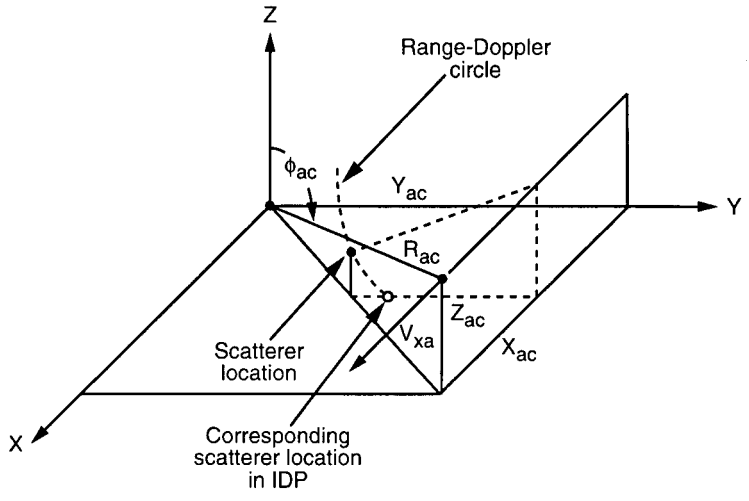


Figure 3.22 Geometry of range-Doppler circle projection.

in planes parallel to the *YZ* plane. All scatterers on a specific iso-range-Doppler circle appear at the identical location in the image. Figure 3.22 illustrates a range-Doppler circle and suggests the geometry of scatterer projection onto the IDP. Figure 2.6 provides a similar perspective. The difference between this projection and that suggested by Figure 3.21 is indicative of geometric distortion.

3.7 RANGE CURVATURE

Range curvature typically introduces significant distortion in a fine-resolution SAR image. The associated space-variant defocus of scatterers in the scene may be significant also. Because these effects are deterministic, it is possible to correct the distortion in the image formation process by an image resampling operation following the two-dimensional FFT. The defocus varies with scatterer location and is not easy to compensate in the final image. This space-variant defocus, in effect, limits the useful size of the image. In many practical applications, the defocus effect is not large enough to be a limitation on imagery exploitation. Section 5.3.2 quantifies this limitation on scene size.

Distortion occurs because surfaces of constant range from the APC at aperture center and surfaces of constant Doppler frequency (more accurately, cosine of the Doppler cone angle) do not form an equally spaced orthogonal grid on a flat ground. As Figure 3.23 suggests, spheres of constant range intersect the ground plane as circles centered at the antenna nadir point, and cones of constant Doppler intersect as hyperbolas symmetrical about the flight line nadir. Figure 2.8 provides a similar view. If an algorithm does not compensate for the curvature and nonorthogonality of this grid, then image distortion is present. Polar format does not naturally compensate, although deterministic distortion

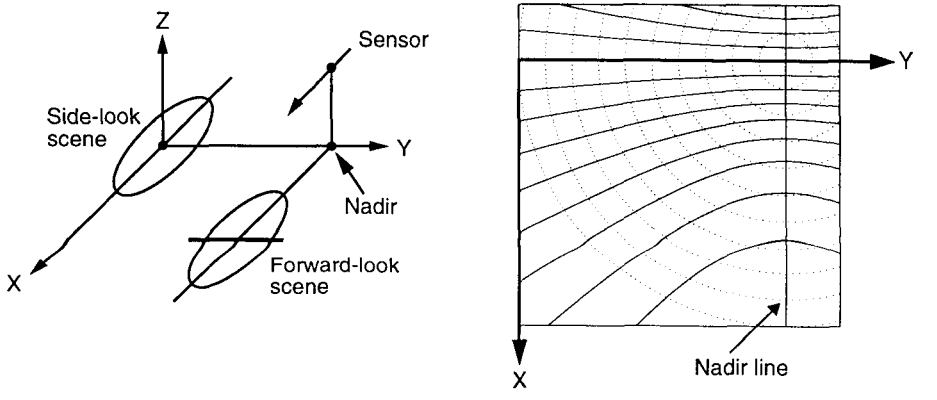


Figure 3.23 Illustration of constant range-Doppler grid: **(a)** Collection geometry; **(b)** Grid of iso-range circles (dotted lines) and iso-Doppler hyperbolas (solid lines) in the *XY* plane.

correction is generally possible in the image domain. The RMA accounts for range curvature and removes its phase effects as an intrinsic part of algorithm procedures.

For instance, a square object in an image without range curvature correction will appear as a keystone shape. Figure 3.24(a) illustrates this distortion for a broadside data collection and Figure 3.24(b) illustrates it for a data collection off broadside (squinted), both at 90-deg incidence angle. The distortion is less symmetric and slightly less severe off broadside since R_a in the denominator is larger off broadside.

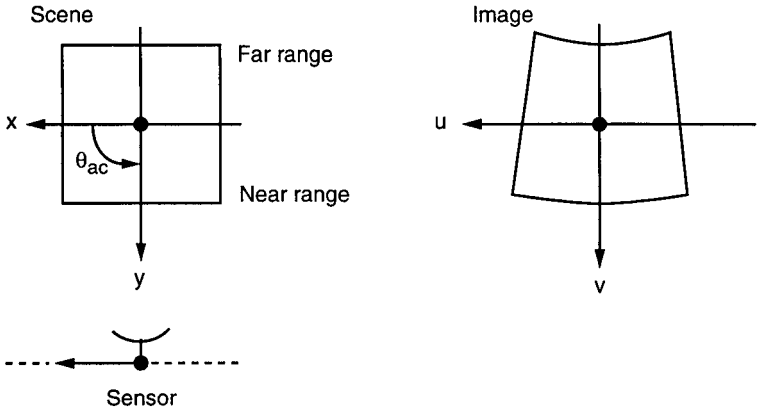
The use of the R_c term of the differential range from (3.58) in g_1 of (3.84) provides the part of the signal history referred to as range curvature. This term has the form

$$(R_\Delta)_{rc} = \frac{r_t^2}{2R_a} - \frac{(\boldsymbol{R}_a \bullet \boldsymbol{r}_t)^2}{2R_a^3} \tag{3.119}$$

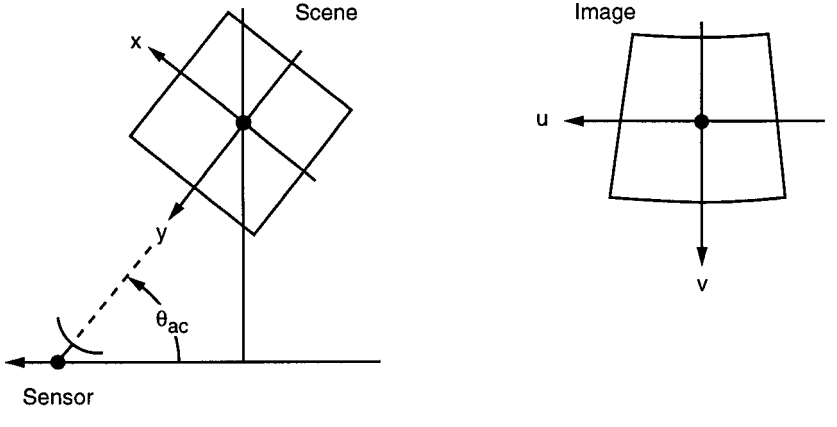
After polar formatting, it provides the space-variant phase effect given by

$$\Phi_{rc} = (g_1)_{rc} = -\frac{K_p}{S_{\phi a}}\left[\frac{r_t^2}{2R_a} - \frac{(\boldsymbol{R}_a \bullet \boldsymbol{r}_t)^2}{2R_a^3}\right] \tag{3.120}$$

For simplicity, it is convenient to examine the case in which the sensor travels in a straight line at constant velocity with only the X component of velocity nonzero; the measured acceleration vector, $\boldsymbol{A}_a$, is zero.



(a)



(b)

Figure 3.24 Keystone distortion: **(a)** Broadside data collection; **(b)** Data collection off broadside.

Use of the R_c part of R_Δ in (3.87) through (3.91) yields the Taylor coefficients representing range curvature. The results are

$$a_{1rc} = -\frac{2\pi}{\lambda_c K_c S_{\theta c}}\left[\frac{(\boldsymbol{P}_a \bullet \boldsymbol{r}_t)^2}{R_{ac}^3} C_{\theta c}(1 + 2S_{\phi c}^2) - \frac{2X_t S_{\phi c}(\boldsymbol{P}_a \bullet \boldsymbol{r}_t)}{R_{ac}^2} - \frac{r_t^2 C_{\theta c}}{R_{ac}}\right] \tag{3.121}$$

$$a_{2rc} = -\frac{2\pi}{\lambda_c K_c}\left[\frac{r_t^2}{R_{ac}} - \frac{(\boldsymbol{P}_a \bullet \boldsymbol{r}_t)^2}{R_{ac}^3}\right] \tag{3.122}$$

$$a_{11rc} = -\frac{2\pi S_{\phi c}^2}{\lambda_c K_c^2 R_{ac} S_{\theta c}^2}\left[X_t^2 - 4X_t S_{\phi c} C_{\theta c}\frac{(\boldsymbol{P}_a \bullet \boldsymbol{r}_t)}{R_{ac}} - (1 - 4S_{\phi c}^2 C_{\theta c}^2)\frac{(\boldsymbol{P}_a \bullet \boldsymbol{r}_t)^2}{R_{ac}^2}\right] \quad (3.123)$$

$$a_{12rc} = 0 \quad (3.124)$$

and

$$a_{22rc} = 0 \quad (3.125)$$

Development of a_1 and a_2 leads to quadratic expressions relating image and scatterer coordinates, useful in digital distortion correction in the image domain. Image distortion from range curvature is entirely an effect of geometry in that it is independent of both radar wavelength and image resolution. Section 3.12.2 provides additional discussion of correction for range curvature distortion.

To consolidate the analysis to this point, it is instructive to present expressions for image coordinates that include the basic imaging effects and range curvature effects for the special case of broadside imaging with no scatterer height out of the *XY* plane. This situation yields

$$u_i = a_1 = x_t + \frac{S_{\phi c}}{R_{ac}} x_t y_t \quad (3.126)$$

and

$$v_i = a_2 = y_t - \frac{1}{2R_{ac}S_{\phi c}}(x_t^2 + y_t^2 C_{\phi c}^2) \quad (3.127)$$

Figure 3.24(a) illustrates the distortion represented by these two equations. The size of distortion l_{rc} over a scene of radius r_o is nominally

$$l_{rc} \approx \frac{r_o^2}{2R_{ac}S_{\phi c}} \quad (3.128)$$

although it naturally varies with location. Table 3.8 quantifies this expression as a function of scene size when $R_{ac}S_{\phi c} = 8660$ m, for example, $R_{ac} = 10{,}000$ m and $\phi_{ac} = 60$ deg. While distortion from range curvature is independent of resolution, distortion in terms of resolution size is the measure that suggests its seriousness.

The QPE coefficient a_{11rc} from (3.123) for the special case of broadside imaging and no scatterer height out of the *XY* plane becomes

$$a_{11rc} = -\frac{2\pi S_{\phi c}^2}{\lambda_c K_c^2 R_{ac}}(x_t^2 - y_t^2 S_{\phi c}^2) \quad (3.129)$$

Table 3.8
Size of Range Curvature Distortion for Broadside Imaging at $R_{ac}S_{\phi c}$ = 8660 m

Scene Radius (m)	*Distortion Size (m)*
100	0.6
500	14.4
1000	57.7
1500	129.9
2000	230.9

The QPE is zero for scatterers at scene center and on the diagonals $x_t = y_t S_{\phi c}$ and $x_t = -y_t S_{\phi c}$. Multiplication of this coefficient by x_p^2 indicates the associated quadratic phase error in azimuth. Use of (3.74) to quantify this quadratic phase error at the edges of the azimuth aperture and setting the QPE allowance to $\pi/2$ rad yields an estimate for allowable scene radius r_o of

$$r_o \leq \frac{2\rho_a}{K_a}\sqrt{\frac{R_{ac}}{\lambda_c}} \tag{3.130}$$

Table 3.9 illustrates this relationship between allowable scene size and resolution for typical radar wavelengths and resolutions; it examines the ability to image a 1200-m radius scene at a slant range of 10 km with K_a = 1.3. Allowable scene size decreases gradually with finer resolution. Parts of the image area outside of the radius given by (3.130) and Table 3.9 will begin to show degradation. For example, at 10 GHz (X-band) and 1-m resolution, noticeable degradation occurs beyond about 888-m radius. Section 5.3.2 quantifies the distortion and quadratic phase effects of range curvature in more detail.

Table 3.9
Limit on Scene Radius (m) from Range Curvature QPE at 10-km Slant Range

	Wavelength (Frequency)			
Resolution	*0.01 m (30 GHz)*	*0.03 m (10 GHz)*	*0.2 m (1.5 GHz)*	*0.6 m (500 MHz)*
10 m	Full size	Full size	Full size	Full size
3 m	Full size	Full size	1032	596
1 m	Full size	888	344	199
0.3 m	461	266	103	60
0.15 m	231	133	52	30

A comparison of Table 3.9 and Table 3.3 (showing the allowable scene radius using rectangular format) indicates the need for and the usefulness of polar format in those situations represented by the table diagonal from lower left to upper right. Table 3.9, in the lower right area, indicates situations that require compensation for range curvature; the range migration and chirp scaling algorithms are reasonable candidates in these cases.

3.8 NONPLANAR MOTION AND THREE-DIMENSIONAL SCENE

The compensation technique for NPM, described initially in Section 3.3.4, correctly compensates scatterers in a selected FTP, usually the ground plane. A scatterer which is either above or below this plane will be misfocused proportionally to its distance out of the FTP. The height above or below which a scatterer experiences unacceptable phase error (nominally $\pi/2$ rad of quadratic phase error) is called the height-of-focus (HOF). For three-dimensional scenes whose height variation exceeds this HOF, space-variant misfocus will occur. This section derives the expression for the HOF limit associated with a data collection involving a quadratic (acceleration) maneuver. Terrain and objects such as buildings and vehicles whose height variation is within this vertical HOF interval of the *XY* focus target plane will image satisfactorily.

A difficulty will arise, however, when this constraint is exceeded either because the nominal ground plane is tilted or is uneven relative to the compensation plane (for example, imaging a sloping terrain without advance warning) or when imaging a complex target with large height variations. At present, the only available approach to compensate for this difficulty is subpatch refocusing. It is not a satisfactory approach unless the height variations are smooth and slowly varying over the scene.

Our signal equation model includes the effects of NPM from a quadratic maneuver. The term

$$N_{pm} = -Z_t S_{\phi a} S_{\theta a} \left[\frac{\cot(\phi_a)}{S_{\theta a}} - \frac{\cot(\phi_{ac})}{S_{\theta c}} \right] \tag{3.131}$$

from (3.107) represents the effects of the nonplanar data collection surface. When (3.131) is inserted into g_1, the result is

$$(g_1)_{npm} = \left[\frac{Z_t \cot(\phi_a)}{S_{\theta a}} - \frac{Z_t \cot(\phi_{ac})}{S_{\theta c}} \right] K_p S_{\theta a} \tag{3.132}$$

which becomes

$$(g_1)_{npm} = \left[\frac{\cot(\phi_a)}{S_{\theta a}} - \frac{\cot(\phi_{ac})}{S_{\theta c}} \right] Z_t Y_p \tag{3.133}$$

In the presence of SAR sensor maneuvers that vary slowly over a coherent aperture time,

this phase term indicates low-frequency phase effects producing various target-height-dependent (from the presence of Z_t) distortion and defocusing of the impulse response.

The model in Section 3.4 includes a specific nonplanar maneuver defined by the measured acceleration vector, $\boldsymbol{A_a} = (A_{xa}, A_{ya}, A_{za})$. This quadratic maneuver causes the angles ϕ_a and θ_a to vary over time in a deterministic fashion. We proceed with a Taylor series expansion of this phase term in the form of (3.132) based on the procedures outlined in Section 3.5 for the case in which motion measurement error vector $\boldsymbol{R_e}$ is zero. This simplification is reasonable to greatly simplify the analysis and preserve the full nature of the NPM effect. In any case, the interaction between small phase effects is usually negligible in practical SAR systems.

The Taylor coefficients representing NPM are available using Equations (3.87) through (3.91). The results are

$$a_{1np} = -\left[\frac{V_{za} - V_{ya}\dfrac{\cot(\phi_{ac})}{S_{\theta c}}}{V_{xa}S_{\theta c} - V_{ya}C_{\theta c}}\right]Z_t \tag{3.134}$$

$$a_{2np} = 0 \tag{3.135}$$

$$a_{11np} = \frac{2\pi}{\lambda_c K_c^2}\left[\frac{R_{ac}S_{\phi c}B_{11}}{(V_{xa}S_{\theta c} - V_{ya}C_{\theta c})^3}\right]Z_t \tag{3.136}$$

$$a_{12np} = 0 \tag{3.137}$$

and

$$a_{22np} = 0 \tag{3.138}$$

The quantity B_{11} in (3.136) is given by

$$B_{11} = B_{xz}S_{\phi c}S_{\theta c} + B_{yx}C_{\phi c} + B_{zy}S_{\phi c}C_{\theta c} \tag{3.139}$$

with

$$B_{xz} = V_{xa}A_{za} - V_{za}A_{xa} \tag{3.140}$$

$$B_{yx} = V_{ya}A_{xa} - V_{xa}A_{ya} \tag{3.141}$$

and

$$B_{zy} = V_{za}A_{ya} - V_{ya}A_{za} \tag{3.142}$$

The quantity B_{11} can be written as

$$B_{11} = \frac{(\boldsymbol{A}_a \times \boldsymbol{V}_a) \bullet \boldsymbol{R}_a}{R_a} \tag{3.143}$$

which represents the LOS component of the cross-product of the velocity and acceleration vectors of the maneuvering sensor. When these two vectors are parallel to each other or coplanar with the slant range vector to scene center, B_{11} vanishes and no quadratic phase error is present.

The quantity a_1 indicates a distortion or natural projection of an elevated scatterer onto the XY plane depending on one's viewpoint. The quantity a_{11} indicates an azimuth quadratic phase error; the phase error is space-variant in that it is proportional to Z_p the scatterer height out of the FTP. Quadratic phase error does not occur in range since a_{22} is zero or in the cross-product direction (range times azimuth) since a_{12} is zero.

It is instructive to examine a simple case that still embodies the character of this NPM effect. We select the situation, possibly a vertical pop-up maneuver, in which the sensor travels with only the X component of velocity nonzero at aperture center. In this case, a_1 is zero and a_{11} is given by

$$a_{11np} = \frac{2\pi}{\lambda_c K_c^2}\left[\frac{R_{ac}S_{\phi c}\left(A_{za}S_{\theta c}S_{\phi c} - A_{ya}C_{\phi c}\right)}{V_{xa}^2 S_{\theta c}^3}\right]Z_t \tag{3.144}$$

Multiplication of this coefficient by x_p^2 indicates the associated quadratic phase error in azimuth. Use of (3.74) to quantify this quadratic phase error and setting the QPE allowance to $\pi/2$ rad yields an estimate Z_{hof} for the HOF of

$$Z_{hof} = \left(\frac{V_{xa}^2 S_{\theta c}^3 S_{\phi c}}{R_{ac} a_{zo}}\right)\left(\frac{4\rho_a^2}{\lambda_c K_a^2}\right) \tag{3.145}$$

with

$$a_{zo} = A_{za}S_{\theta c}S_{\phi c} - A_{ya}C_{\phi c} \tag{3.146}$$

where a_{zo} is the component of APC acceleration perpendicular to the nominal slant plane. Scatterers (with Z_t values) beyond this HOF distance above or below the FTP will have greater than $\pi/2$ rad of QPE. Table 3.10 suggests the size of this HOF while imaging a scene whose height varies 300 m out of the FTP. This table uses the parameter values of V_{xa} = 100 m/s, λ_c = 0.03 m, R_a = 10,000 m, θ_{ac} = 90 deg, ϕ_{ac} = 60 deg and K_a = 1.3. It is clear that this effect poses a serious limitation to fine-resolution imaging during platform maneuvers.

Table 3.10
HOF Distance Z_{hof} as a Function of Resolution and Nonplanar Acceleration

	Out-of-Plane Acceleration (a_{zo})		
Resolution	*10 m/s²*	*1.0 m/s²*	*0.1 m/s²*
3 m	61.5 m	Full scene	Full scene
1 m	6.8 m	68.3 m	Full scene
0.3 m	0.6 m	6.1 m	61.5 m

3.9 MOTION MEASUREMENT ERRORS

Use of the M_e term of the differential range from (3.58) in g_1 of (3.84) provides the part of the signal history which involves error in motion measurement. This M_e term in the form

$$(R_\Delta)_{me} = \frac{(\boldsymbol{R}_a \bullet \boldsymbol{R}_e)}{R_a} - \frac{(\boldsymbol{r}_t \bullet \boldsymbol{R}_e)}{R_a} + \frac{(\boldsymbol{R}_a \bullet \boldsymbol{r}_t)\,(\boldsymbol{R}_e \bullet \boldsymbol{R}_a)}{R_a^3} \tag{3.147}$$

leads to

$$(g_1)_{me} = -\frac{K_p}{S_{\phi a}}\left[\frac{(\boldsymbol{R}_a \bullet \boldsymbol{R}_e)}{R_a} - \frac{(\boldsymbol{r}_t \bullet \boldsymbol{R}_e)}{R_a} + \frac{(\boldsymbol{R}_a \bullet \boldsymbol{r}_t)\,(\boldsymbol{R}_e \bullet \boldsymbol{R}_a)}{R_a^3}\right] \tag{3.148}$$

From this equation, it is possible to derive the effects of position, velocity, and acceleration measurement errors using Equations (3.87) through (3.91).

This development proceeds with three simplifications. First, it examines the case in which the measured acceleration vector, $\boldsymbol{A}_a$, is zero; the sensor travels in a straight line at constant velocity. Second, it examines only space-invariant quadratic phase error; that is, it sets r_t to zero when deriving a_{11}. Measured acceleration does not cause distortion. Both the effects of measured accelerations and the space-variance of quadratic phase error from motion measurement errors are usually negligible. Third, with regard to position measurement error, it considers only the displacement effects since the distortion effects are not significant and serve only to complicate the analysis. The following subsections summarize the results for each type of error effect. First, however, it is necessary to derive the Taylor series coefficients associated with M_e.

For the range rate $(\dot{R}_t - \dot{R}_a)$ at aperture center, the model uses

$$(\dot{R}_\Delta)_{me} = \dot{M}_{e1} + \dot{M}_{e2} \tag{3.149}$$

with inputs from (3.62) and (3.63). When calculating the space-invariant quadratic coefficient, this expression is simplified by setting $\boldsymbol{r}_t = 0$.

The second derivative of R_Δ with respect to time evaluated at aperture center with $\boldsymbol{r}_t = 0$ and $\boldsymbol{A}_a = 0$, saving only those terms which are linear in motion measurement error quantities, is given by

$$(\ddot{R}_\Delta)_{me} \approx \frac{Q_{1me}}{R_a} + \frac{Q_{2me}}{R_a^3} + \frac{Q_{3me}}{R_a^5} \tag{3.150}$$

where

$$Q_{1me} = 2(\boldsymbol{V}_e \bullet \boldsymbol{V}_a) + (\boldsymbol{P}_a \bullet \boldsymbol{A}_e) \tag{3.151}$$

$$Q_{2me} = -2(\boldsymbol{P}_a \bullet \boldsymbol{V}_a)(\boldsymbol{P}_a \bullet \boldsymbol{V}_e + \boldsymbol{P}_e \bullet \boldsymbol{V}_a) - (\boldsymbol{P}_e \bullet \boldsymbol{P}_a) V_a^2 \tag{3.152}$$

and

$$Q_{3me} = 3(\boldsymbol{P}_e \bullet \boldsymbol{P}_a)(\boldsymbol{P}_a \bullet \boldsymbol{V}_a)^2 \tag{3.153}$$

All the quantities in these equations are values at aperture center.

The result for the azimuth coefficient a_1 is

$$a_{1me} = \frac{R_{ac}}{S_{\phi c}}\left[\frac{(\dot{R}_\Delta)_{me} S_{\phi c} - (R_\Delta)_{me} \dot{S}_{\phi c}}{(V_{xa} S_{\theta c} - V_{ya} C_{\theta c})}\right] \tag{3.154}$$

This quantity becomes

$$a_{1me} = \frac{(D_{de} + D_{ve})}{(V_{xa} S_{\theta c} - V_{ya} C_{\theta c})} \tag{3.155}$$

using $\dot{S}_{\phi ac}$ from (3.94) with

$$D_{de} = \frac{(\boldsymbol{P}_a \bullet \boldsymbol{P}_e)(V_{xa} C_{\theta c} + V_{ya} S_{\theta c})}{R_{ac} S_{\phi c}} - (\boldsymbol{P}_e \bullet \boldsymbol{V}_a) \tag{3.156}$$

representing effects of position measurement error and

$$D_{ve} = (\boldsymbol{r}_t - \boldsymbol{P}_a) \bullet \boldsymbol{V}_e - \frac{(\boldsymbol{P}_a \bullet \boldsymbol{r}_t)(\boldsymbol{P}_a \bullet \boldsymbol{V}_e)}{R_{ac}^2} \tag{3.157}$$

representing effects of velocity measurement error. The remaining Taylor series

coefficients are

$$a_{2me} = -\frac{1}{S_{\phi c}}\left[\frac{(\boldsymbol{P}_a \bullet \boldsymbol{P}_e)}{R_{ac}}\right] \tag{3.158}$$

$$a_{11me} = \frac{2\pi}{\lambda_c K_c^2}\left[\frac{2(\boldsymbol{V}_e \bullet \boldsymbol{V}_a) + (\boldsymbol{A}_e \bullet \boldsymbol{P}_a)}{(V_{xa}S_{\theta c} - V_{ya}C_{\theta c})^2}\right] R_{ac}S_{\phi c}^2 \tag{3.159}$$

$$a_{12me} = 0 \tag{3.160}$$

and

$$a_{22me} = 0 \tag{3.161}$$

3.9.1 Scene Center Displacements

Position measurement errors naturally cause scene center displacements, contributing to L_x and L_y in (3.72) and (3.73). LOS velocity error also causes scene center displacement in azimuth, contributing to L_x in (3.72). From (3.155), scene center displacement in x is

$$L_{xme} = -X_{ec}S_{\theta c} + Y_{ec}C_{\theta c} - Z_{ec}p_x - \frac{(\boldsymbol{P}_a \bullet \boldsymbol{V}_e)}{(V_{xa}S_{\theta c} - V_{ya}C_{\theta c})} \tag{3.162}$$

and from (3.158), scene center displacement in y is

$$L_{yme} = -X_{ec}C_{\theta c} - Y_{ec}S_{\theta c} - Z_{ec}\cot(\phi_{ac}) \tag{3.163}$$

with

$$p_x = \frac{V_{za} - (V_{ya}S_{\theta c} + V_{xa}C_{\theta c})\cot(\phi_{ac})}{(V_{xa}S_{\theta c} - V_{ya}C_{\theta c})} \tag{3.164}$$

Scene center displacements do not impact the geometric fidelity of the image. Such displacements are relevant primarily in targeting and geodetic mapping applications for which the absolute geodetic coordinates of a target are important. Displacements may also be a concern in operations that require overlay of two images taken at different squint angles or, more challenging, obtained on two different passes. Two-pass SAR interferometry (Section 9.3) is a good example of this latter situation.

Possible sources of scene center displacement in addition to the measurement errors discussed here include atmospheric propagation effects (bending and speed of light changes) and hardware time delays (filters and waveguide). Such considerations are outside the scope of this presentation.

3.9.2 Geometric Distortion

Velocity measurement errors cause distortion in azimuth, contributing to l_x in (3.72). From (3.155), distortion in x is

$$l_{xme} = \frac{(\boldsymbol{r}_t \bullet \boldsymbol{V}_e)}{(V_{xa}S_{\theta c} - V_{ya}C_{\theta c})} - \frac{(\boldsymbol{P}_a \bullet \boldsymbol{V}_e)\,(\boldsymbol{P}_a \bullet \boldsymbol{r}_t)}{(V_{xa}S_{\theta c} - V_{ya}C_{\theta c})\,R_{ac}^2} \tag{3.165}$$

and distortion in y is

$$l_{yme} = 0 \tag{3.166}$$

Section 5.3.1 quantifies the distortion effects of velocity measurement errors.

3.9.3 Quadratic Phase Error

Along-track velocity error and LOS acceleration measurement error cause quadratic phase error [11]. From (3.159), quadratic phase error in x is

$$Q_{me} = a_{11me}x_p^2 = \frac{2\pi}{\lambda_c}\left[\frac{2\,(\boldsymbol{V}_e \bullet \boldsymbol{V}_a) + (\boldsymbol{A}_e \bullet \boldsymbol{P}_a)}{(V_{xa}S_{\theta c} - V_{ya}C_{\theta c})^2}\right] R_{ac}S_{\phi c}^2\left(\frac{x_p}{K_c}\right)^2 \tag{3.167}$$

Using (3.74), it is possible to quantify this QPE as

$$Q_{me}\big|_{\text{size}} = \frac{\pi\lambda_c K_a^2}{8\rho_a^2}\left[\frac{2\,(\boldsymbol{V}_e \bullet \boldsymbol{V}_a) + (\boldsymbol{A}_e \bullet \boldsymbol{P}_a)}{(V_{xa}S_{\theta c} - V_{ya}C_{\theta c})^2}\right] R_{ac} \tag{3.168}$$

Section 5.3.1 quantifies the quadratic phase effects of velocity and acceleration measurement errors.

3.10 RESIDUAL VIDEO PHASE

An undesirable phase term, designated residual video phase (RVP), is a consequence of the signal dechirp-on-receive approach to spotlight data collection and processing. RVP is identified as the last term in (2.67). It survives the polar formatting operation intact as the last term in (3.25). This effect is not unique to the PFA. It is a consequence of dechirping the SAR signals in range by means of mixing with a reference function in the time domain. The top half of Figure 2.10 illustrates this mixing. This effect is not present in situations that accomplish range compression by means of matched filter processing in the frequency domain.

RVP exists because the difference between two displaced linear FM waveforms includes a constant phase proportional to displacement. In addition to this constant phase, a linear phase, also proportional to displacement, provides the basis for range resolution. RVP impacts SAR imagery because the displacement between the two waveforms varies with time as the two-way range to a scatterer changes over a coherent processing interval. Otherwise, the RVP term would be a constant phase over the aperture time for each scatterer and of no consequence to most SAR imaging applications.

The RVP term is deterministic. Compensation for the defocusing effects of RVP in the image domain is not easy because its effects are space-variant, increasing in severity away from the MCP. In a dechirp-on-receive system, the RVP term can be removed completely from the radar signal in a preprocessing operation by passing the range-dechirped video signal through the digital equivalent of a frequency-dependent delay line. This delay line has the effect of removing the time skew caused by the delay in receiving a signal from a far-range scatterer relative to receiving a signal from a near-range scatterer (bottom half of Figure 2.10). Appendix C presents an analytical basis for this removal along with additional details on RVP.

Because the effects of RVP are not large in most situations, correction may be unnecessary. Correction may be needed primarily when imaging large scenes since the effects increase with scatterer distance from the MCP. Correction may also be needed when using the RMA or the CSA.

For a large scene, it may be possible to divide the scene into separately processed subpatches with dimensions small enough to limit the RVP error. Section 4.8 describes this subpatch processing technique; it is computationally expensive.

In the case of a SAR operating in the spotlight mode, the complete expression for the RVP term, from (3.25), is

$$\Phi_{rvp} = g_2 = 4\pi\frac{\gamma}{c^2}R_\Delta^2 \tag{3.169}$$

This effect becomes larger as the range interval, nominally R_Δ, increases and when γ, the FM chirp rate, is increased. Relative to RVP then, it is desirable to achieve a given bandwidth with a long pulse and a low FM rate rather than with a short pulse and a high FM rate.

In evaluating RVP effects by means of Taylor series expansion of g_2, it is adequate to approximate the differential range by the initial term in (3.58), that is, by (3.106). Additionally, it is acceptable to disregard the NPM term. In both approximations, the discarded quantities are negligible in most situations. For simplicity, it is convenient to examine the case in which the sensor travels in a straight line at constant velocity with only the X component of velocity nonzero; the measured acceleration vector $\boldsymbol{A_a}$ is zero.

The residual video term becomes

$$\Phi_{rvp} = g_2 \approx 4\pi\frac{\gamma}{c^2}S_{\phi a}^2\left[X_t C_{\theta a} + Y_t S_{\theta a} + Z_t S_{\theta a}\frac{\cot(\phi_{ac})}{S_{\theta c}}\right]^2 \tag{3.170}$$

Using the expressions for the derivatives of g_2 in (3.102) and (3.103), the effects of RVP

are available using Equations (3.97) through (3.101). The linear coefficients are

$$a_{1rvp} = -\frac{2\gamma\lambda_c S_{\phi c}}{c^2}\left[\tilde{x}_t\tilde{y}_t + \tilde{y}_t^2 C_{\phi c}^2 \cot(\theta_{ac})\right] \tag{3.171}$$

and

$$a_{2rvp} = 0. \tag{3.172}$$

These expressions use

$$\tilde{x}_t = X_t S_{\theta c} - Y_t C_{\theta c} - Z_t \cot(\phi_{ac}) \cot(\theta_{ac}) = x_t - Z_t \cot(\phi_{ac}) \cot(\theta_{ac}) \tag{3.173}$$

and

$$\tilde{y}_t = X_t C_{\theta c} + Y_t S_{\theta c} + Z_t \cot(\phi_{ac}) = y_t + Z_t \cot(\phi_{ac}) \tag{3.174}$$

which relate to azimuth and range target coordinates, x_t and y_t, as shown. The size of the distortion from RVP l_{rvp} over a scene of radius r_o is nominally

$$l_{rvp} \approx \frac{2\gamma\lambda_c S_{\phi c} r_o^2}{c^2} \tag{3.175}$$

although it naturally varies with location. Table 3.11 quantifies this expression as a function of scene size and wavelength for $\phi_{ac} = 60$ deg and $\gamma = 4.8$ MHz/μs. While distortion from RVP is independent of resolution, distortion in terms of resolution size is the measure that suggests its seriousness.

Table 3.11
Size of RVP Distortion (m)

	Wavelength (Frequency)			
Scene Radius (m)	*0.01 m (30 GHz)*	*0.03 m (10 GHz)*	*0.2 m (1.5 GHz)*	*0.6 m (500 MHz)*
100 m	0.01	0.03	0.2	0.6
500 m	0.2	0.7	4.6	13.9
1000 m	0.9	2.8	18.5	55.4
1500 m	2.1	6.2	41.6	124.7
2000 m	3.7	11.1	73.9	221.7

The quadratic coefficients of the Taylor series expansion of the RVP term are

$$a_{11rvp} = \frac{4\pi\gamma S_{\phi c}^2}{c^2 K_c^2}\left[\tilde{x}_t^2 + 4\tilde{x}_t\tilde{y}_t C_{\phi c}^2 \cot(\theta_{ac}) - \tilde{y}_t^2 M_y\right] \tag{3.176}$$

$$a_{12rvp} = \frac{8\pi\gamma S_{\phi c}^2}{c^2 K_c^2}\left[\tilde{x}_t\tilde{y}_t + \tilde{y}_t^2 C_{\phi c}^2 \cot(\theta_{ac})\right] \tag{3.177}$$

and

$$a_{22rvp} = 0 \tag{3.178}$$

with

$$M_y = 1 - \frac{C_{\phi c}^2}{S_{\theta c}^2}(1 + 2C_{\theta c}^2 - 4C_{\theta c}^2 S_{\phi c}^2) \tag{3.179}$$

The quadratic coefficients are of interest primarily to establish the magnitude of the quadratic phase error; this information is needed to establish whether or not the procedure (Appendix C) to remove the RVP term is necessary. For this purpose, it is adequate to replace the space-variant quantities in a_{11} and a_{12} simply by r_o^2, representing the scene radius. In this case, a reasonable estimate of the size of this QPE is the larger term (depending on the relationship between range and azimuth resolutions) in the expression

$$Q_{rvp}\big|_{\text{size}} = \frac{\pi\gamma}{c^2}\left(\frac{\lambda_c^2 K_a K_r}{2\rho_a\rho_r}\right) r_t^2 + \frac{\pi\gamma}{c^2}\left(\frac{\lambda_c^2 K_a^2}{4\rho_a^2}\right) r_t^2 \tag{3.180}$$

Using ρ_o/K_o to represent these resolution quantities in each dimension, the allowable scene size r_o based on a $\pi/2$ criterion for QPE becomes

$$r_o \le \frac{\rho_o c}{\lambda_c K_o \sqrt{\gamma}} \tag{3.181}$$

Table 3.12 illustrates this relationship between allowable scene size and resolution for typical radar wavelengths and resolutions; it examines the ability to image a 1200-m radius scene with $K_o = 1.3$ and with the FM chirp rate, $\gamma = 4.8$ MHz/μs. Allowable scene size decreases gradually with finer resolution and longer wavelength. Without compensation, the image area outside of the radius given by (3.181) and Table 3.3 will exceed the QPE allowance. However, at 10 GHz (X-band) and 1-m resolution, no noticeable degradation occurs within the 1200-m radius scene considered here. For the parameters in this example, RVP is a possible concern primarily at VHF and lower frequencies or at extremely fine resolution.

Table 3.12
Limit on Scene Radius (m) from Residual Video Phase QPE

	Wavelength (Frequency)			
Resolution	*0.01 m (30 GHz)*	*0.03 m (10 GHz)*	*0.2 m (1.5 GHz)*	*0.6 m (500 MHz)*
10 m	Full size	Full size	Full size	Full size
3 m	Full size	Full size	Full size	526
1 m	Full size	Full size	526	176
0.3 m	Full size	1053	158	53
0.15 m	Full size	526	79	26

3.11 ADDITIONAL ERROR SOURCES

Propagation of the SAR signals through the medium between the sensor and the target area is a source of phase error. Propagation effects may cause integrated sidelobes, scene center displacement, and scene defocus. With respect to propagation effects, partial compensation is possible via range autofocus; also, if available and used, propagation models and/or measurements provide the possibility for nominal compensation. Propagation effects are not likely to be significant for most airborne systems although they may be a factor in a long-range sensor operating at a low grazing angle [12, 13].

Undesirable waveform effects within the transmitter are a source of phase error. The concerns in this category include nonlinearity in the FM waveform, reduction in phase coherence in terms of starting phase and frequency jitter from pulse to pulse, and waveguide dispersion effects. These may cause integrated sidelobes and range defocus. Deterministic correction in the IFP is possible for measurable, stable waveform errors. In the case of a digitally generated waveform, compensation for waveform nonlinearity and waveguide dispersion is possible; predistortion of the waveform during its generation accounts for these effects to yield a correct transmit waveform [14].

Motion during transmission and reception of a pulse introduces undesirable phase into the SAR signal history. Principally it introduces a space-invariant defocusing and some small distortion effects. Being space-invariant, this defocusing can be compensated with a reasonable effort if it is ever sufficiently large to cause a problem. Typically, however, these distortion and defocusing effects are small enough to disregard.

Another error source involves motion between transmit and receive times, that is, a bistatic effect. This effect is small, possibly noticeable in a satellite environment. It is correctable by proper adjustments to the data format.

Other minor and possibly significant error sources abound throughout the hardware and software in a SAR imaging system. Typically, these factors become obvious during system integration and testing if they are significant. Otherwise, a multitude of residual

factors contribute to high-frequency and low-frequency phase effects. With good design and good fortune, these residual factors will cause only a tolerable integrated sidelobe noise level and low-frequency phase errors within the grasp of autofocus procedures.

3.12 RELATIONSHIP BETWEEN TARGET AND IMAGE COORDINATES

Equations (3.72) and (3.73) with scale factors $m_x = 1$ and $m_y = 1$ provide the relationships between target and image coordinates. These relationships are

$$u_i = x_t + P_x Z_t + L_x + l_x \tag{3.182}$$

and

$$v_i = y_t + P_y Z_t + L_y + l_y \tag{3.183}$$

with various contributors to the six defining coefficients, l_x, l_y, L_x, L_y, P_x, and P_y. The Taylor series expansion coefficients, a_1 and a_2, for each source provide these defining coefficients. Image geometric distortion is the difference between this relationship and the desired mapping between scatterer physical location in three-dimensional space and scatterer location in the two-dimensional SAR image. Section 8.5 defines exactly what is meant by a geometrically correct image to enable a calculation of any deviation, that is, distortion. This definition is useful in conjunction with an understanding of the actual relationships, which we summarize next.

3.12.1 Individual Contributors

The following equations summarize individual contributors to these six defining coefficients. First, the basic imaging term yields

$$u_{ib} = a_1 = x_t - Z_t \frac{\cot(\phi_{ac})\, C_{\theta c}}{S_{\theta c}} \tag{3.184}$$

and

$$v_{ib} = a_2 = y_t + Z_t \cot(\phi_{ac}) \tag{3.185}$$

This mapping represents the desired relationship between target and image coordinates.

From a_{1rc} and a_{2rc}, the distortions attributable to range curvature are

$$l_{xrc} = -\frac{1}{2R_{ac}S_{\theta c}S_{\phi c}}\left[\frac{(\boldsymbol{P}_a \bullet \boldsymbol{r}_t)^2}{R_{ac}^2} C_{\theta c}(1 + 2S_{\phi c}^2) - \frac{2X_t S_{\phi c}(\boldsymbol{P}_a \bullet \boldsymbol{r}_t)}{R_{ac}} - r_t^2 C_{\theta c}\right] \tag{3.186}$$

and

$$l_{yrc} = -\frac{1}{2R_{ac}S_{\phi c}}\left[r_t^2 - \frac{(\boldsymbol{P}_a \bullet \boldsymbol{r}_t)^2}{R_{ac}^2}\right] \tag{3.187}$$

From a_{1np} and a_{2np}, the distortions attributable to NPM are

$$l_{xnp} = -\left[\frac{V_{za} - V_{ya}\dfrac{\cot(\phi_{ac})}{S_{\theta c}}}{V_{xa}S_{\theta c} - V_{ya}C_{\theta c}}\right]Z_t \tag{3.188}$$

and

$$l_{ynp} = 0 \tag{3.189}$$

Actually, the quantity l_{xmp} is not a distortion, but rather a contributor to P_x in (3.72).

From a_{1me} and a_{2me}, the displacements attributable to motion measurement errors are

$$L_{xme} = -X_{ec}S_{\theta c} + Y_{ec}C_{\theta c} - Z_{ec}p_x - \frac{(\boldsymbol{P}_a \bullet \boldsymbol{V}_e)}{(V_{xa}S_{\theta c} - V_{ya}C_{\theta c})} \tag{3.190}$$

and

$$L_{yme} = -X_{ec}C_{\theta c} - Y_{ec}S_{\theta c} - Z_{ec}\cot(\phi_{ac}) \tag{3.191}$$

with

$$p_x = \frac{V_{za} - (V_{ya}S_{\theta c} + V_{xa}C_{\theta c})\cot(\phi_{ac})}{(V_{xa}S_{\theta c} - V_{ya}C_{\theta c})} \tag{3.192}$$

The distortions attributable to motion measurement errors are

$$l_{xme} = \frac{\boldsymbol{r}_t \bullet \boldsymbol{V}_e}{(V_{xa}S_{\theta c} - V_{ya}C_{\theta c})} - \frac{(\boldsymbol{P}_a \bullet \boldsymbol{V}_e)\,(\boldsymbol{P}_a \bullet \boldsymbol{r}_t)}{(V_{xa}S_{\theta c} - V_{ya}C_{\theta c})R_{ac}^2} \tag{3.193}$$

and

$$l_{yme} = 0 \tag{3.194}$$

From a_{1rvp} and a_{2rvp}, the distortions attributable to RVP are

$$l_{xrvp} = -\frac{2\gamma\lambda_c S_{\phi c}}{c^2}\left[\tilde{x}_t\tilde{y}_t + \tilde{y}_t^2 C_{\phi c}^2\cot(\theta_{ac})\right] \tag{3.195}$$

and

$$l_{yrvp} = 0 \tag{3.196}$$

These expressions use

$$\tilde{x}_t = X_t S_{\theta c} - Y_t C_{\theta c} - Z_t \cot(\phi_{ac}) \cot(\theta_{ac}) = x_t - Z_t \cot(\phi_{ac}) \cot(\theta_{ac}) \tag{3.197}$$

and

$$\tilde{y}_t = X_t C_{\theta c} + Y_t S_{\theta c} + Z_t \cot(\phi_{ac}) = y_t + Z_t \cot(\phi_{ac}) \tag{3.198}$$

Generally, range curvature is the dominant source of image distortion. It is the source most often calculated and compensated for in high-quality SAR imagery. Section 5.3 quantifies these various sources of image displacement and distortion numerically for a typical X-band data collection system.

3.12.2 Correction for Range Curvature Image Distortion

Range curvature is the primary source of significant, deterministic image distortion which may require compensation by the IFP. The processor removes geometric distortion by means of a two-dimensional resampling of the image pixel array which the processor naturally provides. Use of (3.186) and (3.187) in (3.182) and (3.183) indicates the image location (u_i, v_i) of a scatterer as a function of its physical location (X_t, Y_t, Z_t). The resampling process requires an additional set of equations to indicate the physical location (X_t, Y_t) of a scatterer as a function of its image location (u_i, v_i). Without auxiliary information from other sources, this process necessarily assumes all scatterers are located in the XY plane. With these relationships, the resampling process for distortion correction is able to first move the original (distorted) image samples onto the proper location in the final (undistorted) output image space in order to proceed with interpolation onto an orthogonal, rectilinear output grid. This section discusses this inversion process. Section 4.2 describes the use of digital polyphase filters to do the resampling.

Inversion of (3.182) and (3.183) with the inclusion of (3.186) and (3.187) to obtain expressions for the two-dimensional target coordinates (eventually assuming $Z_t = 0$) as a function of the two-dimensional image coordinates is not a simple task. The transformation that maps from the distorted image space (u, v) to the target space is available also by starting with some earlier equations without inverting (3.186) and (3.187) directly. We outline this alternative approach here and show the results for the case in which the sensor travels in a straight line at constant velocity with only the X component of velocity nonzero; the measured acceleration vector $\boldsymbol{A_a}$ is zero also. For this simple case, (3.186) and (3.187) become

$$l_{xrc} = -\frac{1}{2R_{ac} S_{\theta c} S_{\phi c}} \left[d_t^2 C_{\theta c} (1 + 2S_{\phi c}^2) - 2X_t d_t S_{\phi c} - r_t^2 C_{\theta c} \right] \tag{3.199}$$

and

$$l_{yrc} = -\frac{1}{2R_{ac}S_{\phi c}}\left(r_t^2 - d_t^2\right) \tag{3.200}$$

with

$$d_t = X_t S_{\phi c} C_{\theta c} + Y_t S_{\phi c} S_{\theta c} + Z_t C_{\phi c} = y_t S_{\phi c} + Z_t C_{\phi c} \tag{3.201}$$

This alternative approach begins with the use of (3.49) and (3.92) in (3.87) with (3.67). The intermediate result is

$$u_i = -\frac{Y_{ac}}{V_{xa} S_{\theta c}^2}\left(\frac{\dot{R}_{\Delta c}}{S_{\phi c}} - \frac{R_{\Delta c}\dot{S}_{\phi ac}}{S_{\phi c}^2}\right) \tag{3.202}$$

The desire with this beginning is to develop an expression for X_t in terms of u_i and v_i. The first observation is the ability to replace $R_{\Delta c}$ by

$$R_{\Delta c} = -v_i S_{\phi c} \tag{3.203}$$

based on (3.88) and (3.68). In addition, use of (3.53) and (3.94) eventually leads to

$$X_t = u_i S_{\theta c} + v_i C_{\theta c} - \frac{u_i v_i}{R_{ac}} S_{\theta c} S_{\phi c} - \frac{v_i^2}{R_{ac}} C_{\theta c} S_{\phi c} C_{\phi c}^2 \tag{3.204}$$

This equation is the first of the two needed inversion equations. An expression for the second equation begins by inserting (3.204) into a rearranged version of (3.52) without motion measurement errors and using (3.203) as needed. The result is a cumbersome expression for Y_t. A quadratic approximation to this expression, keeping only the largest term in Z_t, is

$$Y_t \approx -u_i C_{\theta c} + v_i S_{\theta c} - \frac{C_{\phi c}}{S_{\phi c} S_{\theta c}} Z_t + D_{uu} u_i^2 + D_{vv} v_i^2 + D_{uv} u_i v_i \tag{3.205}$$

with the quadratic coefficients

$$D_{uu} = \frac{1}{2R_{ac} S_{\phi c} S_{\theta c}} \tag{3.206}$$

$$D_{vv} = \frac{C_{\phi c}^2\left(1 + 2C_{\theta c}^2 S_{\phi c}^2\right)}{2R_{ac} S_{\phi c} S_{\theta c}} \tag{3.207}$$

and

$$D_{uv} = \frac{C_{\theta c} S_{\phi c}}{R_{ac}} \tag{3.208}$$

Repeating (3.69) through (3.71), these scatterer coordinates relate to azimuth, (negative) ground range, and height coordinates, (x_t, y_t, z_t) by

$$x_t = X_t S_{\theta c} - Y_t C_{\theta c} \tag{3.209}$$

$$y_t = X_t C_{\theta c} + Y_t S_{\theta c} \tag{3.210}$$

and

$$z_t = Z_t \tag{3.211}$$

Figure 3.17(b) illustrates the relationship between this pair of target coordinates.

The transformations above map pixel location in the (distorted) image space to the (undistorted) target space. Correction for geometric distortion requires movement of pixels in the original image to locations in the undistorted or corrected image based on these target positions. It is appropriate to do this transformation with $Z_t = 0$ and (X_t, Y_t) representing the correct image coordinates.

3.13 IMAGE FOCUS ERROR SUMMARY

The quadratic coefficients of the Taylor series expansion of signal phase indicate quadratic phase error that impacts image focus. The quadratic phase error is given by

$$\Phi_{qpe} = a_{11} x_p^2 + a_{12} x_p y_p \tag{3.212}$$

with contributions to the two coefficients from various error sources as calculated earlier. None of the error sources considered here causes quadratic phase error directly in the range coordinate y_p. Individual contributors to these quadratic error coefficients are

$$a_{11rc} = -\frac{2\pi S_{\phi c}^2}{\lambda_c K_c^2 R_{ac} S_{\theta c}^2}\left[X_t^2 - 4X_t S_{\phi c} C_{\theta c} \frac{(\boldsymbol{P}_a \bullet \boldsymbol{r}_t)}{R_{ac}} - (1 - 4S_{\phi c}^2 C_{\theta c}^2) \frac{(\boldsymbol{P}_a \bullet \boldsymbol{r}_t)^2}{R_{ac}^2}\right] \tag{3.213}$$

$$a_{11me} = \frac{2\pi}{\lambda_c K_c^2}\left[\frac{2(\boldsymbol{V}_e \bullet \boldsymbol{V}_a) + (\boldsymbol{A}_e \bullet \boldsymbol{P}_a)}{(V_{xa} S_{\theta c} - V_{ya} C_{\theta c})^2}\right] R_{ac} S_{\phi c}^2 \tag{3.214}$$

$$a_{11np} = \frac{2\pi}{\lambda_c K_c^2}\left[\frac{R_{ac} S_{\phi c} B_{11}}{(V_{xa} S_{\theta c} - V_{ya} C_{\theta c})^3}\right] Z_t \tag{3.215}$$

$$a_{11rvp} = \frac{4\pi\gamma S_{\phi c}^2}{c^2 K_c^2}\left[\tilde{x}_t^2 + 4\tilde{x}_t\tilde{y}_t C_{\phi c}^2 \cot(\theta_{ac}) - \tilde{y}_t^2 M_y\right] \tag{3.216}$$

and

$$a_{12rvp} = \frac{8\pi\gamma S_{\phi c}^2}{c^2 K_c^2}\left[\tilde{x}_t\tilde{y}_t + \tilde{y}_t^2 C_{\phi c}^2 \cot(\theta_{ac})\right] \tag{3.217}$$

Section 3.7 through Section 3.10 quantify these factors numerically while Section 5.3 adds some discussion in this area.

3.14 SUMMARY

In fine-resolution radar imaging, *motion is the solution* and *motion is the problem.* Relative motion between the radar sensor and the imaged scene generates the aspect angle diversity that creates the synthetic aperture array of data necessary to achieve fine azimuth resolution. On the negative side, scatterer MTRC is a consequence of this relative motion. Compensation for measured planar motion and autofocus for motion measurement errors are standard requirements in fine-resolution SAR systems. NPM requires special attention and, even then, leads to a serious HOF limitation. Motion during a pulse causes undesirable phase effects. Motion between transmit and receive pulses leads to a bistatic effect since the antenna location changes between the time of pulse transmission and reception of the backscattered signals.

In early SAR history, motion was primarily a solution: a moving antenna (with coherent pulse transmissions and coherent signal processing) addressed the desire for finer azimuth resolution without an unreasonably large physical antenna aperture. With azimuth resolution of many meters in an X-band SAR, motion measurement was hardly necessary; the more subtle effects of motion were not limiting factors to system performance. With the increased emphasis today on finer resolution and larger scenes, a SAR system design must consider each motion effect as a potential problem. Motion factors impact system design parameters, hardware selection and specification, image formation algorithm selection, processor complexity, and, ultimately, system performance in terms of image quality, image quantity, and timeliness.

In fine-resolution imaging of large scenes, compensation for scatterer MTRC becomes a major consideration in algorithm selection. This consideration motivated the development of the PFA in 1969 and contributes to the importance of the range migration and chirp scaling algorithms in recent years.

This chapter introduces the polar formatting technique, the reasons for its use, and its limitations. It begins with the signal phase equation provided by the IFP after fine motion compensation. It applies the PFA analytically to this equation to distinguish among basic imaging effects, range curvature effects, NPM effects, motion measurement errors, and RVP effects. It provides expressions for the distortion and quadratic phase errors resulting

from these effects. From these expressions, analyses in Chapter 5 quantify these phase effects for practical imaging situations.

The PFA is a viable approach for processing spotlight SAR data collected over either a planar or a nonplanar data collection surface to produce fine-resolution imagery. This algorithm manages the difficulty of MTRC adequately. It allows selection of a FTP in which to optimize compensation for NPM. Attributes and characteristics of the PFA include:

- Compensation for the major part of MTRC;
- Compensation for NPM for scatterers in and near a selectable FTP;
- No compensation for residual MTRC (range curvature);
- Compatibility with two-dimensional FFT processing.

The PFA operates on signal histories after motion compensation to a single scene point and after removal of the chirp in range. Motion compensation to a point effectively transforms data from the azimuth-time (or space) domain to the azimuth-frequency domain. Similarly, dechirp in range transforms the data from the range-time domain to the range-frequency domain. Like the range migration and chirp scaling algorithms, the PFA effectively operates in the two-dimensional spatial-frequency or wavenumber domain.

This chapter provides the modeling and analysis to support use of the PFA in fine-resolution SAR imaging in the spotlight mode. This framework leads to Chapter 4 which discusses techniques to implement the PFA procedures in a digital processing environment.

REFERENCES

[1] Brown, W.M., and R.J. Fredericks, "Range-Doppler Imaging with Motion through Resolution Cells," *IEEE Transactions on Aerospace and Electronic Systems*, Vol. AES-5, No. 1, January 1969, pp. 98-102.

[2] Farrell, J.L., J.H. Mims, and A. Sorrell, "Effects of Navigation Errors in Maneuvering SAR," *IEEE Transactions on Aerospace and Electronic Systems*, Vol. AES-9, No. 5, September 1973, pp. 758-776.

[3] Walker, J., W. Carrara, and I. Cindrich, "Optical Processing of Rotating-Object Radar Data Using a Polar Recording Format," Technical Report RADC-TR-73-136, AD 526 738, Rome Air Development Center, Rome, NY, May 1973.

[4] Munson, D.C., Jr., and R.L. Visentin, "A Signal Processing View of Strip-Mapping Synthetic Aperture Radar," *IEEE Transactions on Acoustics, Speech, and Signal Processing*, Vol. 37, No. 12, December 1989, pp. 2131-2147.

[5] Wu, C., and M. Jin, "Modeling and a Correlation Algorithm for Spaceborne SAR Signals, *IEEE Transactions on Aerospace and Electronic Systems*, Vol. AES-18, No. 5, September 1982, pp. 563-574.

[6] Walker, J.L, "Range-Doppler Imaging of Rotating Objects," *IEEE Transactions on Aerospace and Electronic Systems*, Vol. AES-16, No. 1, January 1980, pp. 23-52.

[7] Banta, E.D., "Limitations on SAR Image Area Due to Motion Through Resolution Cells," *IEEE Transactions on Aerospace and Electronic Systems*, Vol. AES-22, No. 6, November 1986, pp. 799-803.

[8] Ausherman, D.A., A. Kozma, J.L. Walker, H.M. Jones, and E.C. Poggio, "Developments in Radar Imaging," *IEEE Transactions on Aerospace and Electronic Systems*, Vol. AES-20, No. 4, July 1984, pp. 363-400.

[9] Munson, D.C., and J.L. Sanz, "Image Reconstruction from Frequency-Offset Fourier Data," *Proceedings of the IEEE*, Vol. 72, No. 6, June 1984, pp. 661-669.

[10] Goodman, J.W., *Introduction to Fourier Optics*, McGraw-Hill, 1968, pp. 70-74.

[11] Zeoli, G.W., "Effect of Constant Velocity Error on SAR Focus," *IEEE Transactions on Aerospace and Electronic Systems*, Vol. AES-22, No. 5, September 1986, pp. 657-659.

[12] Porcello, L.J., "Turbulence-Induced Phase Errors in Synthetic-Aperture Radar Systems," *IEEE Transactions on Aerospace and Electronic Systems*, Vol. AES-6, No. 5, September 1970, pp. 636-644.

[13] Fante, R.L., "Turbulence-Induced Distortion of Synthetic Aperture Radar Images," *IEEE Transactions on Geoscience and Remote Sensing*, Vol. 32, No. 4, July 1994, pp. 958-961.

[14] Gallaway, W.D., K.F. Luckscheiter, E.H. Cowen, and J.W. Wilhelm, "A Direct Digitally Synthesized Exciter Achieving Near Theoretical Performance for an Operational SAR System," *IEEE National Radar Conference*, Ann Arbor, MI, 20-21 April, 1988, pp. 22-27.

Chapter 4
Digital Polar Format Processing

Motion compensation to accommodate polar format processing of a spotlight SAR signal history involves phase and frequency stabilization of scene center and removal of the chirp in range. These procedures begin the process of readying the signal data for a two-dimensional Fourier transform that converts it into an image. Following motion compensation, samples of the digitized signal data lie at the intersections of radial lines and equally spaced concentric circles in wavenumber space. Figure 3.14 illustrates this input sampling geometry. To perform with computational efficiency, the two-dimensional Fourier transform requires a rectangular array of uniformly spaced samples. A resampling operation converts the input signal, sampled on a polar array, to this desired rectangular data array. The SAR community refers to this resampling as polar-to-rectangular interpolation or *polar interpolation.* Polar interpolation is the digital equivalent of the polar format transformation, which Chapter 3 discusses in detail.

While it is sometimes necessary to implement polar interpolation as a single two-dimensional interpolation, implementation as two one-dimensional interpolation steps presents a lower overall computational burden. The common choice for the interpolator filter is a one-dimensional finite impulse response (FIR) digital filter. This chapter discusses this separable approach to polar interpolation of spotlight SAR signal histories. Section 4.1 begins with an introduction to the resampling techniques required in digital SAR processing. These techniques include the use of FIR filters to change the spacing between collected radar samples. Section 4.2 presents polyphase filters as an efficient implementation of the resampling procedure. Sections 4.3 and 4.4 develop the relationships between polar interpolation input and output sample spacing and discuss the implementation of digital polar interpolation.

Section 4.5 develops expressions for the scale factors that relate final image pixel spacing to scene distances. Section 4.6 discusses the digital implementation of signal history projections to select the focus target and image display planes. Section 4.7 introduces stabilized scene processing in which the orientation of a target within the processed image remains independent of the collection squint angle as the sensor passes by the scene. Section 4.8 presents the use of subpatch processing to reduce the effects of certain types of space-variant phase errors.

While the need for precise interpolation is more obvious with use of the polar format algorithm (PFA), other image formation algorithms generally require accurate data interpolation as well. The range migration algorithm (RMA) in Chapter 10 requires a

one-dimensional interpolation in range to implement the Stolt transformation of (10.9). The tomographic reconstruction algorithm in Appendix B requires a two-dimensional interpolation of complex image samples. The chirp scaling algorithm (CSA) in Chapter 11 ideally requires no interpolation. In theory, the RMA and the CSA have limited resampling requirements. In practice, both likely require additional resampling to provide data with uniform azimuth sample spacing and to compensate for nonplanar sensor motion. The resampling concepts in Section 4.1 and Section 4.2 also apply to these additional interpolation needs.

4.1 SAMPLING RATE CONVERSION

This section discusses the use of FIR filters to accomplish the interpolation of digital signals [1]. The polar input samples collected by the radar represent a two-dimensional, discrete-time signal that requires interpolation onto a rectangular grid. Because it involves fewer computations, the SAR image processor typically divides polar interpolation into the two separate operations of range resampling and azimuth resampling. Thus, it is adequate to consider only one-dimensional sample rate conversion procedures here.

Polar-to-rectangular interpolation employs two special cases of one-dimensional sampling rate conversion. These cases are:

1. Resampling from uniform input spacing to uniform output spacing;
2. Resampling from nonuniform input spacing to uniform output spacing.

The first case describes the resampling operation associated with the range dimension of polar formatting (range interpolation). The second case represents the resampling operation performed in the azimuth dimension (azimuth interpolation). Figure 4.1 depicts both cases of one-dimensional sampling rate conversion. Black dots represent input samples and open circles represent output samples. Section 4.4 discusses these cases in detail.

The use of a FIR filter to alter the sampling rate of a uniformly sampled, discrete-time signal by a rational factor L/M is a one-step process, although it is convenient to model it as a two-step operation. The first step is an upsampling of the signal by an integer factor L; the second step is a downsampling by an integer factor M. Together, these two steps change the sampling rate by the ratio L/M.

4.1.1 Upsampling

To increase the complex sampling rate f_s of a uniformly sampled signal by an integer factor L, it is necessary to interpolate $L-1$ values between each of the original signal samples. The model of this upsampling procedure begins with a bandlimited, continuous-time signal $x_c(t)$ with a discrete-time, sampled representation $x(n) = x_c(nT)$. Here n is the sample number and $T = 1/f_s$ is the sampling interval where f_s satisfies the Nyquist criterion [2]. The Nyquist constraint limits the frequency content of $x(n)$ to $|f| < f_s/2$ where $f_s = 1/T$ is the complex sampling rate in terms of hertz or $f_s = 1$ in terms of

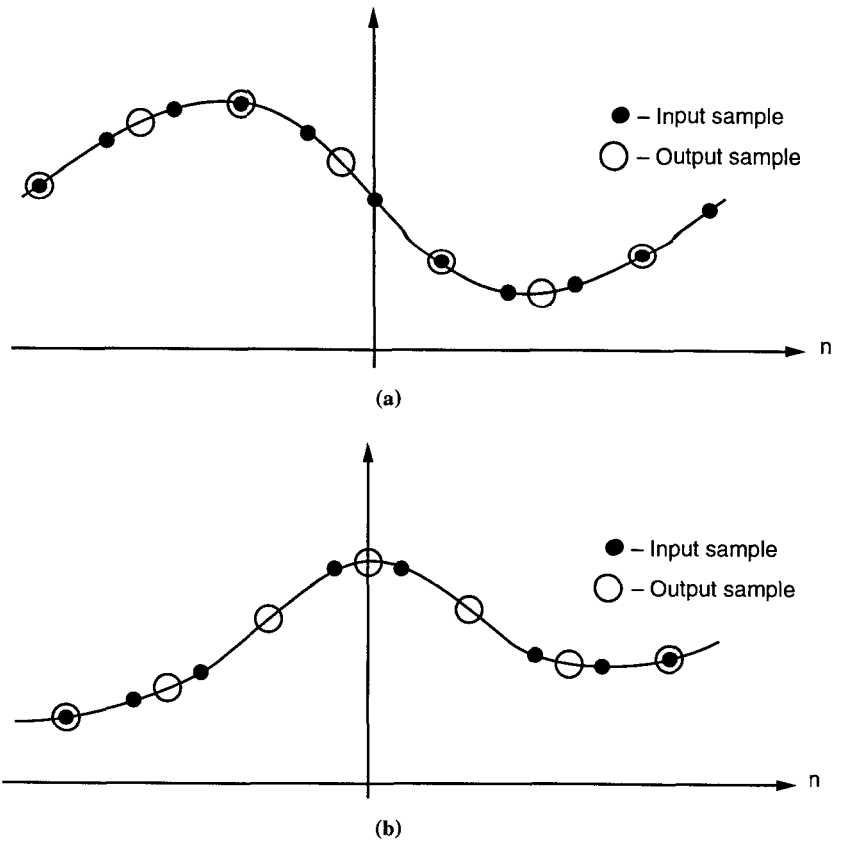


Figure 4.1 Resampling a digital signal: **(a)** Uniform input sample spacing to uniform output sample spacing; **(b)** Nonuniform input sample spacing to uniform output sample spacing.

cycles/sample spacing. We will describe frequency quantities in sampling rate conversion using the cycles/sample spacing perspective.

The sinc reconstruction formula [2] states that a band-limited, continuous-time function is recoverable from its discrete-time samples through a convolution with a sinc function. The mathematical relationship is

$$x_c(t) = \sum_{k=-\infty}^{\infty} x(k)\,\mathrm{sinc}\left(\frac{t-kT}{T}\right) \tag{4.1}$$

where the definition of the sinc function is

$$\mathrm{sinc}(x) = \frac{\sin(\pi x)}{\pi x} \tag{4.2}$$

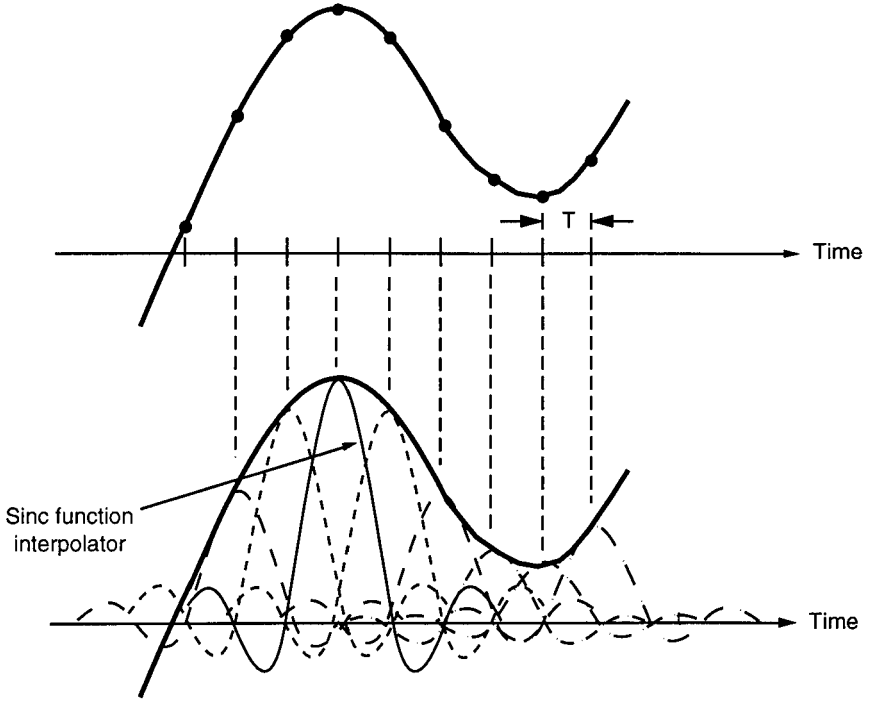


Figure 4.2 Reconstruction of a bandlimited signal from discrete-time samples.

An interpretation of (4.1) is that each digital sample $x(n)$ weights a version of the sinc function shifted to the location of that sample point along the time axis. The sum of these weighted sinc functions yields $x_c(t)$. Figure 4.2 illustrates this interpretation by depicting the recovery of a continuous signal via the sinc reconstruction procedure. Note that only the K^{th} sinc function contributes to the value of $x_c(t)$ at $t = KT$; other sinc functions have zero value at this sample point, but contribute to $x_c(t)$ between the original samples.

The goal of *upsampling* the signal $x(n)$ by a factor L is to produce values of the continuous-time signal $x_c(t)$ at the specific sampling locations $t = mT/L$ from the sequence $x(n)$. Using (4.1), the upsampled sequence $y(m)$ is

$$y(m) = x_c\left(\frac{mT}{L}\right) = \sum_{k=-\infty}^{\infty} x(k)\,\mathrm{sinc}\left(\frac{m}{L} - k\right) \tag{4.3}$$

The infinite-duration sinc function in (4.3) represents an ideal low-pass filter $h(m)$ with

$$h(m) = \mathrm{sinc}\left(\frac{m}{L}\right) \tag{4.4}$$

and a corresponding cutoff frequency $f_C = 1/2L$.

Use of (4.4) in (4.3) yields

$$y(m) = \sum_{k=-\infty}^{\infty} x(k)\, h(m - kL) \tag{4.5}$$

Equation (4.5) has the form of a standard convolution except that $x(n)$ has a sample spacing of T, while the filter $h(m)$ has a sample spacing of T/L. The equation becomes a standard convolution by defining a new sequence $\hat{x}(m)$ where

$$\hat{x}(m) = \begin{cases} x\left(\dfrac{m}{L}\right) & m = 0, \pm L, \pm 2L, \ldots \\ 0 & \text{otherwise} \end{cases} \tag{4.6}$$

Use of (4.6) in (4.5) gives the result

$$y(m) = \sum_{k=-\infty}^{\infty} \hat{x}(k)\, h(m - k) \tag{4.7}$$

which expresses the upsampled output sequence $y(m)$ as the convolution of the new input sequence $\hat{x}(k)$ and an ideal low-pass filter $h(m)$. In practice, a FIR filter approximates the ideal filter $h(m)$ in (4.7) and limits the summation to a reasonable number of terms.

Together, (4.6) and (4.7) provide the following procedure for upsampling $x(n)$. To upsample by an integer factor L, insert $L - 1$ zeros between the original samples of $x(n)$ and low-pass filter the resulting sequence. Figure 4.3 summarizes this procedure.

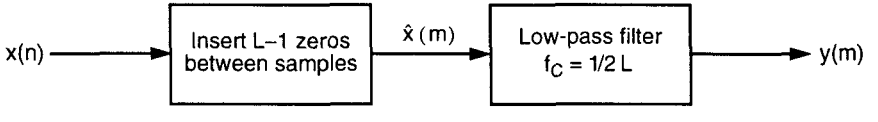


Figure 4.3 Block diagram of the upsampling procedure.

Figure 4.4 describes the upsampling procedure in both the time and frequency domains for the case of $L = 3$. Notice the zero insertion step replicates the spectrum of $x(n)$ by $L - 1$ times. In this example, the filter $h(m)$ has a cutoff frequency of $f_C = 1/6$ cycle/new sample spacing. Figure 4.4 indicates that such a cutoff frequency is necessary to pass the spectrum of $x(m)$ while rejecting the spectral replicas which the zero insertion step introduces.

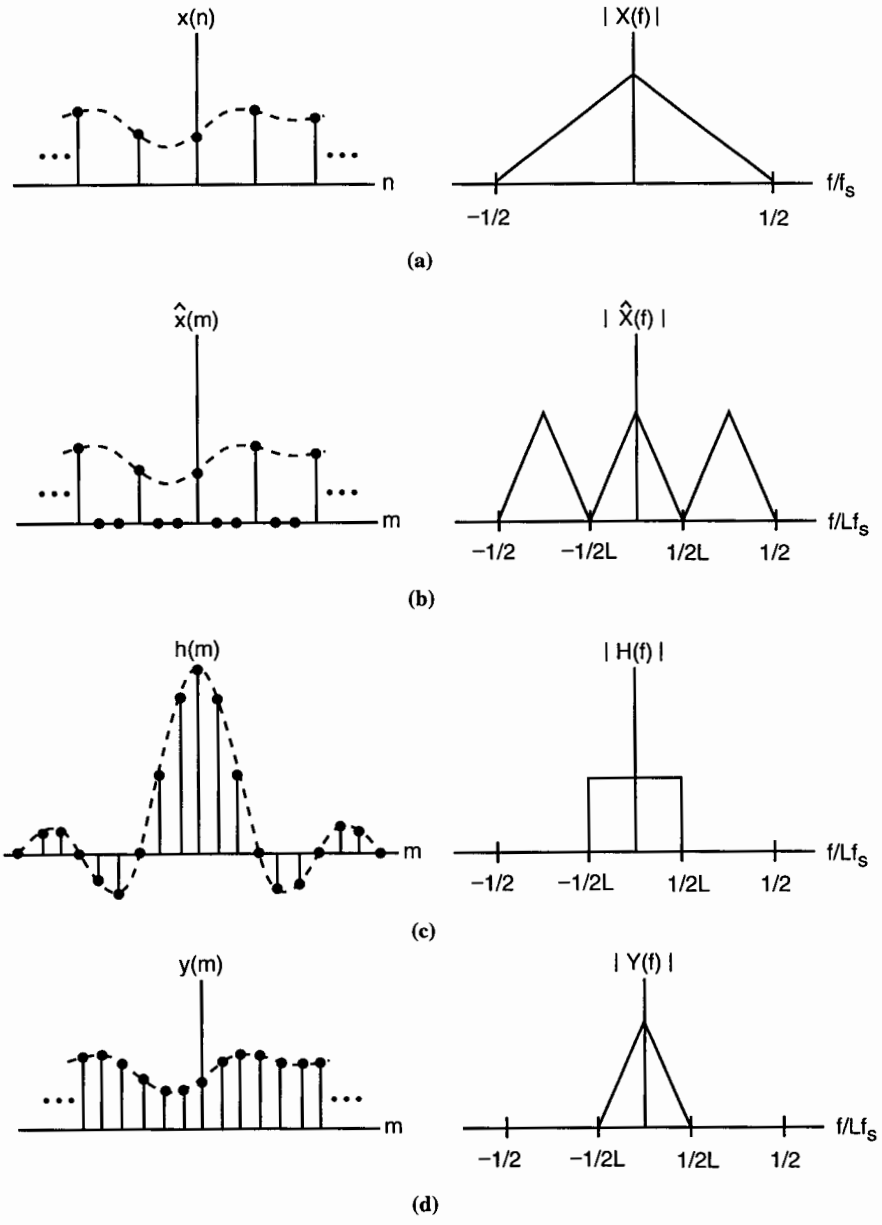


Figure 4.4 Time domain (left) and frequency domain (right) interpretations of upsampling with L = 3: **(a)** Sampled signal; **(b)** Signal after insertion of zeros; **(c)** Ideal low-pass filter; **(d)** Upsampled signal.

4.1.2 Downsampling

This section describes a procedure for reducing the sampling rate of a digital signal $x(n)$ by an integer factor. Downsampling $x(n)$ by an integer factor M implies a reduction of the signal's sampling rate from f_s to f_s/M. To satisfy the Nyquist sampling criterion [2], it is necessary to limit the bandwidth $x(n)$ prior to performing this sampling rate reduction. Specifically, the downsampling procedure must bandlimit $x(n)$ to $|f| < f_s/2M$. Filtering $x(n)$ with an ideal low-pass filter having a cutoff frequency of $f_C = 1/2M$ performs the bandlimiting operation.

Figure 4.5 shows a block diagram of a procedure for downsampling $x(n)$. The first operation performs the necessary bandwidth reduction. After filtering, retaining one of every M of the samples output by the low-pass filter accomplishes the sampling rate reduction without violating the Nyquist criterion. Figure 4.6 depicts these operations in both the time and frequency domains for the case of M = 2.

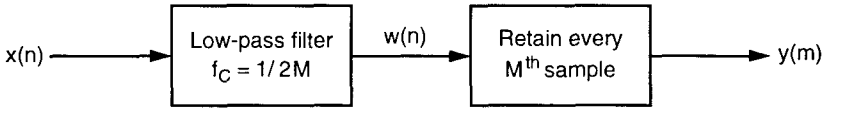


Figure 4.5 Block diagram of the downsampling procedure.

At the low-pass filter output in Figure 4.5, the functional form of the intermediate signal $w(n)$ is

$$w(n) = \sum_{k=-\infty}^{\infty} x(k)\, h(n-k) \tag{4.8}$$

Upon retaining every M^{th} sample, the new downsampled signal becomes

$$y(m) = w(nM) = \sum_{k=-\infty}^{\infty} x(k)\, h(nM-k) \tag{4.9}$$

In practice, a FIR filter approximates the ideal filter $h(k)$ and limits the summation in (4.9) to a reasonable number of terms.

4.1.3 Resampling

The cascading of the upsampling and downsampling operations changes the sampling rate of the signal $x(n)$ by the rational factor L/M. The procedure upsamples $x(n)$ by a factor L and then downsamples the resulting sequence by a factor M. Figure 4.7 shows a block diagram depicting this strategy. To preserve the information content of the original signal, the upsampling operation must precede the downsampling operation. The spectra in

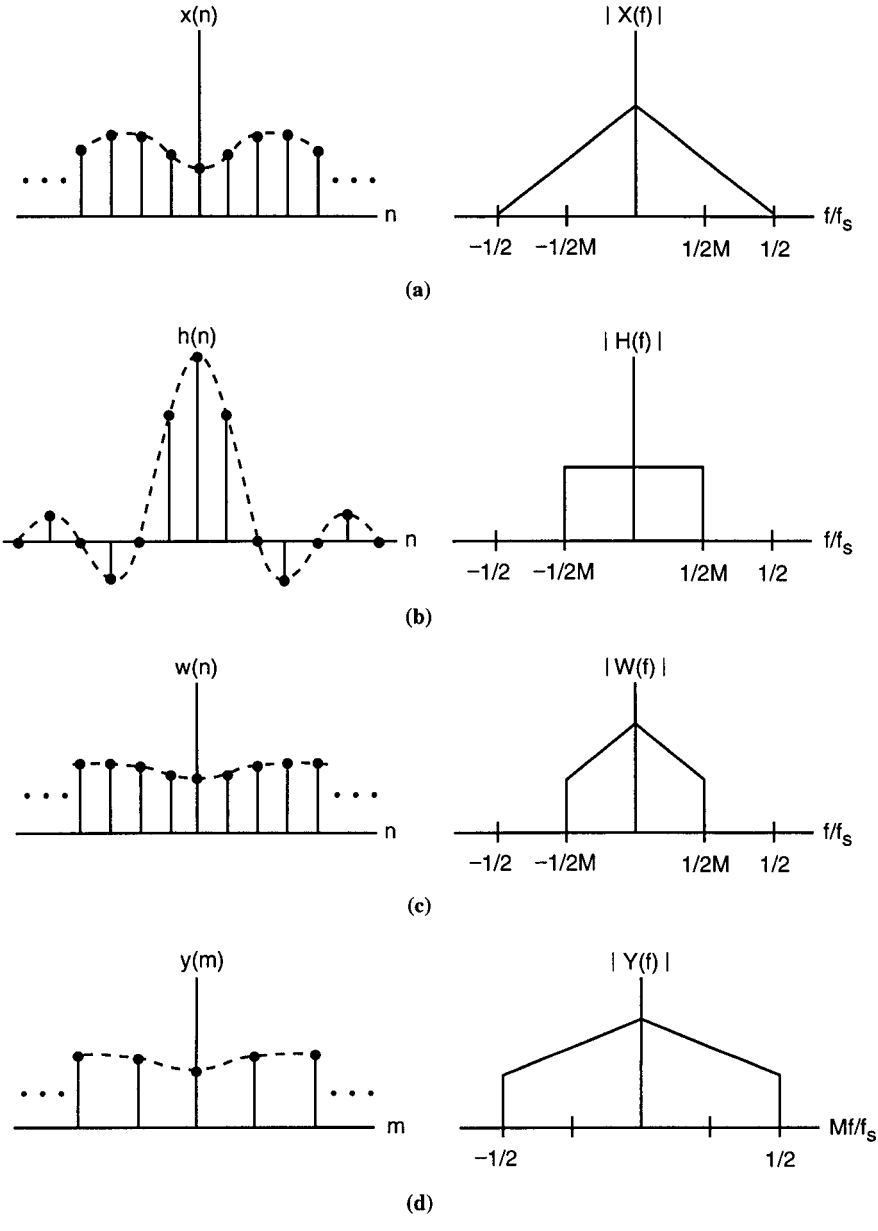


Figure 4.6 Time domain (left) and frequency domain (right) interpretations of downsampling with M = 2: (a) Sampled signal; (b) Ideal low-pass filter; (c) Signal after filter; (d) Downsampled signal.

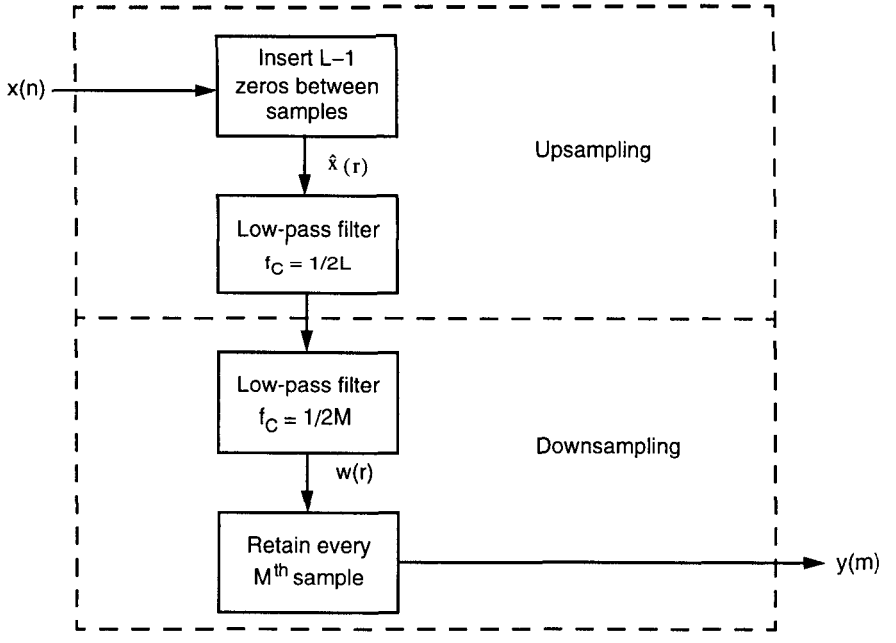


Figure 4.7 Resampling procedure.

Figure 4.4 and Figure 4.6 suggest the basis for this need. One of the two low-pass filtering steps of Figure 4.7 is unnecessary because the filter with the lowest cutoff frequency can perform the work of both filters. This filter $h(r)$ has a cutoff frequency of $f_C = 1/2\max(L, M)$ where the output of the *max*( ) function is the maximum value of its inputs. Regardless of its cutoff frequency, the sampling interval of $h(r)$ is T/L, corresponding to the lowest sampling interval (highest sampling rate) in the entire procedure.

From (4.5), the output of the combined low-pass filters in Figure 4.7 is

$$w(r) = \sum_{k=-\infty}^{\infty} x(k)\, h(r - kL) \tag{4.10}$$

Extracting one out of every M samples from the intermediate sequence $w(r)$ yields the resampled output sequence $y(m)$ given by

$$y(m) = w(mM) = \sum_{k=-\infty}^{\infty} x(k)\, h(mM - kL) \tag{4.11}$$

Equation (4.11) expresses the resampled output signal in terms of the original sampled sequence $x(n)$ and a digital filter $h(r)$. Again, in practice, a FIR filter replaces $h(r)$ to reduce the summation in (4.11) to a finite number of terms.

4.2 POLYPHASE FILTERS

The sample position conversions of polar-to-rectangular interpolation involve a variety of different but similar spatial relationships between input and output sample positions. Rational factor resampling cannot always match these relationships exactly. A common approach is to upsample the FIR resampling filter by a large factor and then downsample it, making approximate location matches through a nearest neighbor selection procedure. This section describes the polyphase filter as an efficient implementation of a FIR filter and discusses procedures for resampling signals using highly upsampled filters.

The choice of the filter upsampling factor involves a tradeoff between storage requirements (based on the number of filter coefficients) and position quantization error. Position quantization errors arising during resampling introduce phase and amplitude errors in the radar signal data. A particular sample positioning error introduces larger phase and amplitude errors in high-frequency signals (representing scatterers near the edges of the scene) than in low-frequency signals; a positioning error causes no errors for a zero-frequency signal (representing a scatterer at scene center).

4.2.1 A Resampling Example

It is instructive to apply (4.11) to a simple example. This example is a case of non-integer downsampling with $L = 2$ and $M = 3$. Figure 4.8 depicts a sampled input sequence $x(n)$ and the desired output sequence $y(m)$. The simple resampling filter $h(r)$ has a length of 7 samples. It is symmetric about its center sample $h(0)$ with the pictorial values shown in the figure. This filter serves to illustrate concepts only; it does not represent a reasonable filter or a filter suitable for polar interpolation.

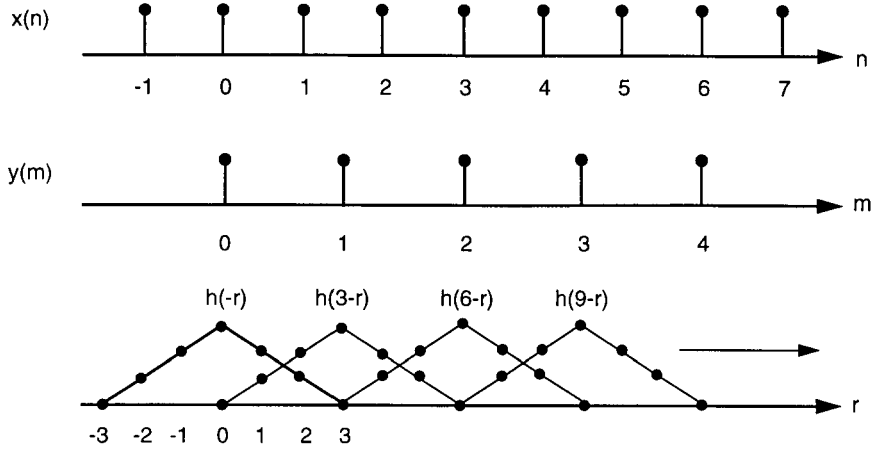


Figure 4.8 Resampling example with a change in sampling rate of 2/3 (downsampling).

Using the illustration, we compute the desired output values $y(m)$ for $m = 0, 1, 2$, and 3 by centering the filter on each output position m and applying the filter weights to each corresponding input sample that falls within the filter's edge-to-edge span. For $m = 0$, the expression in (4.11) becomes

$$y(0) = \sum_{k=-1}^{1} x(k)\, h(-2k) \tag{4.12}$$

Expansion of the right side yields

$$y(0) = x(-1)\, h(2) + x(0)\, h(0) + x(1)\, h(-2) \tag{4.13}$$

A similar expansion for $m = 1, 2$, and 3 produces

$$y(1) = x(0)\, h(3) + x(1)\, h(1) + x(2)\, h(-1) + x(3)\, h(-3) \tag{4.14}$$

$$y(2) = x(2)\, h(2) + x(3)\, h(0) + x(4)\, h(-2) \tag{4.15}$$

$$y(3) = x(3)\, h(3) + x(4)\, h(1) + x(5)\, h(-1) + x(6)\, h(-3) \tag{4.16}$$

The downsampling operation uses $L = 2$ distinct time-varying subsets of filter coefficients to generate the output sequence $y(m)$. These subsets are

$$H_{s1} = [h(-2), h(0), h(2)] \tag{4.17}$$

and

$$H_{s2} = [h(-3), h(-1), h(1), h(3)] \tag{4.18}$$

In addition, the use of subsets H_{s1} and H_{s2} repeats with period $L = 2$, meaning that the coefficients that generate $y(0)$ are the same as those that generate $y(2)$ and $y(nL)$. The index between consecutive filter coefficients within each subset varies by $L = 2$. These properties hold for all resampling ratios L/M, where L and M are integers [3].

Plots of the filter sample subsets H_{s1} and H_{s2} in Figure 4.9 illustrate another interesting characteristic. We plot the H_{s1} subset with its center under the output sample $y(0)$ and the H_{s2} subset with its center under the output sample $y(1)$ because H_{s1} produces $y(0)$ and H_{s2} produces the next output sample $y(1)$. For H_{s1}, the distance from filter center to right edge is 2/3 of one output sample spacing. For H_{s2}, the same distance is one output sample spacing. Thus, the two filter subsets have different fractional sample delays resulting in different linear phase responses when applied to the filtering task. The association of different phase responses with the different subsets of the same filter gives rise to the name *polyphase filter* for this class of resampling filter. The individual subsets of h are the *phasings* of the filter.

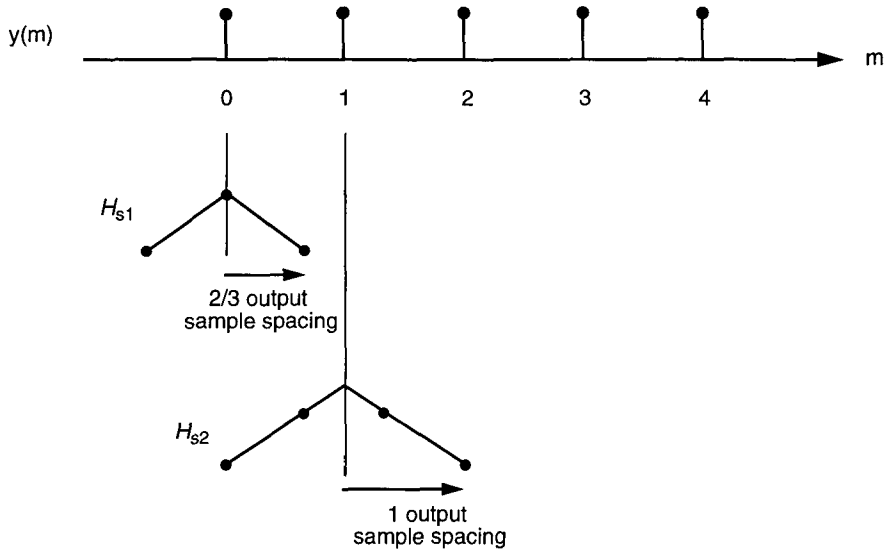


Figure 4.9 Individual phasings of the example resampling filter.

4.2.2 Use of Polyphase Filters

A flexible SAR image formation processor (IFP) must accommodate a wide range of integer and non-integer resampling ratios in two dimensions. The resampling ratios in range and azimuth vary with radar collection parameters, processed image resolution, processed scene size, and required FFT sizes (Section 4.3 and Section 4.4). It is not practical to design a large ensemble of resampling filters to handle all possible cases. The ability to handle a wide range of resampling ratios with a single filter is advantageous. Another important need is computational efficiency in implementing the resampling operation.

A resampling operation using a polyphase filter design addresses the important issues of computational efficiency and flexibility. Computationally, the polyphase filtering procedure operates at the output sampling rate and uses the minimum necessary number of filter coefficients [3]. The polyphase design also supports the goal of using a single, flexible filter. The realization of this flexible filter begins with the design of a low-order FIR filter called the *prototype filter*. The design process seeks to minimize filter length L_f in samples, which relates directly to the computational load of the resampling operation. At the same time, the design process must yield a filter with strong stopband attenuation, a fast passband-to-stopband transition, and low passband ripple in order to achieve high image quality. Balancing the conflicting goals of computational efficiency and flexibility is an important aspect of the filter design process. Many well-documented techniques exist for designing FIR filters that address these performance parameters [2, 4-6].

Once designed, the prototype filter itself requires upsampling by a large factor to create the polyphase filter. Typically, upsampling of the filter uses either Fourier transform techniques or convolution with a truncated sinc function. For example, a representative value for the upsampling factor L_u on a prototype filter consisting of 10 coefficients is 512. Thus, creation of the desired polyphase filter requires upsampling the original 10 sample prototype filter to 5120 samples. Each of the 512 groups of 10 filter samples represent an individual phasing of the filter. The filter upsampling factor (512 in this example) is equivalent to the upsampling factor L in (4.11). By designing a single polyphase filter based on a large value of L, the filter accommodates a broad range of input-to-output phasing relationships and sampling rate changes without significant error. It can approximate closely a required resampling rate by the rational factor L/M. Using this procedure, the IFP need not design a new resampling filter for each resampling ratio requirement. It selects a large integer parameter L once during the filter design process; it selects the integer M on-the-fly to make the ratio L/M as close as possible to the desired rate. Importantly, altering the value of M does not adversely affect the computational load of the overall resampling procedure.

The alignment of zero crossings (nulls) of the filter relative to the input and output sample positions determines the realized frequency characteristics of the resampling operation. To illustrate how this comes about, we analyze how filter cutoff frequency f_C varies with M and L for a filter based on a sinc function.

Section 4.1.3 expresses the required cutoff frequency of a resampling filter as

$$f_C = \frac{1}{2\max(L, M)} \tag{4.19}$$

Figure 4.10 depicts the cases of non-integer upsampling and downsampling. Consider the non-integer upsampling case in Figure 4.10(a) with $L = 3$ and $M = 2$. Assuming that the resampling filter is a discretely sampled sinc function centered at $n = 0$, the first null of the filter occurs L units of n away from filter center. An expression for the filter is then

$$h(n) = \text{sinc}\left(\frac{n}{L}\right) \tag{4.20}$$

Assuming an infinite length filter, the discrete Fourier transform of $h(n)$ to within a scale factor is rect(fL), which has a cutoff frequency of $f_C = 1/2L$; that is, the duration of the rect is $2f_C$. (A practical filter naturally has finite length, but approximates this behavior well with a good design.) In Figure 4.10(a) with $L > M$, the required and realized cutoff frequencies for the resampling filter are equal. Thus, scaling the nulls of the resampling filter to match the sample spacing defined by max(L, M) automatically adjusts the cutoff frequency to that required by the resampling operation in order to prevent signal aliasing. Table 4.1 presents a summary of filter alignments for the various possible cases. A rule of thumb for the filter null alignment is that the filter nulls always align with the signal (input or output) having the lower sampling rate.

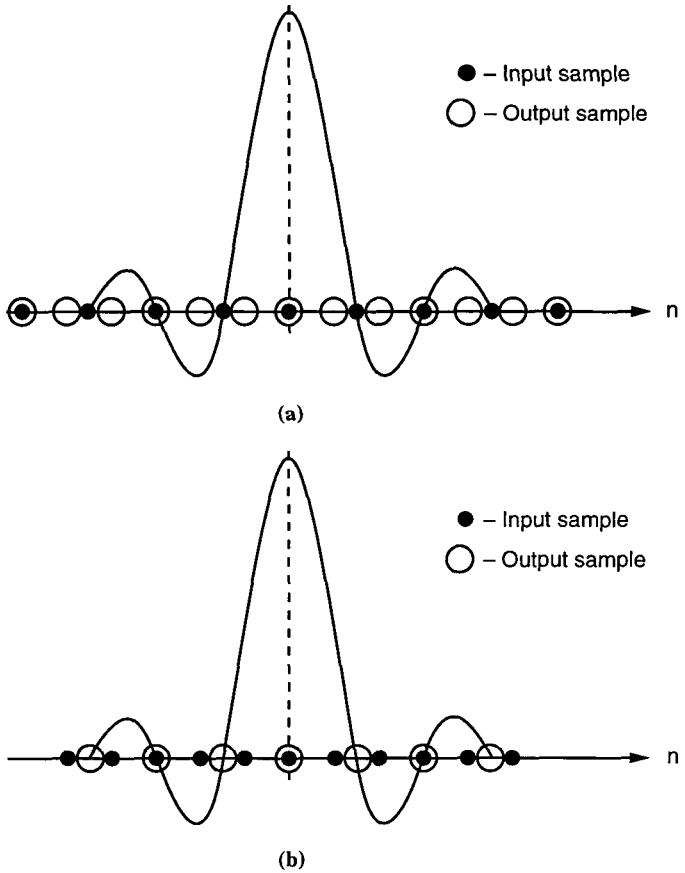


Figure 4.10 Filter sample alignment: **(a)** Non-integer upsampling case ($L > M$) with $L = 3$ and $M = 2$; **(b)** Non-integer downsampling case ($L < M$) with $L = 2$ and $M = 3$.

Table 4.1
Alignment of Resampling Filter Nulls

Case	*Description*	*Filter Null Alignment*
$L > 1, M = 1$	Integer upsampling	With input sample
$L = 1, M > 1$	Integer downsampling	With output sample
$L > M$	Non-integer upsampling	With input sample
$L < M$	Non-integer downsampling	With output sample

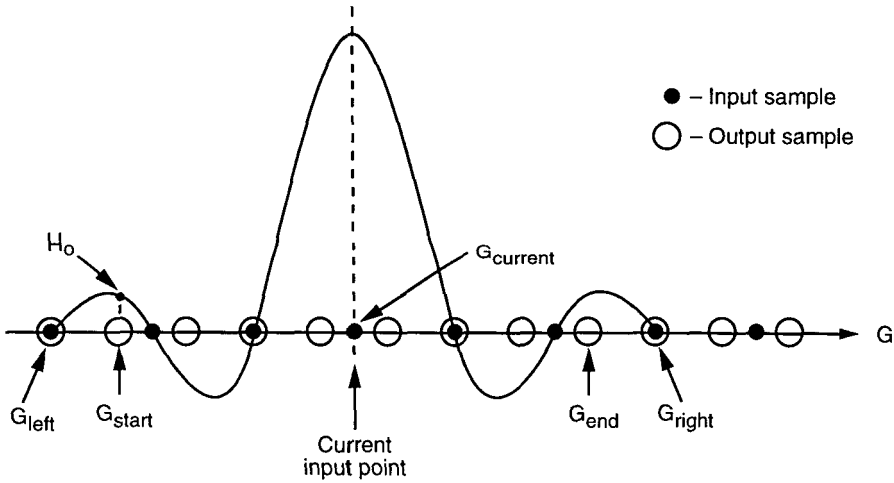


Figure 4.11 Input centered convolution.

4.2.3 Filtering Mechanics

Two ways to implement the filtering process are *input centered convolution* and *output centered convolution*. In each case, the *centered* part of the name refers to the positioning of the center of the resampling filter with respect to the sampled data.

Input centered convolution centers the resampling filter over each input data sample (Figure 4.11). The input sample contributes to each output sample falling within the filter extent. The value of the resampling filter (the filter coefficient) at each output sample location determines the size of each contribution. With a highly upsampled polyphase filter, a nearest neighbor approach chooses the value of the filter at the output sample location. Input centered convolution has an advantage over output centered convolution when implementing a nonuniform-to-uniform resampling such as azimuth polar interpolation (Section 4.4.2). This advantage occurs because input centered convolution offers a simpler implementation than does output centered convolution.

When implementing a digital input centered filtering scheme, it is convenient to scale the output sample spacing to unity and then to express the position of the input samples in terms of scaled output coordinates. Each input point contributes to a number of output points; integer indices access the output points held in digital memory. Unity output scaling allows easier control of the output point multiply-and-accumulate operation.

Input centered convolution proceeds in the following way. The resampling algorithm expresses the location of the current input point $G_{current}$ in output units; typically, $G_{current}$ will be a decimal (non-integer) value. The actual value of the current input is $V_{current}$. Subtracting one-half of the filter length (expressed in scaled output coordinates) from the location of the current input point yields the left edge of the filter G_{left}; adding one-half of the filter length to the location of the current input point yields the right edge G_{right}.

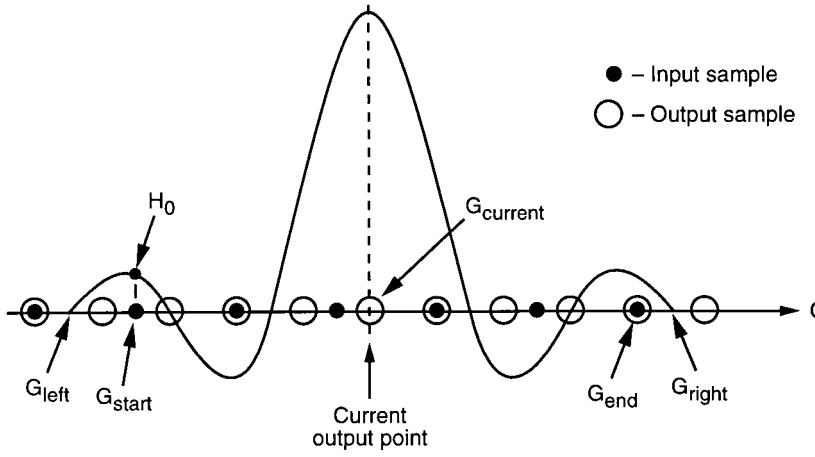


Figure 4.12 Output centered convolution.

Applying an integer ceiling function to the coordinate of the left edge yields the position G_{start} of the first output sample under the filter. The ceiling function $\lceil x \rceil$ indicates the closest integer greater than or equal to a given decimal number x. Applying an integer floor function to the coordinate of the right edge yields the position of the last output grid sample G_{end} under the filter. The floor function $\lfloor x \rfloor$ indicates the closest integer less than or equal to a given decimal number x.

The resampler now requires the value (coefficient) of the resampling filter nearest to each output point. It is convenient to store the filter coefficients in computer memory such that the address of the filter's center sample is zero. Filter values to the left of center will have negative addresses and values to the right of center will have positive addresses. Assuming the resampler uses a polyphase filter derived from a prototype filter with L_f points and L_u phasings, the address of the filter sample H_0 over the first output point is

$$H_0 = \lfloor G_{start} - G_{current} \rfloor L_u \tag{4.21}$$

The contribution that the current input sample makes to the first output sample is $H_0 V_{current}$. Assuming a constant output sample spacing, the change in filter address per output sample is fixed at L_u. The resampler repeats the multiply/accumulate procedure at each output location under the filter until it reaches G_{end}. The resampler centers the filter over the next input sample and repeats the entire procedure. Input centered convolution does not yield a final output value until the entire filter passes over a given output point.

Output centered convolution centers the resampling filter over each output sample (Figure 4.12). The output sample receives contributions from each input sample that falls underneath the extent of the filter. The value of the resampling filter at each input sample location determines the size of each contribution. As is the case of input centered convolution, a nearest neighbor approach chooses the filter value.

When implementing output centered filtering, it is helpful to scale the input sample spacing to unity and then to express each output sample location in terms of scaled input coordinates. Each output point receives contributions from a number of input points. The filtering procedure accesses the input points in computer memory via integer array indices that correspond also to the scaled spacing between input points. The unity input grid scaling allows easy implementation of the input point multiply-and-accumulate operation.

The convolution proceeds as follows. The resampling operation expresses the location of the current output point $G_{current}$ in input units, typically a decimal (non-integer) value. Subtracting one-half of the filter length from the location of the current output point yields the left edge of the filter G_{left}, and adding one-half of the filter length to the location of the current output point yields the right edge G_{right}. Applying an integer ceiling function to G_{left} yields the position G_{start} of the first input sample under the filter. The actual value of the first input point at G_{start} is V_{start}. Applying an integer floor function to G_{right} yields the position G_{end} of the last input sample under the filter.

The resampler now requires the value (coefficient) of the resampling filter nearest to each input point. As in the input centered convolution procedure, the filter is stored in memory with filter center at address zero. Assuming a polyphase filter derived from a prototype filter with L_f points and upsampled by a factor L_u, the address of the filter sample H_0 over the first input point is

$$H_0 = \lfloor G_{start} - G_{current} \rfloor L_u \tag{4.22}$$

The contribution that the current output sample receives from the first input sample is $H_0 V_{start}$. If the input data is uniformly sampled, the change in filter address per input grid sample is L_u. The resampler repeats the multiply and accumulate procedure for each input point under the filter until it reaches G_{end}. The resampler then centers the filter over the next output sample and repeats the entire procedure. Output centered convolution yields a new, complete output sample at each positioning of the filter.

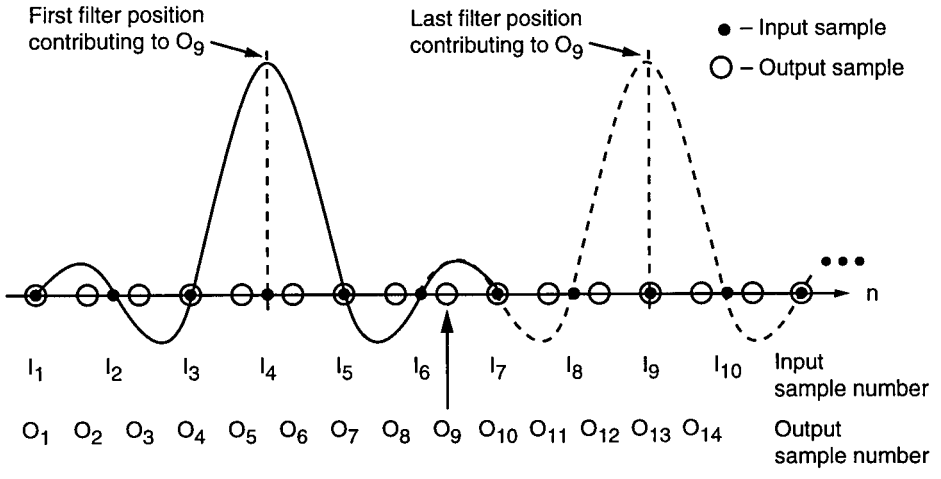
Assuming the use of a symmetric resampling filter, input centered convolution yields the same numerical result as output centered convolution. Figure 4.13 presents an example for the non-integer upsampling case of $L = 3$ and $M = 2$. Figure 4.14 shows the symmetric resampling filter that this example uses. Figure 4.13(a) shows the input centered convolution and only considers those points contributing to output point O_9. Figure 4.13(b) illustrates the output centered convolution, also for output point O_9. The generation of output point O_9 with input centered convolution involves the calculation

$$O_9 = I_4 H_3 + I_5 H_6 + I_6 H_9 + I_7 H_{12} + I_8 H_{15} + I_9 H_{18} \tag{4.23}$$

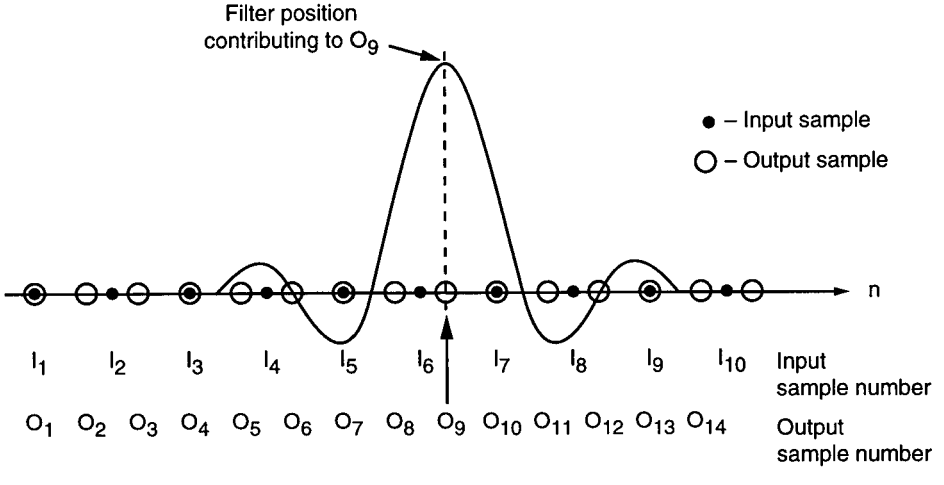
Similarly, the calculation with output centered convolution is

$$O_9 = I_4 H_{17} + I_5 H_{14} + I_6 H_{11} + I_7 H_8 + I_8 H_5 + I_9 H_2 \tag{4.24}$$

Since the filter is symmetric, the filter weights (H_3, H_6, H_9, H_{12}, H_{15}, H_{18}) are equal to (H_{17}, H_{14}, H_{11}, H_8, H_5, H_2), making the two expressions (4.23) and (4.24) equivalent.



(a)



(b)

Figure 4.13 Convolution comparison: **(a)** Input centered convolution; **(b)** Output centered convolution.

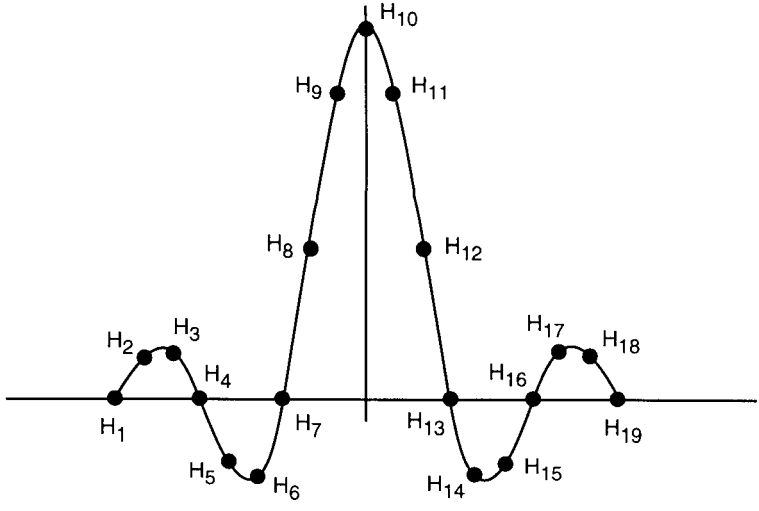


Figure 4.14 Resampling filter that the convolutions in Figure 4.13 use.

4.3 DIGITAL POLAR FORMAT RELATIONSHIPS

The digital IFP receives a two-dimensional array of samples from the radar sensor. This array consists of K samples in range, indexed by k values from 0 to $K-1$. The array contains N_p samples (pulses) in azimuth, indexed by n values from 0 to $N_p - 1$. Following motion compensation procedures, this array is effectively a polar array of samples in radial distance and angle. Two-dimensional storage and processing involve projection of the collected radar data into the $K_x K_y$ plane in wavenumber space (Section 3.3.3). This projection corresponds to using the XY plane as both the focus target plane (FTP) and the image display plane (IDP).

Based on (3.19) and (3.20), the two formatting rules for two-dimensional polar format processing are:

1. Record the K samples within each pulse at radial positions $K_p(n, k)$ proportional to the instantaneous transmitted frequency associated with the return from scene center;
2. Position each of the N_p pulses at an angle $\theta_p(n)$ in processor space equal to the data collection squint angle $\theta_a(n)$.

From (3.22), the first rule in analog form is

$$K_p = K_c \frac{S_{\phi a}}{S_{\phi c} f_c} \left[f_c + \gamma \left(\hat{t} - \frac{2R_a}{c} \right) \right] \tag{4.25}$$

with the constant K_c given by

$$K_c = \frac{4\pi f_c}{c} S_{\phi c} \tag{4.26}$$

The quantity K_c corresponds to the polar radius in $K_x K_y$ space at which the signal returning at $\hat{t} = 2R_a/c$ is stored; $\hat{t}$ is defined as $t - nT$, R_a is the slant range to scene center, c is the speed of light, and T is the interpulse period. Also, f_c is the radar center frequency, γ is the chirp rate, ϕ_a is the instantaneous incidence angle, and ϕ_{ac} is the incidence angle at aperture center with $S_{\phi a} = \sin(\phi_a)$ and $S_{\phi c} = \sin(\phi_{ac})$. Restating (3.20), the second rule is

$$\theta_p(n) = \theta_a(n) \tag{4.27}$$

Using (2.60) in (4.25) for the case $R_o = R_a$, the first rule in digital form is

$$K_p(n,k) = K_c \frac{\gamma}{f_c}\left(\frac{f_c}{\gamma} + \frac{k}{F_s} - \frac{T_p}{2} - \frac{W_r}{c}\right)\frac{S_{\phi a}}{S_{\phi c}} \tag{4.28}$$

where R_o is the reference range used to motion compensate the received radar signal, F_s is the A/D sample frequency, T_p is the pulse length, and W_r (corresponding to Δr in (2.4) and related discussions) is the scene extent in range. Figure 4.15 identifies K_c and illustrates the location of the collected signal samples in the $K_x K_y$ plane. The large dots in this figure indicate the $K \times N_p$ set of collected signal samples.

The transmitted range bandwidth B spans the interval from the radar start frequency f_L to the radar stop frequency f_H. The angular orientation of each pulse in the $K_x K_y$ plane corresponds to the instantaneous squint angle θ_a of the data collection. The sample spacing of the input polar grid is not necessarily uniform in either radius or angle. The sample spacing is, however, adequate from a Nyquist point of view. Using (4.28) and assuming a radar with a positive chirp rate γ, the first sample of pulse n returned from range R_a corresponds to and is stored at a spatial frequency K_L where

$$K_L = \frac{4\pi f_L}{c} S_{\phi a}(n) \tag{4.29}$$

The center sample occurs at a spatial frequency K_C given by

$$K_C = \frac{4\pi f_c}{c} S_{\phi a}(n) = K_c \frac{S_{\phi a}}{S_{\phi c}} \tag{4.30}$$

The last sample occurs at a spatial frequency K_H given by

$$K_H = \frac{4\pi f_H}{c} S_{\phi a}(n) \tag{4.31}$$

For the center pulse, $S_{\phi a}(N_p/2) = S_{\phi c}$ and $K_C(N_p/2) = K_c$.

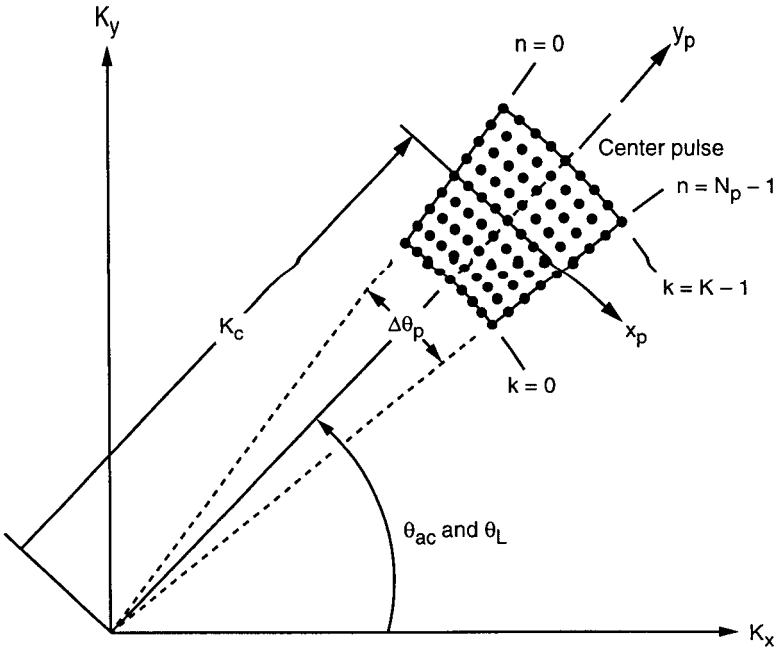


Figure 4.15 Polar storage of radar samples in the spatial-frequency domain.

Based on the complex A/D sampling rate F_s, the radial distance ΔK_p between samples along a pulse is

$$\Delta K_p = \frac{4\pi\gamma}{cF_s} S_{\phi a} \tag{4.32}$$

This sample spacing represents the change in spatial frequency per range sample.

Polar interpolation begins with the placement of the desired rectangular output grid over the grid of polar input samples. In Figure 4.15, we associate the (x_p, y_p) coordinate system centered at $(K_p, \theta_p) = (K_c, \theta_{ac})$ with this rectangular grid. While θ_{ac} need not correspond precisely to a collected pulse position, the following description assumes, for convenience, that it does. The squint angle θ_{ac} in processor space becomes the *image look angle*, designated θ_L. In like fashion, the center sample of the pulse corresponding to θ_{ac} becomes range aperture center in processor coordinates. The y_p axis of the right-handed (x_p, y_p) coordinate system is colinear with the center input pulse at angle θ_{ac} relative to the K_x axis in Figure 4.15. This procedure is *line-of-sight polar interpolation* (LOSPI). With LOSPI, the image display coordinates correspond to range and azimuth coordinates in target space. Reprocessing the data at a different look angle changes the range and azimuth directions in target space and causes the orientation of the imaged scene to rotate with respect to image display coordinates (Section 4.7).

Polar interpolation must compute the value of two key output grid parameters in order to proceed. These parameters are the number of output samples and the spacing between output samples in both the range and the azimuth directions. In SAR, image resolution requirements specify the necessary range bandwidth based on (2.2) and azimuth angular interval based on (2.20). These quantities determine the size of the output rectangular grid. This size fixes the product of the spacing between samples and the total number of samples. The time-bandwidth products of the signal history in range and azimuth after dechirp determine the total number of samples in each dimension. The range time-bandwidth product TB_r uses the IF bandwidth B_{IF} of the dechirped signals from the range interval being imaged. The product of (2.4) and (2.6) yields TB_r as

$$TB_r = \frac{2\gamma W_r}{c}\left(T_p + \frac{2W_r}{c}\right) \tag{4.33}$$

where W_r represents the scene extent in range. Using (2.2), an approximation for this expression in terms of range resolution is

$$TB_r \approx \frac{K_r W_r}{\rho_r} \tag{4.34}$$

where K_r is the range mainlobe-broadening factor. This result assumes that the second term in (4.33) is small. In image formation processing, the appropriate scene size to use is the desired processed scene size. The processor establishes this scene size by downsampling in the range direction during polar interpolation. Similarly, the appropriate range resolution to use in the IFP is the desired processed range resolution, which can be equal to or coarser than the resolution supported by the collected radar bandwidth.

The azimuth time-bandwidth product TB_a equals the number of complex samples required in azimuth to adequately sample the SAR signal. From (2.33), TB_a is

$$TB_a = \frac{K_a W_a}{\rho_a} \tag{4.35}$$

where W_a is the azimuth scene size, and K_a is the azimuth mainlobe-broadening factor. During data collection, the azimuth beamwidth determines the scene size to use when calculating the necessary azimuth sampling rate—the radar pulse repetition frequency (PRF). For image formation processing, the appropriate scene size to use is the desired processed scene size. The processor establishes the desired scene size by downsampling in the azimuth direction during polar interpolation. Similarly, the appropriate azimuth resolution to use in the IFP is the desired processed azimuth resolution, which may be equal to or coarser than the resolution supported by the collected radar data.

For simplicity, we use the same symbols for collected and processed resolutions and for collected and processed scene sizes. This usage assumes that the processor utilizes the full extent and bandwidth of the available signal data; naturally, it is possible to process only a fraction of the available data extent or to downsample the signal data in order to degrade processed resolution or reduce processed scene size.

The range time-bandwidth product in (4.34) provides a minimum sampling requirement in range. Equating the number of range samples required in the rectangular output grid NPH_r to TB_r yields

$$NPH_r = \frac{K_r W_r}{\rho_r} \tag{4.36}$$

Using (2.2) and accounting for the projection of signal data onto the $K_x K_y$ plane in K space, the range spatial-frequency extent of the output grid in $K_x K_y$ becomes

$$\Delta y = \frac{4\pi B S_{\phi c}}{c} = \frac{2\pi K_r S_{\phi c}}{\rho_r} \tag{4.37}$$

Assuming that the desired range resolution is the collected resolution, the range polar interpolation divides this bandwidth over NPH_r samples. Dividing (4.37) by (4.36) yields an expression for the spatial frequency interval k_{gr} between range output samples on the rectangular grid. This expression for k_{gr} is

$$k_{gr} = \frac{2\pi S_{\phi c}}{W_r} \tag{4.38}$$

Similarly, the number of azimuth samples required in the rectangular output grid NPH_a is

$$NPH_a = \frac{K_a W_a}{\rho_a} \tag{4.39}$$

From (3.29), an approximate expression for the necessary azimuth spatial-frequency extent of the output grid in the $K_x K_y$ plane is

$$\Delta x \approx K_c \Delta\theta_p \approx \frac{4\pi \sin(\phi_{ao})\,\Delta\theta}{\lambda_c S_{\phi c}} \tag{4.40}$$

Here ϕ_{ao} is the angle between the XY plane and the plane formed by the X axis and the aperture reference point (ARP) at (X_{ac}, Y_{ac}, Z_{ac}). The expression $\tan(\phi_{ao}) = Y_{ac}/Z_{ac}$ defines this angle. The quantity $\Delta\theta$ is the coherent integration angle in the slant plane. Again assuming that the desired azimuth image resolution is the collected resolution, the azimuth polar interpolation divides this width over NPH_a samples. Dividing (4.40) by (4.39) and using (2.20) yields an expression for the spatial frequency interval k_{ga} between azimuth output samples on the rectangular grid. This expression for k_{ga} is

$$k_{ga} = \frac{2\pi \sin(\phi_{ao})}{W_a S_{\phi c}} \tag{4.41}$$

For an image processed at a 90-deg Doppler cone angle (broadside), $\sin(\phi_{ao})$ is equal to $S_{\phi c}$ and (4.41) simplifies to $2\pi/W_a$.

To accomplish the polar interpolation procedure, the IFP must have values for the four quantities provided by (4.36), (4.38), (4.39) and (4.41). The right-hand sides of these equations indicate the radar and image parameters that the system must communicate to the IFP to enable the processor to proceed.

In practice, the IFP often takes a number of other effects into consideration when determining the processing parameters. In the range direction, for example, interpolation requires sufficient input samples above and below the output grid to support the overhang of the interpolation filter. The processor must begin with slightly more range bandwidth than the desired range resolution indicates. In azimuth, it is reasonable to compute the angular interval $\Delta\theta$ available for azimuth resolution at the low frequency edge of the output grid to avoid unfilled areas in the low frequency corners of the output grid. The IFP must account for overhang of the interpolation filter in the azimuth direction also. The processor accommodates these concerns in azimuth by starting with signal data over slightly more angular interval than the desired azimuth resolution indicates.

4.4 DIGITAL POLAR INTERPOLATION

During polar-to-rectangular interpolation, the processor computes the value of each sample on the rectangular output grid from an appropriately weighted neighborhood of polar input samples. A key factor that affects the requirements on the interpolation weighting function is the change in sampling rate from the input grid to the output grid. The central concern is the desire to reduce the sampling rate of the polar array of input signal samples to compute a more sparse rectangular output grid. This consideration must include both range and azimuth sampling rates.

It is common for the polar interpolator to significantly reduce the azimuth direction sampling rate. The ratio of input samples to output samples in the azimuth direction can approach or exceed 10. The ratio in the range dimension is typically smaller, often as low as 1.1 or 1.2.

It is natural and efficient to store the digitized SAR signals in a rectangular format, indexed in one dimension by the A/D sample number k and in the other dimension by the pulse number n. Figure 4.16 shows the collected signal history data stored in a rectangular format. Conceptually, the PFA requires that the processor store this signal data in a polar format (Section 3.3). In the PFA implementation, a two-dimensional discrete Fourier transform (DFT) of this stored data yields a focused image. For computational efficiency, it is desirable to compute the DFT as a two-dimensional FFT. However, the signal history in polar format does not possess uniform sample spacing in either the range or azimuth dimension. Thus, digital implementation of the PFA requires polar interpolation (resampling) in both dimensions to achieve uniform sampling. Following the polar interpolation step, the signal history has uniform, rectangular sampling, although it is "polar formatted" in common terminology.

Resampling based on one-dimensional FIR filter techniques provides an efficient mechanism for performing polar interpolation. Even with the high efficiency of low-order FIR filters, the polar interpolation procedure often represents an intricate, time-consuming

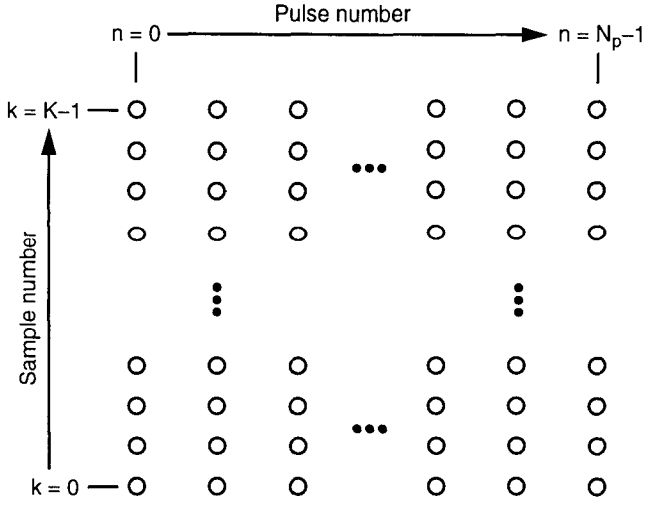


Figure 4.16 SAR signal data stored in rectangular format.

operation in spotlight SAR digital image formation processing. The one-dimensional interpolation approach first resamples the signal history in range (sample number) to produce intermediate sample positions with constant spacing in the range spatial-frequency dimension (Figure 4.17). It then resamples these intermediate output samples in azimuth (frequency) to give uniform spacing in azimuth spatial frequency also (Figure 4.18). As an alternative to these two one-dimensional operations, a single two-dimensional filtering can accomplish the resampling. With an interpolation filter of length L_f, the separable one-dimensional filtering approach has a computational cost proportional to $2L_f$, while the single two-dimensional filtering has a computational cost proportional to L_f^2.

4.4.1 Range Interpolation

In the range dimension, the analog-to-digital (A/D) converter samples each received pulse uniformly in time. The black dots in Figure 4.17 depict these samples. The range interpolation must produce new samples along each pulse at the points where the horizontal output grid lines intersect the polar input pulses in the figure. Open circles represent the output samples of the range interpolator. Resampling in the range direction is a uniform-to-uniform resampling operation. That is, the distances between successive input samples and between successive output samples are constant along each pulse. The range interpolation slightly downsamples the input signal, indicating that the interpolation filter must have a reduced bandwidth, low-pass frequency characteristic.

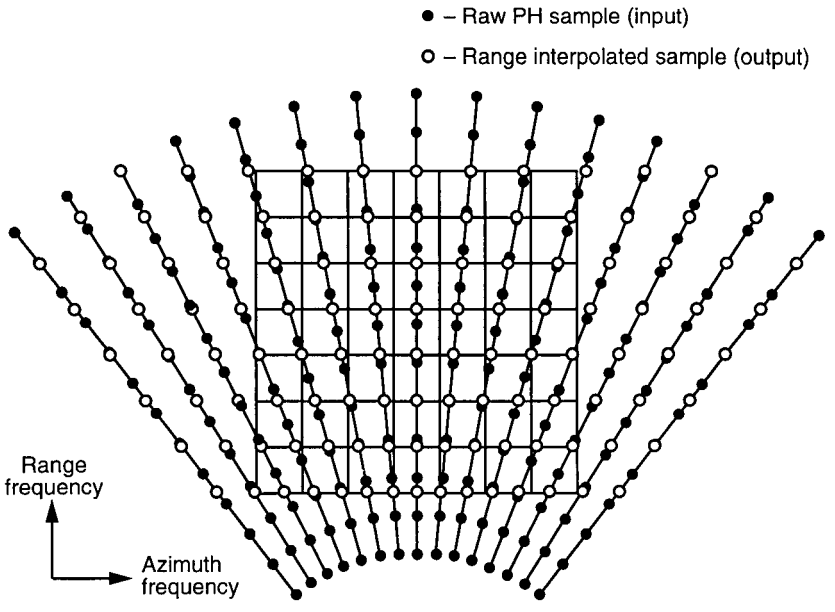


Figure 4.17 Input and output samples for range interpolation.

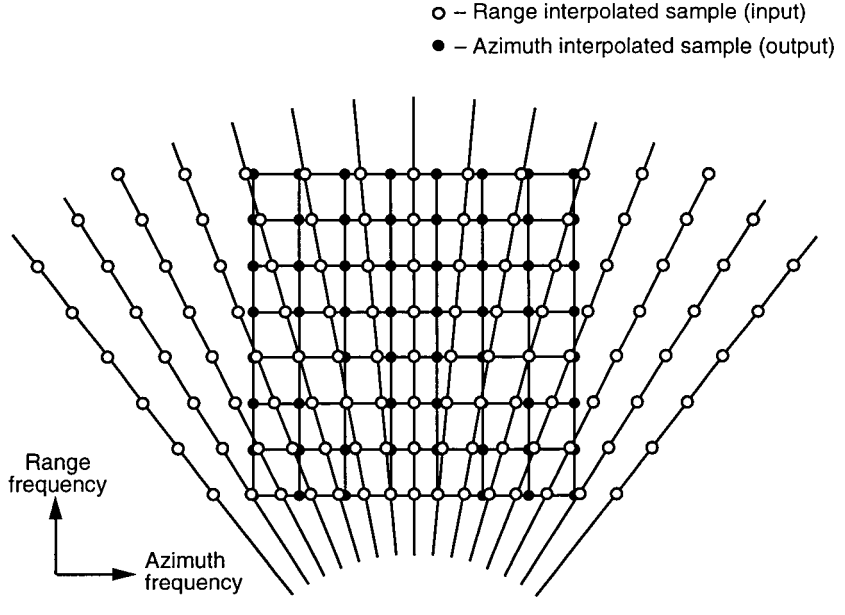


Figure 4.18 Input and output samples for azimuth interpolation.

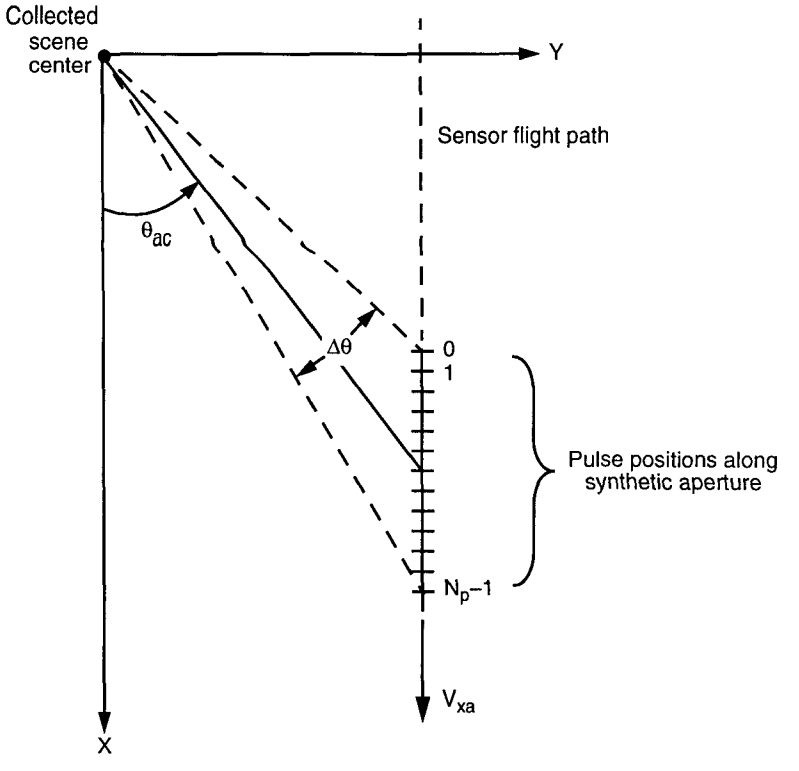


Figure 4.19 A simple imaging geometry.

A simple data collection geometry is useful to illustrate the mechanics of polar interpolation. In this geometry (Figure 4.19), the sensor flies along a straight line in the XY plane parallel to the X axis at velocity V_{xa}. This simplification sets the incidence angle ϕ_a to 90 deg and makes $S_{\phi a}$ in (4.28) through (4.32) equal to unity. The squint angle θ_{ac} at the center of the synthetic aperture interval identifies the squint angle associated with the image. Figure 4.20 indicates the appropriate polar storage format for the input (collected) data samples.

The processor receives a stream of digital data encompassing the desired display squint angle. The first step in range interpolation is to position the rectangular output grid properly with respect to the polar input samples after choosing the angle θ_{ac} about which to form an image. This center angle becomes the look angle θ_L of the image. The next step is to select the image resolution and scene size. It is convenient here to select range and azimuth resolutions equal to each other and range and azimuth scene sizes equal to each other, although this selection is unnecessary in practice. Then, the processor computes NPH_r, NPH_a, k_{gr}, and k_{ga} for the rectangular output grid using (4.36) through (4.41). In the current example, $NPH_r = NPH_a$ and $k_{gr} = k_{ga}$.

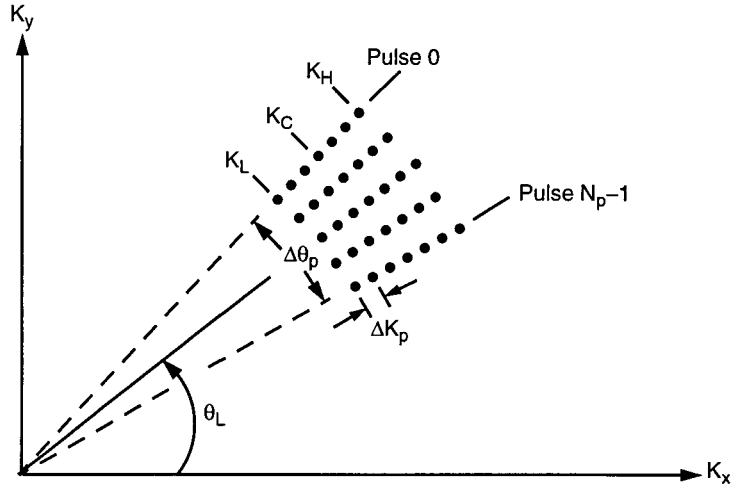


Figure 4.20 Polar formatting for sample imaging geometry.

At this point, we introduce an orthogonal right-handed (U, V) coordinate system for the rectangular output grid (Figure 4.21). The V axis is parallel to the center pulse and points outward from the origin of the (K_x, K_y) coordinate system. The origin of the (U, V) system is that corner sample of the output grid which gives all output samples positive U and V coordinates. The (U, V) system has its own set of units called *output grid units* (OGU). The distances between successive U samples and between successive V samples are one OGU. This scaling sets up the polar interpolation operation as an input-centered resampling procedure.

Associated radial distance $K_p(n, k)$ and angle $\theta_p(n)$ locate each data point on the input polar grid. It is necessary to map only the distance K_p into the (U, V) coordinate system. For the current example with $k_{gr} = k_{ga} = k_g$, the factor $1/k_g$ scales K_p to express it in terms of output grid units. In cases where k_{gr} and k_{ga} are unequal, separate U and V scalings of K_p are necessary. The output grid consists of NPH_r by NPH_a samples.

This (U, V) coordinate system offers a significant advantage when writing computer software to perform polar-to-rectangular interpolation. Computer programs access data storage locations via integer subscripts. Successive data storage locations differ in subscript by unity. Conceptually (and often literally), software realizes the rectangular output grid as a two-dimensional array. The unity OGU scaling of the (U, V) coordinate system greatly simplifies the interpolation computations.

Following the LOSPI approach of Section 4.3 and assuming even-sized sample grids, the center sample of the rectangular output grid is set on top of the middle sample, $k = K/2$, of the center polar input pulse, $n = N_p/2$, as Figure 4.21 suggests. The center sample of the output grid corresponds to the (U, V) coordinates

$$(U_c, V_c) = \left(\frac{NPH_r}{2}, \frac{NPH_a}{2}\right) \tag{4.42}$$

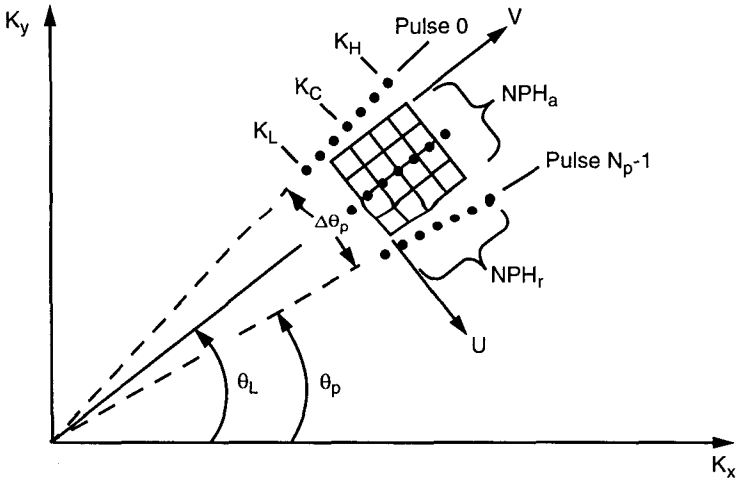


Figure 4.21 Placement of the (U, V) grid over the polar samples.

while, from (4.26), the midpoint of the center pulse occurs at $K_c = 4\pi f_c / c$, where f_c denotes the radar center frequency. It is possible to choose an alternate frequency to use as the aperture center point. Such a change shifts the band of frequencies that contribute to the final image and is useful to study the dependence of target radar cross-section (RCS) on center frequency.

The processor requires a set of coordinate transformation equations mapping (K_p, θ_p) to (U, V). For the current example, these expressions are

$$U = \frac{K_p}{k_g} \sin(\theta_L - \theta_p) + \frac{NPH_a}{2} \tag{4.43}$$

$$V = \frac{K_p}{k_g} \cos(\theta_L - \theta_p) + \frac{NPH_r}{2} - \frac{K_c}{k_g} \tag{4.44}$$

with

$$K_p = K_L + k\Delta K_p \tag{4.45}$$

Here, k indexes the K samples within each input pulse starting with $k = 0$. The pulse index n is implicit in $\theta_p = \theta_p(n)$ and includes N_p pulses starting with $n = 0$. The factor $1/k_g$ properly scales the distance between successive U and V output samples to one OGU.

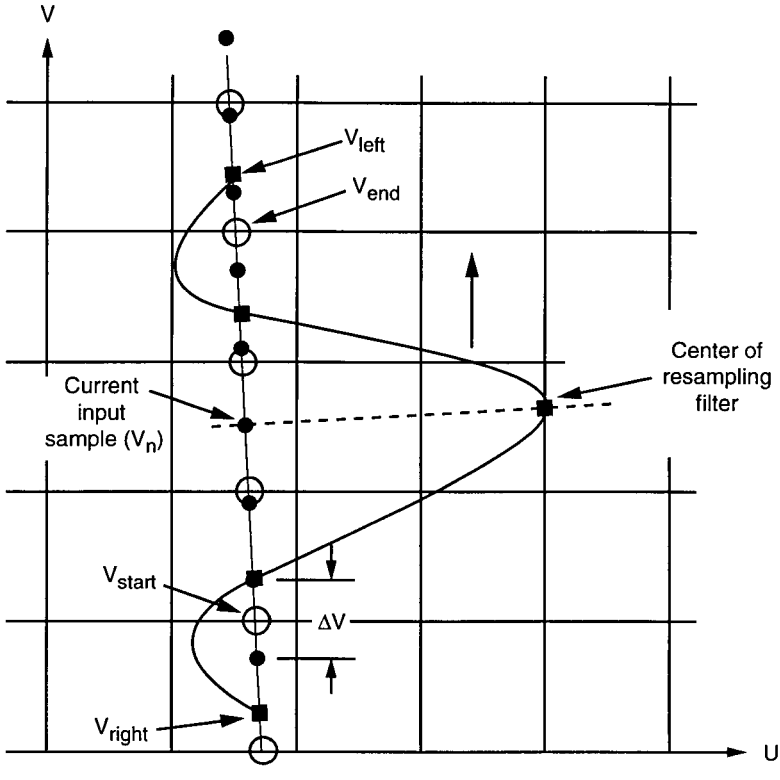


Figure 4.22 Detail of range polar interpolation.

As Section 4.2 describes, the processor aligns the nulls of the range resampling filter with the output grid because the sample rate of the output grid is lower than that of the input pulse. The filter h contains L_f points that are upsampled by a factor L_u, yielding a filter with L_u phasings. The range direction resampling determines the value of the current input pulse at integer values of V. In V units, the filter extends L_{right} units to the right side of its center and L_{left} units to the left side of its center. Address zero stores the center filter sample.

The processor now performs the actual range interpolation (Figure 4.22). It maps the location (K_p, θ_p) of the first sample of the first pulse to a V coordinate using (4.44) and (4.45); this sample is V_0. The processor proceeds likewise for the second sample of the pulse, V_1. The change in V coordinate ΔV is the difference $V_1 - V_0$. Assuming little sensor motion during a pulse, ΔV is constant for any pulse at its given θ_p. Use of ΔV makes unnecessary a sample-by-sample recalculation of the trigonometric function in (4.44).

The processor centers the filter over the first input sample at V_n. It then computes the V coordinate of the filter's right edge as $V_{\text{right}} = V_n - L_{\text{right}}$. Similarly, the V coordinate of the filter's left edge is $V_{\text{left}} = V_n + L_{\text{left}}$.

Application of a ceiling function to V_{right} determines the first V sample to which the current input point contributes; this output grid sample is V_{start}. The ceiling function rounds a number up to the next integer value. Application of a floor function to V_{left} determines the last V sample to which the current input point contributes; this output grid sample is V_{end}. The floor function rounds a number down to the next integer value. Symbolically, we write

$$V_{start} = \lceil V_{right} \rceil \tag{4.46}$$

and

$$V_{end} = \lfloor V_{left} \rfloor \tag{4.47}$$

where $\lfloor \ldots \rfloor$ denotes the integer floor function and $\lceil \ldots \rceil$ denotes the integer ceiling function.

The address of the filter sample over V_{start}, called H_0, is

$$H_0 = \lfloor (V_{start} - V_n) L_u \rfloor \tag{4.48}$$

The contribution that the current input sample makes to output grid point V_{start} is the value of the input sample V_n multiplied by the filter value $h(H_0)$.

The input sample next contributes to sample $V = V_{start} + 1$. The address of the filter sample over this output grid point is $H_0 - L_u$, and the contribution the input point makes to this output point is the value of the input sample at V_n multiplied by $h(H_0 - L_u)$.

After reaching V_{end}, the processor moves the resampling filter up the polar input pulse by one sample, changing its center location by ΔV units. The left and right edges of the filter also move by ΔV units. The use of ΔV avoids the reevaluation of (4.44), saving time and computations. As in the case of the first input sample, the processor applies ceiling and floor functions to V_{right} and V_{left} to obtain V_{start} and V_{end}. It computes the filter sample over V_{start} via (4.48), and contributes the input point to the appropriate output grid points. The interpolation procedure continues until it reaches the last sample of the input pulse.

4.4.2 Azimuth Interpolation

As with range interpolation, the processor can also perform azimuth interpolation on a pulse-by-pulse basis using the intermediate output samples produced by the range interpolation. An alternate approach performs range interpolation on all polar input pulses and buffers the intermediate samples for later use by the azimuth interpolator. Azimuth interpolation is a nonuniform-to-uniform resampling operation. This characteristic is a side effect of the polar formatting since the number of input samples per unit length in the azimuth direction is greater on the inside than on the outside of the polar annulus.

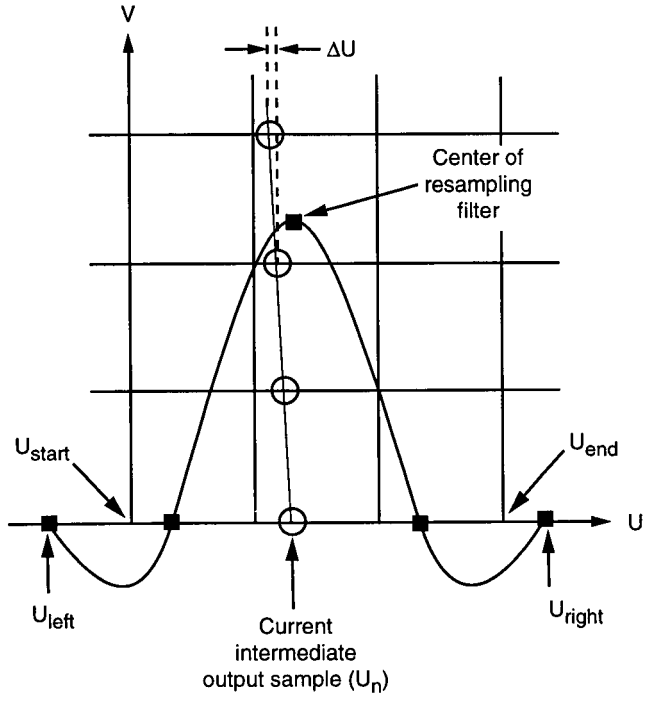


Figure 4.23 Detail of azimuth polar interpolation.

The azimuth interpolation procedure (Figure 4.23) is similar to range interpolation. Significant downsampling typically accompanies the azimuth interpolation, and the resampling filter must possess a low-pass frequency characteristic. The processor aligns the nulls of the resampling filter with the output grid because the output grid has a lower sample rate than that provided by the input pulses. Often, range and azimuth interpolation use the same filter, so the azimuth filter has the same size (L_f samples and L_u phasings) as the range interpolation filter.

The V coordinate of each intermediate output sample starts at zero and runs to $NPH_r - 1$. Since the processor-space squint angle θ_p of each pulse and the look angle θ_L of the image are known, it is useful to rewrite (4.44) to yield K_p in the form

$$\frac{K_p}{k_g} = \frac{V + \dfrac{K_c}{k_g} - \dfrac{NPH_r}{2}}{\cos(\theta_L - \theta_p)} \tag{4.49}$$

Substitution of this equation into (4.43) provides an expression for U in terms of the two

known parameters of the intermediate output samples, the V coordinate and the scene angle θ_p in processor space. Assuming negligible sensor motion during a pulse, this angle is constant along any given pulse. The expression for U becomes

$$U = \left[V + \frac{K_c}{k_g} - \frac{NPH_r}{2} \right] \tan(\theta_L - \theta_p) + \frac{NPH_a}{2} \tag{4.50}$$

The processor uses (4.50) to compute the change ΔU in the U coordinate between each intermediate output sample increment.

Centering the resampling filter over the first intermediate output sample ($V = 0$), the processor computes the U coordinate U_n of this sample, the U coordinate of the right side of the filter U_{right}, and the U coordinate of the left side of the filter U_{left}.

Application of a ceiling function to U_{left} determines the first U sample U_{start} to which the intermediate sample contributes. Application of a floor function to U_{right} determines the last U sample U_{end} to which the intermediate sample contributes. These results have the form

$$U_{\text{start}} = \lceil U_{\text{left}} \rceil \tag{4.51}$$

and

$$U_{\text{end}} = \lfloor U_{\text{right}} \rfloor \tag{4.52}$$

The address of the filter sample that lies on top of U_{start} (called H_0) is

$$H_0 = \lfloor (U_{\text{start}} - U_n) \times L_u \rfloor \tag{4.53}$$

The processor computes the contribution that each intermediate output sample makes to each output grid sample in the same manner that it did in during range interpolation.

After reaching U_{end}, the resampling filter moves up to the next intermediate output sample. This changes its U location by ΔU units. The left and right edges of the filter also move by ΔU units. Application of the floor and ceiling functions of (4.51) and (4.52) yields U_{start} and U_{end}. The processor computes the interpolation filter sample over U_{start} via (4.53) and the input sample contributes to the appropriate output samples.

4.5 IMAGE SCALE FACTORS

After polar interpolation, the IFP forms the desired SAR image by computing the two-dimensional FFT of the $NPH_r \times NPH_a$ output grid samples. This section develops expressions relating spotlight mode SAR image pixel separation to scene distance in range and azimuth.

A rewrite of (4.36) and (4.39) yields expressions for the range extent W_r and azimuth width W_a of the processed image as

$$W_r = \frac{NPH_r\rho_r}{K_r} \tag{4.54}$$

and

$$W_a = \frac{NPH_a\rho_a}{K_a} \tag{4.55}$$

Clearly, W_r is proportional to the number of range samples and W_a is proportional to the number of azimuth samples that the polar interpolator produces.

The processed range and azimuth FFT sample lengths, $NFFT_r$ and $NFFT_a$, can be equal to or greater than the signal history sample lengths. When the FFT and signal history lengths are equal, the scene distances per image pixel, μ_r in range and μ_a in azimuth, are

$$\mu_r = \frac{W_r}{NPH_r} = \frac{\rho_r}{K_r} \tag{4.56}$$

and

$$\mu_a = \frac{W_a}{NPH_a} = \frac{\rho_a}{K_a} \tag{4.57}$$

The quantities μ_r and μ_a have units of distance per pixel. They correspond to the number of distance units in the scene that each pixel in the processed image represents. Here, μ_r compares to $1/m_y$ in (3.73) and μ_a compares to $1/m_x$ in (3.72).

The FFT size exceeds the signal history size when the IFP centers the rectangular output grid in a bed of zeros before performing the FFT. This process of *zero-padding* the size of the FFT naturally increases the number of computations. Zero-padding is generally desirable because it decreases the spacing between image samples. In this case, the scene distances per image pixel become

$$\mu_r = \frac{W_r}{NFFT_r} = \frac{\rho_r}{K_r}\frac{NPH_r}{NFFT_r} \tag{4.58}$$

and

$$\mu_a = \frac{W_a}{NFFT_a} = \frac{\rho_a}{K_a}\frac{NPH_a}{NFFT_a} \tag{4.59}$$

In general, the range distance d_r and azimuth distance d_a between two points in an image separated by P_r pixels in range and P_a pixels in azimuth are

$$d_r = P_r\mu_r \tag{4.60}$$

and

$$d_a = P_a\mu_a \tag{4.61}$$

4.6 SIGNAL HISTORY PROJECTIONS

It is convenient and efficient to combine into the polar interpolation step the signal history projections that compensate nonplanar sensor motion (Section 3.8) and select the IDP (Section 3.3.5). These projections modify the position of, and spacing between, the polar input samples prior to polar-to-rectangular data resampling. In the polar format development of Chapter 3, the expression in (3.35) includes these projections as part of a generalized polar transformation that chooses the XY plane as the focus target plane (FTP) and selects the IDP. Figure 2.22 illustrates these planes in target space. This section briefly reviews these projections and describes their implementation within the digital polar format processor.

4.6.1 Collection Surface to Focus Target Plane

Section 3.3.4 describes a procedure to compensate for nonplanar motion and discusses the FTP concept. Nonplanar motion causes pulse-to-pulse changes in the instantaneous incidence angle ϕ_a in addition to those changes that occur naturally for a planar flight path. Without compensation, these changes in ϕ_a lead to azimuth phase errors throughout the image. The FTP concept is an effective procedure to deal with nonplanar motion. This procedure projects signal history samples orthogonally onto the $\boldsymbol{K}$-space equivalent of the FTP. In this way, a scatterer located in the FTP does not suffer from phase errors induced by nonplanar motion; a scatterer above or below the FTP does experience such errors with a severity that increases with its distance out of the FTP. The $S_{\phi a}$ term in (3.35) accounts for the necessary projection to establish the FTP. By including this term in the mapping of collected data to the (U, V) output grid, the PFA achieves this projection with no increase in computational complexity.

Figure 4.24 illustrates the duality between target space and $\boldsymbol{K}$ space. Figure 4.24(a) shows the FTP as the XY nominal ground plane. The IDP in this example lies between the data collection surface and the FTP. Figure 4.24(b) indicates that selecting the XY plane as the FTP is equivalent to selecting the K_xK_y plane as the projection plane in $\boldsymbol{K}$ space. In general, the orientation of this $\boldsymbol{K}$-space projection plane relative to the K_xK_y plane determines, and is identical to, the FTP orientation relative to the XY plane in target space.

4.6.2 Focus Target Plane to Image Display Plane

During polar interpolation, the IFP selects the IDP in target space by projecting signal history samples into a selected plane in $\boldsymbol{K}$ space (Section 3.3.5). Both the FTP and the IDP naturally include the motion compensation point. The IDP can be the nominal data collection plane, the FTP, or any other plane containing the X axis.

Equation (3.35) in Section 3.3.5 provides a general expression for the polar format transformation K_p that allows the IDP to differ from the FTP. This expression includes provisions for projecting signal history samples onto any plane in $\boldsymbol{K}$ space that includes the K_x axis. In general, the orientation of this projection plane in $\boldsymbol{K}$ space relative to the

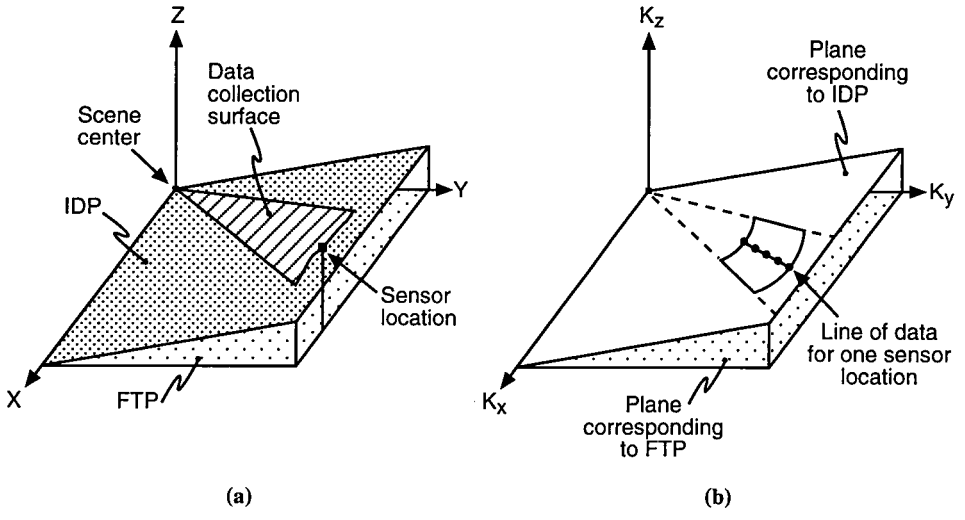


Figure 4.24 Target space and $\boldsymbol{K}$ space duality: (a) FTP and IDP in target space; (b) Corresponding planes in $\boldsymbol{K}$ space.

K_xK_y plane determines, and is identical to, the orientation of the IDP relative to the XY plane in target space. When the FTP is the XY plane, the direction of the projection onto this $\boldsymbol{K}$-space projection plane is orthogonal to the K_xK_y plane. In general, the direction of the projection is orthogonal to the $\boldsymbol{K}$-space equivalent of the FTP. The mapping of signal history samples onto the (U, V) output grid includes this projection. Selection of the IDP during polar interpolation does not increase the computational needs of the digital PFA.

4.7 STABILIZED SCENE POLAR INTERPOLATION

The processor controls scene orientation in the output image by its orientation of the rectangular output grid after polar interpolation. The development of digital polar interpolation in Section 4.4 utilizes LOSPI. This implementation positions the output grid by aligning its center column of data with the center pulse of the signal history aperture (Figure 4.15). LOSPI yields images in which the scene orientation in the output image matches the squint angle of the data collection.

An alternative implementation yields images in which the scene orientation in the output image does not vary with the squint angle of the processed data aperture. This implementation is *stabilized scene polar interpolation* (SSPI). In this case, the radar illumination appears to rotate around a stationary scene when generating multiple images of the scene from various squint angles. It is also possible, but less efficient, to stabilize the scene orientation by resampling output images after image formation via LOSPI. In this section, we illustrate both implementations and describe the procedures for SSPI.

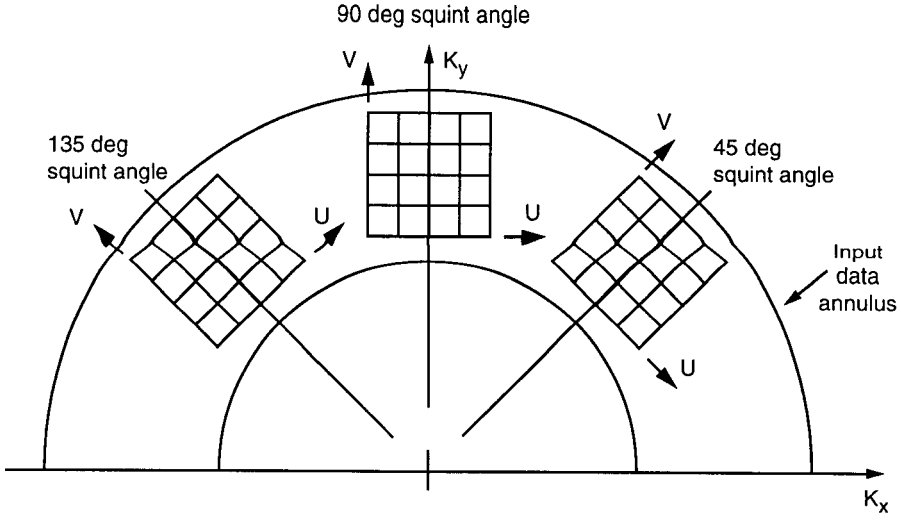


Figure 4.25 Line-of-sight polar interpolation at three different squint angles.

4.7.1 Example with Line-of-Sight Polar Interpolation

Figure 4.25 depicts an input data annulus collected over 180 deg of squint angle. The figure shows polar interpolation output grids at three different squint angles. The squint angle of each image coincides with the mid-aperture squint angle θ_{ac} of the corresponding input data. Figure 4.26 shows images processed from data at the three squint angles in Figure 4.25 and illustrates an example data collection geometry. These images originate from a ground-based spotlight ISAR system operating at X-band (Appendix E). The target is an automobile. The orientation of the imaged scene appears to rotate as the squint angle changes, but the radar illumination is always from the left side. Scene rotation is the key characteristic of LOSPI. While this presentation of images relates easily to imaging a target on a turntable that rotates in front of a fixed illumination beam, LOSPI applies equally well to processing SAR data of a stationary scene collected by an airborne sensor.

4.7.2 Example with Stabilized Scene Polar Interpolation

SSPI stabilizes the scene orientation by rotating the rectangular output grid to maintain a constant grid angle; the *grid angle* of the output grid is the angle between the V axis of the output grid and the K_x axis. The center data column of the output grid is no longer colinear with the center pulse of the signal history aperture. Figure 4.27 illustrates the SSPI output grids and the grid angle for the same three squint angles of Figure 4.25. Figure 4.28 presents the corresponding SSPI images. The grid angle for the stabilized scene images is 90 deg. As the squint angle changes, the radar illumination appears to rotate around the

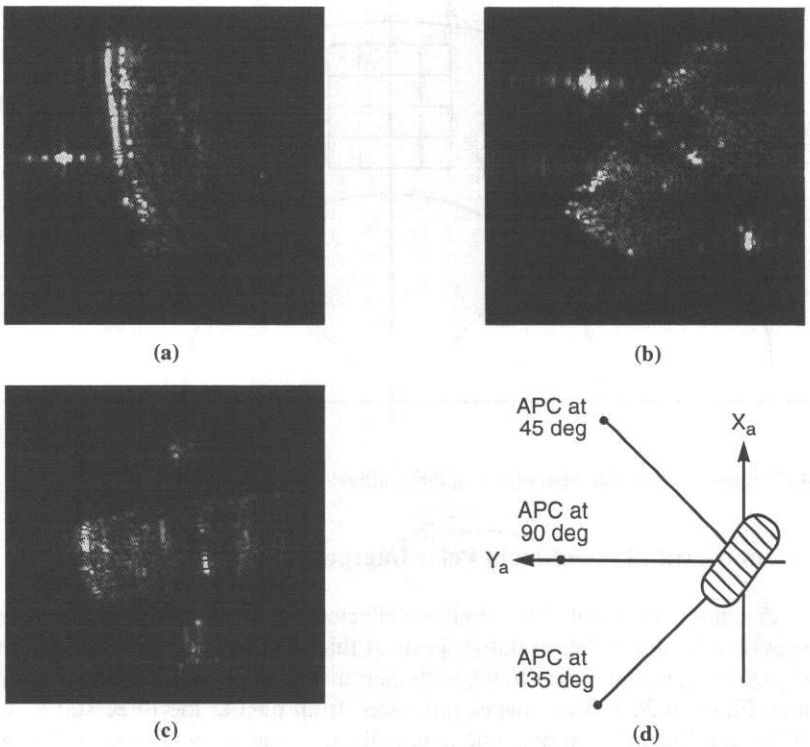


Figure 4.26 SAR images from line-of-sight polar interpolation: **(a)** 45-deg squint angle; **(b)** 90-deg squint angle; **(c)** 135-deg squint angle; **(d)** Example data collection geometry.

stationary scene. This fixed scene orientation is the key characteristic of SSPI. While this presentation of images relates easily to an airborne sensor traveling past or around a stationary scene, SSPI applies equally well to processing SAR data collected by a stationary sensor illuminating a rotating platform.

SSPI is useful in implementing noncoherent integration of SAR images. A stabilized scene greatly facilitates summing together images from multiple squint angles on a pixel-by-pixel basis. While not often practical, noncoherent summation of images from a full 360-deg interval of rotation produces an image of the aggregate radar scattering of the scene or target. For example, Figure 4.29 shows the noncoherent sum of 36 images of the automobile at 10-deg squint angle intervals over 360 deg.

Stabilized scene processing is also useful when making image-based RCS measurements of targets within a scene. With the scene stabilized, a simple fixed-location masking

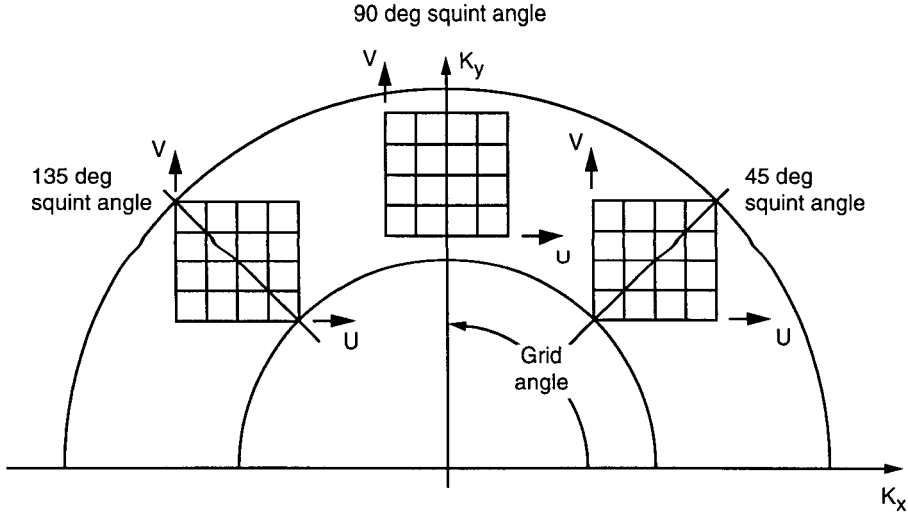


Figure 4.27 Stabilized scene polar interpolation at three different squint angles.

algorithm readily separates target pixels from background pixels. Summing and scaling the energy of pixels inside the mask yields an estimate of the total RCS of the target. As the radar squint angle changes, the location of the target pixels does not vary.

A potential complication with the use of SSPI is an unfilled output grid. Resolution requirements determine the necessary grid size; for a specific output grid size, certain combinations of squint and grid angles can cause regions of the output grid to fall outside the available input data annulus. Figure 4.30 illustrates this situation in which the overhanging areas of the processing aperture contain no signal data. These unfilled regions degrade image resolution and introduce an unconventional sidelobe structure. A reduction in the size of the output grid naturally reduces the unfilled area, but also degrades image resolution.

4.7.3 Considerations in Stabilized Scene Polar Interpolation

The polar interpolation kernel in SSPI usually differs from that in LOSPI. LOSPI often employs two, one-dimensional resampling operations for the sake of efficiency. This is permissible because both the input polar and output rectangular samples are, to a good approximation, oriented in the range and azimuth directions of the output image. This alignment allows the low-pass characteristic of the interpolation filter to adequately band-limit the frequency extent of the final image in the range and azimuth directions, despite the small change in squint angle that occurs over the aperture time.

The one-dimensional interpolation approach can break down when performing SSPI. The breakdown occurs because the input polar samples are no longer aligned with the range and azimuth directions of the output image. Hence, the low-pass characteristic of

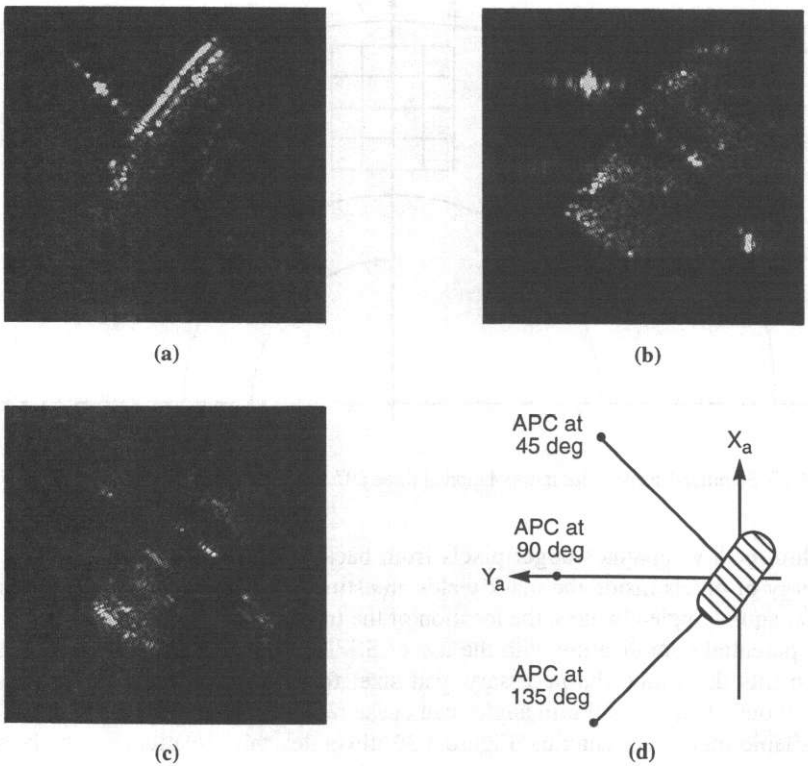


Figure 4.28 SAR images from stabilized scene polar interpolation: **(a)** 45-deg squint angle; **(b)** 90-deg squint angle; **(c)** 135-deg squint angle; **(d)** Example data collection geometry.

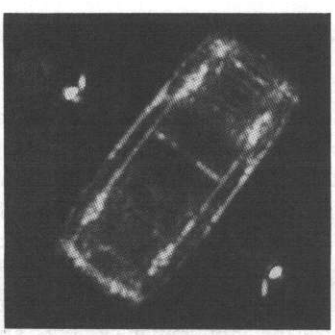


Figure 4.29 A noncoherently averaged image of the automobile (enlarged).

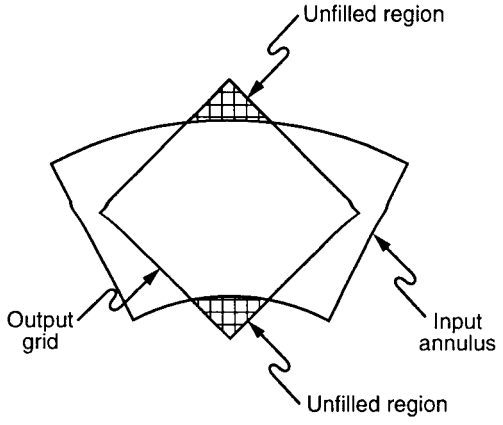


Figure 4.30 Unfilled apertures in SSPI.

the one-dimensional filters may not adequately bandlimit the frequency extent of the final image. Reference [7] provides an excellent discussion of this effect.

To bandlimit the frequency extent of the final image for all grid angles, SSPI must use a two-dimensional, nonseparable interpolation kernel during polar interpolation. The correct procedure orients the filter to align its edges with the rectangular output grid (Figure 4.31). The downside of using a two-dimensional filter is an increased computational requirement relative to the separable approach. With one-dimensional filtering, the number of computations per output grid point is proportional to twice the filter length. With two-dimensional filtering, the number of computations per output grid point is proportional to the *square* of the filter length.

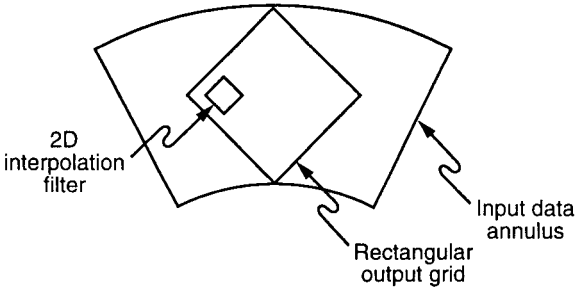


Figure 4.31 Application of a two-dimensional, nonseparable polar interpolation filter.

4.8 SUBPATCH PROCESSING

Space-variant phase errors cause geometric distortion and defocusing that vary with scatterer location within the imaged scene. Because autofocus cannot easily compensate this type of phase error, space-variant defocus can limit scene size in fine resolution spotlight imaging. Range curvature is typically a major factor in limiting scene size when using the PFA for image formation (Section 3.7). One approach to extend this type of limit on scene size involves three steps:

1. Divide the scene into a number of smaller scenes (subpatches);
2. Process each subpatch separately;
3. Mosaic the subpatches together to form an image of the full scene.

The name of this approach is *subpatch processing*. A spotlight SAR processor can use this procedure to focus an image larger than the size limit imposed by common sources of space-variant phase error. This procedure is also useful to divide a large image formation task among multiple digital processors.

Subpatch processing applies the image formation algorithm individually to each subpatch; each subpatch has its own scene center and receives its own motion compensation and algorithm-specific set of operations. For instance, the PFA performs polar interpolation of the input signal data separately for each subpatch. The size of an individual subpatch is small enough to limit scene size-dependent effects to either an acceptable level or to a convenient number of subpatches. Finally, the subpatch processing procedure mosaicks the subpatches together to produce a full-scene image.

Figure 4.32 illustrates a typical subpatch processing procedure. The processor first filters each radar pulse to divide the IF bandwidth, representing the range extent of the scene, into subbands corresponding to range subswaths. It then filters the azimuth bandwidth of each subswath into subbands to form scene subpatches. Coarse motion compensation to a global scene center in separate range (frequency) and azimuth (pulse-to-pulse phase) steps precedes these two filtering operations. Alternatively, the procedure sequentially applies coarse motion compensation to each subpatch center followed by two-dimensional low-pass filtering to isolate data for each subpatch. In this second case, the polar interpolation process can include the low-pass filtering function. In either case, the processor then applies fine motion compensation individually to each subpatch to stabilize the subpatch centers. Because the processor uses the same aperture reference point to motion compensate the individual subpatch scene centers, each subpatch has slightly different range and azimuth orientations (Figure 4.33) with the use of LOSPI. The image mosaicking process must account for this deterministic variation in orientation. The use of SSPI avoids these orientation differences among individual subpatches.

When sizing the subpatches to construct a large image, the processor must include sufficient overlap between subpatch image areas to account for filter overhang of all the resampling filters and to support image rotation to the common output orientation. Reference [7] develops the minimum sampling rate to resample an image from one orthogonal coordinate system to a rotated coordinate system using two one-dimensional interpolators.

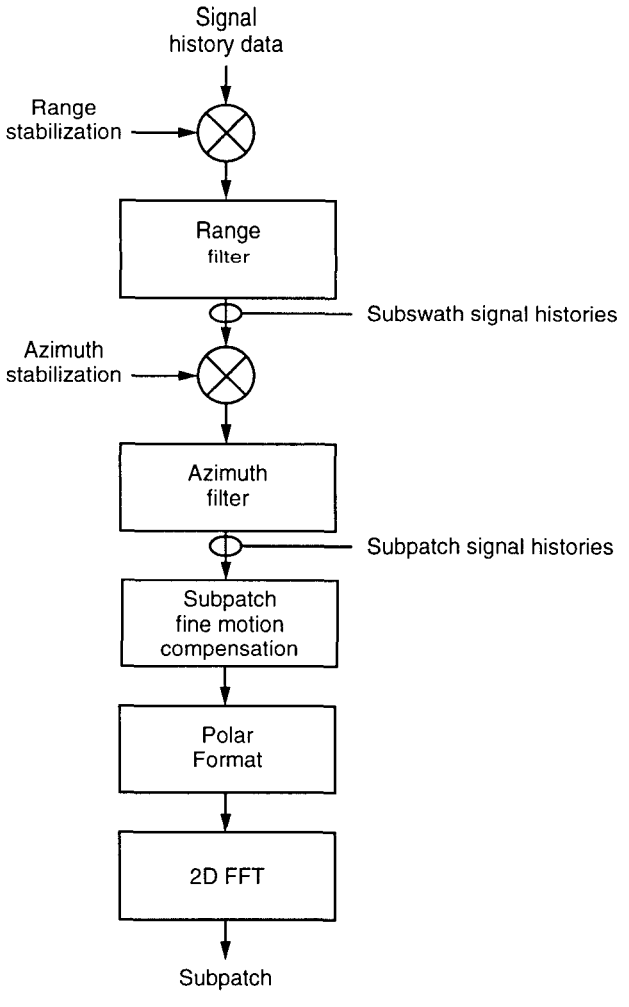


Figure 4.32 Subpatch processing procedure using the PFA.

In addition, the behavior of the amplitude and phase of the final mosaicked image across the subpatch boundaries is a consideration in producing a high-quality output image. The subpatch processor must compensate for the amplitude response of the digital filters that divide the signal history into subpatches. The phase of the complex pixels is usually disturbed and not continuous over the subpatch boundaries. Thus, subpatch processing may not be a reasonable option when image phase is important.

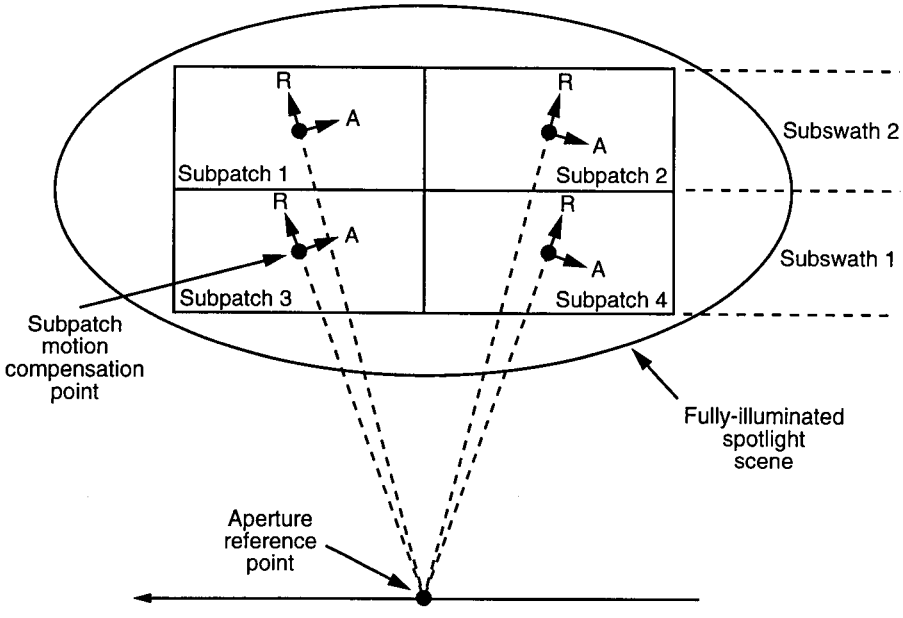


Figure 4.33 Subpatch orientation.

4.9 SUMMARY

The PFA requires a two-dimensional resampling of signal data from the polar grid of input samples to a rectangular output grid. Sampling rate conversion using polyphase filters is an integral part of this resampling procedure. Adjustments to the resampling procedure incorporate compensation for a nonplanar data collection surface and independent selection of both a FTP and an IDP. Selection of the FTP and IDP occurs during range interpolation without additional computational complexity.

REFERENCES

[1] Crochiere, R., and L. Rabiner, *Multirate Digital Signal Processing*, Englewood Cliffs, NJ, Prentice-Hall, 1983.

[2] Oppenheim, A., and R. Schafer, *Digital Signal Processing*, Englewood Cliffs, NJ, Prentice-Hall, 1975.

[3] Crochiere, R.E., and L.R. Rabiner, "Interpolation and Decimation of Digital Signals - A Tutorial Review," *Proceedings of the IEEE*, Vol. 69, No. 3, March 1981, pp. 300-331.

[4] Parks, T.W., and J.H. McClellan, "Chebyshev Approximation for Nonrecursive Digital Filters with Linear Phase," *IEEE Transactions on Circuit Theory*, Vol. CT-19, March 1972, pp. 189-194.

[5] McClellan, J.H., T.W. Parks, and L.R. Rabiner, "A Computer Program for Designing Optimum FIR Linear Phase Digital Filters," *IEEE Transactions on Audio and Electroacoustics*, Vol. AU-21, No. 6, December 1973, pp. 506-526.

[6] Rabiner, L.R., "The Design of Finite Impulse Response Digital Filters Using Linear Programming Techniques," *The Bell System Technical Journal*, Vol. 51, No. 6, July-August 1972, pp. 1177-1198.

[7] Maisel, J., and R. Morden, "Rotation of a Two-Dimensional Signal Set Using One-Dimensional Resampling," *IEEE Transactions on Accoustics, Speech, and Signal Processing*, Vol. ASSP-29, No. 6 December 1991.

Chapter 5
Phase Errors

The ideal representation of each individual scatterer in a spotlight SAR signal history is a signal with a phase that changes linearly over the two-dimensional processing aperture. A two-dimensional Fourier transform of such a constant-frequency signal produces an impulse response with resolution determined by the size of the processing aperture. In practice, undesirable variations in this ideal linear phase are present. Primary causes of these phase variations include uncompensated target or sensor motion and approximations in the image formation algorithm. We categorize these undesirable phase effects as *phase errors*. Phase errors are a concern because they degrade image quality in several ways. Depending on its nature and magnitude, a phase error may cause image geometric distortion, loss of resolution, decrease in image contrast, spurious targets, and a reduction in signal-to-noise ratio (SNR) [1, 2].

To the degree that the motion sensor is able to measure relative motion between targets and the SAR sensor, the image formation processor can eliminate undesired motion effects from the collected signal history. This procedure is the motion compensation that is discussed in Section 2.5 and Section 2.6. Errors in motion measurement lead to phase errors in the signal history. Sources of unwanted phase effects that the image formation algorithm does not remove also lead to phase errors. Typical examples include range curvature, residual video phase, and nonplanar motion.

Part of the SAR system design process is to determine the tolerable levels of uncompensated phase effects and to allocate the phase error budget among various sources. Knowledge of allowable levels of phase errors is particularly important to specify and design the motion sensing subsystem associated with the SAR sensor. If the composite phase error from all contributors is the same for all scatterers in the scene and is not unreasonably large, the image formation processor can often reduce it to an acceptable level by quadratic and higher order autofocus algorithms. Chapter 6 discusses autofocus techniques.

While a number of references discuss various aspects of phase errors in SAR imagery [3-7], this chapter contains a comprehensive discussion of the subject. In this chapter, the authors identify the categories of phase errors, quantify the relationships between phase error magnitude and the level of image degradation, and suggest allowable magnitudes of phase errors for each category; they also quantify the effects of motion measurement error and algorithm approximations with respect to these allowances.

In this discussion, a *phase term* is a complex exponential term of the form $\exp(j\phi)$. A *phase error* refers to the *phase function* ϕ of the phase term. The *instantaneous frequency* of the phase term $\exp(j\phi)$ is the first derivative (or slope) with respect to the data space coordinate of the phase function ϕ divided by 2π. The *spectrum* of the phase term relates to the distribution in frequency of $\exp(j\phi)$, that is, to its Fourier transform. The *frequency* of the phase function ϕ relates to its frequency content, that is, to the Fourier transform of ϕ.

5.1 CLASSIFICATION OF PHASE ERRORS

Phase error categories include low-frequency phase errors, high-frequency sinusoidal phase errors, and wideband phase errors. The low-frequency and high-frequency designations distinguish a phase error by its variation over the processing aperture. It is the frequency of the phase function ϕ relative to the aperture size that determines the low-frequency or high-frequency designation; the instantaneous frequency of the phase term $\exp(j\phi)$ is not a factor in this designation. Wideband phase errors are naturally high frequency. Table 5.1 shows these broad categories along with the general effects of each one on SAR imagery. By separating phase errors into these categories, it is easier to relate phase errors to image effects. The severity with which a phase error degrades image quality varies with the magnitude (size) and frequency of the error.

Table 5.1
Phase Error Categories

Phase Error Category	*Image Effects*
Low-frequency errors (less than one cycle over an aperture)	Geometric distortion; loss of resolution
High-frequency sinusoidal phase errors	Loss of contrast; spurious targets
Wideband phase errors	Loss of contrast; decrease in SNR

Low-frequency errors encompass linear phase errors, quadratic phase errors (QPEs), and higher order phase errors. The higher order terminology refers to a single cycle sinusoidal or a cubic variation in phase over the processing aperture. Quartic and multicycle sinusoids belong in the high-frequency and wideband categories. This differentiation is significant because low-frequency errors affect primarily the mainlobe of the system impulse response while high-frequency errors affect the sidelobe region.

In addition to low-frequency and high-frequency designations, a phase error is either deterministic or random and either space-variant or space-invariant. Deterministic phase errors are of known magnitude and functional form whereas random phase errors are of unknown magnitude or functional form. This differentiation is important because it is easier to remove a deterministic effect in data processing or, at least, to document the

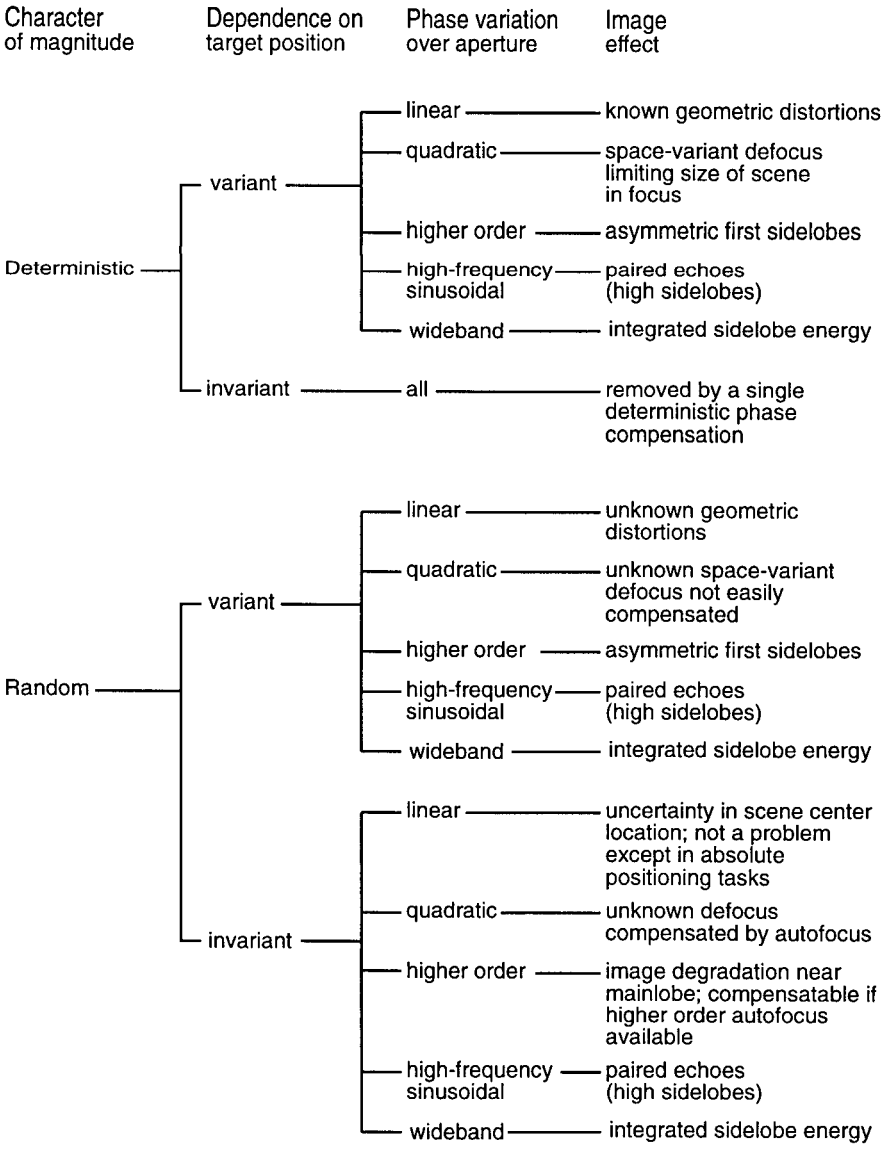


Figure 5.1 Extended classification of phase errors.

effect for the end user of the imagery. A phase error is space-invariant if it is the same for all scatterers in the image; otherwise it is space-variant. This differentiation is important because practical autofocus techniques apply primarily to space-invariant effects. Figure 5.1 summarizes these divisions and lists image effects associated with each one.

Sources of low-frequency phase errors include velocity and acceleration measurement errors by the SAR motion sensor and inherent phase effects in collected data that are not compensated fully by the image formation algorithm. Inherent phase effects include range curvature, the residual video phase term, and nonplanar motion. The effects of the motion measurement errors are largely space-invariant, whereas the algorithm approximations cause space-variant phase errors. Uncompensated vibration of the antenna phase center (APC) is a primary source of space-invariant high-frequency sinusoidal phase errors, while wideband random motion measurement errors by the motion sensor cause space-invariant wideband random phase errors.

5.1.1 Low-Frequency Phase Errors

A *low-frequency phase error* is one having a period larger than the coherent processing interval. In this case, the frequency of the phase function ϕ is less than the reciprocal of the aperture size. The instantaneous frequency of the associated phase term $\exp(j\phi)$ may be of any size. It is common to identify low-frequency phase error by the initial terms of a Taylor series expansion of the phase effect relative to the center of the processing aperture. This procedure is practical because, for low-frequency effects, the higher order terms of the expansion become small. Section 3.5 discusses this procedure. This expansion results in the usual classifications of linear, quadratic, or higher order errors and defines the nature of the phase variation over the processing aperture. Chapter 3 derives the linear and quadratic components of deterministic system phase errors and of phase errors arising from lower frequency motion measurement errors.

Figure 5.2 summarizes the nature of a low-frequency, linear phase error. The horizontal axis X represents position along the data space. By definition, the phase of the linear phase error varies linearly with position across the data space; Figure 5.2(a) indicates this linear phase, $\phi = 2\pi f_e X$. Figure 5.2(b) shows the real component of the associated phase term, $\exp(j2\pi f_e X)$, over one-half of the aperture; the real component is a *cosine* function. Figure 5.2(c) shows the constant instantaneous frequency f_e of the phase term associated with a low-frequency linear phase error. Figure 5.3 illustrates the basis for geometric distortion from this linear phase error. Without this phase error, a Fourier transform of the signal $\exp(j2\pi f_o X)$ in the rectangular aperture of Figure 5.3(a) yields the sinc function of Figure 5.3(b), centered at frequency bin f_o. Multiplication by $\exp(j2\pi f_e X)$ before Fourier transform processing results in the convolution of the original sinc output with Figure 5.3(c), the Fourier transform of this phase term. The result is a displacement in the Fourier transform (image) domain, as Figure 5.3(d) suggests. This displacement is nominally one resolution cell (depending on aperture weighting) for every 2π rad of linear phase error across the aperture. If the frequency of the linear phase term is the same for all scatterers in the scene, the effect is a displacement of the entire scene. If this frequency varies with scatterer position in the scene, the effect is image distortion, that is, a warping of the image geometry relative to the scene geometry.

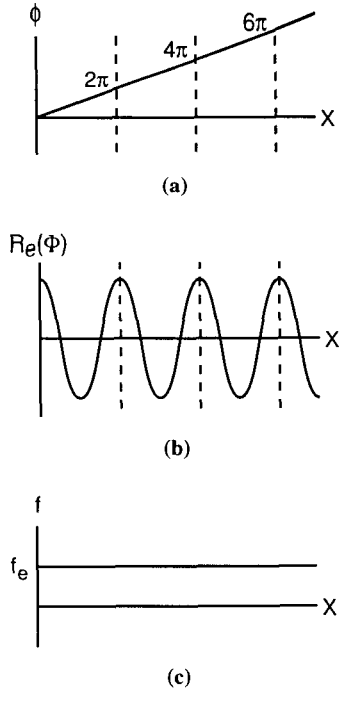


Figure 5.2 Characteristics of a linear phase error (showing variation over one side of aperture): **(a)** Phase function; **(b)** Real component of phase term; **(c)** Instantaneous frequency of phase term.

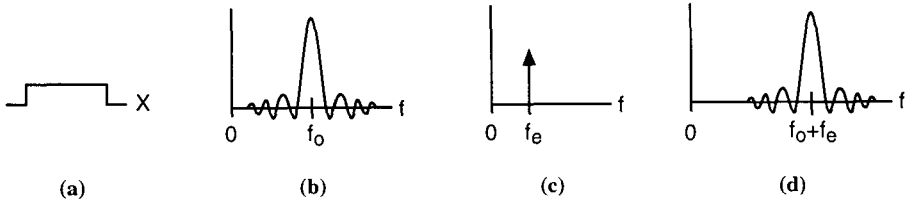


Figure 5.3 Basis for linear phase effect: **(a)** Signal aperture; **(b)** System impulse response without phase error; **(c)** Spectrum of phase term; **(d)** System impulse response with linear phase error.

Similarly, Figure 5.4 summarizes the nature of a low-frequency QPE. By definition, the QPE phase varies quadratically with position across the data space; Figure 5.4(a) indicates this quadratic phase, $\phi = 2\pi\gamma_e X^2$, where γ_e is the quadratic error coefficient. Figure 5.4(b) shows the real component of the associated phase term, $\exp(j2\pi\gamma_e X^2)$; the real component is a sinusoid with instantaneous frequency varying linearly with position

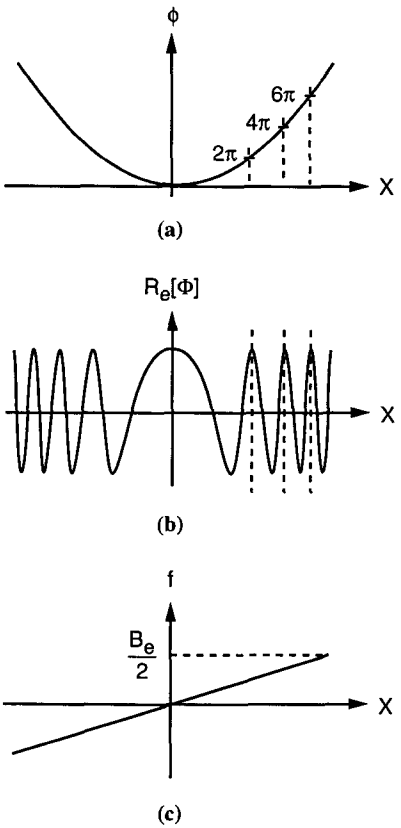


Figure 5.4 Characteristics of a QPE: **(a)** Phase function; **(b)** Real component of phase term; **(c)** Instantaneous frequency of phase term.

from aperture center. Each half of this signal resembles a linear frequency modulation (FM) or chirp signal. Figure 5.4(c) shows the linear frequency variation, $2\gamma_e X$, of the phase term associated with a low-frequency QPE. The maximum and minimum frequencies occur at the edges of the aperture. If the aperture width is L, the maximum frequency is $\gamma_e L$ and the minimum frequency is $-\gamma_e L$ for a bandwidth, $B_e = 2\gamma_e L$.

Figure 5.5 illustrates the basis for image smearing that results from a QPE. Without this phase error, a Fourier transform of the signal $\exp(j2\pi f_o X)$ in the rectangular aperture of Figure 5.5(a) yields the sinc function of Figure 5.5(b), centered at frequency bin f_o. Multiplication by $\exp(j2\pi\gamma_e X^2)$ before Fourier transform processing results in the convolution of the original sinc output with Figure 5.5(c), the Fourier transform of this phase term having bandwidth B_e. As Figure 5.5(d) suggests, multiplication by a phase term of finite bandwidth representing a QPE before Fourier transform processing introduces a

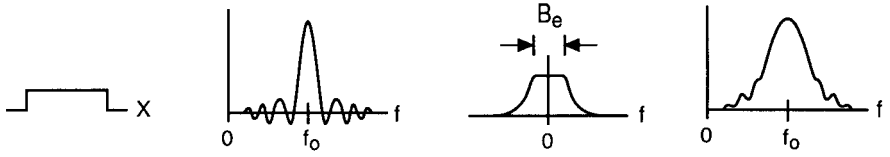


Figure 5.5 Basis for quadratic phase effect: (a) Signal aperture; (b) System impulse response without phase error; (c) Spectrum of phase term; (d) System impulse response with QPE.

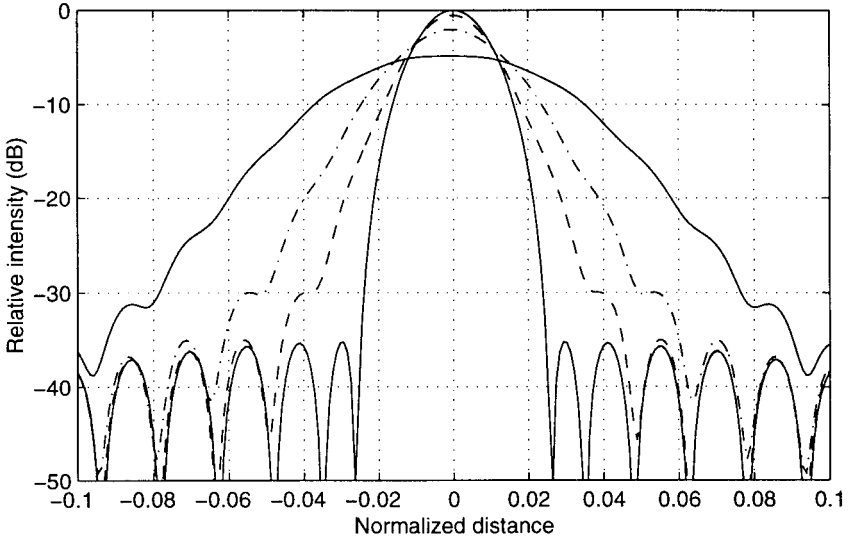


Figure 5.6 System impulse response using −35-dB Taylor weighting with $\bar{n} = 5$ (inside solid curve) and QPEs of $\pi/2$ rad (dashes), π rad (dash dots), and 2π rad (outside solid curve).

spreading out or defocusing in the Fourier transform domain. Thus, a QPE causes defocusing of the system impulse response. If the quadratic coefficient is space-invariant, the effect is uniform defocus over the scene. If the coefficient is space-variant, the effect is defocus that varies in severity over the scene.

Residual uncompensated QPE is a major concern in phase error budgets for a coherent imaging system. Figure 5.6 shows plots of the system impulse response without phase error as a reference and with QPEs of $\pi/2$, π, and 2π rad from center to edge of the aperture. The QPE degrades both the −3-dB width of the mainlobe (that is, the resolution) and the near sidelobe levels. The ordinate of each curve is dB relative to the peak intensity of the error-free impulse response. In this way, the curves show the reduction in intensity of the mainlobe peak as the phase error level increases. These examples use −35-dB

Taylor weighting with $\bar{n} = 5$, a common choice for sidelobe control in SAR imagery (Section D.2). The data aperture that yields the plots in Figure 5.6 consists of 64 signal samples zero-padded to 1024 samples. The FFT of this data results in 1024 frequency bins numbered from −512 to +511. The normalized distance along the abscissa of the impulse response plots is the bin number divided by 1024; it extends from −0.5 to +0.5. Figure 5.6 displays only the center region of this frequency extent in order to show the mainlobe more clearly. The length of the zero-pad affects the aesthetics of the plots but not the normalized scale or the dimensions of the impulse response plots relative to this scale.

Table 5.2 shows the effect of QPE as a function of its magnitude at aperture edge on the −3-dB and − 6-dB widths of the impulse response mainlobe using −35-dB Taylor weighting with $\bar{n} = 5$. We refer to the phase error magnitude at aperture edge as the peak-to-peak QPE level. All mainlobe widths in this table are relative to the −3-dB width without phase error. This table and the plots in Figure 5.6 represent effects with −35-dB Taylor weighting; similar weightings have similar effects while an unweighted (that is, uniform weighting) aperture yields more serious degradation. For reference, Figure 5.7 illustrates the effects of QPE with an unweighted aperture.

Table 5.2
QPE Effects on Mainlobe Width and Intensity using −35-dB Taylor Weighting with $\bar{n} = 5$

QPE Magnitude (rad)	*−3-dB Width of Mainlobe (Resolution)*	*− 6-dB Width of Mainlobe*	*Peak Intensity Loss (dB)*
0	1 (reference width)	1.4	0
$\pi/4$	1.0	1.4	0.1
$\pi/2$	1.1	1.5	0.5
π	1.5	2	2
2π	3.0	4	5
4π	5.5	8	8.5
6π	8.0	12	10
8π	12.0	16	11.5

It is common practice to use $\pi/4$ rad as an acceptable level of uncompensated low-frequency, nonlinear phase errors in order to avoid significant deterioration in image quality. Figure 5.6 and Table 5.2 show that the effect of a $\pi/2$ rad QPE is significant. It broadens the resolution by 10 percent and reduces peak intensity by 0.5 dB.

Cubic phase errors cause asymmetric sidelobes in the system impulse response. Figure 5.8 shows a plot of the system impulse response with a cubic phase error of π rad across the aperture. This phase error distorts the mainlobe and raises sidelobes on one side of the impulse response.

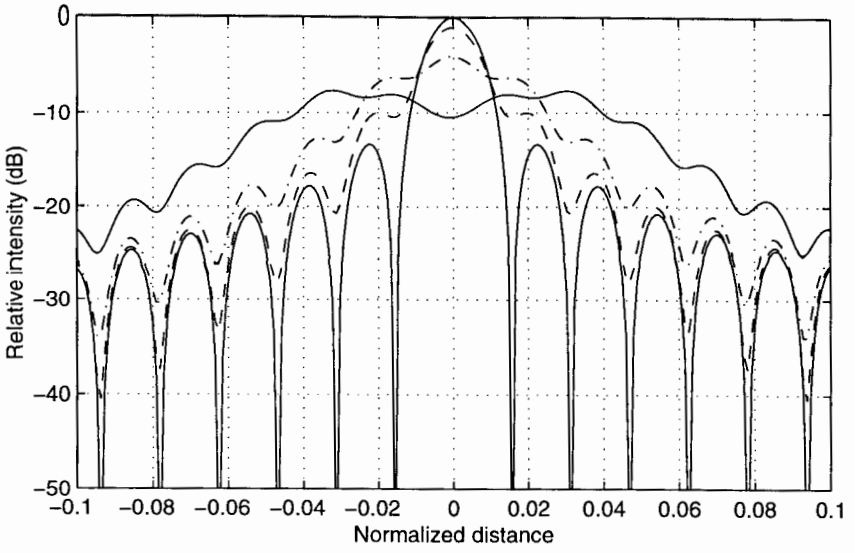


Figure 5.7 System impulse response using uniform weighting (inside solid curve) and QPEs of $\pi/2$ rad (dashes), π rad (dash dots), and 2π rad (outside solid curve).

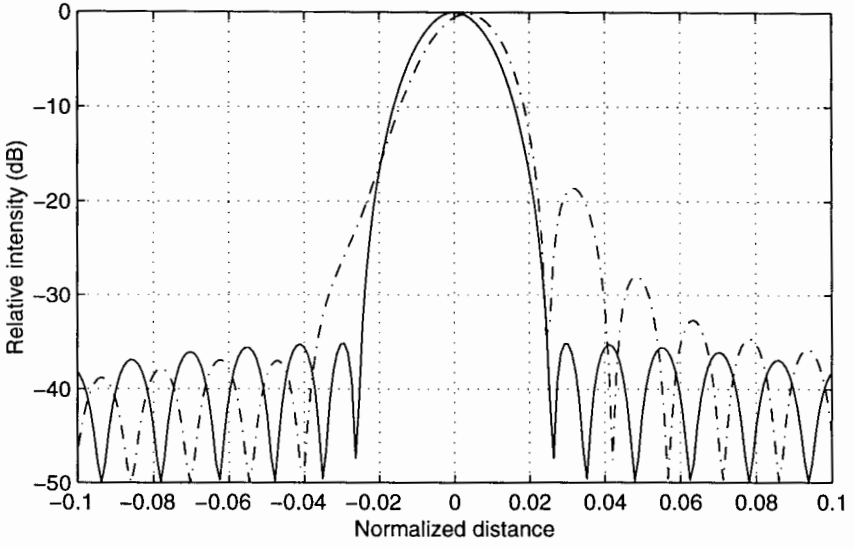


Figure 5.8 System impulse response using −35-dB Taylor weighting with $\bar{n} = 5$ without phase error (solid curve) and with π rad of cubic phase error (dash dots).

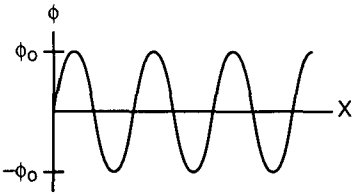


Figure 5.9 Phase function of a sinusoidal phase error (showing one side of aperture).

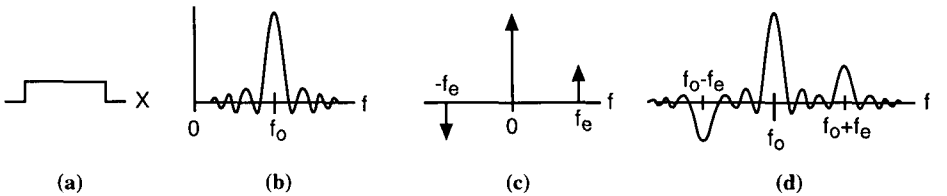


Figure 5.10 Basis for sinusoidal phase effect: **(a)** Signal aperture; **(b)** Impulse response without phase error; **(c)** Spectrum of sinusoidal phase term for $\phi_o << \pi$; **(d)** Impulse response with sinusoidal phase error.

5.1.2 High-Frequency Phase Errors

The classifications of high-frequency phase errors with more rapid variations over the coherent aperture are sinusoidal phase errors, as Figure 5.9 and Figure 5.10 illustrate, or wideband phase errors. The error classification of a specific phase function depends on the coherent aperture interval being examined. In Figure 5.11, the long-term sinusoidal phase variation is nominally a linear phase error over the short aperture interval L_1, a QPE over the interval L_2, and a multicycle sinusoidal phase error over the long interval L_3.

The phase term representing a sinusoidal phase error across the aperture has the form $\exp[j\phi_o \sin(2\pi f_e X)]$. Figure 5.9 illustrates its sinusoidal phase, $\phi_o \sin(2\pi f_e X)$ over one side of the data aperture. A sinusoidal phase error causes paired echoes to appear in the system impulse response [1]. This effect means high peak sidelobes are present, which may be interpreted erroneously as separate targets when, in fact, they are spurious targets. Figure 5.10 indicates the basis for high peak sidelobes from a sinusoidal phase error. Without this phase error, a Fourier transform of the signal $\exp(j2\pi f_o X)$ in the rectangular aperture of Figure 5.10(a) yields the sinc function of Figure 5.10(b), centered at frequency bin f_o. Multiplication by $\exp[j\phi_o \sin(2\pi f_e X)]$ before Fourier transform processing results in the convolution of the original sinc output with Figure 5.10(c), the Fourier transform of this phase term (valid for small ϕ_o). As Figure 5.10(d) suggests, multiplication by a sinusoidal phase term introduces paired echoes related to the two delta functions in the spectrum of the phase term.

In mathematical terms, the source of the error spectrum, and therefore the paired echoes, is evident in the Bessel function approximation to a sinusoidal phase variation [1].

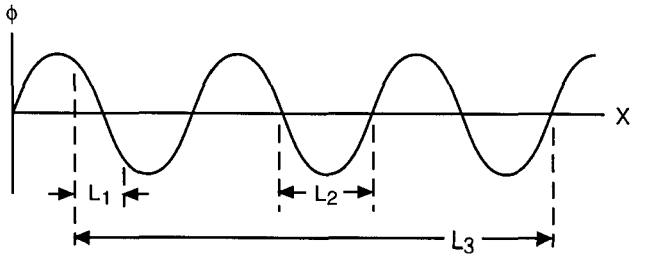


Figure 5.11 Dependence of phase error classification on coherent aperture interval.

This perspective begins by considering an uncompensated sinusoidal phase error Φ_e equal to

$$\Phi_e = \phi_o \sin(2\pi f_e X) \tag{5.1}$$

This phase error, expressed as an infinite summation of Bessel functions of the first kind, becomes

$$e^{j\phi_o \sin(2\pi f_e X)} = \sum_{n=-\infty}^{\infty} J_n(\phi_o)\, e^{j2\pi n f_e X} \tag{5.2}$$

For small ϕ_o, it is reasonable to use the approximation

$$e^{j\phi_o \sin(2\pi f_e X)} \approx J_o(\phi_o) + J_1(\phi_o)\, e^{j2\pi f_e X} + J_{-1}(\phi_o)\, e^{-j2\pi f_e X} \tag{5.3}$$

and to approximate the low-order Bessel functions as

$$J_o(\phi_o) \approx 1 \tag{5.4}$$

and

$$J_1(\phi_o) = -J_{-1}(\phi_o) \approx \frac{\phi_o}{2} \tag{5.5}$$

With these approximations, (5.2) becomes

$$e^{j\phi_o \sin(2\pi f_e X)} \approx 1 + \frac{\phi_o}{2}\left(e^{j2\pi f_e X} - e^{-j2\pi f_e X}\right) \tag{5.6}$$

The presence of a space-invariant sinusoidal phase error in the azimuth signal history coordinate, for example, multiplies the complex signal from each scatterer by (5.6). Multiplication of a signal by this phase term introduces, in addition to the original signal at some frequency f_o, two additional responses of amplitude $\phi_o/2$ relative to the original

signal at frequencies $f_o + f_e$ and $f_o - f_e$. These responses correspond to the two delta functions in the spectrum of the error term in Figure 5.10. These two additional responses, often referred to as *paired echoes*, are really high sidelobes of the impulse response function associated with the sinusoidal phase error. The peak sidelobe ratio (PSR) is the ratio of peak sidelobe intensity to peak mainlobe intensity. From (5.6), the relationship between PSR and a sinusoidal phase error is

$$\text{PSR} = \frac{\phi_o^2}{4} \tag{5.7}$$

Table 5.3 shows the allowable zero-to-peak amplitude ϕ_o of a sinusoidal phase error as a function of PSR requirement. A typical requirement is to stay within a –25-dB allowance for sidelobes near the mainlobe and a –35-dB allowance for other (far) sidelobes. For the values of ϕ_o in Table 5.3, the approximations in (5.4) and (5.5) are adequate and no noticeable decrease in mainlobe peak intensity level occurs.

Table 5.3
Allowable Zero-to-Peak Sinusoidal Phase Error

PSR Requirement (dB)	*Allowable Phase Error ϕ_o (rad)*
–15	0.35
–20	0.20
–25	0.11
–30	0.06
–35	0.04
–40	0.02

Figure 5.12 (solid curve) shows the effect of a 0.11-rad zero-to-peak sinusoidal phase error on system impulse response using –35-dB Taylor weighting. Here, f_e corresponds to 8 cycles of phase error over the processing aperture, causing an effect at 0.125 on the normalized abscissa scale. Similarly, Figure 5.12 (dashes) shows the effect of a 0.06-rad zero-to-peak sinusoidal phase error. It includes 30 cycles of phase error over the processing aperture, causing an effect at 0.469 on the normalized abscissa scale. For comparison, Figure 5.13 shows the Taylor-weighted impulse response without phase error.

Figure 5.14 shows a SAR image with and without the artificial addition of an azimuth sinusoidal phase error to the signal history. The imaged area includes the Iowa River on the north side of Iowa City, Iowa. The sensor and near range are on the left side of the image. In Figure 5.14(a) with the phase error present, f_e corresponds to 100 cycles over the coherent aperture and $\phi_o = 0.35$ rad. This situation corresponds to –15-dB peak sidelobes. These sidelobes are evident in the image, particularly in the duplication of the bridge in the lower part of the image and of the glints off the buildings in the right half of the image. Because this sinusoidal phase error is applied to the signal history after polar formatting the data, it represents a one-dimensional phase error in the azimuth coordinate.

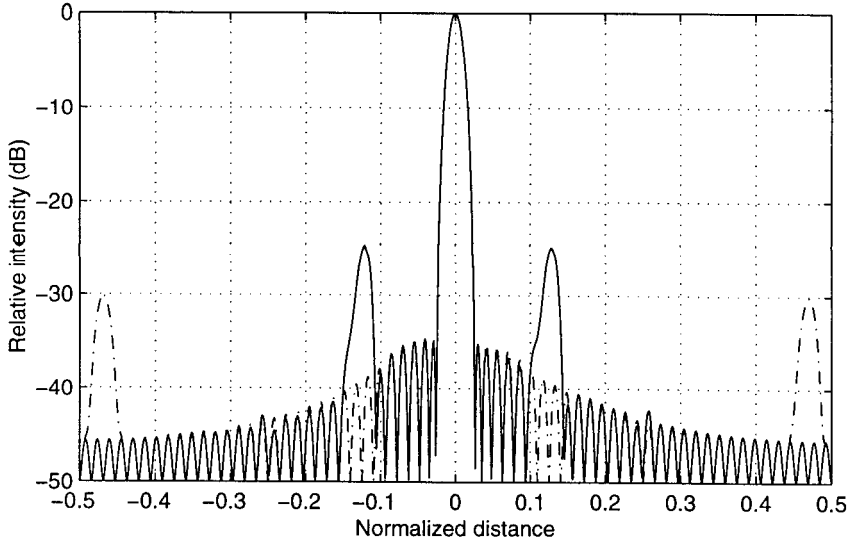


Figure 5.12 System impulse response with 0.11 rad zero-to-peak and 8 cycles of sinusoidal phase error (solid curve) and 0.06 rad zero-to-peak and 30 cycles of sinusoidal phase error (dash dots), both using −35-dB Taylor weighting with $\bar{n} = 5$.

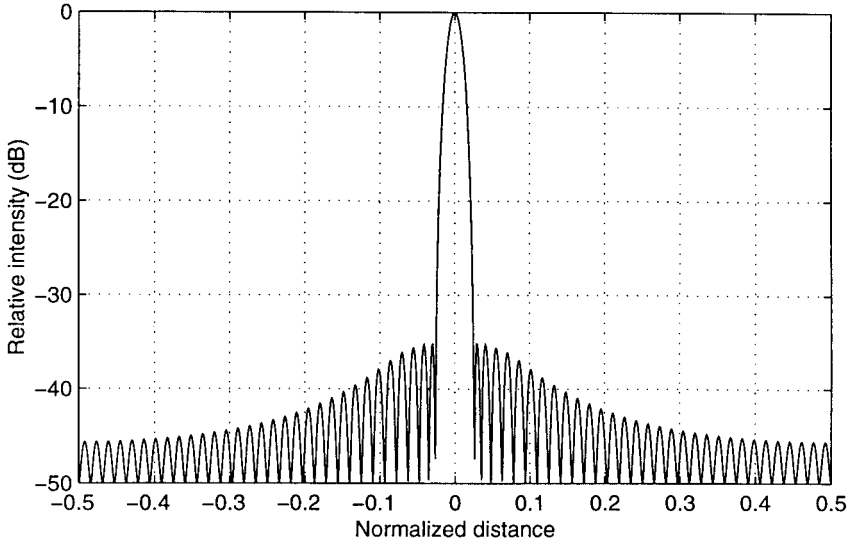


Figure 5.13 System impulse response with no phase error (−35-dB Taylor weighting with $\bar{n} = 5$).



(a)



(b)

Figure 5.14 Images: **(a)** With a sinusoidal phase error; **(b)** Without sinusoidal phase error.

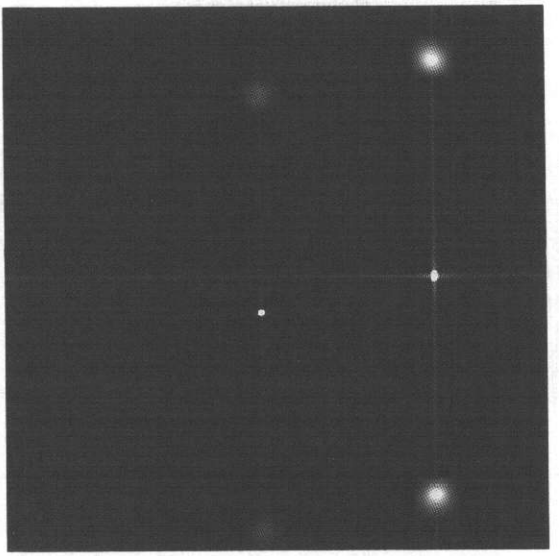


Figure 5.15 Effect of a sinusoidal phase error applied before polar format operation.

The impulse response of each scatterer, then, is similar to the impulse response functions in Figure 5.12 with focused paired echoes about each true scatterer.

In normal SAR operation, a phase effect such as this azimuth sinusoidal phase error is likely to vary with pulse number. Pulse number corresponds to the angle θ_s in the polar format rather than to the azimuth coordinate x_p. The paired echoes resulting from such a realistic error characteristic (for example, from an uncompensated antenna vibration) will not focus. Instead, they smear out in two dimensions over an area into a "fuzzball." The image in Figure 5.15, generated from a simulated signal history with a sinusoidal phase error in azimuth, illustrates these paired echoes. Near range is on the left side of the figure. The image includes a weak scatterer near scene center and a stronger scatterer at far range and mid-azimuth. Associated with each scatterer, two fuzzballs are visible and displaced in azimuth on either side of the main returns. Section 9.4 discusses this effect in detail.

Figure 5.16 displays the phase variation representative of a zero-mean, wideband random phase error with 0.32-rad root mean square (RMS) value across a signal aperture. The effect of wideband phase error is similar to that of sinusoidal phase error except that the wideband phase error spreads out energy widely across the impulse response, governed by the spectral bandwidth of the phase term associated with the phase error. The bandwidth of this phase term corresponds to the bandwidth of the phase function itself. Rather than causing a peak sidelobe, the wideband phase error contributes to a high integrated sidelobe level which results in contrast degradation and noise in the image.

It is essential to keep the RMS value σ_ϕ of wideband phase error significantly less than $\pi/2$ rad (on the order of 0.1 rad). A higher level of phase error causes intolerably

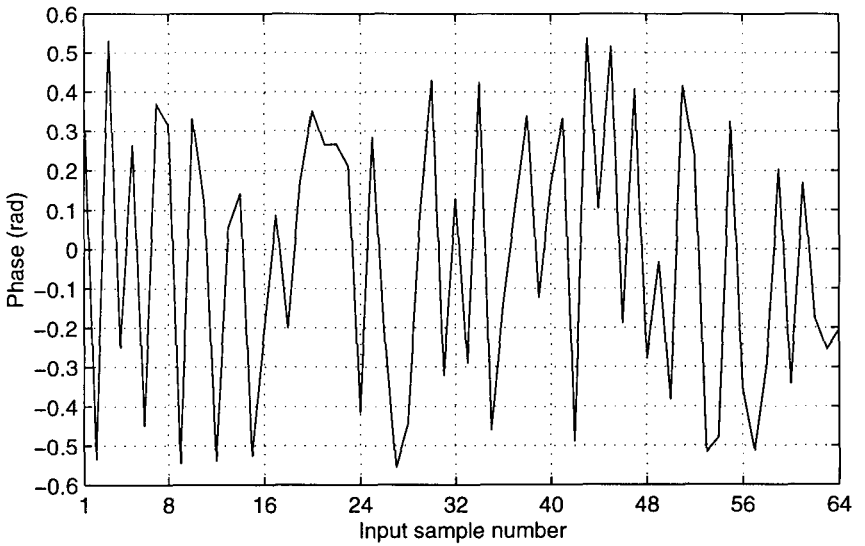


Figure 5.16 Plot of 0.32-rad RMS wideband random phase function over a 64-sample data aperture.

severe image degradation. The principal effect of high-frequency wideband phase error is to increase the integrated sidelobe ratio (ISLR) according to the approximation

$$\frac{\text{increase in sidelobe energy}}{\text{mainlobe energy}} \approx e^{\sigma_\phi^2} - 1 \approx \sigma_\phi^2 \tag{5.8}$$

ISLR is a measure of the ratio of energy in the impulse response sidelobes to the energy in the mainlobe (Section 8.3.3). Here, σ_ϕ^2 is the variance of the zero-mean wideband phase error. It also corresponds to the integrated value of the power spectral density (PSD) of the phase error. In general, the PSD of a quantity is equal to the square of the magnitude of its frequency spectrum. For a specific RMS level of wideband phase error, the height of the associated sidelobes varies inversely with the bandwidth of the phase error; the integrated sidelobe energy remains constant.

An easy way to reach the estimate of ISLR increase in (5.8) is to view the wideband phase error as a combination of (independent) sinusoidal phase errors with varying frequency and amplitude within and nominally filling the bandwidth of the wideband phase error. A sinusoidal phase error of zero-to-peak amplitude ϕ_o contributes two sidelobes to the integrated sidelobe energy. From (5.7), each sidelobe adds $\phi_o^2/4$ to the increase in ISLR. By causing two sidelobes, each sinusoidal phase error contributes twice this amount or $\phi_o^2/2$ to the ISLR increase. The RMS phase ϕ_{rms} of the sinusoidal phase error is equal to $\phi_o/\sqrt{2}$ yielding ϕ_{rms}^2 as the ISLR increase. A set of N sinusoidal phase errors combining to form a wideband phase error of RMS phase $\sigma_\phi \approx \phi_{rms}\sqrt{N}$ results in an ISLR increase of approximately $N\phi_{rms}^2$ which equals σ_ϕ^2.

Table 5.4
Allowable High-Frequency Wideband Phase Error

ISLR Allowance (dB)	*Constraint on RMS Phase Error* σ_ϕ *(rad)*
−5	0.56
−10	0.32
−15	0.18
−20	0.10

Table 5.4 quantifies this relationship between phase error and increase in sidelobe energy. An ISLR allowance of about −20 dB from high-frequency phase error is a typical requirement.

As an example, Figure 5.17 shows the effect of a 0.32-rad RMS wideband random phase error on the one-dimensional impulse response for −35-dB Taylor weighting, which may be compared with the error-free impulse response in Figure 5.13. This phase error (Figure 5.16) results in a one-dimensional ISLR degradation to about −10 dB from −27.5 dB in the error-free case.

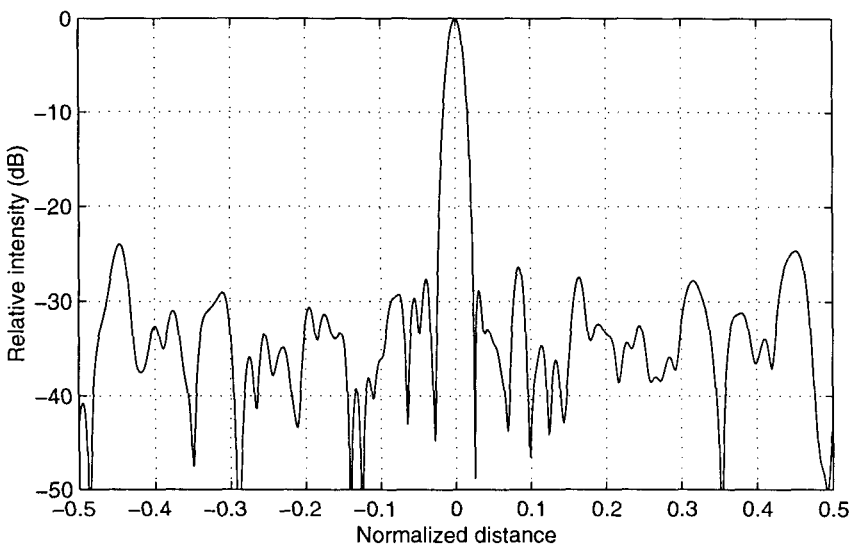


Figure 5.17 System impulse response with 0.32-rad RMS wideband random phase error (−35-dB Taylor weighting with $\bar{n} = 5$).

5.2 MANAGEMENT OF PHASE ERRORS

The actual level of undesirable phase effects in the SAR signal varies dramatically as the signals progress through the radar system and the image formation processor (IFP). Initially, the transmitted signal (from the waveform generator through frequency conversions, amplification, and transmission by the transmit antenna) is relatively free of unwanted phase characteristics. Sources of unwanted phase include nonlinearity in the FM characteristic of the generated waveform, frequency-dependent phase effects in filters, and waveguide dispersion. However, these effects are generally small given today's hardware technology and, although they require attention to achieve fine image quality, they do not threaten the data collection or imaging functions of the system.

While the transmitted signal is benign relative to catastrophic phase effects, the signal returned to the receive antenna may be riddled with undesirable phase effects in azimuth (pulse-to-pulse). The size of these effects may correspond to thousands of radians of phase error. Eventually, motion measurement and motion compensation procedures will eliminate or greatly reduce these undesirable phase effects. Following reception, additional smaller phase effects occur in the receiver hardware, in the A/D conversion process, and in the IFP. If untreated, these effects may seriously compromise image quality, but they generally are not catastrophic to the imaging process.

It is instructive to consider the factors that limit the allowable magnitude of undesirable phase errors at various stages in the SAR system. These factors are particularly relevant in radar systems that include various autofocus or interactive compensation techniques in the IFP to deal with large error effects. They impact the need for and accuracy of motion compensation in the receiver versus compensation in the IFP.

Two different criteria represent absolute limits on these errors. Error magnitudes are unacceptable if:

1. Data from the desired scene is lost;
2. An image is irretrievable from the data.

Scene data may be lost if a large position or velocity measurement error in estimating antenna motions causes the radar to image the wrong area. Scene data may also be lost if a large relative timing error between the transmitter and receiver introduces a range frequency offset that moves the desired scene out of the receiver range window. With current advances in motion sensor technology and clock accuracy and stability, neither of these situations is likely today in a well-designed SAR system during normal operation.

Possibilities which either make an image irretrievable or degrade it unacceptably are more numerous and less remote. These situations include:

- Too much space-invariant quadratic phase error to find the proper focus in a reasonable fashion;
- Too much phase error, which spreads the energy from a scatterer over various processor boundaries or disperses the energy too widely to recover it because of SNR considerations;

- Excessive cubic or higher order phase effects in an image chain that cannot compensate for such effects;
- Space-variant phase effects in an image chain that are too large and cannot be compensated.

In the first case, it is difficult to quantify the magnitude of this limit on space-invariant QPE or to identify the actual cause or source of the limit. However, a limit on the order of 100 rad is a plausible criterion for space-invariant QPE. This limit is different from the autofocus pull-in range, defined as the largest magnitude phase error that an algorithm is able to estimate. Autofocus may fail initially because the pull-in range is exceeded. It may still be possible to find proper focus by adding or subtracting a large space-invariant QPE by trial and error, followed by an attempt to reapply autofocus. However, a large space-invariant QPE usually means that significant space-variant QPE or higher order space-invariant phase error is also present from the same source.

The second case is a qualitative concern and sensitive to processor and algorithm implementation. The final two cases obviously involve design limitations or IFP consequences including implementation cost and processor throughput requirements. With a number of sources of phase errors, cubic and higher order effects increase in proportion to the size of the QPE while space-variant phase effects increase in proportion to the size of the space-invariant phase error. Therefore, a source of large QPE or large space-invariant phase error can be a warning sign of subsequent difficulty even if the image processor can remove these two classes of phase errors.

By application of a one-dimensional or two-dimensional reference function, the processor can compensate for any known or measurable space-invariant effects. Compensation may involve deterministic measurements on point-like targets, use of various other quadratic or higher order focus measurement techniques, or trial-and-error compensations looking for an improvement in the iterated image.

The easiest phase errors in imagery to estimate and compensate are space-invariant QPEs. The mapdrift algorithm (Section 6.1) is one of many autofocus algorithms that is useful in the image formation processor to reduce QPE. It is critical to make allowance for the amount of correction achievable via autofocus (that is, the autofocus pull-in range) when developing system error allocations for a SAR system that incorporates an autofocus capability. The pull-in range for the mapdrift algorithm is typically about 60 rad of QPE.

Space-variant effects are more difficult to manage because they require a different compensation in different parts of the image. One possibility to handle space-variant effects is to divide the scene into subscenes via bandpass filtering of the signal history and to apply the image formation algorithm separately to each subscene. This procedure allows a different, space-invariant compensation for each subscene. Section 4.8 discusses this subpatch processing technique. Another possibility is to divide the full scene into subscenes after forming a large image of the entire scene. The steps in this procedure are to inverse transform each subscene in either or both dimensions, apply the desired subscene-specific compensation, and regenerate the image; it is not necessary to reapply motion compensation and reformat the data for each subscene as is done in the subpatch

processing procedure. Another possibility, which may be applicable for a certain class of error sources, is space-variant compensation of the entire scene by reformatting the signal history. Section 6.6 includes a discussion of space-variant refocus considerations.

System specifications on image quality provide the constraint on allowable phase effects in each phase error category after all compensation procedures are complete. A system performance budget provides an additional link between image quality requirements and allowable phase effects. This budget is a procedure to allocate allowable phase effects among the subsystems. Section 8.2 describes image quality parameters and performance budgeting. Since a major source of phase errors is motion measurement inaccuracy in SAR systems, Section 5.3.1 addresses the image quality requirements that drive motion measurement accuracy.

To avoid a significant deterioration in image quality, a reasonable rule of thumb is to limit uncompensated phase errors to the general guidelines indicated in Table 5.5. It is reasonable to use π rad as a limit on space-variant linear phase errors, thereby allowing geometric distortion on the scale of one-half of the image resolution. Similarly, $\pi/4$ rad is a generally accepted level of low-frequency, nonlinear phase errors to limit mainlobe broadening and peak intensity loss to acceptable levels. Likewise, it is reasonable to use 0.025-rad zero-to-peak sinusoidal phase error as a guideline to limit the peak intensity of spurious sidelobes to –32 dB relative to the mainlobe peak. A guideline on high-frequency wideband phase errors of 0.07 rad RMS is useful to limit added integrated-sidelobe energy in the system impulse response to –23.1 dB relative to the mainlobe energy.

Table 5.5
General Guidelines on Allowable Uncompensated Phase Error Levels

Category of Phase Error	*Acceptable Level*
Space-variant linear	π rad over aperture
Quadratic	$\pi/4$ rad center-to-edge
Cubic (higher order)	$\pi/4$ edge-to-edge
High-frequency sinusoidal	0.025 rad zero-to-peak
High-frequency wideband	0.07 rad RMS

In fact, significant flexibility exists in these acceptable levels as a function of overall system design, trade-offs among parameters, and specific needs of the user of the imagery. A system performance budgeting procedure (Section 8.2) is a necessity to address these system-wide interactions which determine the acceptable levels of residual phase errors.

5.3 MAGNITUDE OF PHASE ERRORS

Phase errors present in a SAR signal history at the time of the final Fourier transform operation lead to defects in the SAR imagery. Following the completion of motion compensation procedures, the major sources of phase errors are:

- Position and motion measurement errors;
- Range curvature;
- Residual video phase;
- Uncompensatable effects of measured nonplanar motion.

While range curvature is a specific limitation of the polar format algorithm, the other error sources are more general in that they are present with each of the available spotlight image formation algorithms. Section 5.3.5 considers additional sources of phase errors.

Table 5.6 and Table 5.7 provide quantitative estimates of the distortion and quadratic phase effect associated with each of the major sources of phase errors as a function of radar system and collection geometry parameters. Chapter 3 provides the basis for the equations in these tables. Section 3.7 through Section 3.10 provide analysis of the individual error sources. Table 3.6 summarizes the assumptions included in the analysis. The following subsections discuss specific items in this table; additionally, Section 5.4 quantifies the effects of motion measurement errors. In these tables, λ_c is the center wavelength, γ is the FM chirp rate, ρ_a and ρ_r are azimuth and range resolutions, V_{xa} is the antenna velocity, R_{ac} is the slant range at aperture center, r_o is the scene radius, K_a and K_r are the azimuth and range mainlobe-broadening factors, $S_{\theta c}$ is the sine of the aperture center squint angle θ_{ac}, and $S_{\phi c}$ is the sine of the aperture center incidence angle ϕ_{ac}.

Table 5.6
Size of Distortion from Major Sources

Source of Distortion	*Expression for Magnitude of Distortion*	*Reference Equation for Derivation*	*Reference for Numerical Example*
Along-track velocity measurement error, V_{xe}	$\frac{X_t V_{xe}}{V_{xa}}$	(3.165)	No table
Range curvature	$\frac{r_o^2}{2R_{ac}S_{\phi c}}$	(3.128)	Table 3.8
Residual video phase	$\frac{2\gamma\lambda_c r_o^2 S_{\phi c}}{c^2}$	(3.175)	Table 3.11

Table 5.7
Size of QPE from Major Sources

Source of QPE	*Expression for Magnitude of Phase Error (rad)*	*Reference Equation for Derivation*	*Reference for Numerical Example*
Along-track velocity measurement error, V_{xe}	$\dfrac{\pi\lambda_c K_a^2 R_{ac} V_{xe}}{4\rho_a^2 V_{xa} S_{\theta c}^2}$	(3.168) and (5.13)	Table 5.8
Line-of-sight acceleration measurement error, A_{elos}	$\dfrac{\pi\lambda_c K_a^2 R_{ac}^2 A_{elos}}{8\rho_a^2 V_{xa}^2 S_{\theta c}^2}$	(3.168) and (5.17)	Table 5.9
Range curvature	$\dfrac{\pi\lambda_c K_a^2 r_o^2}{8\rho_a^2 R_{ac} S_{\theta c}^2}$	(3.129)	Table 3.9
Residual video phase	$\dfrac{\pi\gamma\lambda_c^2 K_a K_r r_o^2}{2c^2 \rho_a \rho_r}$	(3.180)	Table 3.12
Nonplanar motion from acceleration a_{zo} normal to the nominal slant plane	$\dfrac{\pi\lambda_c K_a^2 R_{ac} a_{zo} Z_t}{8\rho_a^2 V_{xa}^2 S_{\theta c}^3 S_{\phi c}}$	(3.144)	Table 3.10

Table 5.7 references other tables which provide numerical examples to size the quadratic phase effects. To keep these quantitative examples simple, the referenced tables address the case of broadside spotlight imaging for which the mid-aperture squint angle θ_{ac} is 90 deg and $S_{\theta c}$ (the sine of this angle) is unity. To size the phase errors, these tables use the relationships

$$\left.\frac{x_p}{K_c}\right|_{\max} = \frac{\lambda_c K_a}{4\rho_a S_{\phi c}} \tag{5.9}$$

from (3.74) with $\sin(\phi_{ao}) = S_{\phi c}$ and

$$\left.\frac{y_p}{K_c}\right|_{\max} = \frac{\lambda_c K_r}{4\rho_r} \tag{5.10}$$

from (3.75). Here K_c is the processing aperture center in $K_x K_y$ space in Figure 3.17(c), which shows the data storage format resulting from the polar format transformation. The quantities x_p and y_p represent the signal history coordinates, centered at aperture center and associated with azimuth and range, respectively. The origin of the (x_p, y_p) coordinate system at $(K_p, \theta_p) = (K_c, \theta_c)$ is the center of the data window being processed.

5.3.1 Errors in Position and Motion Measurement

Inaccuracy in measurements of APC position, velocity, and acceleration is a primary source of undesirable phase effects in SAR imagery. Uncompensated APC motions along the radar line-of-sight (LOS) during a SAR coherent integration time introduce phase effects in the collected signal history, primarily in the azimuth direction. Unless removed, these phase effects will cause various problems in the processed imagery depending on the magnitude and spectral characteristics of the phase effects. The phase effects in the collected data become phase errors in the SAR imagery when the IFP uses motion measurements containing measurement errors to prepare, format, and process the SAR signals into imagery.

The need for accurate motion measurement and proper motion compensation in fine-resolution SAR imaging places severe requirements on radar sensor antenna and pedestal design, measurement accuracy and pulse synchronization of the motion sensor, and algorithms to properly compensate for measured motions. A motion effect of size r_e causes a phase error Φ_e equal to

$$\Phi_e = \frac{4\pi r_e}{\lambda_c} \tag{5.11}$$

This is the usual equation relating phase effect, in radians, to the two-way motion effect. It is the size of r_e relative to radar wavelength that determines the magnitude of the phase effect. It comes from the first terms in (2.67) setting $\hat{t} = 2R_a/c$; the distance r_e represents the change in $R_t - R_a$ attributable to the uncompensated motion. Sources of line-of-sight APC motion include antenna vibrations and deformations as well as rigid-body platform translations and rotations. Causes of these motions include wind gust effects, turbulence, and aircraft maneuvers. Any restrictions imposed on phase errors, in fact, limit uncompensated APC motion only along the radar LOS to the target (except for the effects of nonplanar motion discussed in Section 5.3.4). In reality, comparable motion variations may be present in all directions.

To avoid a significant deterioration in image quality, uncertainty in low-frequency variations in the relative range between scene center and the APC must be limited to the following general guideline. Uncertainty in slowly varying, nonlinear motions along the LOS should be less than $\lambda_c/16$ (where λ_c is the center wavelength of the processed pulse) over the processing aperture. This constraint limits phase errors to $\pi/4$ rad since, using (5.11), it indicates

$$\Phi_e = \left(\frac{4\pi}{\lambda_c}\right)\frac{\lambda_c}{16} = \frac{\pi}{4} \tag{5.12}$$

This requirement refers to quadratic and single-cycle sinusoidal motion primarily.

Incorrect information regarding sensor position leads to an obvious displacement in scene center; the radar sensor images the area it is near, not the area the motion sensor thinks it is near. Position error does not affect image focus in this case. Figure 5.18 illustrates the displacement effect of along-track and cross-track sensor position errors.

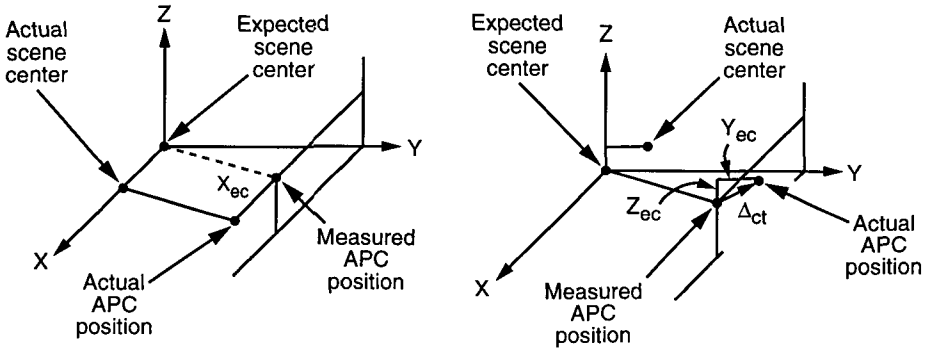


Figure 5.18 Basis for scene center shifts: **(a)** Shift from along-track position error X_{ec}; **(b)** Shift from cross-track position error Δ_{ct} which represents Y_{ec} and Z_{ec} components of position error.

An along-track position error X_{ec} simply displaces the scene center in the along-track direction by a distance equal to X_{ec}. A cross-track position error Δ_{ct} may move the scene center out of the XY plane, in which case the effective ground plane scene center is the projection of this scene center along an iso-range-Doppler circle onto the plane containing the scene.

Incorrect information regarding LOS sensor velocity causes a space-invariant displacement in azimuth of scene center; such an error causes the motion compensation operation not to remove the proper amount of Doppler frequency from scene center, leaving a linear phase error in azimuth. It is important to note that the cross-track component of velocity error is not responsible for this displacement; the LOS component is responsible, as the last term in (3.162) indicates. Figure 5.19 illustrates the displacement effect of a LOS velocity measurement error.

An error in velocity measurement causes a small amount of geometric distortion. For example, when operating in a broadside spotlight mode, an along-track velocity error causes geometric distortion in azimuth because along-track velocity determines the azimuth scale of the image. Thus, a fractional error in along-track velocity corresponds directly to that same fractional error in image azimuth scale.

Along-track velocity error also causes scene defocus in azimuth, while cross-track velocity error does not cause defocus. Along-track velocity error causes a space-invariant defocus in the form of QPE of size

$$Q_{Vxe}\big|_{\text{size}} = \frac{\pi\lambda_c K_a^2}{4\rho_a^2}\left[\frac{V_{xe}}{V_{xa}S_{\theta c}^2}\right]R_{ac} \tag{5.13}$$

from (3.168). To limit this source of QPE to $\pi/4$ rad during a spotlight data collection

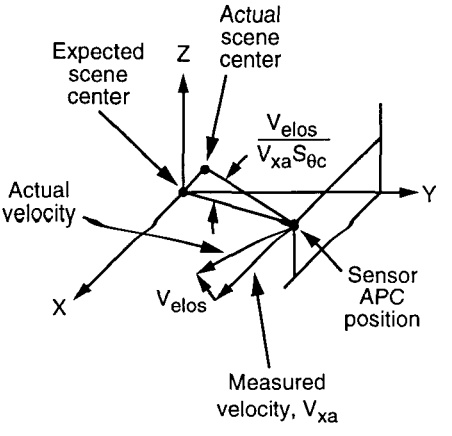


Figure 5.19 Scene center shift from LOS sensor velocity measurement error V_{elos}.

over a stationary target field, the requirement on along-track velocity measurement error V_{xe} is

$$\frac{V_{xe}}{V_{xa}} < \frac{\rho_a^2 S_{\theta c}^2}{\lambda_c K_a^2 R_{ac}} \tag{5.14}$$

This limit results from equating (5.13) to $\pi/4$ rad. Table 5.8 quantifies this limit for typical radar wavelengths and resolutions; it uses R_{ac} = 10,000 m, K_a = 1.3, and θ_{ac} = 90 deg. For instance, an X-band data collection at 1-m resolution must measure along-track velocity to within 0.2 percent (less than 0.2 m/s measurement error at 100 m/s velocity) to limit QPE to $\pi/4$ rad from this source. The use of quadratic autofocus in the image formation processor relaxes this requirement tremendously.

Table 5.8
QPE Limit on Allowable Percent Along-Track Velocity Error (θ_{ac} = 90 deg)

	Wavelength (Frequency)			
Resolution	*0.01 m (30 GHz)*	*0.03 m (10 GHz)*	*0.2 m (1.5 GHz)*	*0.6 m (500 MHz)*
10 m	59.2	19.7	3.0	1.0
3 m	5.3	1.8	0.3	0.09
1 m	0.6	0.2	0.03	0.01
0.3 m	0.05	0.02	0.003	0.001

A heuristic basis for (5.13) is available by calculating the error in R_{ac} associated with V_{xe} and using this quantity in (5.11) for the zero grazing angle and broadside imaging case with $\phi_{ac} = 90$ deg, $\alpha_{dc} = 90$ deg, and $\theta_{ac} = 90$ deg. During the interval from aperture center time to aperture end time, an along-track velocity measurement error V_{xe} causes an along-track distance error of

$$L_e \approx V_{xe}\frac{T_a}{2} \approx \frac{R_a V_{xe}\Delta\theta}{2V_{xa}} \tag{5.15}$$

having used (2.22) for T_a to arrive at the final expression. Thus, L_e is the accumulated position error from the aperture center time to the end of the coherent aperture time. This along-track distance error results in a LOS distance error of

$$r_{elos} \approx L_e\frac{\Delta\theta}{2} \tag{5.16}$$

Figure 5.20 illustrates the geometry associated with this analysis. Use of this quantity in (5.11) with the help of (2.20) yields (5.13) for the case of broadside imaging.

An error in measurement of LOS acceleration also causes scene defocus in azimuth. The QPE from a LOS acceleration measurement error A_{elos} is

$$Q_{Aelos}\Big|_{\text{size}} = \frac{\pi\lambda_c K_a^2}{8\rho_a^2}\left[\frac{A_{elos}}{V_{xa}^2 S_{\theta c}^2}\right]R_{ac}^2 \tag{5.17}$$

from (3.168). Limiting this source of QPE to $\pi/4$ establishes the requirement on acceleration measurement error as

$$\frac{A_{elos}}{V_{xa}^2} < \frac{2\rho_a^2 S_{\theta c}^2}{\lambda_c K_a^2 R_a^2} \tag{5.18}$$

Table 5.9 quantifies this limit for typical radar wavelengths and resolutions; this table uses R_a = 10,000 m, V_{xa} = 100 m/s, K_a = 1.3, and θ_{ac} = 90 deg. For instance, an X-band data collection at 1-m resolution must measure LOS acceleration to within 0.39 cm/s^2 to limit QPE to $\pi/4$ rad from this source. Again, the use of quadratic autofocus in the image formation processor greatly relaxes this requirement.

The basis for (5.17) is illustrated by calculating the error in R_a associated with A_{elos} and using this quantity in (5.11), again for the zero grazing angle, broadside case. The LOS error corresponding to A_{elos} for $T_a/2$ time duration is

$$r_{elos} \approx \frac{1}{2}A_{elos}\left(\frac{T_a}{2}\right)^2 \tag{5.19}$$

Use of this quantity in (5.11) yields (5.17) with the help of (2.20) and (2.22).

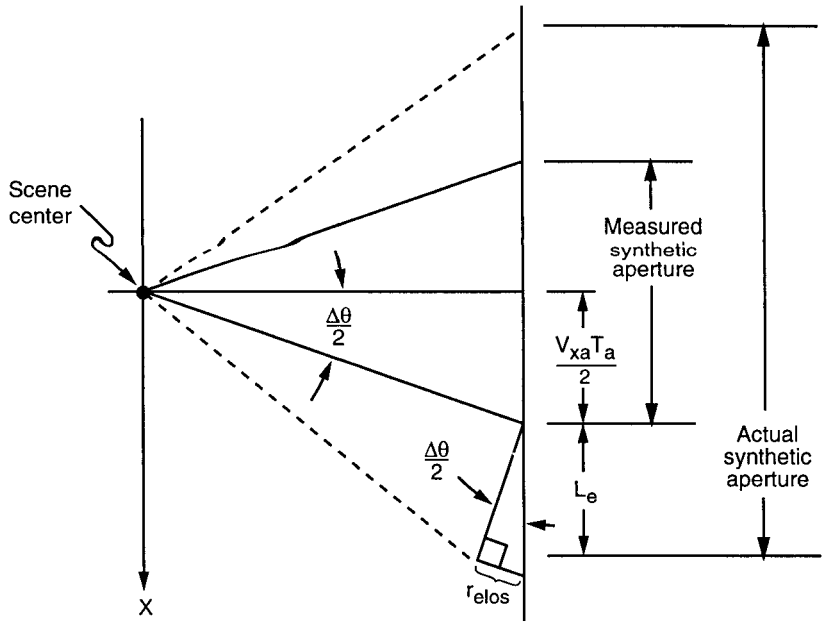


Figure 5.20 Geometry to show effect of error in along-track velocity measurement.

Velocity and acceleration measurement errors also introduce higher order phase effects and space-variant phase effects. These effects are generally small enough to disregard completely, although it is possible to analyze these effects using the Taylor series expansion procedures of Section 3.5.

Table 5.9
QPE Limit on Allowable LOS Acceleration Error (cm/s^2)

	Wavelength (Frequency)			
Resolution	*0.01 m (30 GHz)*	*0.03 m (10 GHz)*	*0.2 m (1.5 GHz)*	*0.6 m (500 MHz)*
10 m	118.34	39.45	5.92	1.97
3 m	10.65	3.55	0.53	0.18
1 m	1.18	0.39	0.06	0.02
0.3 m	0.11	0.04	0.005	0.002

Cross-track velocity measurement error V_{ect} and acceleration measurement error A_{eplos} perpendicular to the LOS do not degrade the image significantly. The first error has little effect on image distortion or image focus because it is perpendicular to the measured velocity vector; its presence does not indicate a significant error in the measured magnitude of the sensor velocity, only an error in direction of the velocity vector. The second error has little effect because, being perpendicular to the LOS, it does not indicate an error in the measurement of the range between the sensor and the scene center; this range is the important quantity with respect to motion compensation and image focus.

Section 3.9 develops the equations which quantify the effects of motion measurement errors. These equations indicate the velocity and acceleration accuracy necessary for the LOS range estimate to be within $\lambda_c/16$. This constraint equates to a two-way path accuracy of $\lambda_c/8$ and yields only $\pi/4$ rad of QPE to avoid significant image quality degradation. To avoid noticeable degradation from phase errors, a conventional SAR motion compensation system measures the variations in relative range to within a small fraction of a radar wavelength over a synthetic aperture interval. The motion sensor achieves this accuracy by a combination of onboard motion-sensing equipment and residual phase error estimation and compensation techniques during data processing stages (autofocus).

These QPEs are correctable via azimuth autofocus; this procedure is routine in many SAR systems via the mapdrift or phase difference algorithms. Chapter 6 describes these two autofocus algorithms and related algorithms applicable to higher order phase errors.

Now we consider the peak sidelobes introduced by sinusoidal APC motions along the radar LOS. An uncompensated, LOS sinusoidal motion error r_e of frequency f_1 and amplitude a_s of the form

$$r_e = a_s \sin(2\pi f_1 t) \tag{5.20}$$

causes a phase error Φ_e equal to

$$\Phi_e = \phi_o \sin(2\pi f_1 t) \tag{5.21}$$

with

$$\phi_o = \left(\frac{4\pi}{\lambda_c}\right) a_s \tag{5.22}$$

If f_1 exceeds the reciprocal of the aperture time T_a, this phase error introduces two peak sidelobes (paired echoes) in the azimuth direction. Otherwise, it broadens the mainlobe similar to other low-frequency phase errors.

Using (5.7), the relationship between the PSR and sinusoidal motion is

$$\text{PSR} = \frac{\phi_o^2}{4} = 4\pi^2 \left(\frac{a_s}{\lambda_c}\right)^2 \tag{5.23}$$

In this form, it is clear that the maximum allowable amplitude a_s of uncompensated

sinusoidal motion error varies linearly with wavelength λ_c for a given PSR requirement. Table 5.10 shows the allowable zero-to-peak amplitude a_s of uncompensated sinusoidal LOS motion as a function of the PSR requirement for $\lambda_c = 0.03$ m (X-band).

Table 5.10
Allowable Sinusoidal Motion for $\lambda_c = 0.03$ m

PSR Requirement (dB)	*Allowable Phase Error ϕ_e (rad)*	*Allowable Amplitude a_s of Sinusoidal Motion (mm)*
−15	0.35	0.84 (0.028 λ_c)
−20	0.20	0.45 (0.015 λ_c)
−25	0.11	0.26 (0.009 λ_c)
−30	0.06	0.14 (0.005 λ_c)
−35	0.04	0.09 (0.003 λ_c)
−40	0.02	0.05 (0.002 λ_c)

Section 5.1.2 indicates that an acceptable requirement is to stay within a −25-dB allowance for sidelobes near the mainlobe and a −35-dB allowance for other (far) sidelobes. In this case, the uncompensated sinusoidal APC motions must be limited to roughly 0.3-mm amplitude at frequencies just above the reciprocal of the coherent integration time and to 0.1 mm at higher frequencies for an imaging system with $\lambda_c = 0.03$ m. Furthermore, the allowable number of such discrete frequency sinusoids must be limited because they contribute to integrated sidelobes.

Motion measurement errors of higher order, that is, those varying or changing direction many times over the azimuth aperture, introduce high-frequency, wideband random phase errors into the signal history. This form of phase error moves additional energy into the sidelobes of the system impulse response, causing a high ISLR and contrast degradation over a densely populated or a distributed-target field.

As before, (5.11) relates phase errors to an uncompensated line-of-sight APC motion. In this way, the measure of high-frequency wideband phase errors σ_ϕ is related to the RMS line-of-sight phase center motion σ_r and via (5.8) to the increase in ISLR by

$$\sigma_\phi = \frac{4\pi\sigma_r}{\lambda_c} = \sqrt{\text{ISLR increase}} \tag{5.24}$$

where σ_r is the standard deviation of the uncompensated APC motion.

Table 5.11 quantifies these relationships as a function of the ISLR allowance for $\lambda_c = 0.03$ m. As (5.24) indicates, the allowable RMS line-of-sight phase center motion σ_r varies linearly with center wavelength λ_c for a given σ_ϕ allowance and corresponding ISLR allowance.

Table 5.11
Allowable Wideband Random Motion for $\lambda_c = 0.03$ m

ISLR Allowance (dB)	*Constraint on Phase Error σ_ϕ (rad)*	*Allowable RMS Motion σ_r (mm)*
−5	0.56	1.34 (0.045 λ_c)
−10	0.32	0.76 (0.025 λ_c)
−15	0.18	0.43 (0.014 λ_c)
−20	0.10	0.24 (0.008 λ_c)

For an imaging system with $\lambda_c = 0.03$ m to stay within an ISLR allowance of −15 dB from this one source, the uncompensated wideband random APC motion would have to be limited to an RMS value of approximately 0.5 mm. Motion compensation would be necessary if the APC motions exceed this limit. While the most obvious compensation involves the use of a LOS accelerometer, the effects of vibrations and deformation of the antenna structure on the location of the APC must also be considered. Difficulty in sensing high-frequency motion implies the need for a higher order autofocus technique in azimuth, such as the phase gradient algorithm described in Section 6.4.

The allowable RMS wideband motion error in (5.24) and Table 5.11 has units of distance while inertial motion sensors measure accelerations as a function of time. Thus, it is common to associate motion measurement error with the PSD of acceleration error $PSD_a(f)$. The acceleration PSD is the square of the magnitude of the acceleration frequency spectrum. The relationship between $PSD_a(f)$ and the PSD of position error $PSD_d(f)$ is

$$PSD_d = \frac{PSD_a}{(2\pi f)^4} \tag{5.25}$$

The RMS line-of-sight phase center motion error σ_r is the integrated value of $PSD_d(f)$ over frequency. Using (5.11), it is possible to relate σ_ϕ^2 and PSD_a by

$$\sigma_\phi^{\,2} = \left(\frac{4\pi}{\lambda_c}\right)^2 \int_0^\infty \left[\frac{PSD_a}{(2\pi f)^4}\right] H_{islr}\, df \tag{5.26}$$

where the weighting function $H_{islr}(f)$, associated with integrated sidelobe energy, is nominally a high-pass filter with cutoff at the reciprocal of the coherent aperture time [8].

It is also reasonable to extract, from the PSD of wideband random motion of a SAR data collection antenna, the contributions to QPEs, linear phase errors, and discrete sinusoidal phase errors. Often in SAR system error allocations, wideband random motion is associated entirely with an ISLR allocation. However, when the motion spectrum has significant energy at periods near the coherent aperture time, it is necessary to assess contributions to linear, quadratic, and single frequency errors as well. This means, for

instance, that a motion compensation system's allocation of QPE must be divided among the along-track velocity uncertainty, the LOS acceleration uncertainty, and the expected value of the contribution to QPE of the wideband random phase errors.

5.3.2 Range Curvature

Range curvature causes geometric distortion, which is a space-variant linear phase effect. Distortion from range curvature is deterministic and readily correctable in the IFP by digitally resampling the processed image. With polar format processing, range curvature distortion is

$$l_{yrc} = -\frac{1}{2S_{\phi c}}\left[\frac{r_t^2}{R_{ac}} - \frac{(\boldsymbol{P}_a \bullet \boldsymbol{r}_t)^2}{R_{ac}^3}\right] \tag{5.27}$$

in range and

$$l_{xrc} = -\frac{1}{2S_{\theta c}S_{\phi c}}\left[\frac{(\boldsymbol{P}_a \bullet \boldsymbol{r}_t)^2}{R_{ac}^3} C_{\theta c}(1 + 2S_{\phi c}^2) - \frac{2X_t S_{\phi c}(\boldsymbol{P}_a \bullet \boldsymbol{r}_t)}{R_{ac}^2} - \frac{r_t^2 C_{\theta c}}{R_{ac}}\right] \tag{5.28}$$

in azimuth.

Range curvature also causes space-variant defocus, which limits the acceptable scene size using the spotlight polar format algorithm. The equation for QPE from range curvature is

$$Q_{rc} = -\frac{2\pi S_{\phi c}^2}{\lambda_c R_{ac} S_{\theta c}^2}\left[X_t^2 - 4X_t S_{\phi c} C_{\theta c}\frac{\boldsymbol{P}_a \bullet \boldsymbol{r}_t}{R_{ac}} - (1 - 4S_{\phi c}^2 C_{\theta c}^2)\frac{(\boldsymbol{P}_a \bullet \boldsymbol{r}_t)^2}{R_{ac}^2}\right]\frac{x_p^2}{K_c^2} \tag{5.29}$$

Using (5.9), the nominal size of this QPE at broadside squint angle is

$$Q_{rc}\big|_{\text{size}} = -\frac{\pi\lambda_c K_a^2}{8\rho_a^2 R_{ac}}\left(X_t^2 - Y_t^2 S_{\phi c}^2\right) \tag{5.30}$$

Section 3.7 discusses range curvature and derives these equations. Range curvature introduces no space-invariant effects. The newer range migration and chirp scaling algorithms intrinsically correct for range curvature effects.

5.3.3 Residual Video Phase

Residual video phase causes distortion and space-variant defocus. It introduces no space-invariant effects. The distortion is deterministic and easily correctable in the processor,

although it is generally small enough to disregard. A frequency-domain algorithm is available to deskew spotlight data and remove the residual video phase error (Appendix C). Without compensation, the residual video phase distortion is

$$l_{yrvp} = 0 \tag{5.31}$$

in range and

$$l_{xrvp} = \frac{2\gamma\lambda_c S_{\phi c}}{c^2}\left[\tilde{x}_t\tilde{y}_t + \tilde{y}_t^2 C_{\phi c}^2 \cot(\theta_{ac})\right] \tag{5.32}$$

in azimuth. From (3.176) and (3.177), the equation for QPE from residual video phase is the sum of

$$Q_{rvpxx} = \frac{4\pi\gamma S_{\phi c}^2}{c^2}\left[\frac{x_p^2}{K_c^2}\right]\left[\tilde{x}_t^2 + 4\tilde{x}_t\tilde{y}_t C_{\phi c}^2 \cot(\theta_{ac}) - \tilde{y}_t^2 M_y\right] \tag{5.33}$$

and

$$Q_{rvp2xy} = \frac{8\pi\gamma S_{\phi c}^2}{c^2}\left[\frac{x_p y_p}{K_c^2}\right]\left[\tilde{x}_t\tilde{y}_t + \tilde{y}_t^2 C_{\phi c}^2 \cot(\theta_{ac})\right] \tag{5.34}$$

These expressions use

$$\tilde{x}_t = X_t S_{\theta c} - Y_t C_{\theta c} - Z_t \cot(\phi_{ac})\cot(\theta_{ac}) = x_t - Z_t \cot(\phi_{ac})\cot(\theta_{ac}) \tag{5.35}$$

$$\tilde{y}_t = X_t C_{\theta c} + Y_t S_{\theta c} + Z_t \cot(\phi_{ac}) = y_t + Z_t \cot(\phi_{ac}) \tag{5.36}$$

and

$$M_y = 1 - \frac{C_{\phi c}^2}{S_{\theta c}^2}(1 + 2C_{\theta c}^2 - 4C_{\theta c}^2 S_{\phi c}^2) \tag{5.37}$$

Using (5.9) and (5.10), the nominal magnitude of this QPE at broadside squint angle is

$$Q_{rvp}\big|_{\text{size}} = \frac{\pi\gamma\lambda_c^2 K_a^2}{2c^2\rho_a^2} r_o^2 \tag{5.38}$$

Here, use of r_o representing scene radius indicates size only, not the exact form of space-variance. Section 3.10 discusses residual video phase and derives these equations; Appendix C provides additional discussion.

5.3.4 Nonplanar Motion

The final error source identified here is uncompensated measured motions in the form of nonplanar motion of the SAR sensor while imaging a three-dimensional scene. This effect causes azimuth defocus of targets out of the selected focus plane. No compensation is known outside of selectively repositioning the focus target plane or applying space-variant (subscene) refocus where appropriate. We consider the case of a quadratic maneuver in which the sensor motion has an X component of velocity, V_{xa}, and three nonzero components of acceleration at aperture center. We use the XY plane as the focus target plane and the image display plane. The equation for QPE from this nonplanar APC motion is

$$Q_{np} = \frac{2\pi}{\lambda_c}\left[\frac{x_p^2}{K_c^2}\right]\left[\frac{R_{ac}S_{\phi c}\left(A_{za}S_{\theta c}S_{\phi c} - A_{ya}C_{\phi c}\right)}{V_{xa}^2 S_{\theta c}^3}\right]Z_t \tag{5.39}$$

Section 3.3.4 discusses nonplanar motion effects while Section 3.8 provides a derivation of this equation.

Using (5.9), the nominal magnitude of this QPE is

$$Q_{np}\big|_{\text{size}} = \frac{\pi\lambda_c K_a^2 R_{ac} a_{zo}}{8\rho_a^2 V_{xa}^2 S_{\theta c}^3 S_{\phi c}} Z_t \tag{5.40}$$

with

$$a_{zo} = A_{za}S_{\theta c}S_{\phi c} - A_{ya}C_{\phi c} \tag{5.41}$$

where a_{zo} represents the acceleration component normal to the data collection surface at aperture center. In these equations, ρ_a is the azimuth resolution, V_{xa} is the antenna velocity, R_{ac} is the slant range to scene center at aperture center, K_a is the azimuth mainlobe-broadening factor, and ϕ_{ac} is the incidence angle at aperture center.

5.3.5 Other Error Sources

Propagation of the SAR signals through the medium between the sensor and the target area adds a source of phase errors. Propagation effects may cause scene center displacement, scene defocus and loss of image contrast. Partial compensation is possible via range autofocus; also, if available and used, propagation models and/or measurements provide the possibility for nominal compensation. Propagation effects are not likely to be significant for most airborne systems, although they may be a factor in a long-range sensor operating at a low grazing angle [9-13].

Waveform error within the transmitter is a source of phase errors. The concerns in this category include nonlinearity in the FM waveform, reduction in phase coherence in terms of starting phase and frequency jitter from pulse to pulse, transmission line reflections, and waveguide dispersion effects. These factors may cause an increase in integrated

sidelobes as well as range defocus. The image formation processor can apply deterministic correction for measurable, stable waveform errors. With digitally generated waveforms, dispersion effects may be precorrected in waveform generation [14].

Motion during transmission and reception of a pulse introduces undesirable phase effects into the SAR signal history, principally a space-invariant defocusing and some small distortion effects. Because it is space-invariant, this defocusing can be compensated sufficiently with a reasonable effort. Typically, however, these distortion and defocusing effects are small enough to disregard.

Another error source involves motion between transmit and receive times, that is, a bistatic effect. This is a small effect, possibly noticeable in a satellite environment. It is correctable by proper adjustments to the data format.

Other minor error sources are likely throughout the hardware and software in a SAR imaging system. Typically, system integration and testing uncovers any of these factors that may require attention.

5.4 REQUIREMENTS ON A PRACTICAL SAR MOTION SENSOR

To avoid significant deterioration in image quality, uncertainty in SAR platform motion and the resulting phase errors are subject to the following general guidelines. Uncertainty in slowly varying, nonlinear motions along the LOS should be less than $\lambda_c/16$ (where λ_c is the center wavelength of the processed pulse) over the processing aperture to limit phase errors to $\pi/4$ rad, making use of (5.11). The value $\pi/4$ rad is a generally accepted level of allowable, uncompensated low-frequency phase errors. Uncertainty in slowly varying (including linear) motions perpendicular to the LOS must be less than one-quarter of the azimuth resolution size over the synthetic aperture interval to limit phase errors to $\pi/4$ rad. Uncertainty in the zero-to-peak amplitude of any sinusoidal LOS motions must be less than $0.015\ \lambda_c$ to limit the peak intensity of spurious sidelobes to –20 dB relative to the mainlobe peak (Table 5.10). The RMS wideband random LOS motion must be less than $0.008\ \lambda_c$ to limit added integrated sidelobe energy in the system impulse response to –20 dB relative to the mainlobe energy (Table 5.11).

The requirements on motion measurement accuracy in terms of residual range uncertainty are generally independent of both radar resolution and data collection characteristics such as slant range and forward velocity. A range accuracy requirement is scaled primarily by radar wavelength for slowly varying motions; radar signal-to-noise parameters, including ISLR, PSR, and signal-to-background ratio (Section 8.4), are also a factor for faster motions. Thus, basic ranging accuracy requirements are essentially platform-independent, with

$$\Delta r_{\text{slow}} < \frac{\lambda_c}{16} \tag{5.42}$$

and

$$\Delta r_{\text{fast}} < 0.008\lambda_c \tag{5.43}$$

representing a good first cut at motion measurement accuracy requirements for a general platform. The differentiation between slow and fast motions depends on the azimuth coherent aperture time (2.22), which varies with radar and platform parameters such as sensor velocity, slant range, and azimuth resolution.

Characterization of the motion accuracy requirements in terms of platform position, velocity, and acceleration errors depends on platform parameters and radar image quality requirements. Table 5.12 illustrates such a characterization for translational motions. While not explicitly illustrated, requirements on rotational motion measurement accuracy are implicit in these translational motion requirements; rotational motion causes an effective translational motion of the APC via the lever arm distance between the motion measurement sensor and the APC. Using Table 5.7, the allowable V_{xe} and A_{elos} levels correspond to $\pi/4$ rad in the absence of quadratic autofocus. Using autofocus with a pull-in range of πN_{pull} rad increases the allowable motion by $4N_{\text{pull}}$ times. The allowance for residual low-frequency motion assumes no use of higher order autofocus. Position measurement error affects only the location of the scene being imaged; allowable position measurement error relates directly to a requirement on scene center location accuracy L_{sc}.

Table 5.12
Characteristics of Translational Motion Measurement Requirements

Motion Measurement Error	*Image Effect*	*Related Specification*	*Allowable Motion*
Position	Scene center offset	Scene location accuracy	$P_e \approx L_{sc}$
LOS velocity	Scene center offset	Scene location accuracy	$V_{elos} \approx \frac{V_{xa} S_{\theta c}}{R_{ac}} L_{sc}$
Along-track velocity	Defocus	Azimuth resolution	$V_{xe} \approx \frac{\rho_a^2 V_{xa} S_{\theta c}^2}{\lambda_c K_a^2 R_{ac}}$
LOS acceleration	Defocus	Azimuth resolution	$A_{elos} \approx \frac{2\rho_a^2 V_{xa}^2 S_{\theta c}^2}{\lambda_c K_a^2 R_{ac}^2}$
Residual low-frequency LOS position	Defocus	Azimuth resolution	$r_e \approx \frac{\lambda_c}{16}$
Sinusoidal (zero-to-peak) LOS position	Peak sidelobes	PSR; spurious targets	$a_s \approx \left(\frac{\lambda_c}{2\pi}\right)\sqrt{\text{PSR}}$
RMS wideband LOS position	Loss of contrast	Multiplicative noise ratio from ISLR	$\sigma_r \approx \left(\frac{\lambda_c}{4\pi}\right)\sqrt{\text{ISLR}}$

For each motion error source, this table indicates the corresponding image effect (or more descriptively, image defect), the relevant system or image quality specification, and the parametric expression for the allowable motion to meet the associated specification. Radar azimuth resolution, slant range, and forward velocity are key parameters. Table 5.13 summarizes the symbols used in Table 5.12.

Table 5.13
Symbols Relating to Motion Error Effects

Symbol	*Definition*
P_e	Uncertainty in platform position
V_{xe}	Uncertainty in along-track component of platform velocity
V_{elos}	Uncertainty in LOS component of platform velocity
A_{elos}	Uncertainty in LOS component of platform acceleration
r_e	Uncertainty in range from the antenna to scene center
a_s	Sinusoidal (zero-to-peak) range error
σ_r	RMS wideband range error
V_{xa}	Platform forward velocity
K_a	Azimuth mainlobe-broadening factor
$S_{\theta c}$	Sine of the squint angle at aperture center
λ_c	Radar wavelength at center frequency
R_{ac}	Slant range between platform and scene center
ρ_a	Azimuth resolution
L_{sc}	Scene location accuracy requirement

Table 5.14 lists nominal parameter values for an example SAR platform corresponding to the system design in Table 2.4, Table 2.5, and Table 2.6. Use of these values in the parametric equations in Table 5.12 provides a rough guideline to platform-dependent requirements on motion measurement accuracy. Table 5.15 presents these results for this X-band SAR with 1-m resolution to show the impact in a typical system configuration.

5.5 MOVING TARGET EFFECTS

In typical ground-imaging applications, the imaged scene is nominally stationary as the SAR sensor passes by and collects radar signals backscattered from targets in the scene. Two common exceptions to this situation are trees on a windy day and ground-moving vehicles. In these situations, target motion is unexpected, unknown, and uncompensated.

Table 5.14
Typical Platform and Image Quality Parameter Values

Symbol	*Platform or Image Quality Parameter*	*Example System Value*
R_{ac}	Slant range	10,000 m
H	Altitude	5000 m
θ_{ac}	Squint angle	90 deg
V_{xa}	Velocity	100 m/s
λ_c	Center wavelength	0.03 m
T_a	Coherent aperture time	1.95 s
K_a	Azimuth mainlobe-broadening factor	1.3
ρ_a	Azimuth resolution	1 m
ρ_r	Range resolution	1 m
PSR	Peak sidelobe ratio	–30 dB
ISLR	Integrated sidelobe ratio	–21 dB
L_{sc}	Scene location accuracy	50 m

Table 5.15
Platform-Dependent Requirements

Symbol	*Motion Measurement Error*	*Requirement for Example System*
P_e	Position	50 m
V_{elos}	LOS velocity	0.5 m/s
V_{xe}	Along-track velocity	0.20 m/s
A_{elos}	LOS acceleration	0.004 m/s^2
r_e	Residual low-frequency motion	1.88 mm
a_s	Sinusoidal (zero-to-peak) motion	0.15 mm
σ_r	RMS wideband motion	0.24 mm

This motion contributes to relative motion between the APC and these particular targets. With respect to relative motion, uncompensated target motion is equivalent to unmeasured APC motion in the opposite direction against a stationary target. As in the case of unmeasured APC motion, the effects of target motion on SAR imagery are image smearing in azimuth and image displacement in angle leading to displacement in azimuth [15].

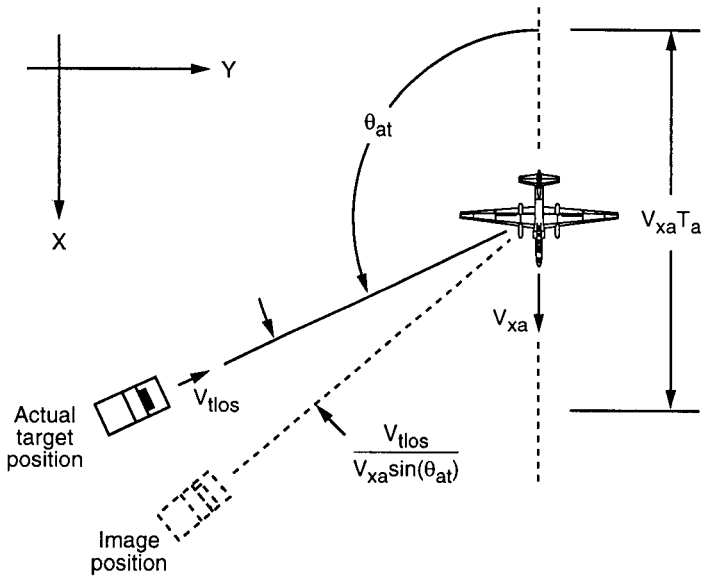


Figure 5.21 Displacement effect of target velocity toward radar.

Image displacement results from a moving target's LOS component of velocity V_{tlos}; Figure 5.21 illustrates the angular displacement of the image with respect to its true squint angle relative to the radar. This displacement is nominally the ratio of the target's LOS velocity V_{tlos} to the cross LOS component $V_{xa}\sin(\theta_{at})$ of radar velocity. Here, θ_{at} is the squint angle between the antenna path and the radar LOS to the moving target. This result is analogous to the last term in (3.162) for the case of uncompensated APC line-of-sight velocity.

Image smearing results largely from a moving target's along-track component of velocity V_{tat}, although other target motions do have some effect. Figure 5.22 illustrates the effect of V_{tat}. The target smearing distance is related to the along-track distance the target travels over the aperture time T_a. This result is available from an estimate of the QPE such a motion causes. From the first row of Table 5.7 describing the analogous APC velocity measurement error effect, the QPE from V_{tat} is of the size

$$Q_{Vtat}\big|_{\text{size}} \approx \frac{\pi\lambda_c K_a^2 R_{ac} V_{tat}}{4\rho_a^2 V_{xa} S_{\theta c}^2} = \frac{\pi K_a V_{tat} T_a}{2\rho_a S_{\theta c}} \tag{5.44}$$

using a version of (2.10) to simplify the expression. A comparison of the bandwidths of an unweighted aperture with and without QPE indicates that a QPE widens the impulse response by one error-free resolution cell for each $\pi/4$ rad of QPE. An estimate of the

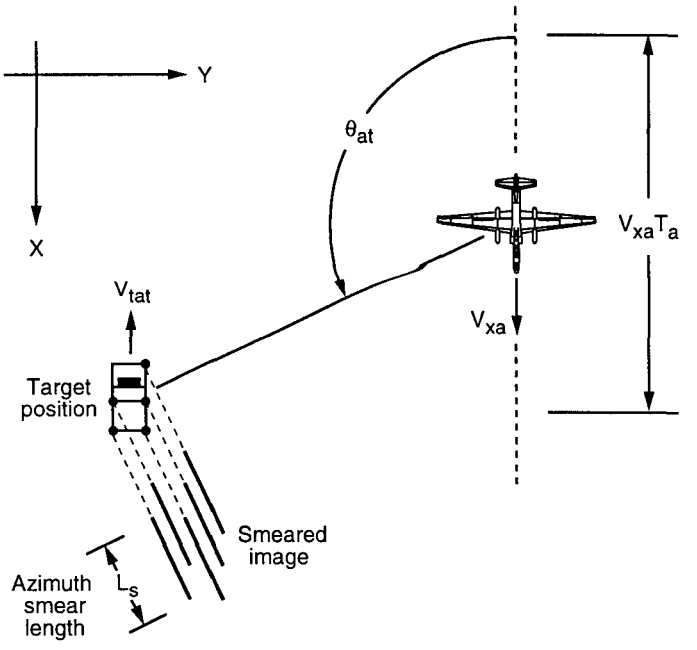


Figure 5.22 Smearing effect of target along-track velocity V_{tat} with uniform aperture weighting.

target smearing is the QPE in (5.44) times ρ_a divided by $\pi/4$. Using $K_a = 0.89$, this estimate yields a smear length L_s given by

$$L_s \approx \frac{1.78 V_{tat} T_a}{S_{\theta c}} \tag{5.45}$$

which is $1.78/S_{\theta c}$ times the along-track distance the target travels over the aperture time. In the presence of a heavy aperture weighting, a specific level of QPE widens the impulse response by roughly one-half of this amount because the weighting suppresses the high-frequency effects toward the edges of the aperture. Table 5.2 suggests agreement with this rule of thumb in the case of −35-dB Taylor weighting and larger levels of QPE; the ratio of defocused-to-focused −3-dB mainlobe widths in the second column approximates one unweighted resolution cell (equal to 1/1.34 weighted resolution cells) for every $\pi/2$ rad of QPE.

5.6 SUMMARY

The output product of the SAR system is imagery. The objective of the spotlight sensor and the early stages of the IFP is to massage the radar signals in order to convert the return from each scatterer in the scene into a complex, single-frequency phase term of the form $\exp[j(K_x X_t + K_y Y_t)]$. This phase term is amenable to a direct two-dimensional Fourier transform to yield an image pixel with resolution corresponding to the RF bandwidth and integration angle of the data collection and with position and amplitude that represents the RCS properties of the target.

Undesirable phase terms occur naturally in the radar signals at various stages of the data collection operation. Some phase terms are inherent in the interaction between the geometry and the radar sensor; others result from hardware limitations in the radar sensor and in the motion sensor. Procedures in the radar receiver begin to remove these undesirable phase terms. The selection and use of algorithms for motion compensation and signal processing in IFP operations removes any residual phase terms within the accuracy of motion sensor data and within the capability of available image formation and autofocus algorithms. Phase terms that the SAR system does not remove successfully become phase errors that compromise the Fourier transform processing of scatterer returns and degrade the resulting image quality.

Phase errors lead to defects in the SAR imagery. Linear phase errors cause a shift in image position. Quadratic and cubic low-frequency phase errors introduce focus difficulties in the imagery for which autofocus techniques can compensate within reasonable limits. High-frequency wideband phase errors increase the energy in the sidelobes of the system impulse response and, therefore, degrade image contrast. Besides contributing to total sidelobe energy, sinusoidal phase errors introduce peak sidelobes (paired echoes) in the azimuth direction which resemble false targets displaced from the true target. It is necessary to restrict the magnitude of these high-frequency effects sufficiently by design or to compensate for them sufficiently (that is, remove by refocusing) to meet the total sidelobe energy and peak sidelobe level specifications of the imaging system.

Error in measurement of APC location is a primary source of phase errors in the azimuth dimension. A processing algorithm that is inadequate due to either an inherent limitation or incomplete implementation is a source of additional phase errors. Phase effects in this category include range curvature, residual video phase, and a nonplanar data collection surface. Of these, range curvature introduces significant image distortion and potentially limits the scene size by the presence of space-variant QPEs increasing in magnitude toward the edges of the imaged area. Nonplanar motion effects severely limit the ability to generate fine-resolution SAR imagery during maneuvers by the SAR platform.

REFERENCES

[1] Klauder, J.R., A.C. Price, S. Darlington and W.J. Albersheim, "The Theory and Design of Chirp Radars," *The Bell System Technical Journal*, Vol. 39, No. 4, July 1960, pp. 745-808.

[2] Harger, R.O., *Synthetic Aperture Radar Systems: Theory and Design*, New York, Academic Press, Inc, 1970, Chapter VI, "Phase and Motion Errors," pp. 129-155.

[3] Develet, J.A., "Influence of Random Phase Errors on the Angular Resolution of SAR Systems", *IRE Transactions on Aerospace and Navigation*, March 1964, pp. 58-65.

[4] Brown, W.M., and C.J. Palermo, "Effects of Phase Errors on Resolution," *IEEE Transactions on Military Electronics*, Vol. MIL-9, No. 1, January 1965, pp. 4-9.

[5] Green, C.A., and R.T. Moller, "The Effects of Normally-Distributed Random Phase Errors on Synthetic Array Gain Patterns," *IRE Transactions on Military Electronics*, Vol. MIL-6, No. 2, April 1962, pp. 130-139.

[6] Blacknell, D., A. Freeman, S. Quegan, I.A. Ward, I.P. Finley, C.J. Oliver, R.G. White, and J.W. Wood, "Geometric Accuracy in Airborne SAR Systems," *IEEE Transactions on Aerospace and Electronic Systems*, Vol. AES-25, No. 2, March 1989, pp. 241-256.

[7] Brown, W.M., "SAR Resolution in the Presence of Phase Errors," *IEEE Transactions on Aerospace and Electronic Systems*, Vol. 24, No. 6, November 1988, pp. 808-814.

[8] Kennedy, T.A., "Strapdown Inertial Measurement Units for Motion Compensation for Synthetic Aperture Radars," *IEEE AES Magazine*, Vol. 3, No. 10, October 1988, pp. 32-35.

[9] Porcello, L.J., "Turbulence-Induced Phase Errors in Synthetic-Aperture Radar Systems," *IEEE Transactions on Aerospace and Electronic Systems*, Vol. AES-6, No. 5, September 1970, pp. 636-644.

[10] Fante, R.L., "Turbulence-Induced Distortion of Synthetic Aperture Radar Images," *IEEE Transactions on Geoscience and Remote Sensing*, Vol. 32, No. 4, July 1994, pp. 958-961.

[11] Quegan, S., and J. Lamont, "Ionospheric and Tropospheric Effects on Synthetic Aperture Radar Performance," *International Journal of Remote Sensing*, Vol. 7, No. 4, 1986, pp. 525-539.

[12] Brown, W.D., and D.C. Ghiglia, "Some Methods for Reducing Propagation-Induced Phase Errors in Coherent Imaging Systems, Part 1, Formalism," *Journal of the Optical Society of America*, Vol. 5, No. 6, June 1988, pp. 942-957.

[13] Ghiglia, D.C., and W.D. Brown, "Some Methods for Reducing Propagation-Induced Phase Errors in Coherent Imaging Systems, Part II, Numerical Results," *Journal of the Optical Society of America*, Vol. 5, No. 6, June 1988, pp. 924-941.

[14] Gallaway, W.D., K.F. Luckscheiter, E.H. Cowen, and J.W. Wilhelm, "A Direct Digitally Synthesized Exciter Achieving Near Theoretical Performance for an Operational SAR System," *IEEE National Radar Conference*, Ann Arbor, MI, 20-21 April 1988, pp. 22-27.

[15] Raney, R.K., "Synthetic Aperture Radar and Moving Targets," *IEEE Transactions on Aerospace and Electronic Systems*, Vol. AES-7, No. 3, May 1971, pp. 499-505.

Chapter 6
Autofocus Techniques

Phase errors present in a SAR signal history at the time of the final Fourier transform operation degrade image quality in several ways. The most serious degradation is often image defocus caused by the presence of uncorrected quadratic and higher order phase errors. Uncompensated motion between the SAR antenna phase center (APC) and the scene being imaged is a primary source of phase errors. Other sources include algorithm approximations, hardware limitations, and propagation effects.

Autofocus techniques improve image focus by removing a large part of any phase errors present after conventional motion compensation and data formatting procedures. Autofocus with respect to SAR imagery refers to the computer-automated estimation and subsequent removal of these residual phase errors. Autofocus generally encompasses two distinct steps:

1. Error estimation;
2. Error compensation.

Error estimation operates on the SAR data and estimates the coefficients of an expansion that models the existing phase error. Elementary autofocus methods may determine only the quadratic coefficient while more elaborate methods estimate higher order coefficients as well. *Error compensation* or *cancellation* uses the coefficient values that the first step provides. The second step involves:

- Building a complex correction vector with phase equal to the negative of the estimated phase error:
- Multiplying the signal history by the correction vector;
- Reprocessing the corrected data with the conventional image formation algorithm.

Some autofocus implementations require explicit knowledge of the set of error coefficients to insert the proper quantities into the correction procedure. In other implementations, the coefficients are implicit in some known composite compensation phase function. For instance, measurements on a high-intensity point scatterer in the image may provide this phase function.

Most SAR autofocus algorithms perform space-invariant compensation in which they apply the same correction vector to all scatterers in the image. Space-invariant compensation is adequate in many operational SAR systems where motion measurement

errors, often along-track velocity error or line-of-sight acceleration error, cause the more significant phase errors; the primary implication of motion errors is space-invariant phase error in azimuth.

This chapter describes five practical autofocus techniques. These techniques are practical in the sense that fielded SAR systems use them. The first four techniques are mapdrift (MD), multiple aperture mapdrift (MAM), phase difference (PD), and phase gradient autofocus (PGA). They represent space-invariant autofocus algorithms. We describe these techniques relative only to one-dimensional phase errors because azimuth phase errors are the primary SAR phase error concern. However, the techniques apply equally to range phase errors. The fifth technique is prominent point processing (PPP). In a simple realization, PPP is also a space-invariant focusing technique. In more refined applications, PPP provides a full motion compensation capability that includes the ability to determine the scene rotation rate for SAR and ISAR applications.

This chapter also details the implementation of these five autofocus techniques and includes image examples to illustrate the focusing capability that each of the four space-invariant algorithms possesses. Section 7.2 illustrates use of the PPP technique to focus an ISAR image. These examples illustrate operation of the algorithms; they do not offer an in-depth performance evaluation or comparison of the algorithms. The chapter concludes with a discussion of space-variant focusing techniques.

6.1 MAPDRIFT

The development of mapdrift in the early to mid-1970s was a significant event in the evolution of fine-resolution imaging radar [1]. The quadratic implementation of MD provides a robust estimate of QPE, historically a major cause of image defocus in SAR data. The MD algorithm, employed by numerous scientific and reconnaissance SAR systems, is the dominant autofocus technique in use today [2-4].

MD directly estimates the quadratic coefficient of the phase error and then, based on this estimate, builds and applies a one-dimensional correction vector to the signal history. Generation and application of the correction vector are simple matters once the quadratic error coefficient is known. This section describes the error estimation procedure of the MD algorithm to estimate a one-dimensional, space-invariant QPE in azimuth.

6.1.1 Overview

Figure 6.1 shows a typical implementation of MD in an image formation processor (IFP) using the polar format algorithm. The IFP performs motion compensation, polar formatting, and range compression before use of the autofocus procedure. In most applications, the MD algorithm uses only a small fraction of the available range bins to derive an estimate of the azimuth QPE coefficient. The algorithm uses this estimate to build and apply an error correction vector. The IFP then compresses the corrected signal data in azimuth to form the output image. The algorithm can iterate the error estimation and correction procedure in order to improve the final result.

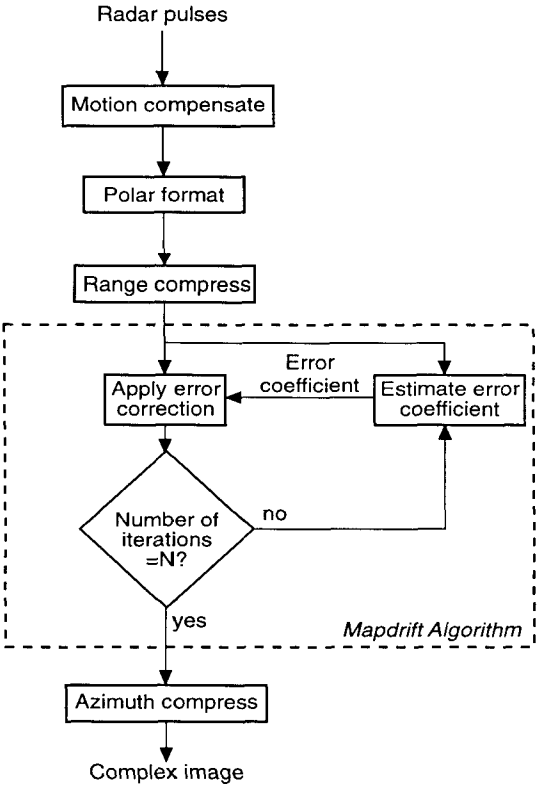


Figure 6.1 Mapdrift autofocus in the image formation processor.

The MD technique divides an aperture of duration T_a into two nonoverlapping subapertures of duration $T_a/2$. The MD concept uses the fact that a QPE across the full processing aperture has a different functional form across two half-length subapertures. To illustrate this idea, Figure 6.2 shows a quadratic error with a center-to-edge phase of Q radians across the full aperture. The phase error across each subaperture consists of a quadratic component, a linear component, and an inconsequential constant component of $Q/4$ radians. The quadratic phase components of the two subapertures are identical with a center-to-edge magnitude of $Q/4$ radians. The linear phase components of the two subapertures have identical magnitudes but slopes of opposite sign.

The linear phase terms across the subapertures shift the images formed from each subaperture. The Fourier shift theorem describes this property [5]. If $s(t)$ and $S(\omega)$ are a Fourier transform pair denoted by $\Im\{s(t)\} = S(\omega)$, this theorem states that

$$\Im\{e^{j\omega_o t} s(t)\} = S(\omega - \omega_o) \tag{6.1}$$

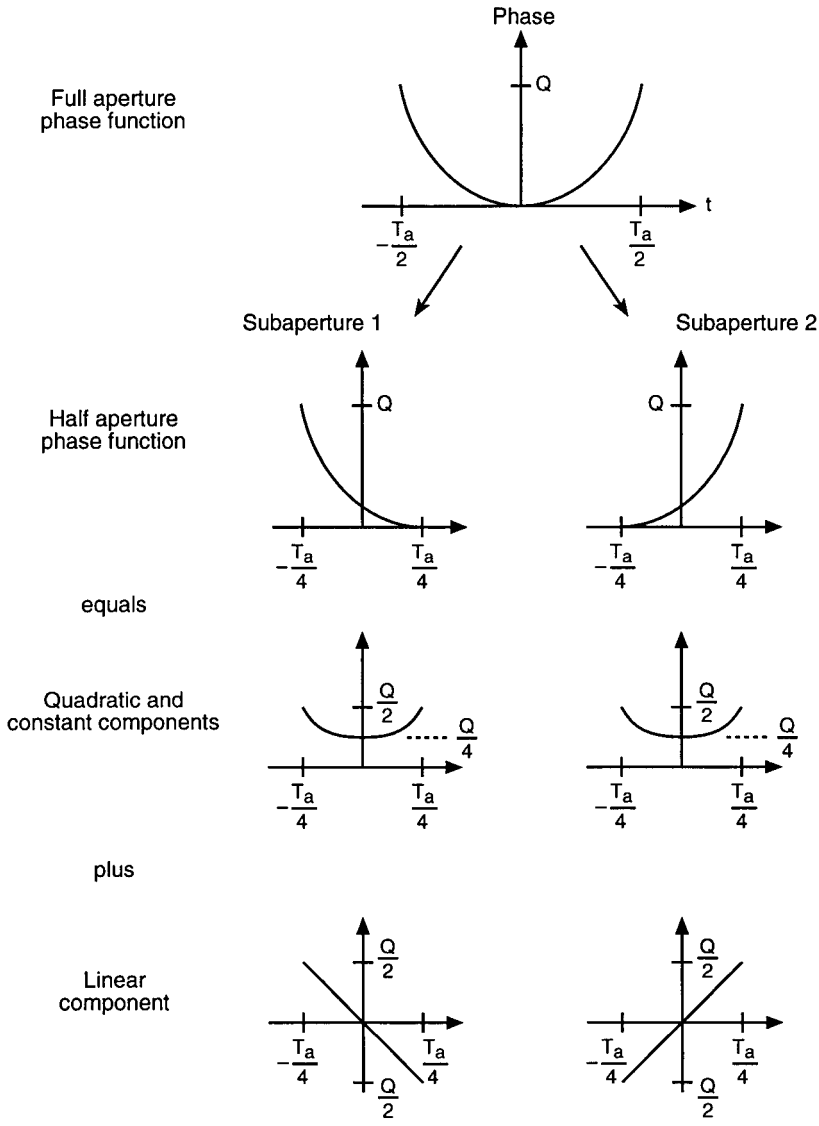


Figure 6.2 Visualization of full aperture QPE over two half apertures.

In words, a linear phase term over the signal $s(t)$ shifts its Fourier transform $S(\omega)$. Since the linear phase terms have opposite signs in the two MD subapertures, the images generated from each subaperture shift in opposite directions. The relative shift between the images is directly proportional to the center-to-edge QPE across the full aperture. The MD

procedure estimates the relative shift (or *drift*) between the image pair by cross-correlating the two intensity images. The location of the cross-correlation peak is a measure of the relative shift. Referring to each intensity image as a *map* leads to the name *mapdrift*.

The two-subaperture MD procedure is able to estimate only a QPE coefficient. Since higher order phase errors also yield different functional forms on the two subapertures, the presence of such errors can compromise MD performance. In the presence of a higher order phase error, the algorithm still provides a quadratic error estimate even though it is more appropriate to describe the actual phase error by a higher order polynomial. This situation occurs when the higher order error yields a different linear phase component on each subaperture.

Figure 6.3 illustrates application of the MD procedure to a simulated signal history from a single point scatterer. The signal history has 2π-rad center-to-edge QPE. Figure 6.3(a) shows the degraded impulse response using the original, full-length aperture. Figure 6.3(b) shows the separate impulse responses from each of the half-length subapertures. As expected, the point impulse response shifts to the left using the first subaperture and to the right using the second subaperture. Relative intensity in these impulse response plots refers to intensity relative to the peak intensity of an error-free impulse response. Figure 6.3(c) shows the result of a cross-correlation of the two impulse responses in Figure 6.3(b). The location Δ_ω of the cross-correlation peak is a measure of the QPE across the full aperture. Figure 6.3(d) shows the corrected impulse response after estimating the phase error level, applying a correction vector, and reprocessing the data with uniform aperture weighting.

6.1.2 Analytical Development

The model for the azimuthal signal $g(t)$ from a single range bin is the product of the error-free signal history $s(t)$ and a complex exponential with quadratic phase. The model for $g(t)$ is

$$g(t) = s(t)\, e^{jat^2} \qquad -\frac{T_a}{2} \le t < \frac{T_a}{2} \tag{6.2}$$

where a is the QPE coefficient to be estimated and T_a is the synthetic aperture duration. The relationship between the center-to-edge phase error Q and the error coefficient is

$$Q = \frac{aT_a^{\,2}}{4} \tag{6.3}$$

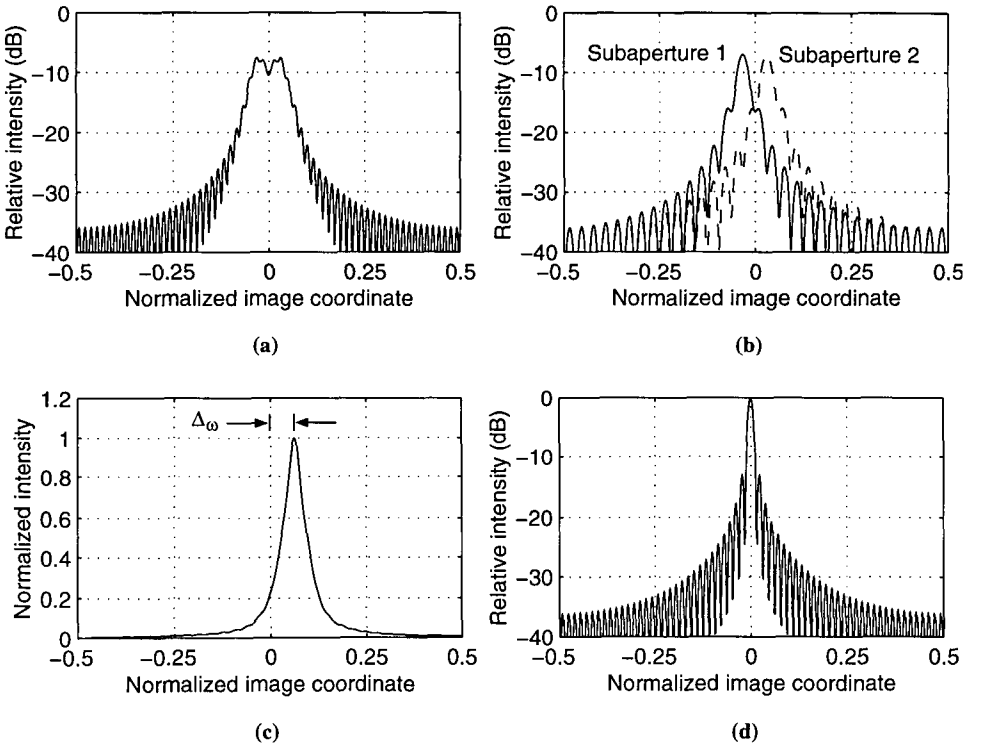


Figure 6.3 Mapdrift example: **(a)** Point target response with 2π rad of QPE; **(b)** Subaperture point target responses; **(c)** Cross-correlation of subaperture responses; **(d)** Point target response after correcting QPE.

The MD procedure begins by dividing $g(t)$ into two subapertures of length $T_a/2$:

$$g_1(t) = g\left(t - \frac{T_a}{4}\right) = s\left(t - \frac{T_a}{4}\right) e^{j\left(at^2 - \frac{aT_a}{2}t + \frac{aT_a^2}{16}\right)} \qquad -\frac{T_a}{4} \le t < \frac{T_a}{4} \tag{6.4}$$

and

$$g_2(t) = g\left(t + \frac{T_a}{4}\right) = s\left(t + \frac{T_a}{4}\right) e^{j\left(at^2 + \frac{aT_a}{2}t + \frac{aT_a^2}{16}\right)} \qquad -\frac{T_a}{4} \le t < \frac{T_a}{4} \tag{6.5}$$

Transformation of each subaperture into the image domain via a Fourier transform yields

$$G_1(\omega) = \int_{-T_a/4}^{T_a/4} g_1(t)\, e^{-j\omega t} dt = \hat{S}_1\left(\omega + \frac{aT_a}{2}\right) \tag{6.6}$$

$$G_2(\omega) = \int_{-T_a/4}^{T_a/4} g_2(t)\, e^{-j\omega t} dt = \hat{S}_2\left(\omega - \frac{aT_a}{2}\right) \tag{6.7}$$

where

$$\hat{S}_1(\omega) = \int_{-T_a/4}^{T_a/4} s\left(t - \frac{T_a}{4}\right) e^{j\left(at^2 + \frac{aT_a^2}{16}\right)} e^{-j\omega t} dt \tag{6.8}$$

and

$$\hat{S}_2(\omega) = \int_{-T_a/4}^{T_a/4} s\left(t + \frac{T_a}{4}\right) e^{j\left(at^2 + \frac{aT_a^2}{16}\right)} e^{-j\omega t} dt \tag{6.9}$$

The MD algorithm relies on the assumption that

$$\left|\hat{S}_1(\omega)\right|^2 = \left|\hat{S}_2(\omega)\right|^2 \tag{6.10}$$

To the extent that (6.10) is valid, it is clear from (6.6) and (6.7) that the two intensity images $\left|G_1(\omega)\right|^2$ and $\left|G_2(\omega)\right|^2$ are shifted versions of the same function. The relative shift between the two images is directly proportional to the QPE coefficient a over the original, full-length aperture. Various methods are available to estimate this shift. The most common estimation method is to measure the peak location of the cross-correlation of the two intensity images as Figure 6.3(c) suggests.

From (6.6) and (6.7), the relative shift between maps (subaperture 2 – subaperture 1) is $\Delta_\omega = aT_a$. A measurement of Δ_ω provides an estimate $\hat{a}$ of the quadratic error coefficient according to

$$\hat{a} = \frac{\Delta_\omega}{T_a} \tag{6.11}$$

From (6.3), the corresponding estimate of center-to-edge QPE is

$$\hat{Q} = \frac{\Delta_\omega T_a}{4} \tag{6.12}$$

Naturally, Δ_ω can be positive or negative depending on the sign of the QPE.

6.1.3 Implementation

A typical MD implementation applies the algorithm to only a small subset of available range bins based on peak (or total) energy content. Experience indicates that use of about 5 percent of the range bins containing the most energy is adequate. An average of the individual estimates of the error coefficient from each of these range bins provides a final estimate. This procedure naturally reduces the computational burden of the algorithm. It also improves the accuracy of the error estimate on the following basis. The range bins with the most energy are likely to contain strong, dominant scatterers with high signal energy relative to clutter energy. The signatures from such scatterers typically show high correlation between the two MD subaperture images (with some exceptions, such as in the case of glinting targets) while clutter is poorly correlated between the two images. In range bins without high signal energy relative to clutter energy, the validity of the assumption in (6.10) deteriorates. This deterioration results in degraded algorithm performance.

It is common practice to apply the MD algorithm iteratively. On each iteration, the algorithm forms an estimate of QPE and applies this estimate to the input signal data. This modified signal data, which presumably contains a smaller phase error than the original data, becomes the starting point for the next iteration. Typically, two to six iterations of MD are sufficient to yield an accurate error estimate which does not change significantly on subsequent iterations. Iteration of the MD procedure greatly improves the accuracy of the final error estimate for two reasons. First, iteration enhances the algorithm's ability to identify and discard those range bins that, for one reason or another, provide anomalous estimates. Averaging the estimates from the surviving range bins improves the composite estimate for the current iteration. Second, the improved focus of the image data after each iteration results in a narrower cross-correlation peak, which leads to a more accurate determination of its location. Accuracy in peak location corresponds to accuracy in the error coefficient estimate.

Figure 6.4 provides an example of focusing an image using the mapdrift algorithm. Figure 6.4(a) shows a 1-m resolution SAR image that has been degraded by a QPE in azimuth with a center-to-edge magnitude of 8π rad. Radar illumination and near range are from the left side of the image. Initially, the mapdrift processor selects a set of 32 range bins containing the most energy. Figure 6.4(b) shows the image resulting from four iterations of mapdrift. After each iteration, the algorithm discards any range bins with a phase error estimate deviating from the mean estimate by more than one standard deviation. Based on this criterion, the algorithm discarded 14 of the original 32 bins during the error estimation procedure. The final QPE estimate after four iterations is 7.97π rad. The residual phase error is a negligible 0.03π rad.

6.2 MULTIPLE APERTURE MAPDRIFT

Extension of the MD algorithm to estimate higher order phase errors is possible by dividing the signal history aperture into more than two subapertures. In general, N subapertures are adequate to estimate the coefficients of an N^{th}-order polynomial error.



(a)



(b)

Figure 6.4 Quadratic mapdrift autofocus example: **(a)** SAR image degraded by phase error; **(b)** SAR image after four iterations of mapdrift.

First reports of the extended algorithm, known as multiple aperture mapdrift (MAM) autofocus, appeared in 1981 in the classified literature [1].

6.2.1 Overview

To illustrate the MAM concept, we examine its treatment of a cubic phase error. To estimate a cubic phase error coefficient, MAM first divides an aperture of duration T_a into three nonoverlapping subapertures, each of length $T_a/3$. As Figure 6.5 indicates, a cubic phase error over the full aperture has a different linear phase and different higher order phase over each of the three subapertures. MAM makes use of this difference in linear phase among the three subapertures. By the Fourier shift theorem of (6.1), the differences in linear phase cause shifts among the images formed independently from each subaperture. A measurement of the relative shift between pairs of intensity images indicates the amount of cubic phase error present over the full aperture. The MAM typically estimates relative shifts by cross-correlating pairs of intensity images. Figure 6.6 shows a block diagram of the N^{th}-order MAM algorithm. The case $N = 2$ corresponds to the quadratic mapdrift algorithm.

A difficulty with the MAM algorithm is that the length of the nonoverlapping subapertures decreases as the MAM order (and the number of subapertures) increases. This decrease in subaperture length degrades both the resolution and the signal-to-noise ratio of targets in the images. These effects reduce the accuracy of the error estimates. In practice, the MAM yields robust error estimates up to approximately fifth order.

The presence of significant phase errors of order higher than the number of subapertures compromises performance of the extended algorithm. For example, a fifth-order polynomial error divided into only three subapertures will wrongly suggest a cubic error. Ideally, the number of subapertures will correspond to the highest order phase error present at a significant level.

6.2.2 Analytical Development

The model for the one-dimensional, space-invariant phase error is the N^{th}-order polynomial

$$\phi_e(t) = \sum_{k=2}^{N} a_k t^k \qquad -\frac{T_a}{2} \le t < \frac{T_a}{2} \tag{6.13}$$

where the a_k quantities are the unknown coefficients of the polynomial error and T_a is the synthetic aperture duration. The actual signal history is the desired signal history multiplied by $\exp[j\phi_e(t)]$. Because constant and linear components of the phase function do not affect image focus, the error model does not include zero-order and first-order terms.

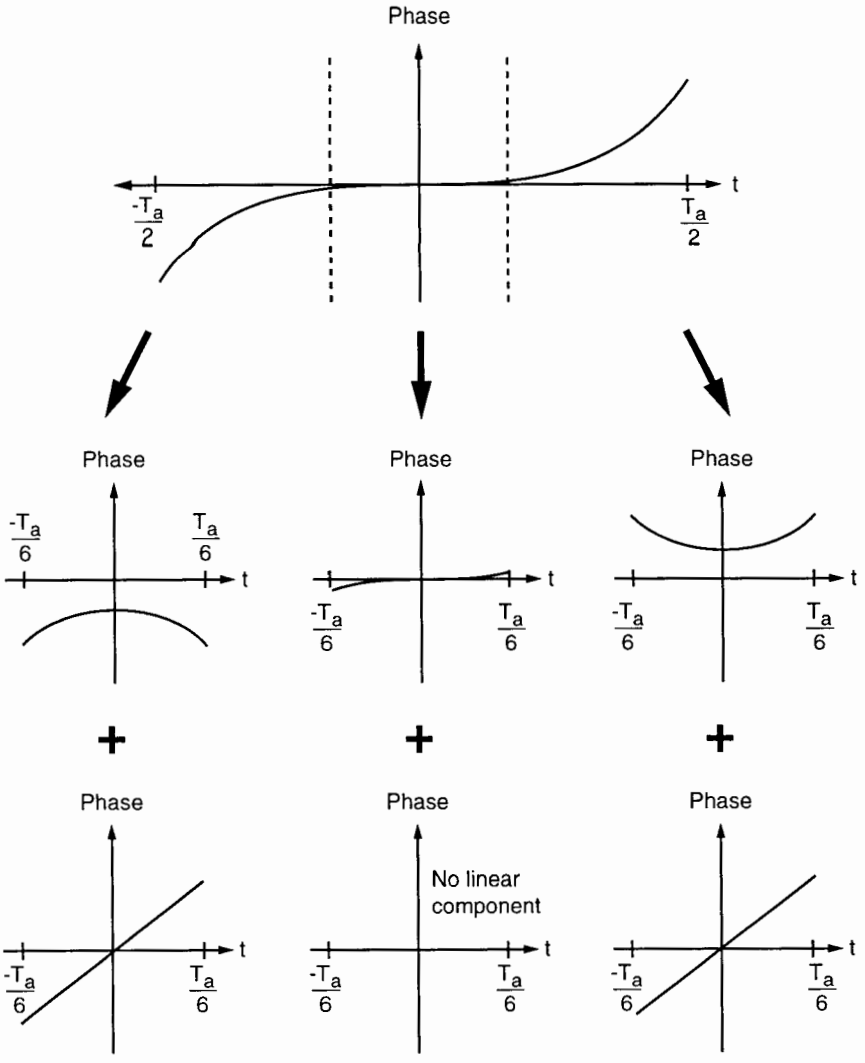


Figure 6.5 Visualization of full-aperture cubic phase error over three subapertures.

The first procedure in the MAM algorithm breaks the signal history into N subapertures. The phase error over the i^{th} subaperture of width T_a/N is

$$\phi_i(t) = \sum_{k=2}^{N} a_k (t + t_i)^k \qquad -\frac{T_a}{2N} \le t < \frac{T_a}{2N} \tag{6.14}$$

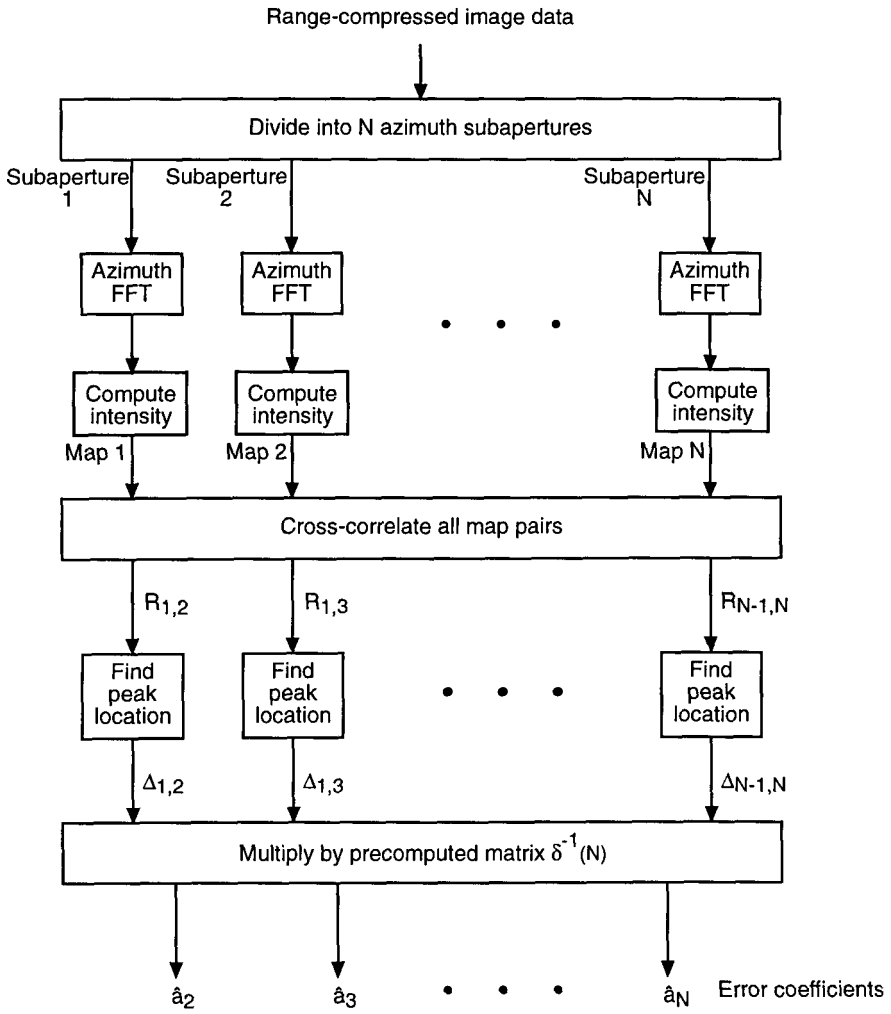


Figure 6.6 Block diagram of multiple aperture mapdrift procedure.

where the center of the i^{th} subaperture t_i is

$$t_i = \left(\frac{i}{N} - \frac{N+1}{2N}\right)T_a \tag{6.15}$$

To include all subapertures, the index i varies from 1 to N. The linear phase error component over each subaperture is the primary interest because this component induces the

relative shift between images originating from each subaperture. The location of the peak of the cross-correlation between each intensity image pair provides a measure of the relative shift between the two images making up the pair. These measurements lead directly to estimates of the second through N^{th} error coefficients. The linear phase on the i^{th} subaperture is

$$\phi_{\text{lin},\,i}(t) = \sum_{k=2}^{N} a_k k t_i^{(k-1)} t \qquad -\frac{T_a}{2N} \le t < \frac{T_a}{2N} \tag{6.16}$$

By the Fourier shift theorem, a linear phase coefficient of Δ in the signal history domain induces a shift of Δ in the image domain. Thus, the shift of the image formed from the i^{th} subaperture in the presence of a polynomial phase error is

$$\text{Shift}_i = \sum_{k=2}^{N} a_k k\, t_i^{(k-1)} \tag{6.17}$$

Cross-correlation of a pair of intensity images determines the relative shift between the two images. The relative shift between the images from the i^{th} and j^{th} subaperture is equal to $Shift_j$ - $Shift_i$. Using (6.17), this relative shift is

$$\Delta_{ij} = \sum_{k=2}^{N} a_k k \left[t_j^{(k-1)} - t_i^{(k-1)} \right] \qquad i < j \tag{6.18}$$

with $i, j \in [1, 2, \ldots, N]$ to include all relative shifts.

This expression describes an overdetermined system of linear equations. In more compact matrix notation, it becomes

$$\underline{\Delta} = \underline{\delta}\underline{a} \tag{6.19}$$

where the shift matrix $\underline{\Delta}$ is

$$\underline{\Delta} = \left[\Delta_{1,2} \cdots \Delta_{1,N} \quad \Delta_{2,3} \cdots \Delta_{2,N} \quad \Delta_{3,4} \cdots \Delta_{N-1,N} \right]^T \tag{6.20}$$

the coefficient matrix $\underline{a}$ is

$$\underline{a} = \left[a_2 \quad a_3 \quad \cdots \quad a_N \right]^T \tag{6.21}$$

and the relational matrix $\underline{\delta}$ is

$$\underline{\delta} = \begin{bmatrix} \delta^2_{1,2} & \delta^3_{1,2} & \cdots & \delta^N_{1,2} \\ \delta^2_{1,3} & \delta^3_{1,3} & \cdots & \delta^N_{1,3} \\ \cdots & \cdots & \cdots & \cdots \\ \delta^2_{1,N} & \delta^3_{1,N} & \cdots & \delta^N_{1,N} \\ \delta^2_{2,3} & \delta^3_{2,3} & \cdots & \delta^N_{2,3} \\ \delta^2_{2,4} & \delta^3_{2,4} & \cdots & \delta^N_{2,4} \\ \cdots & \cdots & \cdots & \cdots \\ \cdots & \cdots & \cdots & \cdots \\ \delta^2_{N-1,N} & \delta^3_{N-1,N} & \cdots & \delta^N_{N-1,N} \end{bmatrix} \tag{6.22}$$

The superscript T in (6.20) and (6.21) denotes a matrix transpose. The notation $\delta^k_{i,j}$ represents the shift between the i^{th} and j^{th} maps caused by a k^{th}-order phase error of unit value (that is, $a_k = 1$). From (6.18), this quantity is

$$\delta^k_{i,j} = \frac{k}{2\pi}\left[t_j^{(k-1)} - t_i^{(k-1)}\right] \tag{6.23}$$

Equations (6.20) and (6.22) have $N(N-1)/2$ entries since there are $N(N-1)/2$ distinct pairs of subapertures.

The polynomial error coefficients are now available as

$$\underline{a} = \underline{\delta}^{-1}\underline{\Delta} \tag{6.24}$$

where $\underline{\delta}^{-1}$ is the $(N-1) \times N(N-1)/2$ pseudo-inverse matrix [6] of $\underline{\delta}$. After cross-correlation of all pairs of maps and estimation of the relative shift between maps, the error coefficients are available by a single matrix multiplication. There is substantial redundancy in the operation described by (6.22) in that estimation of the $N-1$ error coefficients (a_2 through a_N) actually requires only $N-1$ shift measurements. However, the additional correlations help overcome the effects of noise and target signature variation (scintillation) with azimuth subaperture position.

6.2.3 Implementation

It is common to normalize the synthetic aperture time (setting $T_a = 1$) in order to precompute and store the entries of (6.20), and hence the matrix $\underline{\delta}^{-1}$, in the SAR processor.

With $T_a = 1$, the values of $\underline{\delta}$ for $N = 2, 3, 4$ and 5 are

$$\underline{\delta}\,(N = 2) \;=\; 1 \tag{6.25}$$

$$\underline{\delta}\,(N = 3) \;=\; \frac{1}{3}\begin{bmatrix} 2 & -1 \\ 4 & 0 \\ 2 & 1 \end{bmatrix} \tag{6.26}$$

$$\underline{\delta}\,(N = 4) \;=\; \frac{1}{64}\begin{bmatrix} 32 & -24 & 13 \\ 64 & -24 & 14 \\ 32 & 0 & 1 \\ 96 & 0 & 27 \\ 64 & 24 & 14 \\ 32 & 24 & 13 \end{bmatrix} \tag{6.27}$$

$$\underline{\delta}\,(N = 5) \;=\; \frac{1}{125}\begin{bmatrix} 50 & -45 & 28 & -15 \\ 100 & -60 & 32 & -16 \\ 50 & -15 & 4 & -1 \\ 150 & -45 & 36 & -15 \\ 100 & 0 & 8 & 0 \\ 50 & 15 & 4 & 1 \\ 200 & 0 & 64 & 0 \\ 150 & 45 & 36 & 15 \\ 100 & 60 & 32 & 16 \\ 50 & 45 & 28 & 15 \end{bmatrix} \tag{6.28}$$

The corresponding solution matrices $\underline{\delta}^{-1}$ are

$$\underline{\delta}^{-1}\,(N = 2) \;=\; 1 \tag{6.29}$$

$$\underline{\delta}^{-1}\,(N = 3) \;=\; \frac{1}{4}\begin{bmatrix} 1 & 2 & 1 \\ -6 & 0 & 6 \end{bmatrix} \tag{6.30}$$

$$\underline{\delta}^{-1}(N=4) = \frac{1}{24}\begin{bmatrix} -14 & 13 & 27 & -1 & 13 & -14 \\ -16 & -16 & 0 & 0 & 16 & 16 \\ 64 & -32 & -96 & 32 & -32 & 64 \end{bmatrix} \tag{6.31}$$

$$\underline{\delta}^{-1}(N=5) = \frac{1}{144}\begin{bmatrix} -54 & -6 & 48 & 42 & 96 & 48 & -12 & 42 & -6 & -54 \\ 170 & -290 & -460 & 170 & 0 & 46 & 0 & -170 & 290 & -170 \\ 225 & 75 & -150 & -75 & -300 & -150 & 150 & -75 & 75 & 225 \\ -750 & 750 & 1500 & -750 & 0 & -1500 & 0 & 750 & -750 & 750 \end{bmatrix} \tag{6.32}$$

Figure 6.7 shows an example of focusing an image by means of the MAM algorithm. Radar illumination and near range are from the left side of the image. Figure 6.7(a) shows a SAR image degraded by a composite phase error in azimuth consisting of the sum of 6π rad of quadratic error, 6π rad of cubic error, and -6π rad of quartic (fourth-order) error. The MAM algorithm implementation in this example estimates quartic (and lower order) phase error by dividing the SAR signal history into four nonoverlapping subapertures for autofocus processing. The algorithm initially selects 32 range bins for processing. Figure 6.7(b) shows the corrected image after four iterations of the MAM algorithm. During processing, the algorithm discards 17 of the original 32 bins using a criterion based on one standard deviation of the estimated *quadratic* error coefficient. On each iteration, the algorithm discards those bins with a quadratic estimate that is more than one standard deviation away from the mean quadratic estimate. After four iterations, the final error estimates are 6.07π rad of quadratic error, 6.10π rad of cubic error, and -6.03π rad of quartic error.

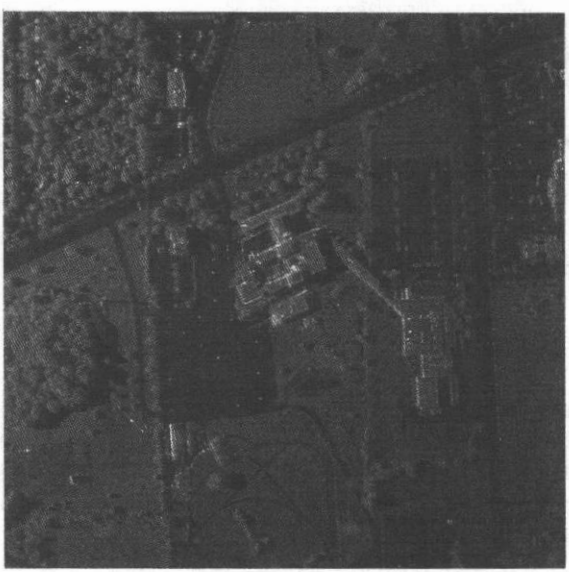
6.3 PHASE DIFFERENCE

Development of the phase difference (PD) algorithm began in the late 1980s [7]. The PD algorithm achieves results comparable to MD with fewer computations. This algorithm is able to generate an accurate quadratic (or higher order) phase error measurement without first cancelling the major portion of the error being measured. This capability eliminates the need for an iterative computation.

This section discusses a simple implementation of the PD, which only estimates QPE. However, extension of this simple implementation of the PD algorithm to estimate higher order errors is possible in a manner similar to the extension of the MD algorithm to the MAM.



(a)



(b)

Figure 6.7 Example of multiple aperture mapdrift autofocus: **(a)** SAR image degraded by composite phase error; **(b)** SAR image after four iterations of multiple aperture mapdrift algorithm.

6.3.1 Overview

The PD algorithm resembles the MD algorithm. Both techniques obtain specific polynomial error coefficients by dividing the processing aperture into two or more subaperture segments. PD and MD differ in the manner in which they manipulate the subaperture data to yield error estimates. MD estimates the error coefficient by determining the relative shift between images formed from each subaperture. PD obtains the error estimate from the Fourier transform of a phase difference function created from the subaperture data. Like MD, the PD algorithm provides a robust estimate of space-invariant QPE. As with MD, it is common to implement the PD algorithm within the image formation chain after motion compensation, data formatting, and range compression.

Figure 6.8 shows the steps in an implementation of the PD algorithm to estimate QPE. PD derives the estimate of the phase error amplitude by dividing the phase history aperture into two azimuth subapertures and multiplying one subaperture by the complex conjugate of the other subaperture from the same range bin. Next, the Fourier transform of the result of this complex multiplication produces the correlation function for each range bin. As with MD, the location of the correlation peak serves as a measure of the relative shift between the images from the two subapertures (although PD does not actually compute the images). Averaging the correlation functions obtained from each range bin yields a good estimate of the QPE without the need for iteration. In this way, PD uses all information in the aperture to derive the error estimate. The PD approach produces a sharper, more discernible cross-correlation peak for a single range bin than does the MD approach. The sharper peak occurs because the conjugate multiplication step of the PD algorithm acts to cancel the common quadratic error across the two subapertures. Averaging over range bins typically yields a better result than using a single iteration of MD. However, MD implementations often make up for this difference through iteration to yield an accurate estimate of the misfocus.

PD estimates a QPE and builds a multiplicative correction vector from the estimate. Application of the same correction vector to the entire aperture of formatted signal history compensates for space-invariant QPE.

6.3.2 Analytical Development

Beginning with the azimuth signal history containing QPE in (6.2), the first step of the PD algorithm divides this signal into two subapertures. The two subaperture signals are $g_1(t)$ and $g_2(t)$ as given in (6.4) and (6.5). The PD algorithm multiplies one subaperture by the complex conjugate of the other subaperture and takes the Fourier transform of the product. This product has the form

$$g_P(t) = g_2(t)\, g_1^*(t) \qquad -\frac{T_a}{4} \le t \le \frac{T_a}{4} \tag{6.33}$$

where T_a is the synthetic aperture duration. The Fourier transform of $g_P(t)$ produces the

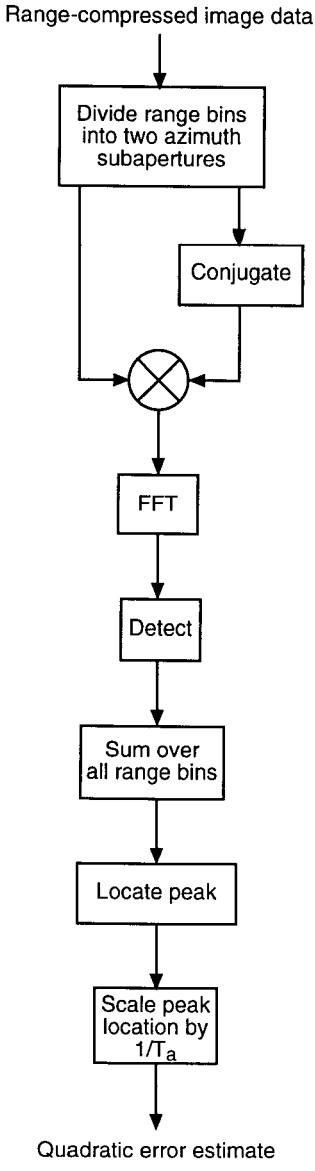


Figure 6.8 Steps in a phase difference autofocus implementation to estimate QPE.

cross-correlation of the complex images from each subaperture in the form

$$G_P(\omega) = \int_{-T_a/4}^{T_a/4} g_P(t)\, e^{-j\omega t} dt = \int_{-T_a/4}^{T_a/4} s\left(t + \frac{T_a}{4}\right) s^*\left(t - \frac{T_a}{4}\right) e^{jaT_a t} e^{-j\omega t} dt \qquad (6.34)$$

In the absence of QPE, the peak of $|G_P(\omega)|$ occurs at zero frequency. With QPE present, the linear phase of the first complex exponential in (6.34) shifts this peak location [7]. The next step averages the magnitude of the correlation function $G_P(\omega)$ over all range bins to increase the signal-to-noise ratio. A determination of the peak location Δ_ω of the averaged correlation function yields an estimate of the QPE coefficient $\hat{a}$ as

$$\hat{a} = \frac{\Delta_\omega}{T_a} \qquad (6.35)$$

Again, Δ_ω can be positive or negative depending on the sign of the QPE.

A principal difference between the PD and the MD algorithms is that PD utilizes the cross-correlation of the *complex* subaperture images given by (6.34) while MD performs a noncoherent cross-correlation of the *intensity* subaperture images. Like the MD and MAM algorithms, the PD algorithm can derive cubic and higher order phase error coefficients by subdividing the signal history aperture into more than two subapertures.

6.3.3 Implementation

The PD procedure uses all range bins to improve the signal-to-noise ratio without needing the iterations common to MD focusing. This procedure generally improves the estimate of space-invariant phase errors over an algorithm that uses only a small percentage of the range bins. Averaging can involve an intensity-weighted average of the individual estimates from each range bin to emphasize error estimates derived from bins with higher energy. An alternative procedure uses the energy in each bin to normalize the correlation peak so that each range bin contributes equally to the overall estimate. In this case, the final estimate is the unweighted average of the estimates from individual range bins.

Use of the PD algorithm to estimate QPE in the misfocused image in Figure 6.4(a) yields an estimate of 7.99π-rad center-to-edge QPE. The actual phase error is 8.00π rad center-to-edge, indicating a small 0.01π-rad residual error.

6.4 PHASE GRADIENT AUTOFOCUS

The phase gradient autofocus (PGA) algorithm for estimating higher order phase errors first appeared in the SAR literature in 1989 [8-11]. The algorithm is unique in that it is not model-based; implementation does not require explicit selection of a maximum order for the phase error being estimated. The PGA algorithm has a well-deserved reputation as a superior algorithm for higher order autofocus. It accurately estimates multicycle phase errors in SAR signal data representing images over a wide variety of scenes.

6.4.1 Overview

Figure 6.9 shows the basic steps in the PGA algorithm. The process begins with the range compressed image and selects a subset of the range bins containing the greatest energy. It performs an azimuth Fourier transform to compress each selected range bin, locates the peak amplitude within each azimuth-compressed range bin, and selects a window of complex pixels from each range bin centered about the azimuth location of the peak amplitude sample. The procedure continues through a number of steps using these groups of pixels from each selected range bin to compute the first derivative (as a function of slow time or azimuth position) of the signal history associated with the windowed image pixels.

These last steps make use of the derivative property of the Fourier transform [5]. This property states that, if $s(t)$ and $S(\omega)$ are a Fourier transform pair denoted by $\Im\{s(t)\} = S(\omega)$, then

$$\Im\{\frac{d}{dt}s(t)\} = j\omega S(\omega) \tag{6.36}$$

Use of this property leads to the first derivative of the time-domain azimuth signal history. Additional steps included in Figure 6.9 fashion this derivative into an estimate of the first derivative of the azimuth phase error as a function of azimuth sample number.

The final step of the PGA algorithm integrates the derivative of the azimuth phase error to calculate the phase error itself as a function of azimuth sample number over the aperture. It is a simple task to convert this estimate of the higher order phase error into an error correction vector. A typical procedure applies the correction vector to the signal history and iterates the algorithm several times on the corrected data in order to reduce residual error.

6.4.2 Analytical Development

To illustrate operation of the PGA algorithm, we consider a single range bin containing one point scatterer. The time-domain signal from the scatterer is

$$g(t) = a_t e^{j[\omega_o t + \phi_o + \phi_e(t)]} \qquad -\frac{T_a}{2} \le t < \frac{T_a}{2} \tag{6.37}$$

Here, a_t, ω_o, and ϕ_o represent the magnitude, frequency, and phase of the signal-history, respectively; the expression $\phi_e(t)$ is the phase error present in the signal history of the scatterer. The PGA algorithm first takes a Fourier transform of the signal in azimuth to obtain

$$G(\omega) = a_t T_a \operatorname{sinc}[T_a(\omega - \omega_o)] e^{j\phi_o} \otimes E(\omega) \tag{6.38}$$

where $E(\omega)$ is the Fourier transform of the complex error function $\exp[j\phi_e(t)]$; the symbol "⊗" denotes convolution. The next step selects and symmetrically windows the

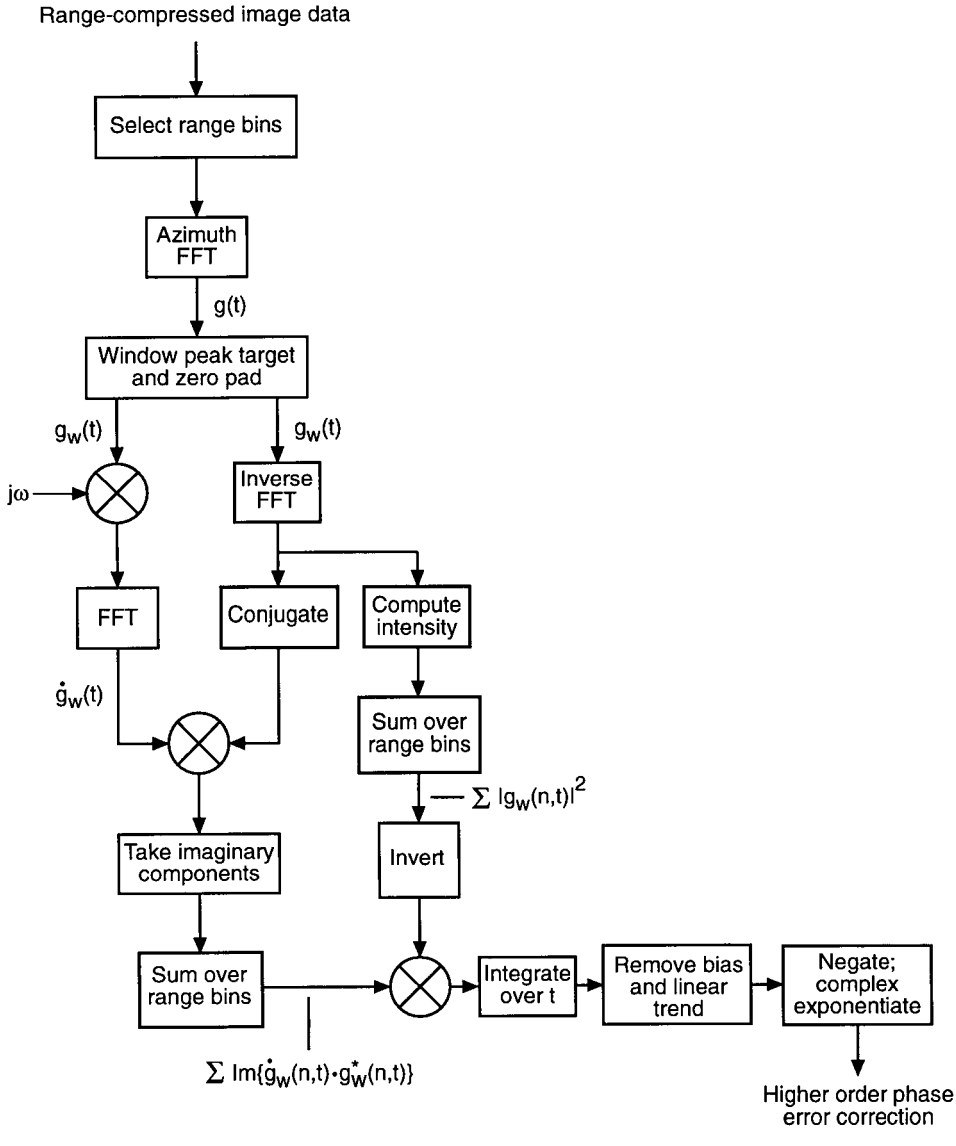


Figure 6.9 Block diagram of the phase gradient autofocus procedure.

peak amplitude pixel within this bin using a weighting function $W(\omega)$ to produce

$$G_w(\omega) = W(\omega - \omega_o)\, a_t T_a \,\mathrm{sinc}\left[T_a(\omega - \omega_o)\right] e^{j\phi_o} \otimes E(\omega) \tag{6.39}$$

Use of the window limits the highest frequency phase error that the PGA is able to estimate and removes other scatterers that could influence the estimate. The high frequency limit decreases as the window length decreases. Taking the inverse Fourier transform of the windowed signal with respect to $\omega - \omega_o$, the PGA process yields

$$g_w(t) = a_t e^{j\phi_o} e^{j\phi_e(t)} \otimes w(t) \tag{6.40}$$

where $w(t)$ is the inverse Fourier transform of $W(\omega)$. The new time-domain function $g_w(t)$ represents the signal history associated with the peak target response in the corresponding image domain. If the window length is long enough to encompass all significant frequency components of $E(\omega)$, then it has little effect on $g_w(t)$ and we can ignore any effects of $w(t)$ in (6.40).

The PGA algorithm also computes the inverse Fourier transform of $j\omega G_w(\omega)$ to obtain the first derivative of $g_w(t)$ via the derivative property of the Fourier transform given by (6.36). For a single point scatterer centered in the window $W(\omega)$, this derivative $\dot{g}_w(t)$ is equal to

$$\dot{g}_w(t) = j\dot{\phi}_e(t)\, g_w(t) \tag{6.41}$$

where $\dot{\phi}_e(t)$ is the time derivative of the phase error. This relationship provides a means to estimate $\dot{\phi}_e(t)$ using the computed values of $\dot{g}_w(t)$.

Assuming the effect of $w(t)$ is small, an estimate of the derivative of the phase error (the phase gradient) in the current example is

$$\hat{\dot{\phi}}_e(t) = \frac{\mathrm{Im}\left[\dot{g}_w(t)\, g_w^*(t)\right]}{\left|g_w(t)\right|^2} \tag{6.42}$$

Integration of (6.42) provides the phase error estimate to within a constant.

For complex scenes containing many range bins, the PGA averages both the numerator and the denominator of (6.42) over many range bins to estimate the gradient. Using N range bins, this estimate has the form

$$\hat{\dot{\phi}}_e(t) = \frac{\sum_N \mathrm{Im}\left[\dot{g}_w(n,t)\, g_w^*(n,t)\right]}{\sum_N \left|g_w(n,t)\right|^2} \tag{6.43}$$

where $g_w(n,t)$ is the signal associated with the windowed target from the n^{th} range bin and $\dot{g}_w(n,t)$ is its derivative. The expression in (6.43) represents a weighted least-squares estimate of the phase error derivative [10].

6.4.3 Implementation

Several variations in implementation of the windowing operation involving $W(\omega)$ in (6.39) offer significant performance improvements in the PGA algorithm. One effective strategy starts the algorithm with a window length much larger than the anticipated phase errors require and reduces the window length on subsequent iterations. The initial window length can include the entire azimuth extent of the image. In this case, the PGA applies the window using circular shifting in such a way that pixels outside of the window extent wrap around to completely fill the window. Typically, each PGA iteration reduces the previous window length between 20 and 50 percent, down to some minimum value. This minimum window value dictates the maximum order phase error that the procedure can estimate. With this strategy, the PGA exhibits excellent performance in estimating phase errors of arbitrarily high order on a wide variety of scenes [11].

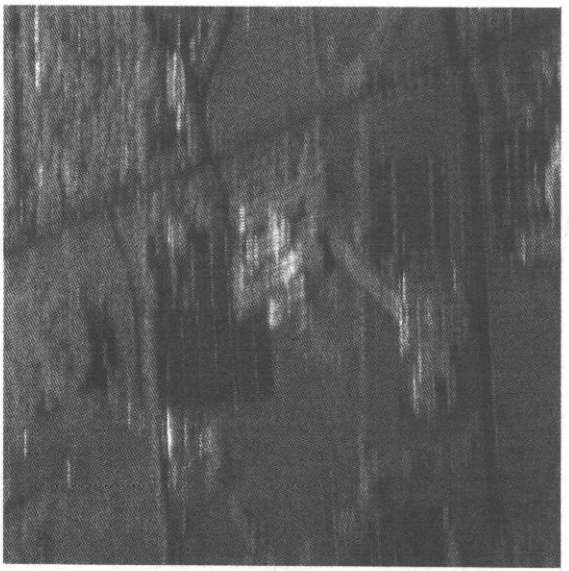
Figure 6.10 demonstrates the use of PGA to perform autofocus in the presence of high-order azimuth phase error across the original signal history. Without autofocus, the signal history produces the image in Figure 6.10(a). Radar illumination and near range are on the left side. Using PGA autofocus on this image yields the result in Figure 6.10(b). Figure 6.10(c) compares the original phase error and the PGA estimate of phase error.

6.5 PROMINENT POINT PROCESSING

One requirement to achieve azimuth phase coherence in SAR data is to account for changes (within a fraction of a wavelength) over time in the distance between the radar APC and the scene being imaged. A second requirement is that the IFP must base the proper formatting of the data on variations in relative aspect angle between the target and the radar over the azimuth processing time. Prominent point processing (PPP) has the potential to accomplish both of these tasks using information in the returned radar signal itself rather than utilizing motion measurement sensors. In this sense, it operates much like an autofocus technique and is considered a refocus technique, although it is not technically *automatic*. Figure 2.19, which outlines the means to achieve azimuth coherence, shows where PPP fits into the scope of fine-resolution spotlight radar imaging.

The PPP technique is an interactive procedure making use of the radar signals returned from the target to obtain azimuth coherence for the SAR signal history. The procedure isolates the signals backscattered from a number of prominent points in the target field. The signal from the first prominent point provides a reference signal to compensate for translational motion effects. Signals from two additional prominent points provide an estimate of rotational motion to improve image quality by aiding data formatting.

It is natural to develop and use the prominent point approach in the framework of the polar format algorithm because the prominent point technique to estimate the image azimuth scale involves the data formatting process. However, single and multiple prominent point implementations are applicable also to spotlight processing with other image formation algorithms.

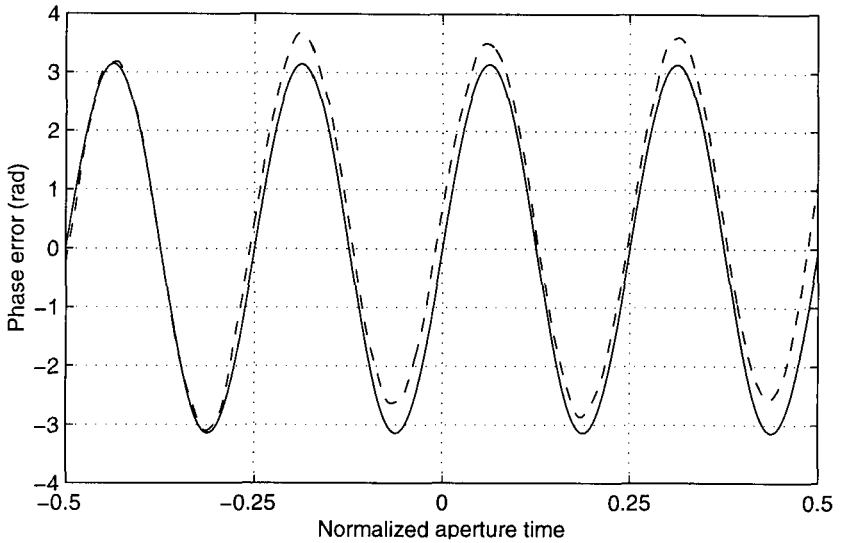


(a)



(b)

Figure 6.10 Example of phase gradient autofocus operation: **(a)** Degraded image; **(b)** Image after eight iterations of PGA.



(c)

Figure 6.10 Example of phase gradient autofocus operation (continued): (c) Induced phase error (dashes) and PGA estimate (solid curve).

Historically, the SAR community has developed and used PPP with a single prominent point to refocus moving targets that are smeared in conventionally processed SAR imagery because of unknown target translations [12]. More broadly, in an airborne SAR data collection, PPP can be useful to augment or replace instrumentation of the SAR antenna to measure its motion. PPP also applies to ISAR imaging of a moving target, with or without motion sensors, from a stationary platform [13]. A multiple prominent point implementation is especially valuable as a means to accomplish both translational and rotational motion compensation (Section 6.5.2).

6.5.1 Single Prominent Point Processing Algorithm

The single PPP algorithm identifies a single dominant point scatterer on the target and measures its pulse-to-pulse range position and phase variation. Using these measurements, the algorithm achieves scene center stabilization (one step in motion compensation) by removing the undesired phase effects of translational motion from the collected signal history. In fact, the algorithm estimates and compensates simultaneously for low- and high-frequency azimuth phase errors from all sources, including undesirable relative motion. There is no need for supplemental autofocus in azimuth unless it is necessary to

compensate for smaller, space-variant effects. The steps of this refocus algorithm are:

1. Identify and isolate a prominent point;
2. Compress (in range) the signal history containing the target;
3. Track the identified prominent point over the aperture time to measure the phase and the range location of its peak response;
4. Use the measurements of the peak location to adjust the frequency of each pulse in the original signal history;
5. Use the measurements of the peak phase to adjust the phase of each pulse in the original signal history;
6. Process the modified signal history with a two-dimensional FFT.

Identification of a prominent point scatterer in the radar signature is possible using either a preliminary, poorly focused, two-dimensional image or the range-compressed signal history. Selection of the prominent point is typically an interactive process requiring user inputs; however, the state of the art is progressing toward automation of this process [14].

In the two-dimensional image domain, a dominant scatterer appears as a poorly focused target which the user of the algorithm must isolate. In the range-compressed signal domain, a scatterer appears as a line meandering across the signal history in the azimuth direction. The sketch in Figure 6.11(a) suggests the appearance of two such prominent point tracks. The algorithm estimates the phase and frequency of the selected scatterer by measuring the phase and the location of its peak response in each range-compressed pulse. It then uses these measurements to adjust the starting phase and the frequency of the SAR signal returned from each transmitted pulse in the original signal history. After these adjustments, the return from the selected prominent point (now the scene center) has zero frequency and constant phase over the entire two-dimensional processing aperture. Range compression of this compensated signal history now generates the signal track of this prominent point scatterer at a constant range. The sketch in Figure 6.11(b) suggests this result. The track of a second target point still meanders somewhat in range during the azimuth aperture interval, particularly in ISAR applications. An azimuth FFT of this range-compressed signal history yields a focused image of the prominent point. The second scatterer, while much improved by the PPP compensation, still does not focus properly. The sketch in Figure 6.11(c) suggests this result with some exaggeration. In SAR and in rotating platform ISAR applications with relatively uniform rotation rates, the track of the second point would likely be much smoother and lead to a better focused image than Figure 6.11 suggests.

An analytical model of this procedure begins with (2.57), following the selection of a prominent point scatterer. This equation indicates that the video signal received from the selected point at pulse n is

$$s_{if1}(n,\hat{t}) = a_1 \text{rect}\left(\frac{\hat{t}-2R_1/c}{T_p}\right) e^{j\Phi_1(n,\hat{t})} \tag{6.44}$$

where range to the selected scatterer $R_1(n)$ replaces $R_t(n)$ and $a_1 = \sqrt{\sigma_1}$ replaces a_t in

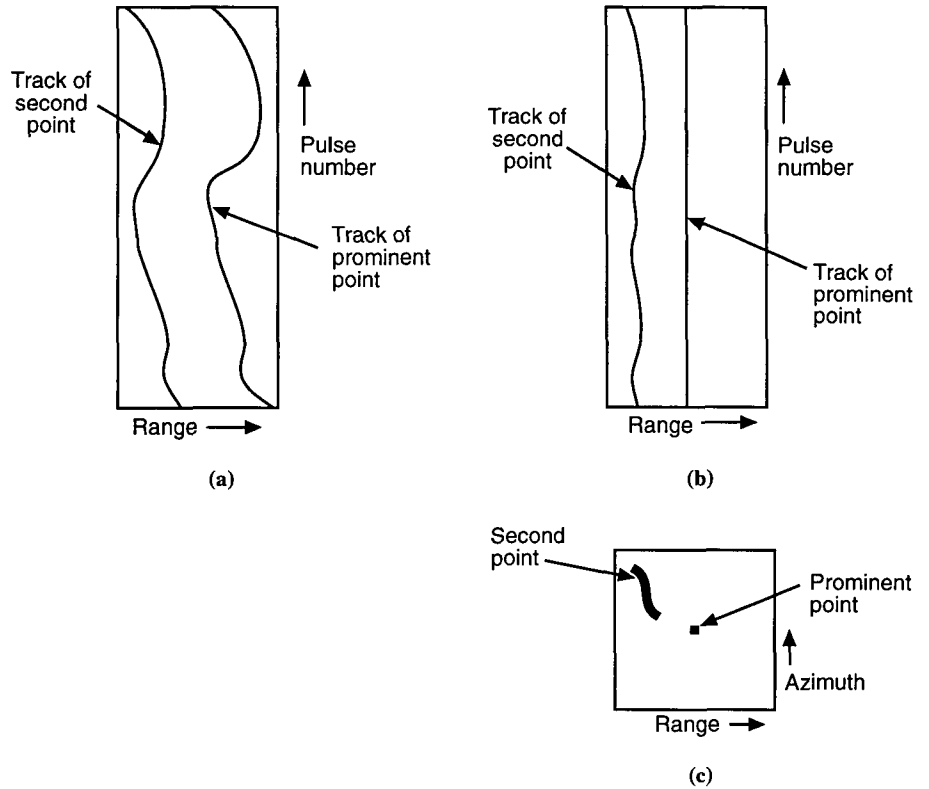


Figure 6.11 Views of prominent point data at various stages in algorithm: **(a)** Tracks before compensation; **(b)** Tracks after compensation; **(c)** Focused prominent point image.

the signal equation. Here, σ_1 is the radar cross-section of the point scatterer. The phase of this signal, $\Phi_1(n, \hat{t})$ has the form

$$\Phi_1(n,\hat{t}) = -\frac{4\pi\gamma}{c}\left(\frac{f_c}{\gamma}+\hat{t}-\frac{2R_o}{c}\right)(R_1-R_o)+\frac{4\pi\gamma}{c^2}(R_1-R_o)^2 \tag{6.45}$$

The quantity $R_o(n)$ is the reference range used to dechirp the received signal.

The second step in the algorithm is to Fourier transform $s_{if1}(n,\hat{t})$ for each pulse in fast time over the parameter $\hat{t}-2R_o(n)/c$. This procedure compresses the signal in range. The result is

$$S_{if1}(n,f_{\hat{t}}) = a_1 T_p \operatorname{sinc}\left[T_p\left(f_{\hat{t}}+\frac{2\gamma}{c}R_{1o}\right)\right] e^{-j\frac{4\pi f_c}{c}R_{1o}} e^{-j\frac{4\pi\gamma}{c^2}R_{1o}^2} e^{-j\frac{4\pi f_{\hat{t}}}{c}R_{1o}} \tag{6.46}$$

using $R_{1o} = R_1 - R_o$ for convenience. The peak intensity of the signal $S_{if1}(n, f_{\hat{t}})$ occurs at $f_{\hat{t}} = -2\gamma R_{1o}/c$. Measurement of this location provides an estimate of the instantaneous differential range R_{1o} between the selected point and the reference range $R_o(n)$. A cross-correlation of the range-compressed returns from successive pulses determines the pulse-to-pulse changes in peak location. At this point, it is acceptable to either subtract off a range frequency term in the original signal history or move the compressed pulses in range using an interpolation routine to align successive pulses. Figure 6.11(b) suggests the result of such an alignment. The necessary frequency adjustment to (2.57) is to multiply by a complex exponential having a phase Φ_{adj} given by

$$\Phi_{adj} = \frac{4\pi\gamma}{c}(R_1 - R_o)\left(\hat{t} - \frac{2R_o}{c}\right) \tag{6.47}$$

The next step of the algorithm is to measure the phase of the peak response of the point. The phase of (6.46) at the peak location is

$$\Phi_{pk1}(n) = -\frac{4\pi f_c}{c}(R_1 - R_o) + \frac{4\pi\gamma}{c^2}(R_1 - R_o)^2 \tag{6.48}$$

The result of multiplying the signal history $s_{if}(n, \hat{t})$ in (2.57) by the frequency adjustment described in (6.47) and by a complex exponential having a phase that is the negative of Φ_{pk1} in (6.48) is

$$s_{if}(n, \hat{t}) = a_t \text{rect}\left(\frac{\hat{t} - 2R_t/c}{T_p}\right) e^{-j\frac{4\pi\gamma}{c}\left(\frac{f_c}{\gamma} + \hat{t} - \frac{2R_1}{c}\right)(R_t - R_1)} e^{j\frac{4\pi\gamma}{c^2}(R_t - R_1)^2} \tag{6.49}$$

for the general scatterer at location (X_t, Y_t, Z_t) and range R_t. This process stabilizes a scene center scatterer (for which $R_t = R_1$) to give any signal from this scatterer a constant phase and zero frequency.

The last step of the single PPP algorithm is to compress this composite signal history in both dimensions (over the azimuth coherent aperture interval as well as the range window). This compression via the two-dimensional Fourier transform focuses the selected prominent point and causes it to appear at the center of the resulting image in Figure 6.11(c).

If the target's relative rotation rate is essentially constant over the coherent data processing interval, this single point compensation alone provides an approximately focused image, especially when the target is small enough that polar formatting is not required. However, when the incremental change in rotation angle is not constant from pulse to pulse, a position-dependent blurring or defocusing of scatterers generally occurs.

In this situation, the IFP must base proper formatting of the data in azimuth on *a priori* knowledge or auxiliary information (such as a flight plan or onboard navigation

data) regarding the variations in relative aspect angle between the target and the radar over the azimuth processing time. In the absence of such information, the processor must assume a constant, arbitrary rotation rate.

Azimuth scale, relating image and target distances in the azimuth direction, depends on this rotation rate; therefore, azimuth scale accuracy depends on auxiliary data accuracy. However, range scale, relating image and target distances in the range direction, is independent of relative motion. Thus, range scale accuracy in PPP is equivalent to that in a motion measurement implementation.

6.5.2 Multiple PPP Algorithm

A multiple PPP image formation algorithm is a powerful approach to achieve signal coherence in azimuth without motion sensors [12, 15]. A well-designed multiple PPP algorithm is able to achieve the desired signal phase coherence in the presence of variations in target rotational motion as well as translational motion. Such an algorithm also estimates the azimuth scale of an ISAR image because it estimates target rotation rate. Another possible way to estimate the azimuth scale factor is to compare the signature of a processed image to the known target extent or size of a distinctive target feature. In contrast, motion compensation of ISAR data from a target instrumented with a motion sensor is able to use measured motion data to avoid this difficulty.

Figure 6.12 provides a simplified block diagram of the multiple PPP algorithm in a typical implementation. Preprocessing activities may include data type conversion, digital quadrature demodulation, and removal of deterministic phase errors in range. Section 7.2 discusses these preprocessing operations in the context of a ground-based ISAR system that images airborne targets.

Initial motion compensation involves the use of whatever data is available. If the PPP application is to image a ground-moving target illuminated during a conventional airborne SAR collection, conventional motion compensation is appropriate utilizing data from the SAR system motion sensor. After conventional processing and extraction of an image chip to include the moving target, additional motion compensation based on any knowledge of the target's movement is a possibility. For instance, it may be useful to assume that the target was traveling at a nominal velocity on a particular road. If the PPP application involves ISAR imaging of a passing aircraft, initial motion compensation utilizing auxiliary information (such as a flight plan, onboard navigation data, or data from an auxiliary tracking sensor) is appropriate. When such data is unavailable, the PPP algorithm generally is able to proceed without it.

Following initial motion compensation and conventional processing, this algorithm sequentially identifies and works with the radar signals from three prominent points on the target. This activity involves a series of three procedures, one related to each prominent point, to account for both translational and rotational motions and to estimate accurately the azimuth scale of the image. The first prominent point provides data to measure and remove translational motion effects. This procedure involves the same steps as the single prominent point algorithm, adjusting the phase and frequency of each pulse in the original

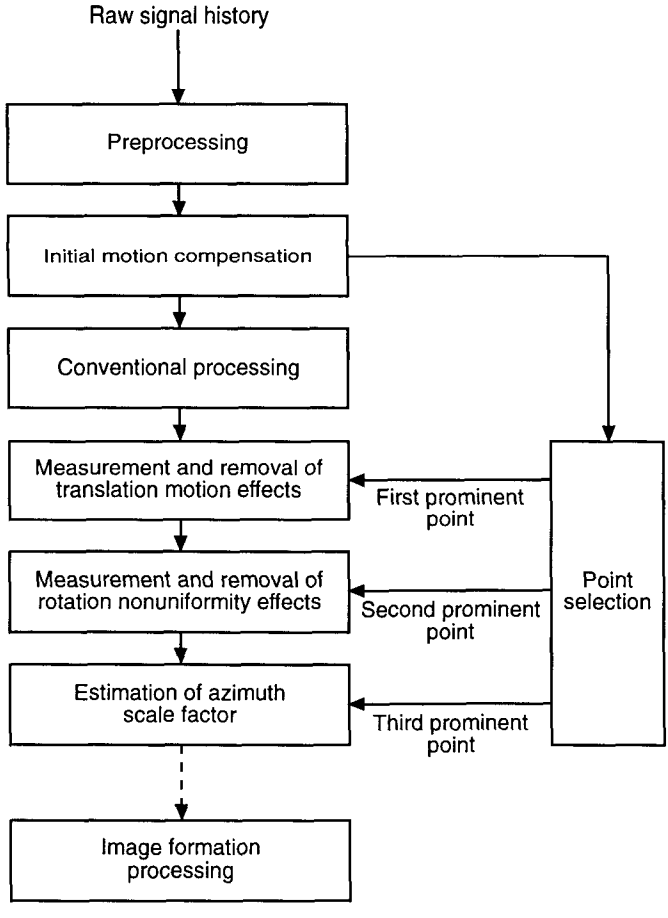


Figure 6.12 Block diagram using multiple PPP algorithm in SAR image formation.

signal history to make the first prominent point become scene center. The second prominent point begins with this adjusted phase history to provide data to estimate and remove the effects of any nonuniformity in the rotation rate of the scene relative to the radar line-of-sight to this new scene center. The steps in using the second prominent point are:

1. Compress the signal history in range;
2. Select a second prominent point and identify its track;
3. Isolate the track of the second prominent point over the aperture time and measure the phase of its peak response for each pulse;
4. Unwrap the phase of the second prominent point over the azimuth aperture;
5. Resample (interpolate) the signal history in azimuth to make the phase of the second prominent point linear in sample number.

Use of the third prominent point begins with this resampled signal history and provides a measure of the actual rotation rate. This measurement leads to an estimate of the azimuth scale factor of the resulting image. The steps involving the third point are:

1. Compress the signal history in range;
2. Select a third prominent point and identify its track;
3. Isolate the track of the third prominent point over the aperture time and measure the phase of its peak response for each azimuth sample;
4. Estimate the component of this phase variation, which is quadratic over sample number;
5. Calculate the display squint angle interval based on the estimated quadratic phase coefficient.

The last block in Figure 6.12 is the image formation processor. Its two steps are:

1. Polar format the signal history;
2. Reprocess the polar-formatted data to achieve the final image.

These IFP steps involve conventional processing operations. Measurements derived from the prominent point signals, rather than radar auxiliary data, provide information for the two-dimensional signal formatting operation.

The beginning stages of an analytical model of the multiple PPP algorithm are identical to the analytical model of the single PPP technique, leading to (6.49). The multiple PPP algorithm now requires the selection of a second prominent point on the target. Using (6.49), the phase of the second point is

$$\Phi_2(n,\hat{t}) = -\frac{4\pi\gamma}{c}\left(\frac{f_c}{\gamma}+\hat{t}-\frac{2R_1}{c}\right)(R_2-R_1)+\frac{4\pi\gamma}{c^2}(R_2-R_1)^2 \tag{6.50}$$

where $R_2(n)$ is the range from the APC to the second point. The next step is a Fourier transform of each pulse with respect to $\hat{t}-2R_1(n)/c$ in order to compress the signal in range. The result is

$$S_{if2}(n,f_{\hat{t}}) = a_2 T_p \operatorname{sinc}\left[T_p\left(f_{\hat{t}}+\frac{2\gamma}{c}R_{21}\right)\right] e^{-j\frac{4\pi f_c}{c}R_{21}} e^{-j\frac{4\pi\gamma}{c^2}R_{21}^2} e^{-j\frac{4\pi f_{\hat{t}}}{c}R_{21}} \tag{6.51}$$

using $R_{21} = R_2 - R_1$, for convenience. The next step isolates the track of the peak response of the second point and measures its phase. The peak occurs at $f_{\hat{t}} = -2\gamma R_{21}/c$, providing a rough estimate of the instantaneous differential range R_{21} between the new selected point and the new reference range $R_1(n)$. The phase of (6.51) at this peak location is

$$\Phi_{pk2}(n) = -\frac{4\pi f_c}{c}R_{21}+\frac{4\pi\gamma}{c^2}R_{21}^2 \tag{6.52}$$

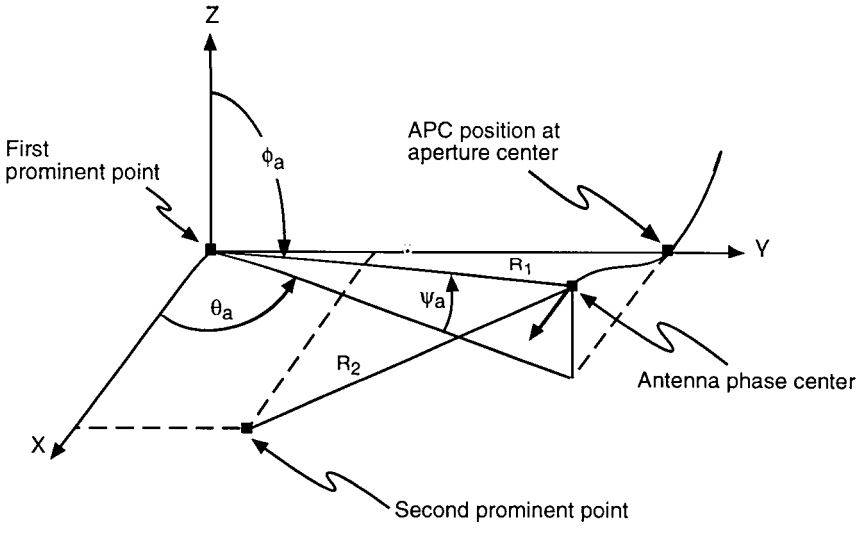


Figure 6.13 Model of data collection geometry associated with PPP.

Because the size of R_{21} is limited to the target size, it is generally acceptable to neglect the phase term in R_{21}^2 in (6.52) as being small. On this basis, the process of unwrapping the phase of this point scatterer from pulse-to-pulse yields an estimate of the variation in differential range between the two selected prominent points as a function of pulse number.

Figure 6.13 identifies a useful data collection geometry model based on these two prominent points. The first prominent point, which becomes scene center, is the origin of the target-fixed XYZ coordinate system. The Y axis passes through the APC position at the center of the azimuth aperture interval. In general, the location of the second prominent point is not known. However, it is possible to place it in the XY plane of this model by appropriate selection of the X axis. The XY plane now contains the set of three points consisting of the first and second prominent points and the APC position at aperture center. Within this coordinate system, the second prominent point has coordinates $(x_2, y_2, 0)$. The model follows Figure 3.17(a) with instantaneous squint angle θ_a and incidence angle ϕ_a.

Now, an expression for R_{21} is needed for use in (6.52). The approximation

$$R_{21} \approx -x_2 \cos(\theta_a) \sin(\phi_a) - y_2 \sin(\theta_a) \sin(\phi_a) \tag{6.53}$$

is available based on (3.105). Generally, it is reasonable to limit the processing aperture to keep variations in θ_a and, hopefully, ϕ_a small enough to utilize small-angle approximations in (6.53). Because each of these angles is centered near a value of $\pi/2$ rad, the use of small-angle approximations leads to

$$R_{21} \approx -x_2 \cos(\theta_a) - y_2 + \frac{y_2}{2}\left(\theta_a - \frac{\pi}{2}\right)^2\left(\phi_a - \frac{\pi}{2}\right)^2 \tag{6.54}$$

Additionally, operating in the range-compressed domain, it is possible to select the second point such that y_2 is small. On this basis, a further approximation of (6.54) yields

$$R_{21} \approx -x_2 \cos(\theta_a) - y_2 \tag{6.55}$$

Now, use of (6.52) and (6.55) yields the result

$$\Phi_{pk2}(n) \approx \frac{4\pi f_c}{c}\left[x_2 \cos(\theta_a) + y_2\right] \tag{6.56}$$

Polar formatting of the SAR signal data requires an expression for the variation in θ_a from pulse-to-pulse. Use of (6.56) for pulse $n = N_p/2$ (aperture center) yields an expression relating change in Φ_{pk2} and change in θ_a. This expression is

$$x_2 \cos\left[\theta_a(n)\right] = \frac{c}{4\pi f_c}\left[\Phi_{pk2}(n) - \Phi_{pk2}\left(\frac{N_p}{2}\right)\right] \approx -x_2 \Delta\theta(n) \tag{6.57}$$

where $\Delta\theta(n)$ is the instantaneous value of $\theta_a(n)$ minus its value at aperture center $\theta_a(N_p/2)$, which is 90 deg. The approximation in this equation is reasonable because θ_a is near 90 deg and changes over only a small angular interval. The change in $\cos(\theta_a)$ is proportional to the change in the unwrapped phase of the second prominent point. However, the constant of proportionality, which is the X coordinate x_2 of the second prominent point, is unknown. Without this constant, it is not possible to polar format the data properly. However, it is possible to format it with the spacing in azimuth proportional to changes in θ_a using a nominal, or best guess, value for x_2. At this point, it is possible to compress the data in both dimensions to obtain a reasonable image.

Figure 6.14(a) indicates an example variation in the unwrapped phase with pulse number. Figure 6.14(b) indicates the necessary positioning of collected pulses to obtain samples at equally spaced intervals of Φ_{pk2} in a modified pulse number coordinate v. In this new format, the approximate relationship in (6.57) suggests that $\Delta\theta = kv$ with k an unknown constant of proportionality. Figure 6.14(c) illustrates the appearance of the prominent point tracks after this resampling of the data. The track of the second prominent point is now slowly and smoothly curved. If the target size is less than $4\rho_a^2/\lambda_c K_a$ then, from (3.7), the data does not require polar formatting; it will produce a well-focused image. However, the azimuth scale factor of the image is not known. Although the procedure linearizes the rotation rate, it does not estimate the value of this constant rotation rate. Thus, the procedure does not estimate the azimuth angular interval which determines azimuth resolution and azimuth scale factor. If the target is large enough, defocus will be evident away from scene center. Figure 6.14(d) illustrates this possibility.

It is often possible to determine this scale factor when target size is large enough to require polar formatting and the data collection involves little rotation out of the XY plane in Figure 6.13. To estimate the azimuth scale factor, the algorithm uses a third prominent

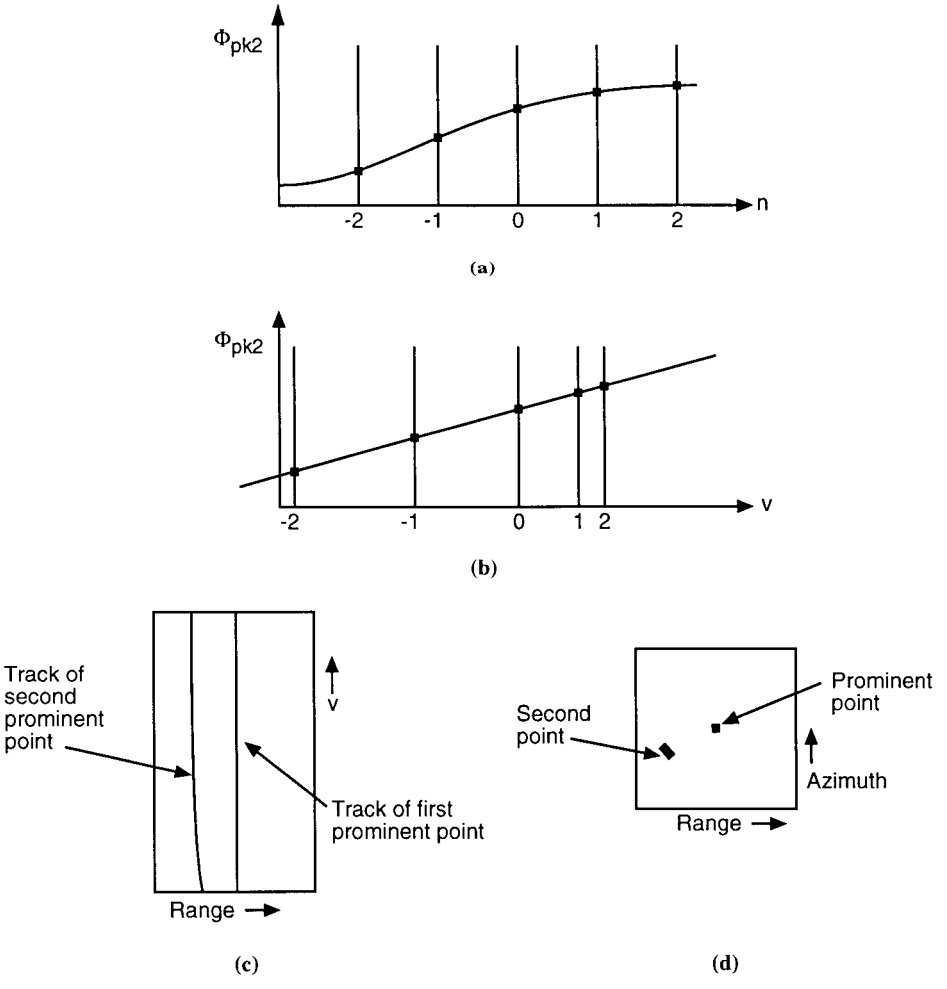


Figure 6.14 Views using second prominent point: **(a)** Unwrapped phase $\Phi_{pk2}(n)$ of second prominent point; **(b)** Variation in pulse spacing to make $\Phi_{pk2}(v)$ linear in v; **(c)** Tracks after use of the second prominent point; **(d)** Appearance of image of two prominent points.

point at coordinates (x_3, y_3, z_3) with no indication of the size of z_3. The process begins with the signal data following stabilization of the first prominent point using (6.47) and (6.48) and nonlinear interpolation in azimuth (over pulse number) to resample Φ_{pk2} at equal increments in v based on (6.57). Figure 6.15(a) illustrates the relationship between v and θ_a after this interpolation. Again, the procedure compresses the signal history in range and measures the phase of the peak response of the third prominent point for each azimuth

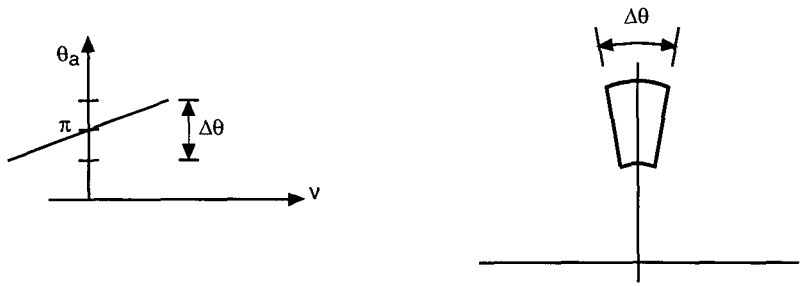


Figure 6.15 Use of squint angle and polar format: **(a)** Squint angle as a function of new azimuth coordinate; **(b)** Polar formatting of data.

sample. The peak phase is approximately

$$\Phi_{pk3}(v) \approx -\frac{4\pi f_c}{c}(R_3 - R_1) \tag{6.58}$$

Similar to (6.53) but with a nonzero Z coordinate, an expression for $R_3 - R_1$ is

$$R_3 - R_1 \approx -x_3 \cos(\theta_a) \sin(\phi_a) - y_3 \sin(\theta_a) \sin(\phi_a) - z_3 \cos(\phi_a) \tag{6.59}$$

Use of $\theta_a = 0.5\pi + kv$ rad, the grazing angle $\psi_a = 0.5\pi - \phi_a$ rad, and the fact that θ_a, ϕ_a, and ψ_a change over small angles leads to the approximation of (6.59) as

$$R_3(v) - R_1(v) \approx x_3 kv - y_3 + \frac{y_3}{2}\left[k^2 v^2 + \psi_a^2(v)\right] - z_3 \sin\left[\psi_a(v)\right] \tag{6.60}$$

In the situations where ψ_a is constant, the coefficient of the quadratic component of this equation is $y_3 k^2/2$. From (6.58), an estimate of this quadratic component is available from the phase measurements of the third prominent point. Therefore, a measure of the scaling factor k is available since y_3 can be measured from the image as the differential range between the third and first prominent points. If K_q is the estimated quadratic phase coefficient, then an estimate of k is available from

$$k = \sqrt{\frac{-cK_q}{2\pi f_c y_3}} \tag{6.61}$$

As (6.60) indicates, significant variations in ψ_a will contribute an error to (6.61). Even then, (6.61) often provides a useful estimate as long as the variations in ψ_a are smaller than, or of comparable size to, the interval $\Delta\theta$. Figure 6.15(b) illustrates the appropriate polar data format using the estimate of $\Delta\theta$.

Three major attributes are desirable for a successful application of the multiple PPP algorithm. First, an implementation of the full algorithm requires three prominent points, each being on the order of 10 dB above the local background. These points ideally are diffraction-limited and rigidly joined point scatterers. Second, for reliable angle estimates, it is desirable that the axis of rotation be oriented approximately in a fixed direction. For three-dimensional targets, it is also desirable that the rotation be nearly perpendicular to the radar line-of-sight. Third, to measure azimuth scale factor it is necessary that the target diameter be large enough to require polar format.

The availability of a strong, isolated scatterer to select as the first prominent point is critical to algorithm performance. At this stage in the algorithm, extremely large phase errors and associated smearing are likely to be present in the signal history. The signatures of various scatterers probably overlap each other and any background clutter.

A proper strategy in choosing the locations of the second and third prominent points relative to the first prominent point will improve algorithm performance. The second prominent point should have a relatively small y_2 component to validate the approximation made in (6.55). The third prominent point should have a relatively large y_3 component to provide a measurable phase effect in (6.60) for estimating target rotation.

The third prominent point and polar formatting may be unnecessary for smaller targets; this simplification limits a large two-dimensional interpolation operation to one dimension only. It may be possible to avoid use of the second prominent point and azimuth interpolation with limited image quality impact. This change will simplify the algorithm and completely eliminate the use of interpolation. In this case, the multiple prominent point algorithm collapses to the single point algorithm of Section 6.5.1.

Automation of the prominent point selection procedure is an active area of current research. Reference [14] describes one applicable technique based on a likelihood ratio for the detection of target scattering centers. This technique uses a score, computed from the likelihood ratio, to indicate the presence of scattering centers, which it then tracks over an aperture via a dynamic programming algorithm.

6.5.3 Selection of Prominent Points

The single prominent point implementation and the first procedure in the multiple PPP algorithm use the return signal from a selected scatterer as the receiver reference function. Ideally, this scatterer is point-like with a complex radar reflectivity that is constant in amplitude and phase over the azimuth processing interval. Also, it is dominant in magnitude over the sum of all other signals in the same range bin in its range-compressed, azimuth signal history space. If a prominent point signal is not dominant relative to the summation of same-range targets, it will not provide an accurate reference phase. Such contamination will introduce high-frequency and low-frequency phase errors in the signal history. These errors may cause target defocus, increased sidelobe energy in the processed image, and a compromise of the relationship between scatterer radar cross-section (RCS) and image peak intensity. Additional discrete targets in the range bin of the selected prominent point will introduce spurious targets (high sidelobes) both in this range bin and about

all other targets in the image. As the prominent point becomes more "prominent" or dominant, perhaps greater than 10 dB in intensity above its range bin competitors, these effects become much less serious. An advanced prominent point algorithm may include a preliminary procedure to reduce the level of interfering signals in the same range bin as the prominent point scatterer. Such a procedure may involve bandpass filtering in the signal domain or spatial filtering in the image domain. In either case, the intent is to limit the azimuth extent of the scene which contributes signals to the range bin occupied by the prominent point.

Selection of a scatterer that is not point-like as the prominent point will degrade image focus and compromise the relationship between scatterer RCS and image intensity, even if it is the only target in the selected range bin. This effect may result in serious degradation if the scatterer selected as the prominent point is not a point scatterer but rather a more complex target within that range resolution cell. An advanced prominent point algorithm may have a set of criteria by which to test a scatterer before accepting it as a prominent point. For instance, the algorithm may reject a return as a prominent point if its amplitude after range compression is not relatively constant from pulse to pulse.

6.6 SPACE-VARIANT REFOCUS

The four autofocus algorithms described above and the single PPP algorithm estimate and apply the same compensation to all targets within the entire image. However, in some SAR and ISAR imaging applications, position-dependent phase errors are dominant and space-variant autofocus becomes a necessity. Space-variant autofocus is inherently challenging because most autofocus algorithms rely on averaging over many scatterers. Generally, larger scenes with space-invariant phase errors offer improved algorithm performance in terms of error estimation accuracy. The common approach to space-variant autofocus is to break a large scene into smaller, possibly overlapping, subimages such that the error present on each subimage is approximately invariant. Each of the small subimages is focused independently using one of the conventional space-invariant autofocus procedures. Upon refocus, individual subimages are reassembled or mosaicked together to yield the full-scene focused image. This approach to space-variant refocus is viable when the space-variant characteristics of the error vary slowly with scene position. Assuming phase errors in azimuth, the procedure is simple if the space-variance depends only on the image range coordinate. It is more difficult when the space-variance depends on the image azimuth coordinate.

An example of the need for space-variant refocus is the imaging of a moving rigid-body target. Space-variant refocus is a possibility because the motion of all scatterers is correlated by the rigid-body nature of the target. In this situation, the multiple PPP algorithm effectively accomplishes space-variant refocus.

Space-variant techniques are also applicable to correct the height-variant azimuth defocus caused by the height-of-focus phase error (Section 3.3.4). This phase error arises in the SAR image of a stationary three-dimensional target in the presence of nonplanar platform motion during the coherent aperture time. However, the space-variance is not

necessarily correlated with image coordinates because scatterer height can be independent of range and azimuth position from image pixel to image pixel. Such a lack of correlation complicates any space-variant compensation. Space-variant autofocus is possibly viable in mapping applications when terrain elevation varies smoothly in range and azimuth, such as when imaging regions with gently sloping terrain or rolling hills.

Limitations and approximations in the image formation algorithm are another source of space-variant phase errors. Such errors are deterministic, yet do not lend themselves easily to compensation in the normal processing signal chain. This situation arises, for instance, with QPE induced by range curvature and polar format processing (Section 3.7). The range curvature phase error is zero at scene center and gradually increases in severity with scatterer distance away from scene center. For SAR systems that do not implement space-variant autofocus, this error source imposes a limit on scene size processed with the polar format algorithm.

Space-variant refocus is also required when imaging targets that experience significant bending, vibration, or other nonrigid-body motion. Examples of such targets include a train moving on a curved track, vibration of an aircraft's wings during flight or while taxiing on a rough runway, and the flexure of a ship in choppy water. These situations involve nonrigid-body motion that is correlated over the target area of interest. The multiple PPP procedure is not applicable to these situations because the algorithm assumes a rigid-body relationship between the three selected prominent points.

In the preceding applications, space-variant compensation by division of the image into subimage patches is possible when the phase error coefficients vary smoothly with spatial coordinates of the image and the error estimation procedure performs adequately over the smaller subimage size. When the space-variance is spatially correlated and slowly varying with image position, we differentiate between two subcases. In the first subcase, the space variance is one-dimensional and orthogonal to the resulting phase error coordinate. An example is a motion-induced azimuth phase error whose magnitude and shape vary slowly with target range coordinate. The target geometry in Figure 6.16(a) suggests this situation. It involves three rigid-body, flexibly joined "train cars" negotiating a tight curve while traveling in range. The radar illuminates the scene from the bottom of the figure. A conventionally processed image of the train is well focused only at the apex of the curve. Scatterers become increasingly defocused as their range separation from the apex increases, as Figure 6.16(b) suggests. (Although not relevant to the current discussion, the train image is also displaced in azimuth due to the moving target effects discussed in Section 5.5.) The distinguishing feature here is that the processor can divide the image into range subswaths and focus each subswath separately. Figure 6.16(b) shows three such subswaths, labeled A, B, and C. The processor can use a space-invariant autofocus algorithm separately on each subswath to estimate phase error coefficients for the subswath. The processor then refocuses each subswath and reassembles or mosaicks them together to yield a full-scene focused image.

In the second subcase, the distinguishing feature is that this space-variant coordinate is not orthogonal to the resulting phase error. The space-variance can be one-dimensional with two-dimensional variance as a possible generalization. Figure 6.17(a) suggests this

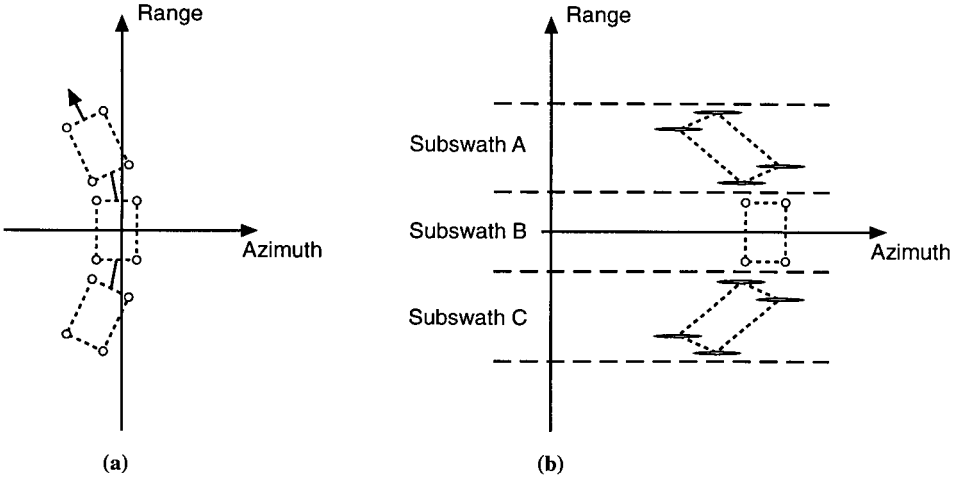


Figure 6.16 Illustration with phase error orthogonal to motion: **(a)** Radar/target geometry with illumination from the bottom; **(b)** Image geometry.

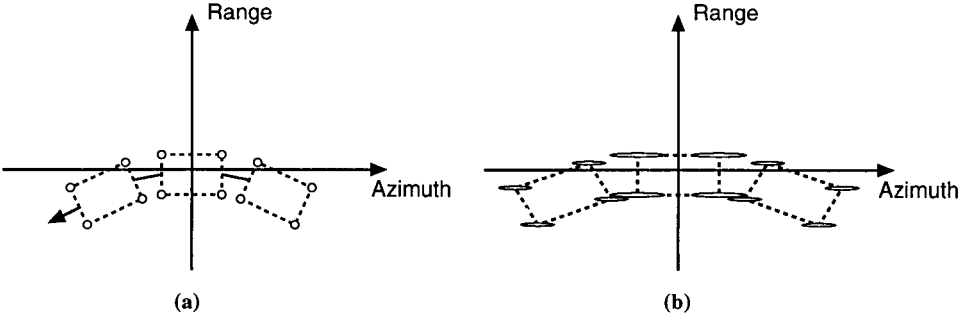


Figure 6.17 Illustration with phase error that is not orthogonal to motion: **(a)** Radar/target geometry with illumination from the bottom; **(b)** Image geometry.

situation. The added difficulty in this subcase is evident. The three flexibly joined vehicles are moving in azimuth. Radar illumination is from the bottom. As Figure 6.17(b) indicates, the space-variance and defocus are both in azimuth. This fact makes it difficult to subdivide the image into subimages consisting of azimuth subswaths because the smeared returns from individual scatterers would be divided among adjacent subimages.

It may be possible and desirable to uncouple the two steps of autofocus, *estimation* and *compensation*, for the space-variant case. In particular, the source of space-variant defocus may be predictable from collateral information such as structural modeling in the

case of nonrigid-body motion. The source might also be deterministic, as is the case for space-variant QPE induced by range curvature and polar format processing. In either case, the real challenge is implementation of a known space-variant compensation function. Such a step is achieved by brute force when it is possible to segregate the imagery from each class of scatterers (a class consisting of members requiring the same refocus coefficients) for application of the appropriate compensation.

6.7 SUMMARY

With the increase in SAR system performance requirements in recent years, automatic refocusing techniques have become increasingly important to avoid degradation in azimuth impulse response. The availability of autofocus permits the SAR system to meet its image quality requirements over a wider operating envelope. Alternatively, autofocus provides a system alternative to attain a specific image quality level with lower fidelity motion measurement instrumentation. The ultimate use of this alternative is in noncooperative ISAR applications that deduce all relative motion entirely from the radar signal data without any motion-sensing instrumentation.

The SAR community has proposed and investigated a number of autofocus algorithms over the years. These algorithms possess varying degrees of sophistication, maturity, and practicality. Table 6.1 summarizes and compares five of these algorithms discussed in this chapter. The use of Table 6.1 requires caution, however, since comparison and evaluation of the algorithms are made difficult by the fact that performance generally varies with scene content and phase error characteristics.

The MD and PD algorithms are viable techniques to measure and remove QPE. Each algorithm provides robust performance over a wide variety of scenes, including both scenes with distinctive (cultural) targets and scenes consisting largely of distributed background terrain. Each algorithm has a large "pull-in" range, defined as the largest magnitude phase error that an algorithm is able to estimate. The two algorithms exhibit similar performance in every category, although MD has a slight edge with its lower computational complexity in many applications. It is feasible to extend each algorithm to handle higher order phase errors up to approximately fifth-order polynomial terms. Extension of the quadratic MD algorithm to higher orders results in the MAM algorithm.

The PGA algorithm exhibits an excellent capability to remove higher order phase errors over a variety of scenes. Although PGA works best on cultural targets, experience indicates robust performance on scenes with a large background clutter content as well.

The PPP algorithms are able to reduce all categories of phase errors if a sufficient number of dominant scattering centers are available on an imaged target or within an imaged scene. The single PPP algorithm corrects space-invariant phase errors, while a version of the algorithm using two prominent points provides a full motion compensation function including angular positioning for both SAR and ISAR applications. A third prominent point is necessary to estimate the azimuth scale factor relating target size to image size in azimuth. Development of practical strategies to automate PPP is an active area of research within the SAR community.

In some imaging applications, position-dependent phase errors are significant and space-variant autofocus is a necessity. A space-variant autofocus technique, such as subscene processing, may be viable depending on the frequency, magnitude, and variation with image spatial coordinates of the phase error.

Table 6.1
Summary of Autofocus Algorithms

Algorithm	*Phase Error Constraints*	*Advantages*	*Disadvantages*
Mapdrift	Quadratic	• Simple implementation • Robust • Good performance on clutter • Large pull-in range • Highly accurate • Low computation	• Quadratic only
Multiple aperture mapdrift	Up to fifth order	• Good performance on clutter • Large pull-in range	• High computation • Performance degrades with increased model order
Phase difference	Quadratic	• Simple implementation • Robust • Good performance on clutter • Large pull-in range • Highly accurate • Non-iterative	• Quadratic only • Moderate computation
Phase gradient autofocus	Arbitrarily high	• Large pull-in range • Robust • Good performance on clutter • Not model based	• Moderate to high computation
Prominent point processing	None	• Highly accurate • Estimates errors caused by any type of unknown motion or other error source • Estimates azimuth scale factor (resolution)	• Interactive (not automatic) • Performance is signature dependent (requires up to three prominent points) • High computation for multiple point algorithm

REFERENCES

[1] Mancill, C.E., and J.M. Swiger, "A Map Drift Autofocus Technique for Correcting Higher Order SAR Phase Errors (U)," *27th Annual Tri-Service Radar Symposium Record*, Monterey, CA, June 23-25, 1981, pp. 391-400.

[2] Curlander, J.C., C. Wu, and A. Pang, "Automated Processing of Spaceborne SAR Data," *Proceedings of IGARSS'82*, Munich, Germany, June 1982, pp. FA-1: 3.1-3.6.

[3] Brown, W.D., and D.C. Ghiglia, "Some Methods for Reducing Propagation-Induced Phase Errors in Coherent Imaging systems. I. Formalism," *Journal of the Optical Society of America A*, Vol. 5, No. 6, June 1988, pp. 924-942.

[4] Ghiglia, D.C., and Brown, W.D., "Some Methods for Reducing Propagation-Induced Phase Errors in Coherent Imaging Systems. II. Numerical Results," *Journal of the Optical Society of America A*, Vol. 5, No. 6, June 1988, pp. 943- 957.

[5] Oppenheim, A.V., and R.W. Schafer, *Digital Signal Processing*, Englewood Cliffs, NJ, Prentice-Hall, Inc., 1975.

[6] Strang, G, *Linear Algebra and its Application*, San Diego, CA, Harcourt Brace Jovanovich, Inc., 1988, Appendix A.

[7] United States Patent No. 4,999,635, G.N. Yoji, "Phase Difference Auto Focusing for Synthetic Aperture Radar Imaging," March 12, 1991.

[8] Eichel, P.H., D.C. Ghiglia, and C.V. Jakowatz, Jr., "Speckle Processing Method for Synthetic Aperture Radar Phase Correction," *Optics Letters*, Vol. 14, No. 1, Jan. 1, 1989.

[9] United States Patent No. 4,924,229, P.H. Eichel, D.C. Ghiglia, and C.V. Jakowatz, Jr., "Phase Correction System for Automatic Focusing of Synthetic Aperture Radar," May 8, 1990.

[10] Eichel, P.H., and C.V. Jakowatz, Jr., "Phase-Gradient Algorithm as an Optimal Estimator of the Phase Derivative," *Optics Letters*, Vol. 14, No. 28, Oct. 15, 1989, pp. 1101-1109.

[11] Wahl, D.E., P.H. Eichel, D.C. Ghiglia, and C.V. Jakowatz, Jr., "Phase Gradient Autofocus--A Robust Tool for High Resolution SAR Phase Correction," *IEEE Transactions on Aerospace and Electronic Systems*, Vol. 30, No. 3, July 1994, pp 827-834.

[12] Werness, S.A., W.G. Carrara, L.S. Joyce, and D.B. Franczak, "Moving Target Imaging Algorithm for SAR Data," *IEEE Transactions on Aerospace and Electronic Systems*, Vol. 26, No. 1, January 1990, pp. 57-67.

[13] Goodman, R.S., L.S. Joyce, and L.S. Cech, "ISAR Image Formation Processing for Airborne Targets," *Proceedings of the 1994 AMTA Symposium*, Long Beach, CA, October 1994, pp. 338-343.

[14] Stuff, M.A., R.C. Sullivan, B.J. Thelen, and S.A. Werness, "Automated Two and Three Dimensional, Fine Resolution, Radar Imaging of Rigid Targets with Arbitrary Unknown Motion," *Proceedings of the 1994 SPIE International Symposium: Algorithms for Synthetic Aperture Radar Imagery*, Orlando, FL, April 1994.

[15] Werness, S.A., M.A. Stuff, and J.R. Fienup, "Two-Dimensional Imaging of Moving Targets in SAR Data," *Record of the Twenty-Fourth Asilomar Conference on Circuits, Systems, and Computers*, Monterey, CA, November 1990.

Chapter 7
Processor Design Examples

This chapter provides two examples of a spotlight SAR image formation processor (IFP). The first example is the common UNIX SAR processor. This software-based IFP processes data from the data collection system (DCS), a representative airborne SAR sensor developed jointly by the U.S. Air Force Wright Laboratory and ERIM. The second example is the ground-to-air imaging radar (GAIR) processor. The GAIR IFP is an inverse SAR (ISAR) processor for use with a ground-based, spotlight imaging radar.

7.1 THE COMMON UNIX SAR PROCESSOR

The common UNIX SAR processor is referred to as CUP (for common UNIX processor). The CUP is a flexible, non-real-time digital IFP. A digital IFP like the CUP feeds large radar data sets through a computationally complex sequence of signal processing operations. The information required to form a single image includes more than 100 megabytes of data for practical systems. The signal processing entails billions of floating point multiplications and additions to produce a single image. Before describing how the CUP achieves this image, we first present an overview of the DCS SAR sensor.

7.1.1 DCS System Overview

The DCS is an air-to-ground SAR imaging system based in a Convair CV-580 aircraft [1]. The system operates at X-band and can collect both stripmap and spotlight mode data. The system is fully polarimetric in that it can record all four linear transmit/receive antenna polarizations (VV, VH, HV, and HH) during a collection. In addition, the DCS can collect and process interferometric data (Section 9.3). Table 7.1 describes the available DCS collection modes. The combination of polarimetry and interferometry means that the system can simultaneously record eight radar video channels. The DCS is also capable of collecting forward-look spotlight SAR data (Section 9.2). Figure 7.1 presents a functional block diagram of the DCS, and Figure 7.2 shows the DCS pedestal with its four antennas.

The exciter unit in Figure 7.1 generates a digital chirp waveform, mixes it up to X-band, and sends it to the transmitter for amplification. The DCS employs a transmit-then-receive approach, using a circulator to couple both the transmitter and receiver to the antennas. The receiver dechirps the echoes received from the illuminated scene by mixing

Table 7.1
DCS Collection Modes

Radar Mode	*Look Direction*	*Resolution*	*Polarization*	*Interferometry*
Stripmap	Side-look	Coarse or fine	Single, dual, or fully polarimetric	Optional
Spotlight	Side-look	Coarse or fine	Single, dual, or fully polarimetric	Optional
Spotlight	Forward-look	Coarse or fine	Single, dual, or fully polarimetric	Optional

them with a delayed replica of the transmitted signal. After a second mixer translates the signals down to baseband, the buffer/formatter digitizes and records the dechirped pulses.

A Honeywell H423 inertial measurement unit (IMU), a Trimble 4000SE GPS receiver, and a barometric altimeter sense aircraft motions. The IMU provides three-axis measurements of aircraft accelerations (translational motion) and ring-laser gyro counts (rotational motion). It passes both types of measurements to a Sandac computer for further real-time processing into aircraft velocity, attitude (roll, pitch, yaw), position, and heading. Motion computation involves procedures similar to those shown in Figure 2.20. The Sandac is a parallel processing, general-purpose computer. The GPS receiver, operating in a real-time differential mode, provides time tags and absolute aircraft position that is accurate to within 10 m. Differential mode GPS requires the use of a second GPS receiver, usually on the ground in the vicinity of the data collection area. Differential mode improves the accuracy of aircraft position measurements by means of processing that combines the airborne and ground-based GPS data sources. It is logical to group a number of data streams together under the single title of auxiliary data, or aux data, for short. These streams are aircraft attitude, velocity, and position data; range to scene center; antenna pointing commands; and antenna attitude measurements. The airborne computers sample each parameter at a 50-Hz rate. The collection system time tags both the aux data and radar video data and records them on a high-density digital tape (HDDT).

After a data collection flight, a ground-based processing facility extracts the recorded aux and video data from the HDDT (Figure 7.3). Data preprocessing software reads the HDDT and separates the multiplexed radar video and aux data channels, placing each in individual computer disk files. The preprocessed video data contains between 2048 and 4096 samples per pulse, depending on the radar mode. Each sample is mathematically real and is one byte long.

During the collection flight, the IMU senses aircraft accelerations and angular rates; it outputs aircraft position in a standard navigational coordinate system. The airborne computers use these measurements to calculate the distance between scene center and the IMU. To apply proper motion compensation and polar format the video data, the IFP needs to know the location of the antenna phase center (APC), not the IMU, with respect to scene center. The distance between the IMU and the APC is the *lever arm*. Changes in the length and attitude of the lever arm over time affect the position of the APC.

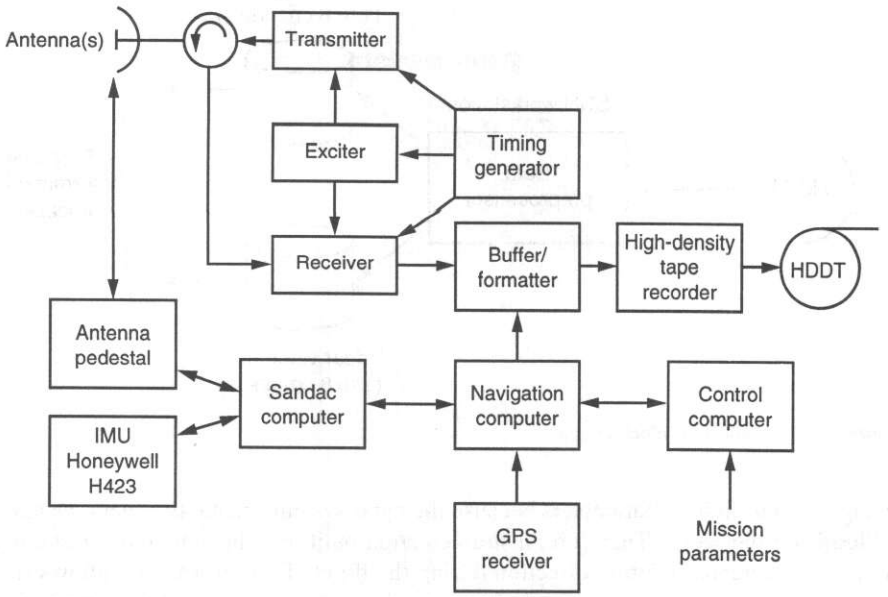


Figure 7.1 DCS block diagram.

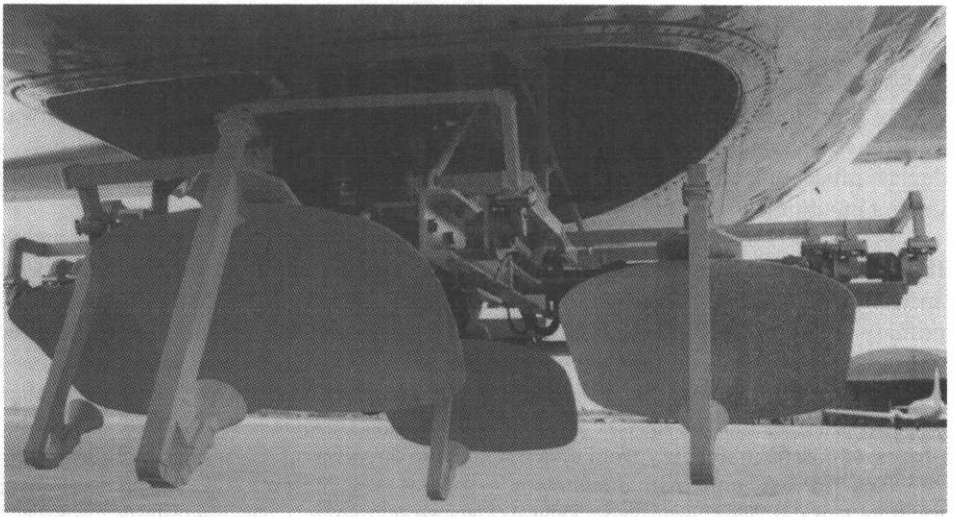


Figure 7.2 The DCS pedestal and antennas.

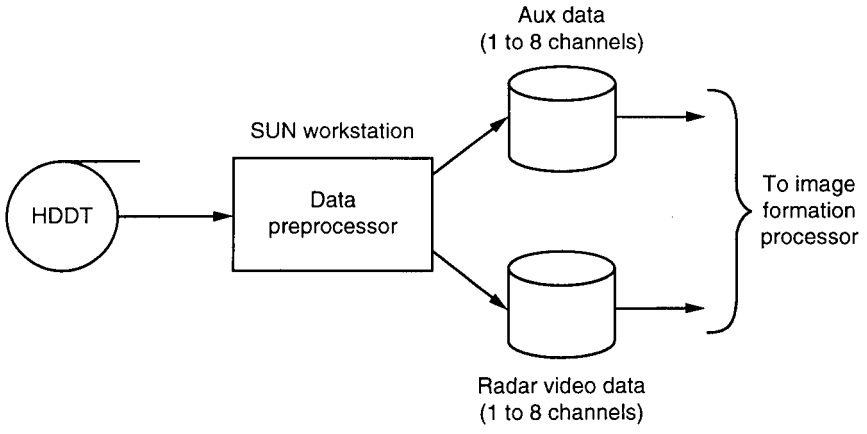


Figure 7.3 Preprocessor block diagram.

Changes occur in both parameters because the radar system constantly steers the antennas to illuminate the scene. Therefore, instrumentation built into the antenna pedestal detects and records antenna pointing direction during the flight. This information allows the IFP to perform a *lever arm correction* during ground processing. The preprocessing software performs this correction for each APC that generates radar signal data during the data collection flight. For each active channel of radar video data, the software writes a unique APC position solution to a separate aux data file associated with that channel.

7.1.2 Processor Overview

A discussion of the CUP begins with a presentation of its data flow diagram in Figure 7.4. A data flow diagram pictorially illustrates the passage of data into and out of a software system. It describes the elements of the processing system in high-level terms only. It depicts processing elements as rectangular boxes, data as arrows, and computer files containing input/output information as pairs of parallel, horizontal lines.

As Figure 7.4 shows, IFP input data comes from two sources: the SAR sensor and the IFP user. User inputs are parameters (such as image resolution, image size, and processing aperture location) that task the IFP to create images from the sensor data. Images are the primary output of the IFP. A secondary output is the header file, which is the set of directives that the IFP uses to form a requested image. The header file also contains values of key parameters that the IFP derives during processing. System users often use these parameters to do image analysis and exploitation, and for diagnostic purposes. The CUP processor can form imagery from data collected in any of the DCS modes in Table 7.1.

The IFP has three main elements: a graphical user interface (GUI), a scene analysis module, and the signal processor. The GUI is a group of Motif-based windows with which the IFP user interacts. The user enters image information (such as resolution, image size,

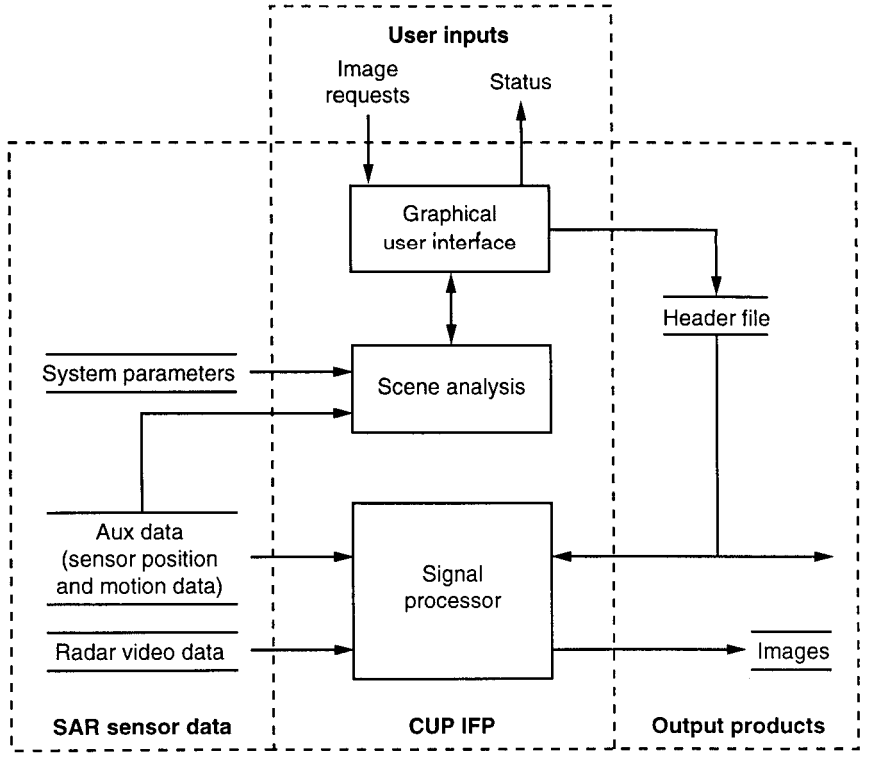


Figure 7.4 CUP data flow diagram.

and sample density) into GUI text boxes. The software limit-checks all inputs and passes them to the scene analysis module.

The scene analysis module combines the user inputs, the system parameters, and subsets of the sensor position data sets. It also verifies that the user inputs for image resolution and aperture position are compatible with the collected sensor data in terms of transmitted bandwidth and data collection interval. A message window on the GUI describes any inconsistency between the user inputs and sensor data. The user must then adjust the input parameters to generate an acceptable processing request. Upon receiving a satisfactory processing request, the GUI generates the header file and passes it to the signal processor.

The signal processor reads the header file to obtain the parameters it needs to form the image that the user described. The signal processor also reads the appropriate subsets of sensor position and video data. After reading the data, it performs the image formation processing and produces the final image. Upon completion, the signal processing software archives key data collection and image formation parameters by writing them to the header file.

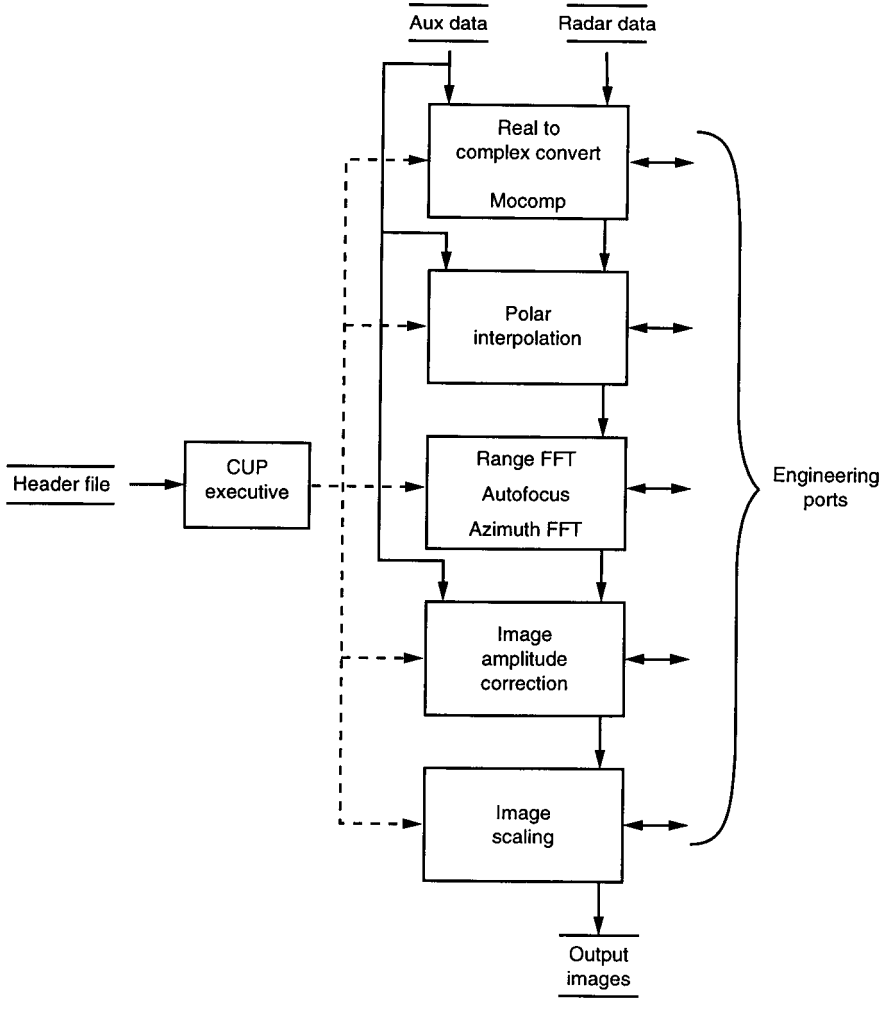


Figure 7.5 Diagram of CUP signal processor architecture.

7.1.3 Signal Processor Software Architecture

Figure 7.5 is a software architecture diagram for the CUP signal processor with its six major software modules. Each module corresponds to a key step in the polar format processing algorithm. Image formation processing begins at the top of the diagram and ends at the bottom. The entire process is under the control of the executive module. The executive module activates and deactivates the individual signal processing modules, passes key parameters, and reports status to the user. The CUP software is written entirely in the C programming language and runs on a standard Sun UNIX workstation.

Because the DCS and CUP are research tools, an important CUP feature is the availability of built-in engineering ports. The engineering ports allow for both the input and output of intermediate results at each major step in the processing chain. This flexibility supports experimentation, data analysis, and processor maintenance. Figure 7.6 provides graphic illustrations of the IFP data stream at selected engineering ports in the signal processor using a synthetic point target signal history. Figure 7.6(a) through Figure 7.6(c) depict the phase of the signal history. In these three images, black represents a signal sample with zero phase and the brightest white intensity represents a phase of 2π rad. Figure 7.6(d) depicts the magnitude of the signal history after range compression, and Figure 7.6(e) depicts the magnitude of the final complex image after range and azimuth compression.

The CUP software uses the preprocessed aux and video data as its input. The executive module initiates a processing operation by reading the aux data that will contribute to the specified image. It then reads the video data. Since the video data is mathematically real, a digital real-to-complex conversion module produces the desired complex (I, Q) signal. If the radar digitizes 2048 real samples, real-to-complex conversion produces 1024 complex samples. Appendix A presents an efficient real-to-complex conversion algorithm similar to that used by the CUP.

The IFP next motion compensates the complex video data by adjusting the phase and frequency of each pulse. The size of the adjustment is proportional to the two-way delay time from antenna phase center to scene center reduced by the reference time delay (or range gate) that the receiver uses during the data collection. To keep the spotlight scene within the range gate of the receiver, the collection system varies the range gate dynamically, in steps. Figure 7.6(a) suggests such a change; the phase discontinuity corresponds to a range gate quantization step of approximately 5 m. Changes in the range gate introduce unwanted, deterministic phase and frequency shifts in the recorded data. The motion compensation module removes these shifts as Figure 7.6(b) suggests. The same software module also compensates the video data for time-invariant, deterministic phase errors in range. Waveguide dispersion (between transmitter and antenna) is one source of these errors; another source is nonlinearity in the chirp generator.

Next, the aux and video data pass to the polar format module. A clamped cubic spline interpolator upsamples the 50-Hz antenna phase center position data to the radar pulse repetition frequency (PRF). The interpolation software uses this position data to derive the location of pulse samples with respect to a rectangular output grid. Each pulse undergoes polar-to-rectangular interpolation, first in the range direction and then in the azimuth direction. The workstation holds the output grid in memory as it processes raw radar pulses and gradually fills this grid. Figure 7.6(c) presents the phase of the data after both range and azimuth interpolation. Chapter 4 discusses digital polar interpolation in detail.

The interpolated signal history next passes to the fast Fourier transform (FFT) module. This module first Fourier transforms the signal history in the range direction. Figure 7.6(d) depicts the range-compressed data produced by this operation. The mapdrift autofocus algorithm (Section 6.1) then operates on the data in the azimuth direction. This algorithm estimates and compensates azimuth quadratic phase errors. Such phase errors

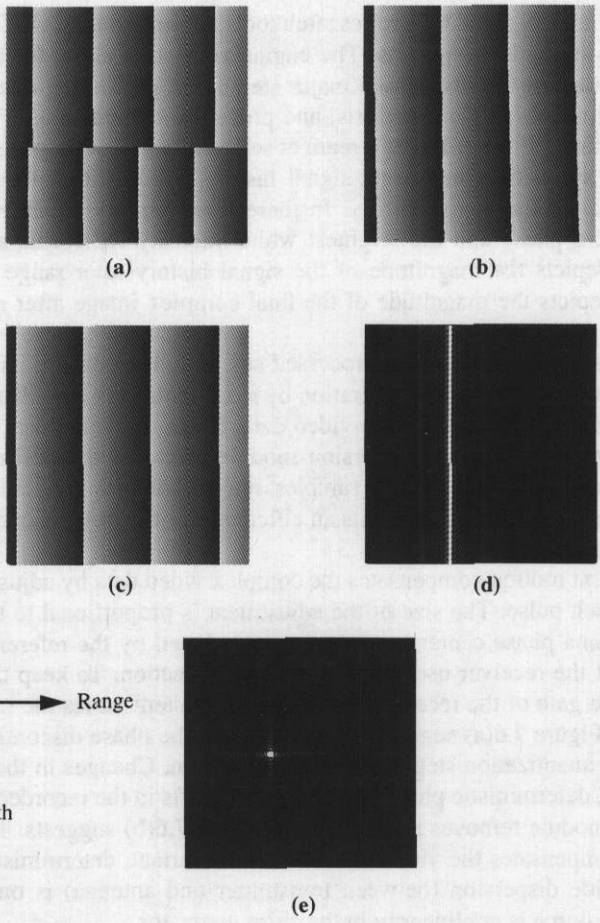


Figure 7.6 IFP data at engineering ports: **(a)** Phase of complex signal before motion compensation; **(b)** Phase after motion compensation; **(c)** Phase after polar interpolation; **(d)** Magnitude of signal after range compression; **(e)** Magnitude of data after two-dimensional compression (image domain).

typically result from errors in measurement of the forward velocity and line-of-sight acceleration components of SAR platform motion. Following completion of the mapdrift autofocus procedure, the software Fourier transforms the signal data in the azimuth direction to form an uncorrected, complex-valued image. Figure 7.6(e) depicts such an image. The term *uncorrected* indicates that the image lacks compensation for amplitude variations and geometric distortions. The CUP does not provide a mechanism for correcting image geometric distortion.

The software passes the uncorrected image to the image amplitude correction module. This module removes image amplitude distortions introduced by the following sources:

- Real-to-complex digital filter;
- Analog receiver filters;
- Range and azimuth polar interpolation filters;
- Range power falloff;
- Range and azimuth antenna pattern.

The final processing step scales the image as the user desires. Typically, the CUP IFP writes output images as unscaled 32-bit floating point numbers that are mathematically complex. Alternatively, the software can scale each image pixel to its calibrated RCS value. It can also scale the image to give the peak pixel amplitude a user-specified value.

CUP image formation execution time depends on a number of factors. The most important factors are the CPU performance of the host workstation, the desired resolution, and the desired image size. Using a Sun Sparc10 workstation, a resolution of 1 m, and an image size of 1000×1000 pixels, the CUP IFP forms a full quality image in about 5 min.

7.2 THE GROUND-TO-AIR IMAGING RADAR PROCESSOR

This section discusses the ground-to-air imaging radar (GAIR) system. The GAIR is an ISAR system that produces high-resolution imagery of airborne targets [2]. It uses a signature-based processing algorithm to accomplish image formation. The processing procedure is the prominent point technique [3, 4], which Section 6.5 discusses in detail. This processing technique utilizes radar returns from isolated, point-like scattering centers to estimate relative motion between the target and radar antenna phase center. The IFP uses these motion estimates to perform traditional spotlight SAR motion compensation and data formatting functions. Remaining signal chain operations are identical to those of a conventional spotlight SAR processor.

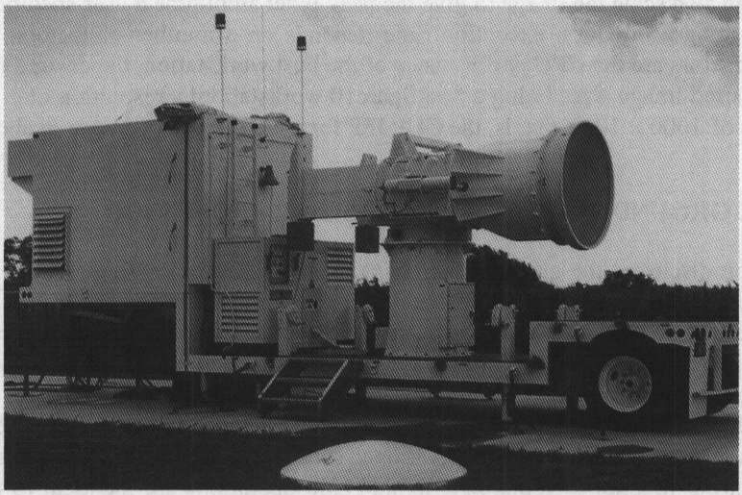
Discussion begins with a brief overview of the GAIR system. A detailed discussion of the GAIR image formation processor and image examples follow.

7.2.1 GAIR System Overview

The GAIR is a ground-based ISAR system. Its mission is to perform radar cross-section (RCS) diagnostic imaging of low-observable airborne targets. Collection of radar data on air vehicles in dynamic flight is important for RCS diagnostic imaging applications. Dynamic imaging is desirable in order to image airborne vehicles with landing gear up, correct control surface positions, realistic structural loading conditions, and full aspect coverage. Previously, such measurements utilized outdoor instrumentation ranges where, typically, landing gear must be engaged and multipath effects due to ground bounce are difficult to mitigate.



(a)



(b)

Figure 7.7 Deployed GAIR system: **(a)** Data acquisition system; **(b)** Close-up of radar pedestal trailer.

Primary design requirements and operational capabilities of the GAIR system include the abilities to:

1. Track low-observable aircraft;
2. Collect ISAR signal history data;
3. Process the collected data into fine-resolution ISAR imagery;
4. Display imagery and overlay a three-dimensional surface model of the imaged target;
5. Maintain absolute RCS calibration.

Table 7.2
GAIR System Parameters

Parameter	Parameter Value for ISAR Imaging	Parameter Value for TRCS Measurement
Waveform	Linear FM; with dechirp-on-receive	Linear FM; with dechirp-on-receive
Processed bandwidth	600 MHz	1.5 MHz
Range resolution	0.3 m	100 m
Azimuth resolution	0.3 m	Not applicable
Integration angle	4 deg	Not applicable
Center frequency	9.44 GHz	9.44 GHz
Pulse width	12 μs	12 μs
PRF	5 kHz	5 kHz
Unambiguous range	2 to 12.8 km	2 to 12.8 km
Antenna type	1.4-m diameter corrugated horn with dielectric lens	1.4-m diameter corrugated horn with dielectric lens
Antenna beamwidth	1.95 deg	1.95 deg
Antenna gain	38.75 dB	38.75 dB
Antenna first sidelobe level	–38 dB one-way	–38 dB one-way
Polarization	VV, VH, HV or HH	VV, VH, HV or HH
Peak transmitter power	9 kW	9 kW

Figure 7.7 shows the GAIR system deployed for field operation. Table 7.2 gives key GAIR operating parameters. Figure 7.8 shows a functional diagram of the GAIR system. The system has the option to measure and record target motion information with a motion measurement subsystem that mounts directly on the target aircraft. This capability allows the processing subsystem to produce images via conventional motion compensation techniques without employing prominent point processing.

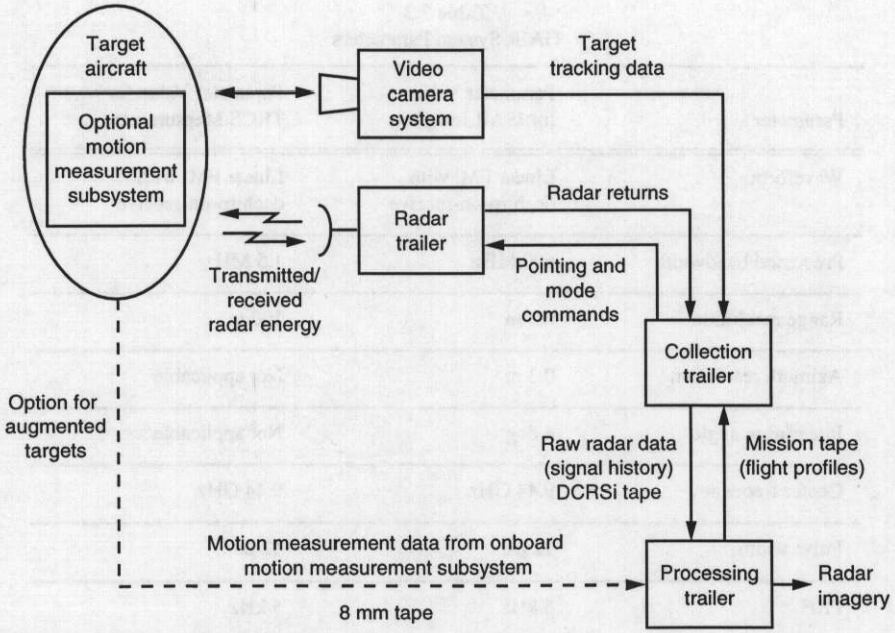
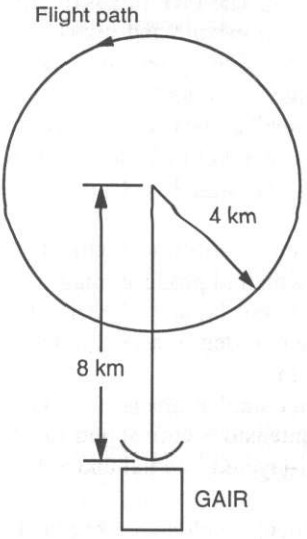


Figure 7.8 Functional diagram of GAIR system.

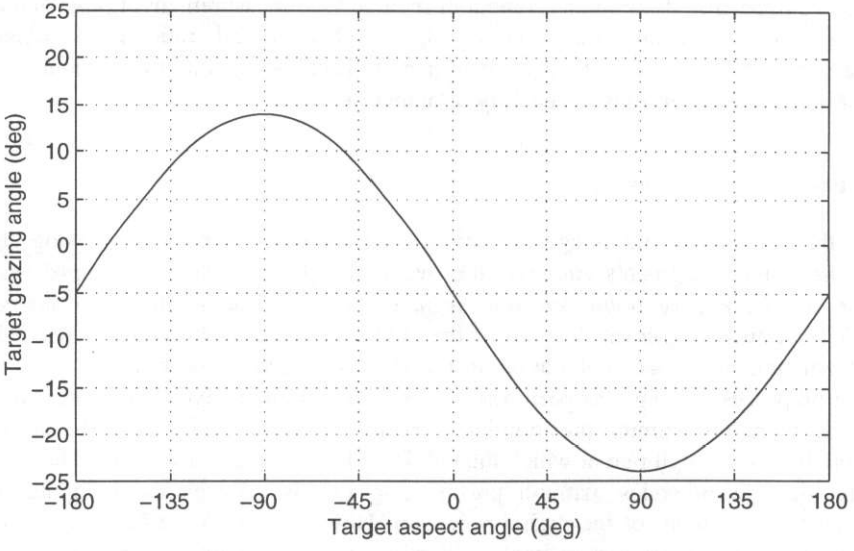
A GAIR mission begins with the definition of a set of flight profiles for the target vehicle to follow during data collection. A system operator designs flight profiles to allow formation of images at desired target aspect and elevation angles. Aspect angles vary from 0 deg for the nose-on view, through 90 deg for the right side view, to 180 deg for the tail-on view. Aspect angles between 180 and 360 deg describe the left side view of the target. Grazing angle is negative when viewing the target from below, 0 deg when viewing from the target "waterline" plane, and positive when viewing from above. Although the GAIR is a ground-based system, it is able to image over a large range of positive grazing angles by banking the target vehicle during a flight profile. Figure 7.9 shows a representative, circular flight profile and the various combinations of aspect and grazing angles that the IFP can process from such a profile.

The GAIR accomplishes target acquisition and angular tracking automatically using a real-time video tracking subsystem. Real-time tracking information, consisting of azimuth and elevation angles to the target, controls the GAIR antenna. Accurate antenna pointing is critical due to the narrow 1.95-deg beamwidth of the system's corrugated horn antenna.

Transmitted pulses alternate between a narrowband waveform and a wideband waveform with linear frequency modulation (FM). The system uses the narrowband pulses for range tracking of the target and for making total RCS (TRCS) measurements. The wideband pulses, which yield the fine-resolution ISAR imagery, have a transmitted



(a)



(b)

Figure 7.9 Example of GAIR target flight profile: **(a)** Radar coordinates; **(b)** Aspect/grazing angle space.

bandwidth of more than 600 MHz, yielding range resolution of 0.3 m when the IFP applies –35-dB Taylor weighting. The PRF of the GAIR is 10 kHz, which leads to effective PRFs of 5 kHz for each (narrowband and wideband) waveform. The GAIR operates in the X-band frequency region. The system uses the dechirp-on-receive procedure of Section 2.3 to achieve fine range resolution over a relatively narrow range swath.

The system mixes wideband echoes received from the target with a replica of the transmitted waveform, down-converts to an intermediate frequency (IF), digitizes the IF signal to 8 bits, and records the signals on high-density digital tape for subsequent processing.

After completion of the data collection segment, an operator interactively chooses signal history apertures from which to produce images by using a display of target trajectory in aspect/grazing angle space. Figure 7.9(b) is an example of such a display. The target must rotate approximately 4 deg in aspect angle to achieve the GAIR cross-range resolution specification of 0.3 m.

Once the IFP processes a complex image, it applies a calibration scale factor to the image so that detected pixel intensities correspond to RCS with units of dB relative to a square meter (dBsm). A multi-layered internal and external calibration scheme maintains calibration accuracy [5].

The system initiates the image exploitation segment by detecting and displaying calibrated images along with a three-dimensional surface model of the target. The exploitation segment projects both the SAR image and the target model into the same viewing plane to facilitate a comparison. Exploitation functions include RCS measurement of point and line scattering sources, feature mensuration, signal-to-background ratio measurements, impulse response plots, and target part identification. Databasing of all measurements and processing parameters ensures traceability of output products.

7.2.2 Processor Overview

The GAIR system performs image formation using a prominent point processing algorithm. Three major segments comprise the overall GAIR processor: the *preprocessing segment*, the *interactive point selection segment*, and the *image formation segment*. Figure 7.10 shows a top-level diagram of the GAIR signal processing chain. All GAIR image formation and image exploitation operations run on UNIX workstations.

The preprocessing segment performs a number of noninteractive signal conditioning operations, including azimuth presumming. Presumming is an important post-collection operation due to the high rate at which the GAIR collects signal history data. The downsampling that accompanies azimuth presumming greatly reduces the computational burden on the remainder of the digital processor. However, before performing presumming, the processor must first estimate and remove a large azimuth (Doppler) carrier frequency from the recorded signal history. Removal of the Doppler carrier is equivalent to performing initial, coarse motion compensation. Noncoherent cross-correlation of range compressed pulses provides a coarse estimate of target motion over the processing aperture. The preprocessing segment uses this motion estimate to perform coarse motion

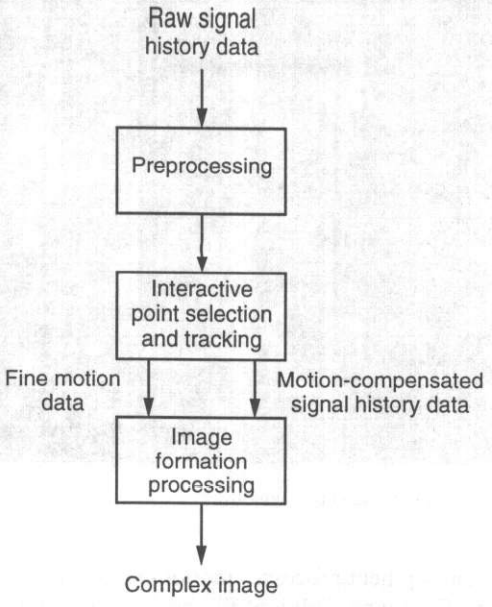


Figure 7.10 GAIR image formation processor.

compensation. This procedure places the radar signals at approximately zero Doppler frequency to correctly prepare the data for the azimuth presumming operation. Azimuth presumming entails low-pass filtering and downsampling of the digitized signal data.

The interactive segment provides a user interface to aid identification and tracking of prominent point scatterers. This segment compresses in range, detects, and displays presummed signal histories produced by the preprocessing segment. A system operator then positions a cursor on a selected scattering center and traces the path that the scatterer follows over the processing aperture. Figure 7.11 shows a display of the point selection window. Radar illumination and near range are on the left side of Figure 7.11. The processor software uses phase information from the selected point, as a function of aperture time, to compensate for target translational motion (Section 6.5).

If necessary, the system operator may optionally select a second prominent point to compensate for nonlinear target rotation over the processing aperture. With appropriate assumptions (Section 6.5), unwrapped phase information extracted from the second prominent point is proportional to the target rotation angle over the processing aperture. Although the total angular interval through which the target rotates is not known precisely, it is satisfactory to estimate this interval based on the planned flight profile. The image formation segment uses the angle information from the second prominent point to perform polar interpolation of the signal history. If the operator does not select a second prominent point, the IFP assumes target rotation at a constant angular rate over the processing aperture.

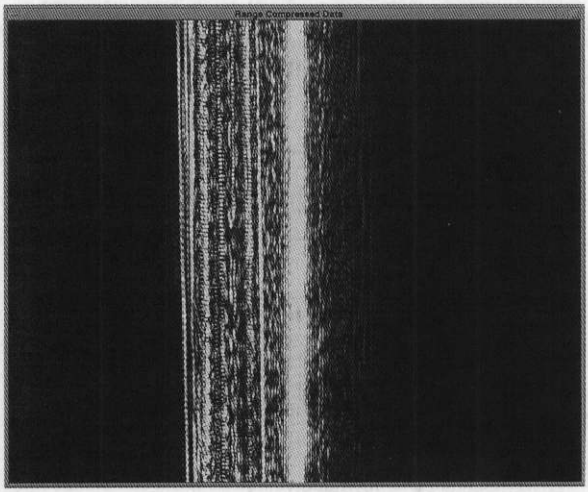


Figure 7.11 Prominent point scatterer selection window.

The image formation segment processes motion-compensated signal history data into fine-resolution imagery. The functionality of this segment is identical to that of a conventional spotlight SAR image formation processor (Section 7.1). Primary operations that this segment performs include polar formatting, aperture weighting, two-dimensional compression, and amplitude equalization in the image domain.

7.2.3 Preprocessing Segment

The GAIR preprocessing segment performs the following signal conditioning operations: quadrature demodulation, range phase error compensation, coarse motion compensation, and azimuth presumming. Figure 7.12 indicates data flow and functionality of the preprocessing segment.

To illustrate the GAIR processing algorithm, it is instructive to follow the signal history corresponding to a single image through the IFP sequence and examine signal characteristics at intermediate processing steps. The selected image is from a straight-line flight profile with a broadside range of 6 km. Figure 7.13 shows the imaged target, a Convair CV-580 aircraft. The duration of the example processing aperture is 1.7 s. This aperture duration corresponds to approximately 4 deg of rotation in target aspect angle over the aperture. The grazing angle at aperture center is –23 deg.

7.2.3.1 Quadrature Demodulation

The GAIR system records 960 real-valued samples for each pulse. Quadrature demodulation converts the pulses into 480 complex values via procedures detailed in Appendix A.

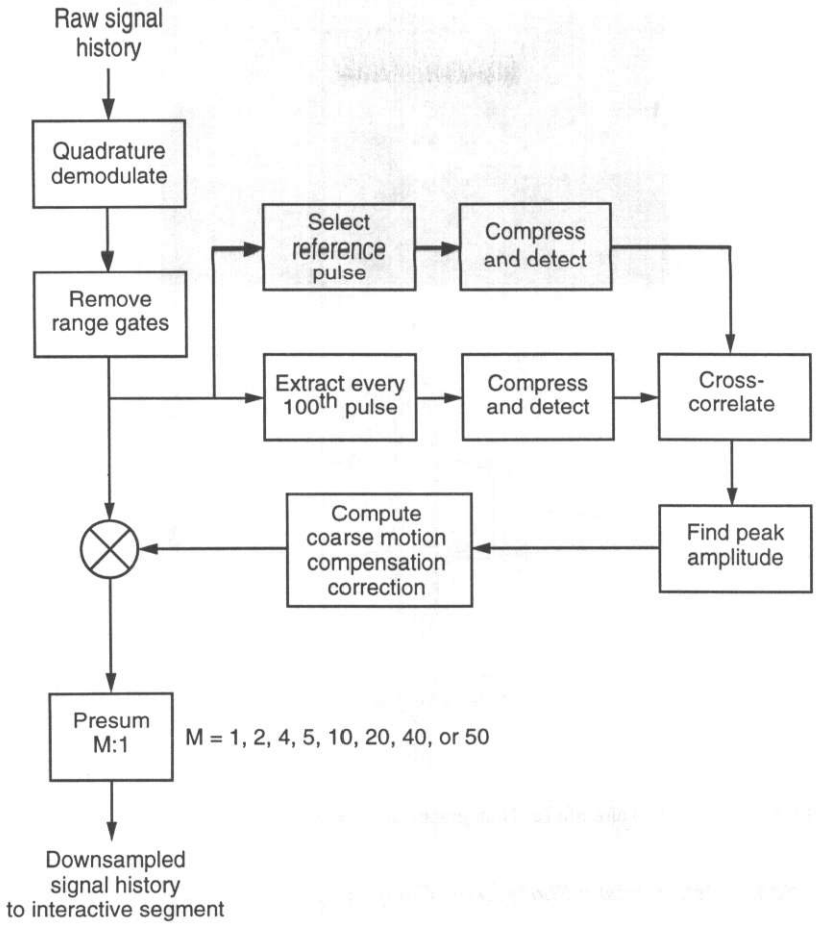
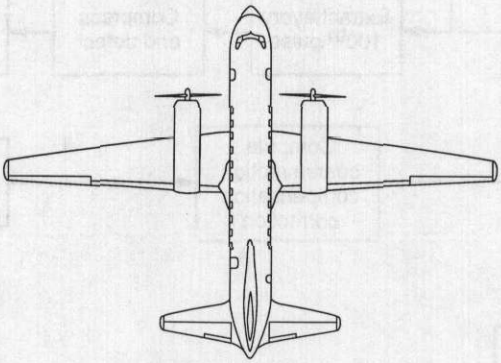


Figure 7.12 Functionality of preprocessing segment.

Figure 7.14 shows a short aperture of range-compressed signal history after quadrature demodulation. Radar illumination in Figure 7.14 is from the left side. The figure shows only half of the GAIR system's 120-m range swath. The range-compressed data contains several dominant scattering centers, including left and right engines, right wingtip, and two X-band antennas—one mounted in the nose and one in the belly of the aircraft. The occasional discontinuities observed in the scatterer tracks in Figure 7.14 are the result of changes in the radar reference function time delay (and range gate) during data collection. These changes involve the parameter $R_o(n)$ in the signal phase equation described by (2.55). To keep the target within the radar's limited swath width, the GAIR changes the range gate in discrete, quantized steps in real time.



(a)



(b)

Figure 7.13 Convair CV-580 aircraft: **(a)** Photograph; **(b)** Plan view.

7.2.3.2 Range Deterministic Phase Error Compensation

It is easy to correct deterministic phase errors in the range dimension of the radar by multiplying each digitized pulse by a precomputed correction vector. Deterministic error sources include nonlinearities in the transmit and receive exciters, analog filters in the receiver, and dispersion in the waveguide connecting the transmitter and receiver to the system antenna.

7.2.3.3 Coarse Motion Compensation

The collection system makes real-time adjustments to the radar range gate during a data collection in order to keep the imaged target within the relatively narrow GAIR range swath. The system records range gate information as auxiliary data. Changes in the range gate parameter cause changes in phase, frequency, and time delay in the demodulated

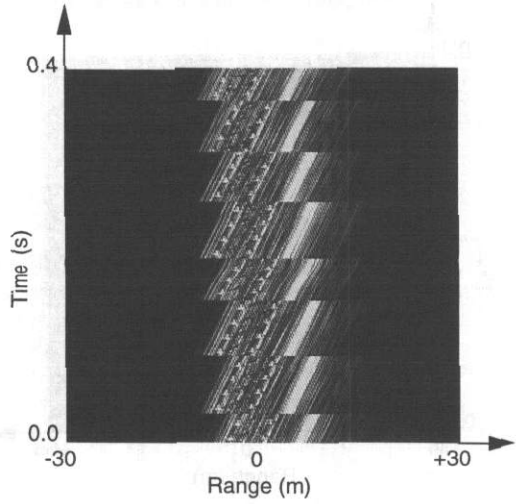


Figure 7.14 Magnitude of range-compressed signal history.

signal history data. Performing single point compensation to a fixed point on the target naturally removes these deterministic effects. However, at this stage in the processing chain, the processor does not yet know the time-varying range to a fixed target point.

A cross-correlation technique is useful to compute a rough estimate of target range. The procedure selects, compresses, and detects a reference pulse from the center of the processing aperture. It then cross-correlates this reference pulse with other compressed and detected pulses in the processing aperture and determines the location of the peak of the correlation function for each cross-correlated pulse. Typically, it is necessary to correlate only 1 out of every 100 pulses for this purpose. The final step fits a low-order polynomial (in azimuth) to the cross-correlation peak locations (in range) and evaluates it for all pulses. The preprocessing segment uses the resulting function as a coarse estimate of instantaneous target range. The purpose of this compensation is only to achieve motion compensation performance that is adequate to permit azimuth presumming.

Figure 7.15 shows the example signal history after coarse motion compensation. Coarse motion compensation effectively removes the range gate-induced discontinuities present in Figure 7.14.

7.2.3.4 Azimuth Presumming

After coarse motion compensation, azimuth presumming ratios as high as 50:1 reduce the large volume of signal data and the computational burden on the remainder of the signal chain. Azimuth presumming by a variable integer ratio M involves low-pass filtering of the signal history with finite impulse response digital filters and retention of one out of

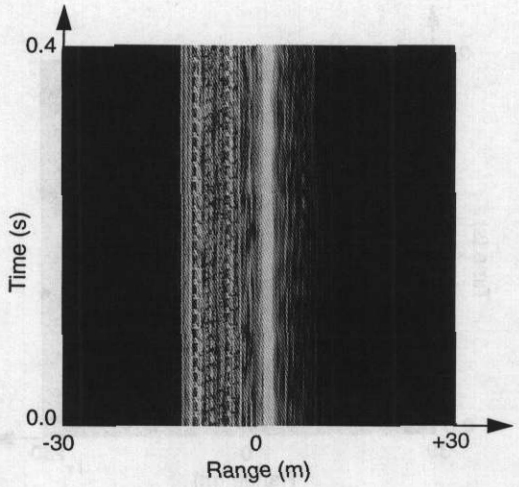


Figure 7.15 Magnitude of range-compressed signal history after coarse motion compensation.

each M filtered pulses. The GAIR IFP allows seven discrete presum ratios; these ratios are 1:1, 2:1, 5:1, 10:1, 20:1, 40:1, and 50:1. To improve computational efficiency, the IFP implements digital filtering associated with the highest downsampling ratios (20:1, 40:1 and 50:1) in two stages.

7.2.4 Interactive Segment

The GAIR interactive segment permits identification and tracking of prominent point scatterers. Figure 7.16 shows the functionality of the interactive segment. The user identifies a point on a display of the magnitude of the range-compressed signal history illustrated in Figure 7.11. The user places a cursor on the desired prominent point trace and indicates its selection by pressing a trackball button. The user selects several points along the trace. The processor fits a low-order polynomial to the selected points and evaluates the polynomial at the effective PRF of the presummed pulses. The resulting curve represents the location of the peak of the selected prominent point as a function of pulse number.

Using the polynomial from the previous step, the processor extracts the phase of the prominent point from the complex range-compressed signal history. The processor typically smooths the extracted prominent point phase, this time with a forward/backward infinite impulse response (IIR) filter. The processor then negates the smoothed phase and applies it as a fine motion compensation phase correction. Figure 7.17 shows the phase extracted from the prominent points identified as point 1 and point 2 in Figure 7.11.

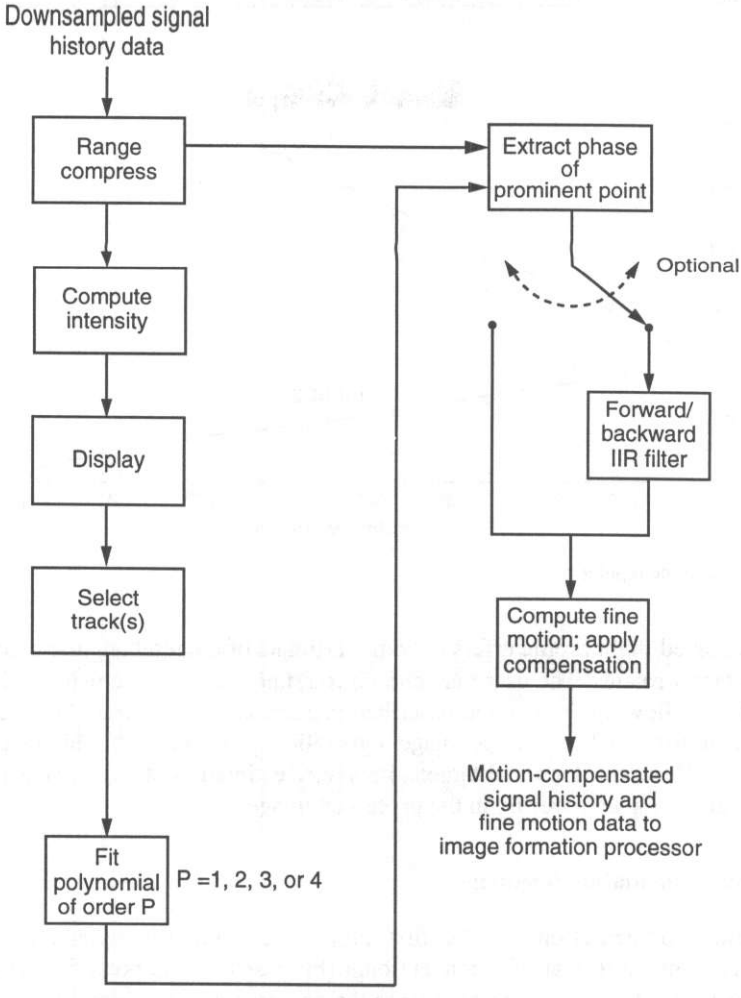


Figure 7.16 Functionality of Interactive segment.

The operator selects a second prominent point in the same manner as the first point. The difference in unwrapped phase between the second and first prominent points is proportional to the variation in target rotation angle over the image formation interval. Knowledge of target rotation is important in order to properly orient radar pulses during the subsequent polar formatting operation. The processor estimates the total angular extent through which the target rotates, and scales the estimated rotation function so that its peak-to-peak variation matches the angular extent of rotation.

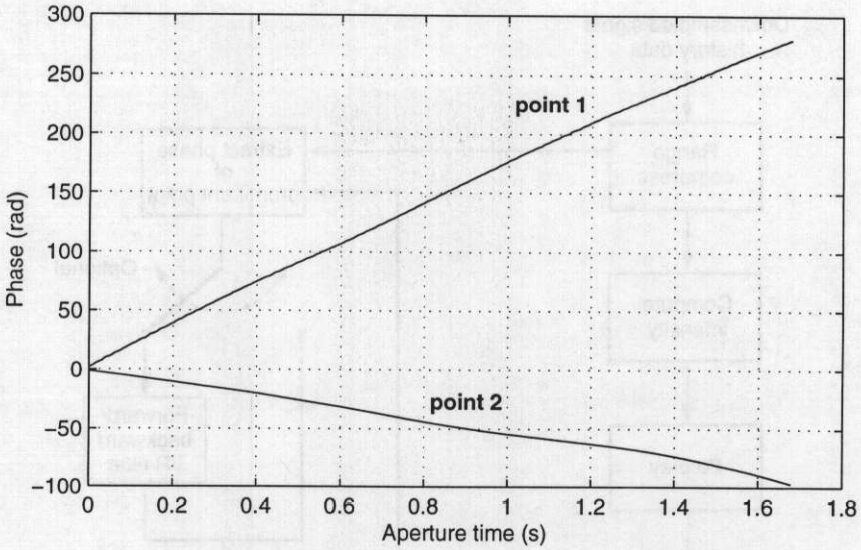


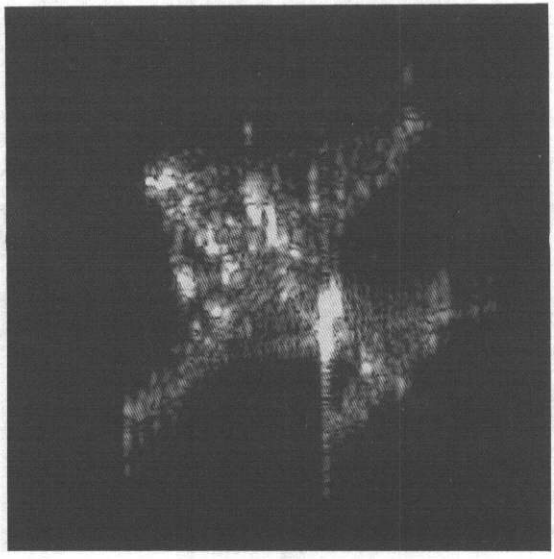
Figure 7.17 Prominent point phase.

The planned flight profile offers an initial estimate of the total angular extent through which the target rotates. The user may choose to refine this estimate using a third prominent point by following the method described in Section 6.5. Accurate knowledge of the angular extent is crucial for precise image registration, since azimuth scale factor depends on this angle. However, for small targets, imprecise estimation of the angular extent does not significantly impact focusing in the processed image.

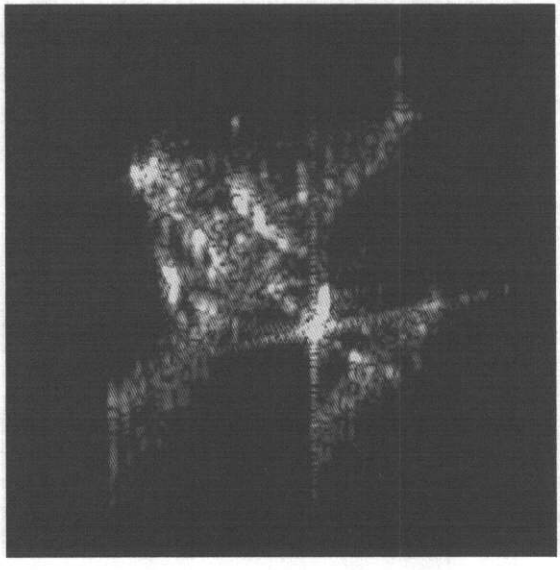
7.2.5 Image Formation Segment

After motion compensation via the first prominent point, the remaining processing sequence is identical to that of a conventional IFP based on the polar format algorithm. Figure 7.18 shows two images formed from the processing aperture that we use throughout this section. The images correspond to a target aspect angle of –40 deg and a grazing angle of –23 deg. The image in Figure 7.18(a) results from single prominent point processing; Figure 7.18(b) shows a slightly improved image using the two-point procedure. Radar illumination and near range are from the left side of these images.

Figure 7.19 shows another set of images from the same target at a nearly nose-on aspect angle. Figure 7.19(a) is the result of single prominent point processing, and Figure 7.19(b) shows the result obtained via the two point procedure. Figure 7.20 shows an image processed slightly off 0-deg aspect using a single prominent point. A large specular flash from the leading edge of the left wing is evident in Figure 7.20.



(a)



(b)

Figure 7.18 Processed ISAR image: **(a)** Single prominent point; **(b)** Two prominent points.

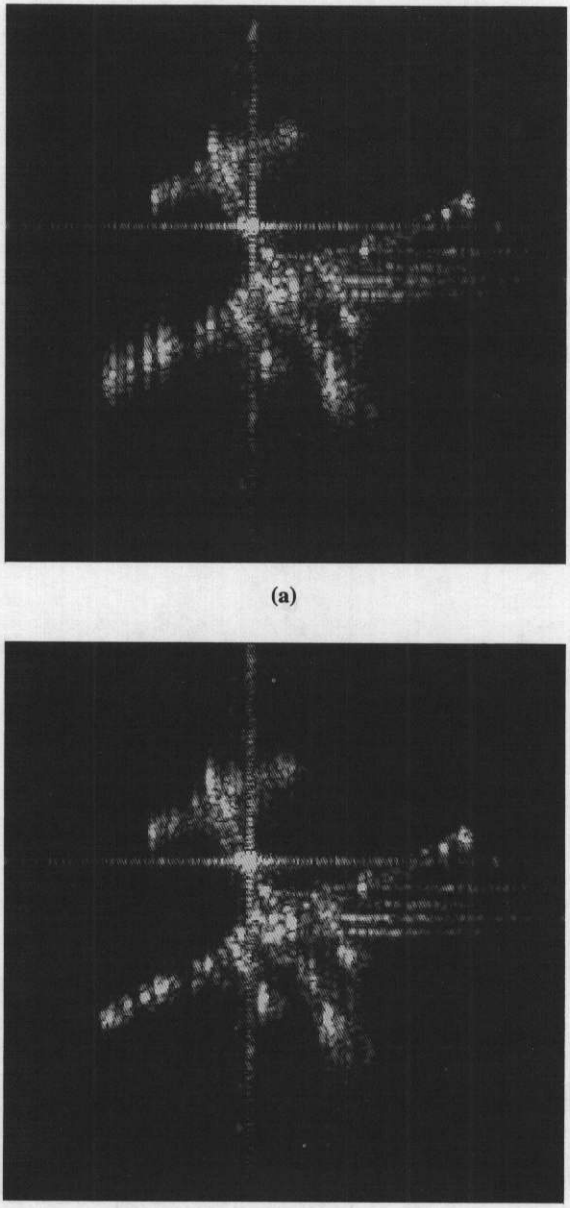


Figure 7.19 ISAR image from nose-on aspect angle: **(a)** Single prominent point; **(b)** Two prominent points.

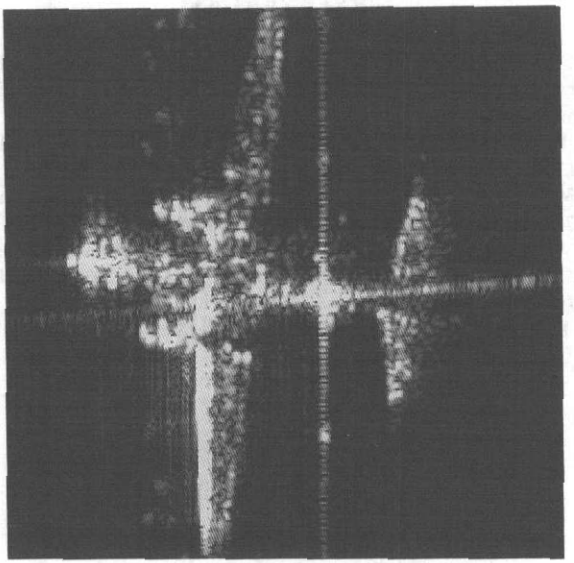


Figure 7.20 ISAR image processed with single prominent point.

7.2.6 Image Exploitation Segment

The GAIR image exploitation segment performs a variety of image exploitation functions and image quality measurements on processed imagery. Such operations include RCS measurement of point, line, and area scattering sources; feature mensuration; signal-to-background ratio measurement; impulse response plots; and target part identification. Databasing of all measurements and processing parameters ensures traceability of output products.

7.3 SUMMARY

The common UNIX processor and GAIR prominent point processor are representative image formation processors for modern fine-resolution imaging SAR systems. Such software-based processors provide flexibility for algorithm testing, experimentation, and improvement. They serve as useful prototypes for high-speed implementations of the same algorithms on high-performance computers and embedded real-time processors. From these working prototypes, system designers can determine the computational requirements and procedures necessary for high-speed processing in operational descendants of the prototypes. This strategy of processor evolution serves to reduce cost and risk at all stages of SAR system development.

REFERENCES

[1] DiMango, M.A., W.T. Hanna, and L. Andersen, "The Data Collection System (DCS) Airborne Platform," *First International Airborne Remote Sensing Conference and Exhibition*, Strasbourg, France, September 1994.

[2] Goodman, R., W. Nagy, J. Wilhelm, and S. Crippen, "A High Fidelity Ground to Air Imaging Radar System," *1994 IEEE National Radar Conference*, Atlanta, GA, March 1994.

[3] Werness, S., W. Carrara, L. Joyce, and D. Franczak, "Moving Target Imaging Algorithm for SAR Data," *IEEE Transactions on Aerospace and Electronic Systems*, Vol. 26, No. 1, January 1990, pp. 57-67.

[4] Goodman, R., L. Joyce, and L. Cech, "ISAR Image Formation Processing for Airborne Targets," *Proceedings of the 1994 AMTA Symposium*, Long Beach, CA, October 1994.

[5] Nagy, W., and E. Johansen, "Ground and Airborne Calibration of the Ground to Air Imaging Radar," *Proceedings of the 1993 AMTA Symposium*, Dallas, TX, October 1993.

Chapter 8
SAR System Performance

The principal product of a SAR system is imagery that provides a visual or digital representation of the radar backscatter characteristics of an illuminated scene. It is reasonable to specify and evaluate a SAR system by functional requirements and by performance requirements with respect to this product. Functional requirements refer to operational capabilities and the type of SAR product. Performance requirements refer to the quantity, quality, and timeliness of the SAR product.

Performance requirements relating to image quantity, image quality, and timeliness are a dominant consideration in the selection of a SAR signal processing algorithm. Image quality requirements relative to scene size are a particularly critical element. While the image formation processor is only one subsystem of the SAR system, it plays two critical roles in its assignment to convert received radar energy into a spatial representation of the scene backscatter coefficient. First, it compensates for a number of deficiencies in other subsystems and, second, it massages the inherent geometry-driven behavior of the received radar data stream into a form amenable to fast, efficient digital signal processing. Scene size, image quality specification levels, and sensor characteristics will influence a wise selection of the image processing algorithm. Requirements on timeliness may also distinguish various approaches to image formation. Timeliness may be in terms of either performance relative to real time or use of computer resources or processing time per image quantity unit.

This chapter discusses SAR system performance in terms of the quality of the SAR image. Image quality does not happen by default. It requires thorough system and subsystem specifications, system parametric design trade-offs, error allocation, and performance prediction. It also requires performance measurement, verification, and monitoring over time.

This chapter defines specific measures of image quality (IQ) that the SAR community uses to specify, design, and verify this aspect of SAR system capability. These IQ metrics relate to image utility in terms of detection, classification, and identification of targets and scene characteristics [1, 2]. Discussion includes a procedure for allocating errors among the various subsystems and components to achieve a specified level of IQ. The chapter concludes with a discussion of the use of test sites for IQ verification.

8.1 IMAGE QUALITY METRICS

Key attributes of image quality include the detectability of scatterers, spatial resolvability of scatterers, relative positioning accuracy of scatterers, and relationship between scatterer radar cross-section and image intensity. These attributes relate to the common tasks of detection, classification, and identification associated with SAR image utility. As primary IQ metrics, the SAR community generally uses resolution, peak sidelobe levels, multiplicative noise ratio (MNR), equivalent backscatter coefficient of additive noise σ_n, and geometric distortion. Resolution commonly refers to the mainlobe –3-dB width of the system impulse response. MNR includes contributions from integrated sidelobe energy, PRF ambiguities, and quantization noise. A definition and discussion of these metrics begins in Section 8.3. Table 8.1 suggests example specification levels for these primary IQ parameters in a spotlight SAR imaging system. Secondary metrics, summarized in Section 8.6, include dynamic range, spurious response levels, image intensity uniformity, RCS calibration accuracy, and mainlobe –18-dB width.

Table 8.1
Example Image Quality Specification Levels

Image Quality Metric	*Example Specification Level*
Resolution (mainlobe –3-dB width)	1 m
Peak sidelobe levels	–30 dB
σ_n, describing additive noise	–28 dB
MNR	–18 dB
Geometric distortion	The larger of 1 resolution cell or 1 percent of the distance involved

The relative importance of the selected IQ parameters, as well as appropriate specification levels, depends on both the characteristics of the scene being imaged and the end use for the SAR imagery. Terrain mapping and discrete target imaging place different demands on the level and character of system noise contributions. Use of imagery for target detection or for target identification influences requirements on system impulse response. The size of the targets being imaged also affects resolution requirements. The imaging of ground vehicles and other smaller targets requires finer resolution than the imaging of buildings, ships, and other larger targets. The importance of shadows to the image analyst is a significant consideration in noise specification.

Given a set of specifications, the radar system designer performs trade-off studies and parametric system designs to configure a satisfactory set of system parameters. In many cases, the system center frequency is part of this trade-off procedure. With a stable system design, the radar project proceeds with subsystem design, hardware build, software development, integration and test, and flight testing. Performance verification with respect to these metrics requires the presence of specific scatterers or types of terrain in the scene

being imaged. Measurements on the intensity of the complex-valued, digital SAR image provide the basis for a judgment of performance.

8.2 SYSTEM PERFORMANCE BUDGET

A methodology to allocate system requirements among subsystems is a necessary part of SAR system design. For instance, an X-band SAR system design may involve a specification on range resolution of 1 m based on image utility studies. A design does not satisfy this system specification simply by using (2.2) to arrive at a need for 200 MHz of transmitter bandwidth. It must factor in such concerns as waveform imperfections, propagation effects, processing algorithm effects, and aperture weighting to arrive at a balanced, consistent design. The methodology that we describe here is a design procedure to take into account a variety of interacting error effects, error sources, and performance-limiting factors to determine the associated levels of achievable system performance. This procedure will help to ensure that the system design is realizable and adequate to meet the system specifications.

A clarification in system-wide allocations is necessary to reflect the possibility of subsequent corrections for deterministic or measurable error effects. Two examples illustrate this possibility. To the degree that amplitude and phase deviations of the transmit waveform from ideal are correctable in the preprocessor, these subsystem deviations can exceed even the eventual system-wide allocations in these areas. To be correctable, such deviations typically must be slowly varying and consistent from pulse to pulse. Similarly, the use of quadratic autofocus in the image formation processor allows individual quadratic phase error sources to greatly exceed the eventual system-wide allocation in this area.

System requirements define minimum performance levels relative to image quality, image quantity, and timeliness. Figure 8.1 outlines an approach to allocate these system requirements among the various radar subsystems, illustrated by the five *SS* (for subsystem) boxes in the figure. The first step in the allocation process is to categorize system requirements and determine the method of allocation. The two broad categories are *functional* requirements and *performance* requirements. Functional requirements define system capabilities, scope and timeliness of performance, and methods for the system to use. Examples of functional requirements for a SAR specification include polarization capability, mode capability (for example, spotlight or stripmap), radiometric calibration capability, operational altitudes or slant ranges, and access area. Access area is the area relative to the sensor location and velocity vector from which the sensor must be able to select and image a scene. Performance requirements may be directly allocable or allocable by means of performance limiting factors (PLFs). Directly allocable performance requirements are parameters whose specification level can be divided or shared directly among the subsystems. PLF-allocable requirements are parameters influenced by a number of separate factors, each of which may have sources in any number of subsystems. In this situation, it is appropriate, first, to allocate each performance requirement among the relevant PLFs. Then, each PLF is allocated directly among the subsystems. This division

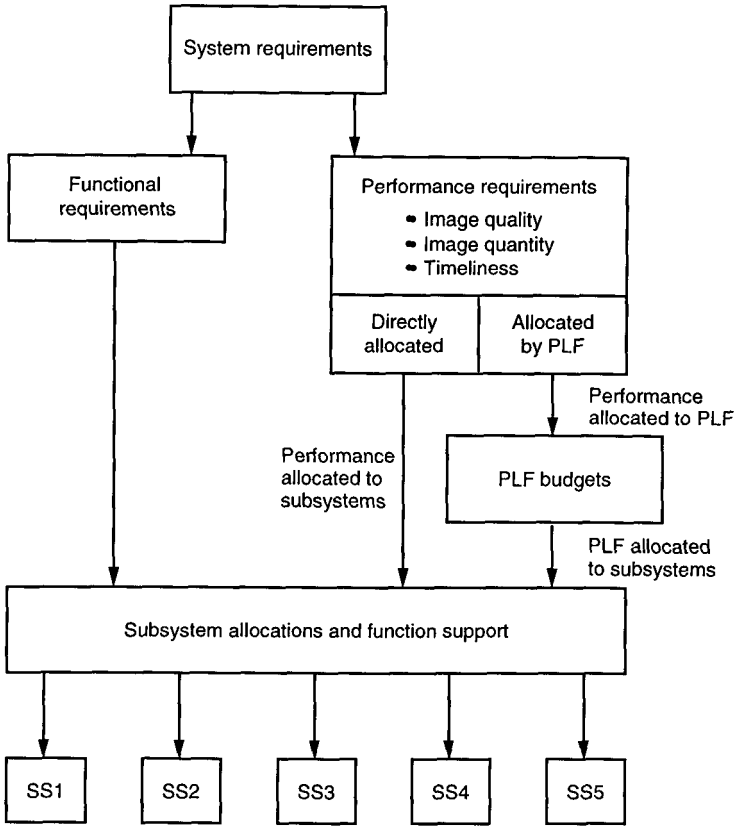


Figure 8.1 Classification and allocation of system requirements.

requires supporting analyses to relate each PLF-allocable requirement to the relevant PLFs. Examples of PLFs include phase errors, amplitude errors, transmitted bandwidth, aperture weighting, coherent data collection angle, and number of quantization bits. Examples of supporting analyses include the discussion and data in Chapter 5 relating phase errors to image degradation and the discussions in Appendix D on aperture weighting effects.

The introduction and use of PLFs is necessary for two reasons. First, the PLFs, rather than the associated performance requirements, are often the measurable quantities at the subsystem and element levels. Second, the same PLF may influence many performance requirements, making it necessary to determine the allowable levels of the PLF for each performance requirement and collectively over all performance requirements. In this situation, it is reasonable to divide the performance requirement specification level among the PLFs rather than among the radar subsystems, within the constraint that the resulting set of PLF allowances must be the same for each performance requirement.

Table 8.2 presents the allocation approach for the primary image quality metrics. Most of these metrics involve use of the performance limiting factors; principally, these PLFs consist of various categories of phase errors. The direct allocation of additive noise involves, principally, the use of the standard radar equation. The direct allocation of geometric distortion involves a single PLF, linear phase error.

Table 8.2
Allocation Approach for Image Quality Metrics

Image Quality Metric	*Allocation Approach*
Mainlobe –3-dB width (resolution)	Through PLFs
Peak sidelobe levels	Through PLFs
σ_n (describing additive noise)	Direct
MNR	Through PLFs
Geometric distortion	Direct

The specification levels on PLF-allocable metrics translate into total system allowances for each PLF. To accomplish this translation, we divide the specification level of each image quality metric individually among the PLFs, but interactively over all metrics. This step generates one set of PLF allowances that simultaneously satisfies all specifications. Table 8.3 indicates a possible format for subsystem allocations of PLF allowances. This table includes a reasonable subset of PLFs together with representative system-wide allowances. The result of this procedure is a division of the system PLF allowances among the subsystems. It is not appropriate to divide the specification levels imposed on the PLF-allocable metrics directly among the subsystems. In the case of a directly allocable metric (such as additive noise), the specification itself is divided among the subsystems.

To verify the adequacy of the set of system-wide allocations of PLFs relevant to impulse response function, it is a common practice to employ an impulse response simulation. This simulation combines all PLFs with random weighting up to each one's allocated value. The purpose of this simulation is to generate typical impulse response functions that would arise, on a statistical basis, from the presence of all effects. A satisfactory result indicates that, on average, the set of proposed PLF levels produces a satisfactory system impulse response function after accounting for the fact that all PLFs are unlikely to occur at maximum value in a particular image.

Table 8.4 offers examples of requirements on subsystems derived from subsystem allocations of PLF. A reasonable format includes the source of the derived requirements. In general, each of the derived subsystem requirements needs a detailed error allocation over the subsystem's elements to demonstrate that each requirement is achievable.

The following sections describe the primary IQ parameters and present the PLFs associated with each parameter. This discussion begins with a consideration of parameters related to system impulse response, continues with a consideration of parameters related to noise, and concludes with a brief definition of the secondary IQ parameters.

Table 8.3
Subsystem Allocations of PLFs

PLF	*System-Wide Allowance*	*Subsystem Allocation*	*Error Sources*
Range quadratic phase error	$\pi/6$ rad	Radar	Waveguide dispersion, beam voltage droop in transmitter and exciters (after corrections)
Azimuth quadratic phase error	$\pi/4$ rad	Motion sensor	Allocation is after autofocus, if available
Range quadratic-to-single-cycle phase error	$\pi/8$ rad interval	Radar	Exciter, RF front-end components
Azimuth quadratic-to-single-cycle phase error	$\pi/8$ rad interval	Motion sensor	Range error, IMU error
Range single-cycle-to-wideband phase error	0.03 rad RMS	Radar	Exciter, RF front-end components
Azimuth single-cycle-to-wideband phase error	0.07 rad RMS	Radar (0.05 rad RMS); Motion sensor (0.05 rad RMS)	Transmitter, frequency generator; IMU error, angle uncertainty
Range low-frequency amplitude error	0.05 relative to average amplitude	Radar	Transmitter, exciter, reflections
Range wideband amplitude error	0.05 RMS relative to average amplitude	Radar	Transmitter, exciter, reflections
Azimuth low-frequency amplitude error	0.05 relative to average amplitude	Radar	Transmitter, antenna pattern
Azimuth wideband amplitude error	0.04 RMS relative to average amplitude	Radar	Transmitter, presummer filter

8.3 REQUIREMENTS RELATING TO SYSTEM IMPULSE RESPONSE

The intensity impulse response of a SAR system, as observed in output radar imagery, is characterized by a mainlobe where most of the energy is concentrated and by sidelobes of varying energy content and spatial distribution. The sidelobe characteristics are influenced primarily by the selected amplitude weighting over the coherent processing aperture, by the presence of undesirable phase effects, and by amplitude weighting introduced throughout the SAR imaging system.

The SAR system is nominally a linear system characterized by a space-invariant impulse response function. In practice, there are factors that contribute nonlinear behavior and space-variant effects. In our spotlight model using the polar format algorithm, the

Table 8.4
Examples of Derived Requirements

Derived Requirement	*Source of Requirement*
Vehicle along-track velocity measurement accuracy	Allocation of low-frequency (quadratic) azimuth phase error
Vehicle line-of-sight acceleration measurement accuracy	Allocation of low-frequency (quadratic) azimuth phase error
Jitter in antenna line-of-sight phase center	Allocation of high-frequency azimuth phase error
Jitter in antenna boresight pointing angle	Allocation of high-frequency azimuth amplitude error
Antenna pointing accuracy	σ_n allocation; requirement on image intensity uniformity
Transmitter chirp linearity	Allocations of low- and high-frequency range phase error

system impulse response is the two-dimensional Fourier transform of the signal history characterized by (3.24). This representation includes various phase effects, but it does not consider noise sources and their impact.

It is common to specify the system impulse response by its mainlobe width and sidelobe structure. Because system requirements can differ in range and cross-range, it is natural to specify the resolution separately in each dimension. Figure 8.2 illustrates an ideal one-dimensional intensity impulse response using uniform weighting. The aperture weighting factor associated with this weighting (either K_r from Section 2.3.2 or K_a from Section 2.4.2) in calculating the theoretical –3-dB width is 0.89. The first sidelobe for the uniform weighting appears 13.3 dB below the mainlobe. Figure 8.3 illustrates the ideal impulse response using –35-dB, $\bar{n} = 5$ Taylor amplitude weighting to suppress sidelobe levels (Appendix D). The aperture weighting factor associated with this weighting is 1.19. Use of this weighting degrades resolution by a factor of 1.34 (the ratio of 1.19 to 0.89) relative to uniform weighting in exchange for much lower sidelobe levels. Normal practice is to transmit additional bandwidth in range and to collect additional angular interval in azimuth to counteract the widening of the impulse response mainlobe by aperture weighting and by allocated amplitude and phase errors. Figure 8.3 includes an example of an envelope specification to limit peak sidelobe levels. This kind of specification does not include a limit on the total integrated sidelobe energy. It is common to specify resolution and peak sidelobe levels individually but to specify integrated sidelobe ratio (ISLR) only indirectly as one contributor to an MNR specification.

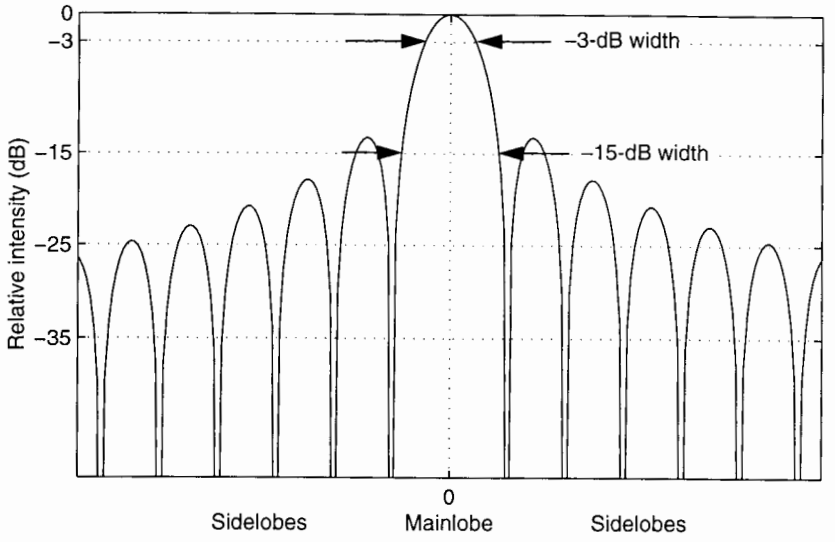


Figure 8.2 Theoretical point target impulse response with rectangular weighting.

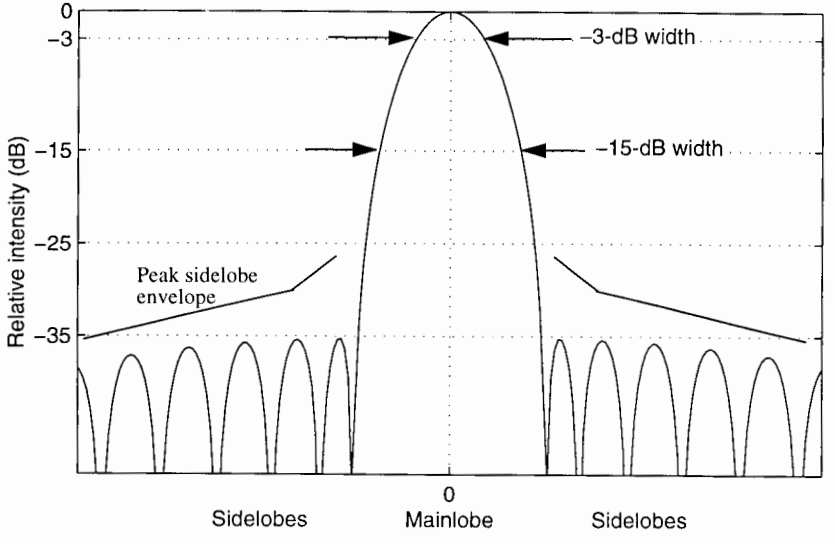


Figure 8.3 Theoretical point target impulse response with −35-dB, $\bar{n} = 5$ Taylor weighting.

8.3.1 Resolution

A common definition of image resolution is the −3-dB width of the intensity impulse response. The physical size of the intended target and the anticipated spacing of its radar scattering centers usually drives the system requirement for resolution. In addition, finer resolution is required as the purpose for or end use of the imagery moves from detection through classification to identification of targets. For instance, detection of ground vehicles often requires a resolution of between 1 and 5 m. On the other hand, SAR imagery involving terrain mapping applications can be useful at resolutions of tens of meters.

The PLFs that impact range resolution are transmitted bandwidth, aperture weighting, low-frequency amplitude effects, and low-frequency phase errors. The factors that limit azimuth resolution at a specific center frequency include the coherent processing angle, aperture weighting, low-frequency amplitude effects and low-frequency phase errors after autofocus. The amplitude and phase errors are nondeterministic sources of degradation. In fact, low-frequency, largely quadratic, phase errors from inaccuracy in antenna phase center (APC) motion measurement are a primary design consideration in the azimuth channel. Table 8.5 presents the relationship between quadratic phase error (QPE) over a −35-dB Taylor-weighted aperture and broadening of the mainlobe. This material, from Section 5.1.1, also indicates the accompanying reduction in peak intensity as energy shifts from the mainlobe to the sidelobes in the presence of phase error. As an example, Figure 8.4 shows the effect of π rad of QPE on the peak intensity and the sidelobe structure of the impulse response function.

Table 8.5
Effects of QPE on Impulse Response with −35-dB, $\bar{n} = 5$ Taylor Weighting

QPE Magnitude (rad)	*−3-dB Width of Mainlobe (Resolution)*	*Peak Intensity Loss (dB)*
0	1.00 (reference width)	0.0
$\pi/4$	1.03	0.1
$\pi/2$	1.09	0.5
π	1.5	2
2π	3.0	5
4π	5.5	8.5
6π	8.0	10
8π	12.0	11.5

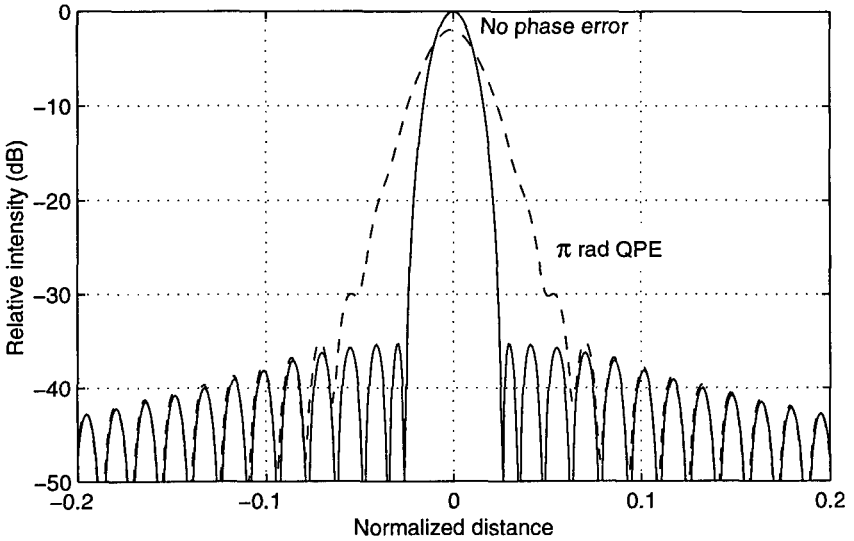


Figure 8.4 Effect of π rad of QPE on impulse response function with –35 dB, $\bar{n}$ = 5 Taylor weighting.

As an example of PLF allocation, Table 8.6 suggests reasonable allocations at X-band for range –3-dB width (resolution). The PLFs are processed bandwidth, aperture weighting to suppress sidelobes, and amplitude and phase errors. Similarly, Table 8.7 suggests similar allocations for an azimuth –3-dB width in which integration angle replaces processed bandwidth. In these tables, the two factors for aperture amplitude weighting and amplitude and phase errors combine to form the mainlobe-broadening factors K_r and K_a in the equations for range resolution (2.2) and azimuth resolution (2.20).

Table 8.6
PLF Allocations at X-Band for Range –3-dB Width

PLF	*Allowance*	*Performance Level*
Bandwidth	180 MHz, unweighted	0.82 m (–3-dB width)
Amplitude weighting	–35 dB; $\bar{n}$ = 5 Taylor	Times 1.19
Amplitude and phase errors	Available from PLF allocation (Table 8.3)	Times 1.03
Net performance		1 m (–3-dB width)

To verify that a SAR system meets its resolution specification, it is standard practice to image a test array containing trihedral (corner) reflectors. Plots of range and azimuth intensity impulse responses provide a direct measurement of the mainlobe –3-dB widths

and the peak sidelobe levels of the system. Figure 8.5 illustrates actual intensity scans from a trihedral corner reflector obtained from a spotlight SAR image. Measures of the mainlobe –3-dB width and nearby peak sidelobe levels are available from these plots. An overlay on each impulse response plot suggests a possible specification limit on allowable peak sidelobe levels and provides a visual verification that the specification is satisfied. The real and imaginary components of the Fourier transform of the isolated impulse response data indicate the phase error and any amplitude effects associated with the impulse response in each dimension. Figure 8.5 includes plots of the phase error associated with the impulse response after the removal of any constant or linear components of phase. In this case, residual phase error is larger in range than it is in azimuth.

Table 8.7
PLF Allocations at X-Band for Azimuth –3-dB Width

PLF	*Allowance*	*Performance Level*
Integration angle	0.0195 rad, unweighted	0.77 m (–3-dB width)
Amplitude weighting	–35 dB; $\bar{n}$ = 5 Taylor	Times 1.19
Amplitude and phase errors	Available from PLF allocations	Times 1.09
Net performance		1 m (–3-dB width)

It is desirable to begin with a complex image to measure image quality parameters related to impulse response. Typically, the original image is sampled between 1.0 and 2.0 samples per resolution cell; it is necessary to upsample the complex impulse response data much more finely to obtain accurate impulse response measurements. Typically, Fourier transforms with zero-padding are used to upsample the image to aid measurements and visualization. The procedure is to window out the impulse response pixels, FFT the selected pixels, add a zero-pad, and perform an inverse FFT. Figure 8.6 illustrates a flow chart to create an upsampled impulse response intensity plot.

The –3-dB width of the impulse response, in pixels, is the number of pixels between the points on each side of, and 3 dB below, the mainlobe peak. Generally, it is necessary to know the location of the impulse response peak and –3-dB width locations to subpixel accuracy. An interpolation, such as a parabolic interpolation, can calculate subpixel locations. To convert the pixel values to units of distance, it is necessary to multiply them by the upsampled image sample density in units of distance per pixel.

Plots of the phase error and any amplitude effects associated with the impulse response in each dimension are useful in reviewing and diagnosing sources of phase and amplitude errors. For instance, an intensity impulse response plot may reveal that the system is not meeting its –3-dB resolution specification. The phase-error plot may reveal that there is a significant quadratic or higher order (low-frequency) phase error present, suggesting incomplete quadratic autofocus correction or the need for higher order autofocus. Similarly, it is not uncommon in an airborne SAR system for the impulse response

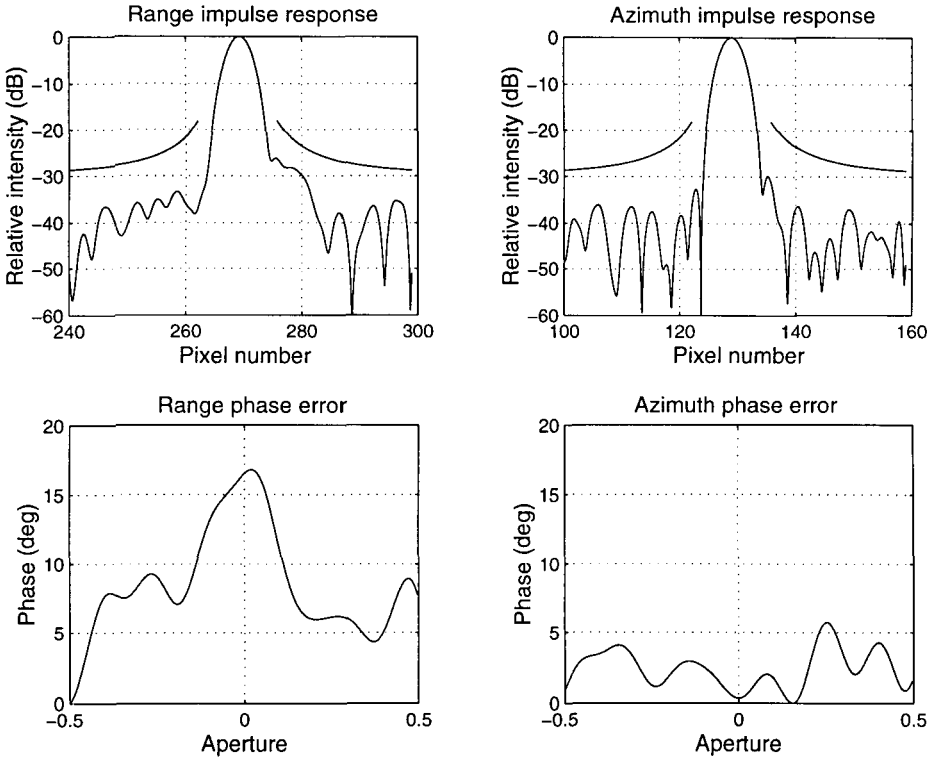


Figure 8.5 Impulse response measurements.

plot to reveal a pair of high sidelobes out a few sidelobes from the mainlobe. In such a case, the phase error plot is likely to reveal a high-frequency sinusoidal phase error indicative of a high-frequency APC vibration, associated with either air turbulence, engine operation, or autopilot system behavior. If the phase plot were smooth, then it is likely that the amplitude plot would indicate a sinusoidal amplitude modulation possibly related to antenna pointing angle jitter. In these ways, valuable system diagnostics information is available.

It is possible to use phase-error plots to provide guidance to correct for higher order phase errors in a particular image. If the phase error on the measured scatterer is indicative of the phase error in the entire image, application of its complex conjugate to the entire signal history will remove the underlying phase error. In range, this procedure can be particularly useful to reduce the impact of imperfections in the transmit waveform. In azimuth, it can provide a higher order focus correction for residual motion error effects reminiscent of single prominent point processing (PPP). As in the case of PPP (Section 6.5), it is important here to select a point-like scatterer with a high radar cross-section relative to the background.

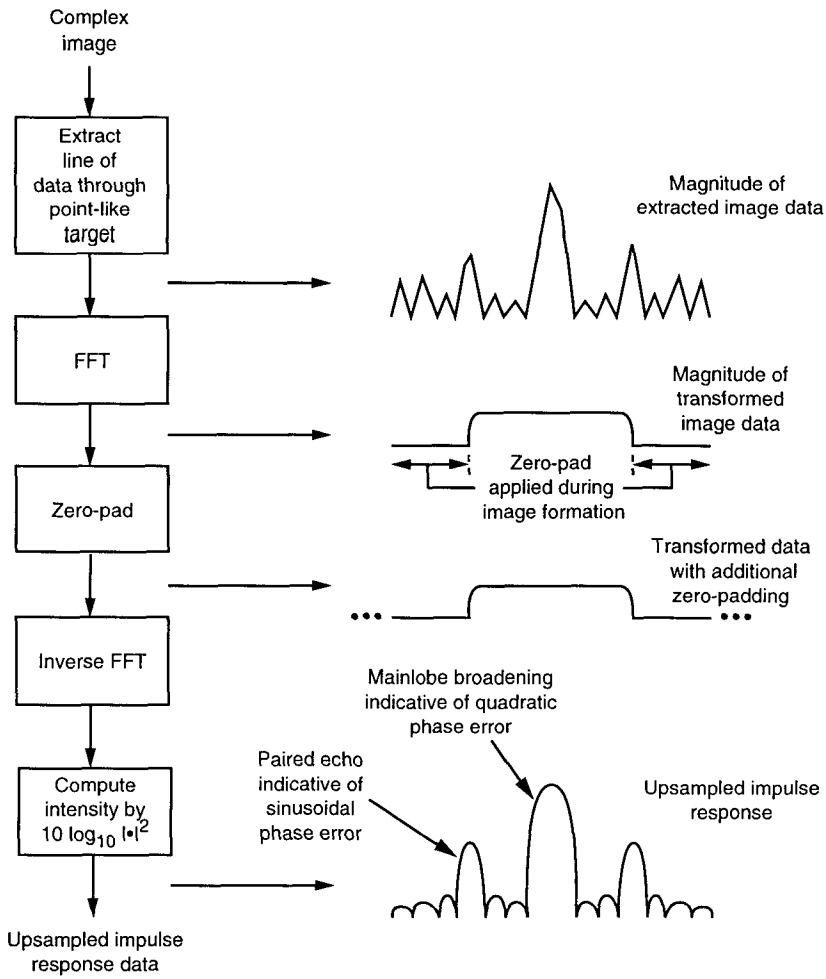


Figure 8.6 Procedure to generate an upsampled magnitude impulse response plot.

Figure 8.7 illustrates a procedure to measure the phase error by examining the complex impulse response of a point-like scatterer. Because the phase of the impulse response may contain phase wraps, the algorithm unwraps the phase before estimating the phase error. The algorithm also removes any constant or linear components of phase. Removal of these components, which may be large but not of interest, is necessary to produce an interpretable phase plot.

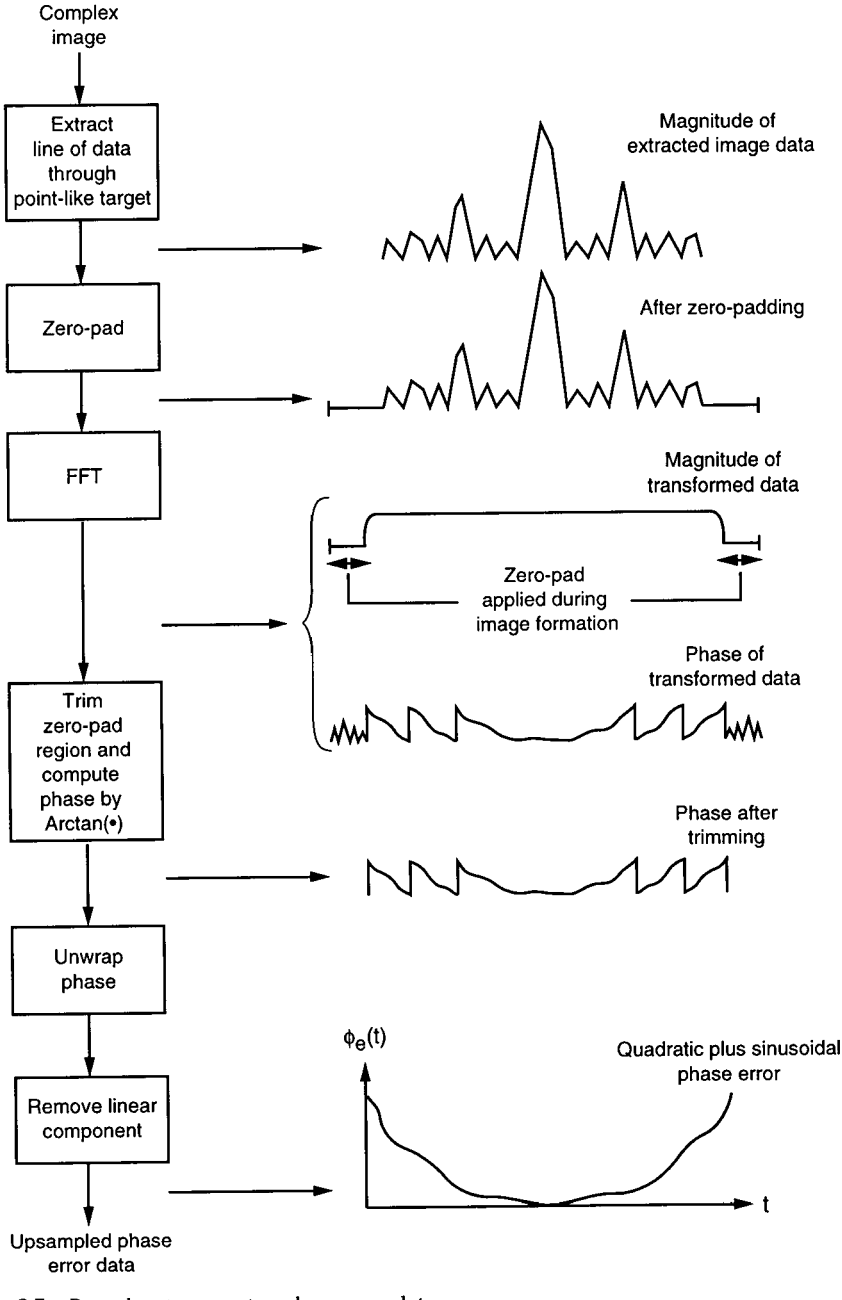


Figure 8.7 Procedure to generate a phase error plot.

8.3.2 Peak Sidelobes

In SAR imaging, it is desirable to limit the peak sidelobes of the impulse response function. High sidelobes confuse the signatures of complex targets consisting of many closely spaced scattering centers and may lead an image analyst to misidentify sidelobes as additional, real targets. The analyst might interpret a bright area emanating from one target as a separate target rather than as a sidelobe of the original target. It is reasonable to base a specification on peak sidelobes on the expected variation in RCS of scattering centers on the targets of interest. The PLFs that influence sidelobe levels are choice of aperture weighting; sinusoidal phase and amplitude errors; and high-frequency, random phase errors. Table 8.8 illustrates typical PLF allocations for the peak sidelobe requirements. Note that this allocation also includes the effects of aperture weighting (in the form of aperture edge effects) and processed bandwidth. The sinusoidal phase and amplitude errors refer to single frequency error effects, as opposed to wideband random errors.

Table 8.8
PLF Allocations for Peak Sidelobes

Performance Limiting Factor	*Allowance*	*Performance (Sidelobe Levels in dB Relative to Mainlobe Peak Intensity)*
Aperture edge effects	−35 dB; $\bar{n}$ = 5 Taylor	−35 dB
Sinusoidal phase error (zero-to-peak)	0.05 rad	−32 dB
Sinusoidal amplitude error (zero-to-peak relative to average)	0.05	−32 dB
Net performance		−30 dB (nominal)

Generally, the sidelobe energy will be concentrated in the range and azimuth directions with little diagonal energy. This happens for two reasons. First, the phase history is typically a rectangular shape with sides aligned to the range and azimuth directions. This alignment causes sidelobes from the limited aperture to dominate in range and azimuth. Second, each individual phase error in the SAR system is primarily in either the range or the azimuth dimension, seldom with any cross-product coupling between the two dimensions. Such phase errors cause an effect specifically in range or in azimuth, not off in some other direction.

The *peak sidelobe ratio* is the ratio of the peak sidelobe intensity to the peak mainlobe intensity. Nominally, the sidelobe regions include the entire area outside the first null of the theoretical weighted impulse response function in the absence of any error effects. An impulse response envelope under which the sidelobes must remain is a convenient method to specify the peak sidelobe levels. It is common practice to allow the first several sidelobes to rise above the level of distant sidelobes. This leniency is a practical necessity to accommodate the natural effects of a limited aperture and the effects of

allocated low-frequency phase errors. Figure 8.5 shows an example of such an envelope specification.

Separable amplitude weighting in the range and azimuth dimensions is the norm in the image formation processor to reduce sidelobe levels at the cost of broadening the mainlobe. Appendix D illustrates this trade-off for some common weightings. A technique to control aperture sidelobes, named *spatially variant apodization* (SVA), is an alternative means to reduce or eliminate sidelobes from isolated bright targets [3]. SVA is a nonlinear technique that improves the appearance of imagery by performing a space-variant reduction of sidelobes over the image area rather than a global, space-invariant reduction of sidelobes. Appendix D discusses the SVA algorithm.

8.3.3 Integrated Sidelobe Ratio

The *integrated sidelobe ratio* (ISLR) is the ratio of all energy in the sidelobes of the system impulse response to energy in the mainlobe. In this definition, the division between mainlobe and sidelobes is the location of the first nulls of the (error-free) system impulse response associated with the aperture weighting function being used. The ISLR is a measure over area, although it is commonly defined and measured in one dimension. A one-dimensional ISLR is a useful measure, particularly in azimuth, because of the importance of motion effects on SAR image quality. The area ISLR in the image, by including all sidelobes in the numerator, is higher than either one-dimensional ISLR.

The significance of integrated sidelobe energy depends, not only on the nature of the sidelobes, but equally importantly on the distribution of scatterers within the scene. For the case of a few widely distributed bright scatterers, the integrated sidelobe energy is not as important as the peak sidelobe levels. High peak sidelobes will contribute false targets and hinder detection of nearby, weak targets. Integrated sidelobe energy is more important when imaging an evenly distributed weaker scene. In an application such as terrain mapping, a high ISLR will degrade contrast and fill in low return and shadow areas.

It is common to regard the ISLR as one input into an MNR specification, rather than to specify it separately. This approach allows for design flexibility. The aperture weighting function and the level of high-frequency phase and amplitude errors influence ISLR. We defer a discussion of ISLR specification to the development of MNR in Section 8.4.1.

8.4 REQUIREMENTS ON SYSTEM NOISE

The decisive factor with respect to signal levels and noise in SAR imagery is the relationship between the signal and the background intensity levels. This relationship is referred to as the signal-to-background ratio (SBR). The signal may be a point-like scatterer indicative of a single target in a resolution cell or a distributed scatterer such as terrain consisting of many scatterers per resolution cell. Most generally, the background includes not only total noise but also background clutter when it is not the object of interest.

Total noise σ_N includes additive noise and multiplicative noise. Additive noise results primarily from thermal noise in the radar receiver. Multiplicative noise is signal-dependent noise; the noise level is proportional to the average signal level. The relationship for total noise is

$$\sigma_N = \sigma_n + (\text{MNR})\,\bar{\sigma}_0 \tag{8.1}$$

where σ_n is the effective backscatter coefficient of additive noise and $\bar{\sigma}_0$ is the average backscatter coefficient of local terrain. MNR is the multiplicative noise ratio, the constant of proportionality between the multiplicative noise level and the average signal level. The term *backscatter coefficient* refers to RCS per unit ground area. Table 8.9 indicates typical values of $\bar{\sigma}_0$ at X-band for common terrain types at a grazing angle near 30 deg [4-6]. In general, $\bar{\sigma}_0$ for a particular terrain area varies with radar frequency, with grazing angle, and with polarization; the values in the table simply provide a generic basis for comparing the noise contributions as discussed here. In a scene with average backscatter coefficient $\bar{\sigma}_0$, the multiplicative noise is equivalent to a terrain of backscatter coefficient $\bar{\sigma}_0$(MNR). Separate sections given later discuss multiplicative and additive noise.

Table 8.9
Average σ_0 at X-Band and 30-deg Grazing Angle for Common Terrain Types

Type of Terrain	*Average Backscatter Coefficient HH Polarization (dB)*	*Average Backscatter Coefficient VV Polarization (dB)*	*Average Backscatter Coefficient HV Polarization (dB)*
Smooth concrete	−35	−30	Not available
Asphalt	−27	−22	−32
Sandy desert	−20	−20	Not available
Plowed, disked ground	−20	−19	Not available
Dry snow	−16	−15	−22
Grasses	−13	−13	−19
Shrubs	−13	−12	−15

The level of total noise determines the distinguishability of terrains with different reflectivity and the detectability of weak targets in low backscatter terrain. Thus, SBR in general is the important factor. With σ_n and MNR as specifications, it is not necessary to include target RCS level σ_t in the system specification. Of course, the specification will choose σ_n and MNR requirements based on the RCS of targets of interest. A less desirable approach is to specify only total noise, rather than σ_n and MNR separately, to give the designer even more flexibility. However, such an approach to noise specification would take away the ability to control performance in extreme situations where either additive or

multiplicative noise may dominate without being unnecessarily restrictive in the more typical situation. An example situation is the differing impact of noise type in an area where bright, discrete targets are important or in a clutter background area where shadows or backscatter coefficient variations are important. For these varying possibilities, a balance between additive and multiplicative noise levels is generally desirable.

In quantifying a relationship between a point target signal and distributed background in an image, signal is measured in terms of peak image intensity and background in terms of the average image intensity. In fact, it is not only the average intensity of the background that is important, but the variation (representing noise spikes) of the intensity about the mean. The mean background can be subtracted out, leaving little noise, were it not for this variation. It is common to assume (with varying degrees of accuracy) that the background mimics random noise by being composed of independent scattering centers of comparable strength and random phase. In this case, the I and Q components are each described by a Gaussian distribution. Distributed clutter or background indicates that each resolution cell contains many such scatterers, randomly positioned leading to the random phase of the backscattered signal from each scattering center. Like the noise component, the amplitude of the ensemble of resolution cells composing the background acquires a Rayleigh distribution in this model. The intensity distribution, then, is characterized by an exponential probability density function. With these statistics, the standard deviation of the background intensity is equal to the mean background intensity. In fact, other models for clutter statistics (and more generally scene statistics) exist and may be more appropriate depending on the situation [6, 7]. When the target is a distributed signal also, it is appropriate to measure both signal and background in terms of the mean image intensity of each quantity.

SBR is closely related to image contrast between two different image areas, one representing the signal and the other representing the background. An extension of the SBR concept to contrast ratio, including the application of contrast ratio to specific classes of radar imaging tasks, begins in Section 8.4.3.

8.4.1 Multiplicative Noise

The principal contributors to multiplicative noise are the integrated sidelobes of the system impulse response, the energy present in the scene as a result of range and azimuth ambiguities, and digital noise. Multiplicative noise energy is distributed throughout the image based on the level of signals either in the neighborhood (integrated sidelobes), in the entire scene (digital quantization noise), or outside the scene (ambiguities). Multiplicative noise is characterized by the *multiplicative noise ratio* (MNR) in the form

$$\text{MNR} = \text{ISLR} + \text{QNR} + \text{AMBR} \tag{8.2}$$

Here, ISLR is the integrated sidelobe ratio, QNR is the quantization noise ratio reflecting primarily A/D quantization noise, and AMBR is the ambiguity ratio.

QNR and AMBR each represent the constant of proportionality between the associated noise level and the average signal level. Quantization noise is typically modeled as white Gaussian noise. A rule of thumb regarding QNR from the quantization of the signal history data is –5 dB per bit; for example, 6 bits corresponds to a QNR of –30 dB. This rule characterizes, in fact, a combination of quantization noise and saturation noise and assumes optimum biasing of the signal level going into the A/D converter relative to the A/D sampling interval [8]. Inputs to the AMBR include range and azimuth ambiguities and processing ambiguities. An antenna pattern with low sidelobes is the primary defense to limit energy from regions corresponding to range and azimuth PRF ambiguities [9, 10]. Azimuth ambiguities occur when the radar PRF does not adequately sample the Doppler frequency of any returned signals; the problem signals typically originate from scatterers illuminated by the edges of the mainlobe or by the sidelobes of the azimuth antenna pattern. Range ambiguities occur when signals, which originate from illumination by a previous pulse, reach the receiver during a range gate associated with a particular transmit pulse. The processor limits its generation of ambiguous energy with the use of adequate sampling and sharp bandpass digital filters with good stopband suppression.

A specification on MNR gives the designer flexibility in trading off the three principal components that contribute to MNR. The performance limiting factors (PLFs) that contribute to ISLR include range and azimuth aperture effects, random, high-frequency phase errors, and wideband amplitude modulation effects. Besides these PLFs, quantization noise and ambiguous energy also contribute to MNR. Table 8.10 provides an example allocation of PLFs and these additional factors for MNR.

8.4.2 Additive Noise

Additive noise is spatially distributed noise present in the image but unrelated to the level of the received radar signal; it is present even when no signal is present. The primary source of additive noise is the thermal noise at the low-noise amplifier input in the front end of the receiver.

It is common to characterize additive noise by σ_n, defined as the effective backscatter coefficient of the additive noise. The quantity σ_n is the equivalent terrain radar backscatter coefficient that would produce a signal in the receiver equal to the receiver noise signal. It is related directly to the common clutter-to-radar-receiver-noise ratio (CNR) by

$$\sigma_n = \frac{\sigma_0}{\text{CNR}} \tag{8.3}$$

CNR is the average image intensity of a diffuse target return divided by the average receiver noise intensity. The common expression for CNR is

$$\text{CNR} = \frac{P_{av}G^2}{2N_oL}\left(\frac{\lambda_c}{4\pi R_a}\right)^3\left[\frac{\sigma_0\rho_r}{K_r V_a \sin(\alpha_{dc})\cos(\psi_{ac})}\right] \tag{8.4}$$

Table 8.10
PLF Allocations for MNR

Performance Limiting Factor	*Allocation*	*Error Contribution*
Range aperture effects	−35 dB; $\bar{n}$ = 5 Taylor	−27.4 dB
Azimuth aperture effects	−35 dB; $\bar{n}$ = 5 Taylor	−27.4 dB
Range wideband phase errors	0.03 rad RMS	−30.4 dB
Azimuth wideband phase errors	0.07 rad RMS	−23.1 dB
Range wideband amplitude errors	0.05 RMS relative to average amplitude	−26.0 dB
Azimuth wideband amplitude errors	0.04 RMS relative to average amplitude	−28.0 dB
Quantization noise • A/D converter • Digital processor	 • 6 bits • 32-bit floating point	 −30.0 dB −60.0 dB
Range PRF ambiguities	PRF choice and range antenna pattern	−50.0 dB
Azimuth PRF ambiguities	PRF choice and azimuth antenna pattern	−30.0 dB
Processing ambiguities	Filters and sampling	−40.0 dB
Net performance		−18.2 dB

CNR varies with ρ_r because receiver noise in the denominator is proportional to the RF signal bandwidth B and therefore inversely proportional to range resolution. Incorporating (8.4) into (8.3), σ_n becomes

$$\sigma_n = \left[\frac{K_r V_a \sin(\alpha_{dc}) \cos(\psi_{ac})}{\rho_r}\right]\left(\frac{2N_o L}{P_{av} G^2}\right)\left(\frac{4\pi R_a}{\lambda_c}\right)^3 \tag{8.5}$$

In these equations:

V_a = antenna velocity
α_{dc} = Doppler cone angle
G = antenna gain
ρ_r = range resolution
$N_o = kT_oF_n$
$k = 1.38\times10^{-23}$ J/K = Boltzmann's constant
T_o = 290 K = standard noise temperature

F_n = receiver noise figure
P_{av} = average transmitted power
R_a = range from antenna to scatterer
λ_c = center transmitted wavelength
ψ_{ac} = grazing angle
K_r = mainlobe-broadening factor in range
L = loss factor.

The quantity N_o is the one-sided receiver noise power spectral density or noise power per unit bandwidth. A typical noise figure F_n might be 3 to 6 dB. The bandwidth associated with this noise power spectral density is contained in ρ_r. The loss factor L includes hardware effects, propagation losses, atmospheric attenuation, and other system losses. Typically, it might be on the order of 5 to 10 dB.

The traditional SAR signal-to-receiver-noise-ratio SNR, where the signal represents the return from a point-like scatterer of radar cross-section σ_t, is

$$\text{SNR} = \frac{P_{av}G^2}{2N_oL}\left(\frac{\lambda_c}{4\pi R_a}\right)^3\left[\frac{\sigma_t}{K_rV_a\rho_a\sin(\alpha_{dc})}\right] \tag{8.6}$$

where $\sigma_t\cos(\psi_{ac})/\rho_a\rho_r$ replaces σ_o in (8.4), the CNR equation.

In SAR imaging, SNR often is not a limiting factor in target detection because, typically, background clutter limits detection first. The signal-to-clutter ratio (SCR) is

$$\text{SCR} = \frac{\sigma_t\cos(\psi_{ac})}{\sigma_o\rho_a\rho_r} \tag{8.7}$$

This equation indicates a limitation on the detection of a target in background clutter regardless of receiver noise. In general, it is the combination of total noise and background clutter that limits detectability.

8.4.3 Contrast Ratio

A consideration of additive and multiplicative noise is essential in the noise trade-off design of the SAR imaging system. However, the user of the imagery may prefer to consider contrast ratio as a measure of image utility. The contrast ratio between two areas of the image is a ratio of the image intensities in the two areas. Contrast ratio is a measurable quantity in the imagery; with adequate test site design, it is possible to derive a good estimate of MNR and a rough estimate of σ_n from contrast ratio measurements to help verify system noise performance. To explore the concept of contrast ratio using the additive and multiplicative noise models, it is helpful to identify two example SAR imaging tasks.

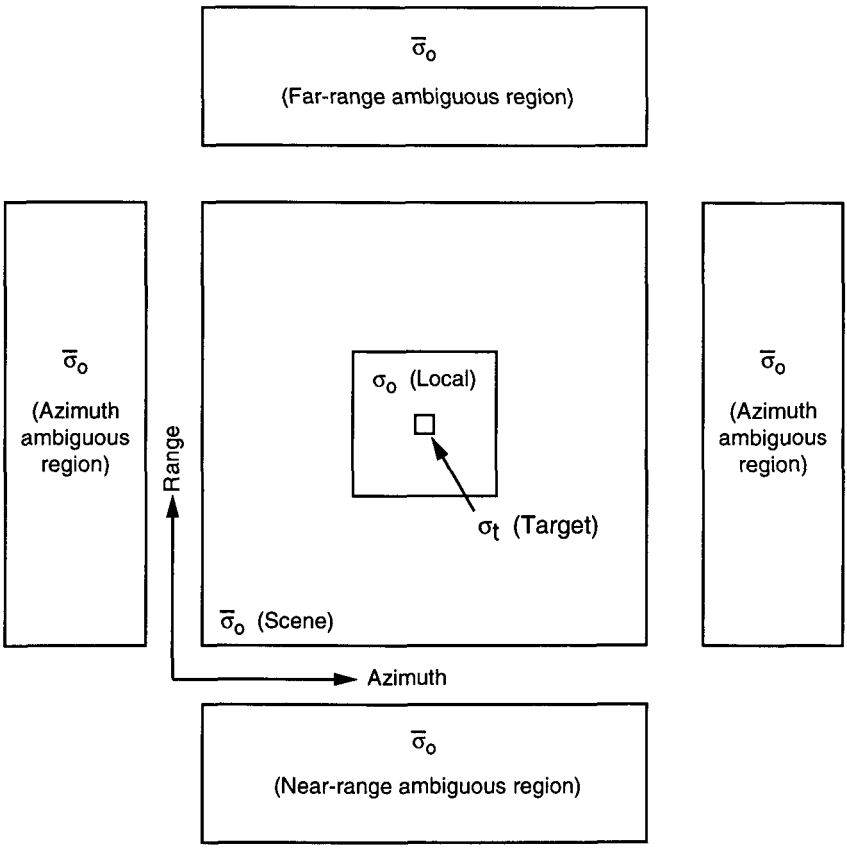


Figure 8.8 Scene model for point target detection.

The first representative task for a SAR imaging system is to detect a point target of RCS σ_t in local clutter of backscatter coefficient σ_o within a larger scene of average backscatter coefficient $\bar{\sigma}_o$. A practical example here would be a task to detect surface mines or mines buried in sand in X-band SAR imagery. In this case, σ_t is the RCS of the mine, perhaps on the order of -10 dBsm for a metallic model; both σ_o and $\bar{\sigma}_o$ are the backscatter coefficient of dry sand, perhaps on the order of -20 dB. Figure 8.8 suggests this situation with the radar (and near range) at the bottom of the figure. The four rectangular areas on each side of the scene are representative of terrain whose returns, attenuated by the ambiguity ratio, fold onto the scene because of range and azimuth ambiguities. The near-range ambiguous region is a factor only in a (long-range) sensor that has a number of pulses in transit at one time.

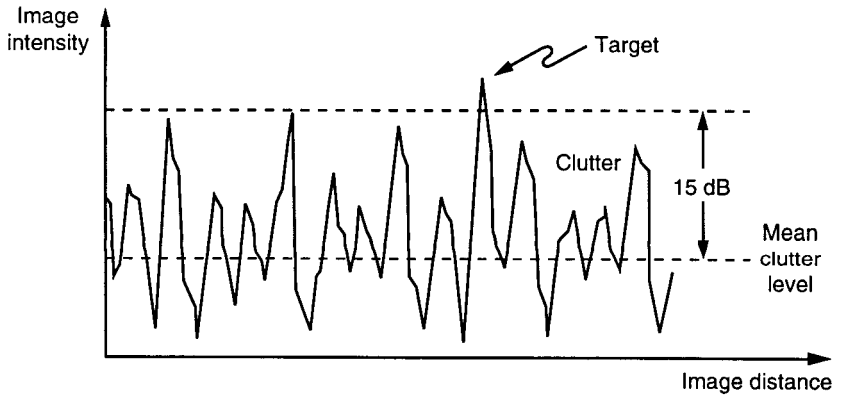


Figure 8.9 Threshold detection of signal in background.

In a task to detect a point target in local clutter, the image point-target-contrast-ratio (PTCR) is important. The PTCR, representing the signal-plus-noise-to-background ratio, is given by

$$\text{PTCR} = \frac{\left[\dfrac{\sigma_t \cos(\psi_{ac})}{\rho_a \rho_r} + \sigma_n + (\text{MNR})\,\bar{\sigma}_o\right]}{[\sigma_o + \sigma_n + (\text{MNR})\,\bar{\sigma}_o]} \tag{8.8}$$

The numerator, or signal, consists of the return from the point target itself plus the additive and multiplicative noise present at the same image location. While not included in this model, it would be necessary to also include in this numerator the return from the local clutter if the target itself does not fill the resolution cell. The denominator is the background or, in a general sense, noise consisting of the local clutter plus the additive and multiplicative noise. A PTCR of 15 dB is often cited as a reasonable requirement for reliable point target detection in the absence of noncoherent integration (NCI). NCI refers to the summation on an intensity basis of multiple images of the same scene taken at different aspect angles or with different segments of the RF spectrum [11-13]. The use of NCI reduces the variance relative to the mean intensity of the background, thereby improving detectability at a given PTCR. In fact, the large PTCR ratio is necessary to distinguish between random background intensity spikes and the bright signal return. The 15-dB requirement is a clear indication of the importance of the variance in the background intensity level. Figure 8.9 illustrates this detection criterion.

The relevance of the SCR introduced in (8.7) is evident from the PTCR equation. In situations where the additive and multiplicative noise contributions are relatively small, the PTCR reduces to the SCR. Consider the example suggested earlier of mine detection in a sandy background environment. Using the values $\sigma_t = -10$ dBsm and $\sigma_o = -20$ dB

in (8.7) produces the result

$$SCR_{mine} = \frac{10 \cos(\psi_{ac})}{\rho_a \rho_r} \text{ m}^2 \tag{8.9}$$

In this situation, resolutions on the order of 1.0 m yield an SCR below 10 dB; this level is hardly adequate for reliable detection, even in the absence of additive or multiplicative noise sources. The PTCR, by including noise in the denominator, indicates that the real situation facing the image analyst is yet more difficult. The conclusion is that finer resolution is required to achieve this type of detection using SAR imagery.

The second representative task for a SAR imaging system is to detect a change in the local clutter from backscatter coefficient σ_{oh} to a lower level σ_{ol} within a larger scene of average backscatter coefficient $\bar{\sigma}_o$. Figure 8.10 suggests this situation with the radar (and near range) at the bottom of the figure. Again, the four rectangular areas on each side of the scene are representative of terrain whose returns, attenuated by the ambiguity ratio, fold onto the scene because of range and azimuth ambiguities. In one extreme, the lower level might be a no-return area or a shadow area. A no-return area is a region that, like a shadow, backscatters no energy to the radar antenna. A flat smooth metallic surface is a typical man-made no return area, while a smooth body of water may serve as a natural no-return area. A practical example of this second task would be the detection of an asphalt highway meandering through an area of grassy vegetation in X-band SAR imagery. In this case, σ_{oh} is the backscatter coefficient of grass, perhaps on the order of -13 dB, while σ_{ol} is the backscatter coefficient of asphalt, perhaps on the order of -26 dB. The surrounding scene possibly includes some rough ground, farm buildings, and trees. The average scene backscatter coefficient $\bar{\sigma}_o$ might be about -10 dB, a reflectivity value a bit higher than grass.

In a task to detect a change in local clutter backscatter coefficient, the image distributed-target-contrast-ratio (DTCR) is important. The DTCR, representing the ratio of the high-signal-plus-noise level to the low-signal-plus-noise level, is given by

$$DTCR = \frac{[\sigma_{oh} + \sigma_n + (MNR)\,\bar{\sigma}_o]}{[\sigma_{ol} + \sigma_n + (MNR)\,\bar{\sigma}_o]} \tag{8.10}$$

The numerator or signal consists of the return from the high local distributed clutter σ_{oh} plus the additive and multiplicative noise present at the same image location. The denominator consists of the low local clutter σ_{ol} plus the additive and multiplicative noise. A DTCR of 1.5 dB is often cited as a reasonable requirement for reliable diffuse area differentiation in the absence of noncoherent integration. Consider the example suggested above of the detection of an asphalt highway meandering through an area of grassy vegetation. The DTCR, using $\sigma_{oh} = -13$ dB and $\sigma_{ol} = -22$ dB, is given by

$$DTCR_{road} = \frac{[0.05 + \sigma_n + 0.1\,(MNR)\,]}{[0.006 + \sigma_n + 0.1\,(MNR)\,]} \tag{8.11}$$

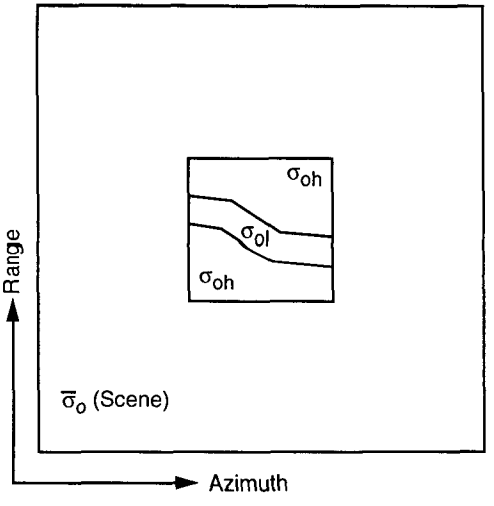


Figure 8.10 Scene model for detection of variation in backscatter coefficient (ambiguous regions not shown).

Assuming MNR is −18 dB, it is obvious from (8.11) that multiplicative noise (0.0016) plays a small role in this situation. A DTCR greater than the 1.5-dB criterion is achieved with a σ_n of less than 0.099 or −10.0 dB. While this situation is somewhat surprising in that the allowable total noise backscatter coefficient (0.101) is larger than that of either signal (0.05 and 0.006), it is not that unusual. The sum of signal plus noise (in the numerator) provides sufficient contrast relative to mostly noise (in the denominator) to permit detection.

8.5 GEOMETRIC DISTORTION

To define, specify, and verify geometric distortion in a SAR image, it is necessary first to clarify exactly what is meant by a geometrically correct image. This definition requires some thought and care because a three-dimensional target field is being mapped onto a two-dimensional image space. Typically, the object field is nominally a large relatively flat surface with minimal "height" or relief extent compared to the other two dimensions. A SAR image most naturally emerges in orthogonal range and Doppler cone angle coordinates. For instance, in an $M \times N$ array of image pixels, succeeding values of m from 1 to M might represent equally spaced range bins while succeeding values of n from 1 to N might represent equally spaced bins in Doppler frequency. From (2.26), Doppler frequency is proportional to the cosine of the Doppler cone angle α_d. If the "reference" image were a representation of the scene in range and $\cos(\alpha_d)$ coordinates, then there would be no geometric distortion.

A reference image more acceptable to the user community is one in which each scatterer in the focus target plane (FTP) appears in its true position with respect to other scatterers in this plane when viewed in a properly scaled image display plane (IDP). In this more acceptable reference image, each scatterer above the FTP appears displaced toward the radar while each scatterer below the FTP appears displaced away from the radar when viewed in a properly scaled IDP. In the nomenclature of Chapters 2 and 3, the desirable relationship between scatterer coordinates (x_t, y_t and Z_t) and IDP coordinates (u_i and v_i representing azimuth and negative range) is defined by

$$u_{id} = x_t + P_x Z_t \tag{8.12}$$

and

$$v_{id} = y_t + P_y Z_t \tag{8.13}$$

Here, x_t, y_t and Z_t represent azimuth, negative range, and height above the FTP. The contributors to P_x and P_y are given in (3.117), (3.118), and (3.188) when the IDP is the FTP. In this case,

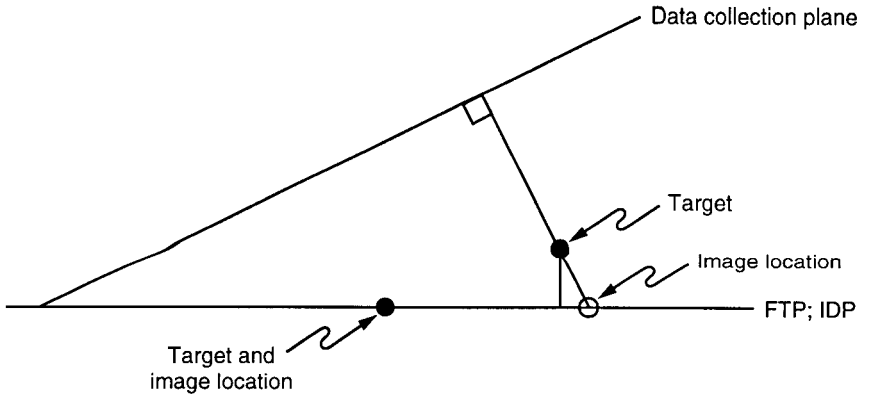
$$P_x = -\frac{\cot(\phi_{ac})\, C_{\theta c}}{S_{\theta c}} - \frac{\left[V_{za} - V_{ya}\dfrac{\cot(\phi_{ac})}{S_{\theta c}}\right]}{(V_{xa}S_{\theta c} - V_{ya}C_{\theta c})} \tag{8.14}$$

and

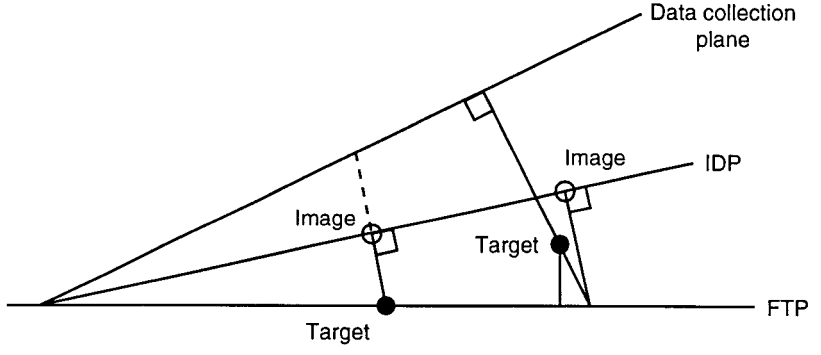
$$P_y = \cot(\phi_{ac}) \tag{8.15}$$

Figure 3.21 and Figure 3.22 illustrate this relationship when the APC is moving at constant velocity V_{xa} in the X direction with V_{ya} and V_{za} both zero. Here $S_{\theta c} = \sin(\theta_{ac})$ and $C_{\theta c} = \cos(\theta_{ac})$ while θ_{ac} and ϕ_{ac} are the values of the data collection squint and incidence angles at the center of the processing aperture. In this more acceptable reference image, the accurate or desirable image location of a scatterer corresponds to the projection of its three-dimensional scene location onto the IDP. This projection occurs along a line perpendicular to the nominal data collection plane. Figure 8.11(a) illustrates this case where the FTP is the IDP. More generally, when the IDP is not the FTP, the accurate or desirable image location of a scatterer involves a two-step projection of its three-dimensional scene location. The first projection is perpendicular to the nominal data collection plane onto the FTP. From there, the second projection is perpendicular to the IDP onto the IDP. Figure 8.11(b) illustrates this general case. Figure 8.11(c) illustrates the case where the IDP is the data collection plane.

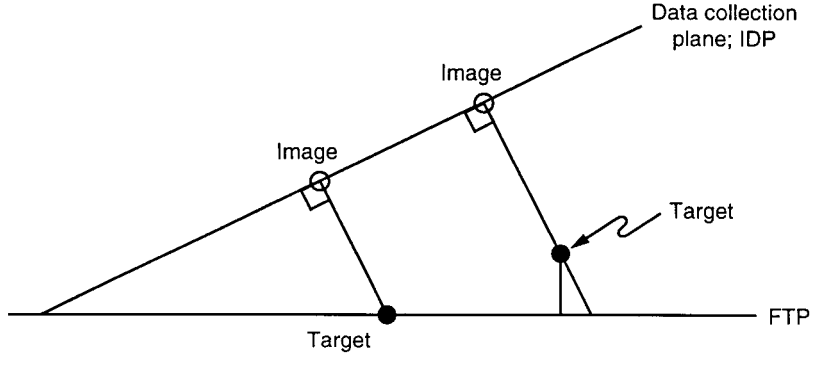
Now it is possible to define geometric distortion as the variation in the image location (u_i, v_i) of a scatterer from the scatterer's desired image coordinates (u_{id}, v_{id}). Equations (3.72) and (3.73), with the image scaling factors (m_x and m_y) equal to unity, reflect this



(a)



(b)



(c)

Figure 8.11 Desirable relationship between scene location and image position in three cases: **(a)** IDP is the FTP; **(b)** IDP is between the FTP and data collection plane; **(c)** IDP is the data collection plane.

definition. These equations are

$$u_i = x_t + P_x Z_t + L_x + l_x(X_t, Y_t, Z_t) \tag{8.16}$$

and

$$v_i = y_t + P_y Z_t + L_y + l_y(X_t, Y_y, Z_t) \tag{8.17}$$

where P_x and P_y are geometry factors relating to the projection of targets onto the IDP, L_x and L_y are image displacements, and l_x and l_y are image distortions in azimuth (x subscript) and negative range (y subscript).

A system specification limiting geometric distortion is important for target identification, such as in ATR algorithms where precise distance measures may be critical factors. Geometric distortion also will impact the utility of large scene images for mapping and geodesy including three-dimensional SAR interferometric mapping (Section 9.3). Sources of image distortion include measurement error in sensor velocity, the uncompensated range curvature term in the polar format algorithm, and the residual video phase effect. Distortion from range curvature arises because the SAR image is naturally a range-Doppler cone angle mapping, not a mapping in IDP coordinates. It is typical to specify the geometric distortion in terms of a tolerance in percentage of distance or in total distance error. Chapter 3 quantifies sources of deterministic geometric distortion in spotlight SAR imagery.

The standard procedure to measure geometric distortion in a SAR image is to measure the image locations of corner reflectors placed throughout a calibration scene and compare these measurements with results from a land survey undertaken to establish the three-dimensional location of each reflector in space. The image location of each corner reflector can be accurately established to within a fraction of a pixel by computing the peak location of its upsampled impulse response.

8.6 SECONDARY IMAGE QUALITY METRICS

This section provides a list of important, although often secondary, SAR image quality (IQ) parameters, along with definitions and representative values in a system specification. Secondary metrics, summarized in Table 8.11, might include system dynamic range, spurious response levels, image intensity uniformity, RCS calibration accuracy, and mainlobe −18-dB width. The selection of primary and secondary IQ parameters for system specification and performance verification is flexible and, ideally, is guided by the end use of the imagery. For example, in our presentation here, RCS calibration accuracy is assigned the secondary label. In fact, the need for calibration, either absolute or relative, and the accuracy levels required vary with image use [14]. In an application such as the ground-to-air imaging radar (GAIR) system (Section 7.2), which was designed to characterize the behavior of stealth targets, RCS calibration accuracy is likely to be the most important consideration [15].

Table 8.11
Secondary Image Quality Metrics

Secondary Image Quality Metric	*Example Specification Level*
System dynamic range	60 dB
Spurious response levels	30 dB below contributing sources
Image intensity uniformity	Less than 1-dB variation
RCS calibration accuracy	Within 1 dB (absolute)
Mainlobe −18-dB width	2 m (for a −3-dB width of 1 m)

The *system dynamic range* describes the interval of RCS over which targets that are simultaneously present within the same scene will image adequately. A target images adequately if its image impulse response satisfies a selected set of image quality specifications. The linear dynamic range is the interval of target RCS over which the peak intensity of the system impulse response is linearly related to the target RCS (before any intentional nonlinear remapping procedure).

Dynamic range is an important consideration in radar system design because the RCS of man-made objects can vary widely. Dynamic range in SAR is a difficult concept to define, to specify, and to measure in a useful way. It involves a number of theoretical and practical aspects. Front-end receiver noise is the primary limit on the minimum discernible signal, or the noise floor, present. Receiver noise (associated with σ_n, although σ_n includes other additive noise sources) determines the minimum diffuse backscatter coefficient that will be visible in the image. The backscatter coefficient of shadows and no-return areas, for instance, will be at or above this level in the image. This fact explains why σ_n is defined as the effective backscatter coefficient of system additive noise.

The maximum useful signal level is more difficult to establish because of the possibility of saturation and clipping of the signal at various stages between the receive antenna and the output image. The receiver front-end, low-noise amplifier gain, any subsequent amplification leading to the A/D converter, and any signal attenuation settings before the A/D conversion affect the maximum useful signal level. The number of A/D bits determines the quantization noise that contributes to system multiplicative noise. The requirement to image *simultaneously* an array of targets with RCS over the dynamic range interval is essential in the specification of system dynamic range. This requirement is needed because of the ease in setting gains and attenuation levels to control the A/D bias level to let through a large signal of any magnitude without distortion at the expense of degrading low-level signals in the digitization process.

A signal from a point target comes into the receiver as a voltage waveform. This voltage varies sinusoidally in time with amplitude proportional to the square root of the target's radar cross-section σ_t. For example, two targets differing by 60 dB in RCS enter the receiver with a 1000:1 voltage ratio, typically along with returns from thousands of other scatterers, all coherently summed. This composite signal represents the temporal

signal that the receiver must process without saturation while preserving the small variations indicative of the weaker signal components. Because the small signals "ride" on top of the composite received signal from all other scatterers, it is not necessary to sample the composite signals over a 60-dB range at the A/D converter. Clipping the analog signal in the A/D converter introduces multiplicative noise, but does not completely remove the weak or strong scatterer information from the composite signal. As the composite signal progresses through the image formation processor, the preservation of high level and low level signals becomes more important. The processor gain that accompanies signal compression, in terms of beam compression ratio (Section 2.4.3) in azimuth and pulse compression ratio (Section 2.3.2) in range, is at work. Coherent signals from large and small RCS scatterers benefit from this processor gain whereas the additive noise and noncoherent clutter returns do not. The number of processor bits per digitized signal sample (processor word size) must eventually accommodate the full 60 dB of intensity interval to preserve two targets differing by 60 dB in RCS.

A *spurious response* is unwanted energy at a location in the imagery not directly indicative of a scatterer at that location. Spurious responses in SAR imagery do not have a uniform distribution. Sources of spurious responses include intermodulation products, harmonics, nonlinear distortions, I and Q imbalance, range and azimuth ambiguities, and signal leakage. The uncertainty of the sources of spurious signals makes their specification and tracking difficult. It is common to specify spurious response levels in relation to the source of the response or in relation to the background noise level. Fortunately, in the well-designed radar system, spurious targets are only an occasional problem, typically associated with an infrequent source such as an unusually high RCS target present in one of the sidelobes of the antenna illumination pattern.

The purpose of a specification on *image intensity uniformity* is to ensure that the return from a uniform, distributed scene is indeed uniform and does not vary significantly with image spatial coordinates. This specification limits the variation of image intensity caused by effects such as antenna illumination pattern, natural power falloff with range to target, and uncompensated frequency-dependent gain of sensor and processor. It is common to specify image intensity uniformity as an allowable variation, such as 1 dB, about the average over an area of relatively uniform backscatter coefficient.

The intensity of an area in a SAR image area is a function of the radar cross-section of the corresponding scene area. Many applications of SAR imagery are satisfied with a relative measure of scene reflectivity; until recently, a requirement on absolute RCS calibration was not common. That situation has been changing in recent years with new demands on sensor capability in terms of polarization diversity, geometric accuracy, and radiometric (RCS calibration) accuracy to contribute to target characterization studies, automatic target cueing, and automatic target recognition (ATR). Some users of SAR data require estimation of the absolute RCS of scatterers or regions found in the imaged scene. Other users of SAR data may require only information about the relative RCS of objects. While absolute calibration implies that RCS values are always estimated to within some absolute error bounds, relative calibration is a comparison of RCS values within the same image or from one image to another.

The absolute RCS calibration of a SAR involves multiple considerations throughout the sensor and the image formation processor [16, 17]. Basically, RCS calibration requires the measurement of the total system transfer function or the transfer function of each of the individual subsystems so that the SAR output image can be directly and absolutely related to the scene reflectivity. To calibrate a SAR system, the system must eventually image a test site containing calibrated reference reflectors, typically trihedral corner reflectors.

In addition to the −3-dB impulse response width, image quality metrics may also include a secondary width such as the −15 or −18-dB width. Such an additional constraint on the shape of the system impulse response is sometimes advisable to control the flaring out of the mainlobe below the −3-dB width.

8.7 TEST SITES FOR IMAGE QUALITY VERIFICATION

The preferred and convincing way to verify that a SAR system meets its performance specifications is to prove it with measurements on actual imagery generated by the system. This step is usually preceded by proving system performance on paper with error budgets, equations, and subsystem measurements of various sorts. Ideally, the final phase of verification involves imaging a ground test site especially designed to provide measurable image features for computing IQ parameters. These test sites generally include carefully engineered, precisely constructed, and accurately calibrated reflector arrays and a sizable no-return area (NRA), properly embedded in the scene. Sometimes, out of necessity, uncalibrated reflectors and a shadow area or a quiet body of water must substitute for precision corners and a NRA in impromptu testing procedures. This section illustrates the basic components of a test site design for IQ verification and discusses some measurement strategies.

8.7.1 Elements of the Test Site

To measure range and azimuth resolution, peak sidelobe levels, ISLR, dynamic range, RCS calibration accuracy, and geometric distortion, it is common to use arrays of trihedral corner reflectors for linear like-polarization operation on transmit and receive (that is, for HH and VV polarization). For linear cross-polarization operation (HV and VH polarization), standard trihedrals give little backscatter energy and are not useful. A version of the trihedral with a gridded mesh covering one side provides a large cross-polarized return [18]. With proper orientation, the dihedral reflector and the tophat reflector on a ground plane are useful for returning a signal in the cross-polarization modes.

Figure 8.12 shows a photograph of a trihedral reflector with triangular sides. The physical size of the trihedral determines its maximum RCS according to the relationship

$$\sigma_t = \frac{4\pi L^4}{3\lambda_c^2} \tag{8.18}$$

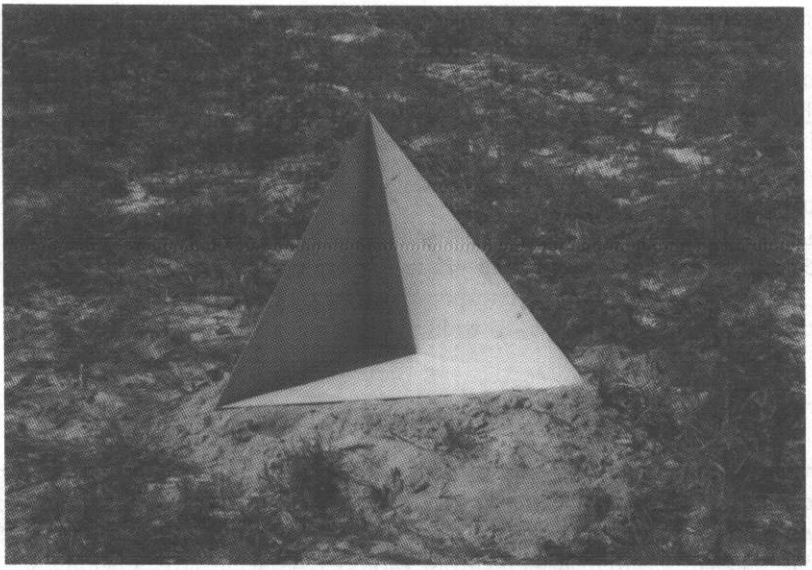


Figure 8.12 Trihedral reflector.

where L is the short dimension of the sides of the trihedral and λ_c is the center wavelength [19]. At a wavelength of 0.03 m, the maximum RCS of a trihedral reflector with sides of 0.2 m is 8.7 dBsm. Versions of the corner reflector with either square sides or a circular treatment to the exposed edge of the sides are also common. The triangular trihedral design is often preferred over alternative versions because it presents a wider beam pattern. A triangular trihedral corner reflector has a broad 40-deg beamwidth in aspect angle while a dihedral reflector has a strong return in aspect angle only normal to its crease.

An isolated corner reflector is useful to estimate the ISLR, one component of the MNR specification. It is important that the corner reflector signatures used for impulse response measurements not interfere with each other or with the signature of the NRA. The corner reflectors for impulse response measurements are placed in areas with a low backscatter coefficient to minimize interference by the background. The reflectors may still have nonideal impulse responses due to multipath effects (Figure 8.13) or interference with the background. For this reason, it is desirable to average measurements on a number of trihedral reflectors to reduce the effects of random errors. Multipath effects are most significant at grazing angles below about 20 deg. When the absolute RCS of a trihedral corner reflector, as well as that of most other reflectors, is important, it is necessary to take into account the strong angular dependence of the RCS of most types of reflectors. Correction factors for elevation and azimuth angles of the radar line-of-sight relative to the reflector's direction of maximum return are essential for accurate calibration [19].

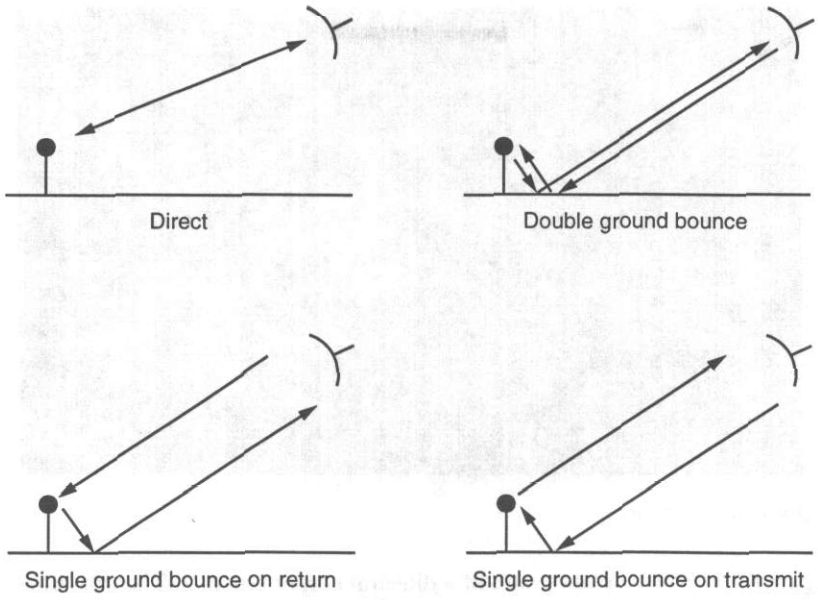


Figure 8.13 Illustration of sources of multipath effects.

The tophat reflector is a solid cylinder on top of a conducting ground plane [20]. The axis of the cylinder is perpendicular to the ground plane. Figure 8.14 shows a photograph of a cylindrical tophat. The tophat reflector is oriented relative to the radar antenna so that a two-bounce reflection off the ground plane and the cylinder returns energy to the antenna. One advantage of the tophat is that it is visible from all aspect angles because of its symmetry. The tophat has a significantly lower RCS than a trihedral corner reflector of comparable size because the curved cylinder of the tophat reflects energy in a wide beam.

The height h and radius r of the tophat reflector determine its RCS at a particular grazing angle, ψ, according to the relationship

$$\sigma_t = \frac{8\pi h^2 r \cos(\psi)}{\lambda_c} \tag{8.19}$$

where λ_c is the center wavelength [20]. This result assumes that the cylinder height, not the size of the ground plane, limits the backscatter area of the reflector (the two-bounce region). With the cylinder axis vertical, this result applies for VV and HH polarizations; there is no HV or HV reflection. If the cylinder is tilted off vertical, HV and VH reflections do occur. At a wavelength of 0.03 m and a nominal grazing angle of 30 deg, the RCS of a 0.2-m high tophat of radius 0.1 m is 4.6 dBsm. The tilted tophat is useful for returning a signal in the cross-polarization modes, although its utility is somewhat limited by its relatively low RCS [20].



Figure 8.14 Tophat reflector.

Figure 8.15 shows a photograph of a dihedral corner reflector. The dihedral reflector has a relatively strong return (similar to a trihedral) for its size. The length l and width w of each side of the dihedral reflector determine its maximum RCS according to the relationship

$$\sigma_t = \frac{8\pi w^2 l^2}{\lambda_c^2} \tag{8.20}$$

This result applies to linear, like-polarization modes when the E-field is parallel or perpendicular to the crease of the dihedral [19, 21]. It applies to linear, cross-polarization modes when the E-field is at 45 deg to the crease of the dihedral. At a wavelength of 0.03 m, the maximum RCS of a dihedral reflector of sides 0.2 m and length 0.2 m is 16.5 dBsm. The dihedral is useful for returning a signal in the cross-polarization modes, although its utility is limited by its narrow aspect angle access.

A typical NRA design consists of flat aluminum panels bolted together to form a flat perfectly conducting plane. Except at normal incidence, the NRA reflects energy away from the source of radiation and returns no energy to the illuminating antenna. An NRA design must minimize the edge effects at the NRA boundaries by designing a smooth height transition to the adjacent terrain. For example, grading the surrounding ground area smoothly up to the edges of the NRA helps to minimize any height discontinuity. Figure 8.16 illustrates a large NRA at a test site. The size of this particular NRA is roughly 10 m on a side although it is not rectangular in shape.

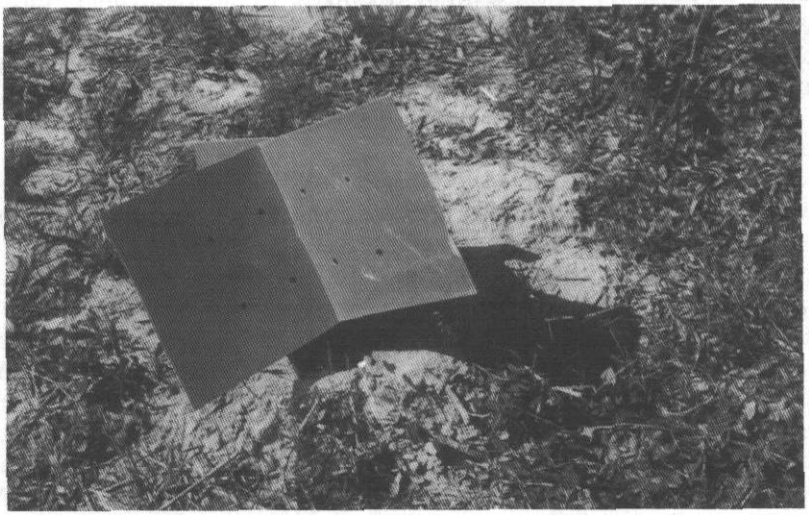


Figure 8.15 Dihedral reflector.



Figure 8.16 Photograph of a no-return area at a test site.

8.7.2 Measurement of System Noise Parameters

Contrast ratio is a measurable quantity in the SAR image, indicative of the system signal-to-background ratio. Under appropriate conditions, contrast ratio measurements provide the basis to derive MNR and, in some instances, σ_n in order to verify system noise performance. Techniques to measure the noise components in a SAR image for verifying

performance use calibrated corner reflectors and precisely controlled terrain with high and low backscatter coefficients.

To measure MNR, a test site setup is necessary in which additive noise is a negligible component of total noise; the design of such a test site is a reasonable task, using background terrain with a large backscatter coefficient to encircle an area with a low backscatter coefficient.

Measurements of integrated sidelobe energy and other multiplicative noise energy are possible using SAR imagery of a scene containing a precision reflector and a no-return area in a fairly homogeneous background of high average backscatter coefficient. The precision reflector provides data for an ISLR measurement. The NRA is needed to measure quantization noise, ambiguous energy that happens to coincide with the location of the NRA, and other distributed multiplicative noise energy. The high average backscatter coefficient of the background ensures that the multiplicative noise in the NRA dominates the additive noise. Measuring the effective backscatter coefficient of the NRA only in a central area away from the boundaries ensures that ISLR from sidelobes near the mainlobe will not be a significant contributor. In this case, the contrast ratio between the average backscatter coefficient of the entire scene to that of the central part of the NRA is an estimate of the MNR components except ISLR. A direct measurement on the image of a dominant RCS reflector provides an estimate of the ISLR. The ISLR measurement is the ratio of energy in the sidelobes to the energy in the mainlobe in the impulse response of the reflector. The system MNR measurement is the sum of these two components. This measurement requires no calibration of absolute RCS. Again, the use of natural low-return areas may be necessary (except with fine-resolution systems) because of the large size required of the no-return area to escape the influence of the first few sidelobes of nearby surrounding scatterers.

In measuring ISLR in an image, a practical question involves the area to integrate over when measuring the sidelobe energy for the numerator of the ISLR metric. A common practice is to integrate until the sidelobes reach the level of the average background.

Actually, the MNR without the ISLR may be so small (see Table 8.10) that additive noise is a significant factor in the NRA despite our best plans. In such a situation, a reasonable approach to MNR verification is to measure the ISLR as above and add to it the calculated ambiguity ratio based on measurements of antenna gain and associated analyses and the calculated quantization noise based on the number of A/D bits. Since these three factors dominate MNR, this approach is reasonable, particularly since the most directly measured quantity of the three, ISLR, is generally the largest of the three.

Measurement of additive noise requires a test site setup in which multiplicative noise is small relative to additive noise; unfortunately, design of such a test site is no easy task. It is reasonable to attempt to measure additive noise with a NRA and measurement procedure similar to that described above for MNR. However, the average backscatter coefficient of the background area should be low to minimize the multiplicative noise in the central area of the NRA. In many situations, it may be difficult to design and implement such a measurement.

Techniques to measure additive noise are not without controversy because, in practice, σ_n is difficult to measure. One approach is to devise methods to measure the inputs into (8.5) that control σ_n. Measuring quantities such as antenna gain and system losses, which may vary with time and imaging geometry, is not always straightforward or accurate, however. A second approach is to collect data with and without the transmitter turned on, duplicating the system configuration and imaging geometry in almost all respects for the two collections. One difference is adjustment of the receiver automatic gain control (AGC) when only thermal noise is present in order for the A/D converter to operate in the same linear region as when the transmitter is on. Requirements to minimize measurement error include taking into account the increased receiver gain, maintaining the same collection parameters (perhaps at a slightly different down-track flight time and location), and using the same processor parameters. The basis for this approach is that only receiver thermal noise is present with the transmitter off, providing a measure of σ_n in the resulting image. The image of a test site with the radar operating normally provides the RCS reference for calibrating the σ_n measurement.

A third approach to measure additive noise is to measure the effective backscatter coefficient in areas of the image such as large shadow areas or in the middle of a large quiet body of water. The idea is that, in the center of these areas, multiplicative noise from ISLR is minimized and the resulting measurements provide, arguably, a reasonable estimate for additive noise. The use of these natural low-return areas is necessary because it likely will not be practical to build a no-return area large enough (in terms of resolution cells) to escape the influence of sidelobe energy from surrounding scatterers. A drawback of this approach is the fact that quantization noise, ambiguous energy, and sidelobe energy from high-frequency phase effects may be present throughout the no-return area.

8.7.3 Example Test Site

Figure 8.17 shows an example of a test site layout that includes the standard target set. The site includes a cylindrical tophat reflector labeled TH1; two isolated, large trihedrals labeled IPR1 and IPR2; two dynamic-range arrays (trihedral corner reflectors) labeled DRA1 and DRA2; four height (vertical) corner reflector arrays labeled HA1, HA2, HA3, and HA5; and a large no-return area (NRA) labeled NRA. The cylindrical tophat reflector (TH1) is placed near the center of this test site to serve as a reference location. Figure 8.18 presents an X-band SAR image of the test site, collected at a grazing angle of 45 deg. The resolution of the image is 1 by 1 m with the radar illumination from the left side. The IDP is the nominal slant plane with a display squint angle of 90 deg. The direct return signatures and the shadows of three large trees are present on the left, or near range, side of the image. A gravel road appears along the bottom of the image.

The two trihedrals, IPR1 and IPR2, provide an opportunity to measure the characteristics of the system impulse response. The short dimension of the trihedral sides is 0.68 m for IPR1 and 0.53 m for IPR2. At X-band (0.03-m wavelength), these targets represent radar cross-sections of 30.0 and 25.6 dBsm, respectively. The background is field grass with a backscatter coefficient in the area of −13 dB. The impulse response corresponding

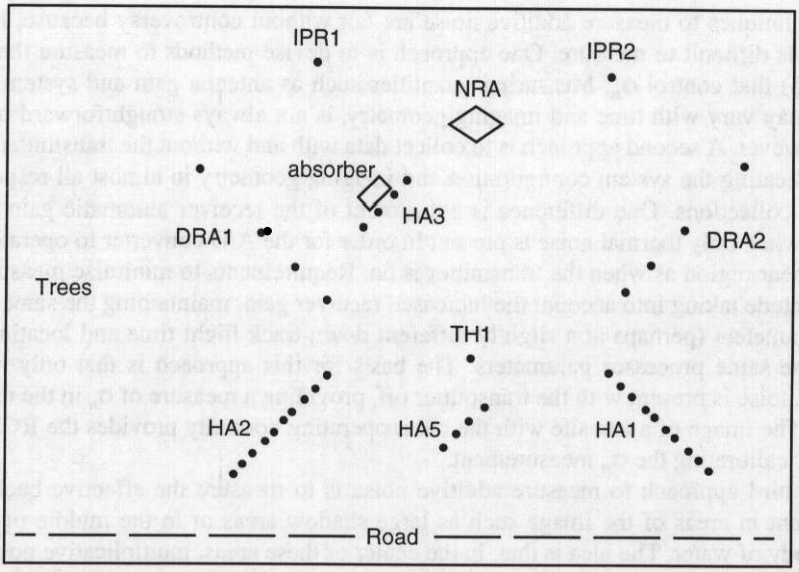


Figure 8.17 Test site layout (not to scale).

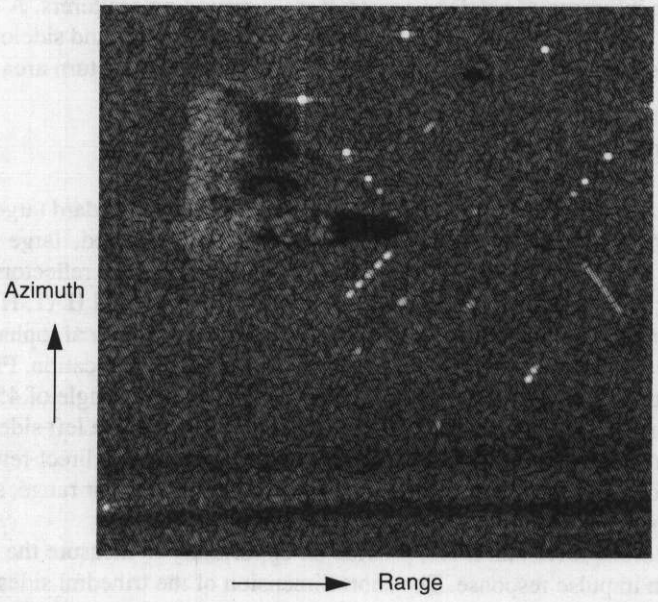


Figure 8.18 Image of test site.

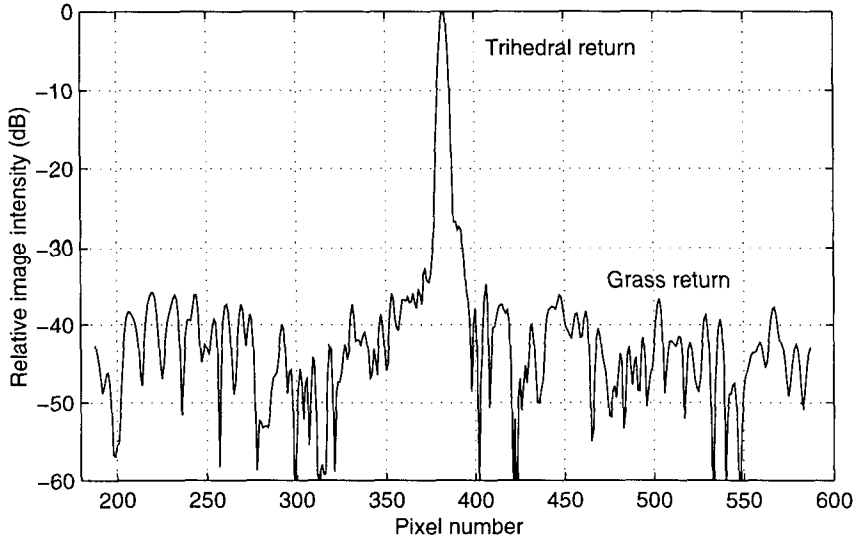


Figure 8.19 Relative intensity plot through image of large trihedral corner reflector.

to each of these large RCS trihedral reflectors dominates the background to provide an accurate measurement of sidelobe characteristics. Figure 8.19 shows a sample intensity plot through the large corner reflector IPR1, taken from the image in Figure 8.18. The peak response of the trihedral return (normalized to 0 dB) represents the 30.0-dBsm RCS of the reflector. The average response of the background is lower by about 42 dB, representing a RCS of about −12 dBsm, corresponding to the −13-dB clutter backscatter coefficient times the 1.4-m^2 (1.5-dB) area of a resolution cell from $\rho_a \rho_r / \cos(\psi_a)$. Figure 8.5 shows both phase and normalized amplitude plots of the central part of this impulse response.

The large NRA in Figure 8.17, is available to provide a rough estimate of the system noise. The size of the large NRA is 12.6 m at its widest point and 7.3 m at its smallest point. It consists of nine flat aluminum panels bolted together to form a flat conducting plane and tilted slightly to ensure proper drainage. The surrounding ground area is graded to the edge of the NRA to minimize any edge effects. With $\bar{\sigma}_0$ equal to about −13 dB in the area, the situation is not ideal to measure either multiplicative or additive noise. If the MNR is about −18 dB, then multiplicative noise in the no-return area will correspond to a backscatter reflectivity of −31 dB. If σ_n is significantly below this value, the NRA offers a measure of MNR; if σ_n is significantly above this value, the NRA offers a measure of σ_n.

Figure 8.20 shows an intensity plot through this large no-return area taken from the image in Figure 8.18. The variance of the return for the grassy area as well as that from the no-return area is evident in this plot. This situation is not ideal since the size of the NRA does not include many resolution cells. The level of the NRA is about 18 dB below that of the grassy area (with backscatter coefficient on the order of −13 dB). This measurement suggests an effective backscatter coefficient of −31 dB for the noise present in this area.

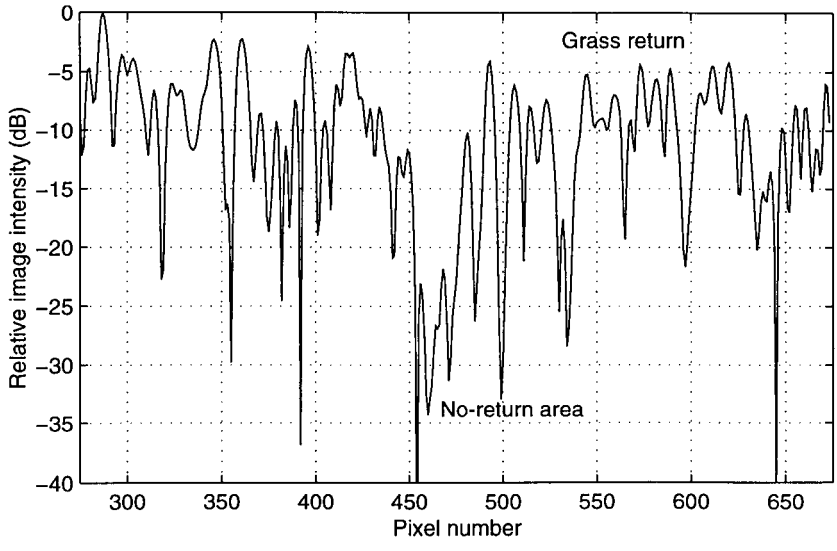


Figure 8.20 Relative intensity plot through image of no-return area.

A system MNR of about −18 dB (largely ISLR) would account for this noise. The value of σ_n associated with this image is below −40 dB, making it unreasonable to use this NRA to measure σ_n. This NRA is too small relative to the resolution cell size, and the background is too high, to make a reliable measurement of additive noise. Even with a larger NRA to escape the influence of near-in sidelobes, there is always some danger that energy from far sidelobes and from ambiguities will contaminate a σ_n measurement. Conversely, a test site with a background of somewhat higher backscatter coefficient than that of this area is desired to provide a good measure of MNR. The large shadow area behind the three trees suggests the type of natural NRA of opportunity that often proves expedient in making noise measurements.

This site includes four vertical trihedral arrays containing targets with known and adjustable heights because it was designed to verify the height accuracy of an interferometric SAR system. The trihedral reflectors in these arrays vary in size from 0.08 to 0.3 m on a side. For the HA3 array, a pad of microwave-absorbing material was placed in front of the reflectors, as suggested in Figure 8.17. The HA5 array has a similar height array as HA3 without the absorbing material. This arrangement is one way to test for the effects of multipath reflections on height measurements by comparing the height estimates from these two arrays.

The site contains two dynamic range arrays (DRA1 and DRA2) to provide the means to estimate the dynamic range of the system. These arrays appear in near range and far range of the imaged scene to ensure that the system properly compensates for variations in signal strength with range. The sizes of the reflectors are 0.22, 0.38, 0.53, and 0.91 m on a side for an RCS variation of 24.7 dBsm. A complete test of system dynamic range typically requires a significantly larger variation in reflector RCS.

8.8 SUMMARY

The SAR user community examines SAR imagery either on photographic film or on softcopy display screens to extract intelligence information. These users may have little concern for, interest in, or knowledge about radar system performance parameters. They simply need to be able to examine images of the appropriate areas, find low-RCS and high-RCS targets, and study target signatures in detail. Basically, they need to detect, classify, and identify targets of various spatial extent and RCS in competing background clutter and noise.

The SAR provider community must quantify the needs of the user in terms of measurable SAR system parameters. The provider community must be able to analyze, specify, budget, test, and validate these parameters. The SAR system designer must be able to predict system performance with respect to these parameters based on engineering design and subsystem measurements; the system designer must be able to relate these performance parameters to SAR image quality. Only in this way can he satisfy the needs of the system users.

To achieve this goal, the SAR community first separates the measures of a SAR system into functional requirements and performance requirements. Functional requirements refer to operational capabilities and the type of SAR product. Performance requirements refer to the quantity, quality, and timeliness of the SAR image.

Functional requirements define system capabilities, scope of performance, and methods for the system to use. Examples of functional requirements for a SAR specification include polarization capability, mode capability, radiometric calibration capability, operational altitudes or slant ranges, and access area.

Performance requirements often emphasize image quality. As primary image quality metrics, the SAR community generally uses mainlobe −3-dB width or resolution, peak sidelobe levels, MNR, equivalent backscatter coefficient of additive noise σ_n and geometric distortion. Additional image quality parameters include system dynamic range, spurious response levels, image intensity uniformity, RCS calibration accuracy, and mainlobe −18-dB width.

The SAR system designer relies on a system and subsystem performance budget methodology to provide system performance in line with system specification. Usually this step proves capability on paper with error budgets, equations, and subsystem measurements of various sorts. Ideally, the final phase involves imaging a ground test site to verify that a SAR system meets its performance specifications by means of measurements on actual imagery generated by the system. A ground test site must be especially designed to provide measurable image features for computing image quality parameters. These test sites generally include carefully engineered, precisely constructed, and accurately calibrated reflector arrays and a sizable NRA, properly embedded within the scene.

REFERENCES

[1] Mitchell, R.H., and S. Marder, "Synthetic Aperture Radar (SAR) Image Quality Considerations," *Image Quality, Proceedings of the SPIE*, Vol. 310, August 1981, pp. 58-68.

[2] Mitchel, R., "SAR Image Quality Analysis Model," PhD dissertation, University of Michigan, 1974.

[3] Stankwitz, H.C., R.J. Dallaire and J.R. Fienup, "Nonlinear Apodization for Sidelobe Control in SAR Imagery," *IEEE Transactions on Aerospace and Electronic Systems*, Vol. AES-31, No. 1, January 1995, pp. 267-279.

[4] Cosgriff, R.L., W.H. Peake, and R.C. Taylor, *Terrain Scattering Properties for Sensor System Design (Terrain Handbook II)*, Engineering Experiment Station, College of Engineering, The Ohio State University, Columbus, May 1960, 118 pages (see also note in [5]).

[5] Bush, T.F., and F.T. Ulaby, "Variability in Measurement of Radar Backscatter," *IEEE Transactions on Antennas and Propagation*, Vol. 24, No. 6, November, 1976, pp. 896-899.

[6] Ulaby, F.T., and M.C. Dobson, *Handbook of Radar Scattering Statistics for Terrain*, Norwood, MA, Artech House, 1989.

[7] Miller, J.M., "Characterization of Clutter and Its Use in Maintaining CFAR Operation," *Electromagnetics*, Vol. 4, 1984, pp. 185-203.

[8] Gray, G.A., and G.W. Zeoli, "Quantization and Saturation Noise Due to Analog-to-Digital Conversion," *IEEE Transactions on Aerospace and Electronic Systems*, Vol. AES-7, No. 1, January 1971, pp. 222-223.

[9] Bayma, R.W., and P. A. McInnes, "Aperture Size and Ambiguity Constraints for a Synthetic Aperture Radar," *1975 IEEE International Radar Conference Record*, 1975, pp 499-504.

[10] Li, F.K., and W.T.K. Johnson, "Ambiguities in Spaceborne Synthetic Aperture Radar Systems," *IEEE Transactions on Aerospace and Electronic Systems*, Vol. AES-19, No. 3, May 1983, pp. 389-396.

[11] Lewis, R.W., "Redundancy in Coherent Imaging Systems," PhD dissertation, University of Michigan, 1973.

[12] Zelenka, J.S., "Comparison of Continuous and Discrete Mixed-Integration Processors," *Journal of the Optical Society of America*, Vol. 66, No. 11, November 1976, pp. 1295-1304.

[13] Moore, R.K., "Tradeoff Between Picture Element Dimensions and Noncoherent Averaging in Side-Looking Airborne Radar," *IEEE Transactions on Aerospace and Electronic Systems*, Vol. AES-15, No. 5, September 1979, pp. 697-708.

[14] Freeman, A., "The Need for SAR Calibration," *Proceedings of the 1989 IEEE International Geoscience and Remote Sensing Symposium (IGARSS)*, Vancouver, Canada, July 1989, pp. 230-233.

[15] Nagy, W.H., and E.L. Johansen, "Ground and Airborne Calibration of the Ground to Air Imaging Radar," *Proceedings of the 1993 AMTA Meeting and Symposium*, Dallas, TX, October 1993, pp. 271-276.

[16] Freeman, A., "SAR Calibration: An Overview," *IEEE Transactions on Geoscience & Remote Sensing*, Vol. 30, No. 6, 1992, pp. 1107-1121.

[17] Larson, R.W., P.L. Jackson, and E.S. Kasischke, "A Digital Calibration Method for Synthetic Aperture Radar Systems," *IEEE Transactions on Geoscience and Remote Sensing*, Vol. GRS-26, No. 6, November 1988, pp. 753-763.

[18] Sheen, D.R., E.L. Johansen, L.P. Elenbogen, and E.S. Kasischke, "The Gridded Trihedral: A New Polarimetric SAR Calibration Reflector," *IEEE Transactions on Geoscience and Remote Sensing*, Vol. GRS-30, No. 6, November 1992, pp. 1149-1153.

[19] Ruck, G.T., D.E. Barrick, W.D. Stuart, and C.K. Krichbaum, *Radar Cross Section Handbook*, Vol. 2, G. T. Ruck, editor, New York, Plenum Press, 1970.

[20] Johansen, E.L., "Top-Hat Reflectors Cap Radar Calibration," *Microwaves*, December 1981, pp. 65-66.

[21] Trebits, R.N., "Radar Cross Section," Chapter 2 in *Techniques of Radar Reflectivity Measurement*, Currie, N.C., editor, Norwood, MA, Artech House, 1984.

Chapter 9
Spotlight Processing Applications

Motion compensation to a scene center location and the polar format algorithm (PFA) apply naturally to the image formation processing of SAR data collected in spotlight mode. The data collection commonly associated with spotlight mode processing involves a single antenna illuminating a fixed patch of terrain to the side of the SAR platform or the inverse SAR equivalent in which the target moves relative to the radar. This chapter discusses four variations to this data collection which also can use spotlight mode processing techniques in the form of motion compensation to scene center and the PFA.

Sections 9.1 and 9.2 present the use of spotlight mode processing in two applications involving variations in the SAR data collection geometry. These applications are stripmap imaging and forward-look imaging. Sections 9.3 and 9.4 discuss the use of spotlight processing in two applications involving exploitation of the complex nature (phase and amplitude) of the SAR image. These applications are interferometric SAR and vibrating target detection. These four examples provide an introduction to the diverse uses of spotlight mode data and roles of spotlight SAR processing.

9.1 SPOTLIGHT PROCESSING OF STRIPMAP SAR DATA

It is common to associate wide-area imaging at coarser resolution with stripmap mode and finer resolution imaging of smaller scenes with spotlight mode. In fact, each mode can possess comparable radar parameters and collect similar signal data. With several preliminary procedures, it is often feasible to process data collected in a stripmap mode with a spotlight image formation processor (IFP) algorithm, such as the PFA. This section describes these procedures and provides examples.

9.1.1 Mode Differences

Two differences between stripmap and spotlight modes are important to this discussion. The first difference concerns the factors that limit azimuth resolution and scene coverage in the two modes. In stripmap mode, antenna beamwidth limits azimuth resolution and data collection length determines azimuth scene coverage. In spotlight mode, the data collection length limits azimuth resolution and antenna beamwidth determines maximum scene coverage in azimuth.

The second difference involves the reference function or motion compensation signal that each mode uses in the radar receiver (Section 2.6.4). While stripmap and spotlight modes can transmit and receive similar signals and perform a similar range-dechirp operation, the spotlight receiver removes the azimuth chirp characteristic from all scatterers whereas the stripmap receiver preserves it.

9.1.2 Stripmap-to-Spotlight Conversion Process

Preparation of stripmap signal data for spotlight PFA processing requires removal of stripmap motion compensation and application of motion compensation to scene center for spotlight data (Section 2.6). A simple model in which the stripmap data collection procedure images at broadside and uses a fixed reference range R_s for motion compensation and dechirp in range illustrates this procedure. This reference range is the distance between the antenna phase center (APC) and the center of the strip being imaged. The stripmap reference signal is

$$s_{ref}^{strip}(n,t) = e^{j\left[2\pi f_c\left(t-\frac{2R_s}{c}\right)+\pi\gamma\left(\hat{t}-\frac{2R_s}{c}\right)^2\right]} \tag{9.1}$$

where n is the radar pulse number, t is instantaneous time, $\hat{t}$ equals $t-nT$, f_c is the radar center frequency, γ is the radar chirp rate, and T is the interpulse period. Application of this reference function to (2.51) provides the stripmap signal data. Using the measured slant range R_a between the APC and a selected scene center as the dechirp reference range in (2.55), the appropriate spotlight reference signal is

$$s_{ref}^{spot}(n,t) = e^{j\left[2\pi f_c\left(t-\frac{2R_a}{c}\right)+\pi\gamma\left(\hat{t}-\frac{2R_a}{c}\right)^2\right]} \tag{9.2}$$

Unlike R_s, the spotlight reference range $R_a = R_a(n)$ is not constant but varies with pulse number n. The difference in phase between reference signals (9.1) and (9.2) is the signal phase that converts stripmap signal data into spotlight signal data. While not essential to this presentation, Section 10.1 offers a more detailed discussion of these two motion compensation strategies and presents the intermediate frequency signals in each case.

The first considerations in setting up a spotlight processor to process stripmap data are azimuth patch size and achievable resolution. In spotlight mode, the system illuminates the same scene during the entire data collection interval. All targets in the scene have the same physical synthetic aperture. In stripmap mode, the antenna illumination pattern slides along-track at the velocity of the collection platform. This motion provides a different synthetic aperture for scatterers at successive along-track locations. The spatial location of the synthetic aperture associated with a particular scatterer changes with the scatterer's along-track location.

To maintain uniform azimuth resolution over the scene, it is necessary to limit the azimuth scene size. The scene must include only scatterers that the sliding stripmap beam illuminates over the necessary cone angle interval $\Delta\theta$ given by (2.20) during the fixed synthetic aperture interval selected on the basis of spotlight mode processing. Referring to Figure 9.1, the allowable azimuth scene size W_a meeting this criterion as a function of azimuth resolution ρ_a and azimuth antenna beamwidth β_a is

$$W_a = 2R_s\left[\tan\left(\frac{\beta_a}{2}\right) - \tan\left(\frac{\Delta\theta}{2}\right)\right] \approx R_s\left(\beta_a - \frac{\lambda_c K_a}{2\rho_a}\right) \tag{9.3}$$

where K_a is the azimuth mainlobe-broadening factor and λ_c is the wavelength that corresponding to radar center frequency f_c. Obviously, β_a must exceed $\Delta\theta$ for this procedure to be viable.

For example, consider an X-band broadside stripmap system with an azimuth antenna beamwidth β_a of 5.3 deg, operating at a reference range R_s of 7500 m. The width W_i of the azimuth illumination at swath center will be

$$W_i = 2R_s\tan\left(\frac{\beta_a}{2}\right) \approx 700\,\text{m} \tag{9.4}$$

From (2.20), an azimuth resolution of 1 m requires a cone angle interval $\Delta\theta$ of 1.12 deg using a center wavelength λ_c of 0.03 m and an azimuth mainlobe-broadening factor K_a of 1.3. The antenna beamwidth easily supports this cone angle requirement. Using (9.3), the maximum azimuth patch size W_a is

$$W_a \approx R_s\left(\beta_a - \frac{\lambda_c K_a}{2\rho_a}\right) \approx 550\,\text{m} \tag{9.5}$$

To image a strip of terrain using a spotlight processing algorithm on signal data collected in the stripmap mode with the parameters assumed here, it is necessary to divide the strip into azimuth patches no larger than 550 m in order to maintain constant azimuth resolution. The spotlight processing algorithm must process each azimuth patch individually.

The procedure to process the stripmap data with spotlight processing techniques first divides the strip of terrain being imaged into patches of azimuth size W_a and selects the appropriate set of radar pulses to form the synthetic aperture for each patch. The next step removes the stripmap motion compensation of (9.1) and applies the spotlight motion compensation of (9.2). The signal data for each patch is now ready for processing with the PFA or other spotlight mode algorithm. Other algorithms may require different treatment of the range or azimuth chirp characteristics of the collected data. The final steps involve the usual spotlight image formation of individual patches and use of a mosaicking algorithm to join the individual patches into a continuous output image.

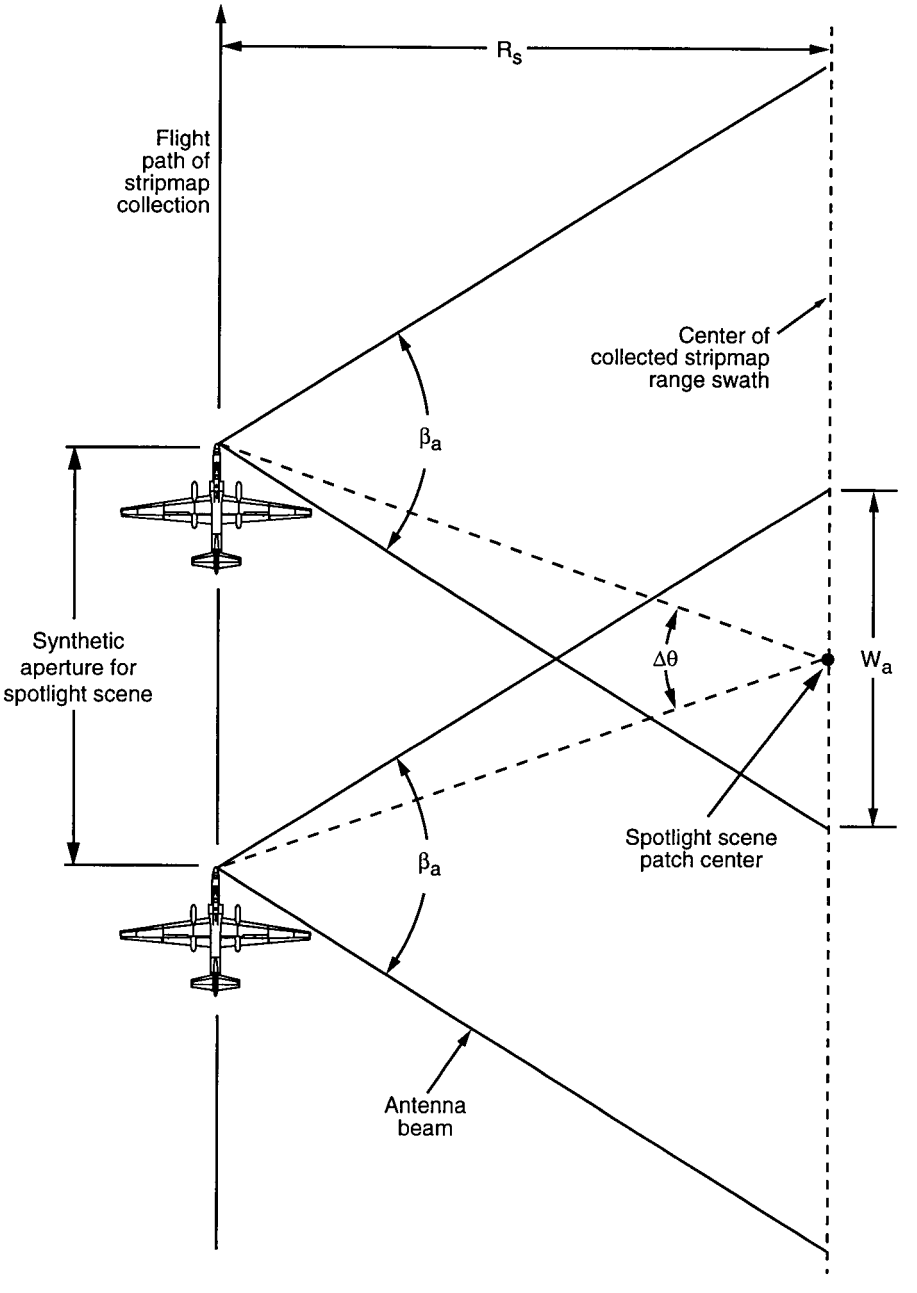


Figure 9.1 Illustration of allowable azimuth scene size in stripmap-to-spotlight data conversion.



Figure 9.2 Spotlight image using stripmap data and the PFA.

9.1.3 Image Example

Figure 9.2 illustrates an image that results from processing collected stripmap signal data as spotlight mode data using the PFA in the common UNIX processor (Section 7.1). Data collection parameters correspond to the values that (9.4) and (9.5) use. The imaged region is the intersection of Interstate I-80 (horizontal) and U.S. Highway 218 (vertical) north of Iowa City, Iowa. Radar illumination is from the left side. Near range is on the left side. The image resolution is 1 m in range and 1 m in azimuth. The image covers 1800 m in range and 530 m in azimuth.

Figure 9.3 illustrates the consequence of exceeding the azimuth scene size limitation of (9.3). The image is the result of reprocessing an area (including that in Figure 9.2) with an azimuth scene size of 800 m, roughly 50 percent larger than the allowable full resolution size. Again, radar illumination is from and near range is on the left side. The degradation in azimuth resolution is particularly noticeable near the top of the image.

9.2 FORWARD-LOOK SAR

A side-look data collection geometry (Figure 2.21) is common in spotlight and stripmap modes. The sensor illuminates an area to the side of the flight path. While stripmap mode most frequently images at a 90-deg cone angle (broadside), spotlight mode imaging can vary over a large cone angle interval fore or aft of broadside. The IFP operates on this side-look data to resolve scattering centers in range and Doppler cone angle. The *forward-look* SAR varies this common collection geometry to illuminate and image an area ahead of and below the sensor velocity vector.



Figure 9.3 Spotlight image using stripmap data that exceeds the azimuth scene size limit of (9.3).

9.2.1 Geometry Model

Figure 9.4 illustrates a typical forward-look geometry. Following the side-look geometry in Section 2.6.1, the origin of the *XYZ* coordinate system is at scene center and the sensor moves in the positive *X* direction. The *XY* plane is the nominal ground plane.

Like side-look SAR, forward-look SAR creates a two-dimensional range-Doppler mapping of the three-dimensional illuminated scene. Forward-look differs in the way its grid of range-Doppler resolution cells intersects the *XY* plane (Figure 9.5). When imaging at broadside in a side-look geometry, lines of constant range and constant Doppler in the *XY* plane are nominally orthogonal. They may intersect each other at a significantly non-orthogonal angle in an off-broadside collection. These intersections divide the *XY* plane into separate resolution cells. In forward-look, these two sets of lines are nominally parallel and do not resolve scatterers in the *Y* direction. Figure 9.6 illustrates this difference by showing sections of the iso-range-Doppler circles for each case. A SAR system has no ability to resolve or separate scatterers that lie on these circles. In both cases, these circles reside in planes parallel to the *YZ* plane. While side-look SAR provides little

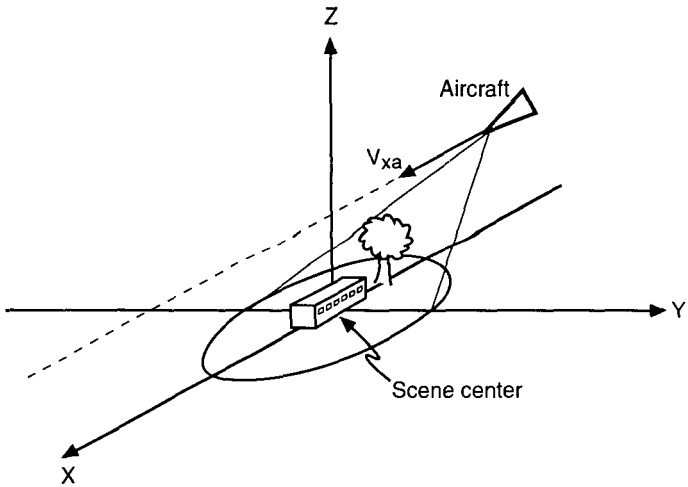


Figure 9.4 Forward-look SAR data collection geometry.

vertical resolution (at low grazing angles), forward-look SAR provides little resolution in the Y direction. However, forward-look SAR does provide Doppler cone angle resolution in the vertical direction (at low grazing angles).

Forward-look SAR offers resolution of scatterers largely in the X and Z directions. Images appear as side-view profiles looking in the Y direction. In contrast, side-look SAR offers resolution largely in the X and Y directions (at low grazing angles) with images appearing as top-view profiles. Figure 9.7 illustrates the difference between side-look and forward-look SAR images.

9.2.2 Image Attributes

Forward-look SAR imagery exhibits two differences relative to side-look imagery. First, targets in forward-look imagery appear in profile and thus offer target height information to a human image interpreter or automatic target recognition (ATR) algorithm. Of course, height information is available at the expense of Y direction information. For cultural targets such as vehicles and buildings, height information can aid in target identification. Second, forward-look imagery can mitigate the effects of range layover (Section 9.3.8.2). In a side-look collection, trees and other tall objects in the background appear in the imagery on top of shorter objects in the foreground. This range layover occurs because the radar wavefronts reach a tall object in the background and a short object in the foreground at the same time. This situation places both scatterers in the same range resolution cell as Figure 9.8 suggests. However, a forward-look SAR collection will locate the tall object in a different image Doppler resolution cell than the shorter object because the two objects (at the same range) have different range rates.

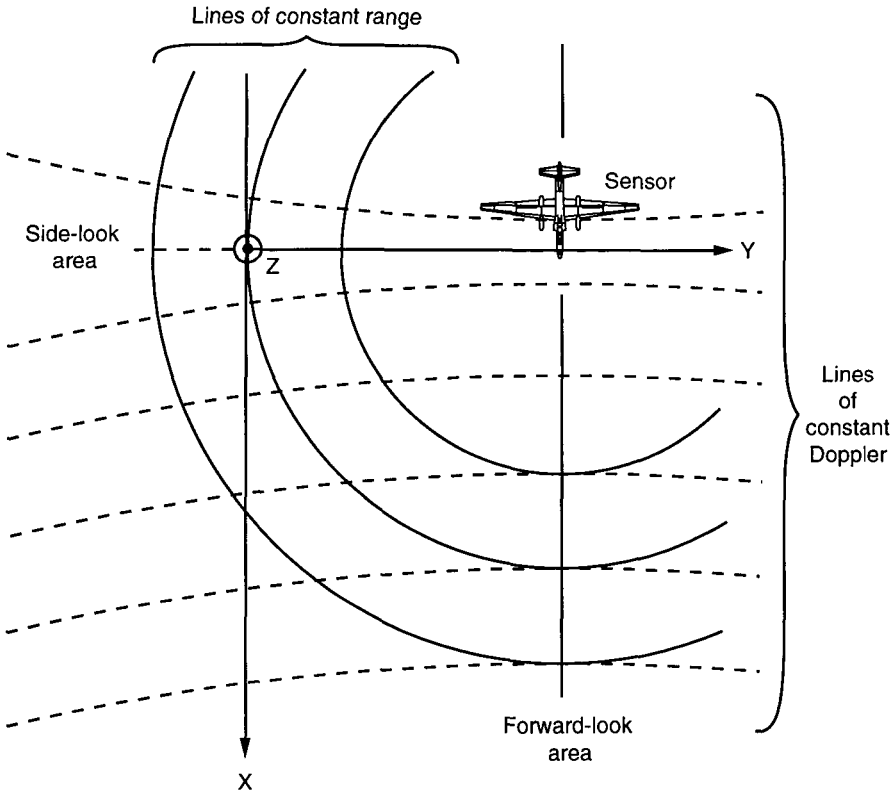
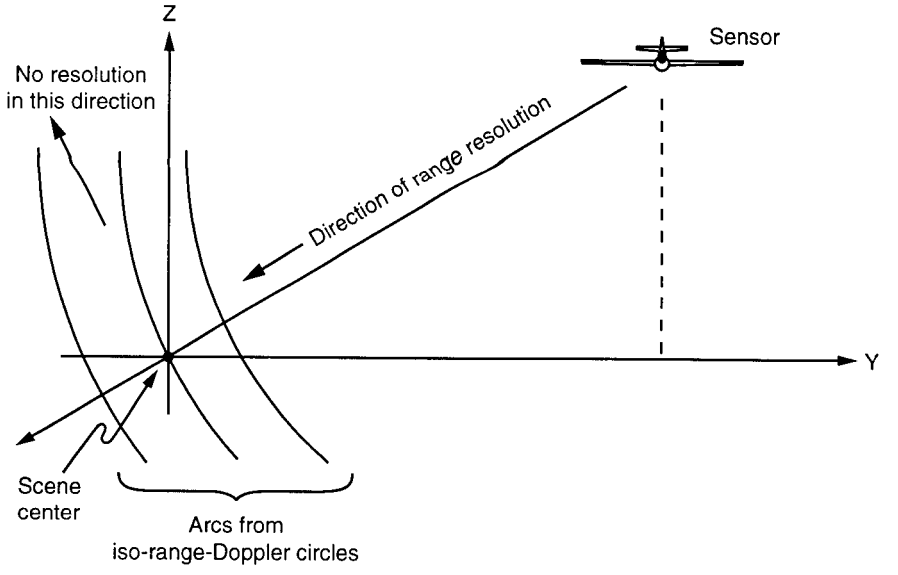


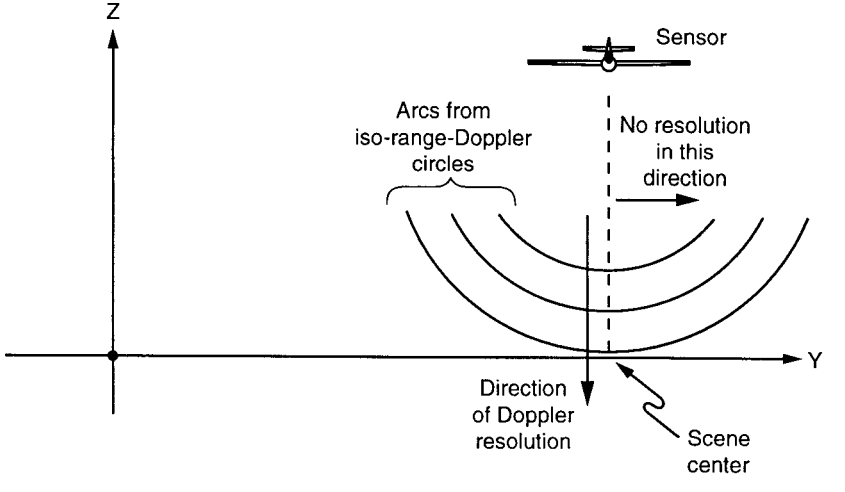
Figure 9.5 Circles of constant range (solid lines) and hyperbolas of constant Doppler (dashes) in the *XY* plane.

In fact, forward-look SAR trades the Doppler resolution in X associated with side-look SAR for Doppler resolution nominally in Z (at low grazing angles). As the arcs from iso-range-Doppler circles in Figure 9.6(b) suggest, a lack of resolution along these arcs causes scatterers separated only in the *Y* direction to project onto each other and coincide in the two-dimensional range-Doppler image. In a sense, layover in the *Y* direction in forward-look SAR replaces range layover in side-look SAR. Because the *Y* direction is usually rich in scatterers, the layover effects in forward-look SAR can be a serious concern that is difficult to avoid in an operational environment.

One method to reduce this effect uses an antenna with a narrow azimuth beam to illuminate a smaller scene. The smaller cross-track ground footprint of the narrow beam limits the number of targets likely to be present on each iso-range-Doppler circle.

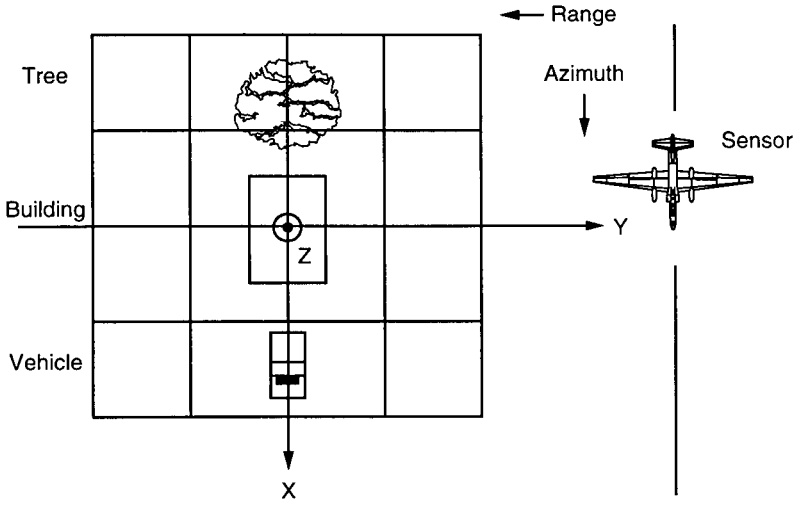


(a)

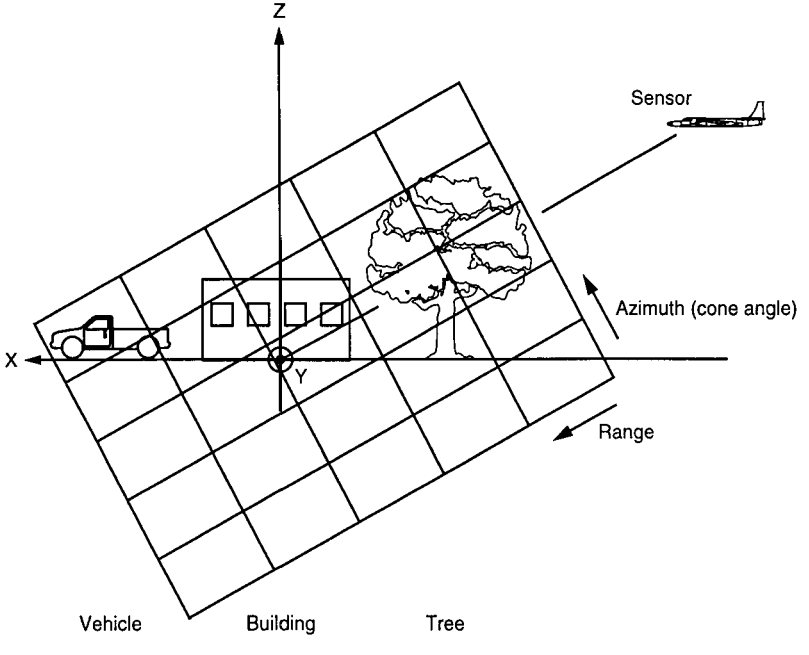


(b)

Figure 9.6 Directions of range and Doppler resolution: **(a)** Side-look SAR; **(b)** Forward-look SAR.



(a)



(b)

Figure 9.7 Illustration of image geometries: **(a)** Side-look SAR; **(b)** Forward-look SAR.

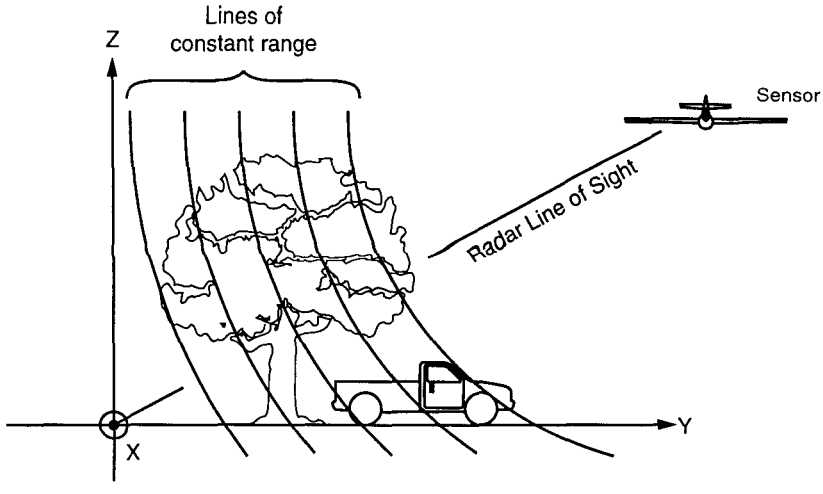


Figure 9.8 Tall scatterer layover onto shorter targets in the foreground in side-look SAR imagery.

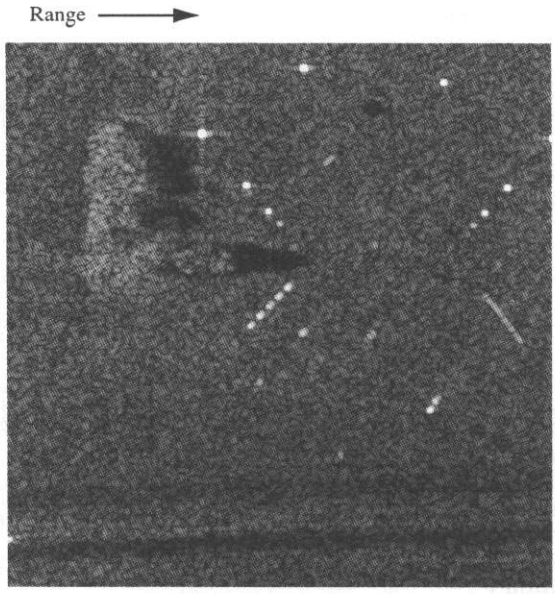
9.2.3 Image Examples

A processor designed for side-look SAR can form images from forward-look SAR data. An exchange of the Z component and Y component values for the sensor positions and velocities in the auxiliary data stream of the forward-look system effectively synthesizes a forward squint, zero grazing angle, side-look collection geometry. Once the processor exchanges the positional auxiliary data, IFP function to process forward-look data is identical to that for side-look data.

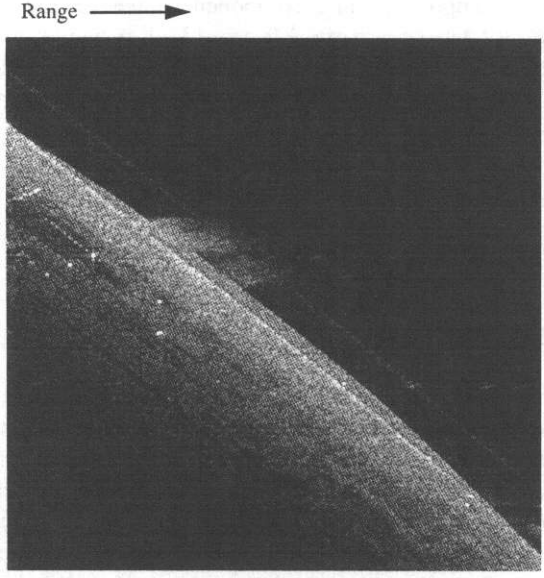
Figure 9.9 shows a side-look image and a forward-look image of a corner reflector test array. The same PFA spotlight processor generated both images. The forward-look image suffers from lack of resolution in the Y direction. It does, however, resolve the height of the trees in the scene.

9.3 INTERFEROMETRIC SAR

The usual SAR range-Doppler digital image is a two-dimensional array of complex numbers that represent image pixels. The magnitude of a pixel is a measure of the radar reflectivity of scatterers within the corresponding area of the scene. Pixel position within the array associates each scatterer with a specific iso-range-Doppler circle; range is scatterer distance from the antenna phase center (APC), while Doppler cone angle is the angle between the line-of-sight (LOS) vector from the antenna to the scatterer and the antenna velocity vector. The scatterer's position on the iso-range-Doppler circle, representing its depression angle, is unknown. Whether imaging terrain or cultural targets, information about this angle is needed to estimate the relative heights of scatterers in the scene.



(a)



(b)

Figure 9.9 Images of a radar test site from two geometries: **(a)** Side-look SAR; **(b)** Forward-look SAR.

Two conventional approaches to obtain information about scatterer height using SAR imagery are stereo radargrammetry using two SAR intensity images of a scene obtained from different perspectives and exploitation of range layover and shadow effects in a single SAR image (Section 9.3.8). The use of interferometric techniques with SAR imagery to provide height information is an active research area that represents a maturing technology today [1-6]. Interferometric SAR (IFSAR) is the preferred approach because it promises to provide a continuous (pixel-by-pixel) height map with reasonable height resolution over a large area.

SAR interferometry using spotlight imagery is best suited for examining cultural targets and smaller natural scenes. The fine resolution associated with spotlight mode SAR is valuable to resolve scattering centers in range and azimuth; the higher signal-to-clutter ratio associated with fine resolution helps to provide accurate height estimates. SAR interferometry using stripmap imagery is particularly useful in developing digital terrain elevation (DTE) maps of large areas of terrain. The wide-swath, continuous-mapping capability of stripmap SAR is essential to this application. While IFSAR techniques apply equally well to spotlight, stripmap, and scan mode systems [7], we limit discussion here to spotlight mode interferometry using single-pass, dual-antenna SAR data.

9.3.1 Nature of SAR Interferometry

A SAR interferometer measures scatterer height by comparing the phase of corresponding pixels in two SAR images of the same geographical area, obtained from slightly different depression angles. The phase difference arises from the difference in path length to a scatterer in the scene from each antenna. A simple implementation of a SAR interferometer uses two antennas separated by a fixed distance horizontally in a plane orthogonal to the platform velocity vector. This separation is the *interferometric baseline* or simply the baseline. The baseline introduces the small depression angle difference between the two images that SAR interferometry requires. Ideally, the remaining data collection geometry parameters and radar system parameters remain the same for the two images.

Figure 2.9 illustrates the basis for SAR interferometry in the context of normal SAR imaging. The image from the first antenna locates a scatterer on one iso-range-Doppler circle without being able to determine the scatterer's position, or elevation angle, on the circle. The image collected from the second antenna locates the scatterer on a second iso-range-Doppler circle. In the absence of errors, the two circles intersect at a single point in the illuminated volume to determine the three-dimensional location of the scatterer.

By using the phase information inherent in a SAR image, SAR interferometry is sensitive to distances on the order of radar *wavelength* rather than radar *resolution*. The SAR interferometric technique is applicable to both distributed scatterers found in terrain and concentrated scatterers found on hard targets. A high scatterer signal-to-background ratio (SBR) is necessary for a meaningful single-pixel phase comparison in which the phase estimate will have a small standard deviation [8]. Area-averaging filters are useful in reducing the phase noise in areas of distributed scattering. Interferometric techniques will fail in areas of no return, such as shadows, and in low return areas, such as calm water.

One way to collect IFSAR data is to make two sensor collection passes with a single-antenna, single-channel system. An advantage of this two-pass, single-antenna system is that an existing single-channel SAR sensor can collect interferometric data without modification. This technique requires a stable, high-performance navigation subsystem. This subsystem ensures that the two data collection passes have accurately known and nearly identical data collection geometries with the necessary baseline separation. At a minimum, the platform should employ an inertial sensor (aided by a global positioning system (GPS) during collection) and differential GPS to provide additional motion data accuracy during interferometric processing. A significant disadvantage to this approach is that changes in terrain condition, propagation effects, or weather conditions between the two collection passes will affect the interferometric phase measurements and ultimately contaminate the terrain height measurement.

Use of a dual-antenna, dual-channel radar system is another way to realize an IFSAR system. In this system, a single data collection pass provides the necessary two-channel interferometric data in a controlled fashion. The dual-antenna system requires a second antenna and must handle twice the analog-to-digital (A/D) and data recording rates in order to simultaneously collect the two data streams. Typically, radome and antenna sizes limit the baseline length of a two-antenna system to a small, easily measurable distance. The single-pass approach provides interferometric data without pass-to-pass alignment problems and without the possibility of temporal changes in terrain inherent in a two-pass system. It must, however, account for any rotation of the baseline during a data collection.

9.3.2 Interferometry Model

Figure 9.10 provides the basic geometry to model a SAR interferometer. A rigid baseline B_i separates two antennas, A1 and A2. This separation causes the two antennas to illuminate the scene at slightly different depression angles relative to the baseline. Here ψ is the nominal depression angle from the center of the baseline to the scatterer relative to the baseline. The model assumes that the platform travels at constant velocity in the X direction while the baseline remains parallel to the Y axis at a constant height Z_{ac} above the XY plane. The radar system transmits and receives pulses alternately on antenna A1 and on antenna A2.

A spotlight signal equation in the form of (3.24) describes the signal data collected by each antenna. The two sets of signal data differ primarily because of the small differences in the data collection geometry. The IFP polar formats the data separately for each channel. The IFP produces one complex image from each antenna's data stream and makes the appropriate adjustments to achieve pixel-to-pixel alignment of corresponding scatterers in the two images.

The phase of an image pixel representing multiple scatterers in the same resolution cell consists of both a deterministic component and an unknown random component (Section 3.6.1). A data collection for SAR interferometry adheres to special conditions to ensure that the random component of the phase is nearly identical in the two images. The deterministic phase in a single image is due to the two-way propagation path between the

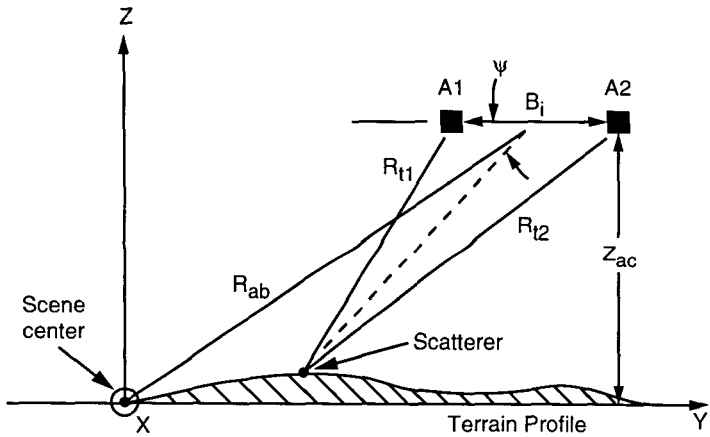


Figure 9.10 Interferometric SAR geometry.

associated antenna and the target. The constant a_o in the Taylor series expansion of the signal phase (3.66) provides this deterministic phase.

With proper preparation and data handling procedures, it is possible to compute the elevation angle of the radar LOS to a scatterer relative to the baseline from the (deterministic) phase difference between corresponding pixels in a pair of images collected with a known baseline. Knowledge of this elevation angle allows a calculation of scatterer height above a reference plane.

We may write the complex quantities representing a corresponding pair of image pixels, P_1 and P_2, from image 1 and image 2 as

$$P_1 = a_1 e^{j(\theta_1 + \Phi_1)} \tag{9.6}$$

and

$$P_2 = a_2 e^{j(\theta_2 + \Phi_2)} \tag{9.7}$$

The quantities a_1 and a_2 represent the amplitudes of each image pixel. Generally, these amplitudes are approximately equal. The quantities θ_1 and θ_2 are the random components of pixel phase. They represent the vector summations of returns from all unresolved scatterers within the resolution cell and include contributions from receiver noise. With proper system design and operation, θ_1 and θ_2 are nearly equal. The quantities Φ_1 and Φ_2 are the deterministic contribution to the phase of the image pixel. The desired function of the interferometer is to provide a measure of the phase difference, $\Phi_1 - \Phi_2$.

Based on (3.104), approximations to Φ_1 and Φ_2 from a scatterer at (X_t, Y_t, Z_t) are

$$\Phi_1 \approx -\frac{4\pi}{\lambda_c}(R_{t1} - R_{ab}) \tag{9.8}$$

and

$$\Phi_2 \approx -\frac{4\pi}{\lambda_c}(R_{t2} - R_{ab}) \tag{9.9}$$

The quantities R_{t1} and R_{t2} are the distances from each APC to the scatterer at the center of the synthetic aperture and λ_c is the radar center wavelength. Following the common practice of using the same reference range for each image, the quantity R_{ab} is the distance from the middle of the baseline to scene center at the center of the synthetic aperture.

Multiplication of one image and the complex conjugate of the second image on a pixel-by-pixel basis yields the phase difference between corresponding pixels in the two images. This complex product produces the interferogram I with

$$I = P_1 P_2^* \tag{9.10}$$

where * denotes the complex conjugate operation. With θ_1 and θ_2 nearly equal and a_1 and a_2 nearly equal, the two images differ primarily in how the slight difference in collection depression angles affects Φ_1 and Φ_2. Ideally then, each pixel in the interferogram has the form

$$I = a^2 e^{-j\left[\frac{4\pi}{\lambda_c}(R_{t1} - R_{t2})\right]} = a^2 e^{j\phi_{12}} \tag{9.11}$$

using $a_1 = a_2 = a$. The amplitude a^2 of the interferogram corresponds to image intensity. The phase ϕ_{12} of the interferogram becomes

$$\phi_{12} = \frac{4\pi (R_{t2} - R_{t1})}{\lambda_c} \tag{9.12}$$

which is the quantity used to derive the depression angle to the scatterer relative to the baseline and, eventually, information about scatterer height relative to the XY plane. Use of the approximation

$$R_{t2} - R_{t1} \approx B_i \cos(\psi) \tag{9.13}$$

from Figure 9.10 in (9.12) yields

$$\phi_{12} \approx \frac{4\pi B_i \cos(\psi)}{\lambda_c} \tag{9.14}$$

Here ψ is the nominal depression angle from the center of the baseline to the scatterer relative to the baseline. No phase difference indicates that $\psi = 90$ deg and the scatterer is in the plane through the center of and orthogonal to the baseline. The interferometric phase involves many radians of phase for scatterers at other depression angles since the range difference $R_{t2} - R_{t1}$ will be many wavelengths. In practice, however, an interferometric system does not easily measure the total pixel phase difference. Rather, it measures

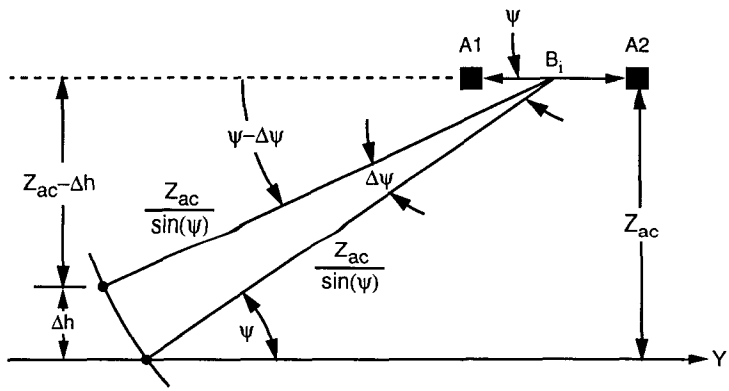


Figure 9.11 Geometry for converting relative depression angle into relative height.

only the phase difference that remains after subtracting all full 2π intervals present (modulo-2π). To estimate the actual depression angle to a particular scatterer, the interferometer must measure the total pixel phase difference of many cycles. This information is available, for instance, by unwrapping the raw interferometric phase measurements beginning at a scene location in a plane through the center of and orthogonal to the baseline. Section 9.3.5 suggests other approaches to determining total phase difference between corresponding pixels.

Rather than seek the absolute depression angle to a scatterer and the scatterer height, it is common to seek only the relative depression angle and relative height among scatterers within a scene. The differential of (9.14) with respect to ψ provides this relative measure. This differential is

$$\Delta\phi_T = -\left(\frac{4\pi B_i}{\lambda_c}\right)\sin(\psi)\,\Delta\psi \tag{9.15}$$

or

$$\Delta\psi = -\left[\frac{\lambda_c}{4\pi B_i \sin(\psi)}\right]\Delta\phi_{12} \tag{9.16}$$

This result indicates that two pixels in the interferogram that differ in phase by $\Delta\phi_{12}$ represent scatterers differing in depression angle by $\Delta\psi$. From the collection geometry in Figure 9.11, a change $\Delta\psi$ in depression angle is related to a change Δh in height (at the same range from mid-baseline) by

$$Z_{ac} - \Delta h = \frac{Z_{ac}\sin(\psi - \Delta\psi)}{\sin(\psi)} \tag{9.17}$$

A useful small-angle approximation to (9.17) yields

$$\Delta h \approx Z_{ac} \cot(\psi)\, \Delta\psi \tag{9.18}$$

Substituting (9.16) into this equation provides the result

$$\Delta h \approx -\left[\frac{\lambda_c Z_{ac} \cot(\psi)}{4\pi B_i \sin(\psi)}\right] \Delta\phi_{12} \tag{9.19}$$

The depression angle ψ varies significantly across a large range swath. The relationship between Δh and $\Delta\phi_{12}$ naturally varies with $\cot(\psi)/\sin(\psi)$ as (9.19) indicates. For instance, using $\lambda_c = 0.03$ m, $Z_{ac} = 5000$ m, and $B_i = 1$ m, a phase difference between two image pixels of 0.105 rad at $\psi = 30$ deg corresponds to a 4.34-m height difference in the corresponding scene area. At $\psi = 45$ deg, this phase difference corresponds to a 1.77-m height difference, while, at $\psi = 60$ deg, it corresponds to a 0.84-m height difference.

9.3.3 Processing Requirements

The PFA is a suitable choice to process each of the images of an interferometric SAR data collection in spotlight mode. The motion histories of the two antennas may differ because of platform attitude variations (primarily roll in the case of a side-look collection). For this reason, it is important to individually motion compensate the data sets from each antenna. While any slight image defocus that may result from a lack of this differential motion compensation is not a concern by itself, any uncompensated phase errors that cause image defocus may also affect the phase of image pixels.

In addition to the usual operations required to process a single SAR image, the interferometric processor must spatially register the two images to within a small fraction of a resolution cell to ensure that corresponding image pixels represent the same area of terrain. Registration of two single-pass IFSAR images requires special attention to detail in both azimuth and range.

In the azimuth direction, a typical single-pass IFSAR system transmits and receives pulses alternately with each antenna, A1 and A2 in our model. This procedure introduces a small aspect angle offset between the pulse trains of the two signal histories. The polar interpolator easily removes this offset when it performs azimuth resampling.

In the range direction, the difference in signal delay between the two channels is the dominant source of misregistration. This difference arises from differential path lengths within the receiver hardware and from the LOS projection of the interferometer baseline. Any difference in propagation path between the two channels displaces one image in range with respect to the other. Because this range offset is deterministic and time-invariant, the processor removes it easily.

Following image registration, the processor performs the pixel-by-pixel complex multiplication indicated in (9.10) between the image from antenna A1 and the complex conjugate of the image from antenna A2. This operation generates the complex interferogram. To convert the interferometric phase data into relative heights, the processor performs two additional procedures. The first procedure removes the deterministic interferometric phase variation associated with flat, level terrain. This operation is *interferogram leveling*, or leveling for short. This phase difference arises naturally because $R_{t2} - R_{t1}$ in (9.12) is clearly nonzero for scatterers in the ground plane. The leveling procedure simply multiplies the interferogram by the conjugate of (9.12) evaluated at all range-Doppler values for the case $Z_t = 0$. This process leaves only phase variations related to terrain height above or below the XY plane.

The second procedure filters the interferogram in order to average the pixel-to-pixel phase noise associated with radar system noise, image misregistration, and speckle effects caused by the complex nature of SAR imagery. A simple filter that is quite effective is a complex box average. This filter sums the complex pixels within a rectangular (box) area, divides by the number of pixels within the box, and outputs the resulting complex value. The filter repeats this procedure for each pixel in the interferogram. A large box size decreases the uncertainty in the height measurement at the cost of reduced sensitivity to higher frequency spatial variations in terrain height. Adaptive filtering techniques are a possibility to filter clutter areas without disturbing the more rapid height variations associated with cultural targets and natural terrain features. Optimal filtering for this application is an area of active study.

9.3.4 Height Measurement Error

Equation (9.19) provides the relationship between the variation in scatterer height Δh and the phase $\Delta\phi_T$ of the associated pixel in the complex, leveled interferogram. It is reasonable to assess root mean square (RMS) measurement error σ_h in interferometer-derived height in terms of RMS phase noise σ_ϕ present in the underlying phase values. From (9.19), the relationship between these two quantities is

$$\sigma_h = \left[\frac{\lambda_c Z_{ac} \cot(\psi)}{4\pi B_i \sin(\psi)}\right]\sigma_\phi \tag{9.20}$$

A number of quantities affect σ_ϕ by causing decorrelation in the phase between the two images. Three of these quantities are the image SBR, the depression angle difference corresponding to the interferometric baseline, and the misregistration between the two images. Table 9.1 summarizes the symbols applicable to the following analysis.

The relationship between RMS phase noise and the magnitude of the complex correlation coefficient μ between two images is [1, 9]

$$\sigma_\phi^2 = \frac{1}{2N}\left(\frac{1-\mu^2}{\mu^2}\right) \tag{9.21}$$

Table 9.1
Symbols Relating to Interferometric Phase Standard Deviation

Symbol	*Definition*
μ_c	Correlation coefficient due to interferometric depression angle difference
μ_m	Correlation coefficient due to range and azimuth image misregistration
μ_n	Correlation coefficient due to radar additive and multiplicative noise
ρ_r	Range resolution
ρ_a	Azimuth resolution
B_i	Interferometric baseline length
ψ	Depression angle or grazing angle relative to XY plane
λ_c	Radar wavelength at center frequency
Z_{ac}	Altitude of the interferometric baseline above the reference plane
N	Number of independent resolution cells used in complex box average
$\Delta\rho_r$	Misregistration between images in the range direction
$\Delta\rho_a$	Misregistration between images in the azimuth direction

A correlation coefficient with magnitude near unity is desirable. The quantity N represents the number of independent resolution cells included in the complex box average when filtering the interferogram to smooth its phase. Generally, N is less than the number of interferogram pixels in the box because the number of pixels per resolution cell usually exceeds unity.

In this model, μ has three principal components given by the relationship

$$\mu = \mu_c \mu_m \mu_n \tag{9.22}$$

where

$$\mu_c = \left[1 - \frac{2\rho_r B_i \sin(\psi)^2}{\lambda_c Z_{ac} \cot(\psi)}\right] \tag{9.23}$$

$$\mu_m = \operatorname{sinc}\left(\frac{\Delta\rho_r}{\rho_r}\right)\operatorname{sinc}\left(\frac{\Delta\rho_a}{\rho_a}\right) \tag{9.24}$$

and

$$\mu_n = \frac{\mathrm{SBR}}{1 + \mathrm{SBR}} \tag{9.25}$$

The first component μ_c of μ in (9.22) is the clutter correlation coefficient. It represents the effect of the coherent summation of multiple scatterers within a resolution cell from slightly different depression angles in the two images. The second component μ_m is the image pixel correlation coefficient. It represents the reduction in correlation from image misregistration in range $\Delta\rho_r$ and in azimuth $\Delta\rho_a$. The final component μ_n is the signal correlation coefficient. It represents degradation involving the presence of background noise from radar additive and multiplicative noise sources that differ between the two images. It is common to work (9.25) and (9.22) into (9.21) to obtain an alternate expression

$$\sigma_\phi^2 = \frac{1}{2N\mu_c^2\mu_m^2}\left[(1-\mu_c^2\mu_m^2) + \frac{2}{\text{SBR}} + \frac{1}{\text{SBR}^2}\right] \tag{9.26}$$

From (9.26), a useful approximation for the radar SBR contribution to RMS phase noise is

$$\sigma_{\phi n}^2 \approx \frac{1}{N(\text{SBR})} \tag{9.27}$$

Use of (9.26) or (9.27) in (9.20) yields an expression for the RMS height measurement error. For example, with $N = 9$ representing a complex averaging with a 3×3 resolution cell box and SBR = 10 dB, the approximate expression in (9.27) yields $\sigma_{\phi n} = 0.105$ rad. Using $\lambda_c = 0.03$ m, $Z_{ac} = 5000$ m, $\psi = 30$ deg, and $B_i = 1$ m in (9.20), a 0.105-rad RMS phase noise corresponds to a 4.34-m RMS height error in the related scene area.

Another factor affecting phase noise is the possibility of changes in the terrain between the two data collections. A correlation coefficient associated with this factor is difficult to quantify. This factor is relevant only in a single-antenna, dual-pass IFSAR collection. Both nature and humans can significantly alter the terrain in terms of precipitation (from rainfall or irrigation), wind, plant growth, construction, and vehicle incursions. Similarly, tropospheric propagation changes, likely related to weather between passes, can contribute to decorrelation between the two images.

9.3.5 Absolute Height Information

The model for a SAR interferometer in Section 9.3.2 concludes with (9.19), which relates relative height Δh to pixel phase difference $\Delta\phi_T$ between the two images. When absolute height information is important, (9.14) is the applicable equation. This equation involves many radians of phase for scatterers away from $\psi = 90$ deg. In practice, an interferometric SAR measures pixel phase difference modulo-2π, not absolute phase difference. It cannot directly recover any integer multiples of 2π, but measures only the remaining fractional part. For example, it is not possible to distinguish a pixel with a phase value of $\pi/6$ from one with a phase value of $\pi/6 \pm 2\pi n$, where n is an integer. From (9.14), the indistinguishable phase differences, formed by adding and subtracting $2\pi n$, lead to an ambiguous set of possible depression angles. This $2\pi n$ ambiguity is the reason why, without additional information or extra effort, the SAR interferometer measures relative height

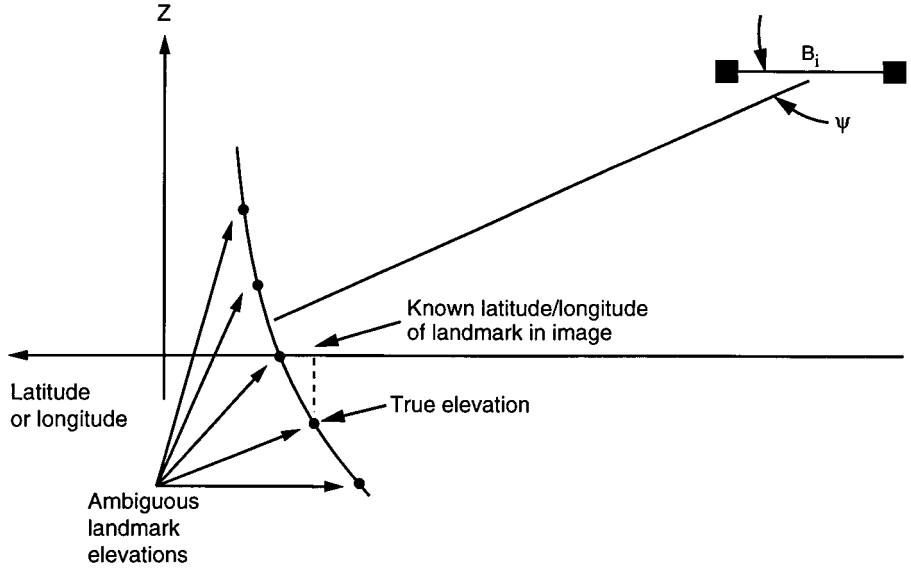


Figure 9.12 Resolution of angle ambiguity knowing target latitude or longitude.

variations (from depression angle differences) within the image area via (9.19) rather than absolute height (from absolute depression angle) above a geodetic datum via (9.14).

There are a number of approaches to removing height ambiguity. One approach is to place geodetically located reference points in the imaged scene. The precise knowledge of the three-dimensional position of both the reference points and the radar sensor permits manual (or automatic) resolution of the angle ambiguity. This procedure is useful to verify interferometric system operation. Other less demanding scene information can also be useful. For instance, knowing the latitude or longitude of a landmark in the scene is adequate to resolve the angle ambiguity with no altitude information. Figure 9.12 illustrates this approach. The known latitude or longitude of the landmark permits the identification of its true depression angle from the set of ambiguous possibilities. This information provides the value of n in the $2\pi n$ absolute phase ambiguity for one image location. One data point is adequate to determine the absolute phase over the entire interferogram and, therefore, to provide absolute height information over the entire image area.

An automated approach, called *split-bandwidth processing*, is especially applicable to systems with large range bandwidth [10]. This approach divides the radar's range bandwidth in half and forms an interferogram from each half. Each interferogram has a different center frequency and, hence, a different value of λ_c. Because of this wavelength difference, the two interferograms have different ambiguity intervals. This, in turn, can be used as a vernier to resolve the angle ambiguity (Figure 9.13). This approach is difficult to implement because it forms an insensitive interferometer and because of propagation and multipath effects. Another active research direction to resolve the ambiguity is to make an

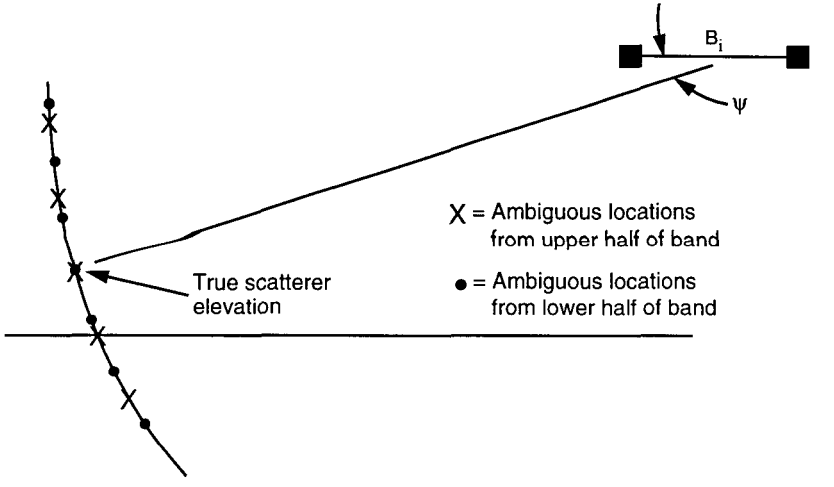


Figure 9.13 Resolution of angle ambiguity with split-bandwidth processing.

extremely accurate measurement of the difference in range $(R_{t2} - R_{t1})$ to a dominant area of the scene by measuring the misregistration between the images from the two interferometric channels. A measurement of this range difference, accurate to within a small fraction of λ_c, would provide the value of n in the $2\pi n$ absolute phase ambiguity since this range difference is between $n\lambda_c/2$ and $(n+1)\lambda_c/2$ in value.

9.3.6 Orthorectification

A desirable step to improve the utility of interferogram data is orthorectification, which corrects the interferogram for the range layover effect (Section 9.3.8.2) and produces a DTE map. An orthorectification algorithm calculates the corresponding (X, Y, Z) physical location of each pixel in the interferogram. In a broadside SAR imaging geometry, the azimuth direction is not affected by range layover, so orthorectification involves adjusting only the range position of each pixel based on the calculated interferometric height above the reference plane. Information required to determine a pixel's three-dimensional position includes the pixel height from its interferometric phase, the data collection geometry and imaging parameters, and the pixel row and column positions in the interferogram image array. The orthorectification algorithm produces an array of three-dimensional position vectors. With appropriate scaling, this array represents a DTE map. Both stripmap and spotlight images, whether single pass or dual pass, require orthorectification to correct for range layover effects.

The output points generated by an orthorectification algorithm do not lie on a regularly spaced grid. A pixel's final range location is a function of the collection geometry and its height. The orthorectification output of (X, Y, Z) position coordinates proceeds into



Figure 9.14 Spotlight SAR image of an area near Iowa City, Iowa.

a resampling algorithm for construction of a rectangular grid of pixels, regularly spaced in X and Y. Nearest-neighbor resampling approaches are often adequate to accomplish this task; otherwise, weighted neighborhood operators are available.

It is reasonable to apply the orthorectification process to images and interferograms alike. This procedure produces a matched pair of data, namely, the scene radar cross-section (RCS) in the image and the corresponding height map in the DTE map. The orthorectification algorithm requires the pixel height information contained in the interferogram in order to orthorectify the SAR image properly.

9.3.7 Image Examples

This section concludes with an example of IFSAR imagery and the associated three-dimensional data products. Figure 9.14 is a spotlight mode image of an area near Iowa City, Iowa. The purpose of this collection was to evaluate the suitability of SAR DTE in the studies of floodplains and flood prediction. This slant-plane image, collected in March 1994, has a ground range coverage of 1800 m and an azimuth coverage of 800 m. Image resolution is 1 m in range and 1 m in azimuth; pixel spacing is 0.67 m. Figure 9.15 shows the level, but unfiltered, interferogram derived from the pair of interferometric SAR images. Figure 9.16 represents the result of filtering the raw interferogram by passing a complex averaging box filter over the data. This result included two filtering passes using a filter size of 15×15 pixels (10×10 resolution cells).



Figure 9.15 Leveled and unfiltered interferogram derived from Iowa City image pair.

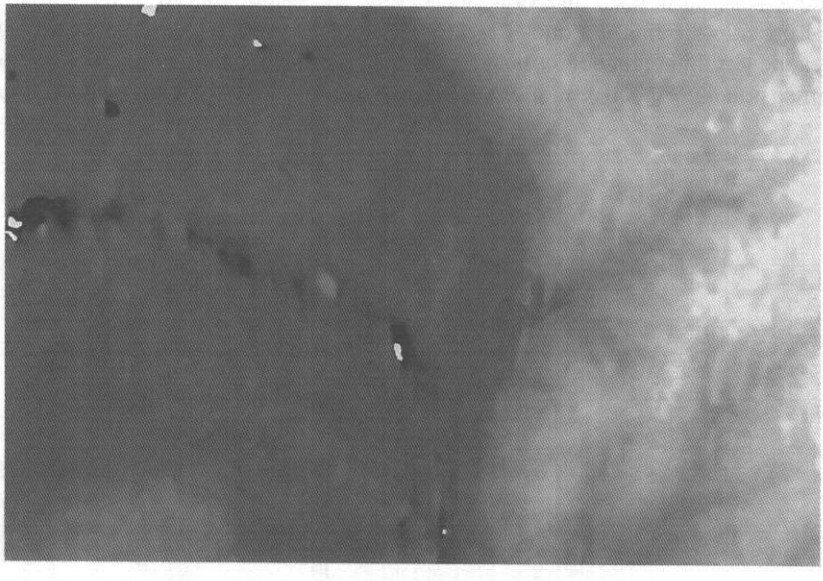


Figure 9.16 Leveled and filtered interferogram derived from Iowa City image pair.

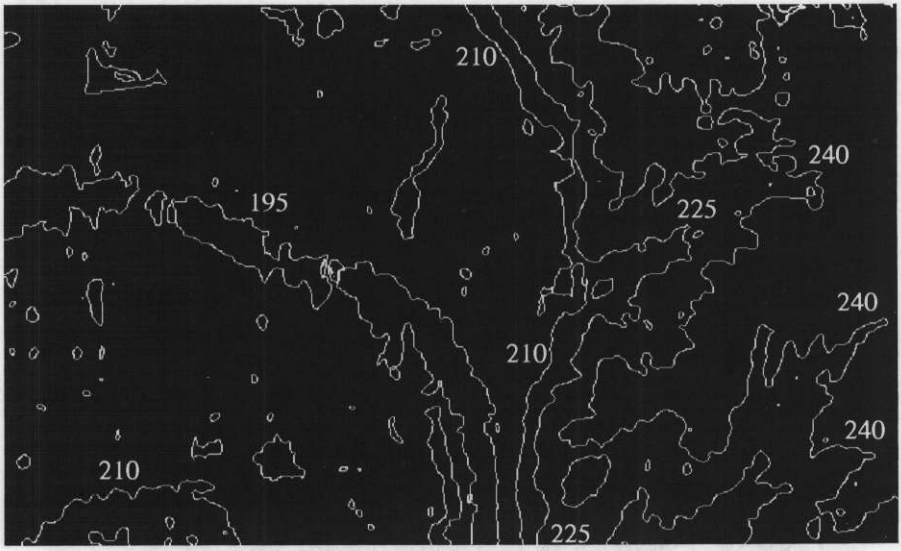


Figure 9.17 Terrain height contours generated from the SAR-derived DTE data.

Orthorectification of the interferogram in Figure 9.16, resampling it to a grid with 2-m sample spacing in each direction, and scaling the height data to meters above mean sea level provide the final product, a DTE map. Use of a commercial software package generates the terrain height contours in Figure 9.17 from DTE data. Figure 9.18 presents a three-dimensional perspective plot of the imaged area from the SAR-derived DTE data.

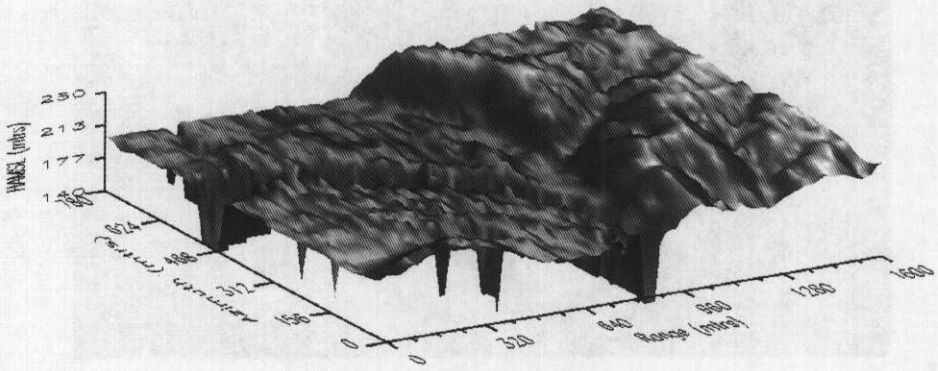


Figure 9.18 Perspective plot generated from the SAR-derived DTE data.

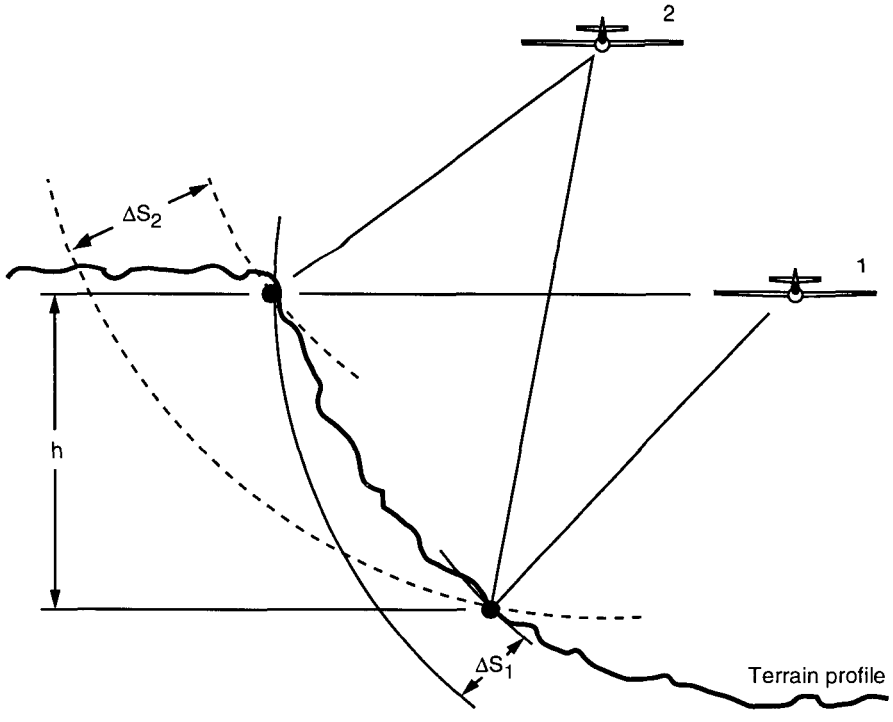


Figure 9.19 Height measurement from stereo radargrammetry.

9.3.8 Other Approaches to Height Measurement

Two approaches for obtaining limited height information about a scatterer using SAR imagery (without interferometry) include stereo radargrammetry and exploitation of range layover and shadow effects. These approaches generally do not provide a continuous (pixel-by-pixel) height map with reasonable height resolution. Because they depend on objects in the scene, neither range layover nor shadow exploitation is appropriate for reliable measurement of terrain height.

9.3.8.1 Stereo Radargrammetry

Stereo radargrammetry, or stereo SAR, employs techniques similar to those used in stereo optical systems. Stereo SAR requires two images obtained at significantly different radar depression angles. Two separate collection passes over an area of interest are necessary to produce such images. Figure 9.19 illustrates this collection geometry. The IFP forms the

two images in the usual way. Analysts determine object height by measuring the relative position shifts (ΔS_1 and ΔS_2 in Figure 9.19) between objects in the two images. It is possible to measure the shifts in object location between the images either manually or by means of an automated cross-correlation operation. Because an object's radar scattering is a strong function of both grazing and aspect angle, accurate location of the same feature in both images is often difficult. Thus, the height measurement capability of stereo SAR depends largely on radar resolution and the presence of distinguishable image features [11]. The procedure also requires intensive involvement by a human operator. These factors limit the use of stereo SAR.

9.3.8.2 Range Layover

Height measurement from range layover is applicable to single SAR images containing targets with scatterers elevated above the background terrain. Trees, water towers, and radio towers are good examples of such targets. An elevated scatterer appears in a SAR image at a range that is closer to the radar than that which a scatterer directly below it would appear. In a squinted imaging geometry, the scatterer is also displaced in azimuth. Range layover is always normal to the along-track direction, regardless of the squint angle of the data collection. This fact is evident from an examination of the geometry of the iso-range-Doppler circles in Figure 2.6. Figure 9.20 illustrates range layover for the case of a broadside imaging geometry. The radar wavefronts reach the elevated scatterer before reaching scatterers at ground level. From the radar's perspective, the elevated target is nearer than the ground scatterers. Based on a measurement of the amount of layover ΔL in an image collected at broadside with the ground plane as the image display plane (IDP), object height h is available from

$$h \approx \frac{\Delta L}{\tan(\psi)} \tag{9.28}$$

The actual range difference ΔR is approximately $\Delta L \cos(\psi)$.

9.3.8.3 Shadows

An elevated scatterer is often part of a larger object that casts a radar shadow. Trees and buildings are good examples of such objects (Figure 9.21). Unlike range layover, a shadow is always cast in the LOS direction (range) and away from the radar (behind the object). Based on a measurement of the length d of the shadow in an image with the ground plane as the IDP, object height is available from

$$h = d \tan(\psi) \tag{9.29}$$

Also, a shadow naturally suggests the shape of an object to some degree.

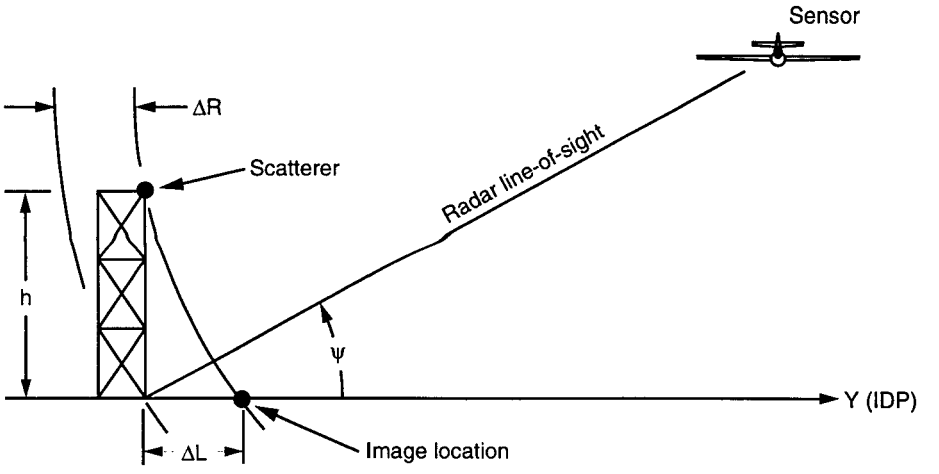


Figure 9.20 Measurement of height h from range layover ΔL.

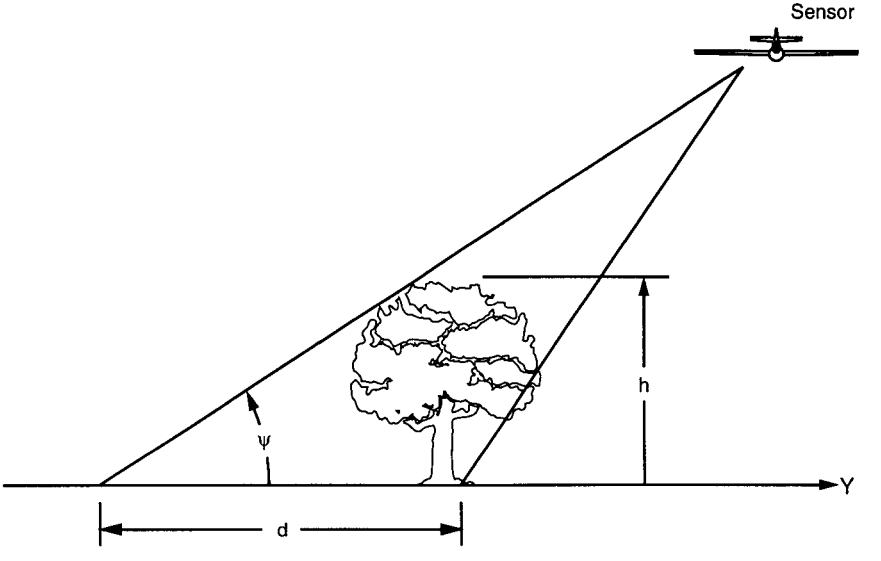


Figure 9.21 Measurement of height h from shadow length d.

9.4 VIBRATING TARGET DETECTION

Uncompensated sinusoidal motion of the SAR antenna phase center introduces paired echoes in the impulse response function of each scatterer in a SAR image scene (Section 5.1.2). Target motion and antenna motion have similar effects in SAR imaging because the relative motion between the APC and the scatterer is the important quantity. Thus, sinusoidal vibration of a scatterer being imaged by a SAR produces a sinusoidal phase effect in the signal history from that scatterer. This phase effect generates paired echoes about the mainlobe response for that scatterer (Section 5.1.2). As is usual with uncompensated motion effects, the paired echoes occur in azimuth.

The presence of these paired echoes about a scatterer or target in a SAR image is an indication that the scatterer is vibrating with a component of motion in the radar LOS direction. A number of factors complicate detection of this paired echo response. First, the response is weak compared to the intensity of the mainlobe of the vibrating target. Second, each paired echo is smeared over an area rather than concentrated like a point scatterer when using any of the wavenumber algorithms (including the PFA) to process the data. This smearing is a consequence of storing the data, effectively, in a nonrectangular format. Finally, noise and background clutter in the scene interfere with the paired echo response.

It may be possible to detect and characterize a vibrating target by exploitation of the SAR signals returned from it. Regarding a target that vibrates during an associated operation, it is possible to detect the following:

- Status of the operation (on or off) by the presence or absence of paired echoes associated with the target;
- Frequency of the operation by the location of the paired echoes;
- Magnitude of the operation by the intensity of the paired echoes relative to the mainlobe intensity;
- Character of the operation by the bandwidth of the paired echo response.

The input data for vibration detection and characterization is a single spotlight SAR complex image. The IFP motion compensates and polar formats this image in the normal ways. The basis for vibration detection and characterization is that a LOS component of sinusoidal motion produces paired echoes; vibration characteristics determine the amplitude, phase, and location of these echoes.

This section develops an analytical model for the effects of a sinusoidal vibration of constant amplitude and fixed, single frequency on the SAR signal history and on the resulting image of a vibrating point scatterer. It develops the equation for the phase compensation needed to focus the resulting paired echoes to a size comparable to the image of the scatterer itself. This focusing improves the probability of detection in a clutter plus noise environment.

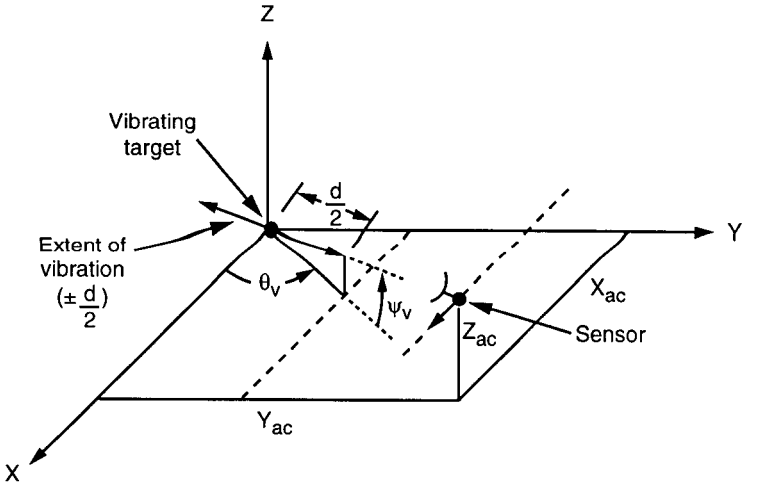


Figure 9.22 Data collection geometry with vibrating target.

9.4.1 Data Collection Model

To analyze the effects of target vibration in spotlight SAR imagery, the SAR data collection model in Figure 3.17(a) with the APC moving in the X direction at constant velocity is adequate. As Figure 9.22 shows, the XY plane is the nominal ground plane being imaged; it contains the vibrating target located at the origin of the XYZ coordinate system. At the center of the synthetic aperture time, the APC location is (X_{ac}, Y_{ac}, Z_{ac}) with components of APC position (X_{ac}, Y_{ac}, Z_{ac}) and velocity $(V_{xa}, 0, 0)$. Based on (3.27), the relevant signal equation for a point scatterer of radar cross-section σ_t is

$$s_o(K_p, \theta_p) = a_t \sum_{n=0}^{N_p-1} \left[\sum_{k=0}^{K-1} e^{j\Phi_p(K_p, \theta_p)} \right] \tag{9.30}$$

with $a_t = \sqrt{\sigma_t}$ where, from (3.28),

$$\Phi_p(K_p, \theta_p) = -\frac{K_p}{S_{\phi a}} (R_t - R_a) \tag{9.31}$$

This result discards the small residual video phase term, which is not relevant with respect to vibration analysis.

From (3.58) and (3.106), the appropriate expression for $R_t - R_a$ is the basic imaging term

$$(R_t - R_a)_{\text{basic}} = -S_{\phi a} \left\{ X_t C_{\theta a} + \left[Y_t + Z_t \frac{\cot(\phi_{ac})}{S_{\theta c}} \right] S_{\theta a} \right\} \tag{9.32}$$

Use of (9.32) in (9.31) yields

$$\Phi_p(K_p, \theta_p) = K_p \left\{ X_t C_{\theta a} + \left[Y_t + Z_t \frac{\cot(\phi_{ac})}{S_{\theta c}} \right] S_{\theta a} \right\} \tag{9.33}$$

where the target coordinates are nominally zero, but vary with time based on the vibration parameters of frequency f_v, peak-to-peak amplitude d, and phase at aperture center ϕ_v. Target movement d_v is given by

$$d_v(t) = \frac{d}{2} \sin(2\pi f_v t + \phi_v) \tag{9.34}$$

We assume that the vibration frequency is low relative to the radar PRF; therefore the variable t relates to sampled (slow) time or, equivalently, to pulse number n. Unlike earlier models developed for imaging stationary targets, the target coordinates (X_t, Y_t, Z_t) vary with time according to

$$X_t = \frac{d}{2} \cos(\psi_v) \cos(\theta_v) \sin(2\pi f_v t + \phi_v) \tag{9.35}$$

$$Y_t = \frac{d}{2} \cos(\psi_v) \sin(\theta_v) \sin(2\pi f_v t + \phi_v) \tag{9.36}$$

and

$$Z_t = \frac{d}{2} \sin(\psi_v) \sin(2\pi f_v t + \phi_v) \tag{9.37}$$

Figure 9.22 illustrates the geometry of this vibration, where ψ_v and θ_v identify the direction of vibration.

Substituting (9.35) through (9.37) into (9.33), the contribution of vibration to signal phase becomes

$$\Phi_p(K_p, \theta_p) = 2k_c U_p d \left(\frac{K_p}{K_c} \right) \sin(2\pi f_v t + \phi_v) \tag{9.38}$$

where

$$U_p(\theta_p) = \left\{ C_{\psi v} C_{\theta v} C_{\theta a} + \left[C_{\psi v} S_{\theta v} + \frac{\cot(\phi_{ac})}{S_{\theta c}} S_{\psi v} \right] S_{\theta a} \right\} S_{\phi c} \tag{9.39}$$

with

$$k_c = \frac{\pi}{\lambda_c} \tag{9.40}$$

The quantity K_c, given by (3.23), is the value of K_p at aperture center. This result uses the identities $C_{\psi v} = \cos(\psi_v)$, $C_{\theta v} = \cos(\theta_v)$, $S_{\theta v} = \sin(\theta_v)$, and $S_{\psi v} = \sin(\psi_v)$. An important point here is that U_p varies slowly over the coherent aperture while the vibration sinusoid varies through a few to many cycles over the coherent aperture.

9.4.2 Effect of Vibration

From (5.6), the approximation

$$e^{j\phi_o \sin(2\pi f_v t + \phi_v)} \approx 1 + \frac{\phi_o}{2}\left[e^{j(2\pi f_v t + \phi_v)} - e^{-j(2\pi f_v t + \phi_v)}\right] \tag{9.41}$$

is useful to analyze the effect of a sinusoidal vibration. This expression relates to (9.38) with the substitution

$$\phi_o = 2k_c U_p d\left(\frac{K_p}{K_c}\right) \tag{9.42}$$

which is much smaller than unity as long as d is much less than the radar center wavelength λ_c. Because U_p and K_p/K_c vary slowly, it is adequate to consider ϕ_o to be fixed at aperture center values ($U_p = U_c$ and $K_p = K_c$) when applying (9.41) to (9.38). Therefore, the signal associated with the vibrating target becomes

$$s_{vib}(K_p, \theta_p) = a_t e^{j\Phi_p(K_p, \theta_p)} \approx a_t e^{j\phi_t}\left\{1 + k_c d_{los}\left[e^{j(2\pi f_v t + \phi_v)} - e^{-j(2\pi f_v t + \phi_v)}\right]\right\} \tag{9.43}$$

The quantity ϕ_t represents the basic image phase associated with the target itself and, equally, with each paired echo (Section 3.6.1). This equation provides a model of the vibration-induced phase effect on the image of a vibrating target with

$$d_{los} = U_c d \tag{9.44}$$

Here, d_{los} is the mid-aperture LOS peak-to-peak amplitude of vibration. Besides the phase that (9.43) indicates, the basic phase associated with SAR image pixels (Section 3.6.1) is present on the entire vibrating target signature.

A sinusoidal vibration translates directly into a pulse-to-pulse (that is, t-dependent) sinusoidal phase effect in the SAR signal history for that target. It results in a pair of high azimuth sidelobes or paired echoes. Figure 5.15 illustrates this effect of sinusoidal phase errors in SAR imagery. In this figure, the paired echoes appear around every target because the antenna vibration causes the same relative motion for all targets. In the case of a vibrating target, only the scatterers that are vibrating will show the paired echo response.

Based on (5.7), the peak intensity of each paired echo in the image relative to that of the vibrating target is

$$\text{PSR} = (k_c d_{los})^2 = \left(\frac{\pi}{\lambda_c} d_{los}\right)^2 \tag{9.45}$$

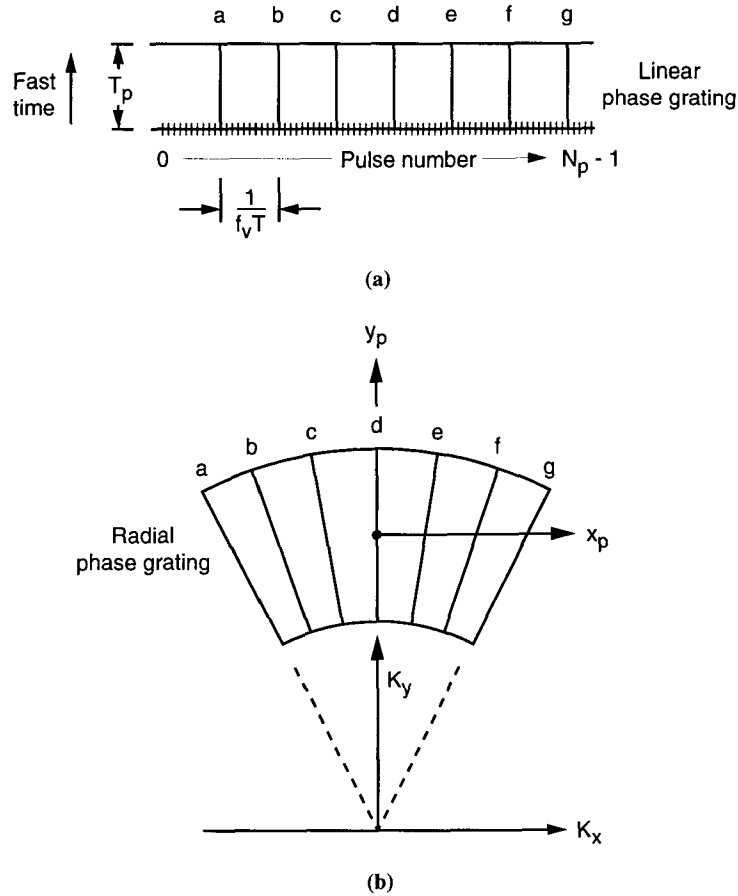


Figure 9.23 Constant phase lines from target sinusoidal vibration: **(a)** Rectangular format; **(b)** Polar format.

This relationship is valid only when the paired echo is focused as well as the vibrating target is focused. In this case, a measurement of peak sidelobe ratio (PSR) in the SAR image provides an estimate of d_{los} using this equation.

9.4.3 Smearing of Paired Echoes

A sinusoidal phase modulation, as seen in (9.38), usually generates focused paired echoes in one-dimensional Fourier analysis. In stripmap SAR and in spotlight SAR recorded in a rectangular format, a sinusoidal vibration produces a linear phase grating in azimuth in the two-dimensional SAR data format. Figure 9.23(a) illustrates this point. This signal has constant frequency over the full data window. Such a constant frequency signal produces

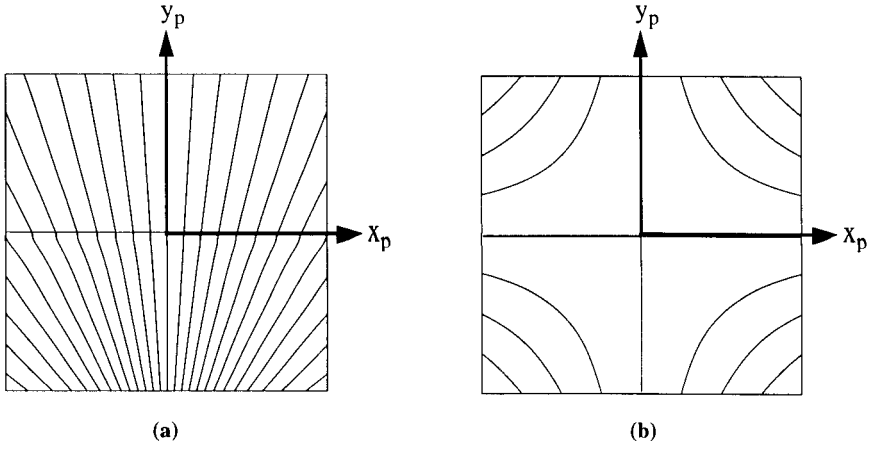


Figure 9.24 Components of sinusoidal vibration phase in polar format: **(a)** Full phase; **(b)** Nonlinear phase.

focused paired echoes, not smeared points. The process of polar formatting during fine-resolution spotlight signal processing takes this linear phase grating and warps it into a radial phase grating as Figure 9.23(b) suggests. The lines of constant phase arise from a pulse-to-pulse sinusoidal phase shift; however, the formatting stores these successive pulses, not side by side, but in this polar arrangement, angle by angle.

This polar phase grating consists largely of a linear grating in azimuth (x_p); however, it possesses a significant cross-product ($x_p y_p$) quadratic phase in the azimuth and range signal history coordinates. We illustrate this effect in Figure 9.24 and derive it analytically in Section 9.4.4.

Analysis in Section 9.4.4 will show that the linear component includes N_v cycles over the coherent azimuth aperture time T_a where

$$N_v = f_v T_a \tag{9.46}$$

Each cycle corresponds to a ρ_a / K_a distance of azimuth displacement of the paired echo from the vibrating scatterer causing it. Thus, displacement D_v in the azimuth direction is

$$D_v = \frac{\rho_a}{K_a} f_v T_a \tag{9.47}$$

Here K_a is the excess aperture factor in azimuth required to compensate for the resolution loss due to the aperture weighting function used for sidelobe control. The paired echoes before refocus subtend an angle equal to the azimuth coherent processing angle of the SAR data. The size of the smear S_v is roughly

$$S_v = D_v \Delta\theta = \frac{\lambda_c}{2} f_v T_a \tag{9.48}$$

after use of (2.20) for ρ_a. Figure 9.25 illustrates the geometry of these effects.

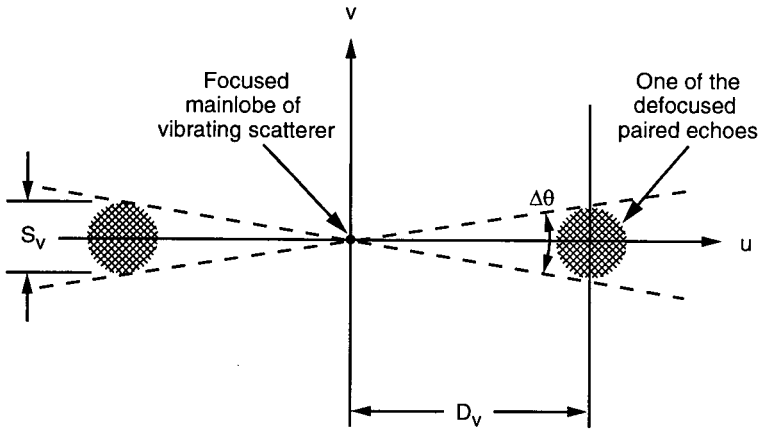


Figure 9.25 Geometry of smeared paired echoes.

9.4.4 Phase Adjustment to Focus Paired Echoes

From (9.43), the signal representing one of the vibration-induced paired echoes is

$$s_{pe}(t) \approx \pm a_t e^{j\phi_t} (k_c d_{los}) e^{\pm j(2\pi f_v t + \phi_v)} \tag{9.49}$$

The $\pm$ sign distinguishes between the two paired echoes. Because the phase term in ϕ_t includes no $\pm$ sign, the paired echoes lack a complex conjugate phase relationship.

To proceed with the analysis, we need an expression for time t as a function of data format coordinates K_p and θ_p. Equation (3.48) leads to the expression

$$t = \frac{Y_{ac}[\cot(\theta_p) - \cot(\theta_{ac})]}{V_{xa}} \tag{9.50}$$

showing that t varies with coordinate θ_p only. Figure 3.18 identifies x_p and y_p as signal history coordinates, centered at aperture center and associated with azimuth and range, respectively. We desire an expression for the phase of each paired echo in terms of x_p and y_p. Using (9.50) in (9.49), this phase $p(x_p, y_p)$ is

$$p(x_p, y_p) = \pm \left(2\pi f_v \frac{Y_{ac}}{V_{xa}} \right) [\cot(\theta_p) - \cot(\theta_{ac})] \pm \phi_v + \phi_t \tag{9.51}$$

The vibration analysis proceeds with a Taylor series expansion of this phase about the point $(x_p, y_p) = (0, 0)$ or identically $(K_p, \theta_p) = (K_c, \theta_c)$. An expression for this expansion is

$$p(x_p, y_p) = a_0 + a_1 x_p + a_2 y_p + a_{11} x_p^2 + a_{12} x_p y_p + a_{22} y_p^2 + \text{higher order} \tag{9.52}$$

which acknowledges but does not include the higher order terms (including cubic) because they are generally small.

Using (3.76) through (3.80), the expressions for the coefficients in (9.52) are

$$a_0 = p|_c = \phi_t \pm \phi_v \tag{9.53}$$

$$a_1 = -\frac{1}{K_c}\frac{dp}{d\theta_p} = \frac{2\pi f_v Y_{ac}}{K_c V_{xa} S_{\theta c}^2} \tag{9.54}$$

$$a_2 = \frac{dp}{dK_p} = 0 \tag{9.55}$$

$$a_{11} = \frac{1}{2K_c^2}\frac{d^2p}{d\theta_p^2} + \frac{1}{2K_c}\frac{dp}{dK_p} = \pm\frac{2\pi f_v Y_{ac} C_{\theta c}}{K_c^2 V_{xa} S_{\theta c}^3} \tag{9.56}$$

$$a_{12} = \frac{1}{K_c^2}\frac{dp}{d\theta_p} - \frac{1}{K_c}\frac{d^2p}{dK_p d\theta_p} = \mp\frac{2\pi f_v Y_{ac}}{K_c^2 V_{xa} S_{\theta c}^2} \tag{9.57}$$

and

$$a_{22} = \frac{1}{2}\frac{d^2p}{dK_p^2} = 0 \tag{9.58}$$

All derivatives are evaluated at aperture center. Use of

$$x_k = \frac{x_p}{K_c} \tag{9.59}$$

and

$$y_k = \frac{y_p}{K_c} \tag{9.60}$$

yields the relevant vibration echo quadratic phase (defocus) effect in the form

$$Q_{vib}(x_k, y_k) = \pm\left[\frac{2\pi f_v Y_{ac}}{V_{xa} S_{\theta c}^3}\right]\left[x_k^2 C_{\theta c} - x_k y_k S_{\theta c}\right] \tag{9.61}$$

The first term is a quadratic phase error in azimuth and the second term is a cross-product quadratic phase, that is, a function of the product of the range and azimuth coordinates. When imaging near broadside (θ_{ac} near $\pi/2$ rad), the azimuth term is small and the cross-product term dominates.

The idea is to compensate for this quadratic effect by multiplying the signal history by a conjugate expression before the two-dimensional FFT needed to compress the signal. In such a case, the paired echo signal becomes

$$s_{pe2}(t) \approx a_m k_c d_{los} e^{j(a_0 + a_1 x_p)} \tag{9.62}$$

This expression includes the $a_o = \phi_t \pm \phi_v$ constant phase and the linear (in x_p) phase effect. The linear term signifies the displacement in azimuth of the echo. Again, the $\pm$ designation distinguishes between the two paired echoes. In addition to the quadratic phase effects (which have been removed), cubic and higher order phase terms occur; however, they are significantly smaller than the quadratic terms.

The size of the displacement, indicated by a_1, is available by comparing a_1 to the first term in (9.33). From (9.33), the linear coefficient relating frequency (in x_p coordinate where $x_p = K_c \cos\theta_p$) to x_t position is

$$C_{xp} = \frac{4\pi S_{\phi c}}{\lambda K_c} \tag{9.63}$$

Division of a_1 by C_{xp} yields the displacement D_v in azimuth resulting from the a_1 term. The result is a D_v of

$$D_v = \frac{f_v Y_{ac} \lambda}{2 V_{xa} S_{\theta c}^2 S_{\phi c}} = \frac{\rho_a}{K_a} f_v T_a \tag{9.64}$$

using (2.20) and (2.22). This result is the source of (9.47) above.

9.4.5 Vibration Detection Process

Figure 9.26 illustrates the vibrating scatterer characteristic in the SAR image before and after focusing the smeared paired echoes; in this image space, u and v represent azimuth and range coordinates, respectively. Besides refocus by the phase compensation indicated by (9.61), it may be necessary to take into account the distortion caused by range curvature to properly locate the pair of focused paired echoes. This figure suggests the appearance of an intensity scan along the range bin containing the vibrating scatterer and shows how a thresholding technique may indicate the presence of a vibration. The location and intensity of the echoes relative to the mainlobe indicate the frequency of vibration from (9.64) and the LOS amplitude of vibration from (9.45).

Clutter is typically the factor that limits sensitivity to vibration detection in a well-designed, low-noise SAR system; otherwise, additive noise and multiplicative noise may be significant factors. The additive noise may be primarily radar thermal noise and the multiplicative noise likely arises from azimuth sidelobes induced by uncompensated antenna motion. Because antenna vibration exactly mimics target vibration, the two sources cannot readily be distinguished.

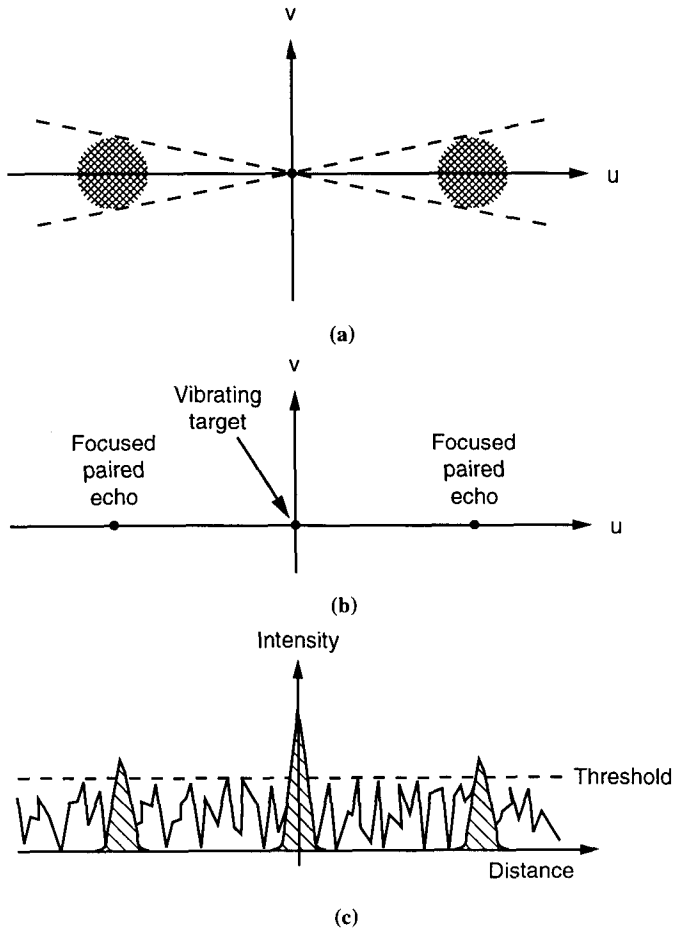


Figure 9.26 Vibration detection: (**a**) Smeared echoes; (**b**) Effect of refocus; (**c**) Thresholding approach.

Demanding coincidental detection of two corresponding paired echoes may reduce the probability of false alarms in this vibration detection process. Similarly, adding the two echoes in phase to gain a factor of two in signal level relative to clutter level may increase the probability of detection.

Additional considerations in vibration detection include the size and RCS characteristics of the target itself and the nature of the vibration in time and space coordinates. The target may be a single point scatterer, multiple point scatterers, linear or dihedral targets, or a distributed area target. The nature of the vibration includes its bandwidth and the

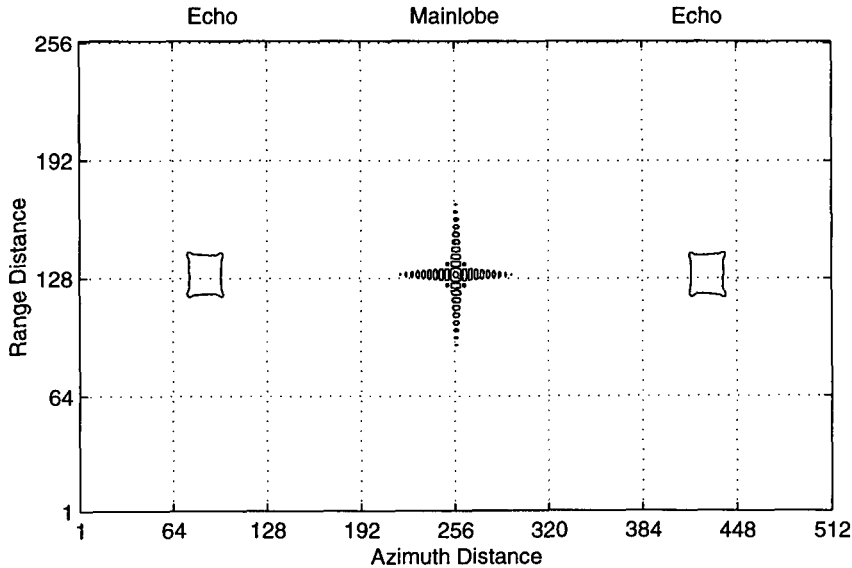


Figure 9.27 Contour plot in usual SAR image.

variations in vibration amplitude and phase over the target area. At one extreme, the vibration may involve primarily a discrete frequency; at the other extreme, it may encompass wideband random motion. The spatial nature of the vibration refers to the mode structure of an area target.

9.4.6 Simulated Examples with Vibrating Targets

To illustrate vibrating target effects, a computer program generates a signal history containing the returns from a point target at scene center vibrating sinusoidally at a constant frequency and amplitude. The signal history is polar formatted. Thus, it includes the two paired echoes displaced in azimuth associated with a vibrating target within the polar format processing structure. The signal history has the form of (9.30).

Figure 9.27 shows a two-dimensional contour plot of a scatterer and its two echoes in the SAR image. This image is the result of a two-dimensional FFT of the polar formatted signal history for the case of broadside spotlight imaging. The target is vibrating at 10 Hz with $d_{los} = 0.1\lambda_c$. The paired echoes on either side of the target are smeared over an area much larger than the size of the target mainlobe. The aperture time is about 4.25 s. From (9.46), this aperture time yields $N_v = 42.5$ cycles. At four pixels per resolution cell sampling, the paired echoes are displaced roughly 170 pixels in azimuth from the mainlobe target return, as we expect from (9.47). In summary, application of the PFA to this

simulated spotlight mode data produces a well-focused target at scene center and two appropriately sized and displaced paired echoes of energy from the phase modulation caused by the target vibration component along the radar line of sight.

Figure 9.28 shows a normalized intensity scan in the azimuth direction along range bin number 128 in Figure 9.27 containing the vibrating scatterer. The size of each smeared paired echo is about 22 pixels in azimuth. At 170 pixels distance, this size corresponds to an angular spread of 0.129 rad, consistent with the coherent processing angle of 0.130 rad and in agreement with (9.48). The echo intensity is roughly −24 dB relative to the mainlobe peak intensity, while (9.45) indicates a focused paired echo will appear −10 dB below the mainlobe peak. The smearing over 22 pixels or 5.5 resolution cells in two dimensions (14.8-dB decrease in echo intensity) accounts for this difference. The rightmost and leftmost returns are second-order terms of the expansion indicated by (9.41).

Application of the focus correction calculated in (9.61) will focus one of the paired echoes for constant velocity motion of the data collector. This equation changes sign between the two paired echoes. Figure 9.29 shows an azimuth intensity scan of the same area after applying the phase compensation to focus the smeared paired echo on the left in Figure 9.28. The result is that the first smeared paired echo on the left is focused and has the size of the originally focused mainlobe. The original mainlobe centered at pixel 257 is now defocused by the amount the now-focused paired echo was originally defocused. Focusing the echo increases its intensity by 14 dB while defocusing the mainlobe decreases its intensity by 14 dB. In agreement with the intensity scan in Figure 9.29, the defocused mainlobe intensity will now be −4 dB relative to the focused echo rather than 24 dB, having added 28 dB to the refocusing process. The first paired echo on the right has increased its defocus since the focus correction was of the wrong sign for this paired echo. The defocus of the rightmost second-order term is increased also because of the sign of the focus correction. Similarly, the defocus of the leftmost second-order term is reduced but not eliminated because the sign of the focus correction is proper but its magnitude is only half that required by this second-order paired echo. Figure 9.29, then, shows the result of applying the focus correction calculated as necessary to focus one of the paired echoes to the mainlobe, to the other first-order paired echo, and to the second-order paired echo. The mainlobe, which was well-focused initially, now possesses the initial characteristics of the first sidelobe; the second sidelobe received the proper magnitude of phase correction but the wrong sign, causing its smear to double from the original situation.

After multiplication by this focus correction, a two-dimensional FFT of the signal history produces an image in which one smeared paired echo is focused while the mainlobe return at scene center and the second paired echo are defocused a corresponding amount. Clearly, one requirement to produce an output in which all three scatterer attributes are focused (to aid relative comparison) is that the signals from each must be compensated differently. Proper space-variant phase compensation will remove the phase effect and focus the smeared paired echo to a size comparable to the signature of the target mainlobe response.

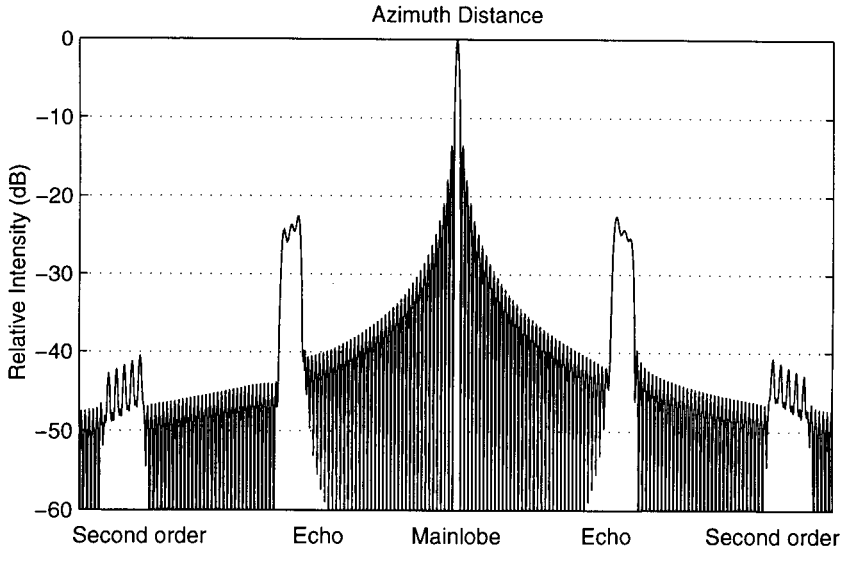


Figure 9.28 Intensity scan in azimuth direction along range bin containing the vibrating scatterer.

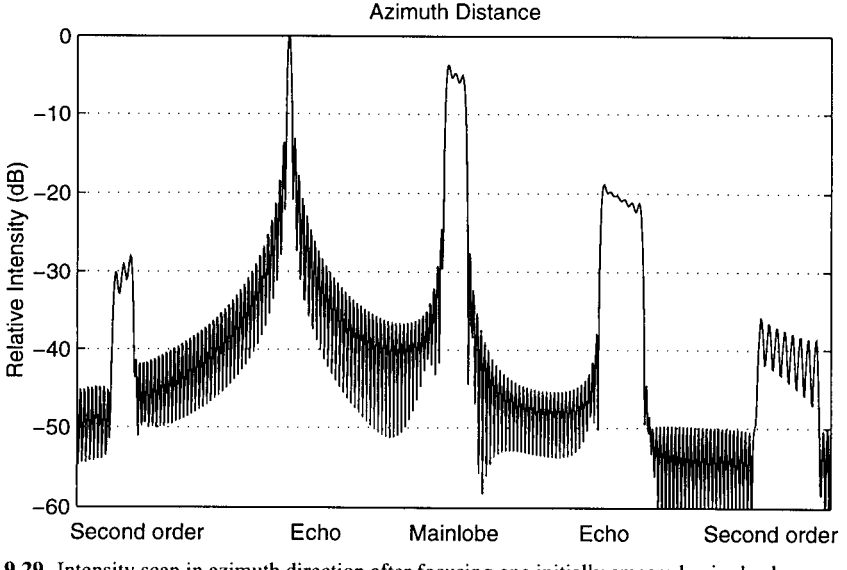


Figure 9.29 Intensity scan in azimuth direction after focusing one initially smeared paired echo.

9.5 SUMMARY

The examples in this chapter illustrate the diversity of applications for spotlight processing algorithms. While each of these examples uses the PFA, the range migration and chirp scaling algorithms are potential choices also. A trade-off process similar to that suggested in Chapter 12 determines the appropriate algorithm. Additional radar applications for these algorithms include *bistatic SAR imaging* [12, 13] using separately located transmit and receive antennas and *passive SAR imaging* [14] involving the simultaneous collection by two separately located broadband microwave receivers of incoherent thermal radiation originating from the scene of interest. Bistatic imaging and passive imaging are each amenable to processing with modified polar format algorithms based on the unique features of the signal data and collection geometries.

REFERENCES

[1] Rodriguez, E., and J.M. Martin, "Theory and Design of Interferometric Synthetic Aperture Radars," *IEE Proceedings-F*, Vol. 139, No. 2, April 1992, pp. 147-159.

[2] Zebker, H., and R.M. Goldstein, "Topographic Mapping from Interferometric Synthetic Aperture Radar Observations," *Journal of Geophysical Research*, Vol. 91, April 1986, pp. 4993-4999.

[3] Held, D.N., and J.D. O'Brien, "Norden Systems' 2-Dimensional Interferometric Synthetic Aperture Radar Flying Testbed," *Proceedings of the 1992 IEEE International Geoscience and Remote Sensing Symposium (IGARSS)*, Houston, TX, 26-29 May, 1992, pp. 646-648.

[4] Zebker, H.A., S.N. Madsen, J. Martin, K.B. Wheeler, T. Miller, Y. Lou, G. Alberti, S. Vetrella, and A. Cucci, "The TOPSAR Interferometric Radar Topographic Mapping Instrument," *IEEE Transactions on Geoscience and Remote Sensing*, Vol. 30, No. 5, September 1992, pp. 933-940.

[5] Li, F.K., and R.M. Goldstein, "Studies of Multibaseline Spaceborne Interferometric Synthetic Aperture Radars," *IEEE Transactions on Geoscience and Remote Sensing*, Vol, 28, No. 1, January 1990, pp. 88-97.

[6] Gabriel, A.K., and R.M. Goldstein, "Crossed Orbit Interferometry: Theory and Experimental Results form SIR-B," *International Journal of Remote Sensing*, Vol. 9, No. 5, 1988, pp. 857-872.

[7] Sos, G.T., H.W. Klimach, and G.F. Adams, "High Performance Interferometric SAR Description and Capabilities," *Proceedings of the 10th Thematic Conference on Geologic Remote Sensing*, San Antonio, Texas, 9-12 May 1994, Vol. 2, pp. 637-650.

[8] Adams, G.F., J.L. Auterman, G.T. Sos, and J.A. Voisinet, "Terrain Height Measurement by Fine Resolution Interferometric SAR," *Proceedings of the 9th Thematic Conference on Geologic Remote Sensing*, Pasadena, California, 8-11 February 1993, pp. 1121-1131.

[9] Just, D., and R. Bamler, "Phase Statistics of Interferograms with Applications to Synthetic Aperture Radar," *Applied Optics*, Vol. 33, No. 20, July 1994, pp. 4361-4368.

[10] Madsen, S.N., and H.A. Zebker, "Automated Absolute Phase Retrieval in Across-Track Interferometry," *Proceedings of the International Geoscience and Remote Sensing Symposium, IGARSS 1992*, Vol II, 1992.

[11] Leberl, F.W., *Radargrammetric Image Processing*, Artech House, Norwood, MA, 1990.

[12] Willis, N.J., *Bistatic Radar*, Artech House, Norwood, MA, 1991.

[13] Lee, P.K., and T.F. Coffey, "Space-Based Bistatic Radar: Opportunity for Future Tactical Air Surveillance," *IEEE International Radar Conference*, 1985, Arlington, VA, pp. 322-329.

[14] United States Patent No. 4,794,395, I. Cindrich, W.G. Carrara, I.J. LaHaie, and A.M. Tai, "Passive Interferometric Imaging Receiver System," 27 December 1988.

Chapter 10
Range Migration Algorithm

Three publications by Cafforio, Prati, and Rocca describe a new algorithm for digital SAR image formation processing [1-3]. The algorithm, known as the range migration algorithm (RMA), originates from techniques long used in the field of seismic signal processing for imaging the earth's substrata [4, 5]. Initial publications on the RMA treat the case of an image formation processor (IFP) for stripmap SAR systems carried by airborne or satellite platforms [3]. Subsequent papers demonstrate the application of range migration processing to spotlight data [6, 7]. This chapter develops the RMA from the perspective of spotlight SAR image formation. The concepts and analysis presented here extend easily to an understanding of stripmap data processing as well.

Unlike the polar format algorithm (PFA), the RMA does not assume that illuminating wavefronts are planar. Hence, RMA images do not suffer from the space-variant defocusing and geometric distortion that wavefront curvature induces with use of the PFA. In addition, the RMA is often competitive with the PFA in terms of computational efficiency. These characteristics make the RMA particularly attractive for imaging situations that involve severe differential range curvature over the scene of interest (Section 3.1.2). Such situations include imaging large scenes at fine resolution, imaging at short ranges, and imaging with a low center frequency.

One drawback to RMA processing of spotlight data is that the RMA generally requires a higher along-track sampling rate than the PFA. This requirement can become troublesome as azimuth time-bandwidth product increases. Section 10.1 discusses the origin of this sampling requirement, and Section 10.4.1 quantifies it.

Section 10.1 sets up convenient imaging geometry and signal models to analyze and understand the RMA. It presents a motion compensation requirement that is a necessary prerequisite for RMA processing. Section 10.2 describes the operation and functionality of the RMA using simulated data examples to illustrate each step of the algorithm. Section 10.3 presents a detailed analytical development of the RMA. Section 10.4 discusses a number of practical topics pertaining to RMA processing of spotlight SAR data. Finally, Section 10.5 illustrates RMA processing using SAR signal data from two applications. The first application involves fine-resolution imaging of a large scene at L-band. The second application is ultra-wideband (UWB) SAR imaging for foliage penetration (FOPEN). Chapter 12 provides a comparison between the RMA and other spotlight image formation algorithms.

10.1 SIGNAL MODEL

The data collection geometry in Figure 10.1 provides the basis for a convenient SAR signal model to analyze the RMA. To simplify analysis of the RMA, the SAR sensor traverses a straight-line flight path parallel to the X axis. It travels at constant velocity and altitude to image an area of terrain in a squinted spotlight mode. The radar transmits and receives pulses at a fixed pulse repetition interval to maintain uniform spatial sampling along the flight path. The RMA processes a batch of pulses collected over a synthetic aperture length L to form an image of the spotlight scene.

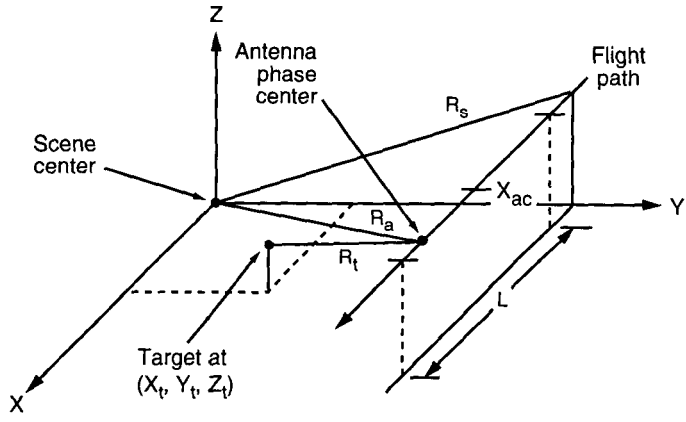


Figure 10.1 Data collection and imaging geometry.

The geometry model in Figure 10.1 uses a Cartesian coordinate system with origin at the center of the scene being imaged. The X axis of this system is parallel to and in the same direction as the SAR platform velocity vector. The fixed slant range distance between the flight path and swath center is R_s. The center of the synthetic aperture has along-track coordinate X_{ac}. Point scatterer analysis assumes a single point reflector within the imaged scene at coordinates (X_t, Y_t, Z_t). The distance $R_t(X_a)$ between the radar and this scatterer varies as a function of along-track position X_a. As in previous chapters, it is convenient to suppress notation depicting the dependency of this quantity on X_a and simply write R_t. Similarly, the range between the radar and the center of the imaged scene is $R_a(X_a)$, or simply R_a.

We develop the RMA for a SAR system using a linear FM (chirp) waveform with dechirp-on-receive (Section 2.6). This waveform strategy is common in fine-resolution SAR systems. However, the RMA is also applicable to chirp systems that do not employ dechirp-on-receive and to systems that do not use chirp waveforms. To apply the RMA to these other radar waveforms, it is necessary to first convert collected radar signals into the range spatial-frequency domain. This domain is available as the range Fourier transform

of fully compressed range signals. A preprocessing operation before the actual RMA must perform this conversion.

In the data collection model of Figure 10.1, the SAR system transmits a pulse at position (X_a, Y_a, Z_a) along the flight path. The radar receives a return from the point scatterer and demodulates it using a delayed replica of the transmitted pulse. Based on (2.57), the resulting intermediate frequency signal is

$$s_{if}(X_a, \hat{t}) = a_t \operatorname{rect}\left(\frac{X_a - X_{ac}}{L}\right) \operatorname{rect}\left(\frac{\hat{t} - 2R_t/c}{T_p}\right) e^{j\Phi_{if}(X_a, \hat{t})} \tag{10.1}$$

with

$$\Phi_{if}(X_a, \hat{t}) = -\frac{4\pi\gamma}{c}\left(\frac{f_c}{\gamma} + \hat{t} - \frac{2R_a}{c}\right)(R_t - R_a) + \frac{4\pi\gamma}{c^2}(R_t - R_a)^2 \tag{10.2}$$

We write (10.1) and (10.2) as continuous functions of along-track sensor position rather than discrete pulse number n. The quantity T_p is the transmitted pulse length, c is the speed at which microwave energy propagates, f_c represents the center transmit frequency, γ is the chirp rate, and a_t is the square root of the scatterer's radar cross section σ_t. The symbol $\hat{t}$ is defined by $\hat{t} = t - nT$, where T is the period between successive pulse transmissions.

The first rect function in (10.1) limits the received data in azimuth to an aperture of length L centered at coordinate X_{ac}. This length establishes azimuth resolution. For simplicity, (10.1) assumes the backscattered amplitude and phase characteristics of the point scatterer do not vary with frequency or aspect angle and that the radar is stationary during pulse transmission and reception. This model disregards antenna gain, amplitude effects of propagation on the signal, and any additional time delays due to atmospheric effects.

The signal phase in (10.2) results from demodulating, or motion compensating, received signals with a reference function that is based on line-of-sight range to scene center R_a. The reference function is a replica of the transmitted signal delayed by an amount $2R_a/c$, which varies with along-track sensor position. Figure 10.2 illustrates this reference function for the case of broadside imaging. The azimuth phase of a scene center scatterer is nominally $-4\pi R_a/\lambda_c$, where $\lambda_c = c/f_c$ is the center wavelength of the radar. The motion compensation reference function matches this phase and cancels it. After application of the reference, the scene center scatterer has no phase variation.

Unlike the PFA, the RMA requires demodulation of input signal history data based on a *fixed* reference range. Such a signal history is available by replacing the reference range R_a in (10.2) with the constant reference range R_s. This procedure results in a new signal with phase

$$\Phi_{if}(X_a, \hat{t}) = -\frac{4\pi\gamma}{c}\left(\frac{f_c}{\gamma} + \hat{t} - \frac{2R_s}{c}\right)(R_t - R_s) + \frac{4\pi\gamma}{c^2}(R_t - R_s)^2 \tag{10.3}$$

The SAR sensor can obtain this signal by demodulating received echoes in real time using

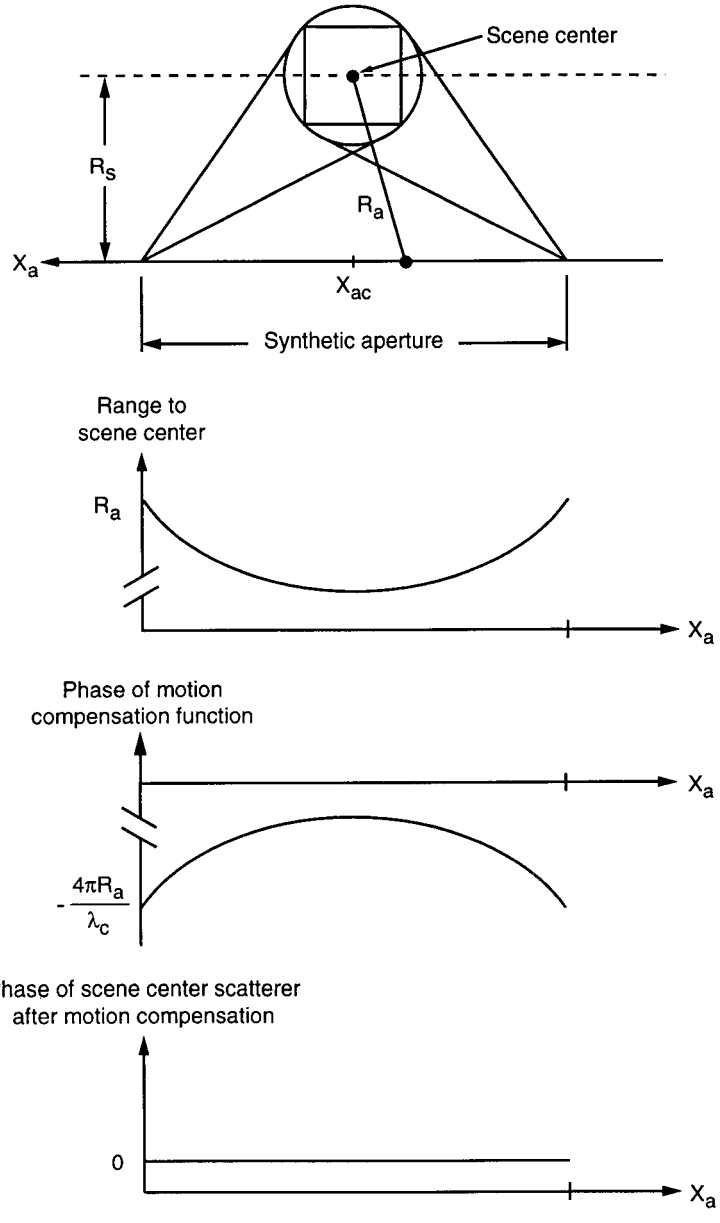


Figure 10.2 Motion compensation strategy for conventional spotlight imaging (compensation to a point).

a fixed time delay of $2R_s/c$ rather than the variable delay that spotlight SAR usually employs. Alternatively, it is acceptable to mix the standard spotlight signal in (10.1) with a new reference function that yields (10.3) as a result. In either case, the RMA expects data in the form of (10.3). An interpretation of (10.3) is a SAR signal with motion compensation to a moving scene point moving at the nominal sensor velocity. Figure 10.3 illustrates compensation to a moving point, or line. *Stripmap* SAR commonly employs this motion compensation strategy in which the azimuthal phase of the motion compensation reference function remains constant. A scatterer at scene center retains its approximately quadratic phase variation in azimuth after application of the reference function.

The second term in (10.3) is an unwanted phase effect known as residual video phase (RVP). It is specific to chirp systems that dechirp in the time domain as the above model does. If the variation of this term is small over a synthetic aperture, we can safely ignore it. Otherwise, the IFP must remove it in a preprocessing operation known as *range deskew* (Appendix C). The current model, with its emphasis on fine-resolution imaging, will remove the RVP term. After removal of RVP through range deskew, the signal becomes

$$s_{rd}(X_a, \hat{t}) = a_t \text{rect}\left(\frac{X_a - X_{ac}}{L}\right) \text{rect}\left(\frac{\hat{t} - 2R_s/c}{T_p}\right) e^{j\Phi_{rd}(X_a, \hat{t})} \tag{10.4}$$

with

$$\Phi_{rd}(X_a, \hat{t}) = -\frac{4\pi\gamma}{c}\left(\frac{f_c}{\gamma} + \hat{t} - \frac{2R_s}{c}\right)(R_t - R_s) \tag{10.5}$$

The second rect function in (10.4) indicates that the range deskew operation shifts the signal in $\hat{t}$. The return from a point anywhere in the scene now coincides in time with that of a point at range R_s. Figure 10.4 shows the two-dimensional support of the SAR signal received from a scene center scatterer before and after range deskew for the case of broadside imaging. Figure 10.4(a) corresponds to (10.1), while Figure 10.4(b) corresponds to (10.4). Radar illumination and near range are on the left side in Figure 10.4.

Although (10.2) represents a SAR signal with motion compensation to a point and (10.3) represents a SAR signal with motion compensation to a line, both possess a RVP term. The part of this term that varies over the synthetic aperture causes difficulty in image formation (Appendix C). In general, this part of the RVP term is larger with motion compensation to a line than with motion compensation to a point. This difference occurs for two reasons. First, RVP is proportional to the square of the quantity $R_t - R_s$ in the former case and to the square of $R_t - R_a$ in the later case. Typically, $R_t - R_s$ can be substantially larger than $R_t - R_a$. Second, because R_s is constant, the variation in $R_t - R_s$ is much larger than the variation in $R_t - R_a$ over the synthetic aperture. For instance, a scatterer at scene center, where $R_t = R_a$, has zero RVP with motion compensation to a point. This same scatterer can have a significant RVP level with motion compensation to a line. Because RMA requires motion compensation to a line, the use of the RMA in a fine-resolution SAR system often implies that the processor must first perform range deskew. These same systems may safely ignore RVP when processing via image formation algorithms that utilize motion compensation to a point.

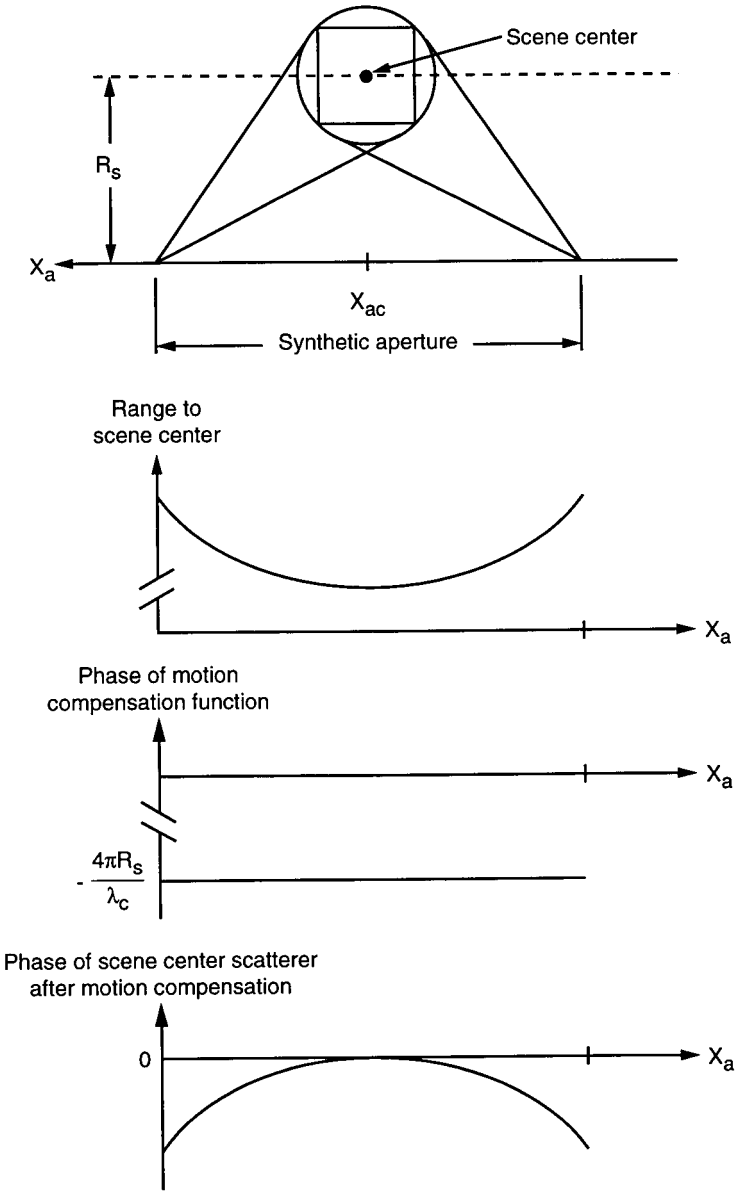


Figure 10.3 Motion compensation strategy required for RMA processing (compensation to a line).

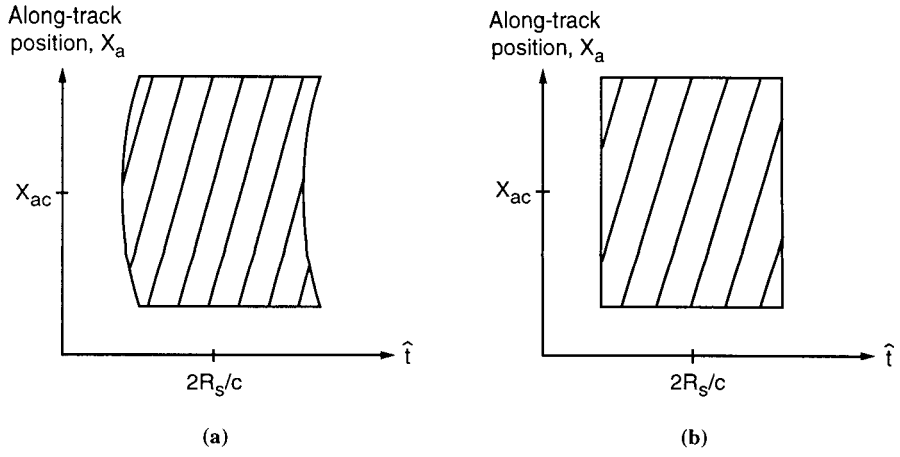


Figure 10.4 Two-dimensional support of SAR signal: (**a**) Received data; (**b**) Data after range deskew.

Motion compensation to a line and range deskew are preprocessing operations rather than actual components of the RMA. Figure 10.5 shows the location of these operations in the overall SAR image formation processor. The IFP in Figure 10.5 does not include a provision to compensate for nonplanar motion (Section 3.3.4). If needed, the IFP can easily include a module to compensate for this effect.

10.2 ALGORITHM OVERVIEW

This section provides a heuristic overview of the RMA and illustrates its basic operation with simulation examples based on the data collection geometry in Figure 10.6. Generation of these examples uses the signal model of (10.4), the accompanying assumptions in Section 10.1, and the radar system parameters in Table 10.1. The simulation parameters provide a useful illustration only; they do not represent any specific SAR system.

Figure 10.7 shows the magnitude of the simulated scatterers in Table 10.1 after range compression. In this domain, the energy from each scatterer follows a curved path in range and along-track position. The variation in range to a scatterer over the spotlight synthetic aperture is known as *motion through resolution cells* (MTRC). Figure 10.8 quantifies the MTRC associated with the three simulated point scatterers. Discussions of the RMA commonly use stripmap terminology in which the nonlinear component of MTRC is range curvature (Section 3.2.1). The variation in range curvature over the scene is *differential* range curvature. Image formation algorithms vary in their ability to accommodate differential range curvature. The real strength and benefit of the RMA derives from its ability to compensate severe differential range curvature. This chapter illustrates how the RMA achieves such compensation in the two-dimensional spatial-frequency domain.

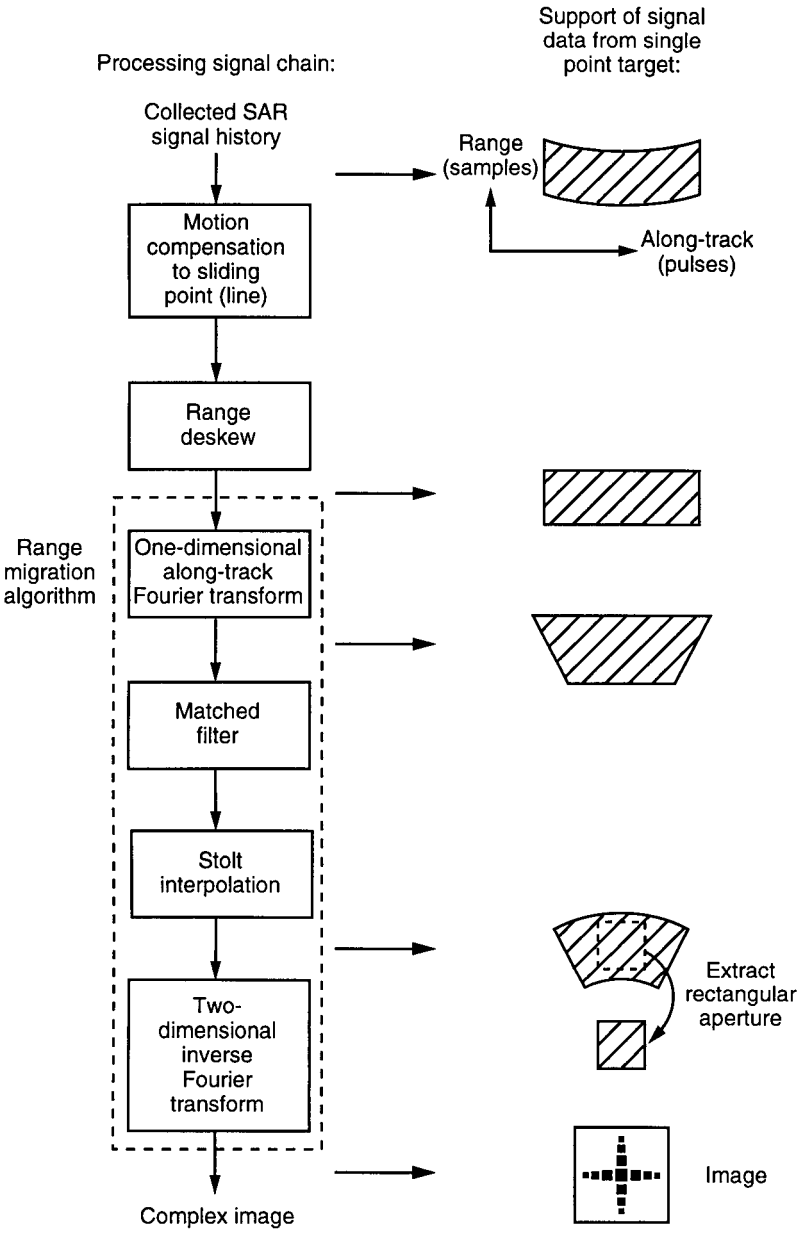


Figure 10.5 Image formation processor using the RMA.

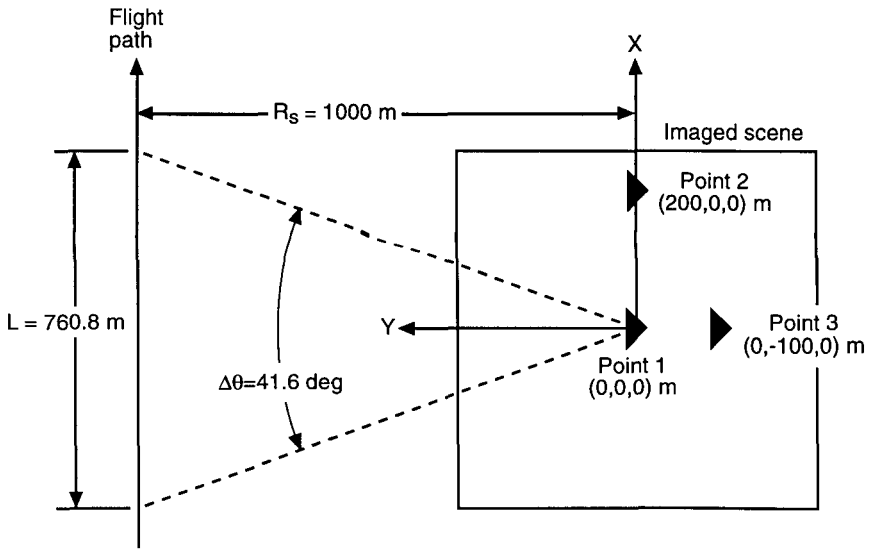


Figure 10.6 Simulation geometry.

Figure 10.9 presents a simplified block diagram of the RMA. The figure includes only the essential functions of RMA operation. The input is SAR signal data after motion compensation to a line and after range deskew. This section describes each of these signal processing functions.

10.2.1 Along-Track Fourier Transform

The RMA differs from the polar formation algorithm immediately in that its first operation is a Fourier transform in the along-track dimension. The IFP performs this transform prior to range compression and prior to removing the azimuth chirp from the signal history. It is helpful to first explore the characteristics of the transformed signal before discussing the motivation behind this initial RMA operation.

Figure 10.10 relates the RMA perspective here to the PFA perspective in Figure 3.12. The principal difference is that the RMA signal history remains in the $K_X K_Y$ slant plane in wavenumber space while the PFA development projects the signal history to the $K_x K_y$ plane to establish the XY plane as the image display plane (IDP). In the RMA presentation, the IDP is the nominal data collection plane. Note that $K_x = K_X$ and that K_R is common to both presentations.

Figure 10.11 shows the magnitude of the two-dimensional signal history from point 1 of Figure 10.6 after performing an azimuth FFT. Figure 10.11 shows the result of the transform for one simulated point only (rather than all three simultaneously) to make the discussion clear. The vertical axis is range spatial frequency. In the dechirped SAR signal,

Table 10.1
System Parameters for Simulation Example

Parameter	*Description*	*Value*
Δ_X	Along-track sample spacing	0.6 m
T_p	Pulse length	4 μs
W_r	Range scene size	575.3 m
W_a	Azimuth scene size	442.9 m
f_c	Radar center frequency	242.4 MHz
γ	Chirp rate	33.375 MHz/μs
B	Processed bandwidth	133.5 MHz
F_s	Complex sampling rate	128 MHz
ρ_r	Range resolution	1.0 m
ρ_a	Azimuth resolution	1.0 m
K_r	Range mainlobe-broadening factor	0.89
K_a	Azimuth mainlobe-broadening factor	0.89
R_s	Broadside slant range to scene center	1000 m
ϕ_{ac}	Image incidence angle	90 deg
θ_{ac}	Image squint angle	90 deg (broadside)
L	Synthetic aperture length	760.8 m
$\Delta\theta$	Coherent processing angle interval	41.6 deg
	Number of scatterers	3
	Scatterer locations:	
(X_1, Y_1, Z_1)	Point 1 coordinates	(0, 0, 0) m
(X_2, Y_2, Z_2)	Point 2 coordinates	(200, 0, 0) m
(X_3, Y_3, Z_3)	Point 3 coordinates	(0, −100, 0) m

range spatial frequency is RF frequency scaled by $4\pi/c$. This quantity has units of radians per unit length and is denoted by the symbol K_R. It varies from a minimum value of $4\pi(f_c - B/2)/c$ to a maximum value of $4\pi(f_c + B/2)/c$. The parameters f_c and B are the SAR system center frequency and transmitted bandwidth in units of hertz.

The horizontal axis of Figure 10.11 is azimuth spatial frequency. This quantity is equivalent to negative Doppler frequency expressed in units of radians per unit length rather than in units of temporal frequency. We represent azimuth spatial frequency with the symbol K_X. The signal data output from the azimuth FFT has K_X values ranging from π/Δ_X to $-\pi/\Delta_X$, where Δ_X is the interpulse sample spacing in units of distance.

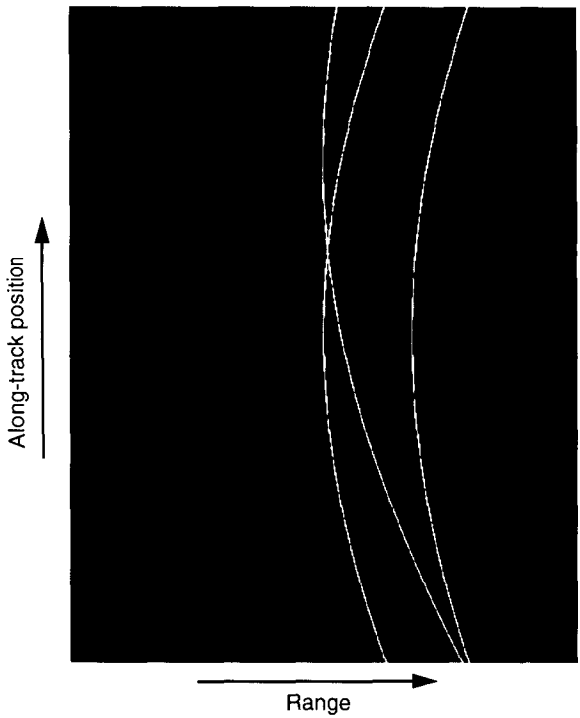


Figure 10.7 Simulated signal history after range compression.

Based on (2.26), the Doppler frequency of a signal from a scatterer at a cone angle α_d relative to the antenna velocity vector is

$$f_d = \frac{2V_a \cos(\alpha_d)}{\lambda} \tag{10.6}$$

where λ is instantaneous transmitted wavelength and V_a is velocity. Multiplication by $-2\pi/V_a$ yields azimuth spatial frequency as

$$K_X = -\frac{4\pi \cos(\alpha_d)}{\lambda} \tag{10.7}$$

We include the negative sign to align the X and K_X axes in the same direction in Figure 10.10. Here, azimuth spatial frequency relates to the negative of Doppler frequency in the right-looking data collection perspective that we use in this book. The two-dimensional support of the signal data in Figure 10.11 "fans out" with increasing range frequency because azimuth spatial frequency varies with transmitted wavelength as (10.7) indicates.

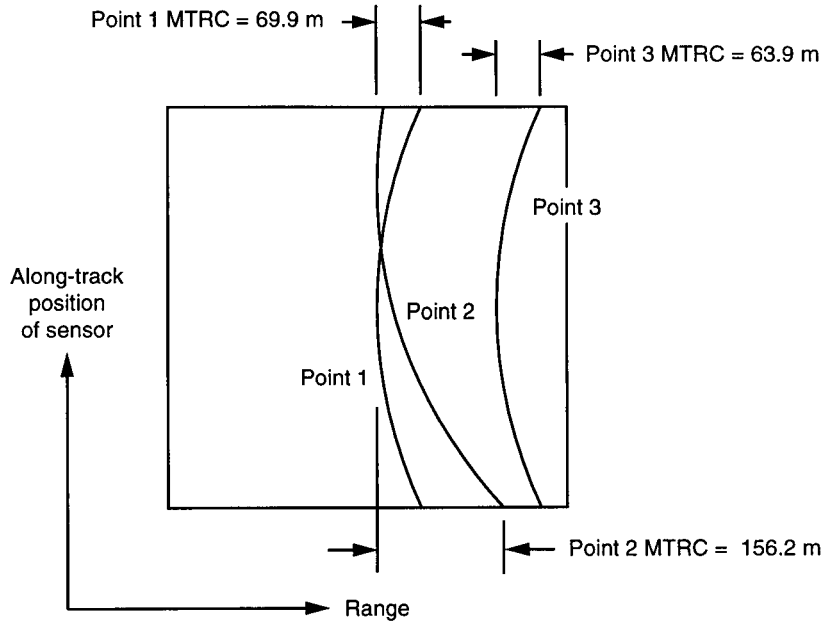


Figure 10.8 Magnitude and shape of MTRC associated with simulated scatterers.

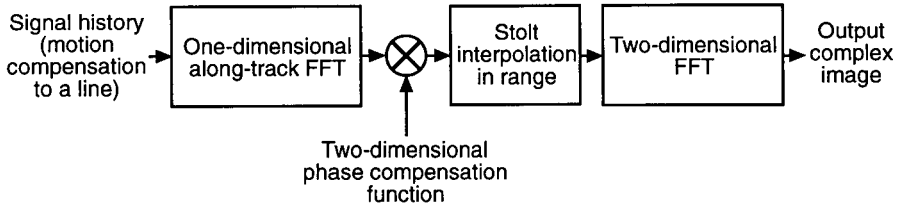
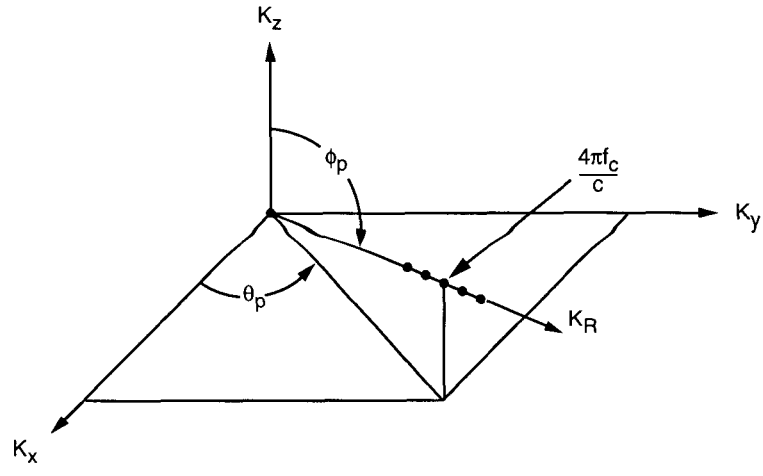
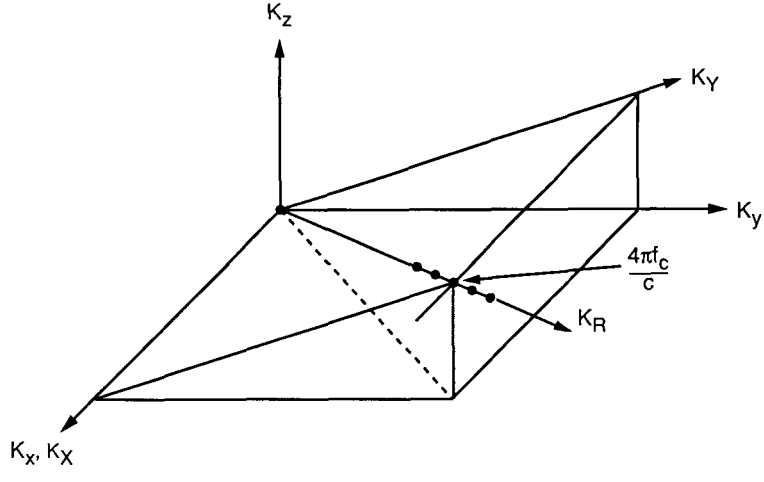


Figure 10.9 Block diagram of range migration algorithm.

Figure 10.12 shows what the azimuth transformed SAR signal would look like after a range compression via a range Fourier transform. As in Figure 10.7, the point scatterers in Figure 10.12 follow curved trajectories. Now, however, the two scatterers at the same broadside range (point 1 and point 2) follow identical trajectories. Being at differing along-track locations, they map into different segments of the same arc. Examination of Figure 10.12 suggests that we can equalize range curvature across the imaged range extent by performing a remapping of the data in the range direction that varies with azimuth frequency. That is, we remap or warp the data depicted in Figure 10.12 as a function of azimuth frequency K_X. The RMA achieves this warping by performing a one-dimensional interpolation in the range frequency coordinate K_R. Section 10.2.3 discusses this operation, known as the Stolt interpolation [2].



(a)



(b)

Figure 10.10 Wavenumber space: **(a)** Polar format algorithm perspective from Figure 3.12; **(b)** Range migration algorithm perspective.

10.2.2 Matched Filtering

The second step in the RMA (Figure 10.9) is application of a two-dimensional phase compensation to the azimuth-transformed signal. This operation perfectly corrects the range curvature of all scatterers at the same range as scene center. It only partially compensates scatterers at other ranges. In effect, the operation performs motion compensation to scene

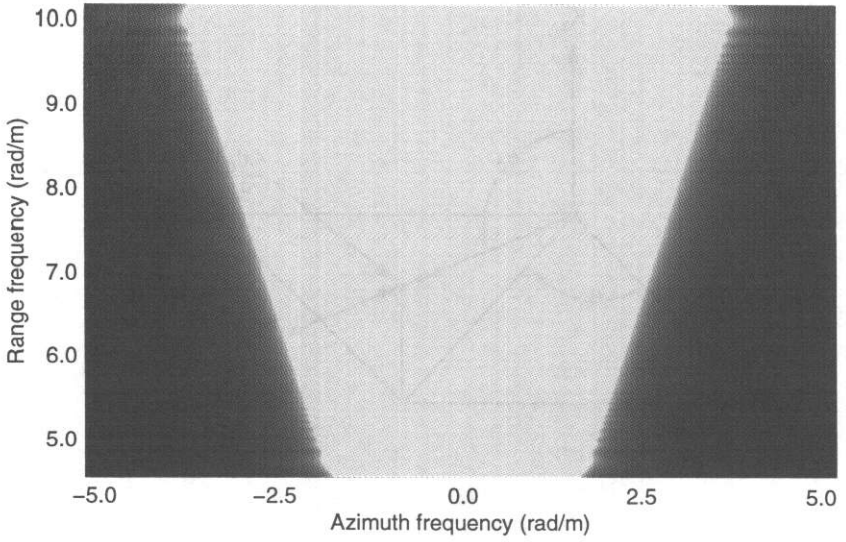


Figure 10.11 Magnitude of two-dimensional signal history after azimuth Fourier transform.

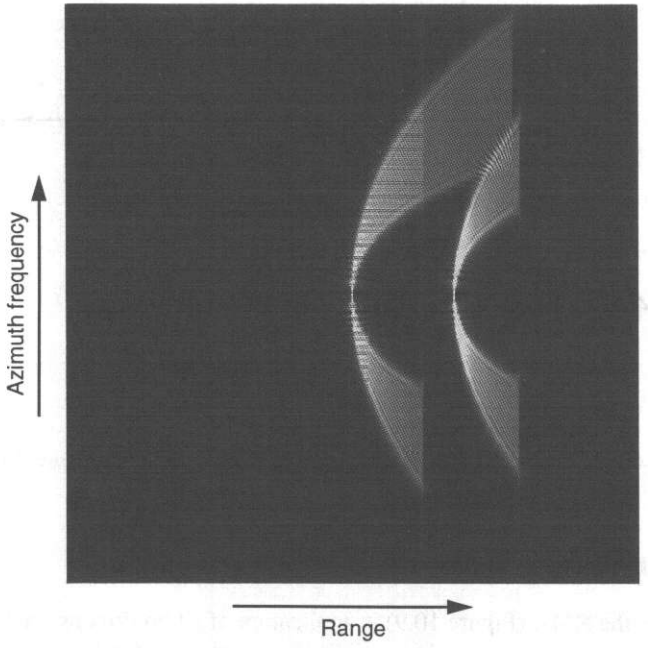


Figure 10.12 Magnitude of azimuth-transformed signal history after range compression.

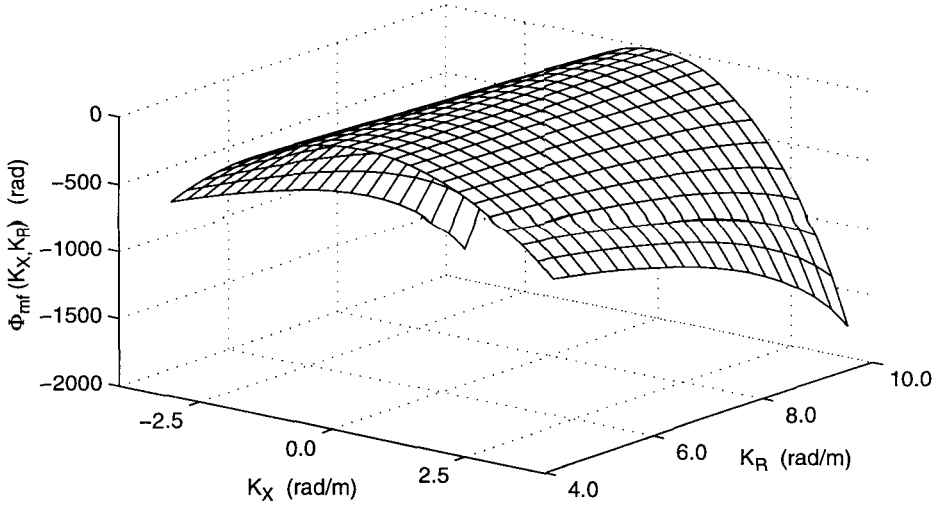


Figure 10.13 Phase of two-dimensional reference function (matched filter).

center, or azimuth dechirp, in the azimuth-frequency domain K_X rather than in the along-track collection domain X_a. The operation implements the two-dimensional matched filter needed to compress all scatterers having minimum range R_s.

Section 10.3 will show that the phase of the two-dimensional matched filter is

$$\Phi_{mf}(K_X, K_R) = -R_s K_R + R_s \sqrt{K_R^2 - K_X^2} \tag{10.8}$$

Figure 10.13 shows a surface plot of this two-dimensional phase function for the ongoing simulation example. The figure shows that the phase compensation of (10.8) is approximately quadratic in K_X and approximately linear in K_R. The K_X-dependent linear phase component corrects the range curvature of a scatterer at scene center.

To summarize RMA operations up to this point, the algorithm transforms the azimuth chirped data into the K_X domain in order to circumvent the along-track dependency of range curvature. The resulting two-dimensional signal is still chirped in the K_X dimension; the size of this chirp varies with range frequency. The RMA removes the chirp in the azimuth spatial-frequency domain via the phase function of (10.8). Also, application of (10.8) corrects the range curvature of all scatterers having minimum range R_s. Residual range curvature is still present on those scatterers with a minimum range that is different than R_s. In spotlight SAR data, the matched filter undercompensates the curvature of scatterers at ranges nearer than scene center and overcompensates the curvature of scatterers at ranges farther than scene center. It is the job of the next operation to remove the residual range curvature of all scatterers.

10.2.3 Stolt Interpolation

The third step performed by the RMA is known as Stolt transformation. It simultaneously compensates the range curvature of all scatterers by an appropriate warping of the SAR signal data. The warping is primarily a K_X-dependent stretching of the signal in the range dimension. The Stolt transformation operates on signal data in the (K_X, K_R) domain.

In the (K_X, K_R) domain, the signal from a single point scatterer is a sinusoid in the K_R coordinate. Before stretching, the frequency of the sinusoid for a specific scatterer varies with K_X. Stretching a one-dimensional sinusoid has the effect of lowering its frequency. The Stolt transformation lowers the range frequency of a scatterer by the correct amount as a function of K_X to make the frequency of the sinusoid constant for all K_X; the relation between range frequency reduction and K_X is such that the residual range curvature arcs are "straightened out" and the range response is made to reside in a single range frequency bin. In addition to the stretching performed by the Stolt transformation, a K_X-dependent shift of the signal in the K_R dimension is necessary to preserve the phase of each point over the all azimuth frequencies. Figure 10.14 illustrates how the Stolt transformation corrects range curvature for scatterers at differing ranges.

The Stolt transformation performs a one-dimensional mapping to a new domain denoted by K_Y, where K_Y is given by

$$K_Y = \sqrt{K_R^2 - K_X^2} \tag{10.9}$$

For discrete-time video signals, the RMA processor implements the Stolt transformation using digital interpolation filters, such as those used for polar interpolation in Chapter 4. Collected data samples are spaced uniformly in K_R. The interpolation resamples the data in K_R to give output samples that are uniformly spaced in K_Y. Figure 10.15 depicts the two-dimensional samples of the simulated data set in both the (K_X, K_R) domain and the (K_X, K_Y) domain. Lines of constant K_R in (K_X, K_R) space map into circles in (K_X, K_Y) space. Figure 10.16 illustrates the relationship between Stolt interpolation input sample locations and output sample locations in (K_X, K_Y) space.

Figure 10.17 is a plot of the input-output relationship for the ongoing simulation example for three values of K_X. Input and output locations are identical for $K_X = 0$ (that is, no resampling is necessary). The slope of the linear component of the mapping increases with increasing K_X, indicating that the mapping increases the amount by which signals are stretched as K_X increases. For high values of K_X, the mapping becomes increasingly nonlinear, as the curve for the value $K_X = 4.0$ rad/m shows. From (10.9), it is clear that the mapping is the same for negative and positive values of K_X. Figure 10.18 shows the magnitude of the simulated data of this section after Stolt interpolation. This magnitude is not constant due to interference between the signals from the three individual scatterers.

Figure 10.19 shows the phase of each of the three individual simulated scatterers before and after Stolt interpolation. The figure displays phase over a small rectangular region taken from the center of each point's two-dimensional signal support. In the figure, black represents a signal sample with zero phase while the brightest white intensity represents a phase of 2π rad. The sharp discontinuities in the figure represent phase wraps.

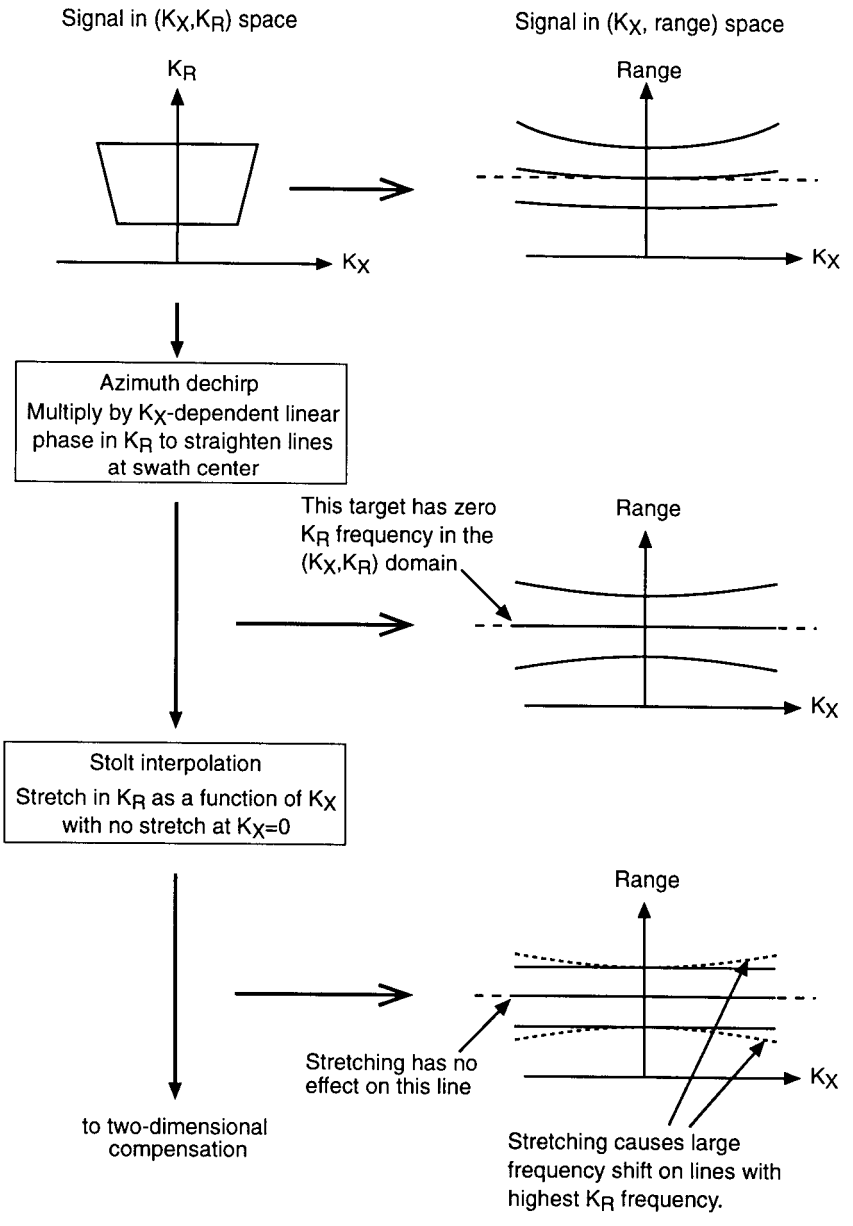


Figure 10.14 Illustration of K_X-dependent range resampling to correct range curvature.

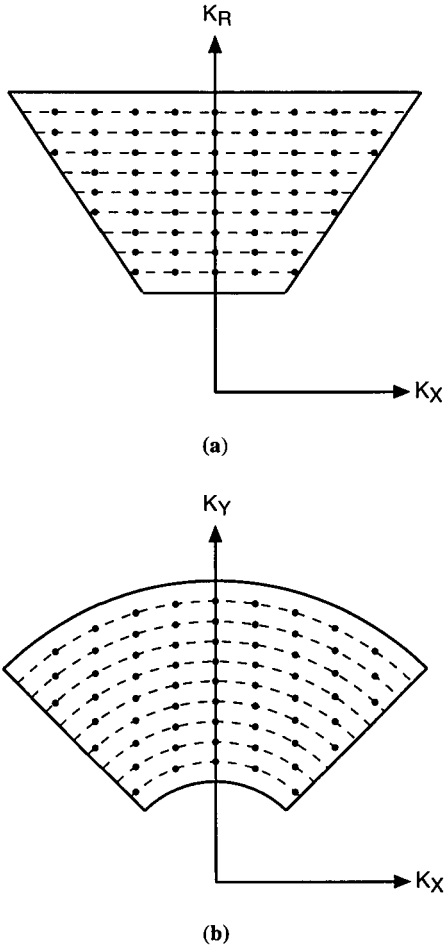


Figure 10.15 Two-dimensional signal support and sample locations: **(a)** In (K_X, K_R) domain before Stolt interpolation; **(b)** In (K_X, K_Y) domain after Stolt interpolation.

The constant phase of the scene center scatterer (point 1) is unaffected by the Stolt mapping, as Figure 10.19(a) and Figure 10.19(b)show. Figure 10.19(c) shows that the phase of point 2, the scatterer which is offset in azimuth only, is a linear grating in K_X prior to Stolt interpolation. Since this scatterer has no residual range curvature after the matched filter operation, the Stolt interpolation has no effect, as Figure 10.19(d) shows. The phase of point 3, the scatterer which is offset in range only, is left with residual range curvature after the matched filtering operation. This residual curvature accounts for the curved lines of constant phase in Figure 10.19(e). The Stolt interpolation straightens these lines of constant phase to form the linear phase grating of Figure 10.19(f). Notice that point 3 has

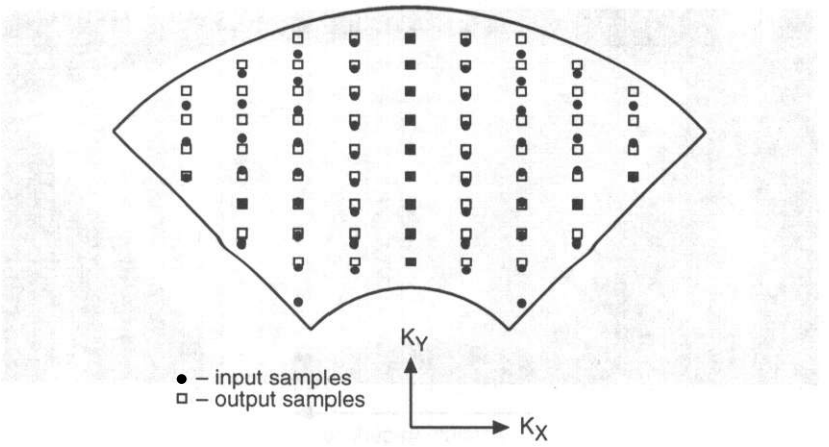


Figure 10.16 Stolt interpolation.

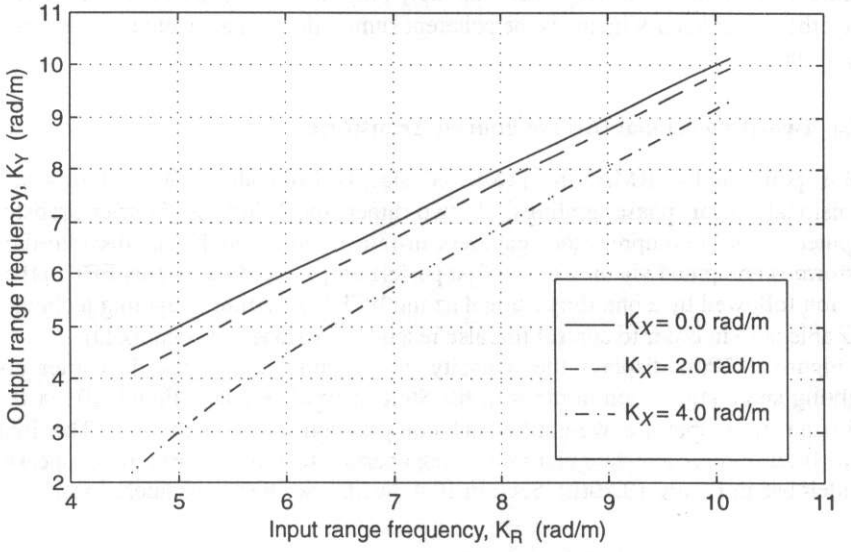


Figure 10.17 Input-output relationship of Stolt interpolation in simulation example.

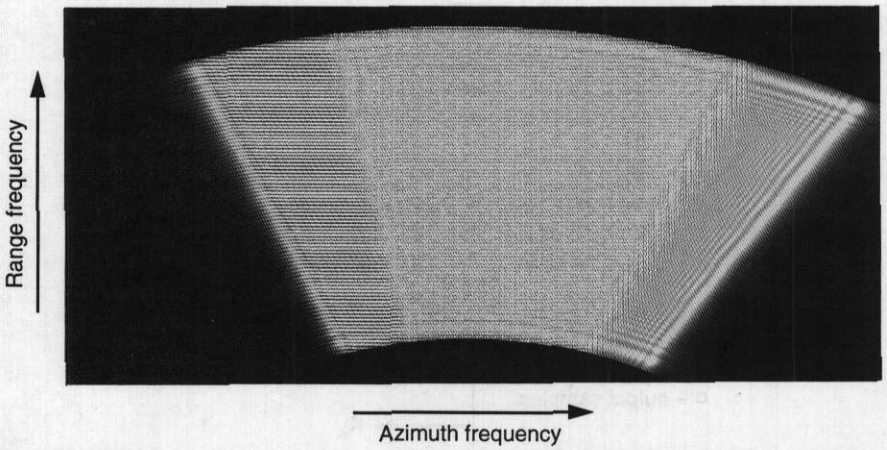


Figure 10.18 Magnitude of simulation data after Stolt interpolation.

linear phase in the K_Y dimension, with no phase variation in K_X. These attributes are consistent with a scatterer that is displaced from scene center in range only. Figure 10.19 presents the data for the three points separately only to illustrate operation of the RMA. In reality, the signal history includes the coherent summation of data from all scatterers in the imaged scene.

10.2.4 Two-Dimensional Inverse Fourier Transform

At this point in the RMA, the processed signals from all point scatterers are two-dimensional linear phase gratings. A two-dimensional inverse Fourier transform is computed to fully compress the scatterers in range and azimuth. For discrete data, this transform is computed via the FFT by first performing a one-dimensional FFT in the range direction followed by a one-dimensional azimuth FFT. Aperture weighting techniques are applicable here in order to control impulse response sidelobes (Appendix D).

Figure 10.20(a) displays the intensity of the simulated signal data after aperture weighting and compression in range of the Stolt-interpolated data. Figure 10.20(b) shows the image after aperture weighting and compression in azimuth also. The image in Figure 10.20(c) uses a rectangular processing aperture to avoid the irregular appearance of the sidelobes in Figure 10.20(b). Section 10.4.3 addresses these considerations.

10.3 ANALYTICAL DEVELOPMENT

This section provides an analytical development of the RMA. Section 10.1 developed the SAR video signal for a single point scatterer after range dechirp. Here, we propagate this signal model through the RMA image formation procedure to show how the algorithm recovers the complex reflectivity of an illuminated point scatterer.

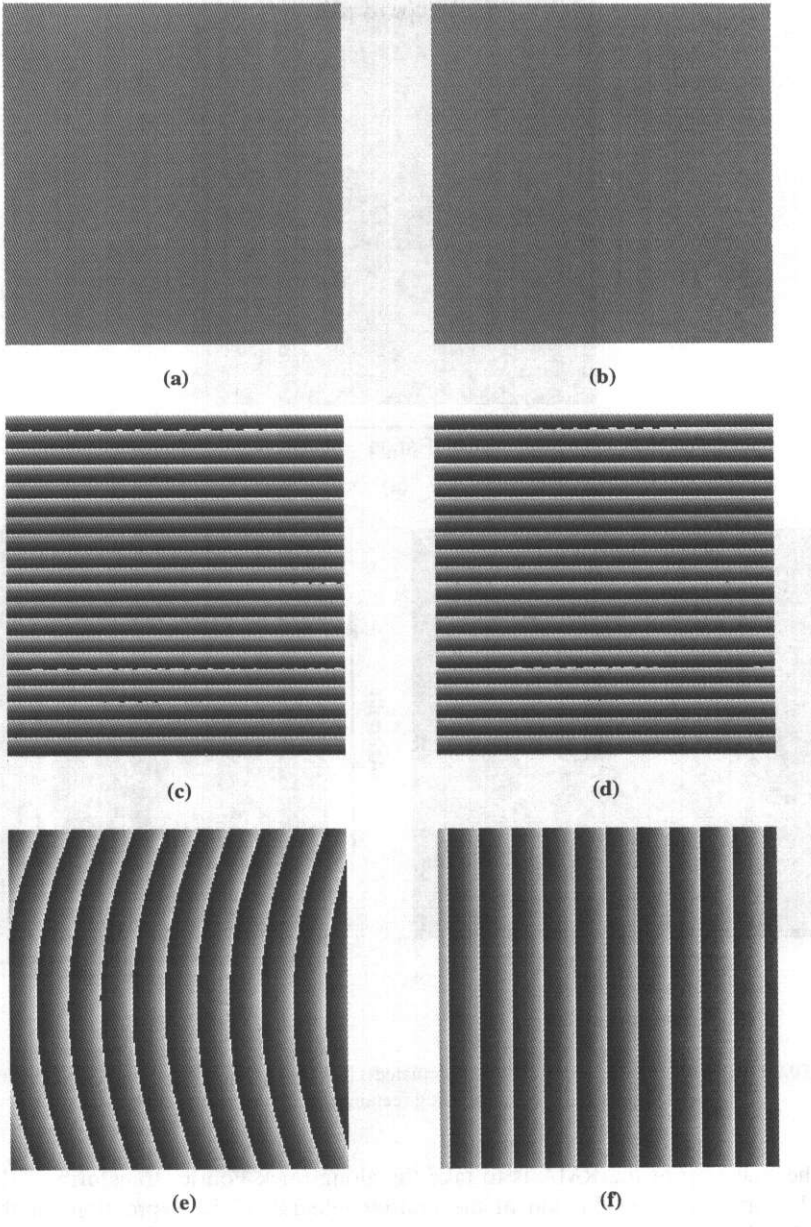


Figure 10.19 Phase of simulated point scatterers before and after Stolt interpolation (horizontal axis is range frequency, vertical axis is azimuth frequency): **(a)** Point 1 before interpolation; **(b)** Point 1 after interpolation; **(c)** Point 2 before interpolation; **(d)** Point 2 after interpolation; **(e)** Point 3 before interpolation; **(f)** Point 3 after interpolation.

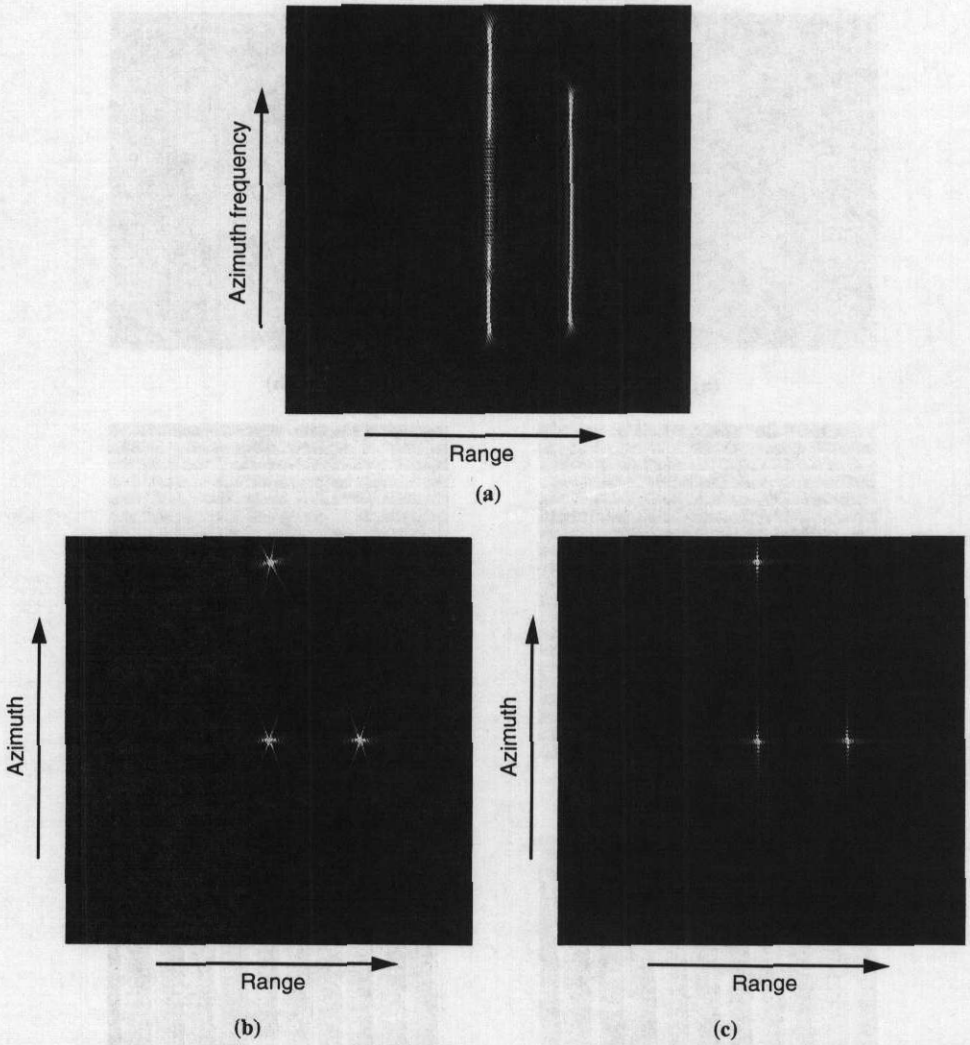


Figure 10.20 Stolt-interpolated signal history (simulated): **(a)** After range compression; **(b)** After range and azimuth compression; **(c)** Image using rectangular processing aperture.

The first step of the RMA is to take the along-track Fourier transform of the SAR signal history. Direct evaluation of the Fourier integral of the expression for the SAR video signal is not easy. However, an integration technique known as the principle of stationary phase (PSP) makes the integration tractable. Section 10.3.1 describes the PSP and provides an example of its application. Section 10.3.2 applies the PSP to the problem of computing the azimuth Fourier transform of the SAR video signal.

The processor can readily remove the space-invariant phase terms that appear in the signal data after the azimuth transform by multiplication with the appropriate reference function. This multiplication represents a matched filtering operation in azimuth. A change of variables results in a two-dimensional linear phase grating for all scatterers. For discrete time (sampled) signals, an interpolation using finite impulse response digital (FIR) filters achieves the change of variables. The resulting signal is uniformly sampled in range and cross-range. A two-dimensional FFT then compresses this signal in both dimensions to produce the complex image.

10.3.1 Principle of Stationary Phase

We employ an integration technique known as the *principle of stationary phase* (PSP) to evaluate the Fourier transform of the azimuth chirped signal [8]. This integration method applies to integrals of the form

$$S(K_X) = \int_a^b s(X)\, e^{j\varphi(X)}\, dX \tag{10.10}$$

in which $s(X)$ is a slowly varying function while $\varphi(X)$ changes by many cycles over the interval of integration. Under these conditions, contributions to the above integral over most of the X interval tend to cancel each other, and thus add little to the overall value of the integral. An exception occurs for contributions at the stationary points of the phase $\varphi(X)$, defined as those values of X for which

$$\frac{d}{dX}[\varphi(X)] = 0 \tag{10.11}$$

These points in the integration interval may contribute substantially to the integral in (10.10).

The PSP states that the integral of (10.10) has its greatest contributions from those values of X which are stationary points of $\varphi(X)$ on the interval $[a,b]$. Evaluation of the integral involves two steps:

1. Determine the location of the stationary point(s) of $\varphi(x)$;
2. Evaluate the *integrand* of (10.10) at the stationary point(s).

If X^* is the only stationary point on $[a,b]$, then an approximation for the integral is

$$\int_a^b s(X)\, e^{j\varphi(X)}\, dX \approx \left[\frac{-\pi}{2\varphi''(X^*)} e^{-j\frac{\pi}{2}}\right]^{\frac{1}{2}} s(X^*)\, e^{j\varphi(X^*)} \tag{10.12}$$

For the radar signal processing of interest here, the factor in square brackets in (10.12), including magnitude and phase, is essentially constant and we need not consider it in the following analysis.

An illustrative application of the PSP involves the computation of the Fourier transform of a chirp waveform using PSP. The expression

$$s(X) = \text{rect}\left(\frac{X}{L}\right)e^{j\pi bX^2} \tag{10.13}$$

describes this waveform where L is the chirp duration and b is the chirp rate parameter. The Fourier transform of the function $s(X)$ is

$$S(K_X) = \Im\{s(X)\} = \int_{-\infty}^{\infty} \text{rect}\left(\frac{X}{L}\right)e^{j\pi bX^2} e^{-jK_X X}\,dx \tag{10.14}$$

Relative to (10.12), $\varphi(X)$ in (10.14) is

$$\varphi(X) = \pi bX^2 - K_X X \tag{10.15}$$

The relationship

$$\frac{d}{dx}[\varphi(X)] = 2\pi bX - K_X = 0 \tag{10.16}$$

indicates a stationary point at

$$X^* = \frac{K_X}{2\pi b} \tag{10.17}$$

Evaluation of (10.14) proceeds by substituting (10.17) for X^* in the right-hand side of (10.12) and disregarding the complex factor inside the brackets. The result is

$$S(K_X) \approx \text{rect}\left(\frac{K_X}{2\pi bL}\right)e^{-j\frac{K_X^2}{4\pi b}} \tag{10.18}$$

The rect function correctly indicates the nominal bandwidth of the chirp waveform. The exponential function correctly identifies the quadratic phase relationship across this bandwidth. This result clearly is only an approximation since both functions in the Fourier transform pair cannot have compact support. However, (10.18) is a useful engineering approximation, particularly in coherent radar problems emphasizing phase rather than magnitude.

10.3.2 Along-Track Fourier Transform Analysis

The analytical development of the RMA now proceeds by making the following substitutions for convenience

$$K_R = \frac{4\pi\gamma}{c}\left(\frac{f_c}{\gamma} + \hat{t} - \frac{2R_s}{c}\right) \tag{10.19}$$

and

$$t' = t - nT - \frac{2R_s}{c} = \hat{t} - \frac{2R_s}{c} \tag{10.20}$$

With these definitions, (10.4) and (10.5) become

$$s_{rd}(X_a, K_R) = a_t \text{rect}\left(\frac{X_a - X_{ac}}{L}\right)\text{rect}\left(\frac{t'}{T_p}\right)e^{-jK_R(R_t - R_s)} \tag{10.21}$$

The Fourier transform of (10.21) with respect to X_a yields

$$S(K_X, K_R) = \int s_{rd}(X_a, K_R)\, e^{-jK_X X_a} dX_a \tag{10.22}$$

Substitution of (10.21) into (10.22) gives

$$S(K_X, K_R) = \alpha \int \text{rect}\left(\frac{X_a - X_{ac}}{L}\right)e^{-jK_R R_t} e^{-jK_X X_a} dX_a \tag{10.23}$$

with

$$\alpha = a_t \text{rect}\left(\frac{t'}{T_p}\right)e^{jK_R R_s} \tag{10.24}$$

To evaluate (10.23) using the PSP, we must determine the stationary points of its phase. The phase function φ in (10.12) now corresponds to

$$\varphi(X_a, K_R) = -K_R R_t - K_X X_a \tag{10.25}$$

From Figure 10.1, we have

$$R_t = \sqrt{(X_a - X_t)^2 + R_B^2} \tag{10.26}$$

with $R_B = \sqrt{(Y_a - Y_t)^2 + (Z_a - Z_t)^2}$; here Y_a and Z_a are constant at Y_{ac} and Z_{ac}, respectively. Here, R_B is the minimum range to the scatterer occurring when $X_a = X_t$.

Substituting (10.26) into (10.25) and equating the first derivative to zero gives

$$\frac{\partial}{\partial X_a}[\varphi(X_a, K_R)] = -\frac{K_R(X_a - X_t)}{\sqrt{(X_a - X_t)^2 + R_B^2}} - K_X = 0 \tag{10.27}$$

Solving (10.27) for X_a yields

$$X_a^* = -\frac{R_B K_X}{\sqrt{K_R^2 - K_X^2}} + X_t \tag{10.28}$$

as the stationary point.

We now compute the transformed signal by substituting (10.28) into the integrand of (10.23). The phase of $S(K_X, K_R)$ is

$$\Phi(K_X, K_R) = \angle S(K_X, K_R) = -K_R R_t - K_X X_a + K_R R_s \tag{10.29}$$

The last term of (10.29) is the phase contribution from the complex constant α. Substituting the value X_a^* for X_a in (10.29) yields

$$\Phi(K_X, K_R) = -K_X X_t - R_B\sqrt{K_R^2 - K_X^2} + K_R R_s \tag{10.30}$$

after some manipulation.

Similarly, the magnitude of $S(K_X, K_R)$ is available by substituting the value X_a^* for X_a in the rect( ) function of (10.23). The resulting magnitude is

$$\left|S(K_X, K_R)\right| = a_t \operatorname{rect}\left(\frac{K_R - 4\pi f_c/c}{4\pi\gamma T_p/c}\right)\operatorname{rect}\left(\frac{K_X R_B}{L\sqrt{K_R^2 - K_X^2}} + \frac{X_{ac} - X_t}{L}\right) \tag{10.31}$$

using the substitution

$$t' = \frac{cK_R}{4\pi\gamma} - \frac{f_c}{\gamma} \tag{10.32}$$

in the first rect function. The corresponding expression for K_R is

$$K_R = \frac{4\pi\gamma}{c}\left(\frac{f_c}{\gamma} + t'\right) \tag{10.33}$$

The constant signal magnitude shown in (10.31) is an approximation. The development of (10.31) ignores propagation attenuation in the received signal model (10.4) and neglects

the amplitude term (10.12) of the PSP. In addition, the sharp discontinuities at the edges of the limited, along-track duration signal cause amplitude ripple in the K_X domain. However, despite these considerations, the constant magnitude assumption of (10.31) is adequate for typical SAR systems operating at modest range over a relatively narrow range swath.

The magnitude and phase of the azimuth Fourier transform of the range-deskewed signal data are available in (10.31) and (10.30), respectively. This azimuth Fourier transform is

$$S(K_X, K_R) = |S(K_X, K_R)| e^{-j\Phi(K_X, K_R)} \tag{10.34}$$

10.3.3 Matched Filtering Analysis

Multiplication of (10.34) by a reference function containing the conjugate of all space-invariant phase terms performs the RMA matched filtering operation. Space-invariant terms refer to phase terms that do not depend on scatterer coordinates (X_t, Y_t, Z_t). The phase of the matched filter is

$$\Phi_{mf}(K_X, K_R) = -K_R R_s + R_s \sqrt{K_R^2 - K_X^2} \tag{10.35}$$

After application of the matched filter, the signal becomes

$$S_2(K_X, K_R) = |S(K_X, K_R)| e^{-j\left[K_X X_t + (R_B - R_s)\sqrt{K_R^2 - K_X^2}\right]} \tag{10.36}$$

where $|S(K_X, K_R)|$ is unchanged from (10.31).

10.3.4 Stolt Interpolation Analysis

At this point, $S(K_X, K_R)$ is a two-dimensional linear phase grating for all scatterers in the same range bin as scene center (all scatterers having the same R_B). A change of variables, known as the Stolt interpolation, converts $S_2(K_X, K_R)$ into a linear phase grating for scatterers at all ranges. The appropriate change of variables is

$$\sqrt{K_R^2 - K_X^2} \rightarrow K_Y \tag{10.37}$$

Application of this transformation yields the desired signal

$$S_3(K_X, K_Y) = |S(K_X, K_R)| e^{-j[K_X X_t + K_Y (R_B - R_s)]} \tag{10.38}$$

The signal from a point scatterer located anywhere in the imaged scene now has linear

phase in K_X and K_Y and nominally constant magnitude over the two-dimensional support. A two-dimensional inverse Fourier transform with kernel $\exp[j(K_X X_a + K_Y Y_s)]$ compresses the signal in both range and azimuth. The quantity Y_s represents negative range relative to scene center. The peak of the impulse response occurs at location $X_a = X_t$ and $Y_s = R_B - R_s$ in the IDP. This representation means that the scene center location corresponds to $Y_s = 0$. Scatterers located closer to the ARP have positive values for Y_s.

For the discrete-time problem, sampling of the signal in (10.36) is uniform in K_X and K_R. It is desirable to perform range and azimuth compression via a two-dimensional inverse FFT. In order to use the FFT, the processor must resample the signal from K_R to constant spacing in K_Y. Efficient resampling is possible through the use of FIR polyphase digital filters. This resampling technique (Section 4.3) is similar to the range dimension interpolation step of polar formatting (Section 4.4).

10.4 ASPECTS OF RANGE MIGRATION PROCESSING

This section discusses a number of practical considerations for range migration processing of spotlight SAR data. It begins with a review of along-track sampling requirements for spotlight SAR and the RMA, and then discusses RMA processing for squinted (non-broadside) imaging geometries. Section 10.4.3 describes the space-variant nature of the impulse response in RMA-processed imagery. Section 10.4.4 presents a computational shortcut that is sometimes applicable to the Stolt interpolation. The final subsection presents a qualitative discussion of the similarities and differences between the RMA and the PFA; Chapter 12 adds to this comparison and includes computational complexity.

10.4.1 Along-Track Sampling Requirements

The RMA requires input signal histories with motion compensation to a moving point (a line) rather than to a fixed scene point. This requirement carries with it a potentially serious penalty in terms of along-track sampling requirements.

From Section 10.1, signals with motion compensation to a line correspond to signals with a chirp characteristic in the azimuth dimension. Equation (2.28) gives the bandwidth of this chirp, which is also the Doppler bandwidth due to a point scatterer observed over a cone angle interval $\Delta\theta$. This bandwidth is

$$B_d \approx \frac{2V_a \Delta\theta \sin(\alpha_{dc})}{\lambda} \tag{10.39}$$

where λ is the instantaneous transmitted wavelength, V_a is the along-track ground speed, and α_{dc} is the Doppler cone angle at aperture center. Presence of the azimuth chirp requires a minimum azimuth sampling rate equal to B_d for unambiguous sampling.

In contrast, the common approach to collecting and processing spotlight signal history data is to perform motion compensation to a fixed scene point. This compensation

strategy eliminates the azimuth chirp. The resulting bandwidth from (2.32) is

$$B_a \approx \frac{2V_a W_a \sin(\alpha_{dc})}{\lambda R_{ac}} \tag{10.40}$$

where W_a is the azimuth extent of the imaged scene and R_{ac} is slant range to the motion compensation point at midaperture. Thus, when processing with azimuth dechirp, the quantity W_a/R_{ac} drives the along-track sampling rate. This quantity is approximately the angle subtended by the azimuth extent of the imaged scene. Because RMA processing does not remove the azimuth chirp, the angle $\Delta\theta$ in (10.39) drives along-track sampling requirements.

Depending on specific system and operational parameters, the difference between sampling requirements for azimuth chirped signals and dechirped signals can be enormous. Generally, RMA processing of azimuth chirped data requires a higher azimuth sampling rate than image formation algorithms (such as polar format) that operate on dechirped signals. This increased sampling rate can impose a significant computational burden on the RMA processor relative to other algorithms.

Spotlight systems typically remove most of the azimuth chirp in real time to reduce the pulse repetition frequency. To use the RMA on such data, the processor must first upsample the collected signal data in order to unambiguously reinstate the azimuth chirp.

The requirement for a high sampling rate can be a severe limitation of the RMA. References [6, 9] propose and demonstrate techniques to overcome this requirement. These techniques add complexity to the overall image formation algorithm. Methods to alleviate the RMA azimuth sampling requirement are an active area of research.

10.4.2 Processing Squinted Data

The presence of an azimuth carrier frequency in spotlight SAR signal data collected in a squinted geometry distinguishes this data from that collected in a broadside geometry. With the aid of Figure 10.21, we discuss the origin and effect of this azimuth carrier frequency. Figure 10.21(a) illustrates a squinted data collection geometry with the synthetic aperture center at the location X_{ac}. Figure 10.21(b) indicates the variation in range between the APC and a scatterer at scene center over the synthetic aperture interval. The nonlinear component (nominally quadratic) of this variation introduces the azimuth chirp to the signal history; the linear component introduces an azimuth carrier frequency that shifts the signal spectrum away from zero frequency. Figure 10.21(c) shows this spectrum in wavenumber space shifted away from $K_X = 0$. In the context of RMA processing, the spectrum in Figure 10.21(c) represents the two-dimensional support of the SAR data after the initial along-track discrete Fourier transform. This support clearly differs from that in Figure 10.15(a) for a broadside collection. RMA processing continues with matched filtering and Stolt interpolation. Figure 10.21(d) shows the signal support after Stolt interpolation to compare to that in Figure 10.15(b) for a broadside collection. The last step of image formation extracts an aperture of data from the Stolt-interpolated signal and performs a two-dimensional discrete Fourier transform to generate an image.

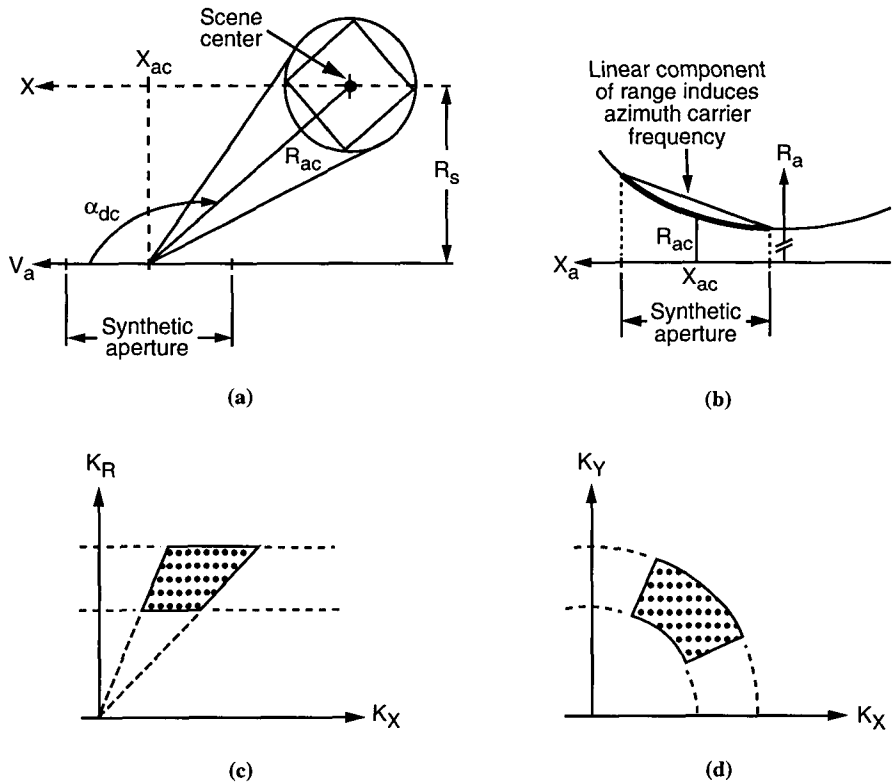


Figure 10.21 RMA processing of squinted data: **(a)** Data collection geometry; **(b)** Variation in range to scene center; **(c)** Signal support in (K_X, K_R) space before Stolt interpolation; **(d)** Signal support in (K_X, K_Y) space after Stolt interpolation.

The samples of the Stolt-interpolated signal history lie on lines of constant K_X and K_Y. These sampling locations result in a stabilized scene orientation with image pixels along lines of constant range and along-track coordinates. A two-dimensional resampling (rotation) of the Stolt-interpolated signal can produce imagery at other orientations, such as range by azimuth. This resampling is necessary if it is desirable to process the signal data over the largest possible rectangular aperture.

It is almost always desirable to remove the azimuth carrier corresponding to center wavelength prior to the along-track Fourier transform of the RMA. In highly squinted geometries, removal of this carrier dramatically reduces the required along-track sampling rate of the signal history and relieves an unnecessary computational burden on the RMA processor. In fact, the typical spotlight SAR system removes the carrier frequency, along with the azimuth chirp, in real time during data collection. Figure 10.22(a) shows the SAR signal in (K_X, K_R) space after removal of the azimuth carrier frequency or *squint removal.* Comparing Figure 10.22(a) with Figure 10.21(d) shows that squint removal simply shifts

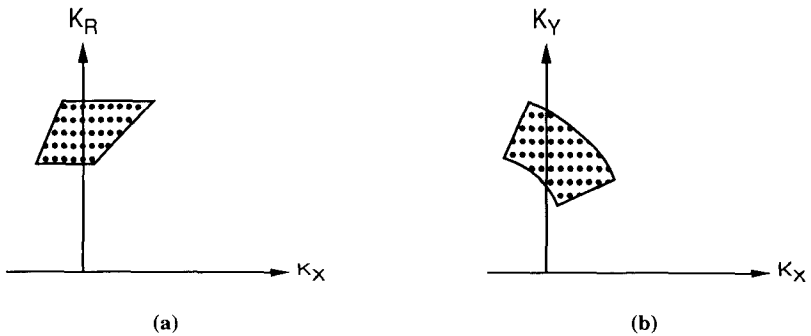


Figure 10.22 Squint removal operation for RMA processing: **(a)** Signal support in (K_X, K_R) space; **(b)** Signal support in (K_X, K_Y) space.

the spectrum in azimuth. Figure 10.22(b) shows the signal in (K_X, K_Y) space after Stolt interpolation. The Stolt transformation performs the identical mapping here as in Figure 10.21. The Stolt transformation treats (K_X, K_R) samples as if they possess the azimuth carrier, even though they are now centered about zero azimuth frequency. Rotation of the processing aperture to maximize the size of a rectangular data aperture or to orient the output image applies equally well to data with or without squint removal.

10.4.3 Space-Variant Impulse Response

During spotlight data collection, the starting and ending cone angles over which the SAR observes a particular point scatterer vary with scatterer position. This fact causes scatterers to possess varying amounts of *range walk* in addition to range curvature. Range walk is defined as the linear component of MTRC. This linear component causes a shift of the scatterer's azimuth spectrum to center it about some nonzero carrier frequency. The size of the carrier varies with the size of the range walk and, therefore, with scatterer position. After the initial azimuth Fourier transform of the RMA, all scatterers do not possess identical two-dimensional signal support. Rather, their spectra are skewed slightly relative to one another. Figure 10.23 illustrates this effect by sketching the two-dimensional signal support for each point scatterer in the simulation example. Figure 10.23(a) shows the signal support after the initial azimuth Fourier transform. Figure 10.23(b) shows the signal support after Stolt interpolation.

This position-dependent skew effect propagates through the matched filter operation and the Stolt interpolation. The final step of the RMA procedure is a two-dimensional Fourier transform. The skew causes the shape of the processing aperture to vary with scatterer location in the scene. This variation in aperture shape leads to a space-variant impulse response. This effect is not always of concern because (1) it is only visible on strong, dominant scatterers in the SAR scene; and (2) the effect does not degrade processed resolution, it merely alters the distribution of impulse response sidelobes. The

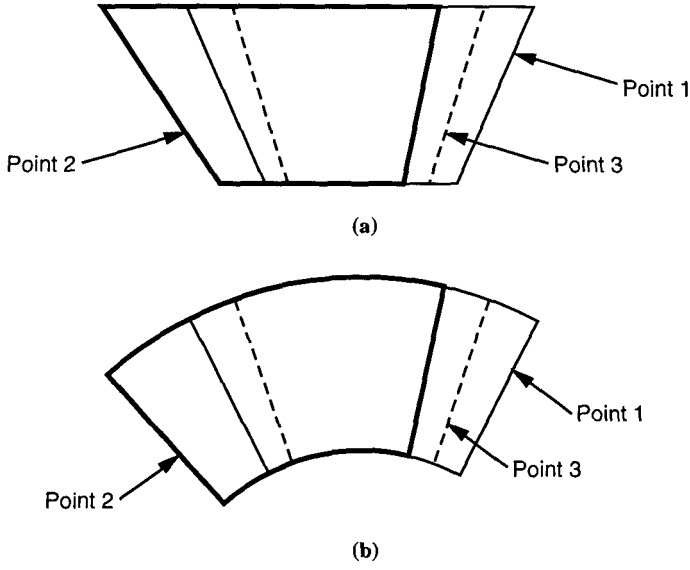


Figure 10.23 Support of simulated point scatterers: (**a**) In (K_X, K_R) space; (**b**) In (K_X, K_Y) space after Stolt interpolation.

space-variant impulse response can be circumvented by collecting SAR data over a larger angular aperture than is strictly needed to achieve the desired azimuth resolution. The azimuth frequency extent of the signal history can be trimmed (at both ends) after the Stolt interpolation of the RMA. This process ensures that the spectrum of every scatterer fills a common processing aperture shape (for example, rectangular). Figure 10.24 illustrates this data processing approach.

10.4.4 Approximation for Stolt Interpolation

A simple operation to approximate the Stolt interpolation step can be adequate when the variations in K_X and K_R are much smaller than K_{Rc}, the value of K_R that corresponds to center frequency [1]. SAR systems with small bandwidth-to-center-frequency ratios and small coherent integration angles are more likely to satisfy these constraints. In this case, the range migration processor can replace the Stolt change of variables in (10.37) with

$$K_Y \approx K_R - \frac{K_X^2}{2K_{Rc}} \tag{10.41}$$

This operation replaces the nonlinear Stolt interpolation with a K_X-dependent shift in the K_R dimension. A convenient implementation of this shift is a complex multiply in the azimuth-frequency/range-position domain to add a K_X-dependent phase that is linear in

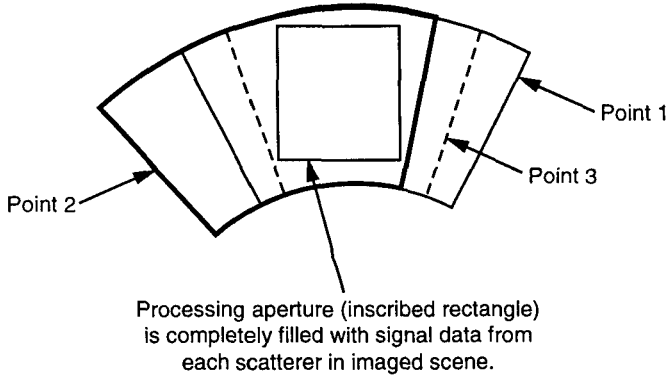


Figure 10.24 Data handling approach to maintain space-invariant impulse response.

range position. Use of (10.41) avoids any need for the digital resampling associated with the exact Stolt interpolation.

Use of (10.41) accomplishes a necessary azimuth phase adjustment. It does not compensate at all for the effects of differential range curvature in the range dimension. Because a formatting approximation of this type introduces phase errors that increase with scatterer distance from scene center, its use limits scene size. Some insight into this limitation is available in the discussion of CSA limitations in Section 11.4.

10.4.5 Relation between Range Migration and Polar Format Algorithms

Figure 10.25 shows simplified block diagrams for the RMA and the PFA. Both algorithms assume that input data is dechirped in range. However, the RMA operates on azimuth chirped data, while the PFA operates on azimuth dechirped data.

The mathematical development of the PFA assumes that illuminating wavefronts are planar. The reality of curved wavefronts (range curvature) leads to residual phase errors in processed imagery. One such error, a space-variant linear phase error, causes geometric (keystone) distortion. Since this phase error is deterministic, the digital processor easily compensates the resulting geometric distortion by digitally resampling (warping) a processed image from distorted pixel coordinates to undistorted coordinates.

Wavefront curvature also induces a space-variant quadratic phase error (QPE) that frequently causes problems for the PFA. Referred to as range curvature QPE, this phase error leads to position-dependent defocusing. Range curvature also introduces higher order phase errors, but these errors are typically small. Section 3.7 discusses range curvature in detail. The magnitude of the range curvature QPE increases quadratically with scatterer distance from scene center and reaches a maximum value at the edges of the scene. The usual approach to handling this error in a PFA-based processor is to simply limit processed scene dimensions to some maximum size. By constraining the scene size,

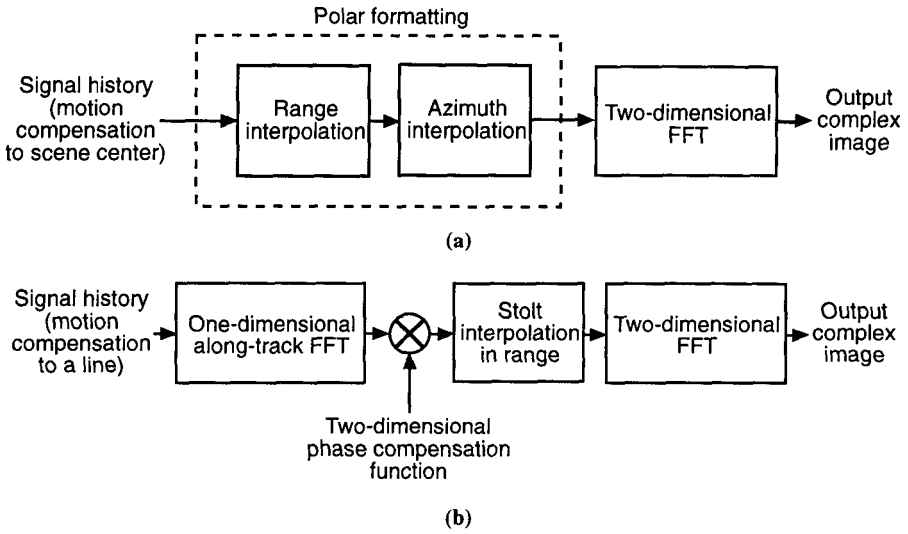


Figure 10.25 Processor block diagrams: **(a)** Polar format algorithm; **(b)** Range migration algorithm.

the processor can hold the range curvature QPE below some acceptable level at the edges of an image. If necessary, larger scenes can be produced by mosaicking smaller images (subpatches) together.

The RMA does not suffer from any range curvature distortions or defocusing effects. This algorithm exactly solves the range curvature problem. The analytical development of the RMA in Section 10.3 makes no planar wavefront assumptions or approximations. The results of that development are valid within the limits of the applicability of the principle of stationary phase.

Despite the foregoing differences, several similarities between the two algorithms are evident. First, the shape of the signal support after Stolt interpolation in Figure 10.15 resembles the polar data storage annulus of the PFA. Figure 10.26 compares the data formats of the PFA and the RMA. For a scene center scatterer (point B), the two algorithms have identical storage formats. Both algorithms store digitized signal histories in a two-dimensional polar format in which samples representing the same RF frequency from different pulses map into circles.

Another interesting similarity between these algorithms is the manner in which their respective data storage formats fan out with increasing RF frequency. Figure 10.26(b) indicates that the PFA data format takes its shape by storing pulses according to the data collection angle θ. Figure 10.26(c) shows that the RMA format takes its shape from the fact that Doppler bandwidth increases linearly with increasing range frequency. Thus, after the azimuth Fourier transform of the RMA, the two-dimensional signal support is wider at high range (RF) frequencies than at low range frequencies. For scatterers displaced in azimuth from scene center (points A and C), the RMA signal support shifts according to the Doppler cone angles over which the sensor observes a particular scatterer

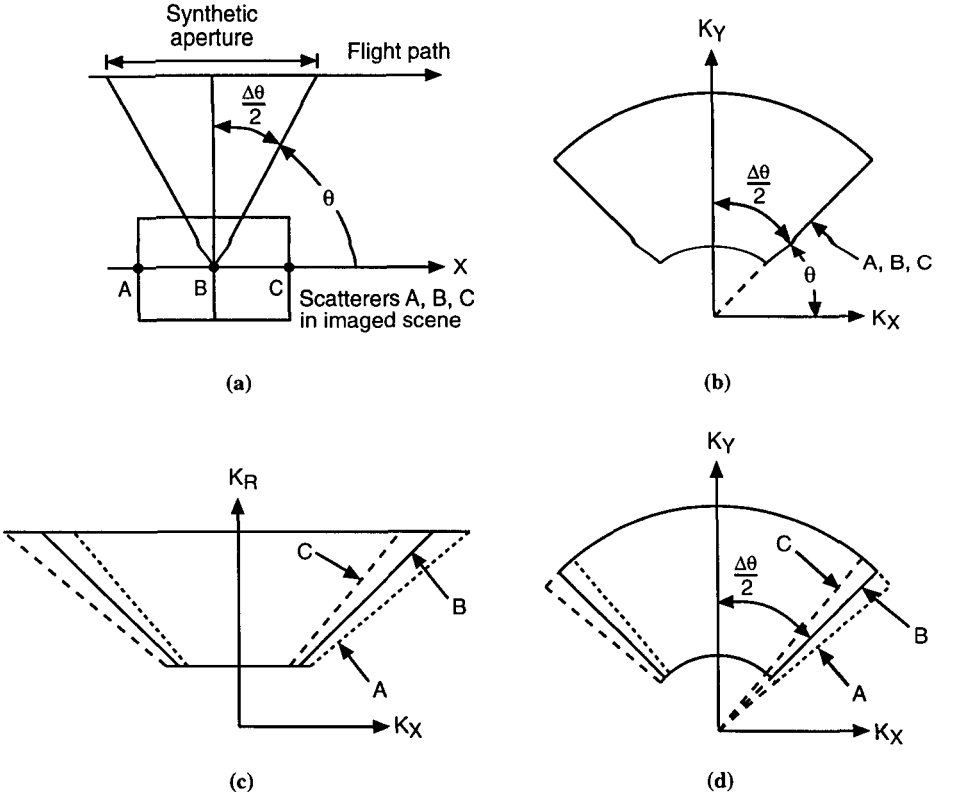


Figure 10.26 Comparison of polar format and range migration data storage formats for spotlight SAR: **(a)** Data collection domain; **(b)** Polar format data storage; **(c)** Range migration data storage before Stolt interpolation; **(d)** Range migration data storage after Stolt interpolation.

location, whereas the PFA formats all scatterers in exactly the same manner. This scatterer-dependent skewing of the signal support contributes to the improved focusing performance of the RMA.

10.5 APPLICATIONS OF RANGE MIGRATION PROCESSING

This section describes two applications using RMA processing. Both examples originate from the experimental P-3 SAR system (Appendix E), a multimode radar that flies aboard a Navy P-3 aircraft [10]. The first example demonstrates RMA processing of L-band P-3 imagery with moderate resolution and large scene size. The second example describes formation of SAR imagery for foliage penetration (FOPEN) applications. It discusses RMA processing of fine-resolution imagery collected in the P-3 ultra-wideband (UWB) mode.



Figure 10.27 SAR image of airfield near Key West, Florida.

10.5.1 L-Band SAR

Figure 10.27 shows an RMA-processed, L-band image of an airfield near Key West, Florida. Table 10.2 gives associated radar system and processing parameters. The scene size is approximately 5×2.5-km range by azimuth, with radar illumination and near range on the left side of the image. The image has uniform weighting in both dimensions, resulting in processed resolutions of 1.1 m in range and 0.6 m in azimuth.

Figure 10.28 is an expanded view of the runway near the center of the L-band image. This area contains an array of trihedral reflectors of various cross sections suitable for assessing image quality. The short slant range (5 km) of the image and large integration angle (10 deg) suggest the presence of significant differential range curvature. In such a situation, the RMA excels relative to other algorithms. In fact, the PFA is an inappropriate choice for processing this image. From (5.30), the residual range curvature quadratic phase error that would result from polar format processing is 216 rad for a scatterer at zero



Figure 10.28 Expanded view of runway showing corner reflector array.

azimuth and near or far range in the L-band scene. This large phase error is unacceptable for practical uses of SAR imagery.

10.5.2 Ultra-Wideband SAR for FOPEN

Ultra-wideband SAR is finding important applications in the areas of foliage penetration (FOPEN) radar and ground-penetrating radar (GPR). The UWB mode of the P-3 SAR system supports FOPEN and GPR studies [11, 12]. This fine-resolution imaging mode operates in the VHF/UHF frequency bands. Table 10.3 lists key system and processing parameters. Figure 10.29 shows a UWB image of the University of Michigan biological experiment station near Pellston, Michigan. This image has 0.33-m resolution in range and 0.66-m resolution in azimuth, with −30-dB Taylor weighting in both dimensions. Radar illumination and near range are on the left side of the image.

Figure 10.30(a) shows a close-up view of the clearing near the center of the image in Figure 10.29. The figure identifies two large trihedral reflectors, two trucks, two greenhouses, and an array of plant monitors. The trihedral reflectors, shown in Figure 10.30(b) and Figure 10.30(c), help to assess image quality. Their large physical size is necessary due to the long wavelength of the P-3 UWB mode. The two trucks, parked in foliage, illustrate FOPEN radar. Figure 10.30(d) and Figure 10.30(e) are photographs of the trucks in surrounding foliage. The trucks, though mostly obscured in the photographs, are clearly visible through the foliage in the radar image.

Table 10.2
System and Processing Parameters for L-Band Image

Parameter	*Description*	*Value*
f_c	Radar center frequency	1.25 GHz
	Waveform	Linear FM without dechirp-on-receive
	Polarization	VV
B	Processed bandwidth	120 MHz
R_{ac}	Slant range to scene center	4972 m
θ_{ac}	Image squint angle	90 deg (broadside)
Ψ_{ac}	Image grazing angle	25 deg
L	Synthetic aperture length	870 m
$\Delta\theta$	Coherent integration angle	10 deg
	Aperture weighting	Uniform
ρ_r	Range resolution	1.1 m
ρ_a	Azimuth resolution	0.6 m
W_r	Range scene size	5028 m
W_a	Azimuth scene size	2510 m

Due to its large integration angle (31.7 deg) and relatively short range (6 to 14 km), the P-3 UWB system experiences severe differential range curvature relative to that which the L-band mode faces. Again, the RMA is particularly well suited for this application whereas use of the PFA would result in an intolerable 33.1 rad of QPE from range curvature. This phase error level using the PFA is considerably smaller than that for the L-band example in Section 10.5.1 because the UWB image has a smaller scene size.

10.6 SUMMARY

An important attribute of the RMA for SAR image information is its ability to completely compensate scatterer MTRC. Fine-resolution, large scene images processed by the RMA do not suffer the geometric distortion or residual quadratic phase error inherent in conventional PFA processing. The RMA corrects the range curvature of every scatterer in a processed scene simultaneously and can process both stripmap and spotlight mode SAR data. A disadvantage of the RMA is its need to operate on azimuth chirped data, necessitating high along-track sampling rates at the front-end of the RMA processor. This difficulty may be acute in highly squinted SAR systems. Methods to alleviate this problem remain an active area of research [6, 9].

Table 10.3
System and Processing Parameters for P-3 UWB Image

Parameter	*Description*	*Value*
f_c	Radar center frequency	469.5 MHz
	Waveform	Linear FM with dechirp-on-receive
	Polarization	HH
B	Processed bandwidth	509 MHz
R_{ac}	Slant range to scene center	6240 m
θ_{ac}	Image squint angle	90 deg (broadside)
Ψ_{ac}	Image grazing angle	30 deg
L	Synthetic aperture length	3543 m
$\Delta\theta$	Coherent integration angle	31.7 deg
	Aperture weighting	–30-dB Taylor
ρ_r	Range resolution	0.33 m
ρ_a	Azimuth resolution	0.66 m
W_r	Range scene size	800 m
W_a	Azimuth scene size	1200 m

References [13-17] provide additional information on the RMA and related algorithms. References [15-17] offer a comparison of the RMA, range-Doppler processing, and the chirp scaling algorithm. Range-Doppler processing is the conventional image formation approach in stripmap SAR systems. Related to the RMA, the chirp scaling algorithm is the subject of Chapter 11.

REFERENCES

[1] Rocca, F., C. Cafforio, and C. Prati, "Synthetic Aperture Radar: A New Application for Wave Equation Techniques," *Geophysical Prospecting 37*, 1989, pp. 809-830.

[2] Cafforio, C., C. Prati, and F. Rocca, "SAR Data Focusing Using Seismic Migration Techniques," *IEEE Transactions on Aerospace and Electronic Systems*, Vol. 27, No. 2, March 1991, pp. 194-206.

[3] Cafforio, C., C. Prati, and F. Rocca, "Full Resolution Focusing of SEASAT SAR Images in the Frequency-Wave Number Domain," *Proceedings of the 8th EARSeL Symposium*, Capri, Italy, 1988, pp. 336-355.

[4] Stolt, R.H., "Migration by Fourier Transform," *Geophysics*, Vol. 43, No. 1, February 1978, pp. 23-48.

[5] Gazdag, J., and P. Sguazzero, "Migration of Seismic Data," *Proceedings of the IEEE*, Vol. 72, No. 10, October 1984, pp. 1302-1315.



Figure 10.29 P-3 ultra-wideband SAR image processed with the range migration algorithm.

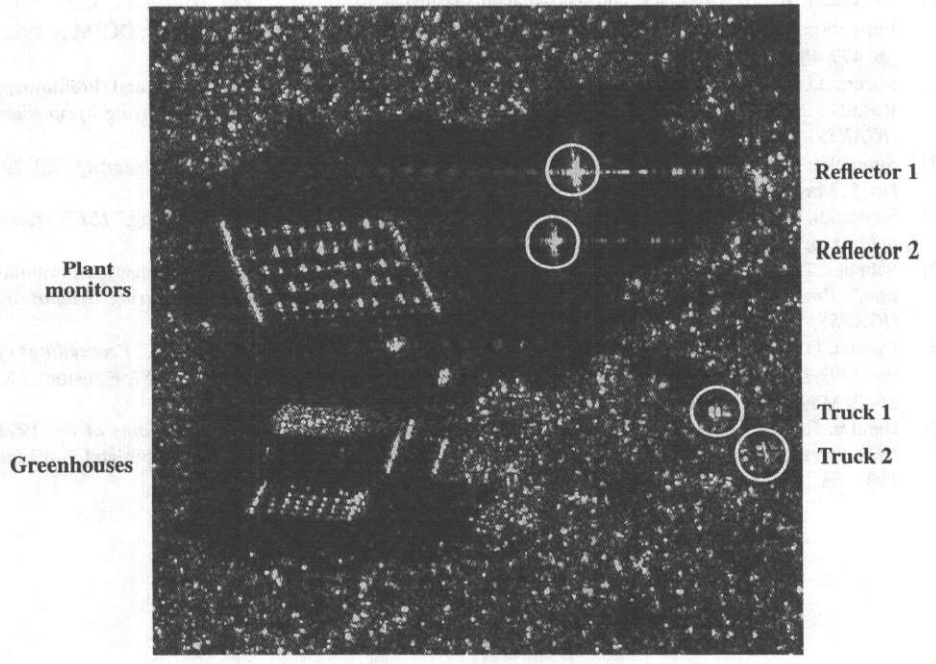
[6] Prati, C., A.M. Guarnieri, and F. Rocca, "Spot Mode SAR Focusing with the ω-k Technique," *Proceedings of the 1991 IEEE International Geoscience and Remote Sensing Symposium (IGARSS)*, Espoo, Finland, 3-6 June 1991, pp. 631-634.

[7] Milman, A.S., "SAR Imaging by ω-k Migration," *International Journal of Remote Sensing*, Vol. 14, No. 10, 1993, pp. 1965-1979.

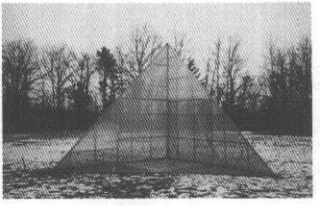
[8] Born, M., and E. Wolf, *Principles of Optics*, New York, Pergamon Press, 1959, Appendix III.

[9] Golden, A., S.C. Wei, K.K. Ellis, and S. Tummala, "Migration Processing of Spotlight SAR Data," *Proceedings of the SPIE Symposium on Algorithms for SAR Imagery*, Orlando, FL, April 1994, pp. 25-35.

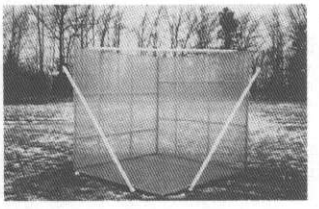
[10] Sullivan, R., A. Nichols, R. Rawson, C. Haney, F. Darreff, and J. Schanne, Jr., "Polarimetric X/L/C-Band SAR," *Proceedings of the 1988 IEEE National Radar Conference*, Ann Arbor, MI, 20-21 April 1988, pp. 9-14.



(a)



(b)



(c)



(d)



(e)

Figure 10.30 Expanded view of clearing in P-3 UWB image: **(a)** SAR image; **(b)** Reflector 1 (trihedral with 4.9 m sides); **(c)** Reflector 2 (trihedral with 2.5 m sides); **(d)** Truck 1; **(e)** Truck 2.

[11] Goodman, R., S. Tummala, and W. Carrara, "Issues in Ultra-Wideband, Widebeam SAR Image Formation," *Record of the 1995 IEEE International Radar Conference*, Washington, DC, May 1995, pp. 479-485.

[12] Sheen, D.R., C.M. Strawitch, and T.B. Lewis, "UHF Wideband SAR Design and Preliminary Results," *Proceedings of the 1994 IEEE International Geoscience and Remote Sensing Symposium (IGARSS)*, Pasadena, CA, August 1994, pp. 289-291.

[13] Soumekh, M., "Echo Imaging Using Physical and Synthesized Arrays," *Optical Engineering*, Vol. 29, No. 5, May 1990, pp. 545-554.

[14] Soumekh, M., "A System Model and Inversion for Synthetic Aperture Radar Imaging," *IEEE Transactions on Image Processing*, Vol. 1, No. 1, January 1992, pp. 64-76.

[15] Scheuer, T.E., and F.H. Wong, "Comparison of SAR Processors Based on a Wave Equation Formulation," *Proceedings of the 1991 IEEE International Geoscience and Remote Sensing Symposium (IGARSS)*, Espoo, Finland, 3-6 June 1991, pp. 635-639.

[16] Dendal, D., and J.L. Marchand, "Ω-K Techniques Advantages and Weaker Aspects," *Proceedings of the 1992 IEEE International Geoscience and Remote Sensing Symposium (IGARSS)*, Houston, TX, 26-29 May 1992, pp. 366-368.

[17] Bamler, R., "A Systematic Comparison of SAR Focussing Algorithms," *Proceedings of the 1991 IEEE International Geoscience and Remote Sensing Symposium (IGARSS)*, Espoo, Finland, 3-6 June 1991, pp. 1005-1009.

Chapter 11
Chirp Scaling Algorithm

The *chirp scaling algorithm* (CSA) is a computationally efficient variation to the range migration algorithm (RMA) for SAR image formation [1-7]. The CSA is attractive because it requires only FFTs and complex multiplies; it requires no interpolations. These attributes lead to efficient implementations on FFT-based signal processors and high-speed parallel processors. The CSA achieves its unique properties by approximating the Stolt transformation of the RMA. With this approximation, the CSA does not totally compensate for motion through resolution cells (MTRC). However, interest in and use of the CSA is widespread within the SAR community because of the algorithm's ease of implementation and reasonable compensation of MTRC. The CSA can process SAR data collected in either stripmap or spotlight mode.

Like the RMA, the CSA operates on SAR signal data with motion compensation to a line rather than to a fixed point (Section 10.1). Unlike the RMA, the CSA requires signal data that is chirped in the range dimension. Systems that utilize the chirp waveform but do not employ dechirp-on-receive provide such signals.

Section 11.1 models SAR signal data collected without dechirp-on-receive processing. Section 11.2 introduces the CSA with a heuristic explanation of its signal processing operations. Section 11.3 provides an analytical development of the algorithm. Section 11.4 discusses some limitations of the CSA in its most elementary realization. An example in Section 11.5 demonstrates application of the CSA to fine resolution L-band imagery.

11.1 SIGNAL MODEL WITHOUT DECHIRP-ON-RECEIVE

Figure 11.1 presents the spotlight SAR imaging geometry relevant to this presentation of the CSA. At position (X_a, Y_a, Z_a), the SAR system transmits a chirp waveform and receives an echo from a point scatterer of radar cross-section σ_t at scene coordinates (X_t, Y_t, Z_t). Based on (2.51), the received signal is

$$s_r(X_a, t) = a_t \text{rect}\left(\frac{X_a - X_{ac}}{L}\right) \text{rect}\left(\frac{\hat{t} - 2R_t/c}{T_p}\right) e^{j2\pi f_c\left(t - \frac{2R_t}{c}\right)} e^{j\pi\gamma\left(\hat{t} - \frac{2R_t}{c}\right)^2} \tag{11.1}$$

The amplitude a_t is equal to $\sqrt{\sigma_t}$, f_c represents center frequency, T_p is the transmitted

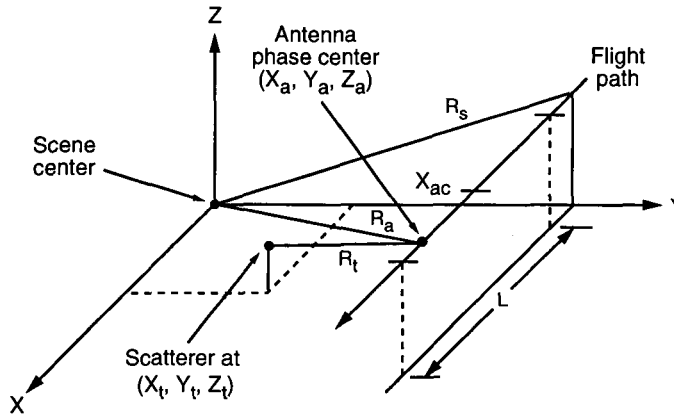


Figure 11.1 SAR imaging geometry for development of chirp scaling algorithm.

pulse length, γ is the chirp rate, c is the speed at which microwave energy propagates, X_{ac} is the aperture reference point (ARP) or center of the synthetic aperture of length L, and R_t is the distance between the sensor antenna phase center (APC) and the point scatterer. The expression $\hat{t} = t - nT$ represents fast time and T is the pulse repetition interval.

For simplicity, we write the slow-time dependence of (11.1) as a function of the continuous along-track position X_a rather than the discrete pulse number variable n. The first rect function limits the received data to a synthetic aperture of length L centered at X_{ac} in Figure 11.1. The signal model assumes that the backscattered amplitude and phase characteristics of the point scatterer do not vary with frequency or aspect angle and that the radar is stationary during pulse transmission and reception. This model also ignores antenna gain, atmospheric propagation effects on signal amplitude, and the effects of any time delays in the SAR system hardware.

We assume that the sensor traverses a straight-line flight path parallel to the X axis, making Y_a and Z_a constant at Y_{ac} and Z_{ac}, respectively. The quantity R_s in Figure 11.1 is the distance between the APC and scene center when $X_a = 0$. The quantity $R_t = R_t(X_a)$ varies with along-track sensor position X_a only. An expression for R_t is

$$R_t = \sqrt{(X_a - X_t)^2 + (Y_{ac} - Y_t)^2 + (Z_{ac} - Z_t)^2} \tag{11.2}$$

where (X_a, Y_{ac}, Z_{ac}) is the measured position of the APC. We assume no error in measurement of the APC location, making (X_a, Y_{ac}, Z_{ac}) also the actual position of the APC.

The minimum range to the scatterer, which we refer to as the broadside range R_B, occurs along the flight path when $X_a = X_t$. An expression for R_B is

$$R_B = \sqrt{(Y_{ac} - Y_t)^2 + (Z_{ac} - Z_t)^2} \tag{11.3}$$

Figure 11.2 shows the two-dimensional support of the SAR signal from a point scatterer

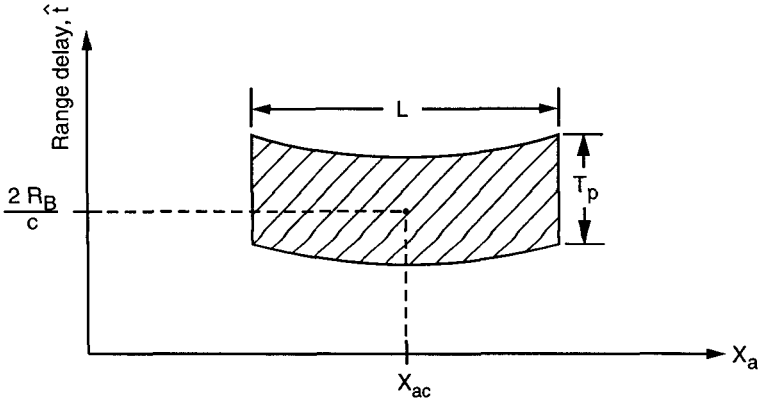


Figure 11.2 Two-dimensional support of SAR signal from a scatterer at $X_t = X_{ac}$.

located at $X_t = X_{ac}$. In the case of broadside imaging, X_{ac} is equal to zero. The signal support (in range delay) has constant width T_p and a center delay that varies with X_a.

The SAR system model in Section 2.6 demodulates received signals using a replica of the transmitted waveform delayed by the two-way propagation time to scene center. This dechirp-on-receive operation removes the wideband chirp modulation and the RF carrier from radar echoes before analog-to-digital conversion. In the CSA case, the appropriate reference function for demodulating and motion compensating the received signal is

$$s_{ref}(t) = e^{j2\pi f_c\left(t-\frac{2R_s}{c}\right)} \tag{11.4}$$

The presence of the constant R_s in this reference function indicates demodulation of the received signals using a constant range delay. This constant range delay introduces only an inconsequential constant phase in the demodulated signal, which we discard. In a realistic data collection, R_s varies over time because Y_a and Z_a vary due to effects such as atmospheric turbulence that cause the SAR platform to traverse a nonideal flight path.

In one interpretation, use of (11.4) as a reference function represents motion compensation to a scene point moving along-track at the nominal sensor velocity rather than to a fixed point at scene center (Section 10.1). Referred to as motion compensation to a line, this approach is typical of most *stripmap* SAR systems.

The signal that results from mixing the received signal of (11.1) and the complex conjugate of the reference function of (11.4) is

$$s(X_a, \hat{t}) = a_t \text{rect}\left(\frac{X_a - X_{ac}}{L}\right)\text{rect}\left(\frac{\hat{t} - 2R_t/c}{T_p}\right)e^{-j\frac{4\pi f_c}{c}R_t}e^{j\pi\gamma\left(\hat{t}-\frac{2R_t}{c}\right)^2} \tag{11.5}$$

after discarding the constant phase term in R_s.

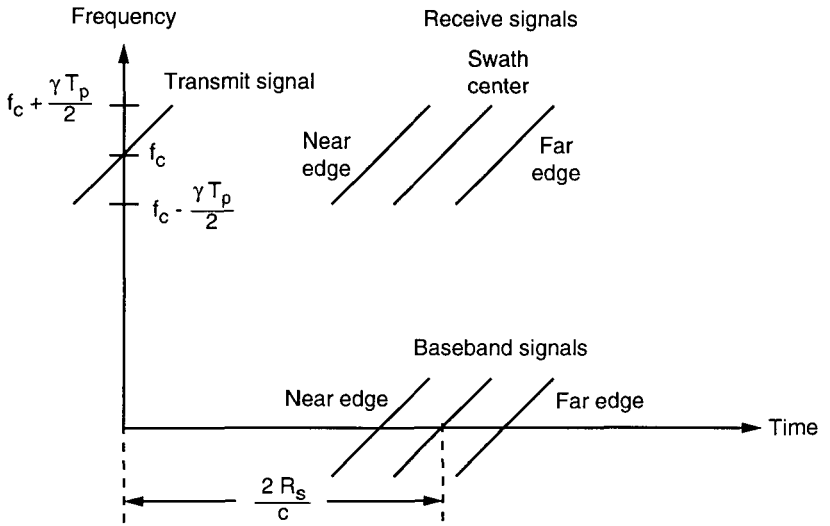


Figure 11.3 Time-frequency diagram for non-dechirped SAR system.

The phase of the first exponential term in (11.5) varies with the range R_t. This phase variation over a synthetic aperture supplies the Doppler bandwidth that leads to azimuth resolution. In the imaging geometry of Figure 11.1, the variation in R_t and the phase of the Doppler imaging term is approximately quadratic over the synthetic aperture. Since a chirp signal also has quadratic phase, it is common to say that the SAR signal history represented by (11.5) is chirped in azimuth as well as in range. A typical spotlight SAR system removes the majority of this azimuth chirp in real time during data collection. In such a case, a preprocessing operation is necessary to reinstate the azimuth chirp in order to proceed with CSA processing.

The second exponential term in (11.5) is the range chirp of the baseband signal. Figure 11.3 shows the relationship between time and frequency for a single transmitted pulse in a SAR system without dechirp-on-receive. Upon reception, the receiver translates the signal from the RF carrier frequency f_c to baseband via (11.4) without affecting the chirp modulation. The presence of the chirp modulation makes it necessary to digitize the entire chirp bandwidth. The CSA operates on this high-bandwidth signal.

In summary, CSA analysis begins with (11.5). This equation describes the two-dimensional signal history from a single point scatterer at coordinates (X_t, Y_t, Z_t) within an imaged scene. The signal data contains both range and azimuth chirp characteristics. The CSA requirement for data chirped in range and azimuth does not necessarily constrain the SAR data collection. A preprocessing operation can reapply range and azimuth chirps prior to image formation processing if they are not present in the collected signal history.

11.2 ALGORITHM OVERVIEW

The CSA, like the RMA, belongs to a class of image formation algorithms known as *wavenumber domain* algorithms because they operate primarily in the wavenumber or spatial-frequency domain. The RMA operates in the azimuth-frequency/range-frequency domain, while CSA operates in both the azimuth-frequency/range-time (or range-position) domain and the azimuth-frequency/range-frequency domain. Unlike the RMA, the CSA requires range-chirped signal data. Figure 11.4 shows a block diagram of the CSA procedure. CSA processing requires only FFTs and complex multiplications to form a SAR image. This attribute makes hardware and software implementations of the CSA simple relative to algorithms that require sophisticated interpolations.

In general, fine-resolution SAR image formation is a difficult task for large scenes because of the presence of differential range curvature (Section 3.2.1 and Section 10.2). Figure 11.5(a) depicts three point scatterers in a scene imaged by a spotlight SAR at a 90-deg (broadside) Doppler cone angle. Figure 11.5(b) illustrates the collected signal history data as it would appear after range compression. In this domain, each scatterer follows a curved, hyperbolic trajectory in response to variations in range over the synthetic aperture. The nonlinear component of each scatterer's trajectory is range curvature; the variation in range curvature over the scene is differential range curvature. We will show that the CSA performs specific processing steps designed to equalize the range curvature of all scatterers in the scene. After these operations, a space-invariant matched filtering step simultaneously focuses all scatterers.

In this section, we illustrate CSA operation using a two-dimensional simulation. Figure 11.5(a) illustrates the collection geometry and shows the locations of three point scatterers in the simulated scene. Table 11.1 lists the SAR parameters that the simulation uses. We choose these parameters to challenge the image formation processor (IFP) with respect to the severity of differential range curvature; they do not necessarily represent a practical SAR system design. Figure 11.6 shows the magnitude of the simulated signal history. The vertical dimension is the azimuth coordinate X_a, with positive X_a to the top of the figure. The horizontal dimension corresponds to time within a pulse (range or fast time), with increasing time to the right. The returns from points 1 and 2 overlap causing the amplitude modulation seen in the near range signals; the return from point 3 appears separately at far range to the right of the figure.

11.2.1 Azimuth Fourier Transform

The first CSA operation computes the azimuth Fourier transform of the signal history, transforming the data into the azimuth-frequency/range-time domain. (In Section 11.3, we refer to this domain as the azimuth-frequency/range-position domain.) The CSA equalizes range curvature in the azimuth-frequency domain rather than azimuth-position (data collection) domain. In the azimuth-position domain, range curvature is a function of both the broadside range and azimuth coordinate of a scatterer. In the azimuth-frequency domain, however, range curvature does not depend on the azimuth coordinate of a scatterer.

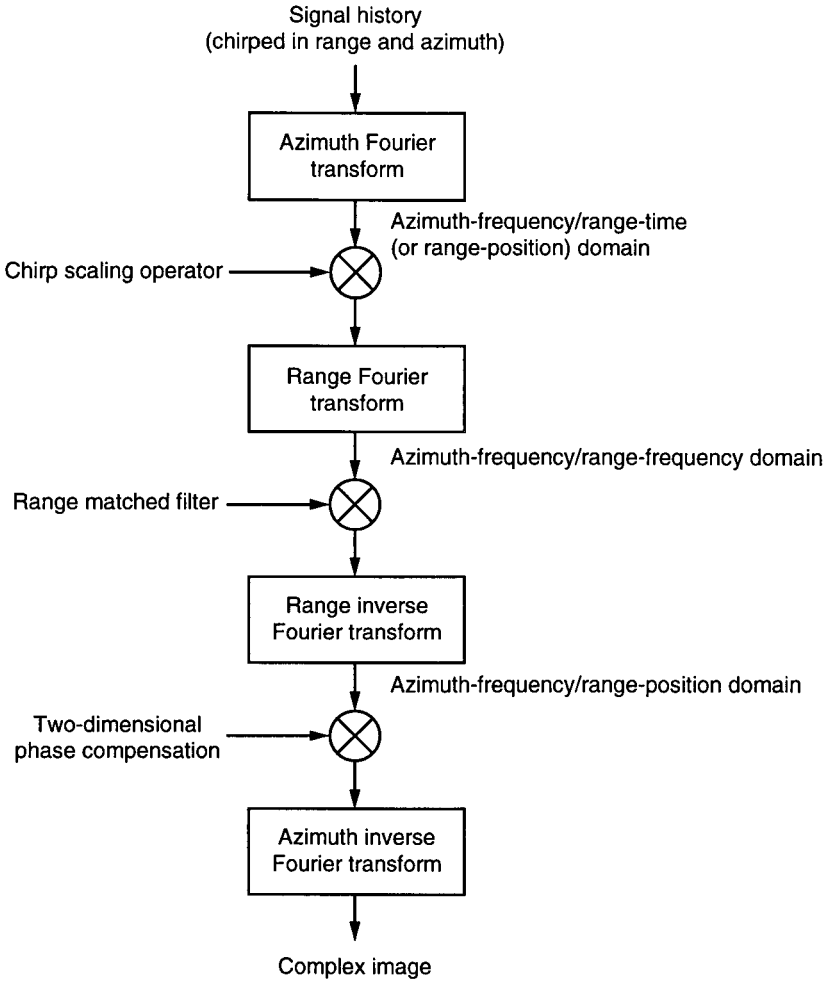


Figure 11.4 Block diagram of the chirp scaling algorithm.

Figure 11.7 shows the magnitude of the simulated signal history after the azimuth Fourier transform. The azimuth spectra of points 1 and 2 overlap, with the spectrum of point 2 being offset in azimuth frequency (toward the top of the figure). The azimuth spectrum of point 3 is centered at zero spatial frequency since the synthetic aperture is symmetrical about this scatterer.

Figure 11.8 shows the result of range compressing the data in Figure 11.7 and removing from all scatterers the range curvature associated with a point at scene center. This range curvature correction procedure provides adequate compensation for point 2 as well as the scatterer at scene center (point 1). However, close inspection of Figure 11.8

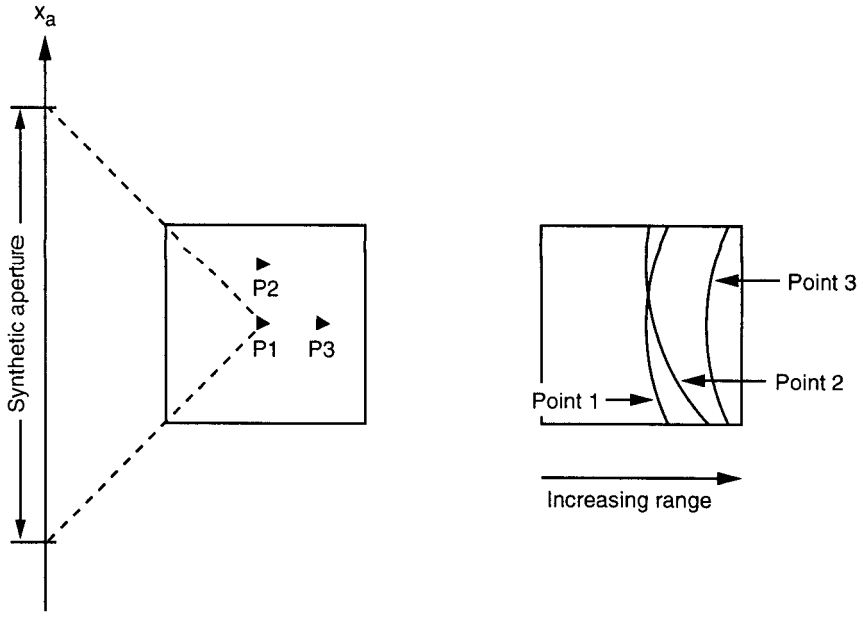


Figure 11.5 Range curvature in spotlight SAR: **(a)** Collection geometry; **(b)** Signal history after range compression.

shows the presence of residual range curvature on point 3. Being displaced in range, point 3 is improperly compensated because it possesses a different amount of range curvature than point 1. However, the image formation algorithm can equalize range curvature across the range swath by performing a remapping or warping operation in the range dimension that varies as a function of azimuth frequency. The RMA achieves this effect by an interpolation in the range-frequency direction of the two-dimensional frequency domain. Section 11.2.2 discusses how the CSA equalizes range curvature by performing an azimuth frequency-dependent modification, or *scaling*, of the original range chirp rate.

11.2.2 Chirp Scaling Operation

The second step of the CSA modifies the range chirp rate as a function of azimuth frequency to equalize the range curvature of scatterers at all ranges. The chirp scaling operation multiplies the azimuth-transformed signal data by a two-dimensional, complex exponential reference function. Figure 11.9 shows the effect of this chirp scaling operation for a particular (nonzero) azimuth frequency. The upper drawing shows the phase of three radar signals as a function of range time (fast time). These signals correspond to three point scatterers spread across the radar range swath. The middle drawing shows the phase of the complex conjugate of the chirp scaling operator. This phase also represents a chirp

Table 11.1
System Parameters for Chirp Scaling Simulation Example

Parameter	*Description*	*Value*
Δ_X	Along-track sample spacing	0.4 m
T_p	Pulse length	1.0 μs
W_r	Range scene size	617.8 m
W_a	Azimuth scene size	400.0 m
f_c	Radar center frequency	422.4 MHz
γ	Chirp rate	133.5 MHz/μs
B	Processed bandwidth	133.5 MHz
F_s	Complex sampling rate	200 MHz
ρ_r	Range resolution	1.0 m
ρ_a	Azimuth resolution	0.8 m
K_r	Range mainlobe-broadening factor	0.89
K_a	Azimuth mainlobe-broadening factor	0.89
R_s	Broadside slant range to scene center	1000 m
ϕ_{ac}	Image incidence angle	90 deg
θ_{ac}	Image squint angle	90 deg (broadside)
L	Synthetic aperture length	400.0 m
$\Delta\theta$	Coherent processing angle interval	22.6 deg
	Number of scatterers	3
	Scatterer locations:	
(X_1, Y_1, Z_1)	Point 1 coordinates	(0, 0, 0) m
(X_2, Y_2, Z_2)	Point 2 coordinates	(100, 0, 0) m
(X_3, Y_3, Z_3)	Point 3 coordinates	(0, −200, 0) m

waveform, but with a much lower chirp rate than that of the transmitted SAR signal. The bottom diagram shows the signal phase after the chirp scaling operation. The operation slightly increases the chirp rate of all signals and adds a linear phase that increases with target distance from scene center. In the subsequent matched filtering operation, this linear phase component shifts the range location of a point target response nearer to scene center. The size of this shift increases linearly with a target's distance from scene center. As Figure 11.10 suggests, the net result is that the chirp scaling operator changes the range scale factor. In addition, the chirp scaling operation introduces a range-dependent phase term that a subsequent step of the CSA easily removes.

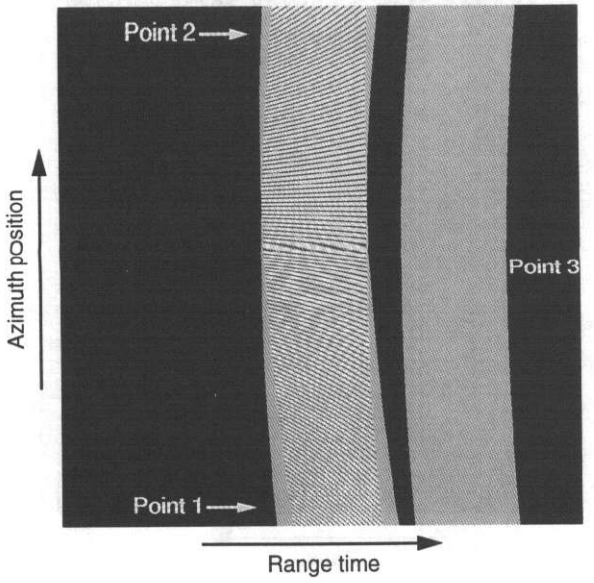


Figure 11.6 Magnitude of simulated signal history in azimuth-position/range-time domain.

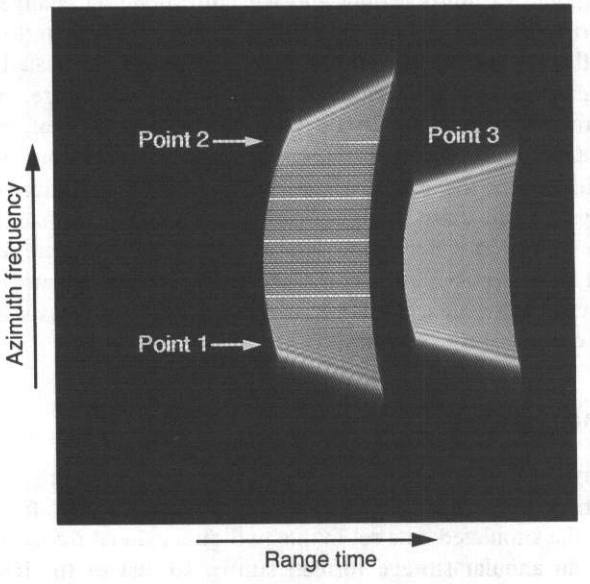


Figure 11.7 Data in azimuth-frequency/range-time domain after computing the azimuth Fourier transform of the simulated signal history.

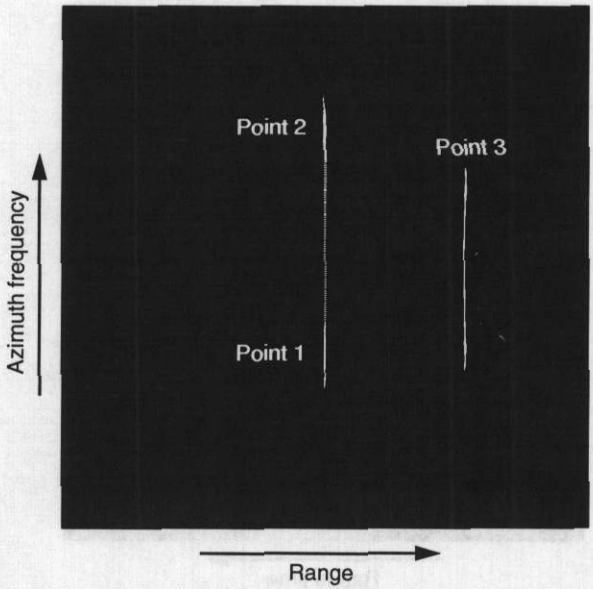


Figure 11.8 Differential range curvature in azimuth-frequency/range-position domain.

It is the change in range scale factor that equalizes the range curvature arcs of Figure 11.8. The amount of chirp scaling and the corresponding change in range scale factor vary appropriately with azimuth frequency to force all targets to have the same range curvature as that of a target at a selected reference range. The usual procedure is to select the broadside range to scene center R_s as this reference range. At zero azimuth frequency, this operation does not modify the chirp rate. The amount of chirp rate modification increases as azimuth frequency increases or decreases away from zero.

Figure 11.11 illustrates the effect of the chirp scaling operation on the data of Figure 11.8. It shows that the chirp scaling procedure is able to equalize the range curvature of all scatterers in the simulated scene. No residual range curvature remains on point 3. We point out that in actual CSA operation range curvature is not removed totally at this point in the algorithm; rather, all scatterers have the same curvature as scatterers at range R_s possess prior to chirp scaling.

11.2.3 Range Compression

Following the chirp scaling operation, a range Fourier transform of the azimuth-frequency/range-time signal brings the data into the two-dimensional frequency domain. Figure 11.12 shows the simulated data set in this two-dimensional frequency domain. The data now occupies an annular storage format, similar to that of the RMA example in Chapter 10 after Stolt interpolation (Figure 10.18). We emphasize that the CSA reaches this format via the chirp scaling multiply without explicitly interpolating the signal data.

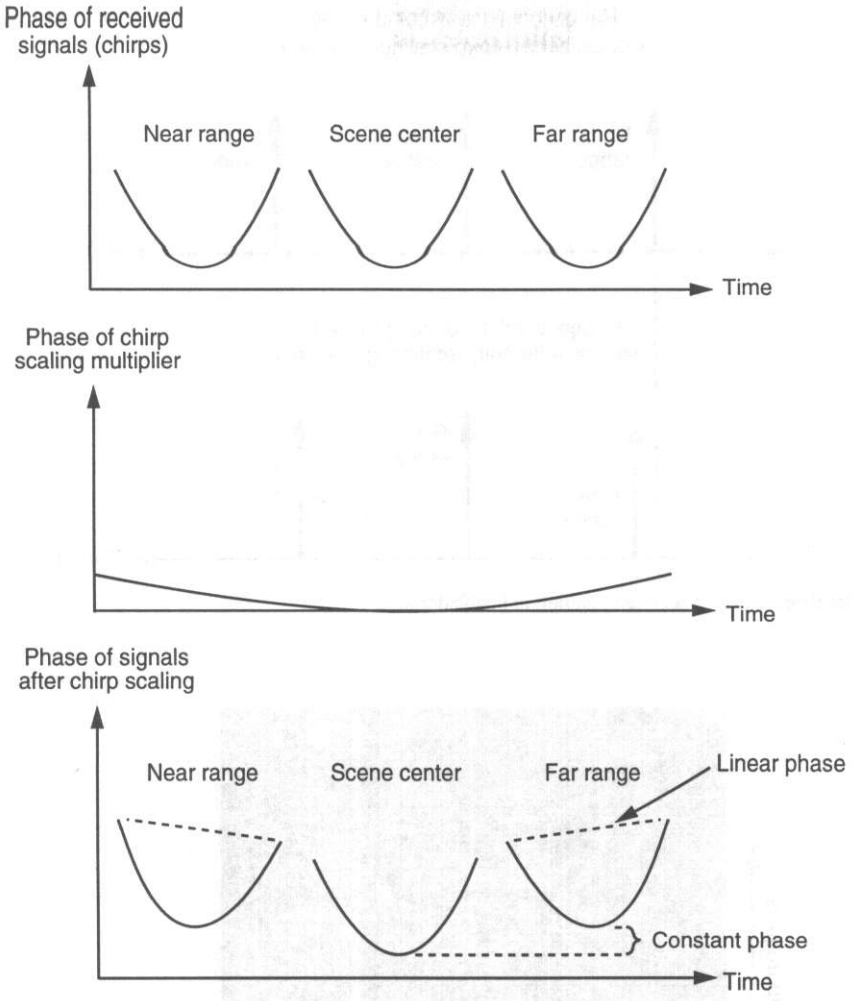


Figure 11.9 Effect of chirp scaling operation on phase signals from scatterers at three ranges.

At this point in the CSA, multiplication by a two-dimensional reference function (matched filter) removes the equalized range curvature from all scatterers in the scene. The matched filter also removes the wideband range chirp characteristics from the signal data of all scatterers. A range-dependent phase effect resulting from the previous chirp scaling operation is still present in the data. To remove this effect, the CSA first performs a range inverse Fourier transform which compresses all targets in range (Figure 11.11). The CSA is then able to perform azimuth matched filtering and compensate the residual range-dependent phase effect in the azimuth-frequency/range-position domain.

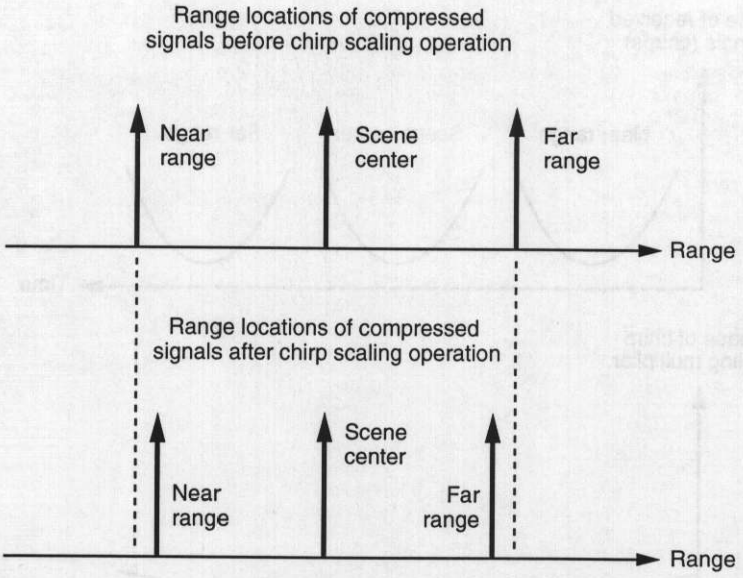


Figure 11.10 Effect of chirp scaling operation in image domain.

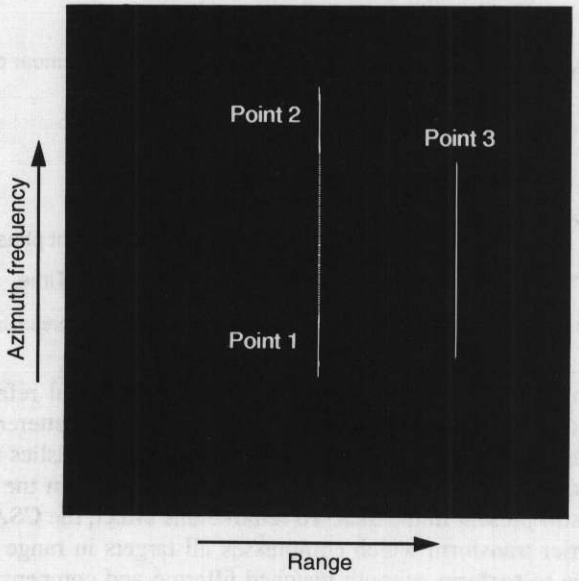


Figure 11.11 Trajectories of point targets after chirp scaling operation and range curvature correction.

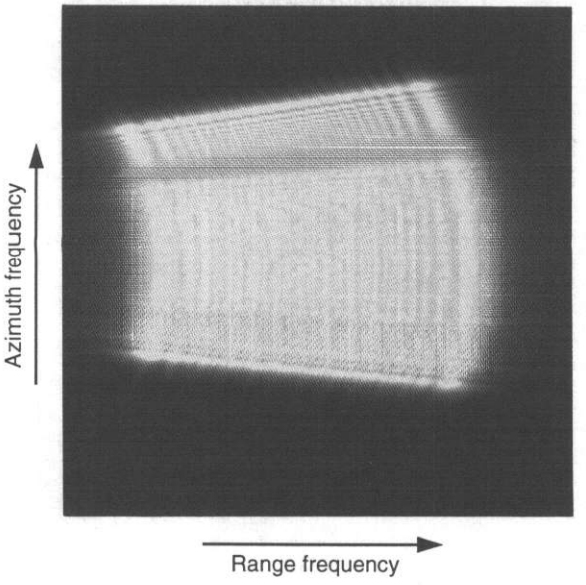


Figure 11.12 Simulated data in frequency domain after chirp scaling operation and range Fourier transform.

11.2.4 Two-Dimensional Phase Compensation

The third multiplication in Figure 11.4 compensates the residual range-dependent phase effect resulting from the chirp scaling operation and performs azimuth matched filtering. Sample-by-sample multiplication of the range-compressed signal by a two-dimensional, complex exponential accomplishes these procedures.

11.2.5 Azimuth Inverse Fourier Transform

The final CSA operation is a one-dimensional inverse Fourier transform to compress the signal in azimuth. Figure 11.13 shows the resulting fully compressed image for the simulation example of this section.

The CSA processor can apply two-dimensional aperture weighting before the range inverse Fourier transform in order to control impulse response sidelobes in the final image. Appendix D discusses several applicable techniques to manage image sidelobes.

When applying aperture weighting, not all scatterers have precisely the same signal support in the two-dimensional frequency domain. This subtlety causes the processing aperture shape to vary with scatterer location in the scene. This variation in aperture shape leads to a space-variant impulse response when processing spotlight SAR data with the CSA (and the RMA). Section 10.4.3 presents a method to control this effect. For typical systems and operational parameters, the variation in impulse response shape over a scene is often small and negligible.

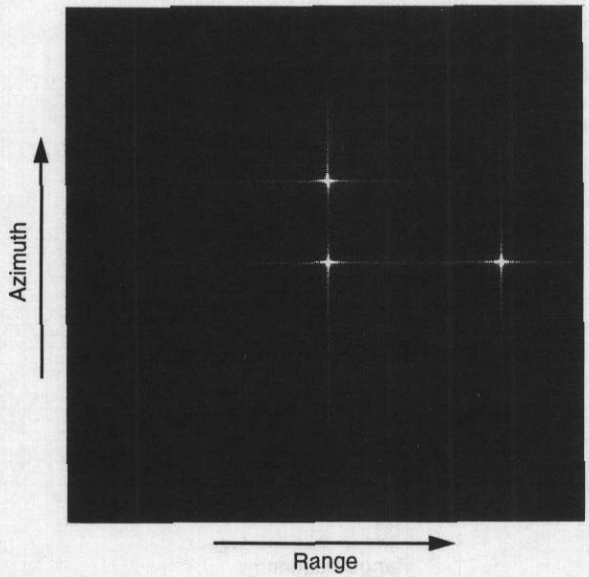


Figure 11.13 Fully compressed simulated SAR image.

11.3 ANALYTICAL DEVELOPMENT

This section presents an analytical development of the chirp scaling algorithm following Figure 11.4. The starting point is the SAR signal of (11.5). This equation models the received and demodulated signal from a single point scatterer at an arbitrary location within an illuminated scene. In the following development, the SAR sensor travels along a straight line parallel to the X axis. Figure 11.1 illustrates this data collection geometry.

11.3.1 Azimuth Fourier Transform

The initial CSA step computes the azimuth Fourier transform of the SAR signal data to reach the azimuth-frequency/range-time domain. A closed-form expression for this transform is not available. Instead, we approximate the transform by applying the principle of stationary phase (PSP) discussed in Section 10.3.1 in a four-stage procedure introduced in [2]. Figure 11.14 provides a roadmap for this procedure. It begins with application of the PSP to determine the range Fourier transform of the signal history, followed by an azimuth Fourier transform of the resulting expression, and a simplifying approximation. The approximation makes it possible to determine the inverse Fourier transform in the range dimension to obtain the desired azimuth Fourier transform of the original expression. It is convenient to express this result in terms of the range position variable Y_s, which is the spatial equivalent to the fast time variable $\hat{t}$.

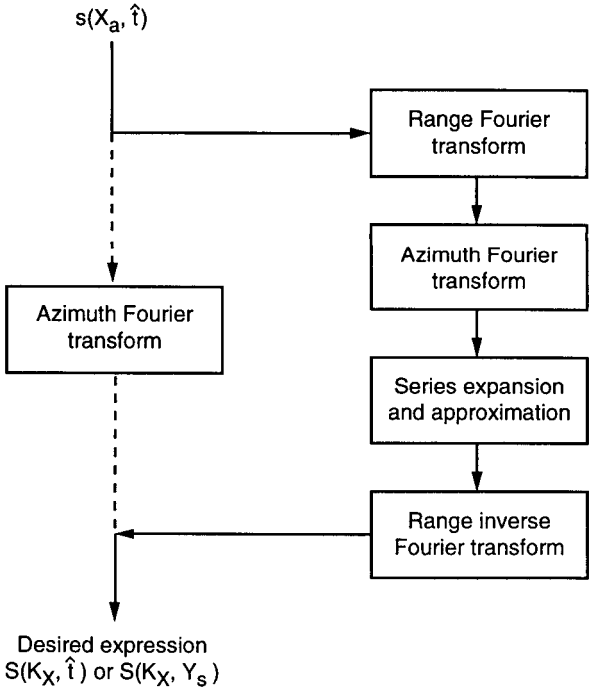


Figure 11.14 Evaluating the azimuth Fourier transform of the SAR signal model.

The range Fourier transform of (11.5) in the parameter $\hat{t} - 2R_s/c$ is

$$S(X_a, f_{\hat{t}}) = \int s(X_a, \hat{t})\, e^{-j2\pi f_{\hat{t}}\left(\hat{t} - \frac{2R_s}{c}\right)} d\hat{t} \tag{11.6}$$

where $f_{\hat{t}}$ is the frequency domain counterpart to $\hat{t}$. We apply the PSP to evaluate this expression. The phase of the integrand of (11.6) is

$$\Phi_1(X_a, \hat{t}) = -\frac{4\pi f_c R_t}{c} + \pi\gamma\left(\hat{t} - \frac{2R_t}{c}\right)^2 - 2\pi f_{\hat{t}}\left(\hat{t} - \frac{2R_s}{c}\right) \tag{11.7}$$

The procedure to determine the stationary point of (11.6) computes the derivative of (11.7) with respect to $\hat{t}$ and equates the result to zero. The derivative is

$$\frac{\partial}{\partial \hat{t}}\Phi_1(X_a, \hat{t}) = 2\pi\gamma\left(\hat{t} - \frac{2R_t}{c}\right) - 2\pi f_{\hat{t}} \tag{11.8}$$

Equating this derivative to zero and solving for $\hat{t}$, the stationary point $\hat{t}^*$ is

$$\hat{t}^* = \frac{f_{\hat{t}}}{\gamma} + \frac{2R_t}{c} \tag{11.9}$$

We approximate the range Fourier transform of (11.5) by substituting (11.9) for $\hat{t}$ in the integrand of (11.6) to obtain

$$S(X_a, f_{\hat{t}}) = A_1 \text{rect}\left(\frac{X_a - X_{ac}}{L}\right)\text{rect}\left(\frac{f_{\hat{t}}}{\gamma T_p}\right) e^{-j(2\pi f_c + 2\pi f_{\hat{t}})\frac{2R_t}{c}} e^{-j\frac{\pi f_{\hat{t}}^2}{\gamma}} e^{j2\pi f_{\hat{t}}\frac{2R_s}{c}} \tag{11.10}$$

The coefficient A_1 represents complex amplitude factors not important to this development. The range-dimension variable $f_{\hat{t}}$ in (11.10) represents the temporal frequency of demodulated signals. At this point, it is convenient to rewrite (11.10) in terms of spatial frequency with units of rad/unit distance. Although not necessary to the CSA development, this change better conveys the essential aspects of image formation in the wavenumber or spatial-frequency domain. To make this change, we define the quantities

$$K_{Rc} = \frac{4\pi f_c}{c} \tag{11.11}$$

$$\Delta K_R = \frac{4\pi f_{\hat{t}}}{c} \tag{11.12}$$

$$K_R = K_{Rc} + \Delta K_R \tag{11.13}$$

and

$$b = \frac{8\pi\gamma}{c^2} \tag{11.14}$$

The quantity K_R in (11.13) represents instantaneous transmitted (radian) frequency scaled by the factor $2/c$. Equation (11.13) corresponds to (10.19) in the analytical development of the RMA. The quantity K_{Rc} in (11.11) is the value of K_R at the radar center frequency, while ΔK_R in (11.12) represents the variation in K_R over the transmitted bandwidth. Note that ΔK_R may be negative or positive, but K_R is always positive. Equation (11.14) scales the temporal chirp rate into units of radians per unit length squared. In terms of these new quantities, (11.10) becomes

$$S(X_a, \Delta K_R) = A_1 \text{rect}\left(\frac{X_a - X_{ac}}{L}\right)\text{rect}\left(\frac{2\Delta K_R}{bcT_p}\right) e^{-jK_R R_t} e^{-j\frac{\Delta K_R^2}{2b}} e^{jR_s \Delta K_R} \tag{11.15}$$

The next step determines the azimuth Fourier transform of (11.15) in the form

$$S_2(K_X, \Delta K_R) = \int S(X_a, \Delta K_R) e^{-jK_X X_a} dX_a \tag{11.16}$$

Here, the Fourier transform kernel involves spatial frequency and K_X is the frequency domain counterpart to X_a. The phase of the integrand of (11.16) is

$$\Phi_2(X_a, \Delta K_R) = -K_R R_t - \frac{\Delta K_R^2}{2b} + R_s \Delta K_R - K_X X_a \tag{11.17}$$

Equating to zero the first derivative of (11.17) with respect to X_a (recalling that R_t is a function of X_a) and solving for X_a, the stationary point for use with PSP analysis is

$$X_a^* = \frac{-K_X R_B}{\sqrt{K_R^2 - K_X^2}} + X_t \tag{11.18}$$

with R_B given by (11.3).

Substituting the stationary point X_a^* for X_a in the integrand of (11.16) yields the signal in the azimuth-frequency/range-frequency domain as

$$S_2(K_X, \Delta K_R) = a_2(K_X, \Delta K_R) e^{-jR_B\sqrt{K_R^2 - K_X^2}} e^{-j\frac{\Delta K_R^2}{2b}} e^{jR_s \Delta K_R} e^{-jK_X X_t} \tag{11.19}$$

with

$$a_2(K_X, \Delta K_R) = A_2 \operatorname{rect}\left(\frac{K_X R_B}{L\sqrt{K_R^2 - K_X^2}} + \frac{X_{ac} - X_t}{L} \right) \operatorname{rect}\left(\frac{2\Delta K_R}{bcT_p} \right) \tag{11.20}$$

Here, A_2 represents a new amplitude coefficient. We will see in Section 11.3.7 that the linear phase of the last term in (11.19) positions the target at azimuth coordinate X_t.

The final step to achieve the desired azimuth-frequency/range-time signal (now range-position) requires the range inverse Fourier transform of (11.19). Following [2], this step begins by rewriting the phase of (11.19) as

$$\Phi_{S2}(K_X, \Delta K_R) = -R_B K_{Rc} A_X \left(1 + \frac{2\Delta K_R}{A_X^2 K_{Rc}} + \frac{\Delta K_R^2}{A_X^2 K_{Rc}^2} \right)^{1/2} - \frac{\Delta K_R^2}{2b} + R_s \Delta K_R - K_X X_t \tag{11.21}$$

with

$$A_X^2(K_X) = 1 - \frac{K_X^2}{K_{Rc}^2} \tag{11.22}$$

The analysis continues by assuming that the fractions inside the brackets in (11.21) are small relative to unity and replacing the square root of the bracketed expression by the first terms of its Taylor series expansion. SAR systems with small bandwidth-to-center-frequency ratios and small coherent integration angles are more likely to fit this approximation.

The Taylor series expansion yields the approximate relationship

$$\left(1+\frac{2\Delta K_R}{A_X^2 K_{Rc}}+\frac{\Delta K_R^2}{A_X^2 K_{Rc}^2}\right)^{1/2} \approx 1+\frac{1}{2}\left(\frac{2\Delta K_R}{A_X^2 K_{Rc}}+\frac{\Delta K_R^2}{A_X^2 K_{Rc}^2}\right)-\frac{1}{8}\left(\frac{2\Delta K_R}{A_X^2 K_{Rc}}+\frac{\Delta K_R^2}{A_X^2 K_{Rc}^2}\right)^2 \tag{11.23}$$

We substitute (11.23) into (11.21) and use the result in (11.19). Discarding cubic and higher order terms in ΔK_R produces the result

$$S_2(K_X, \Delta K_R) \approx a_2(K_X, \Delta K_R)\, e^{-jR_B K_{Rc} A_X}\, e^{j\left(R_s - \frac{R_B}{A_X}\right)\Delta K_R}\, e^{-j\frac{\Delta K_R^2}{2b_m}}\, e^{-jK_X X_t} \tag{11.24}$$

with

$$b_m(K_X) = \frac{b}{1-\dfrac{bR_B K_X^2}{K_{Rc}^3 A_X^3}} \tag{11.25}$$

The development of (11.25) combines all terms containing the quantity ΔK_R^2 into a single expression involving a generalized chirp rate b_m. This generalized chirp rate varies with azimuth frequency K_X and with broadside target range R_B. The K_X dependence is an important aspect of the CSA. The range dependence in (11.25) is typically either less significant or not significant in SAR systems with small coherent integration angles or small range scene sizes.

The inverse Fourier transform of (11.24) with respect to ΔK_R converts the signal to the azimuth-frequency/range-position domain. This inverse transform is

$$S_3(K_X, Y_s) = \frac{1}{2\pi}\int S_2(K_X, \Delta K_R)\, e^{j\Delta K_R Y_s} d(\Delta K_R) \tag{11.26}$$

where Y_s represents range position relative to scene center. In this representation, the scene center location corresponds to $Y_s = 0$; the range coordinate Y_s increases in the direction away from the ARP. For application of the PSP to (11.26), the stationary point is

$$\Delta K_R^* = b_m\left(Y_s + R_s - \frac{R_B}{A_X}\right) \tag{11.27}$$

Use of (11.27) for ΔK_R in the integrand of (11.26) yields

$$S_3(K_X, Y_s) = a_3(K_X, Y_s)\, e^{-jR_B K_{Rc} A_X} e^{j\frac{b_m}{2}\left(Y_s + R_s - \frac{R_B}{A_X}\right)^2} e^{-jK_X X_t} \tag{11.28}$$

with

$$a_3(K_X, Y_s) \approx A_3 \,\mathrm{rect}\left(\frac{K_X R_B}{LK_{Rc}} + \frac{X_{ac} - X_t}{L}\right) \mathrm{rect}\left[\frac{2b_m\left(Y_s + R_s - \frac{R_B}{A_X}\right)}{bcT_p}\right] \tag{11.29}$$

and a new amplitude coefficient A_3. Equation (11.28) is an approximate expression for the azimuth Fourier transform of the SAR point target signal in (11.5). This result uses the range position variable Y_s rather than the time delay variable $\hat{t}$ present in (11.5). The first rect function in (11.29) results from the approximation

$$\mathrm{rect}\left(\frac{K_X R_B}{L\sqrt{(K_{Rc} + \Delta K_R^*)^2 - K_X^2}} + \frac{X_{ac} - X_t}{L}\right) \approx \mathrm{rect}\left(\frac{K_X R_B}{LK_{Rc}} + \frac{X_{ac} - X_t}{L}\right) \tag{11.30}$$

This simplification neglects the range dependence of the data support in azimuth. It preserves the K_X displacement of this support as a function of scatterer azimuth location X_t.

11.3.2 Chirp Scaling Operation

The second step of the CSA procedure multiplies (11.28) by the conjugate of a reference function, the *chirp scaling operator*, that modifies the generalized range chirp rate b_m. The size of this modification varies with K_X. The form of the chirp scaling operator is

$$S_{ref1}(K_X, Y_s) = e^{-j\frac{b_m D}{2}(Y_s - Y_{ref})^2} \tag{11.31}$$

where Y_{ref} is a constant reference range and $D(K_X)$ is a modification parameter that varies with K_X. An appropriate choice for D eliminates differential range curvature from the SAR signal data (Section 11.3.3). The usual procedure chooses $Y_{ref} = 0$, meaning that this operator does not affect scatterers at distance R_s from scene center. Since the generalized chirp rate b_m depends only weakly on R_B (the minimum broadside range to each target), it is reasonable to approximate (11.31) as a space-invariant reference function. In practice, the IFP makes this approximation by replacing R_B in (11.25) by R_s. The analysis does not make this approximation although, for simplicity, it does set $Y_{ref} = 0$.

11.3.3 Range Fourier Transform

The third step in the CSA procedure takes the range Fourier transform of the product of (11.28) and the complex conjugate of (11.31) with $Y_{ref} = 0$. The Fourier kernel

is $\exp(-j\,\Delta K_R Y_s)$. The phase within the Fourier integral of this product is

$$\begin{aligned}\Phi_4(Y_s, \Delta K_R) &= \frac{b_m}{2}(1+D)\,Y_s^2 - b_m\left(\frac{R_B}{A_X} - R_s + \frac{\Delta K_R}{b_m}\right)Y_s \\ &\quad + \frac{b_m}{2}\left(R_s - \frac{R_B}{A_X}\right)^2 - R_B K_{Rc} A_X - K_X X_t\end{aligned} \tag{11.32}$$

Using the PSP to evaluate this transform, we take the first derivative of (11.32) with respect to Y_s and equate the result to zero. Solving for Y_s yields the stationary point Y_s^* in the form

$$Y_s^* = \frac{\dfrac{R_B}{A_X} - R_s + \dfrac{\Delta K_R}{b_m}}{1+D} \tag{11.33}$$

Substitution of Y_s^* for Y_s in the Fourier integral under consideration produces an approximation for the desired range transform $S_5(K_X, \Delta K_R)$. With this procedure, the phase of $S_5(K_X, \Delta K_R)$ becomes

$$\begin{aligned}\Phi_5(K_X, \Delta K_R) &= -\left(\frac{1}{1+D}\right)\frac{\Delta K_R^2}{2b_m} + \frac{R_s \Delta K_R}{1+D}\left(1 - \frac{1}{A_X}\right) + \frac{(R_s - R_B)\,\Delta K_R}{(1+D)\,A_X} \\ &\quad + \frac{b_m}{2}\left(\frac{D}{1+D}\right)\left(\frac{R_B}{A_X} - R_s\right)^2 - R_B K_{Rc} A_X - K_X X_t\end{aligned} \tag{11.34}$$

The first three terms of (11.34) contain the range frequency variable ΔK_R. The first term is quadratic in ΔK_R; it originates from the high bandwidth chirp waveform that the SAR transmits. A comparison with the corresponding term in (11.24) indicates the effect of the chirp scaling operator. The second term is linear in ΔK_R; its linear coefficient varies with azimuth frequency because A and D vary with K_X. This term represents the range curvature of scatterers having a broadside range equal to R_s. The CSA processor removes these two terms in a subsequent matched filtering operation. The third term is linear in ΔK_R; its linear coefficient varies with K_X and also with scatterer range location since it includes the range R_B. The K_X variation is undesirable whereas the R_B variation is desirable. The appropriate selection of the parameter D in (11.31) removes the K_X dependence; equating the denominator of the third term to unity yields this selection for D in the form

$$D = \frac{1}{A_X} - 1 \tag{11.35}$$

With this choice, the third term has the linear phase $(R_s - R_B)\,\Delta K_R$; it positions each scatterer at the proper range ($Y_s = R_B - R_s$) in the range-position domain. Scatterers beyond scene center map to positive Y_s while scatterers closer to the APC map to negative Y_s. In the CSA here, Y_s has the opposite sign convention of the Y_s in the RMA development.

Use of (11.35) to evaluate (11.34) at the stationary point yields the SAR signal in the two-dimensional frequency domain after the chirp scaling operation. This signal is

$$S_5(K_X, \Delta K_R) = a_5(K_X, \Delta K_R)\, e^{j\Phi_5(K_X, \Delta K_R)} \tag{11.36}$$

Using a new amplitude factor A_5, we approximate the support by the rectangle

$$a_5 \approx A_5 \,\mathrm{rect}\left(\frac{K_X R_B}{L K_{Rc}} + \frac{X_{ac} - X_t}{L}\right)\mathrm{rect}\left(\frac{2\Delta K_R}{bcT_p}\right) \tag{11.37}$$

The phase $\Phi_5(K_X, \Delta K_R)$ consists of six terms. These phase terms are

$$\Phi_5(K_X, \Delta K_R) = \Phi_A + \Phi_B + \Phi_C + \Phi_D + \Phi_E + \Phi_F \tag{11.38}$$

with

$$\Phi_A = -\frac{A_X \Delta K_R^2}{2b_m} \tag{11.39}$$

$$\Phi_B = -(1 - A_X) R_s \Delta K_R \tag{11.40}$$

$$\Phi_C = \frac{b_m}{2}(1 - A_X)\left(\frac{R_B}{A_X} - R_s\right)^2 \tag{11.41}$$

$$\Phi_D = -R_B K_{Rc} A_X \tag{11.42}$$

$$\Phi_E = (R_s - R_B)\Delta K_R \tag{11.43}$$

and

$$\Phi_F = -K_X X_t \tag{11.44}$$

11.3.4 Two-Dimensional Matched Filtering

The next step is the two-dimensional matched filtering of $S_5(K_X, \Delta K_R)$ in (11.36). This process multiplies (11.36) by (the conjugate of) a two-dimensional reference function. This matched filtering step removes the common range chirp from the signal of (11.36) to prepare for range compression. The matched filter also removes the effects of range curvature from all scatterers.

The appropriate matched filter is

$$S_{ref2}(K_X, \Delta K_R) = e^{j(\Phi_A + \Phi_B)} \tag{11.45}$$

The CSA processor neglects a weak R_B dependence in (11.45) from b_m in Φ_A; it replaces R_B by the constant R_s to evaluate the matched filter. With the two-dimensional multiply

of (11.36) by the complex conjugate of (11.45), the signal of a point target becomes

$$S_6(K_X, \omega_{\hat{t}}) = a_5(K_X, \Delta K_R)\, e^{j(\Phi_C + \Phi_D + \Phi_E + \Phi_F)} \tag{11.46}$$

This result, representing the second multiply in Figure 11.4, disregards the slight mismatch (using R_s rather than R_B) between the signal and the practical matched filter. An inverse Fourier transform of (11.46) with respect to ΔK_R achieves range compression.

11.3.5 Range Inverse Fourier Transform

Evaluation of the range inverse Fourier transform of (11.46) with kernel $\exp(jY_s\Delta K_R)$ does not require use of the PSP. A direct evaluation produces

$$S_7(K_X, Y_s) = a_7(K_X)\,\mathrm{sinc}\left[\frac{bcT_p}{4\pi}(Y_s + R_s - R_B)\right] e^{j(\Phi_C + \Phi_D + \Phi_F)} \tag{11.47}$$

With a new amplitude factor A_7, the expression

$$a_7(K_X) = A_7 \mathrm{rect}\left(\frac{K_X R_B}{LK_{Rc}} + \frac{X_{ac} - X_t}{L}\right) \tag{11.48}$$

describes the support in azimuth of the range-compressed signal.

11.3.6 Two-Dimensional Phase Compensation

Multiplication of (11.47) by the conjugate of the final two-dimensional reference function

$$S_{\mathrm{ref3}}(K_X, Y_s) = e^{j(\Phi_C + \Phi_D)} \tag{11.49}$$

removes the two remaining range-dependent phase terms, Φ_C and Φ_D. Now, a one-dimensional inverse Fourier transform compresses the resulting signal in azimuth.

11.3.7 Azimuth Inverse Fourier Transform

The final step compresses the product of (11.47) and the conjugate of (11.49) in azimuth via an inverse Fourier transform with kernel $\exp(jX_aK_X)$. The impulse response becomes

$$S_8(X_a, Y_s) = A_8\,\mathrm{sinc}\left[\frac{LK_{Rc}}{2\pi R_B}(X_a - X_t)\right]\mathrm{sinc}\left[\frac{bcT_p}{4\pi}(Y_s + R_s - R_B)\right] e^{-j4\pi X_a\left(\frac{X_{ac} - X_t}{\lambda_c R_B}\right)} \tag{11.50}$$

with a new amplitude factor A_8 to complete the CSA analytical model. This expression represents azimuth resolution (approximately $\lambda_c R_B/2L$ from $2\pi R_B/LK_{Rc}$) and range resolution (approximately $c/2\gamma T_p$ from $4\pi/bcT_p$) consistent with (2.10) and (2.2). The wavelength λ_c corresponds to radar center frequency f_c.

11.4 ALGORITHM LIMITATIONS

The analysis that supports CSA relies on a number of approximations. In particular, it assumes the applicability of the PSP on multiple occasions and it uses the (relatively accurate) approximation of (11.23). In addition, practical implementations of CSA disregard the dependence of b_m on R_B in implementing the chirp scaling operator of (11.31) and the matched filter of (11.45). Use of the space-invariant matched filter is a primary limiting factor in CSA performance [4]. SAR systems with small bandwidth-to-center-frequency ratios and small coherent integration angles are more likely to satisfy these assumptions.

From another perspective, the CSA replaces the ideal nonlinear Stolt interpolation of the RMA by a linear interpolation that the IFP implements via a complex multiply in the signal history domain. The CSA implements only the shift and linear components of the Stolt mapping. (A procedure in Section 10.4.4 involves the shift component alone.) The quadratic chirp scaling operator of the CSA effects the linear component of mapping; a later phase multiply provides the shift. This linear approximation becomes inadequate as resolution becomes finer and scene size increases.

The CSA makes minor adjustments to the range chirp rate as a function of Doppler frequency. This operation can lead to a practical algorithm limitation. To adjust the range dechirp function, the CSA must operate on signal history data that is chirped in range. This requirement can lead to difficulty when applying the CSA to SAR systems that employ dechirp-on-receive, as fine-resolution systems typically do. To utilize dechirped data, the CSA must reapply the original chirp to the signal history. The rechirping process must first upsample each range record to support the full wideband chirp. Each digitized pulse requires upsampling by the ratio B/B_{IF} where B is the transmitted RF bandwidth and B_{IF} is the bandwidth of the intermediate frequency dechirped pulse. Such upsampling can be a major computational and memory bottleneck. For example, if a dechirp-on-receive system with $B/B_{IF} = 4$ digitizes 4096 complex samples, rechirping requires more than 16,000 complex samples—a large amount of data to store and process.

Below, we examine the Stolt mapping to quantify the limitation that CSA acquires by its linear approximation to the ideal nonlinear Stolt interpolation. The objective is to estimate the level of phase errors that this approximation can introduce. (A similar process can quantify the limitation of the shift-only procedure in Section 10.4.4.)

Section 10.3.4 defines the Stolt mapping by the transformation

$$K_Y = \sqrt{K_R^2 - K_X^2} \tag{11.51}$$

where K_X is azimuth spatial frequency, K_R is range frequency, and K_Y is the spatial frequency in the newly mapped range dimension. Expressions for these quantities are

$$K_X = -\frac{4\pi f}{c}\cos(\alpha_d) \tag{11.52}$$

and

$$K_R = \sqrt{K_X^2 + K_Y^2} = \frac{4\pi f}{c} = K_{Rc} + \Delta K_R \tag{11.53}$$

In these relationships, f corresponds to radar instantaneous frequency and α_d is the cone angle to a scatterer relative to the antenna velocity vector. K_X relates to the negative of Doppler frequency in the right-looking data collection perspective that we use in this book (Section 10.2.1). It follows that

$$K_Y = \frac{4\pi f}{c}\sin(\alpha_d) \tag{11.54}$$

Figure 10.15 in Section 10.2.3 shows the two-dimensional data storage format before and after the Stolt interpolation.

Equation (11.53) indicates that K_R is proportional to radar transmit frequency. This means that errors encountered when mapping K_R to K_Y will manifest themselves primarily as a range dimension phase error. The magnitude of the phase error increases linearly with a target's distance from the reference range bin because of the increase in spatial frequency; the error also varies somewhat with K_X. Thus, the CSA approximation results in a residual two-dimensional, space-variant phase effect in the final image.

An estimate of the size of the phase error induced by the CSA approximation begins with an estimate of the positional error in the Stolt mapping in the CSA implementation. An estimate of the Stolt mapping error is available by evaluating the second-order term in K_R of a Taylor series expansion of (11.51) about K_{Rc}, the value of K_R corresponding to center frequency f_c. The CSA approximation ignores this term and higher order terms. The second-order term dominates the remaining higher order terms and offers a reasonable estimate of the error. The Taylor series expansion of K_Y about $K_R = K_{Rc}$ for each K_X through the second-order term yields

$$K_Y \approx \sqrt{K_{Rc}^2 - K_X^2} + \frac{K_{Rc}\Delta K_R}{\sqrt{K_{Rc}^2 - K_X^2}} + b_2 \tag{11.55}$$

The second-order term b_2 has the form

$$b_2 = -\frac{K_X^2 \Delta K_R^2}{2\left(K_{Rc}^2 - K_X^2\right)^{3/2}} \tag{11.56}$$

Given a value of K_X, the maximum value of the Taylor series term b_2 occurs at the extremes of K_R. K_R has its maximum value K_{Rmax} at the highest frequency f_H of the transmitted radar signal. Similarly, K_R takes on its minimum value K_{Rmin} at the lowest frequency f_L. Thus, K_{Rmin} and K_{Rmax} are given by

$$K_{Rmin} = \frac{4\pi f_L}{c} \tag{11.57}$$

$$K_{Rmax} = \frac{4\pi f_H}{c} \tag{11.58}$$

and

$$K_{Rc} = \frac{2\pi (f_L + f_H)}{c} = \frac{4\pi f_c}{c} \tag{11.59}$$

It is reasonable to use the maximum value of K_X in (11.56) to evaluate the largest effect of b_2. For the broadside imaging case, the maximum K_X value, K_{Xmax}, occurs when α_d varies from $\pi/2$ rad by one-half the integration angle $\Delta\theta$ necessary for the desired azimuth resolution. Based on (2.19) and accepting a frequency-dependent requirement on $\Delta\theta$ to fill out the processing aperture rectangle in $\boldsymbol{K}$ space, the integration angle is available from

$$2\sin\left(\frac{\Delta\theta}{2}\right) = \frac{K_a c}{2\rho_a f} \tag{11.60}$$

Substituting $\sin(\Delta\theta/2)$ for $\cos(\alpha_d)$ in (11.52) yields an expression for K_{Xmax} in the form

$$K_{Xmax} = \frac{\pi K_a}{\rho_a} \tag{11.61}$$

It is appropriate that K_{Xmax} is constant for all K_Y in order to maintain a rectangular aperture in $\boldsymbol{K}$ space.

The b_2 term represents a distortion in the signal history format; such a distortion affects higher frequency signals more than lower frequency signals. Use of (11.56) to estimate phase error requires a relationship between distortion in $\boldsymbol{K}$ space and resulting phase error. Computation of the signal phase change per unit of spatial frequency along K_Y in $\boldsymbol{K}$ space provides this relationship. The desired relationship is the quantity $\Delta\phi_L/\Delta K_Y$, where $\Delta\phi_L$ is the linear phase along K_Y associated with a target that is at a distance Y_t from center range of the scene and ΔK_Y is the extent of the signal in K_Y. This quantity represents the phase error per unit distortion error in the K_Y transformation because of the approximation error in (11.55). The expression $\Delta\phi_L$ is

$$\Delta\phi_L = \frac{2\pi K_r Y_t}{\rho_r} \tag{11.62}$$

representing one cycle of signal for each $1/K_r$ resolution cell distance from center range. Here K_r is the mainlobe-broadening factor in range.

The deviation ΔK_Y in K_Y is approximately the interval of K_R, which is K_{Rmax} minus K_{Rmin} and equals ΔK_R. The estimate for ΔK_Y is

$$\Delta K_Y \approx \frac{4\pi (f_H - f_L)}{c} = \frac{2\pi K_r}{\rho_r} \tag{11.63}$$

Use of (11.62) and (11.63) yields

$$\frac{\Delta\phi_L}{\Delta K_Y} = Y_t \tag{11.64}$$

The final estimate of the peak phase error E_{pk} induced by the CSA approximation is this ratio times b_2, which yields

$$E_{pk} \approx \frac{-K_{Xmax}^2 (K_{Rmax} - K_{Rc})^2}{2\left(K_{Rc}^2 - K_{Xmax}^2\right)^{3/2}} Y_t \tag{11.65}$$

With some imagination, appropriate substitutions to evaluate this phase error in terms of resolution are K_{Xmax} from (11.61), $K_{Rmax} - K_{Rc}$ in the form

$$K_{Rmax} - K_{Rc} = \frac{4\pi (f_H - f_c)}{c} = \frac{\pi K_r}{\rho_r} \tag{11.66}$$

and $K_{Rc}^2 - K_{Xmax}^2$ in the form

$$K_{Rc}^2 - K_{Xmax}^2 = \left[\frac{4\pi f_c}{c}\right]^2 \left[1 - \left(\frac{cK_a}{4f_c\rho_a}\right)^2\right] \tag{11.67}$$

Using these relationships in (11.65) yields

$$E_{pk} \approx -\frac{2\pi}{\left[1 - \left(\frac{cK_a}{4f_c\rho_a}\right)^2\right]^{3/2}} \left[\frac{c}{f_c}\right]^3 \left[\frac{K_a}{4\rho_a}\right]^2 \left[\frac{K_r}{4\rho_r}\right]^2 Y_t \tag{11.68}$$

admittedly a rough but useful perspective. In Section 12.3.3, we quantify the impact of this phase effect on allowable range swath. A similar expression arises by sizing the phase error that results from using a space-invariant version of (11.45) as the matched filter.

11.5 ALGORITHM APPLICATIONS

Figure 11.15 displays a SAR image processed using the CSA. The image originates from the P-3 multimode SAR [8] using the system and processing parameters in Table 11.2. Section 10.5 and Appendix E discuss this radar system. The imaged scene is a wooded area near Portage, Maine. Displayed scene size is 2.5×1.4 km (range $\times$ azimuth). Radar illumination and near range are at the top of the image. The image has uniform weighting in both dimensions, resulting in a processed resolution of 1.1 m in both range and azimuth. Figure 11.16 is an expanded view of the clearing near the top of the CSA image. The clearing contains a number of corner reflectors deployed to assess image quality.

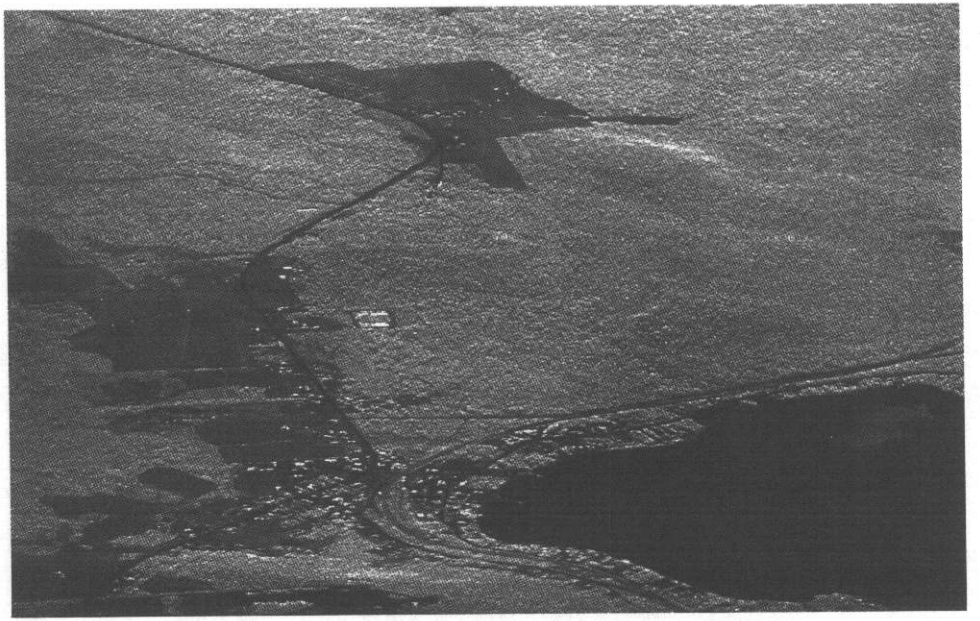


Figure 11.15 SAR image using the chirp scaling algorithm.

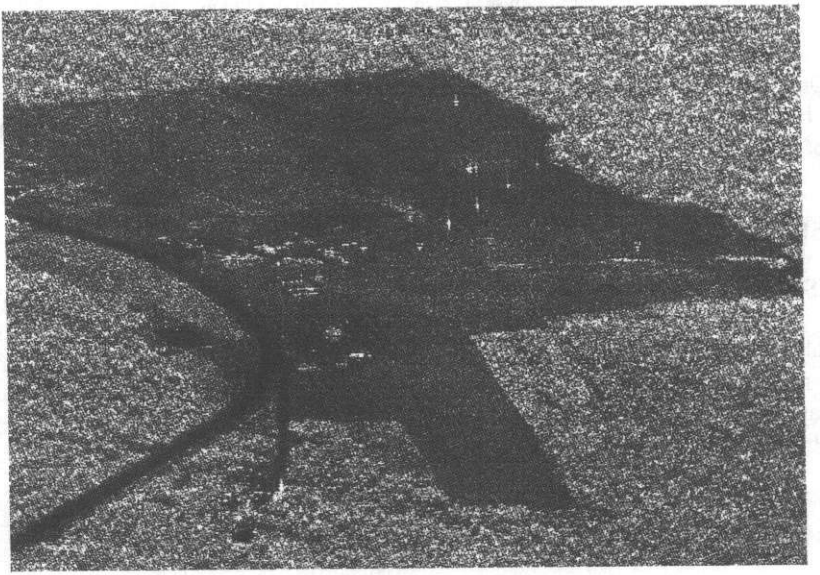


Figure 11.16 Expanded view of clearing containing engineering array.

Table 11.2
System and Processing Parameters for Chirp Scaling Image

Parameter	*Description*	*Value*
f_c	Radar center frequency	1.25 GHz
	Waveform	Linear FM without dechirp-on-receive
	Polarization	VV
B	Processed bandwidth	120 MHz
R_{ac}	Slant range to scene center	6864 m
θ_{ac}	Image squint angle	90 deg (broadside)
Ψ_{ac}	Image grazing angle	21.7 deg
L	Synthetic aperture length	667 m
$\Delta\theta$	Coherent integration angle	5.6 deg
	Aperture weighting	Uniform
ρ_r	Range resolution	1.1 m
ρ_a	Azimuth resolution	1.1 m
W_r	Range scene size	2450 m
W_a	Azimuth scene size	1420 m

One of the primary advantages of the CSA is simplicity of implementation. In fact, the C language software forming the image in Figure 11.15 consists of fewer than 200 lines of code.

11.6 SUMMARY

The CSA is attractive because of its excellent focusing ability and implementation simplicity. The algorithm requires only FFTs and complex vector multiplies without any interpolations. Because of these unique properties, it has become the subject of widespread research interest. The CSA is well suited for processing imagery from spaceborne, stripmap SAR systems [9-11]. Modifications to the chirp scaling operation improve the algorithm's ability to process squinted SAR data [12-14].

REFERENCES

[1] Raney, R.K., and P.W. Vachon, "A Phase Preserving SAR Processor," *1989 IEEE International Geoscience and Remote Sensing Symposium (IGARSS)*, Vancouver, Canada, 10-14 July 1989, pp. 2588-2591.

[2] Raney, R.K., "A New and Fundamental Fourier Transform Pair," *Proceedings of the 1992 IEEE International Geoscience and Remote Sensing Symposium (IGARSS)*, Houston, TX, 26-29 May 1992, pp. 106-107.

[3] Runge, H., and R. Bamler, "A Novel High Precision SAR Focussing Algorithm Based on Chirp Scaling," *Proceedings of the 1992 IEEE International Geoscience and Remote Sensing Symposium (IGARSS)*, Houston, TX, 26-29 May 1992, pp. 372-375.

[4] Raney, R.K., H. Runge, R. Bamler, I.G. Cumming, and F.H. Wong, "Precision SAR Processing Using Chirp Scaling," *IEEE Transactions on Geoscience and Remote Sensing*, Vol. 32, No. 4, July 1994, pp. 786-799.

[5] Raney, R.K., "An Exact Wide Field Digital Imaging Algorithm," *International Journal of Remote Sensing*, Vol. 13, No. 5, 1992, pp. 991-998.

[6] Cumming, I.G., F.H. Wong, and R.K. Raney, "A SAR Processing Algorithm with No Interpolation," *Proceedings of the 1992 IEEE International Geoscience and Remote Sensing Symposium (IGARSS)*, Houston, TX, 26-29 May 1992, pp. 376-379.

[7] Jin, M.Y., F. Cheng, and M. Chen, "Chirp Scaling Algorithms for SAR Processing," *Proceedings of the 1993 IEEE International Geoscience and Remote Sensing Symposium (IGARSS)*, Tokyo, Japan, August 1993, pp. 1169-1172.

[8] Sullivan, R., A. Nichols, R. Rawson, C. Haney, F. Darreff, and J. Schanne, Jr., "Polarimetric X/L/C-Band SAR," *Proceedings of the 1988 IEEE National Radar Conference*, Ann Arbor, MI, 20-21 April 1988, pp. 9-14.

[9] Wong, F.H., I.G. Cumming, and R.K. Raney, "Processing Simulated Radarsat SAR Data with Squint by a High Precision Algorithm," *Proceedings of the 1993 IEEE International Geoscience and Remote Sensing Symposium (IGARSS)*, Tokyo, Japan, August 1993, pp. 1176-1178.

[10] Martinez, A., and J.L. Marchand, "Implementation and Quality Analysis of a CSA SAR Processor," *Proceedings of the 1993 IEEE International Geoscience and Remote Sensing Symposium (IGARSS)*, Tokyo, Japan, August 1993, pp. 1179-1181.

[11] Chang, C.Y., M.Y. Jin, and J.C. Curlander, "SAR Processing Based on the Exact Two-Dimensional Transfer Function," *Proceedings of the 1992 IEEE International Geoscience and Remote Sensing Symposium (IGARSS)*, Houston, TX, 26-29 May 1992, pp. 355-359.

[12] Davidson, C.W., I.G. Cumming, and M.R. Ito, "An Approach for Improved Processing in Squint Mode SAR," *Proceedings of the 1993 IEEE International Geoscience and Remote Sensing Symposium (IGARSS)*, Tokyo, Japan, August 1993, pp. 1173-1175.

[13] Huang, Y., and A. Moreira, "Airborne SAR Processing Using Chirp Scaling and a Time Domain Subaperture Algorithm," *Proceedings of the 1993 IEEE International Geoscience and Remote Sensing Symposium (IGARSS)*, Tokyo, Japan, August 1993, pp. 1182-1184.

[14] Moreira, A., and Y. Huang, "Airborne SAR Processing of Highly Squinted Data Using a Chirp Scaling Algorithm with Integrated Motion Compensation," *IEEE Transactions on Geoscience and Remote Sensing*, Vol. 32, No. 5, September 1994, pp. 1029-1040.

Chapter 12
Comparison of Image Formation Algorithms

Earlier chapters describe three algorithms that can form fine-resolution digital imagery from spotlight SAR data. These algorithms are the polar format algorithm (PFA), range migration algorithm (RMA), and chirp scaling algorithm (CSA). This chapter locates each algorithm in the end-to-end implementation of the image formation processor (IFP), quantifies the computational requirements of each algorithm, and summarizes the functional and qualitative aspects of each algorithm. Appendix B introduces tomographic processing as a fourth algorithm, which this comparison does not include.

Both system requirements and algorithm capabilities influence the selection of an algorithm for a particular SAR application. Sensor parameters and characteristics of the associated signal data—in combination with image quality, image quantity, and timeliness requirements—specify the challenge to the IFP. Algorithm attributes include:

- Number of arithmetic operations to form an image;
- Memory requirements to form an image;
- Match between signal processing operations (for example, digital filtering and FFTs) that an algorithm requires and available processing hardware;
- Image quality attributes;
- Compatibility with procedures auxiliary to image formation.

Image quality attributes include the presence of residual phase errors and the introduction of image artifacts. A key compatibility consideration is the ability to efficiently insert a feed-forward autofocus procedure (such as the mapdrift algorithm) into the image formation process. A difficulty here can greatly increase overall computational complexity.

Each algorithm has distinct capabilities, procedural requirements, and limitations, both in functional aspects and in speed and operational considerations. Yet the PFA, the RMA, and the CSA are similar in their effect on input SAR data. In general, polar storage of data from each scatterer is ideal for processing spotlight data. The PFA achieves this format for a scatterer at scene center and approximately achieves it for scatterers near scene center. The CSA achieves this format for scatterers at mid-range and approximately achieves it for scatterers near mid-range. The RMA achieves this format for all scatterers.

This chapter presents procedures and considerations in evaluating an IFP algorithm for a particular application. It does not offer an absolute comparison of the algorithms. An absolute comparison naturally depends on specific sensor parameters and application requirements.

12.1 IMAGE FORMATION ALGORITHM MODELS

An evaluation of the adequacy of an image formation algorithm to satisfy a particular application requires consideration of the strengths and weaknesses of the entire processor signal chain. The processor signal chain includes mainline algorithm steps, functional requirements, and sensor-dependent operations. Mainline algorithm steps include phase compensations, data resampling, aperture weighting, and signal compression. Table 12.1 summarizes the functional considerations that earlier chapters present and the operational counts that this chapter develops (Section 12.2). Considerations that impact the operational load include motion compensation, signal projections, signal and image sampling rate adjustments, FFT operations, and autofocus. The next three sections successively present a model of the processor signal chain for each algorithm. These models separate mainline steps from procedures that depend on sensor parameters and characteristics.

Table 12.1
Algorithm Comparison Chart

IFP Algorithm	*Range Curvature Correction*	*Residual Video Phase Compensation*	*Planar Motion Compensation*	*Nonplanar Motion Compensation*	*Operational Load (real ops per pixel)*
Polar format	Partial	Possible	Compensation to point	Possible	280 (for one example)
Range migration	Complete	Possible	Compensation to line	Possible	230 (for one example)
Chirp scaling	Approximate	Unnecessary	Compensation to line	Possible	235 (for one example)

12.1.1 Polar Format Algorithm

Figure 12.1 shows a block diagram of a spotlight SAR digital image formation processor (IFP) using the PFA. Dashed lines represent processing elements that typically must be present in the signal chain yet are not integral parts of the PFA. Consideration of these ancillary elements is important when designing a processor since their presence or absence can dramatically change the signal flow and complexity of the processor.

The PFA operates on radar signal histories after removal of the chirp in range and motion compensation to a single scene point. Motion compensation to a point effectively transforms data from the azimuth-time (or azimuth-position) domain to the azimuth-frequency domain. Similarly, dechirp in range transforms the data from the range-time domain to the range-frequency domain. Thus, the PFA operates in the two-dimensional spatial-frequency or wavenumber domain.

For small angular processing intervals, it is acceptable to implement the polar format as two passes of a one-dimensional interpolation filter (Chapter 4). In this procedure, the processor first interpolates the signal data in the range dimension and continues with

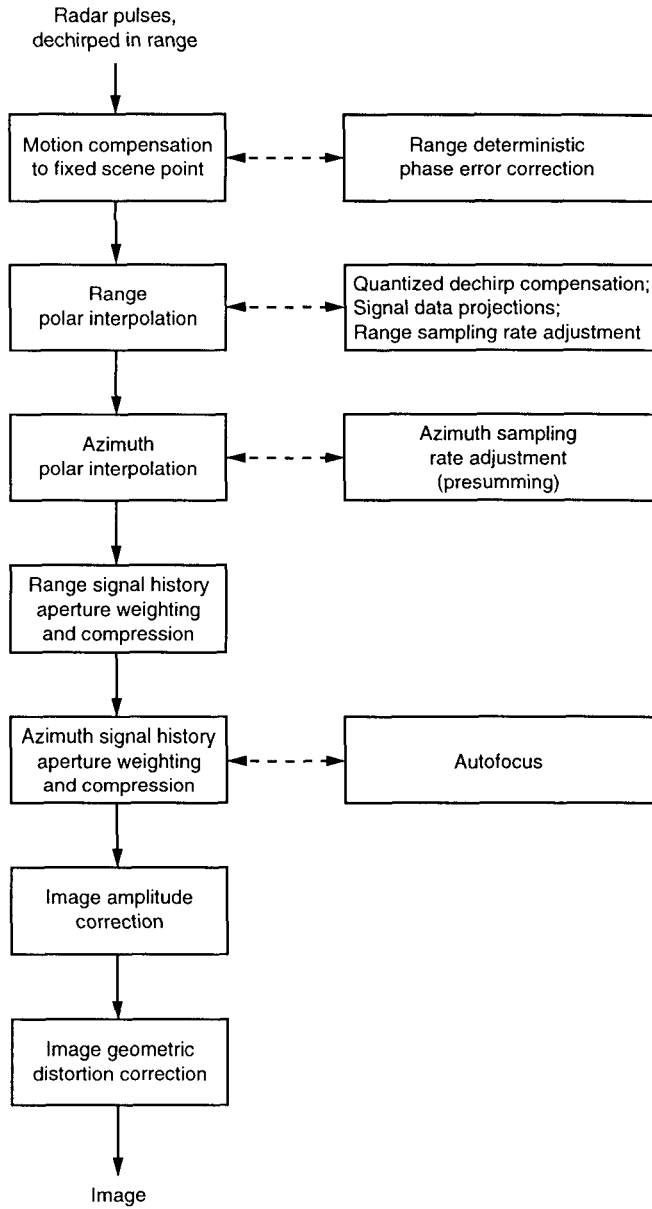


Figure 12.1 Spotlight SAR processor using the PFA.

interpolation in the azimuth direction. Then, a two-dimensional FFT forms the complex image. As Figure 12.1 suggests, the processor can perform several functions in parallel with the range and azimuth interpolation steps. These additional functions involve changes in the data sample spacing and fit easily into the resampling operations that naturally occurs during polar formatting. These functions include compensating for phase errors that a nonplanar data collection surface introduces (Section 3.8 and Section 4.6.1), changing the output image display plane (Section 4.6.2), accounting for nonuniform spatial sampling in the azimuth direction, presumming the signal data in azimuth, and removing the effects of a quantized dechirp reference delay (Section 2.6.4). The opportunity to package these compensations into a single resampling step makes the PFA an efficient image formation approach for many fine-resolution SAR systems.

12.1.2 Range Migration Algorithm

Figure 12.2 illustrates the steps in a spotlight SAR processor using the RMA. The RMA operates on signal histories with motion compensation to a line (Section 10.1) rather than to a fixed point. The motion compensation to a line produces a signal history that is chirped in azimuth. In range, however, the RMA operates on a signal history that is dechirped. The first step of the RMA is a one-dimensional FFT in the azimuth dimension. After this step, the RMA operates in the range-frequency/azimuth-frequency (Doppler) domain. Operations in this two-dimensional spatial-frequency domain involve a two-dimensional signal phase adjustment, a one-dimensional interpolation in the range dimension, and a two-dimensional FFT to generate the output complex image. Depending on the characteristics of the SAR sensor and the data collection geometry, a number of preprocessing operations may be necessary prior to the first azimuth FFT. These operations include azimuth resampling to reduce data rates and achieve constant azimuth sample spacing and range resampling to alleviate the effects of a nonplanar data collection surface. Range resampling also serves to remove the effects of a quantized dechirp reference delay (Section 2.6.4).

12.1.3 Chirp Scaling Algorithm

Figure 12.3 shows the steps of a spotlight SAR processor using the CSA. The CSA is a variation to the range migration procedure. Like the RMA, the CSA must operate on signal data with motion compensation to a line rather than to a fixed point. Unlike the RMA, the CSA can only accept linear FM data without dechirp in range. If the range chirp is not present in the digitized signal history data, a preprocessing step must reapply the range chirp at the original chirp rate. The CSA operates in the range-time/azimuth-frequency domain for some operations and in the two-dimensional spatial-frequency domain for others.

By itself, the CSA has the attractive property that it requires only FFTs with no resampling operations [1]. However, depending on the exact characteristics of the sensor

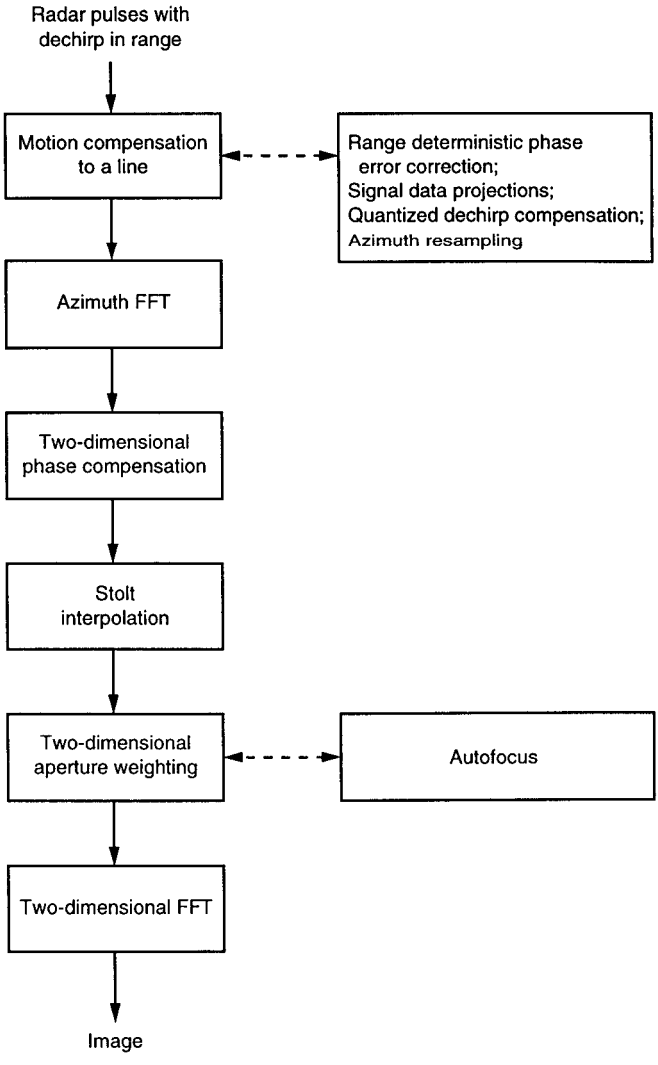


Figure 12.2 Spotlight SAR processor using the RMA.

and data collection geometry, azimuth and range resampling of the signal history may be necessary before CSA processing. The processor may need to resample in azimuth to produce a signal history with a constant azimuth sample spacing. If the input signal history is dechirped in range, the processor may need to resample (upsample) each pulse in range in order to reapply the range chirp.

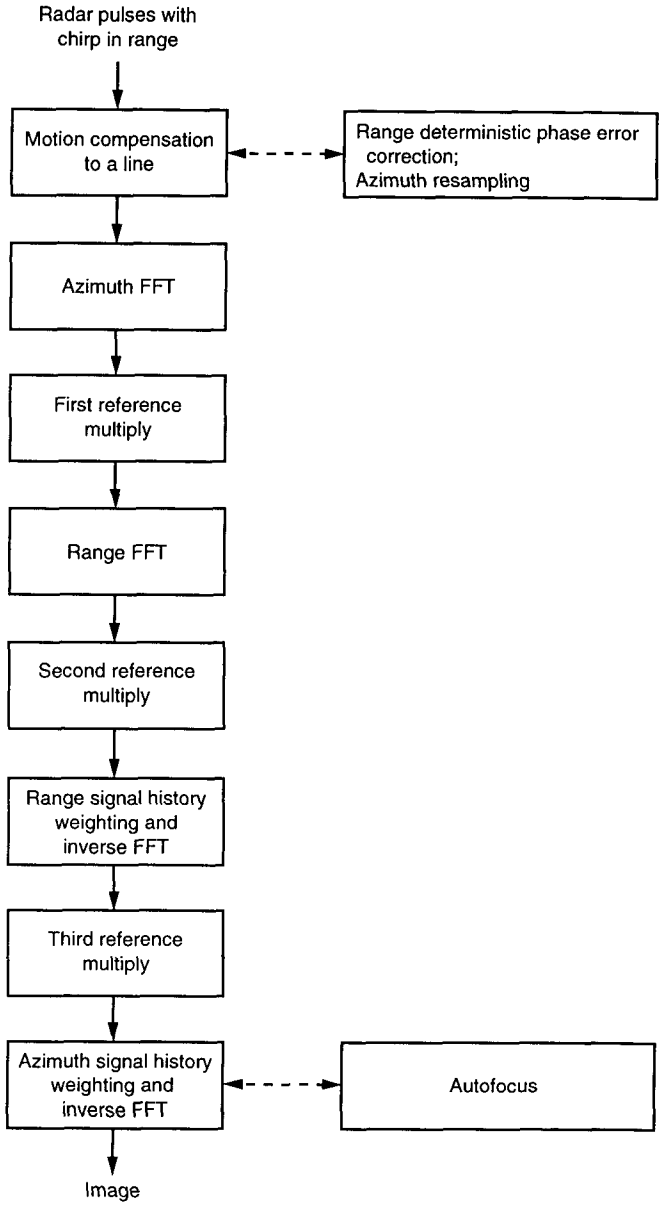


Figure 12.3 Spotlight SAR processor using the CSA.

12.2 COMPUTATIONAL COMPLEXITY

Many possible approaches exist to evaluate the computational complexity of an algorithm. This section presents an approach based on estimating the number of complex operations for each major step in the algorithm. A complex operation is one radix-2 FFT butterfly. A single radix-2 FFT butterfly consists of one complex multiply and two complex additions; the butterfly equates to four floating point multiplies and six floating point additions for a total of ten floating point (real) operations. Assuming equal computational cost for multiplies and additions, it is reasonable to use the 10-to-1 conversion from complex to floating point operations at all stages of evaluation, not just for the FFTs. The complex operation count C_{fft} for an FFT of size N is [2]

$$C_{fft} = \left(\frac{N}{2}\right) \log_2 N \tag{12.1}$$

In analyzing non-FFT stages, a complex multiply operation consisting of four floating point multiplies and two additions counts as one complex operation. Motion compensation and reference multiplications involve complex multiplies. A complex-by-real multiply consists of two floating point multiplies and counts as one-half of a complex operation. The range and azimuth phase history weighting operations in the PFA are examples of complex-by-real multiplies.

The complex operations count C_p to perform an interpolation is available by expanding (4.11) or an equivalent expression and counting the number of operations necessary to compute each output point. For N output points, this procedure generalizes to

$$C_p = 0.4N[\,(L_f - 1)\,DSR + 1\,]\,M_k \tag{12.2}$$

where L_f is the length of the interpolation filter expressed in output samples and DSR is the downsampling ratio (the total number of input samples divided by the total number of output samples). The factor M_k is an estimation margin that adjusts for the filter coefficient indexing characteristics specific to digital resampling. A typical value for M_k is 1.25, making (12.2) equal to

$$C_p = 0.5N[\,(L_f - 1)\,DSR + 1\,] \tag{12.3}$$

Equation (12.3) applies to polar-to-rectangular interpolation, Stolt interpolation, azimuth resampling, and image resampling.

The complex operations count approach slightly overestimates the total operations count for a given algorithm. In so doing, however, it does provide a margin for uncounted machine cycles such as array index generation, submodule setup, and memory access. Typical spotlight SAR data and image sizes quickly produce operations counts in the millions and tens of millions. These estimates are rounded up to the nearest one hundred thousand. Multiplication of the estimate of an algorithm's total number of complex operations by ten converts the estimate to floating point operations. Dividing this count by the number of image pixels produces an estimate of the number of floating point operations per pixel (ops/pixel).

The radar system and geometry parameters in Table 2.4 through Table 2.6 provide a useful example to illustrate a comparison of IFP algorithms. These parameters describe a 1-m resolution, air-to-ground spotlight SAR system. Table 12.2 summarizes the radar parameters that are important to this algorithm comparison together with key processing parameters. This comparison assumes a broadside spotlight collection with video data in the format that each algorithm requires. The PFA and RMA begin with radar pulses that are dechirped in range while the CSA begins with pulses that are chirped in range. This starting point puts the three algorithms on a roughly equal footing for evaluation of computational requirements. We further simplify the comparison by considering only the mainline steps of each algorithm. Except for autofocus, the additional sensor-dependent functions largely accompany mainline steps without added computational burden. Figure 12.1 through Figure 12.3 display these ancillary operations on the right side, connected to the mainline algorithm by dashed lines. Autofocus is often an essential step in air-to-ground image formation processing; to first order, it impacts each algorithm equally and does not impact the comparison. This evaluation assumes an output image size of 1024×1024 pixels and an image sample density S_d of 1 sample per resolution cell.

Table 12.2
Key System Parameters in Operations Count Analysis

Parameter	*Description*	*Value*
λ_c	Radar center wavelength	0.03 m
R_{ac}	Slant range at aperture center	10 km
V_{xa}	Sensor along-track velocity	100 m/s
T_a	Synthetic aperture time	1.95 s
K_r, K_a	Mainlobe-broadening factors	1.23, 1.30
ρ_r, ρ_a	Range and azimuth resolutions	1, 1 m
W_r, W_a	Range and azimuth scene sizes	1024, 1024 m
N_{ir}, N_{ia}	Range and azimuth image sizes	1024, 1024 pixels
S_d	Image sample density (pixels/resolution cell)	1, 1
K	Complex samples per pulse (range)	reduced to 1024
N_p	Pulses over synthetic aperture (azimuth)	reduced to 1024
H_{fp}	Polar interpolation filter length	10 samples
H_{fs}	Stolt interpolation filter length	10 samples

Table 12.3 through Table 12.5 detail the operations count per pixel for each of the algorithms under consideration in the X-band imaging situation that Table 12.2 describes. We obtain these numbers by applying (12.1) and (12.3) to each block of Figure 12.1

Table 12.3
Operations Count for the PFA

Algorithm Element	*Complex Operations (millions)*
Motion compensation	1.05
Range polar interpolation	5.24
Azimuth polar interpolation	5.24
Range weighting	0.52
Range FFT	5.24
Azimuth weighting	0.52
Azimuth FFT	5.24
Image amplitude correction	1.05
Image distortion correction	5.24
Total Complex Operations	29.36
Real Operations	293,600,000
Real Operations per Pixel	280

Table 12.4
Operations Count for the RMA

Algorithm Element	*Complex Operations (millions)*
Motion compensation	1.05
Azimuth FFT	5.24
Two-dimensional phase compensation	1.05
Stolt interpolation	5.24
Two-dimensional aperture weighting	1.05
Two-dimensional FFT	10.49
Total Complex Operations	24.12
Real Operations	241,170,000
Real Operations per Pixel	288

through Figure 12.3. These tables suggest that the three IFP algorithms are comparable in terms of operations count per pixel in this case. The FFTs dominate the operations counts for each of the three algorithms. The operations count for each algorithm depends on radar center frequency, platform velocity, radar PRF, the imaging geometry, and final image resolution. Looking beyond this specific example, larger differences in the total operations per pixel are common. Additionally, the ancillary signal processing operations not considered in this presentation often greatly increase the final operations count.

Table 12.5
Operations Count for the CSA

Algorithm Element	*Complex Operations (millions)*
Motion compensation	1.05
Azimuth FFT	5.24
First reference multiply	0.52
Range FFT	5.24
Second reference multiply	0.52
Range aperture weighting	0.52
Range inverse FFT	5.24
Third reference multiply	0.52
Azimuth aperture weighting	0.52
Azimuth inverse FFT	5.24
Total Complex Operations	24.64
Real Operations	246,420,000
Operations per Pixel	235

12.3 ADDITIONAL ASPECTS OF ALGORITHM PERFORMANCE

This section moves beyond the topic of computational complexity. It considers additional algorithm performance factors and limitations that impact evaluation of the PFA, RMA, and CSA for imaging radar systems.

12.3.1 Polar Format Algorithm

The PFA compensates for scatterer motion through range and Doppler resolution cells in fine-resolution, spotlight mode SAR. This compensation is incomplete and leaves a residual space-variant phase effect referred to as range curvature. Consequently, images of

large scenes can suffer from geometric distortion, quadratic defocus, and higher order image smearing. The geometric distortion is deterministic. Thus, the digital resampling of a processed image from distorted pixel locations to undistorted coordinates (Section 4.5) easily removes this distortion. The quadratic phase error (QPE) induced by range curvature is also deterministic, but difficult to remove with postprocessing procedures because it is space-variant. Section 3.7 develops an equation to describe the QPE. For the broadside imaging case, the magnitude of this phase error increases with target distance from the scene diagonals given by $X_t = \pm Y_t S_{\phi c}$ for scatterers in the XY plane with scene coordinates $(X_t, Y_t, 0)$. Here $S_{\phi c}$ is $\sin(\phi_{ac})$ with ϕ_{ac} being the value of the incidence angle at aperture center. The usual method to deal with this phase error limits the processed scene size to hold the QPE to an acceptable level. Higher order phase errors induced by range curvature are not a factor.

Table 12.6 indicates the scene diameter that the PFA can process at various radar wavelengths and resolutions while limiting range curvature phase error to $\pi/2$ rad. Based on (3.130), this table examines the ability to image a scene of 8000-m diameter at a range of 10 km with $K_a = 1.3$. Allowable scene size decreases gradually with finer resolution.

Table 12.6
Limit on Scene Diameter (m) from Range Curvature QPE at 10-km Slant Range

	Wavelength (Frequency)			
Resolution	*0.01 m (30 GHz)*	*0.03 m (10 GHz)*	*0.2 m (1.5 GHz)*	*0.6 m (500 MHz)*
10 m	Full size	Full size	6880	3972
3 m	Full size	5329	2064	1192
1 m	3077	1776	688	397
0.3 m	923	533	206	119
0.15 m	462	266	103	60

To produce a 2.4 × 2.4-km scene (a reasonable goal) with 1-m resolution at 1.5 GHz *and* limit the range curvature QPE to $\pi/2$ rad, the PFA processor must divide the desired scene into four subswaths in range, each with four subpatches in azimuth. After forming these 16 subimages using the PFA, the digital processor must mosaic them together to yield an image meeting the scene size goal. At X-band, only 4 subimages are necessary to produce a 2.4 × 2.4-km scene. Section 4.8 discusses this *subpatch processing* approach to polar format processing of SAR data.

The subpatch processing approach is extremely inefficient. For the 1.5-GHz case at 1-m resolution, it is necessary to process the signal history 16 times in order to produce an output image. Another difficulty with subpatch processing is that phase and amplitude discontinuities are inevitable at the subpatch boundaries. Amplitude discontinuities affect the interpretability of processed images, while phase discontinuities affect image utility for exploitation techniques that use image phase.

12.3.2 Range Migration Algorithm

Chapter 10 provides a complete description of the RMA. Key attributes of the RMA are:

1. It solves exactly the problem of scatterer motion through resolution cells and leaves no geometric (keystone) distortion or residual quadratic phase error;
2. It requires signal histories dechirped in range and chirped in azimuth;
3. It can process SAR data in both stripmap and spotlight modes;
4. No subpatch or subswath boundaries are present in RMA-generated images.

These attributes indicate the appeal of the RMA. It readily accommodates a large scene without undesirable effects on image quality.

A disadvantage of the RMA is its need to operate on azimuth-chirped data (Section 10.1). This requirement necessitates high along-track sampling rates at the front end of the processor. This difficulty is not unique to the RMA; the CSA and most stripmap image formation algorithms also operate on azimuth-chirped signal history data.

Another potential disadvantage of the RMA arises in its application to fine-resolution systems. Chapter 5 discusses the residual video phase (RVP) effect, which exists in chirp-waveform systems that dechirp in the range-time domain. Section 10.1 states that the RVP error is generally larger in the RMA processor than in the PFA processor. RVP is safely ignored in many fine-resolution systems that utilize the PFA. However, these same systems often cannot neglect RVP when performing RMA processing. Hence, the RMA may require the additional burden of range deskew. If RVP is large enough to warrant compensation, the IFP may eliminate it using the range deskew algorithm of Appendix C. Although simple to implement, range deskew can significantly degrade processor throughput since it requires computation of the forward and inverse FFT of every radar pulse.

12.3.3 Chirp Scaling Algorithm

The CSA is attractive because of its implementation simplicity. The algorithm requires only FFTs and complex vector multiplies without any interpolations. The CSA for SAR image formation is a computationally efficient approximation to the RMA. The nature of the approximation is, in effect, to replace the nonlinear Stolt transformation of the RMA by a linear transformation implemented by a complex multiplication in the time domain. The CSA implements only the shift and linear components of the Stolt transformation, ignoring the higher order components of the Stolt mapping. This approach becomes inadequate as resolution becomes finer and scene size increases. Eventually, this approximation leads to unacceptable transformation errors that cause two-dimensional, space-variant phase effects in the final image.

To adjust the range dechirp function, the CSA must operate on signal history data that is chirped in range. This need can lead to difficulty when applying the CSA to SAR systems that employ dechirp-on-receive (as many fine-resolution systems do). To utilize the CSA, a preprocessor must rechirp the signal histories from these systems at the original chirp rate. The rechirping process must first upsample the data from each range

record to support the full wideband chirp by the ratio B/B_{IF}, where B is the transmitted RF bandwidth and B_{IF} is the dechirped IF bandwidth associated with scene size in range. Such upsampling can be a major computational and memory bottleneck. For example, the spotlight SAR design in Table 2.4 through Table 2.6, possesses a ratio of RF to IF bandwidth of 5.5 from 185MHz/33.62MHz. Rechirping each of these pulses requires a 5.5-fold increase in the number of complex samples, which represents a large impact on data storage and processing requirements.

A determination of the applicability of the CSA to a particular radar imaging system requires an estimate of the phase error that the Stolt approximation of the CSA causes. From (11.68), an expression for allowable range scene extent W_R (based on $2Y_t$) to limit phase error to $\pi/2$ rad is

$$W_R \approx \frac{\lambda_c}{2}\left[\frac{4\rho_a}{\lambda_c K_a}\right]^2\left[\frac{4\rho_r}{\lambda_c K_r}\right]^2\left[1-\left(\frac{\lambda_c K_a}{4\rho_a}\right)^2\right]^{3/2} \tag{12.4}$$

Table 12.7 quantifies this limit on W_R at typical radar wavelengths and resolutions. It examines the ability to image a 8000-m range swath scene with $K_a = 1.30$ and $K_r = 1.23$. These results suggest that the CSA may not an acceptable IFP algorithm for imaging larger scenes at lower frequency and finer resolution. The CSA can be a satisfactory choice at coarser resolutions and at X-band and K_u-band frequencies.

Table 12.7
Limit (m) on Scene Size W_R Imposed by the CSA Stolt Approximation

	Wavelength (Frequency)			
Resolution	*0.01 m (30 GHz)*	*0.03 m (10 GHz)*	*0.2 m (1.5 GHz)*	*0.6 m (500 MHz)*
10 m	Full size	Full size	Full size	Full size
3 m	Full size	Full size	Full size	Full size
1 m	Full size	Full size	6218	219
0.3 m	Full size	Full size	47	1
0.15 m	Full size	933	2	None

12.4 SUMMARY

Image resolution, scene size, and radar center frequency are primary influences on the ability of an image formation algorithm to process SAR signal data with adequate image quality. Other factors influence the efficiency and timeliness of the image formation process. These factors involve system requirements such as the use of dechirp-on-receive, the need for radar mode flexibility, necessary ancillary operations such as azimuth pre-summing and autofocus, and any image formation hardware constraints. Other factors

involve algorithm requirements including operations counts and signal processing functions required by the algorithm such as FFTs and interpolations.

Table 12.8 summarizes key attributes of three SAR image formation algorithms with respect to factors important in algorithm selection. The question of operations counts requires evaluation on a case-by-case basis.

Table 12.8
Key Algorithm Attributes

Parameter	*PFA*	*RMA*	*CSA*
Signal input (range)	Dechirped	Dechirped	Chirped
Signal input (azimuth)	Dechirped	Chirped	Chirped
Motion compensation	To a point	To a line	To a line
Treatment of motion through resolution cells	Partial (range curvature remains)	Complete	Approximate
Mode processing capability	Spotlight Stripmap (with limits)	Spotlight Stripmap	Spotlight Stripmap
Resolution capability	Limited by range curvature (varies with scene size and radar center frequency)	Unlimited by processor	Limited by approximation to Stolt interpolation (varies with scene size and radar center frequency)
Scene size	Limited by range curvature (varies with resolution and radar center frequency)	Unlimited by processor	Limited by approximation to Stolt interpolation (varies with resolution and radar center frequency)
Signal processing functions	FFTs and two one-dimensional interpolations	FFTs and a one-dimensional interpolation	FFTs without interpolation
Autofocus availability	Feed-forward	Feed-forward	Feed-forward
Operations counts	Case-dependent	Case-dependent	Case-dependent

REFERENCES

[1] Bamler, R., "A Systematic Comparison of SAR Focussing Algorithms," *Proceedings of the 1991 IEEE International Geoscience and Remote Sensing Symposium (IGARSS)*, Espoo, Finland, 3-6 June 1991, pp. 1005-1009.

[2] Blahut, R.E., *Fast Algorithms for Digital Signal Processing*, Reading, MA, Addison-Wesley, 1985.

Appendix A
A Fast Algorithm for Digital Quadrature Demodulation

SAR image formation requires making phase and frequency adjustments to the received signal history. The received signals are naturally time-varying voltage waveforms, that is, real-valued signals. By converting these signals into in-phase and quadrature components, a simple multiplication of each sample with the appropriate complex number achieves the desired phase adjustment to that signal sample. The radar system can perform this conversion either before or after digitization of the signals. The conversion procedure is known as *quadrature demodulation*. Figure A.1 shows the common technique for obtaining these components directly from the received analog signals. Following analog quadrature demodulation, the radar system digitizes the two output signal components simultaneously via two analog-to-digital (A/D) converters.

This appendix presents an efficient algorithm to obtain the in-phase and quadrature components of received signals after digitization. Digital implementation of this operation has several advantages over the equivalent analog implementation of Figure A.1. The digital approach easily maintains amplitude and phase balance between the two mixers (Figure A.1) involved in the procedure. Also, the digital implementation tightly controls the magnitude and phase responses of the two low-pass filters.

The quadrature demodulation procedure for a digital signal involves:

1. Shifting the signal frequency to remove its offset carrier frequency;
2. Low-pass filtering the baseband signal to remove high-frequency sidebands resulting from the first step;
3. Downsampling the low-pass filtered signal to reduce the sampling rate.

A description of this procedure begins with a real-valued, bandlimited signal $s_r(m)$ consisting of M real samples, with $m = 0, 1, \ldots, M - 1$. The real sampling rate F_{rs} produces a spacing of $1/F_{rs}$ between samples. Most radar system designs place $s_r(m)$ on an offset (carrier) frequency equal to one-quarter of the A/D sampling rate. Such a design minimizes the required bandwidth of the radar's data acquisition subsystem. Digital quadrature demodulation exploits this relationship between A/D rate and carrier frequency to significantly reduce the required computations [1].

The first step in the digital procedure removes the carrier frequency f_{vo} by means of multiplication of $s_r(m)$ by a complex exponential with phase $-2\pi f_{vo}m/F_{rs}$. The result

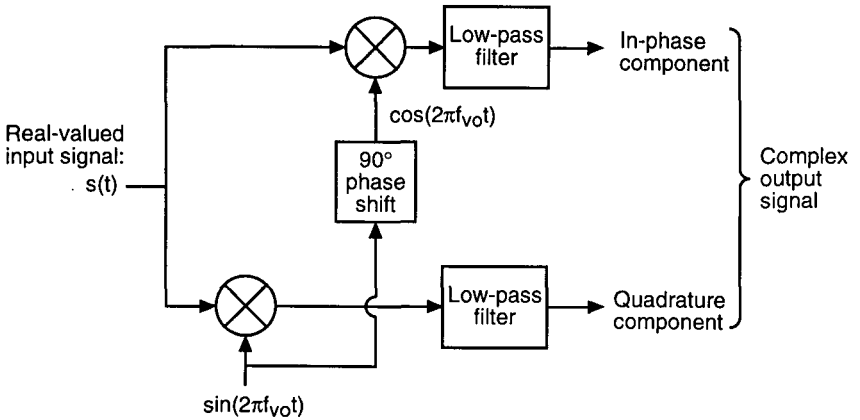


Figure A.1 Analog quadrature demodulation.

of this step is

$$s_c(m) = s_r(m)\, e^{-j2\pi\left(\frac{f_{vo}}{F_{rs}}\right)m} \qquad m = 0, 1, \ldots, M-1 \tag{A.1}$$

The resulting signal $s_c(m)$ is a complex sequence of length M. Figure A.2 illustrates carrier frequency removal in the frequency domain. Figure A.2(a) depicts the spectrum of a real-valued signal $s_r(m)$. Since the signal is real-valued, its spectrum is symmetric about zero frequency [2]. The multiplication in (A.1) circularly shifts the entire spectrum of $s_r(m)$ to the left by an amount f_{vo}. Figure A.2(b) shows this shift.

Having assumed that $f_{vo}/F_{rs} = 1/4$, the complex exponential in (A.1) has the properties that every other real sample is zero, every other imaginary sample is zero, and all other real and imaginary samples alternate between +1 and −1. The first few values of the exponential in (A.1) are

$$e^{-j\frac{\pi}{2}m} = \begin{cases} 1+j0 & m=0 \\ 0-j1 & m=1 \\ -1+j0 & m=2 \\ 0+j1 & m=3 \\ 1+j0 & m=4 \\ \vdots & \vdots \end{cases} \tag{A.2}$$

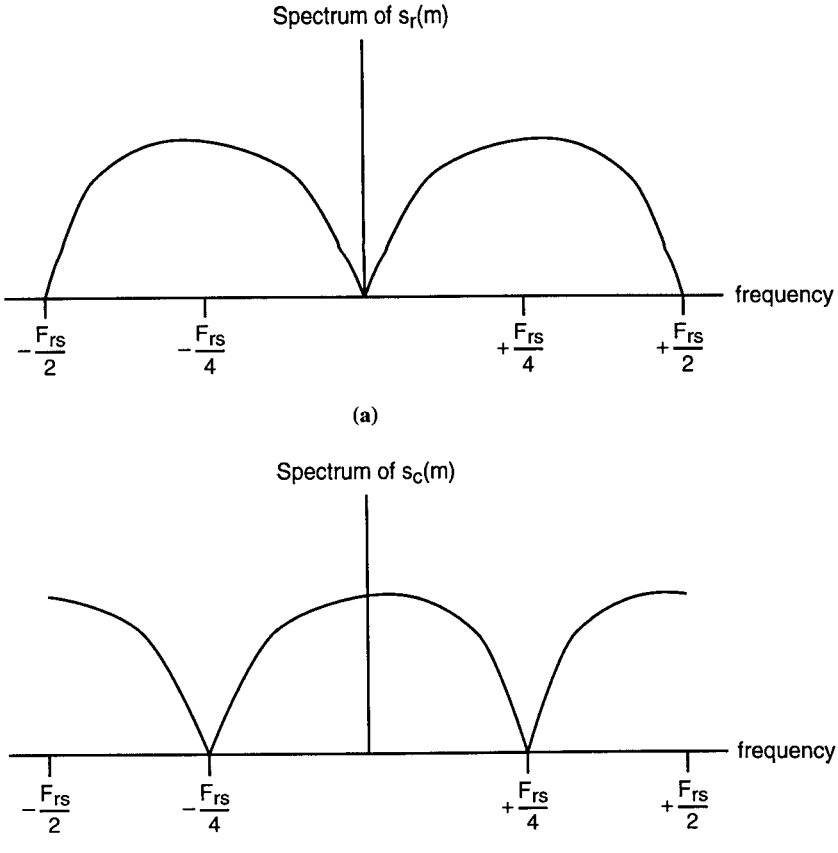


Figure A.2 Carrier frequency removal: **(a)** Original signal spectrum; **(b)** Spectrum after removing carrier.

In terms of $s_r(m)$, the complex product $s_c(m)$ is

$$s_c(m) = \begin{cases} s_r(0) + j0 & m = 0 \\ 0 - js_r(1) & m = 1 \\ -s_r(2) + j0 & m = 2 \\ 0 + js_r(3) & m = 3 \\ s_r(4) + j0 & m = 4 \\ \vdots & \vdots \end{cases} \tag{A.3}$$

Thus, it is easy to compute $s_c(m)$ by negating $s_r(m)$ for appropriate values of m and inserting zeros as real or imaginary components where necessary. Implementation in a digital processor may skip subsequent multiplications involving one of the zero components of $s_c(m)$, so it is not necessary to either insert zeros or calculate the products.

The next step low-pass filters $s_c(m)$ to remove the high-frequency sidebands arising from the mixing operation. Figure A.2(b) shows these sidebands. An optimal finite impulse response (FIR) halfband filter performs this filtering. For odd length filters, such filters have the property that all even-numbered filter coefficient are zero except for the center coefficient. Figure A.3 shows an example halfband FIR filter. Figure A.3(a) illustrates the impulse response *h(m)* of a 29-point filter. All even samples of this particular filter are zero except for the center sample *h(14)*. Figure A.3(b) shows the magnitude of the filter's frequency response.

The digital filtering operation reduces total signal energy by one-half because it completely removes one sideband. The filter requires a gain of 2.0 to preserve unity gain for the overall demodulation algorithm. In this way, the algorithm converts a real-valued input signal into a complex signal having the same magnitude.

Low-pass filtering leaves the resulting complex signal oversampled by a factor of two. Downsampling (decimation) of the signal to prevent an unnecessary computational burden involves discarding every other sample at the output of the low-pass filter. Proper design of the digital filter preceding the downsampling operation keeps aliasing signal components below an acceptable level.

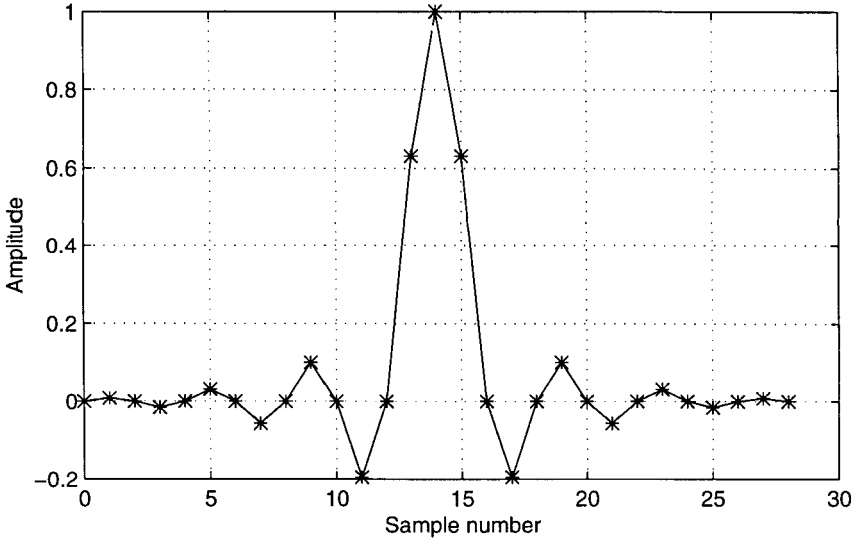
Consider the low-pass filter *h(m)* with $m = 0, 1, \ldots, M_F$ and M_F an even number so that the filter has odd length and possesses the properties noted above. We assume the filter procedure properly zero-pads $s_c(m)$ at each end to accommodate filter overhang during filtering; this means that $s_c(m) = 0$ for all $m < 0$ and $m > M - 1$. This consideration is necessary because the filter produces $M/2$ complex output samples using the M real input samples. The complex sequence *y(m)* output from the filter is the convolution

$$y(m) = \sum_{k=0}^{M_F} s_c(m-k)\, h(k) \qquad m = 0, 1, \ldots, M + M_F - 1 \qquad \text{(A.4)}$$

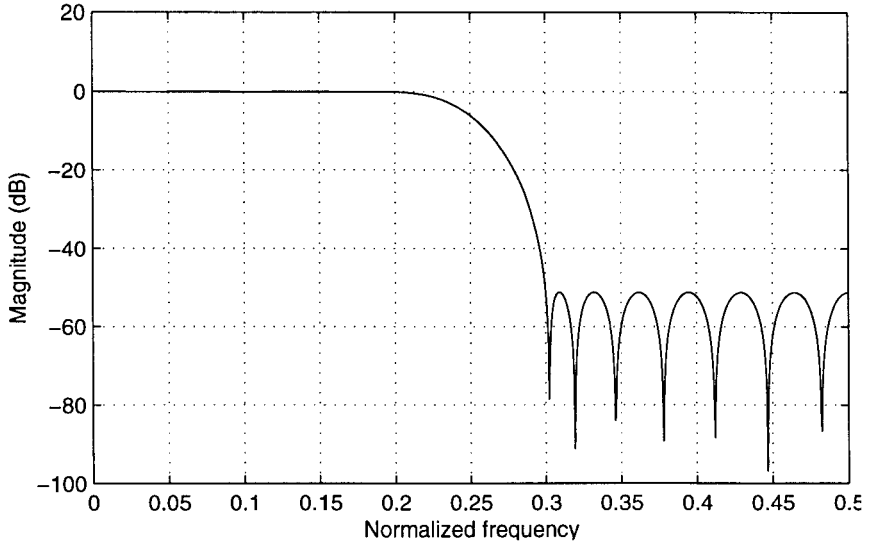
Since the filter is downsampling by a factor of 2, it computes $y(m)$ for only odd values of m, to eliminate half of the computations. This procedure corresponds to taking every other output sample, beginning with the second point, to produce the output $y'(r) = y(2r+1)$ with $r = 0, 1, \ldots, (M + M_F)/2 - 1$, assuming for simplicity that M is also even. The downsampled sequence $y'(r)$ becomes

$$y'(r) = \sum_{k=0}^{M_F} s_c(2r+1-k)\, h(k) \qquad r = 0, 1, \ldots, \frac{M + M_F}{2} - 1 \qquad \text{(A.5)}$$

The output signal contains half as many points as the input signal.



(a)



(b)

Figure A.3 Example halfband FIR filter: **(a)** Impulse response *h(m)*; **(b)** Magnitude of frequency response.

Since the filter coefficients are real-valued, the real and imaginary components of the output sequence are

$$\mathrm{Re}\{y'(r)\} = \sum_{k=0}^{M_F} h(k)\,\mathrm{Re}\{s_c(2r+1-k)\} \qquad r = 0, 1, \ldots, \frac{M+M_F}{2}-1 \qquad \text{(A.6)}$$

$$\mathrm{Im}\{y'(r)\} = \sum_{k=0}^{M_F} h(k)\,\mathrm{Im}\{s_c(2r+1-k)\} \qquad r = 0, 1, \ldots, \frac{M+M_F}{2}-1 \qquad \text{(A.7)}$$

Examination of (A.2) reveals that $\mathrm{Re}\{s_c(r)\}$ is zero for odd values of r and $\mathrm{Im}\{s_c(r)\}$ is zero for even values of r. The filter need not compute multiplications involving such terms, again reducing computations during low-pass filtering. A rewrite of (A.6) and (A.7) to reflect this property yields the real and imaginary components of the output signal as

$$\mathrm{Re}\{y'(r)\} = \sum_{l=0}^{M_F/2-1} h(2l+1)\,\mathrm{Re}\{s_c(2r-2l)\} \qquad \text{(A.8)}$$

$$\mathrm{Im}\{y'(r)\} = \sum_{l=0}^{M_F/2} h(2l)\,\mathrm{Im}\{s_c(2r-2l+1)\} \qquad \text{(A.9)}$$

with $r = 0, 1, \ldots, (M+M_F)/2-1$. Substitution of the value $2l+1$ for k in (A.6) and the value $2l$ for k in (A.7) yields (A.8) and (A.9). The rewriting process includes adjustment of the summation limits in (A.8) and (A.9) by noting that when M_F is even there are $M_F/2$ odd filter samples and $M_F/2+1$ even filter samples.

When computing the imaginary component of filter outputs, (A.9) indexes only even filter coefficients. However, values of the filter are zero for all even coefficients except the middle one with value $h(M_F/2)$. This consideration leads to the result that

$$\mathrm{Im}\{y'(r)\} = h\left(\frac{M_F}{2}\right)\mathrm{Im}\left\{s_c\left(2r-\frac{M_F}{2}+1\right)\right\} \qquad r = 0, 1, \ldots, \frac{M+M_F}{2}-1 \qquad \text{(A.10)}$$

Equation (A.8) indexes only odd filter coefficients and offers no further reduction in computations when computing the real component of filter outputs. The signal $y'(r)$ contains $(M+M_F)/2$ complex samples; only the middle $M/2$ samples are valid due to filter overhang at both ends of the sequence.

A single multiply computes the imaginary component of each filter output sample. Total computational load for each complex output sample is $M_F/2-1$ real additions and $M_F/2+1$ real multiplications. This fast algorithm represents an almost eightfold reduction in computations compared to a conventional implementation of the same high-quality digital filter.

REFERENCES

[1] Mitchel, R.L., "Creating Complex Signal Samples from a Band-Limited Real Signal," *IEEE Transactions on Aerospace and Electronic Systems*, Vol. 25, No. 3, May 1989.

[2] Oppenheim, A.V., and R.W. Schafer, *Digital Signal Processing*, Englewood Cliffs, NJ, Prentice-Hall, Inc., 1975.

Appendix B
Tomographic Processing of Spotlight Data

This book describes three algorithms for spotlight SAR image formation. Chapter 3 presents the polar format algorithm (PFA). Chapters 10 and 11 discuss two wavenumber domain approaches, the range migration algorithm (RMA) and the chirp scaling algorithm (CSA), respectively. Chapter 12 compares and contrasts these three algorithms.

This appendix provides a qualitative introduction to a fourth algorithm called tomographic processing or tomographic reconstruction (TR). The medical community uses X-ray-based tomography [1] for noninvasive examinations of the body's internal organs, while the manufacturing world employs tomographic imaging for nondestructive parts testing. TR provides another path for computing an image from spotlight SAR data.

Many excellent publications describing TR techniques are available. In particular, [2] provides a rigorous development of TR for spotlight SAR image formation. Additional information is available in [3-5]. As we will see, TR carries a high computational burden, which limits its use in many operational systems. For these reasons, this book assigned TR to an appendix and presents it in less detail than other image formation approaches.

B.1 TOMOGRAPHIC RECONSTRUCTION

A discussion of the TR algorithm begins with the spotlight SAR collection geometry in Figure B.1. For simplicity, this model considers a two-dimensional (X, Y) geometry in which radar wavefront curvature across the scene is less than the width of a range resolution cell. Additionally, the sensor travels in a perfect circle around scene center at a constant angular rotation rate. Figure B.1 shows the positions of three scatterers (A, B, and C) within the imaged scene.

As the sensor travels along its circular flight path, the radar transmits linear FM pulses at a constant rate. The system dechirps each returned pulse by mixing it with a delayed version of the transmitted pulse. The dechirp delay time is equal to the two-way time delay experienced by a pulse returned by a scatterer at scene center (Section 2.6.4). This dechirping procedure causes the returned signal from each scatterer to be a sinusoid with frequency proportional to the scatterer's differential range at the time of each pulse transmission. Differential range is $R_t - R_a$, where R_t is the distance from the antenna phase center (APC) to the scatterer, and R_a is the distance from the APC to scene center.

The radar line-of-sight (LOS) vector is a line from the radar APC to scene center. At pulse n, the radar LOS vector *slices* through the scene at the angle θ_n relative to the X axis

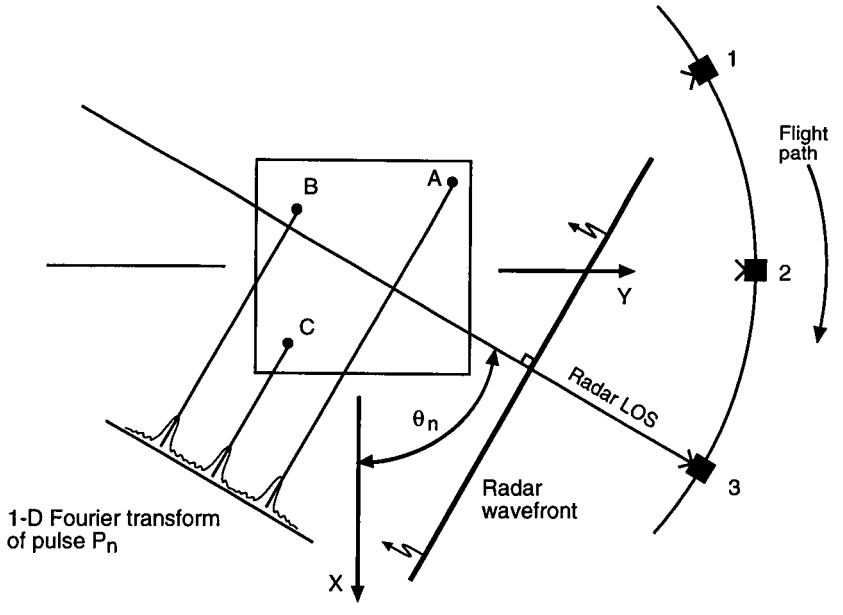


Figure B.1 Spotlight SAR collection scenario.

in Figure B.1. On a pulse-by-pulse basis, the imaging process effectively *projects* each scatterer in the scene onto the current radar LOS in a range bin corresponding to scatterer distance from the APC. A single pulse resolves scatterers in range only, so many scatterers can occupy the same range bin. Since the current model assumes negligible wavefront curvature, the imaging process projects scatterers perpendicular to the radar LOS.

A one-dimensional Fourier transform compresses each pulse in range and maps scatterers into their current range bins. As the radar follows its path around the scene, the range to each scatterer and the projection along the radar LOS changes. For instance, scatterers B and C project onto different range bins along the radar LOS when the sensor is at positions 1 and 3. They project onto the same range bin when the radar is at position 2.

The TR algorithm applies the projection-slice theorem of the Fourier transform to compute the image. A mathematical development of the projection-slice theorem is available in many references [2, 6, 7]. The projection-slice theorem states that the Fourier transform of a one-dimensional projection of a two-dimensional function $f(x, y)$ made at angle θ_n is a slice through the two-dimensional Fourier transform of $f(x, y)$ at angle θ_n.

In this SAR imaging example, each radar pulse slices through the radar scene and projects scatterers onto the radar LOS. Whereas some algorithms convert the signals from many pulses simultaneously into a reflectivity image using a two-dimensional Fourier transform, TR generates an image by projecting the range-only Fourier transform of each radar LOS slice individually *back* onto a two-dimensional grid of image pixels. This operation gives rise to the term *backprojection* to describe the TR algorithm.

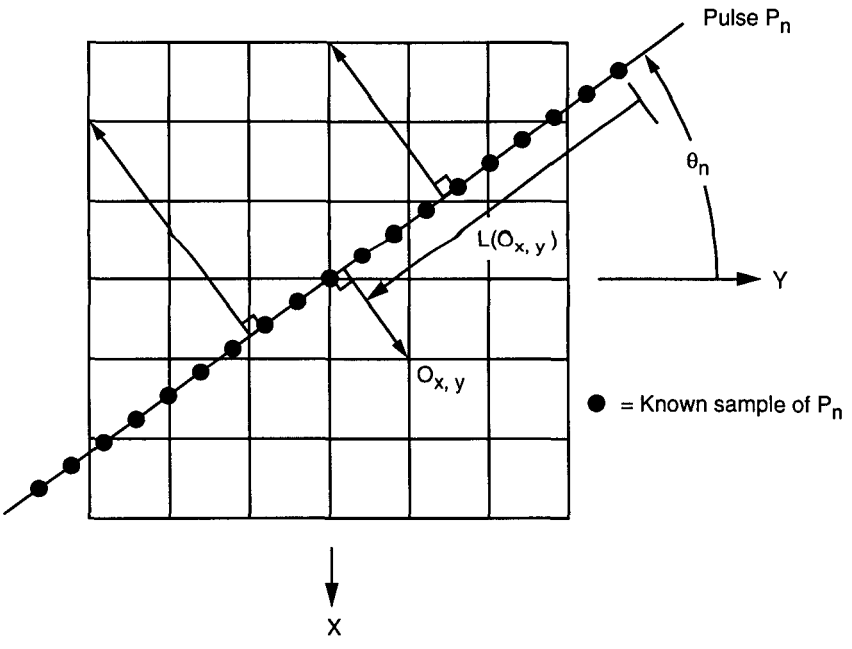


Figure B.2 Backprojecting P_n onto the output image grid.

The reconstruction calculation (Figure B.2) begins by placing a rectangular output grid over the (X, Y) plane of Figure B.1. The second step Fourier transforms pulse P_n to resolve individual scatterers in range and places that result in the (X, Y) plane at angle θ_n. The third step determines the input range bin $L(O_{x,y})$ associated with each pixel $O_{x,y}$ on the output grid by projecting $O_{x,y}$ onto P_n. The last step for pulse P_n coherently adds the input value in range bin $L(O_{x,y})$ to each output grid pixel $O_{x,y}$. Reconstruction continues by repeating this process on successive pulse and adding to the output grid pixels.

Typically, the location $L(O_{x,y})$ does not correspond to an exact sample point on P_n. Accordingly, an interpolation procedure determines the value of P_n at each location $L(O_{x,y})$; this one-dimensional interpolation is along the pulse. The interpolation techniques suggested in Section 4.2.3 are applicable to the TR interpolation task.

B.2 ALGORITHM ATTRIBUTES

In practice, application of TR to spotlight SAR image formation often must account for wavefront curvature. It must also account for range variations caused by a noncircular flight path and a nonzero, changing grazing angle [2]. Reference [8] offers a modified tomographic backprojection algorithm for use with spotlight SAR data in the presence of significant wavefront curvature.

One favorable attribute of TR is that it gradually constructs the final image result as it incorporates successive pulses. Image resolution starts low (coarse) and improves with backprojection of each additional pulse. This behavior can be useful in automatic target detection (ATD) applications. For example, a TR-based image formation processor (IFP) might initially process only a small fraction of the collected pulses to form a coarse-resolution image for evaluation by an ATD algorithm to test for the presence of targets of interest. If the ATD result is positive, the IFP could continue with the backprojection to improve image resolution; if it is negative, the IFP stops processing to conserve processing resources.

A second favorable attribute of TR is that it maps well to a parallel processing hardware architecture [9] because the reconstruction operation occurs on a pixel-by-pixel basis. In the extreme, a massively parallel architecture could assign each output grid pixel to a unique processing element. More practically, a single processing element is able to handle a neighborhood of output grid pixels. The PFA, because of its inherent two-dimensional polar-to-rectangular interpolation, adapts less readily to such parallelization.

The computational burden of TR is high relative to other image formation algorithms. For fine-resolution SAR imaging, TR may require as much as one hundred times more floating point operations per output image pixel than polar formatting requires [9].

Finally, it is often difficult to integrate autofocus algorithms into TR for real-time operation. Autofocus techniques typically apply phase error compensations in the azimuth direction of the signal history domain. TR has no processing stage where uncompressed azimuth signal data is available. Instead, TR forms an image directly. To compensate for phase errors, it is, therefore, necessary to inverse Fourier transform the misfocused TR image in azimuth, estimate and apply the correction, then forward Fourier transform the data to obtain a focused image. The two extra Fourier transforms can significantly increase the computational complexity of the TR processor relative to other image formation approaches.

REFERENCES

[1] Scudder, H.J., "Introduction to Computer Aided Tomography," *Proceedings of the IEEE*, Vol. 66, No. 6, June 1978, pp. 628-637.

[2] Munson, D.C., J.D. O'Brien, and W.K. Jenkins, "A Tomographic Formulation of Spotlight-Mode Synthetic Aperture Radar," *Proceedings of the IEEE*, Vol. 72, No. 8, August 1983, pp. 917-925.

[3] Mensa, D.L., S. Halevy, and G. Wade, "Coherent Doppler Tomography for Microwave Imaging," *Proceedings of the IEEE*, Vol. 71, No. 2, February 1983, pp. 254-261.

[4] O'Sullivan, J.D., "A Fast Sinc Function Gridding Algorithm for Fourier Inversion in Computer Tomography," *IEEE Transactions on Medical Imaging*, Vol. MI-4, No. 4, December 1985, pp. 200-207.

[5] Pan, S.X., and A.C. Kak, "A Computational Study of Reconstruction Algorithms for Diffraction Tomography: Interpolation versus Filtered Back Propagation," *IEEE Transactions on Acoustics, Speech and Signal Processing*, Vol. ASSP-31, No. 5, October 1983, pp. 1262-1275.

[6] Mersereau, R.M., and A.V. Oppenheim, "Digital Reconstruction of Multidimensional Signals from Their Projections," *Proceedings of the IEEE*, Vol. 62, No. 10, October 1974, pp. 1319-1338.

[7] Herman, G.T., editor, *Image Reconstruction from Projections*, New York, Springer-Verlag, 1979.

[8] Bauck, J.L., and W.K. Jenkins, "Tomographic Processing of Spotlight-Mode Synthetic Aperture Radar Signals with Compensation for Wavefront Curvature," *IEEE 1988 International Conference on Acoustics, Speech and Signal Processing*, New York, NY, 11-14 April 1988.

[9] Desai, M.D., and W.K. Jenkins, "Convolutional Backprojection Image Reconstruction for Spotlight Mode Synthetic Aperture Radar," *IEEE Transactions on Image Processing*, Vol. 1, No. 4, October 1992, pp. 505-517.

Appendix C
Removal of Residual Video Phase

From Section 3.10, an undesirable residual video phase (RVP) term is a consequence of the signal dechirp-on-receive approach to spotlight data collection and processing. This effect is not unique to the polar format algorithm. It is a consequence of dechirping the SAR signals in range by means of mixing with a reference function in the time domain. It is absent in situations that use matched filter processing in the frequency domain (after a range Fourier transform of the chirped signals) to accomplish range compression.

The RVP term is deterministic. Compensating for the defocusing effects of RVP in the image domain is not easy because these effects are space-variant, increasing in severity away from the motion compensation point. The use of multiple motion compensation points in a subpatch processing procedure (Section 4.8) is one way to reduce the impact of RVP. More desirably, a preprocessing operation is available to completely remove the RVP term from the radar signal by passing the range-dechirped video signal through the digital equivalent of a frequency-dependent delay line. This appendix presents an analytical basis for removal of the RVP term.

C.1 PRESENCE OF RVP

RVP exists because the difference between any two displaced linear FM waveforms includes a constant phase proportional to the displacement. RVP impacts SAR imagery because the displacement between the two waveforms varies over a coherent processing interval as the two-way time delay to a target changes. Otherwise, the RVP term would be a constant phase over the aperture time for each target point and of no consequence to most SAR imaging applications.

Chapter 2 provides the expression for the signal with limited along-track duration from a point scatterer with radar reflectivity coefficient σ_t. From (2.66) and (2.67), this signal is

$$s_o(n,\hat{t}) = a_t \sum_{n=0}^{N_p-1} \left[\text{rect}\left(\frac{\hat{t} - 2R_t/c}{T_p} \right) e^{j\Phi(n,\hat{t})} \right] \tag{C.1}$$

with phase

$$\Phi(n,\hat{t}) = -\frac{4\pi\gamma}{c}\left(\frac{f_c}{\gamma} + \hat{t} - \frac{2R_a}{c} \right)(R_t - R_a) + \frac{4\pi\gamma}{c^2}(R_t - R_a)^2 \tag{C.2}$$

Here, $a_t = \sqrt{\sigma_t}$, n is an index corresponding to pulse number, the expression $\hat{t} = t - nT$ represents fast time or time within a signal received from a specific transmitted pulse and referenced to the time of pulse generation, γ is the linear FM rate, f_c is the transmitted center frequency, T is the pulse repetition interval, T_p is the length of the transmitted pulse, R_t is the distance between the antenna phase center (APC) and the scatterer, and R_a is the distance between the APC and scene center. Equation (C.1) models the SAR video signal after the fine motion compensation operation. The last term in (C.2) is the RVP effect.

C.2 COMPENSATION WITH A FREQUENCY-DEPENDENT DELAY

First, it is helpful to examine removal of the RVP term heuristically. Assuming a positive linear FM rate, it is desirable to delay high intermediate frequencies in time relative to low intermediate frequencies to align the signals from all scatterers in time (Figure C.1). This alignment requires a frequency-dependent time delay t_d related to frequency by

$$t_d = \frac{f}{\gamma} \tag{C.3}$$

This delay removes the original time delay difference between signals from different ranges. Analysis given later in this Appendix shows that application of this new delay introduces a multiplicative term of phase $-\pi f^2/\gamma$ into the original signal and removes the RVP term from the signal history. To implement this new delay, it is necessary to filter each range record (pulse) by a linearly dispersive filter exhibiting the time delay characteristic of (C.3). The effect of a time delay t_d on a constant frequency (f_1) signal with phase $\phi_v = 2\pi f_1 t$ is to multiply the signal by a constant amplitude signal with phase $\phi_d = -2\pi f_1 t_d$. In general, t_d is related to ϕ_d by $-2\pi t_d = d\phi_d/df$.

Taking the time derivative of (C.2), the instantaneous frequency is

$$f = \frac{1}{2\pi}\frac{d\Phi}{d\hat{t}} \tag{C.4}$$

Evaluating this derivative yields

$$f = -\frac{2\gamma}{c}R_\Delta\left(1-\frac{2}{c}\frac{dR_\Delta}{d\hat{t}}\right)-\frac{2\gamma}{c}\left(\hat{t}-\frac{2R_a}{c}+\frac{f_c}{\gamma}\right)\frac{dR_\Delta}{d\hat{t}} \tag{C.5}$$

using $R_\Delta = R_t - R_a$ for convenience. Relative to the effects of the time delay of (C.3), the approximation

$$f \approx -\frac{2\gamma}{c}R_\Delta \tag{C.6}$$

is adequate. It indicates that scatterers that are nearer than R_a have a positive frequency in this representation while those that are more distant have a negative frequency.

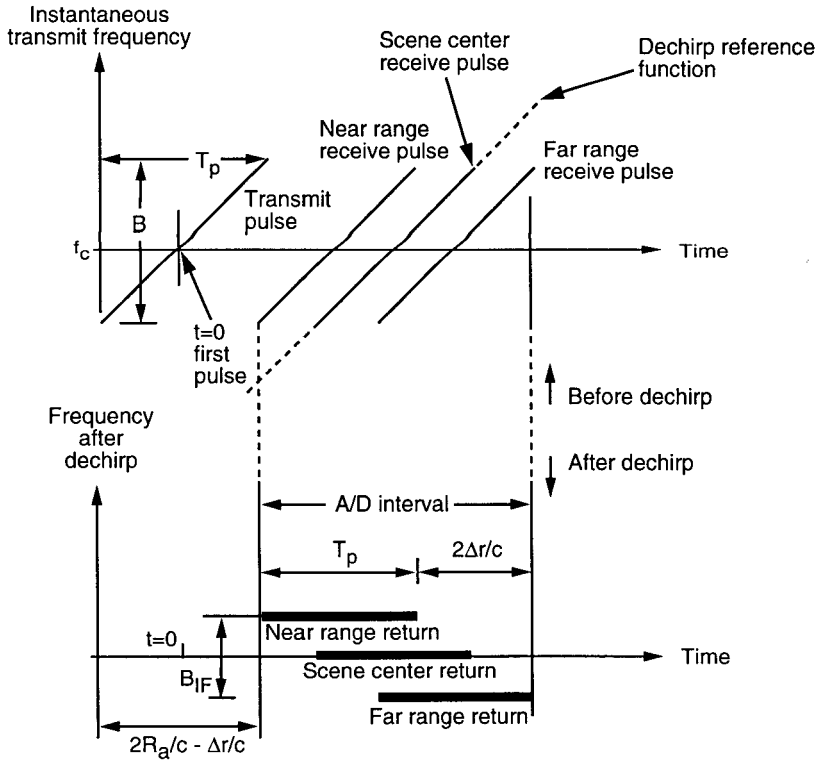


Figure C.1 Frequency-dependent signal skew.

Figure C.1 indicates this characteristic for a scene of range extent Δr corresponding to an IF bandwidth B_{IF} equal to $2\gamma\Delta r/c$.

The result of passing the signal of phase Φ through the delay line with $t_d = f/\gamma$ is the new phase $\Phi_{rd} = \Phi - \pi f^2/\gamma$, which, on substitution of the expression in (C.6) for f, becomes

$$\Phi_{rd}(n,\hat{t}) = -\frac{4\pi\gamma}{c}\left(\hat{t} - \frac{2R_a}{c} + \frac{f_c}{\gamma}\right)R_\Delta \tag{C.7}$$

This expression is the desired phase for a target at range R_t and reference range R_a. The RVP term has been eliminated.

We now examine removal of the RVP term in a more rigorous, analytical fashion. Figure C.2 illustrates the block diagram of the filtering process involving a Fourier transform, a complex multiply, and an inverse Fourier transform.

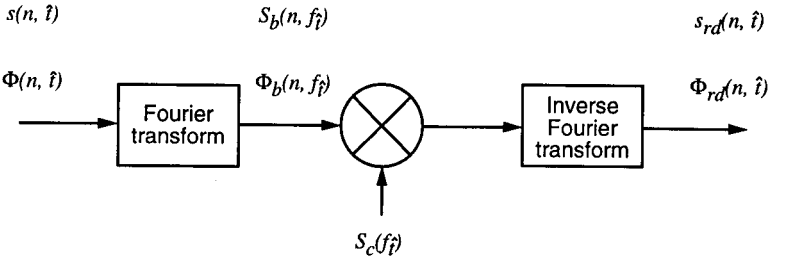


Figure C.2 Block diagram of deskew procedure.

To compensate for RVP, the first step takes the Fourier transform of the signal $s(n, \hat{t})$ of (C.1) on a pulse-by-pulse basis with respect to $\hat{t}-2R_a/c$. For pulse n, the result is

$$S_b(n, f_{\hat{t}}) = a_t T_p \operatorname{sinc}\left[T_p\left(f_{\hat{t}} + 2\frac{\gamma}{c}R_\Delta\right)\right] e^{j\Phi_b(n, f_{\hat{t}})} \tag{C.8}$$

with

$$\Phi_b(n, f_{\hat{t}}) = -\frac{4\pi f_c}{c}R_\Delta - \frac{4\pi\gamma}{c^2}R_\Delta^2 - \frac{4\pi f_{\hat{t}}}{c}R_\Delta \tag{C.9}$$

This equation is an expression for the range-compressed signal from pulse n for a scatterer at range R_t.

In this $(n, f_{\hat{t}})$ domain, the next step is to multiply the signal $S_b(n, f_{\hat{t}})$ by an appropriate $f_{\hat{t}}$-dependent phase term, $S_c(f_{\hat{t}})$. Here, the coordinate $f_{\hat{t}}$ is directly related on a pulse-to-pulse basis to the image domain range direction to the target. This compensation term is given by

$$S_c(f_{\hat{t}}) = e^{-j\left(\pi f_{\hat{t}}^2/\gamma\right)} \tag{C.10}$$

The next step is to proceed with an inverse Fourier transform of the product of (C.8) and (C.10) with respect to $f_{\hat{t}}$ to return to the $(n, \hat{t})$ domain. The result is

$$s(n, \hat{t}) = a_t I e^{j\Phi_{rd}(n, \hat{t})} \tag{C.11}$$

with

$$\Phi_{rd}(n, \hat{t}) = -\frac{4\pi\gamma}{c}\left(\hat{t} + \frac{f_c}{\gamma} - \frac{2R_a}{c}\right)R_\Delta \tag{C.12}$$

and

$$I = T_p\int_{-\infty}^{\infty} \operatorname{sinc}(T_p F)\, e^{-j\frac{\pi}{\gamma}F^2} e^{j2\pi F\left(\hat{t} - \frac{2R_a}{c}\right)} dF \tag{C.13}$$

In (C.13), F is given by

$$F = f_{\hat{t}} + \frac{2\gamma}{c} R_{\Delta} \tag{C.14}$$

Were it not for the presence of the term involving F^2 in the integral, (C.13) would become

$$I \Rightarrow \text{rect}\left(\frac{\hat{t} - 2R_a/c}{T_p} \right) \tag{C.15}$$

which leads to the desired result. The integrand in (C.13) has significant magnitude only for $-1/T_p < F < 1/T_p$. So, the desired result is reached if

$$e^{-j\pi/\gamma T_p^2} \approx 1 \tag{C.16}$$

Now γT_p^2 is the pulse compression ratio or time bandwidth product of the SAR range dimension as shown in (2.3). For any SAR of moderate or finer range resolution, this quantity is at least in the thousands, (C.16) is valid, and (C.15) is a reasonable approximation for (C.13).

After RVP compensation, the signal is

$$s_{rd}(n, \hat{t}) = a_t \, \text{rect}\left(\frac{\hat{t} - 2R_a/c}{T_p} \right) e^{j\Phi_{rd}(n, \hat{t})} \tag{C.17}$$

with

$$\Phi_{rd}(n, \hat{t}) = -\frac{4\pi\gamma}{c}\left(\hat{t} + \frac{f_c}{\gamma} - \frac{2R_a}{c} \right) R_{\Delta} \tag{C.18}$$

In the process of compensating for the RVP, the frequency-dependent delay also changes the relative timing among returns from different ranges. These effects are evident by examining the signal beginning as (C.1) after this RVP compensation operation. The form of the rect( ) function in (C.17) indicates that the signals from targets at all ranges have been aligned in time to coincide with the return from a target at range R_a. This was not the case in (C.1). This change is referred to as "range deskew." Figure C.3 illustrates range deskew. The absence of the R_{Δ}^2 phase term in (C.18) seen in (C.2) indicates that the RVP term has been removed.

C.3 UTILITY OF RVP COMPENSATION

Besides correcting for RVP, the frequency-dependent delay also improves the characteristics of the time-bandwidth plot of the dechirped video signal. This improvement permits more efficient data rates and simplifies the application of aperture weighting to the entire collected bandwidth in range (Section 3.10).

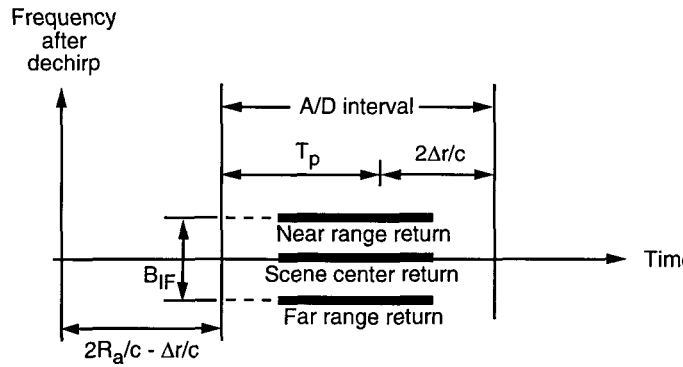


Figure C.3 SAR signal after range deskew.

Because the effects of RVP are small in many situations, correction is often unnecessary. Large scenes that have only one motion compensation point may require correction because the effects increase with target distance from the motion compensation point. Equations (5.33) and (5.34) describe the amount of quadratic phase error from RVP and indicate whether RVP contributes significantly to space-variant quadratic phase error. From these equations, the size of the quadratic phase error from the RVP effect is

$$Q_{rvp}\big|_{\text{size}} = \frac{\pi\gamma\lambda_c^2 K_a^2}{2c^2\rho_a^2} r_o^2 \tag{C.19}$$

where r_o is a nominal scene radius and λ_c is the center wavelength associated with f_c. Typically, this phase error represents a small effect.

RVP also introduces geometric distortion into a SAR image. Section 3.10 describes and quantifies this distortion. The distortion effects of RVP, more than its quadratic phase effects, are likely to be significant. However, the SAR processor is able to compensate for the distortion effects of RVP readily in the image domain. This compensation generally can proceed without significant additional computational burden if the processor already compensates for distortion from other sources. From (3.175), the size of the distortion from the RVP term is

$$l_{rvp} = \frac{2\gamma\lambda_c S_{\phi c} r_o^2}{c^2} \tag{C.20}$$

As Table 3.11 suggests, this distortion can easily exceed a resolution cell in size. Removing the RVP term with the above range deskew procedure also eliminates RVP-induced distortion and any need for image domain RVP distortion correction.

Appendix D
Sidelobe Control in SAR Imagery

A system impulse response with low sidelobes is important in SAR imagery because sidelobes contribute to multiplicative noise and may interfere with nearby scatterers. The primary sources of sidelobes are the finite data processing aperture and the presence of phase errors in the SAR data. The use of aperture weighting, or windowing, smooths the transition from data to the absence of data at the aperture edges. This process reduces the level of the sidelobes that arise from the finite data collection and processing apertures. Conventional aperture weighting is a linear operation which involves multiplication of a finite-extent SAR signal by a real function with amplitude decreasing monotonically away from aperture center. In the ideal case, the space-invariant impulse response of the spotlight SAR system is the two-dimensional Fourier transform of the chosen weighting function. The impact of phase errors on this impulse response is covered in Chapter 5.

In this appendix, we summarize the use of Taylor and Hanning weighting functions in SAR image formation processing to reduce the finite aperture sidelobes and illustrate the effect of each weighting on SAR images. Additional material is readily available on these traditional weighting functions [1-3]. This appendix includes a tutorial discussion of a recently developed sidelobe reduction technique termed *spatially variant apodization* (SVA) [4, 5]. Unlike conventional approaches, the SVA technique is nonlinear and better applied in the image domain than in the signal history domain. The appendix concludes with a comparison of SVA and conventional aperture weighting methods.

D.1 FINITE APERTURES

Finite apertures occur naturally in SAR imaging due to the physical and practical limitations of data collection and processing. Collected SAR data consists of finite-length pulses in range and a finite number of pulses in azimuth. A spotlight SAR system encodes information about each scattering center as a two-dimensional complex sinusoidal signal within the signal history. The amplitude of the sinusoid relates to the RCS of the scattering center while the orientation and frequency of the sinusoid relate to the position of the scatterer. The digital image formation processor maps these sinusoids into the image domain by performing a two-dimensional FFT over this limited data set.

Because the system impulse response is the Fourier transform of the data aperture, it is normal to trim the limited available data to fill either a rectangular or a circular aperture

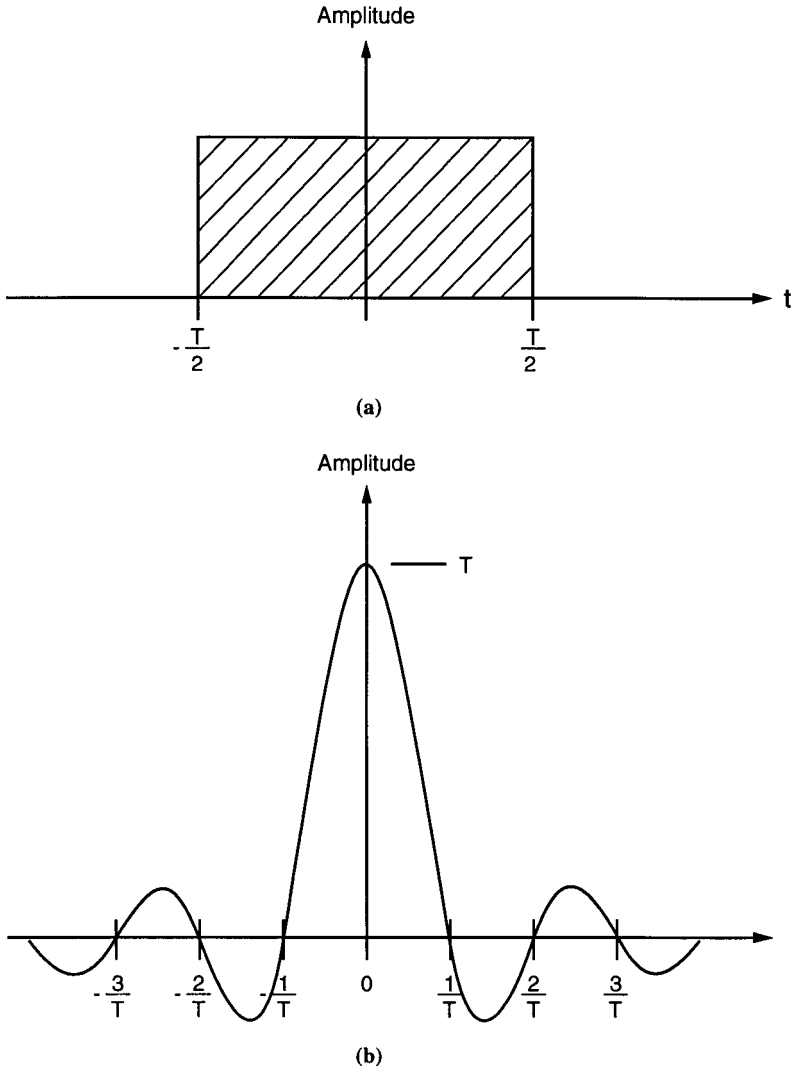


Figure D.1 Fourier transform pair associated with a uniformly weighted rectangular aperture: **(a)** Aperture amplitude weighting; **(b)** Impulse response function.

to obtain a reasonable pattern of sidelobes. If the amplitude of the aperture function is constant, we refer to the aperture as *unweighted* or *uniformly weighted.* The two-dimensional Fourier transform of the unweighted rectangular aperture is a two-dimensional $\sin(\pi f)/\pi f$ or sinc function. Figure D.1 illustrates the Fourier transform pair in one dimension for a uniformly weighted rectangular aperture.

Figure D.2 Image using a uniformly weighted rectangular aperture.

The first sidelobe of the impulse response associated with uniform weighting appears 13.3 dB below the mainlobe. With an aperture extent T, the interval to the first nulls of the impulse response is $1/T$ units on each side of the mainlobe peak, for a null-to-null mainlobe width of $2/T$. Subsequent nulls are spaced each $1/T$ units. The −3-dB width of the mainlobe intensity is $0.89/T$. The integrated sidelobe ratio (ISLR) of the one-dimensional sinc function is −9.7 dB. The two-dimensional ISLR associated with this aperture is −6.7 dB. Figure D.2 shows a SAR image processed using an unweighted rectangular aperture. The radar sensor and near range are on the left side of the image. Additional information about this image is available in Section E.1.

Processing a discrete-time signal using the discrete Fourier transform (DFT) produces a sampled sinc function for the impulse response associated with a uniformly weighted aperture. Sampling a discrete signal with uniform weighting at N time instances with a spacing of Δt seconds between samples generates a digitized signal of duration $T = N\Delta t$. The null-to-null mainlobe width of the associated impulse response is $2/N\Delta t$; the −3-dB width of the mainlobe intensity is $0.89/N\Delta t$. Computing the impulse response via an M-point DFT with $M \geq N$ yields a frequency spacing between adjacent samples in the impulse response of $1/M\Delta t$. In common terms, this procedure corresponds to using a

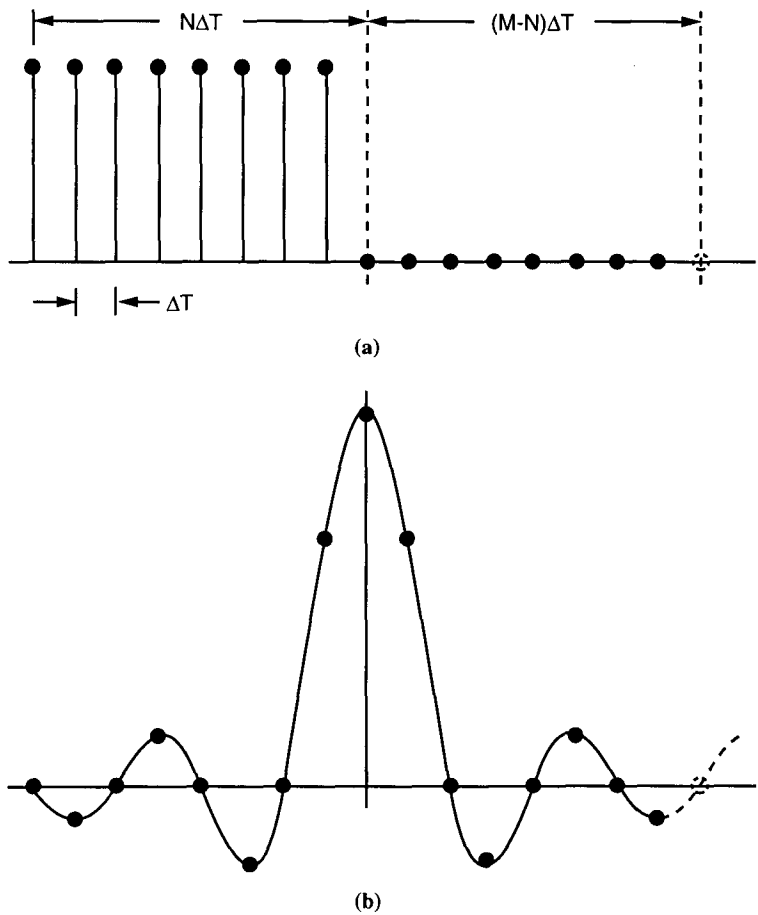


Figure D.3 Illustration of discrete sampling: (**a**) Discrete-time signal; (**b**) Discrete-frequency impulse response.

zero-pad of size $M - N$ around the signal data. In terms of samples, or pixels, the resulting sampled sinc function has mainlobe null-to-null and −3-dB widths of $2M/N$ pixels and $0.89M/N$ pixels, respectively. When transforming an N-point uniformly weighted aperture with an N-point DFT (that is, $M = N$), the impulse response has null-to-null width of 2 pixels and −3-dB width of 0.89 pixels. Figure D.3 illustrates this sampling geometry for the case of $M = 16$ and $N = 8$.

A circular aperture is common in optical systems as a practical alternative to a rectangular aperture. Early SAR processing systems used optical processing to form images [6].



Figure D.4 Image using circular aperture weighting.

The circular aperture provides a system impulse response whose sidelobes appear as rings around a circular mainlobe response; the Fourier transform of an unweighted circular function is a two-dimensional, circular Bessel function of the first kind. Figure D.4 shows an image from the same SAR data used to produce Figure D.2, but processed using a uniform circular aperture weighting.

Digital image formation processing generally does not use circular aperture weighting. Besides being somewhat clumsy to implement digitally, the circular aperture usually discards a significant portion of the available signal and slightly broadens the –3-dB width to $1.03/T$ where T is now the radius of the circular aperture. The two-dimensional ISLR of the circular aperture is –7.1 dB, not too different from that of the rectangular aperture. The first sidelobe of the uniform circular aperture is 17.6 dB below the mainlobe peak versus that of the rectangular aperture which is 13.3 dB below.

D.2 COMMON WEIGHTING FUNCTIONS

The uniform rectangular and circular weighting functions in Section D.1 have unity amplitude over the entire aperture. Nonuniform amplitude weighting is useful to decrease the sidelobe levels below those of uniform weighting for a given aperture shape. Nonuniform amplitude weighting is applied to SAR imagery by multiplying the signal history prior to the Fourier transform by a real function with amplitude typically decreasing monotonically and symmetrically away from aperture center.

Two common weighting functions are Taylor weighting [7] and Hanning weighting [2]. The SAR community commonly uses Taylor weighting for image formation processing because it provides strong, selectable sidelobe suppression with a minimum broadening of the mainlobe. Hanning weighting is popular in many signal processing applications although it is not particularly common in SAR signal processing. We introduce Hanning weighting primarily because of its relevance to the SVA algorithm discussed in Section D.3.

The discrete Taylor window is specified by three parameters N, $\bar{n}$, and SLL where:

1. N is the number of coefficients in the Taylor window;
2. $\bar{n}$ is the number of nearly constant-level sidelobes adjacent to the mainlobe;
3. SLL is the peak sidelobe level (in dB) relative to the mainlobe peak.

Popular choices for values of these parameters in SAR processing include SLL = −30 dB with $\bar{n} = 4$ and SLL = −35 dB with $\bar{n} = 5$, with N dictated by the number of range or azimuth signal history samples being processed. The N Taylor coefficients are computed as the sum of a constant and $\bar{n} - 1$ cosine functions according to

$$\text{Tay}(n) = 1 + 2 \sum_{m=1}^{\bar{n}-1} F_m \cos\left[\frac{2\pi m\,(n - N/2 + 1/2)}{N}\right] \tag{D.1}$$

for $n = 0, 1, \ldots, N-1$. The cosine weights in (D.1) are determined by

$$F_m = \frac{(-1)^{(m+1)} \prod_{i=1}^{\bar{n}-1} \left[1 - \dfrac{m^2/\sigma^2}{A^2 + (i - 1/2)^2}\right]}{2 \prod_{\substack{j=1 \\ j \neq m}}^{\bar{n}-1} (1 - m^2/j^2)} \tag{D.2}$$

where

$$A = \frac{\ln\left(B + \sqrt{B^2 - 1}\right)}{\pi} \tag{D.3}$$

$$B = 10^{-\frac{\text{SLL}}{20}} \tag{D.4}$$

and

$$\sigma^2 = \frac{(\bar{n})^2}{A^2 + (\bar{n} - 1/2)^2} \tag{D.5}$$

The quantity SLL in (D.4) is expressed as a negative number (for example, –30 dB). The above computational procedure requires that $\bar{n} \geq 2A^2 + 1/2$.

Figure D.5 shows a 64-point Taylor window for the case of $\bar{n} = 5$ and $SLL = -35$ dB. Figure D.6 shows the impulse response associated with the window of Figure D.5. The frequency axis of Figure D.6 has been normalized, which corresponds to sampling the window function of Figure D.5 with a sampling interval of unity. For this case, Taylor weighting produces a –3-dB mainlobe width equal to $1.19/T$; this width is 1.34 times that of the unweighted aperture, which is $0.89/T$. Figure D.7 shows an image from the same SAR data used to produce Figure D.2, but processed using Taylor weighting with SLL = –35 dB and $\bar{n} = 5$.

A modified Taylor window is available that avoids the abrupt termination, or pedestal, at the aperture edges and yields superior rolloff of distant impulse response sidelobes [8]. The cost of the improved sidelobe performance is a slightly wider mainlobe. Even though the broadening of the mainlobe is slight, the modified Taylor window is not particularly common in high-resolution SAR processing. Another variation of Taylor weighting achieves a suppression of selected sidelobes by modifying the Taylor window to force the nulls associated with the selected sidelobes to move closer together [9].

The Hanning weighting function is described by

$$\text{Hann}(n) = 1 - \cos\left[\frac{2\pi n}{N}\right] \tag{D.6}$$

with n varying from 0 to $N - 1$. Figure D.8 shows a 64-point Hanning window and Figure D.9 shows its associated impulse response. Hanning weighting reduces the first sidelobe to 31.5 dB below the mainlobe peak but increases the –3-dB impulse response mainlobe width to $1.43/T$ with a null-to-null mainlobe width of $4/T$. Again, reduction in sidelobe levels is accomplished at the expense of mainlobe broadening which equates to loss of resolution in the SAR image.

The SAR system designer must account for the resolution loss that results from nonuniform aperture weighting. The factors K_a and K_r in (2.2) and (2.20) for range and azimuth resolution acknowledge this weighting effect. As an example, to achieve the same resolution using Taylor weighting with $SLL = -35$ dB and $\bar{n} = 5$ as with uniform weighting, 34 percent more bandwidth must be processed in range and 34 percent more angular interval must be processed in azimuth. The downside of processing extra data in range and azimuth is that the radar must collect the additional data, which complicates the design and extends motion compensation performance requirements. It also increases computation and data storage requirements in image formation processing. Such trade-offs are part of the system performance budgeting for resolution as discussed in Chapter 8.

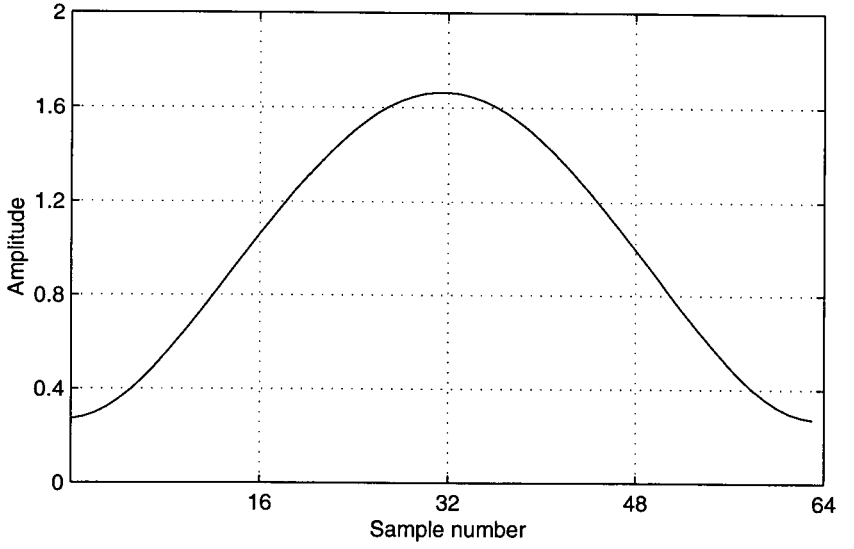


Figure D.5 Taylor window with SLL = −35 dB and $\bar{n} = 5$.

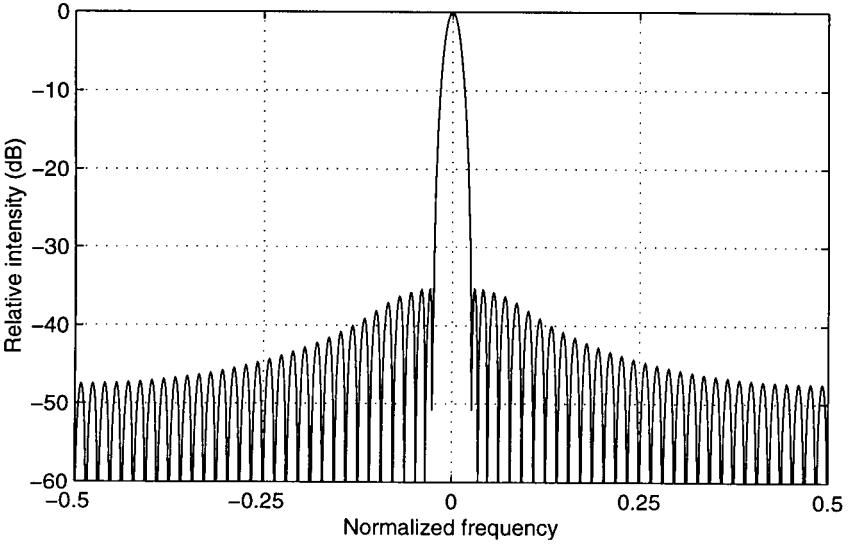


Figure D.6 Impulse response of 64-point Taylor window with SLL = −35 dB and $\bar{n} = 5$.



Figure D.7 Image using a rectangular aperture with Taylor weighting.

D.3 SPATIALLY VARIANT APODIZATION

S*patially variant apodization* (SVA) is a processing operation on a complex SAR image. Use of SVA significantly reduces impulse response sidelobe levels of locally dominant, high-RCS concentrated targets while preserving the mainlobe width associated with an unweighted aperture. The application of SVA also reduces the sidelobe energy associated with groups of targets and with areas of distributed scattering centers. This appendix provides a simple one-dimensional introduction to SVA beginning with descriptions of two similar but less complex concepts. A detailed development, including an analysis of the two-dimensional case, is available in the literature [4, 5, 10, 11].

SVA involves a nonlinear procedure which improves the appearance of imagery by performing a space-variant reduction of sidelobes over the image area. Unlike conventional aperture weighting, it does not perform a global, space-invariant reduction of sidelobes over the entire image. The "spatially variant" part of the name arises from the fact that the resulting image impulse response after application of SVA is not the same for all scatterers. Rather, the impulse response (in particular, its sidelobe levels) varies over the area of the image because of interactions that SVA causes among scatterers in local neighborhoods.

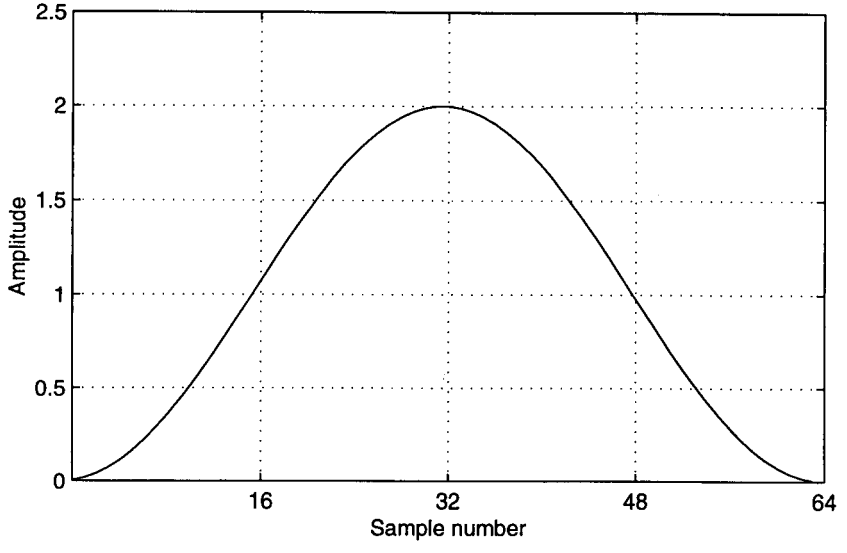


Figure D.8 Hanning aperture weighting.

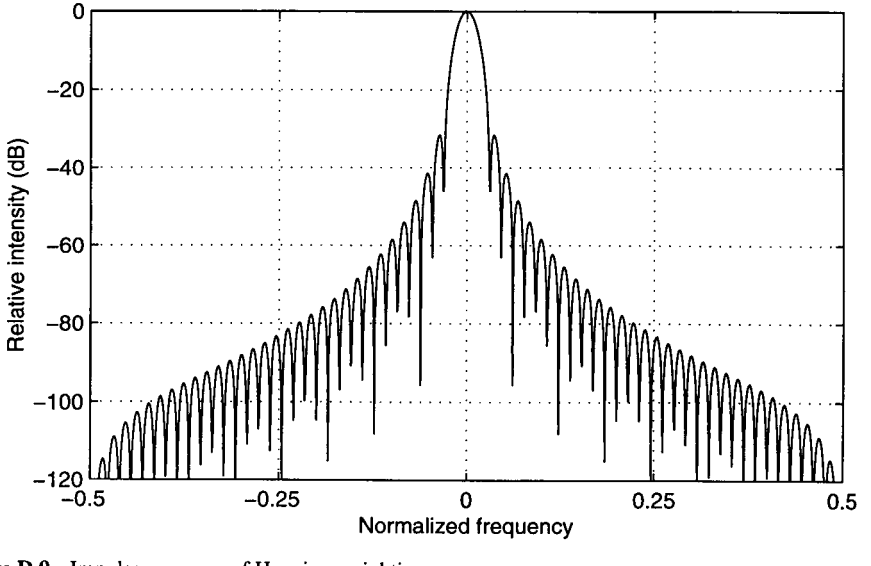


Figure D.9 Impulse response of Hanning weighting.

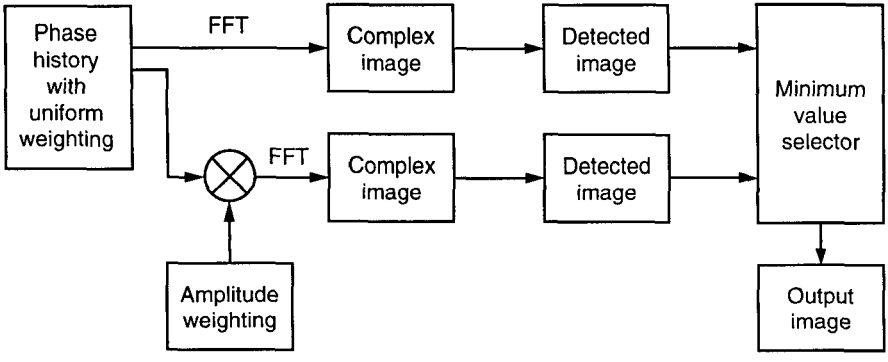


Figure D.10 Procedure for dual apodization.

The SVA algorithm arose as a computationally efficient extension of two simple concepts referred to as *dual apodization* (DA) and, more generally, *complex dual apodization* (CDA). The motivation behind these concepts is to improve the mainlobe and sidelobe characteristics of specific image areas. For instance, one goal is to remove, or at least suppress, the sidelobes of high RCS concentrated scatterers; such bright scatterers commonly include range and azimuth streaks of sidelobes in the image which draw the attention of the user. A second goal is to maintain the finer resolution associated with uniform weighting in areas that do not contain concentrated targets but consist largely of distributed terrain-like returns. These concepts depend on an ability to distinguish between pixels that contain primarily mainlobe energy and those that contain primarily sidelobe energy in the SAR image.

This presentation first describes dual apodization, then follows with a discussion of complex dual apodization leading up to SVA. The DA concept is particularly straightforward and easy to understand. Figure D.10 illustrates this procedure. DA utilizes two *detected* images, generated separately from the same signal history. One image is generated using an unweighted aperture while the second image is generated using a second weighting, for instance Hanning or Taylor weighting. The DA procedure operates on these two images to generate an improved output image on the following basis. The algorithm compares the two images on a pixel-by-pixel basis and selects the minimum value of each pixel pair as the value for the corresponding output pixel. Figure D.11 indicates the outcome of this process on an area of the image consisting of an isolated point target using Hanning weighting for the second image. The dash-dotted curve is the result with uniform weighting, the solid curve with Hanning weighting, and the cross-hatched area is the result of using DA. With DA, the impulse response of an isolated point target preserves the narrow mainlobe width of the sinc function and the lower sidelobe levels associated with the Hanning weighting. It is not reasonable to generalize this observation and suggest that this impulse response is representative of the system impulse response. In fact, dual apodization produces an image with a space-variant impulse response. Figure D.12 shows

a similar result for four point scatterers with the third one −25 dB in peak intensity relative to the other three scatterers. The dash-dotted curve is the result with uniform weighting and the solid curve with Hanning weighting. The cross-hatched area is the result that DA produces. Clearly, a significant interaction among targets is possible whose result depends on the local scatterer distribution. The local scene characteristics affect the impulse response via the nonlinear operation that DA applies to corresponding pixels in the two input images.

Complex dual apodization (CDA) utilizes two complex images rather than detected images. Again, the CDA process generates the two images separately from the same signal history, one using an unweighted aperture and the second using Hanning weighting. Being complex-valued images, each image pixel has both real (I or in-phase) and imaginary (Q or quadrature) components. The CDA procedure compares these two images on a pixel-by-pixel basis. It generates corresponding pixels in an output image on the following basis:

- If the I components in the two images for a particular pixel have opposite signs, it sets the I component of the corresponding output pixel to zero magnitude;
- If the I components have the same sign, it gives the output pixel's I component the value from the image that has the smaller absolute I component value;
- It follows the same steps for the Q component.

A key to this algorithm is that the width between the first nulls of the impulse response mainlobe associated with Hanning weighting is twice that width associated with the unweighted aperture. Figure D.11 illustrates this point. CDA is effective in eliminating sidelobes from the impulse response for an isolated point target because the sidelobes of the Hanning weighted and unweighted apertures have opposite signs. When a sidelobe is present, indicated by opposite signs in the comparison of corresponding pixels, the algorithm eliminates the sidelobe by setting the corresponding output pixel equal to zero. By setting the output pixel equal to zero in this case, the algorithm effectively utilizes some specific (but unknown) weighting between uniform and Hanning in a dual apodization procedure. The unknown weighting yields an impulse response for which the minimum input pixel value between the two images is zero. Hence, the CDA algorithm is effectively applying DA but using a continuum of weighting functions while only computing two weightings explicitly—uniform and Hanning. Even more effectively than simple dual apodization, the output of this algorithm tends to preserve the narrow mainlobe width of the sinc function while suppressing its sidelobe levels.

SVA is an extension and efficient implementation of the DA and the CDA concepts. SVA derives its efficiency from its ability to compute the desired CDA output image using a single complex image obtained with an unweighted aperture. This ability eliminates the need to generate the second input image required by CDA. We will describe only one-dimensional SVA applied to imagery sampled at the Nyquist rate although the principle easily extends to two dimensions and to imagery sampled at other than the Nyquist rate [5]. By Nyquist-sampled, we mean the unweighted image possesses two complex samples per mainlobe null-to-null width.

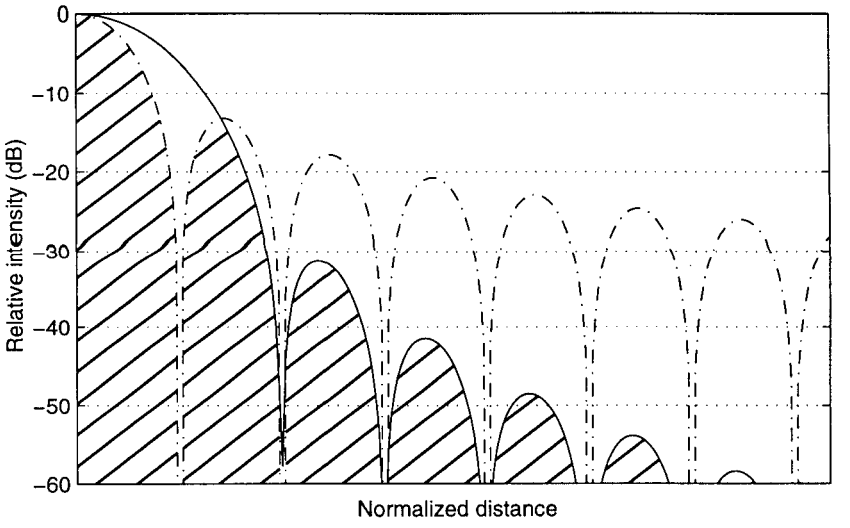


Figure D.11 Sidelobes using uniform weighting (dash dots), Hanning weighting (solid line), and dual apodization (cross-hatches).

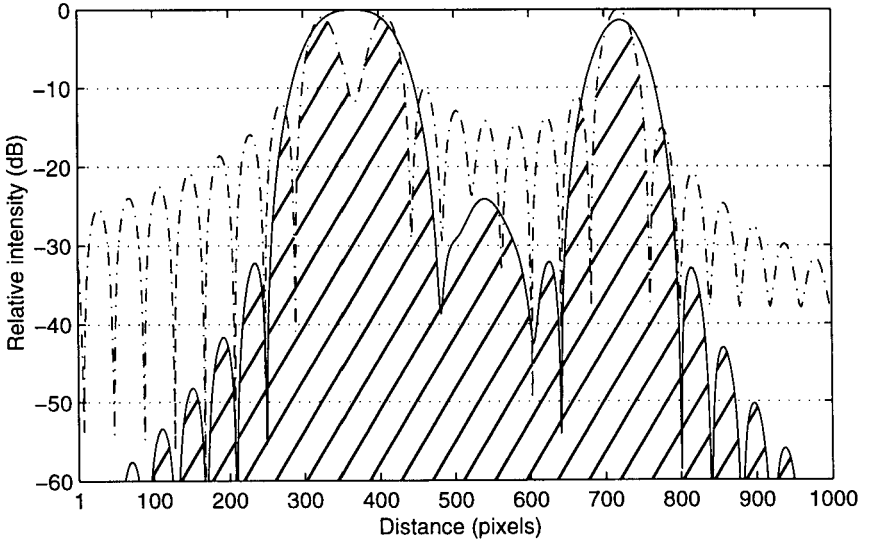


Figure D.12 Performance of dual apodization (cross-hatches) on a grouping of four scatterers at pixel locations 325, 410, 540, and 720 compared to uniform weighting (dash dots) and Hanning weighting (solid line).

The SVA algorithm takes advantage of the special properties of a cosine-on-pedestal weighting function applied to complex Nyquist-sampled imagery. The family of cosine-on-pedestal weighting functions for an aperture of N pixels is represented by

$$C(n) = 1 + 2w\cos\left(\frac{2\pi n}{N}\right) \tag{D.7}$$

with $|n| \leq N/2$. When the constant w is zero, the weighting is uniform (all pedestal) and when w is 0.5, the weighting is Hanning (all cosine). The Hanning function from (D.7) differs from (D.6) in the sign of the cosine term because the two expressions have their origins at different sample numbers. In fact, the two expressions are equivalent.

The discrete Fourier transform of $C(n)$ in (D.7) is

$$c(m) = \delta(m) + w\delta(m-1) + w\delta(m+1) \tag{D.8}$$

where $\delta(m)$ is the Kronecker delta function. This three-sample function represents the system impulse response of a complex Nyquist-sampled image using the aperture weighting $C(n)$.

The SVA algorithm operates in the image domain using complex image data derived from unweighted signal history data. Operating in one dimension, the SVA algorithm convolves $c(m)$ with each line of pixels in the image. In effect, this convolution produces output pixels that would result had the aperture weighting $C(n)$ been applied initially to the signal history. In the simplest I-Q-independent implementation [4], the algorithm selects w on a pixel-by-pixel basis to minimize separately the magnitude of the I and Q components subject to the constraint that w not exceed 0.5. This constraint is consistent with use of cosine-on-pedestal weightings where $w = 0$ represents uniform weighting while $w = 0.5$ represents Hanning weighting. Values between these two extremes represent other weightings within the cosine-on-pedestal family. The effective weighting applied, then, varies from pixel to pixel as w is changed. Values of w outside this constraint cause the weighting function $C(n)$ to include negative values.

Let $s(m)$ represent individually the I and Q image pixel components (on separate passes through the algorithm). The SVA algorithm proceeds by convolving the initial image with the weighting function $c(m)$. The m^{th} output value, designated $o(m)$, of this convolution is

$$o(m) = s(m) + w[s(m-1) + s(m+1)] \tag{D.9}$$

The value $w_u(m)$ of w which minimizes the intensity $|o(m)|^2$ of $o(m)$ is given by

$$w_u(m) = \frac{-s(m)}{s(m-1) + s(m+1)} \tag{D.10}$$

We obtain (D.10) by equating the first derivative of $|o(m)|^2$ with respect to w to zero and

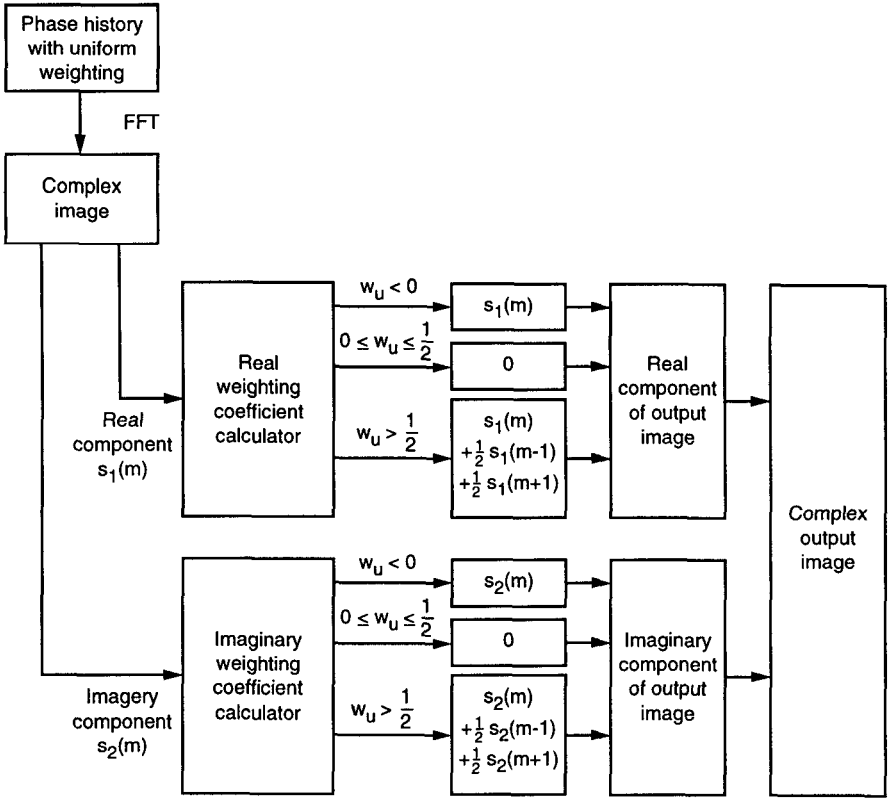


Figure D.13 Procedure for spatially variant apodization.

solving for w. Using the constraint that w be between and including 0.0 and 0.5, the SVA procedure to yield the value $y(m)$ for the I (and separately, Q) component of the m^{th} output pixel is

$$y(m) = \begin{cases} s(m) & \text{for } w_u(m) < 0 \\ 0 & \text{for } 0 \le w_u(m) \le 0.5 \\ s(m) + 0.5\,[s(m-1) + s(m+1)] & \text{for } w_u(m) > 0.5 \end{cases} \qquad \text{(D.11)}$$

The algorithm applies (D.11) separately to derive the I and Q components of the complex pixels. Figure D.13 illustrates the steps in this SVA procedure.

Inspection of (D.10) indicates that, for $w_u(m)$ to be negative, the pixel $s(m)$ must have the same sign as the sum of its neighboring pixels, $s(m-1) + s(m+1)$. This occurs in a Nyquist-sampled sinc function if the pixel is in the mainlobe, in which case one of the

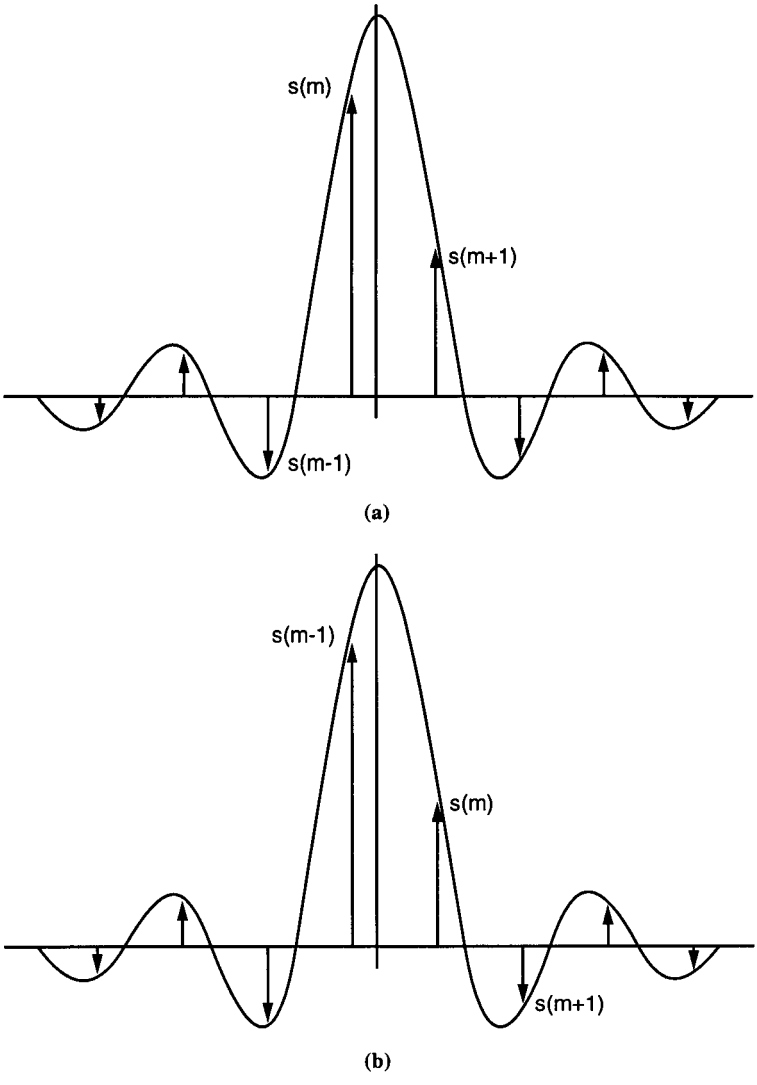


Figure D.14 Example of mainlobe pixels in SVA algorithm: **(a)** Left pixel; **(b)** Right pixel.

neighboring pixels will be in a sidelobe and have a negative value and the other will be in the mainlobe and have a positive value with a greater magnitude than the negative neighbor. Thus, when $w_u(m)$ is negative, the input pixel $s(m)$ must be a mainlobe pixel; in this case, the output is set equal to $s(m)$ to maintain the mainlobe pixel value produced by uniform weighting. Figure D.14 shows an example of this situation in which the input pixel $s(m)$ is a mainlobe pixel.

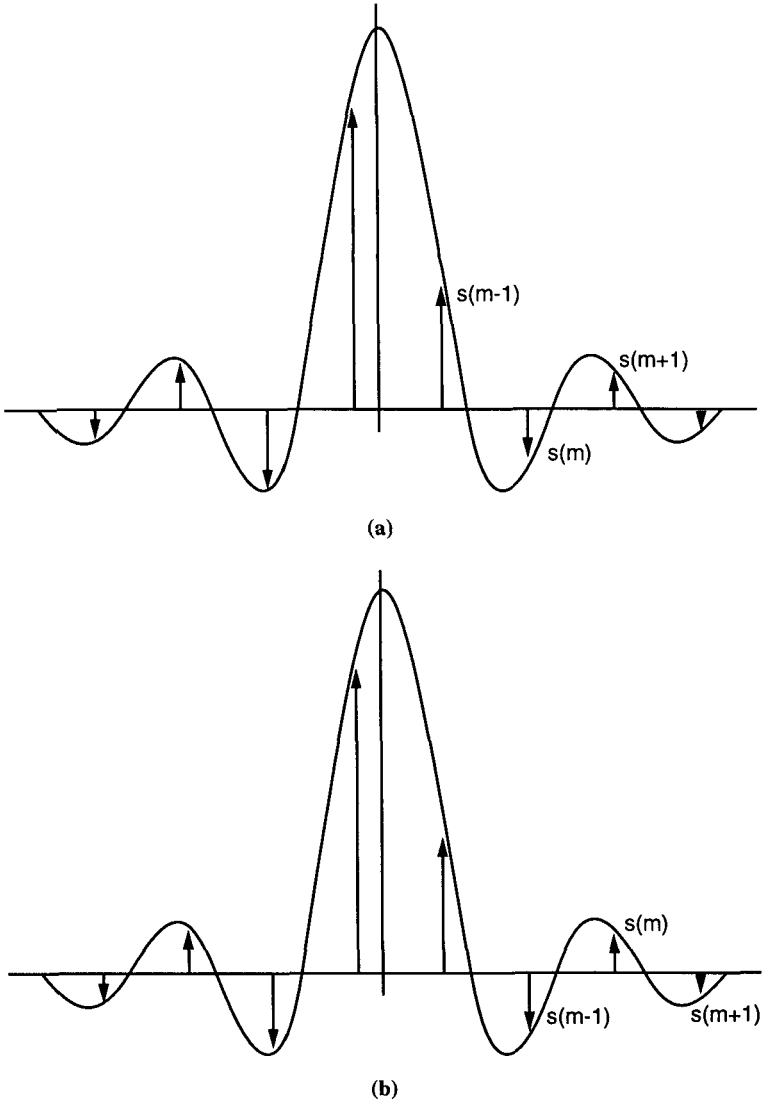


Figure D.15 Example of sidelobe pixels in SVA algorithm: **(a)** Near mainlobe; **(b)** Away from mainlobe.

When $w_u(m)$ has a value of 0.0 to 0.5, the input pixel has the opposite sign as the sum of its neighboring pixels. This occurs in a Nyquist-sampled sinc function if the input pixel is in the sidelobes. Therefore, the algorithm sets the corresponding output pixel equal to zero in order to remove the sidelobe energy. The input pixel represents a sidelobe because

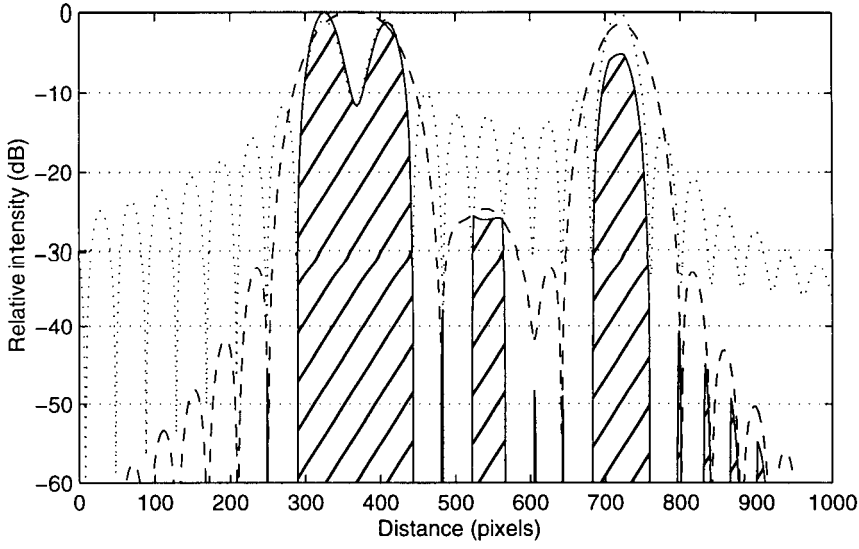
the sidelobes of a sinc function oscillate in sign for each pixel causing both neighbors to have the opposite sign of the middle pixel. Figure D.15 illustrates this point with an example in which the input pixel $s(m)$ is a sidelobe pixel.

When $w_u(m)$ is greater than 0.5, the input pixel again has the opposite sign as the sum of its neighboring pixels. Now, however, the absolute value of the sum of the neighboring pixels is less than double the absolute value of the original pixel. This situation suggests that the input pixel is in a mainlobe but includes energy from sidelobes of other scatterers. Here, the algorithm chooses $w = 0.5$, representing Hanning weighting with low sidelobes. In this way, SVA attempts to improve the interaction between the mainlobe and interfering sidelobes.

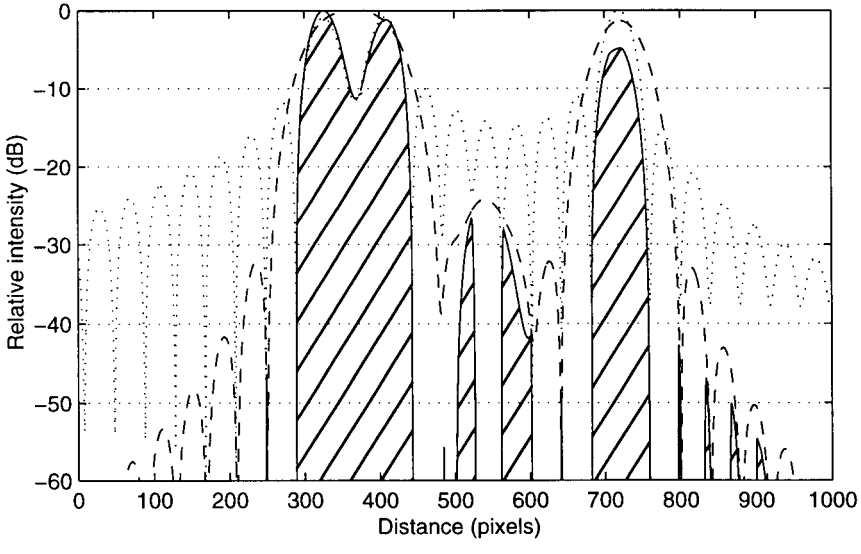
The SVA algorithm is effective because it eliminates or suppresses the areas of the image in which pixels oscillate in sign from pixel to pixel, as sinc function sidelobes do, and it preserves areas that do not oscillate, indicative of a mainlobe area of the sinc function. Figure D.16 shows a simulation result of applying SVA to a scene consisting of four adjacent point scatterers with the third one −25 dB in peak intensity relative to three other scatterers. The dotted curve is the result with uniform weighting and the solid curve with Hanning weighting. The hatched area is the result of using SVA. The two cases in this figure differ in the relative phase of the third, lower-intensity scatterer. Because a significant interaction among targets is possible, the result depends on the local scatterer phase and amplitude distributions.

For an image consisting of a single point target, the algorithm clearly works well. When multiple point targets or areas of distributed scattering centers are present, algorithm performance is less predictable, but usually excellent. The performance of SVA on typical SAR imagery with assorted types and sizes of scatterers, although not easily analyzed, is favorable in terms of image appearance. The algorithm itself is robust with respect to the presence of additive noise and modest levels of low-frequency phase errors [11]. Additive noise does not prevent the algorithm from reducing sidelobe energy down to the noise level [5].

Figure D.17 illustrates the result of applying a two-dimensional version of SVA to the image with uniform weighting in Figure D.2. A comparison among these two images and the image with Taylor weighting in Figure D.7 suggests that SVA virtually eliminates the sidelobes of strong scatterers while preserving the sharpness of their mainlobes. Figure D.18 provides a second comparison between images processed using SVA and using Taylor weighting with $SLL = -35$ dB and $\bar{n} = 5$. Again, the SVA procedure offers a superior result. Intensity scans through a dominant scatterer in each image offer a good demonstration of the behavior of these three methods of sidelobe control. Figure D.19 provides two such comparisons. Figure D.19(a) shows intensity scans through the same image point in the SVA image of Figure D.18(b) and a corresponding image with uniform weighting. Figure D.19(b) shows intensity scans through the same image point in the SVA image of Figure D.18(b) and the image with Taylor weighting of Figure D.18(a). The scan through the SVA image maintains the narrow mainlobe width of the uniform weighting and the low sidelobes of the Taylor weighting.



(a)



(b)

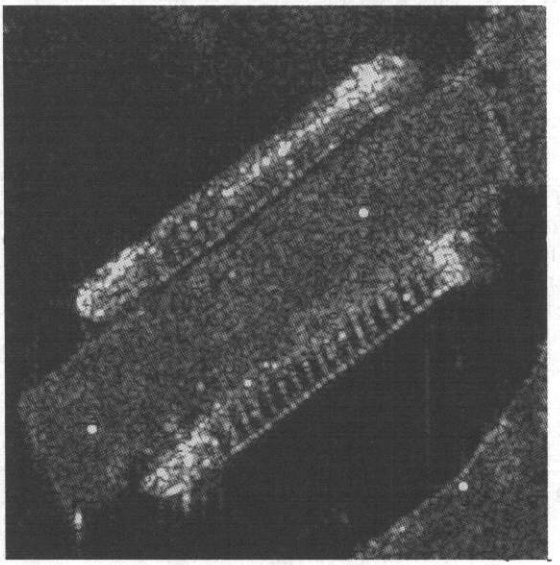
Figure D.16 Performance of SVA (solid with cross-hatches) compared to uniform (dots) and Hanning (dashes) weightings: **(a)** A grouping of four scatterers at pixel locations 325, 410, 540, and 720; **(b)** Same four scatterers with different relative phases.



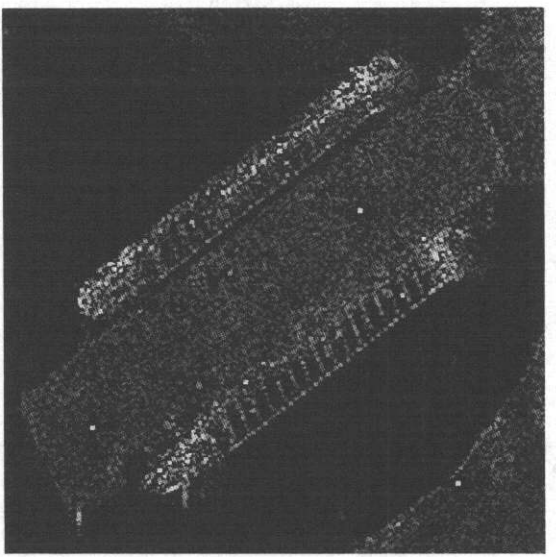
Figure D.17 SVA image.

D.4 SUMMARY

Table D.1 summarizes the characteristics of various aperture weighting functions. The desire for ISLR less than –21 dB and peak sidelobes below –30 dB, without an unreasonable penalty in broader mainlobe width, makes Taylor weighting with $SLL = -35$ dB and $\bar{n} = 5$ a common choice in SAR digital signal processors. The SVA algorithm has some attractive features and shows promise for use in future image formation processing systems.

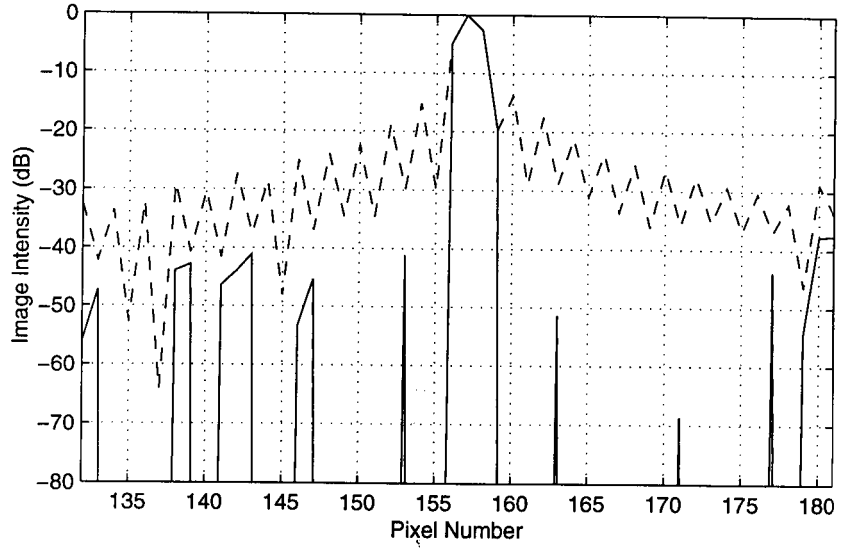


(a)

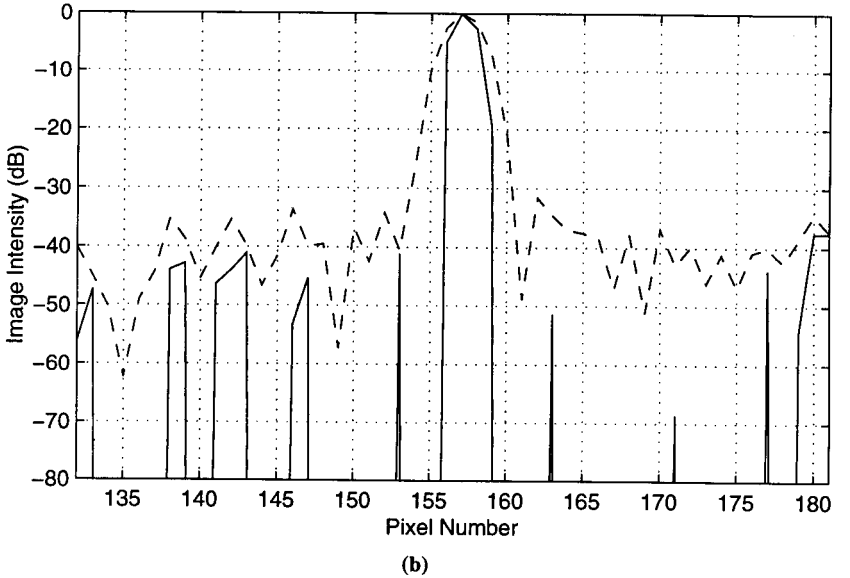


(b)

Figure D.18 Comparison of weighting techniques: **(a)** Image using Taylor weighting; **(b)** Image using SVA.



(a)



(b)

Figure D.19 SVA impulse response of a single scatterer: **(a)** Unweighted aperture (dashes) and SVA (solid line); **(b)** Taylor weighting (dashes) and SVA (solid line).

Table D.1
Aperture Weighting Comparison

Weighting	*First Sidelobe Level (dB)*	*−3-dB Mainlobe Width*	*One-Dimensional ISLR (dB)*	*Two-Dimensional ISLR (dB)*	*Implementation Considerations*
Uniform rectangular	−13.3	$0.89/T$	−9.7	−6.7	No additional operations needed
Uniform circular	−17.6	$1.03/T$	−10.1	−7.1	Circular data support required after polar format interpolation
Taylor with SLL = −35 dB and $\bar{n} = 5$	−35.0	$1.19/T$	−27.5	−24.5	Real-by-complex multiply for each pixel
Hanning	−31.5	$1.43/T$	−34.3	−31.3	Real-by-complex multiply for each pixel
SVA in two dimensions	Variable	$0.89/T$	Variable	Variable	Convolution; pixel comparison

REFERENCES

[1] Oppenheim, A.V., and R. Schafer, *Digital Signal Processing*, Englewood Cliffs, NJ, Prentice Hall, 1975.

[2] Harris, F., "On the Use of Windows for Harmonic Analysis with the Discrete Fourier Transform," *Proceedings of the IEEE,* Vol. 66, No. 1, January 1978, pp. 51-83.

[3] Embree, P.M., and B. Kimble, *C Language Algorithms for Digital Signal Processing,* Englewood Cliffs, NJ, Prentice Hall, 1991.

[4] Stankwitz, H.C., R.J. Dallaire, and J.R. Fienup, "Spatially Variant Apodization for Sidelobe Control in SAR Imagery," *Proceedings of the 1994 IEEE National Radar Conference*, March 1994.

[5] Stankwitz, H.C., R.J. Dallaire, and J R. Fienup, "Nonlinear Apodization for Sidelobe Control in SAR Imagery," *IEEE Transactions on Aerospace and Electronic Systems*, Vol. AES-31, No. 1, January 1995, pp. 267-279.

[6] Cutrona, L.J., E.N. Leith, L.J. Porcello, and W.E. Vivian, "On the Application of Coherent Optical Processing Techniques to Synthetic Aperture Radar," *Proceedings of the IEEE,* Vol. 54, No. 8, August 1966, pp. 1026-32.

[7] Taylor, T., "Design of Line-Source Antennas for Narrow Beam Width and Low Sidelobes," *IRE Transactions on Antennas & Propagation*, Vol. AP-3, January 1955.

[8] Rhodes, D., "On the Taylor Distribution," *IEEE Transactions on Antennas and Propagation*, Vol. AP-20, No. 2, March 1972, pp. 143-145.

[9] Elliot, R.S., "Design of Line-Source Antennas for Sum Patterns with Sidelobes of Individually Arbitrary Heights," *IEEE Transactions on Antennas and Propagation*, Vol. AP-24, No. 1, January 1976, pp. 76-83.

[10] United States Patent No. 5,349,359, Dallaire, R.J. and H.C. Stankwitz, "Spatially Variant Apodization," 20 September 1994.

[11] Dezellem, R., J. Adams, D. Mensa, and K. Vaccaro, "Non-Linear Windowing for ISAR Images," *Proceedings of the 1994 Antenna Measurements Techniques Association Symposium*, Long Beach, CA, 3-7 October, 1994, pp. 320-325.

Appendix E
Description of SAR Images

This appendix groups each image included in this book according to its originating SAR system. It also describes each SAR system and provides additional image parameters and information.

E.1 DATA COLLECTION SYSTEM

The ERIM data collection system (DCS) is a fine-resolution air-to-ground SAR imaging system on board a Convair CV-580 aircraft [1]. Developed jointly by the U.S. Air Force Wright Laboratory and ERIM, the DCS X-band radar sensor operates in stripmap and spotlight modes. The DCS can also collect single-pass interferometric SAR data and forward-look SAR data. The radar system is fully polarimetric and records the four linear transmit/receive antenna polarizations during a collection. Table 7.1 provides a full description of DCS collection modes. The DCS motion sensor includes an inertial measurement unit and a differential global positioning system receiver. Table E.1 describes each DCS image that appears in this book.

E.2 GROUND-TO-AIR IMAGING RADAR

The ERIM ground-to-air imaging radar (GAIR) is an X-band, fine-resolution, ground-based inverse SAR (ISAR) system [2-4]. The GAIR performs radar cross-section (RCS) diagnostic imaging of low-observable airborne targets. The system can record each of the four linear transmit/receive polarization combinations, one at a time. It produces imagery with 30-cm range and azimuth resolution. Section 7.2 provides a more complete description of the GAIR and Table 7.2 presents key system parameters. Table E.2 describes the GAIR images that appear in this book.

Table E.1
Images from the DCS Sensor

Figure	*Band*	*Mode*	*Range × Azimuth Resolution (m)*	*Range × Azimuth Image Size (m)*	*Scene Description*
1.1	X	Spotlight side-look	1 × 1	630 × 630	Office building in Ann Arbor, MI
5.14	X	Spotlight side-look	1 × 1	680 × 680	Iowa River on north side of Iowa City, IA; (a) with and (b) without added sinusoidal phase error
6.4	X	Spotlight side-look	1 × 1	680 × 680	Office building; (a) with added quadratic phase error and (b) after autofocus
6.7	X	Spotlight side-look	1 × 1	680 × 680	Office building; (a) with added quadratic, cubic, and quartic phase errors and (b) after autofocus
6.10	X	Spotlight side-look	1 × 1	680 × 680	Office building; (a) with added sinusoidal phase error and (b) after autofocus
8.18	X	Spotlight side-look	1 × 1	190 × 190	Radar test array near Willow Run airport in Ypsilanti, MI
9.2	X	Stripmap side-look	1 × 1	1250 × 530	Interstate I-80 north of Iowa City, IA
9.3	X	Stripmap side-look	1 × 1	1250 × 800	Interstate I-80 north of Iowa City, IA; using same Figure 9.2 data and excessive azimuth scene size
9.9(a)	X	Spotlight side-look	1 × 1	190 × 190	Radar test array near Willow Run airport in Ypsilanti, MI
9.9(b)	X	Spotlight forward-look	1 × 1	190 × 190	Radar test array near Willow Run airport in Ypsilanti, MI
9.14	X	Spotlight side-look	1 × 1	1250 × 800	Iowa River on the north side of Iowa City, IA
9.15	X	Spotlight side-look	1 × 1	1250 × 800	Figure 9.14 scene; Leveled and unfiltered interferogram derived from SAR image
9.16	X	Spotlight side-look	1 × 1	1250 × 800	Figure 9.14 scene; Leveled and filtered interferogram derived from Figure 9.15 interferogram

Table E.1 (continued)
Images from the DCS Sensor

Figure	*Band*	*Mode*	*Range × Azimuth Resolution (m)*	*Range × Azimuth Image Size (m)*	*Scene Description*
9.17	X	Spotlight side-look	2.5 × 2.5	1250 × 800	Figure 9.14 scene; Terrain height contours derived from Figure 9.16 interferogram
9.18	X	Spotlight side-look	2.5 × 2.5	1250 × 800	Figure 9.14 scene; Perspective plot of terrain height data derived from Figure 9.17 data
D.2	X	Spotlight side-look	1.1 × 1.1	660 × 660	University of Michigan football stadium, Ann Arbor, MI; with unweighted rectangular aperture
D.4	X	Spotlight side-look	1.1 × 1.1	660 × 660	University of Michigan football stadium, Ann Arbor, MI; using unweighted circular aperture
D.7	X	Spotlight side-look	1.1 × 1.1	660 × 660	University of Michigan football stadium, Ann Arbor, MI; using Taylor weighting
D.17	X	Spotlight side-look	1.1 × 1.1	660 × 660	University of Michigan football stadium, Ann Arbor, MI; using spatially variant apodization
D.18 (a)	K_u	Spotlight side-look	1 × 1	400 × 400	Freighters docked near Toledo, OH; using Taylor weighting
D.18 (b)	K_u	Spotlight side-look	1 × 1	400 × 400	Freighters docked near Toledo, OH; using spatially variant apodization

E.3 ROTATING PLATFORM FACILITY

The ERIM rotating platform facility is a ground-based, fine-resolution ISAR system. It operates in the X, K_a, and W radar bands. The target area is a 6-m-diameter circular table installed flush with the surrounding ground surface. The radar is horizontally located 43 m away from table center. The sensor height is variable to illuminate the scene at any grazing angle between 0 and 15 deg. The rotating platform facility is a resource for RCS and scattering studies of both smaller targets and scale models of larger targets. Table E.3 describes the rotating platform images.

Table E.2
Images from the GAIR Sensor

Figure	*Band*	*Mode*	*Range × Azimuth Resolution (m)*	*Range × Azimuth Image Size (m)*	*Scene Description*
7.11	X	Spotlight ISAR	0.3 × not applicable	60 × not applicable	In-flight Convair CV-580 aircraft; range compressed data before coarse motion compensation
7.14	X	Spotlight ISAR	0.3 × not applicable	60 × not applicable	In-flight Convair CV-580 aircraft; range compressed data before coarse motion compensation
7.15	X	Spotlight ISAR	0.3 × not applicable	60 × not applicable	In-flight Convair CV-580 aircraft; range compressed data with coarse motion compensation
7.18	X	Spotlight ISAR	0.3 × 0.3	45 × 45	In-flight Convair CV-580 aircraft; processed using (a) single and (b) dual PPP algorithm
7.19	X	Spotlight ISAR	0.3 × 0.3	45 × 45	In-flight Convair CV-580 aircraft; processed using (a) single and (b) dual PPP algorithm
7.20	X	Spotlight ISAR	0.3 × 0.3	30 × 30	In-flight Convair CV-580 aircraft; processed at head-on aspect angle with single PPP algorithm

E.4 P-3/SAR SYSTEM

The P-3/SAR is a multimode, fully polarimetric imaging radar that flies aboard a Navy P-3 aircraft [5]. Built by ERIM and the Naval Air Warfare Center (NAWC), the P-3/SAR system operates in the X, L, and C radar bands and can image simultaneously in all three bands. The system supports stripmap and spotlight modes with range resolutions down to 1.125 m. Recently, ERIM and NAWC completed a modification to this system for the Advanced Research Projects Agency (ARPA). This modification permits collection of wideband polarimetric SAR data at low-frequency (509 MHz bandwidth between the frequencies of 215 and 900 MHz); it supports 0.33-m range resolution and 0.66-m azimuth resolution [6, 7]. Table E.4 describes the P-3/SAR images that appear in this book.

Table E.3
Images from the Rotating Platform Sensor

Figure	*Band*	*Mode*	*Range × Azimuth Resolution (m)*	*Range × Azimuth Image Size (m)*	*Scene Description*
4.26	X	Spotlight ISAR	0.06 × 0.06	8 × 8	Automobile at three aspect angles with LOSPI
4.28	X	Spotlight ISAR	0.06 × 0.06	8 × 8	Automobile at three aspect angles with SSPI
4.29	X	Spotlight ISAR	0.06 × 0.06	8 × 8	Noncoherent sum of 36 separate images of automobile over 360 deg of target rotation

Table E.4
Images from the P-3/SAR Sensor

Figure	*Band*	*Mode*	*Range × Azimuth Resolution (m)*	*Range × Azimuth Image Size (m)*	*Scene Description*
10.27	L	Stripmap side-look	1.1 × 0.6	5028 × 2510	Airfield near Key West, FL
10.28	L	Stripmap side-look	1.1 × 0.6	960 × 880	Close-up of runway in the image in Figure 10.27
10.29	VHF/ UHF	Stripmap side-look	0.33 × 0.66	800 × 1200	Biological experiment station near Pellston, MI
10.30	VHF/ UHF	Stripmap side-look	0.33 × 0.66	180 × 180	Close-up of concealed vehicles in the image in Figure 10.29
11.15	L	Spotlight	1.1 × 1.1	2450 × 1420	Wooded area near Portage, ME
11.16	L	Spotlight	1.1 × 1.1	560 × 364	Close-up of engineering array in the image in Figure 11.15

E.5 SIMULATED IMAGES

Images in Figure 3.7, Figure 5.15, Figure 7.6, Figure 10.20, and Figure 11.13 originate from computer-generated signal histories; they illustrate various properties of SAR imagery, but do not use actual SAR sensor data.

REFERENCES

[1] DiMango, M.A., W.T. Hanna, and L. Andersen, "The Data Collection System (DCS) Airborne Platform," *First International Airborne Remote Sensing Conference and Exhibition*, Strasbourg, France, September 1994.

[2] Goodman, R., W. Nagy, J. Wilhelm, and S. Crippen, "A High Fidelity Ground to Air Imaging Radar System," *1994 IEEE National Radar Conference*, Atlanta, GA, March 1994.

[3] Nagy, W., and E. Johansen, "Ground and Airborne Calibration of the Ground to Air Imaging Radar," *Proceedings of the 1993 AMTA Symposium*, Dallas, TX, October 1993.

[4] Goodman, R., L. Joyce, and L. Cech, "ISAR Image Formation Processing for Airborne Targets," *Proceedings of the 1994 AMTA Symposium*, Long Beach, CA, October 1994.

[5] Sullivan, R., A. Nichols, R. Rawson, C. Haney, F. Darreff, and J. Schanne, Jr., "Polarimetric X/L/C-Band SAR," *Proceedings of the 1988 IEEE National Radar Conference*, Ann Arbor, MI, 20-21 April 1988, pp. 9-14.

[6] Goodman, R., S. Tummala, and W. Carrara, "Issues in Ultra-Wideband, Widebeam SAR Image Formation," *Proceedings of the 1995 IEEE International Radar Conference*, Washington, D.C., May 1995 (in press).

[7] Sheen, D.R., C.M. Strawitch, and T.B. Lewis, "UHF Wideband SAR Design and Preliminary Results," *Proceedings of the 1994 IEEE International Geoscience and Remote Sensing Symposium (IGARSS)*, Pasadena, CA, August 1994.

Acronyms

Acronym	*Corresponding Phrase*	*Description*
A/D	analog-to-digital	Section 2.1.2
AGC	automatic gain control	Section 8.7.2
AMBR	ambiguity ratio	Section 8.4.1
APC	antenna phase center	Section 2.6.1
ARP	aperture reference point	Section 2.6.1
ATD	automatic target detection	Section 2.1.5
ATR	automatic target recognition	Section 2.1.5
BCR	beam compression ratio	Section 2.4.3
CDA	complex dual apodization	Section D.3
CNR	clutter-to-(radar receiver) noise ratio	Section 8.4.2
CPU	central processing unit	Section 7.1.3
CSA	chirp scaling algorithm	Chapter 11
CUP	common UNIX processor	Section 7.1
D/A	digital-to-analog	Section 2.1.2
DA	dual apodization	Section D.3
DCS	data collection system	Section 7.1.1
DTCR	distributed target contrast ratio	Section 8.4.3
DFT	discrete Fourier transform	Section 4.4
DTE	digital terrain elevation	Section 9.3.6
FFT	fast Fourier transform	Section 1.4.2
FIR	finite impulse response	Section 4.0
FM	frequency modulation	Section 2.3
FOPEN	foliage penetration	Section 10.5.2
FTP	focus target plane	Section 3.3.4

Acronym	*Corresponding Phrase*	*Description*
GAIR	ground-to-air imaging radar	Section 7.2
GPR	ground-penetrating radar	Section 10.5.2
GPS	global positioning system	Section 2.1.3
GUI	graphical user interface	Section 7.1.2
HDDT	high-density digital tape	Section 7.1.1
HOF	height-of-focus	Section 3.3.4
IDP	image display plane	Section 3.3.5
IF	intermediate frequency	Section 2.3.2
IFP	image formation processor	Section 2.1.4
IFSAR	interferometric synthetic aperture radar	Section 9.3
IMU	inertial measurement unit	Section 2.5.3.4
INS	inertial navigation system	Section 2.5.3.4
IQ	image quality	Section 8.0
ISAR	inverse synthetic aperture radar	Section 2.7
ISLR	integrated sidelobe ratio	Section 5.1.2
LOS	line-of-sight	Section 5.3.1
LOSPI	line-of-sight polar interpolation	Section 4.3
LPI	low probability of intercept	Section 2.3
MAM	multiple aperture mapdrift	Section 6.2
MCP	motion compensation point	Section 2.6.1
MD	mapdrift (algorithm)	Section 6.1
MNR	multiplicative noise ratio	Section 8.4
MTRC	motion through resolution cells	Section 3.1.2
NCI	noncoherent integration	Section 8.4.3
NPM	nonplanar motion	Section 3.3.4
NRA	no-return area	Section 8.7.1
OGU	output grid unit	Section 4.4.1

Acronym	*Corresponding Phrase*	*Description*
PCR	pulse compression ratio	Section 2.3.2
PD	phase difference (algorithm)	Section 6.3
PFA	polar format algorithm	Chapter 3
PGA	phase gradient algorithm	Section 6.4
PLF	performance limiting factor	Section 8.2
PPP	prominent point processing	Section 6.5
PRF	pulse repetition frequency	Section 2.1.1
PSD	power spectral density	Section 5.1.2
PSP	principle of stationary phase	Section 10.3.1
PSR	peak sidelobe ratio	Section 5.1.2
PTCR	point-target contrast ratio	Section 8.4.3
QNR	quantization noise ratio	Section 8.4.1
QPE	quadratic phase error	Section 5.5.1
RCS	radar cross-section	Section 2.2
RF	radio frequency	Section 2.1.2
RMA	range migration algorithm	Chapter 10
RMS	root mean square	Section 5.1.2
RVP	residual video phase	Section 3.10
SAR	synthetic aperture radar	Section 1.1
SBR	signal-to-background ratio	Section 8.4
SCR	signal-to-clutter ratio	Section 8.4.2
SNR	signal-to-noise ratio	Section 8.4.2
SSPI	stabilized scene polar interpolation	Section 4.7
SVA	spatially variant apodization	Section D.3
TR	tomographic reconstruction	Appendix B
TRCS	total radar cross-section	Section 7.2.1
UAV	unmanned aerial vehicle	Section 1.5
UHF	ultra-high frequency	Section 10.5.2
UWB	ultra wideband	Section 10.5.2
VHF	very high frequency	Section 10.5.2

Symbols

Symbol	*Definition*	*Reference*
a_t	Amplitude associated with scatterer RCS; $a_t = \sqrt{\sigma_t}$	Section 2.6.3
a_{zo}	Component of measured APC acceleration normal to nominal slant range plane at aperture center	Equation (3.146)
A_a	Measured APC acceleration vector at aperture center	Section 2.6.3
A_e	APC acceleration measurement error vector at aperture center	Section 2.6.3
A_{elos}	LOS component of APC acceleration measurement error at aperture center	Section 5.3.1
A_{xa}	X component of measured APC acceleration at aperture center	Section 2.6.3
A_{xe}	X component of APC acceleration measurement error at aperture center	Section 2.6.3
A_{ya}	Y component of measured APC acceleration at aperture center	Section 2.6.3
A_{ye}	Y component of APC acceleration measurement error at aperture center	Section 2.6.3
A_{za}	Z component of measured APC acceleration at aperture center	Section 2.6.3
A_{ze}	Z component of APC acceleration measurement error at aperture center	Section 2.6.3
B	Transmitted RF bandwidth; $B = \gamma T_p$	Section 2.3.2
B_a	Azimuth scene bandwidth after dechirp	Section 2.4.5
B_d	Doppler bandwidth of a single scatterer before azimuth dechirp	Section 2.4.4
B_i	Interferometric baseline	Section 9.3.2
B_{IF}	IF bandwidth (after range dechirp) associated with Δr	Equation (2.4)
BCR	Beam compression ratio	Section 2.4.3
CNR	Clutter-to-(radar receiver) noise ratio	Section 8.4.2
d_a	Azimuth distance between two points in an image	Section 4.5
d_r	Range distance between two points in an image	Section 4.5
DTCR	Image distributed-target-contrast ratio	Section 8.4.3

Symbol	*Definition*	*Reference*
f_c	Radar center transmit frequency	Section 2.3.2
f_d	Doppler frequency	Section 2.4.4
F_s	Radar A/D sampling frequency	Section 2.6.5
G	Real antenna one-way gain	Section 8.4.2
ISLR	Integrated sidelobe ratio	Section 8.3.3
k	Sample number within a radar pulse	Section 2.6.5
k_{ga}	Spatial frequency interval between azimuth output grid samples in processor space	Section 4.3
k_{gr}	Spatial frequency interval between range output grid samples in processor space	Section 4.3
K	Number of samples on each radar pulse	Section 2.6.5
K_a	Mainlobe-broadening factor associated with azimuth resolution	Section 2.4.2
K_c	Radian spatial frequency corresponding to f_c at aperture center with $K_c = 4\pi f_c S_{\phi c}/c$	Section 3.3.3
K_C	Radian spatial frequency corresponding to f_c with $K_C = 4\pi f_c S_{\phi a}/c$	Section 4.3
K_H	Radian spatial frequency corresponding to $f_c + B/2$	Section 4.3
K_L	Radian spatial frequency in processor space corresponding to $f_c - B/2$	Section 4.3
K_p	Radial wavenumber coordinate in PFA processor space	Section 4.3
ΔK_p	Distance between samples on a pulse in PFA processor space	Section 4.3
K_r	Mainlobe-broadening factor associated with range resolution	Section 2.3.2
l_x	x component (azimuth) of image distortion	Section 3.5.1
l_y	y component (negative range) of image distortion	Section 3.5.1
L	Synthetic aperture length	Section 2.4.1
L_f	Digital filter length in samples	Section 4.2.3
L_u	Digital filter upsampling factor	Section 4.2.3
L_x	X component (azimuth) of image displacement	Section 3.5.1
L_y	Y component (negative range) of image displacement	Section 3.5.1

Symbol	*Definition*	*Reference*
m_x	Image scaling factor in x (azimuth) direction	Section 3.5.1
m_y	Image scaling factor in y (negative range) direction	Section 3.5.1
MNR	Multiplicative noise ratio	Section 8.4.1
n	Pulse number	Section 2.6.5
n_c	Pulse number associated with aperture center	Section 2.6.3
n_Δ	Pulse number relative to n_c where $n_\Delta = n - n_c$	Section 2.6.3
N_p	Number of pulses over data aperture	Section 2.6.5
$NFFT_a$	Azimuth FFT length (in samples)	Section 4.5
$NFFT_r$	Range FFT length (in samples)	Section 4.5
NPH_a	Azimuth extent (in samples) of interpolated signal history	Section 4.3
NPH_r	Range extent (in samples) of interpolated signal history	Section 4.3
$\boldsymbol{P_a}$	APC position vector at aperture center	Section 2.6.3
$\boldsymbol{P_e}$	APC position measurement error vector at aperture center	Section 2.6.3
PCR	Pulse compression ratio; PCR = γT_p^2	Equation (2.3)
PTCR	Image point-target-contrast ratio	Section 8.4.3
Δr	Range swath associated with receiver range gate; similar to W_r	Section 2.3.2
r_{elos}	Error in measurement of line-of-sight range	Section 5.3.1
r_o	Nominal scene radius	Section 3.2.2
$\boldsymbol{r_t}$	Target location vector	Section 2.6.1
r_t	Scatterer distance from scene center; amplitude of $\boldsymbol{r_t}$	Section 2.6.1
$\boldsymbol{R_a}$	Measured slant range vector	Section 2.6.1
R_a	Measured distance between APC and scene center; amplitude of $\boldsymbol{R_a}$	Section 2.6.1
R_{ac}	Amplitude of slant range vector at aperture center	Section 3.3.3
R_Δ	Expression for differential range $R_t - R_a$	Section 3.2.2
$R_{\Delta c}$	Differential range at aperture center	Section 3.4.3
$\dot{R}_\Delta$	Time rate-of-change of differential range	Section 3.2.2

Symbol	*Definition*	*Reference*
R_o	Reference range corresponding to time delay of range dechirp signal	Section 2.6.4
R_q	Range estimation and quantization error; $R_q = R_o - R_a$	Section 2.6.4
R_s	Fixed reference range applicable to stripmap mode data collection	Section 9.1.2
R_t	Distance between true APC location and a particular scatterer	Section 2.6.3
$\dot{R}_t$	Time rate of change of R_t denoted range rate	Section 2.2
R_B	Minimum distance between the APC and a scatterer during the coherent aperture interval	Section 11.1
SBR	Signal-to-background ratio	Section 8.4
SCR	Signal-to-clutter ratio	Section 8.4.2
SNR	Signal-to-(receiver) noise ratio	Section 8.4.2
t	Continuous or real time; sometimes denoted slow time	Section 2.1.1
$\hat{t}$	Time within a received pulse designated fast time; $\hat{t} = t - nT$	Section 2.1.1
t_d	Round-trip time delay between antenna phase center and a scatterer	Section 2.6.3
T	Pulse repetition interval or interpulse time	Section 2.1.1
T_a	Coherent aperture time associated with synthetic aperture L	Section 2.4.2
T_p	Length of transmitted RF pulse	Section 2.3.1
T_s	Two-way time delay associated with range swath Δr	Section 2.3.2
T_S	A/D sampling interval; $T_S = T_s + T_p$	Section 2.3.2
TB_a	Scene time-bandwidth product in azimuth after azimuth dechirp	Section 2.4.5
TB_r	Scene time-bandwidth product in range after range dechirp	Section 4.3
u_i	Image coordinate corresponding to azimuth in target space	Section 3.5.1
v_i	Image coordinate corresponding to negative range in target space	Section 3.5.1
$\boldsymbol{V}_a$	Measured APC velocity vector at aperture center	Section 2.6.3
V_a	Amplitude of measured APC velocity vector $\boldsymbol{V}_a$ at aperture center	Section 2.4.2
$\boldsymbol{V}_e$	APC velocity measurement error vector at aperture center	Section 2.6.3
V_{xa}	X component of measured APC velocity at aperture center	Section 2.6.3

Symbol	*Definition*	*Reference*
V_{xe}	X component of velocity measurement error at aperture center	Section 2.6.3
V_{ya}	Y component of measured APC velocity at aperture center	Section 2.6.3
V_{ye}	Y component of velocity measurement error at aperture center	Section 2.6.3
V_{za}	Z component of measured APC velocity at aperture center	Section 2.6.3
V_{ze}	Z component of velocity measurement error at aperture center	Section 2.6.3
W_a	Azimuth scene size	Section 2.4.5
W_r	Range scene size; similar to Δr	Section 4.3
x_p	Wavenumber domain coordinate associated with azimuth dimension and centered on signal data in processor space	Section 3.3.3
x_t	x component (azimuth) of scatterer location in target space	Equation (3.69)
X_a	X component of measured APC position	Section 2.6.1
X_{ac}	X component of measured APC position at aperture center	Section 2.6.3
X_e	X component of APC position measurement error	Section 2.6.3
X_{ec}	X component of APC position measurement error at aperture center	Section 2.6.3
X_t	X component of scatterer location	Section 2.6.3
y_p	Wavenumber domain coordinate associated with negative range dimension and centered on signal data in processor space	Section 3.3.3
y_t	y component (negative range) of scatterer location in target space	Equation (3.70)
Y_a	Y component of measured APC position	Section 2.6.1
Y_{ac}	Y component of measured APC position at aperture center	Section 2.6.3
Y_e	Y component of APC position measurement error	Section 2.6.3
Y_{ec}	Y component of APC position measurement error at aperture center	Section 2.6.3
Y_t	Y component of scatterer location	Section 2.6.3
z_t	z component of scatterer location in target space; $z_t = Z_t$	Equation (3.71)
Z_a	Z component of measured APC position	Section 2.6.1
Z_{ac}	Z component of measured APC position at aperture center	Section 2.6.3

Symbol	*Definition*	*Reference*
Z_e	Z component of APC position measurement error	Section 2.6.3
Z_{ec}	Z component of APC position measurement error at aperture center	Section 2.6.3
Z_{hof}	Height-of-focus distance introduced by nonplanar motion	Section 3.8
Z_t	Z component of scatterer location	Section 2.6.3
α_d	Instantaneous Doppler cone angle	Section 2.6.1
α_{dc}	Doppler cone angle at aperture center	Section 2.6.1
β_a	Half-power one-way azimuth beamwidth of real antenna	Section 2.4.1
β_e	Half-power one-way elevation beamwidth of a real antenna	Table 2.4
β_o	Slope angle between the IDP and the XY plane	Figure 2.22
β_s	Half-power beamwidth of synthetic aperture	Equation (2.14)
γ	Chirp rate of linear FM waveform	Section 2.3.2
γ_a	Chirp rate associated with signal received across synthetic aperture	Section 2.4.4
λ_c	Wavelength corresponding to center frequency	Section 2.4.1
μ	Interferometric image complex correlation coefficient; $\mu = \mu_c \mu_m \mu_n$	Section 9.3.4
μ_a	Azimuth image scale factor in units of distance/pixel (compares to $1/m_x$)	Section 4.5
μ_c	Correlation coefficient due to interferometric depression angle difference	Equation (9.23)
μ_m	Correlation coefficient due to misregistration between interferometric image pair	Equation (9.24)
μ_n	Correlation coefficient associated with background noise	Equation (9.25)
μ_r	Range image scale factor in units of distance/pixel (compares to $1/m_y$)	Section 4.5
ϕ_a	Instantaneous incidence angle	Section 2.6.1
ϕ_{ac}	Incidence angle at aperture center	Section 2.6.1
ϕ_p	Instantaneous incidence angle in wavenumber (processor) space associated with the data collection incidence angle ϕ_a	Figure 3.12

Symbol	*Definition*	*Reference*
ϕ_s	Instantaneous display incidence angle	Section 2.6.1
ϕ_{sc}	Display incidence angle at aperture center	Section 2.6.1
ψ_a	Instantaneous grazing angle	Section 2.6.1
ψ_{ac}	Grazing angle at aperture center	Section 2.6.1
ψ_s	Instantaneous display grazing angle	Section 2.6.1
ψ_{sc}	Display grazing angle at aperture center	Section 2.6.1
ρ_a	Azimuth resolution	Section 2.4.1
ρ_r	Range resolution	Section 2.3.1
$\Delta\rho_a$	Misregistration in azimuth direction between interferometric image pair	Section 9.3.4
$\Delta\rho_r$	Misregistration in range direction between interferometric image pair	Section 9.3.4
σ_n	Effective backscatter coefficient of additive noise; $\sigma_n = \sigma_o/\text{CNR}$	Section 8.4.2
σ_N	Radar system total noise; $\sigma_N = \sigma_n + (\text{MNR})\bar{\sigma}_o$	Equation (8.1)
σ_o	Radar backscatter coefficient of terrain (RCS per unit ground area)	Section 8.4
$\bar{\sigma}_o$	Average backscatter coefficient of local terrain	Section 8.4
σ_t	Scatterer radar cross-section	Section 2.6.3
θ_a	Instantaneous squint angle	Section 2.6.1
θ_{ac}	Squint angle at aperture center	Section 2.6.1
θ_p	Instantaneous squint angle in wavenumber (processor) space associated	Figure 3.12
θ_s	Instantaneous display squint angle	Section 2.6.1
θ_{sc}	Display squint angle at aperture center	Figure 4.15
θ_L	Image look angle; equivalent to θ_{sc}	Section 4.3
$\Delta\theta$	Coherent integration angular interval associated with azimuth resolution	Section 2.4.2
$\Delta\theta_p$	Coherent integration angular interval in IDP associated with $\Delta\theta$	Equation (3.30)
ω_c	Filter cutoff frequency	Section 4.1.1
ω_s	Radian sampling frequency	Section 4.1.1

Index

A/D conversion 18, 69–70
Ambiguity ratio 333
Angle
  display grazing 61
  display squint 61
  Doppler cone 22, 59
  grazing 59
  grid 193
  incidence 59, 61
  slope 59
  squint 60
Antenna phase center 57
Aperture
  reference point 57
  time 14, 40–41
Aperture weighting 211, 507–515
  See also complex dual apodization
  See also spatially variant apodization
Apodization 515–524
Autofocus 245–287
  mapdrift 246–252
  multiple aperture mapdrift 252–260
  phase difference algorithm 260–264
  phase gradient 264–268
  prominent point processing 268–282
  space-variant considerations 282–285
Azimuth
  bandwidth 43
  chirp 409, 428–433, 446
  chirp rate 42–43
  dechirp 43, 99, 143–144
  presumming 18, 20, 44–45, 307
  resolution 31–45
  scene size 190
Azimuth resolution 31–45
  performance limiting factors 325
  real beam 32
  synthetic aperture 33–37

Backprojection 496
Backscatter coefficient
  of additive and total noise 331–335
  of local terrain 331
  table of values 331
Bandwidth
  Doppler 32, 42–45, 428
  range 29, 176–178
Beam compression ratio 41
Bistatic SAR 18

Chirp rate
  azimuth 42–43
  range 27
Chirp scaling algorithm 443–470
  analytical development 456–464
  compared with RMA and PFA 443, 474–486
  computational complexity 479–482
  IFP block diagram 478
  limitations 465–468, 484–485
Clutter-to-noise ratio 333
Coherence
  SAR requirements for 46–56
Common UNIX processor 289–297
  software architecture 294–297
Complex dual apodization 517–519
Computational complexity
  estimation method 479
  of IFP algorithms 480–482
Cone angle 59
Contrast ratio 335–339
Convolution
  input and output centered 171–173
Cubic phase error 210–211

Data collection system (DCS) 289–292
  image list 532–533
Dechirp-on-receive 28–30, 66–68, 402, 445, 484
Deskew 405–407, 505

Differential range 84–86, 116–119
Display grazing angle 61
Display squint angle 61
Distortion
  See geometric distortion
Distributed-target-contrast-ratio 338
Doppler
  bandwidth 32, 42–45
  cone angle 22, 59
  Iso-Doppler cones 22–26
Downsampling 18, 163
Dual apodization 517–519
Dynamic range 343

Error budgets 317–320
Error sources 223–236

Filters
  FIR 158–173
  for digital quadrature demodulation 490
  matched 413–415, 427, 453
  polyphase 166–171
Focus target plane 57, 107–109, 191
Foliage penetration 435, 437
Forward-look SAR 361–367

Geometric distortion 148–150, 339–342
  definition of 339
  from range curvature 233
  from residual video phase 233–234, 506
  table of sources 223
Geometry
  data collection 57–61
  data format 111–113
  forward-look SAR 362–363
  ISAR 73–75
  stripmap mode 360
Grazing angle 59
Ground-penetrating radar 437
Ground-to-air imaging radar 297–313
  and prominent point processing 303
  image list 534
  system overview 297–302

Hanning aperture weighting 512

Image displacement 240
Image display plane 59, 109–119, 191, 340, 409
Image distortion 132–136, 148–152, 223
Image exploitation 21, 313
Image formation processor 20
Image intensity uniformity 344
Image phase 127, 370–374
Image processor 20
Image quality 316–350
  measurement 325, 345–350
  metrics 316, 343
  requirements and specification 316–319
Image scale factors 120, 189–190
Images
  description of SAR images 531–536
Impulse response
  See resolution
  See system impulse response
Incidence angle 59, 61
Integrated sidelobe ratio
  definition 330
  for various aperture weightings 529
  phase error effects on 218
Interferometric SAR 24–26, 367–383
  absolute height extraction 377–378
  and digital terrain elevations 379
  geometry model 370–374
  height resolution of 375–377
  IFP requirements 374–375
  image examples 380–382
  interferogram filtering 375
  interferogram leveling 375
  interferogram, definition of 372
  orthorectification 379–380
Interpolation 157–175
  and sinc reconstruction 159
  azimuth 187–189
  downsampling 163
  LOSPI 192–193
  range 181–187
  resampling 163–165
  SSPI 177, 192–197
  upsampling 158–161
  See also polar interpolation 157
Inverse SAR (ISAR) 72–75
  and ground-to-air imaging radar 297–302
  and prominent point processing 268–281
Iso-range-Doppler contours 21–23, 133

Lever arm correction 51–55, 290–292
Linear FM waveforms 27–30, 61–63, 443–446

Mapdrift autofocus 246–252
  analytical development 246–251
  implementation 249–252
Monostatic SAR 18

Motion compensation 403–407
and coherence 49
equations for 70
fine 68
for ISAR systems 73, 306–310
for spotlight mode 66, 403–404
for stripmap mode 67, 405–406, 445
real time 19, 55, 67, 68
Motion during a pulse 56, 63, 147
Motion effects 48–56
categories 55–56
compensation procedures for 49
measurement and phase errors 225–233
Motion sensor
function in SAR 19
SAR requirements on 236–238
types 53–55
Motion through resolution cells 6, 71, 92, 407
Moving targets
and phase error effects 238–241
imaging 297–313
Multiple aperture mapdrift 252–260
analytical development 254–258
implementation 258–260
Multiplicative noise ratio 331–335
performance limiting factors 334

Noise
additive 331, 333
measurement of 349
multiplicative 331, 332
quantization 333
requirements 330–339
total 331
Nonplanar motion 235, 407

Ops count 479–482
Optical processing 6–7
Orthorectification 379–380

P-3 SAR
description 436–439, 468
image list 535
Peak sidelobe ratio 214, 329
Performance limiting factor 317
Performance budget 317–320
Phase coherence 46–49
Phase difference algorithm 260–264
analytical development 262
implementation 264
Phase equation
See signal model

Phase errors 203–243
allowable levels of 222
and distortion 120
and integrated sidelobe ratio 218
and peak intensity loss 323
and peak sidelobe levels 214
and position measurement errors 225–233
and resolution degradation 323
and scene displacements 120
categories of 204
effects on impulse response 210
expressions for magnitude of 223–224
from motion measurement errors 140, 225–233
from nonplanar sensor motion 139, 235
from range curvature 233
from residual video phase 234, 506
high frequency 212–219
low frequency 206–211
management of 220–222
other sources 235
Phase gradient autofocus 264–268
analytical development 265–267
implementation 268
Plane
data collection 58
focus target 57, 107–109, 191
image display 59, 109–119, 191, 339–342, 409
projections in polar interpolation 191–192
slant 59
Point-target-contrast ratio 337
Polar format algorithm 6–8, 81–111
analytical model 97–106
and nonplanar sensor motion 137–139
and range curvature 132–136
applied to stripmap data 357–359
compared with RMA 401, 433–435
compared with RMA and CSA 474–486
computational complexity 479–482
differential range approximation 117
geometry model 111–112
history 6–8
IFP block diagram 475
with motion measurement errors 140–143
Polar interpolation 175–189
azimuth direction 187–189
line-of-sight 177, 193
range direction 181–187
signal history projections 191–192
stabilized scene 193–195
subpatch processing 198–199
Polyphase filters 166–171

Presumming 18, 20, 44–45, 307
Principle of stationary phase 423–426, 456–464
Projection-slice theorem 496
Prominent point processing (PPP) 268–282
  example use of 308–310
  geometry model 277
  historical background 270
  multiple PPP algorithm 274–281
  single PPP algorithm 270–274
Pulse compression 26–28
Pulse repetition frequency (PRF) 15
Pulse repetition interval 15

Quadratic phase error 206–211
  from motion errors 143
  from nonplanar motion 138
  from range curvature 135
  from residual video phase 146
  image example 253
  table of sources 224
Quadrature demodulation
  analog 488
  digital 487–491
  in GAIR system 304
Quantization noise ratio 333

Radar cross section
  calibration 343–344
  diagnostic imaging 297
  of a dihedral 348
  of a top hat 347
  of a trihedral 345
  table of common terrain 331
Range
  bandwidth 29
  chirp 402–403, 446
  chirp rate 27
  dechirp 28, 99
  differential 116–119
  gate 14, 295, 305–307
  layover 384
  rate 22
  resolution 26–28
  scene size 190
  skew 30
  slant 58
Range curvature 88–90, 128–132, 412–420, 447
  and polar format 132–136
  differential 407, 436, 447, 452, 461
  in stripmap mode 90
  size of geometric distortion 223
  size of quadratic phase error 233
Range migration algorithm 401–442
  analytical model 420–428
  compared with PFA 401, 433–435
  compared with PFA and CSA 474–486
  computational complexity 479–482
  geometry model 402
  IFP block diagram 477
  overview 407–418
  signal phase model 402–405
Range rate 84–86, 116–119
Range resolution
  linear FM waveform 28
  performance limiting factors 324
  short pulse 27
Range walk 90, 431
Ratio
  ambiguity 333
  beam compression 41
  clutter-to-noise 333
  distributed-target-contrast 338
  multiplicative noise 332
  peak sidelobe 214, 329
  point-target-contrast 337
  pulse compression 28
  quantization noise 333
  signal-to-clutter 335
  signal-to-noise 335
Rectangular format
  definition 6
  example image 94
  example signal history 8, 98
  limitations of 90–95
Resampling
  general considerations 163–165
  with polyphase filters 166–173
Residual video phase 501–506
  and deskew 405, 505
  general discussion 143–146, 405
  in polar format signal phase 106
  size of quadratic phase error 234, 506
  source of 30, 501
Resolution
  azimuth 31–45
  measurement in imagery 325–328
  performance limiting factors 324–325
  range 26–28
  See system impulse response
Rotating platform
  and MTRC 6, 92
  image list 535

Sampled signal 69, 175–177
Scan mode 4, 369
Scene center 58
Shadows 384
Short pulse 27
Sidelobe control 212–219, 231, 329–330, 507–526
Signal model
  CSA 443–446, 456–464
  PFA 67–72, 97–111
  phase equation 61–72
  prominent point processing 270–281
  RMA 402–407, 420–428
  stripmap mode 357–358
Signal phase equation 56, 61–72
  See also signal model
Signal-to-clutter ratio 335
Signal-to-noise ratio 335
Sinc reconstruction formula 159
Sinusoidal phase error 212–217
  and vibrating targets 386–397
  error budget 214, 236–237
  image example 216–217
Slant plane 59
Slant range 58
Slant range vector 58
Slope angle 59
Space-variant autofocus 282–285
Spatial-frequency domain
  See wavenumber space
Spatially variant apodization 515–524
Spotlight mode 5–9
  data collection geometry 58
  differences from stripmap 357
  forward-look 361–367
  See also interferometric SAR
  See also inverse SAR
  See also vibrating target
Spurious response 344
Squint angle 60
Stepped-frequency waveform 30–31
Stereo radargrammetry 383
Stolt interpolation 416–420, 427–428
  approximation for 432–433
Stripmap mode 4, 357–361
  differences from spotlight 357
  image example 361
  polar format processing of 357–359
  proper motion compensation 358
Subpatch processing 144, 198–199
Synthetic aperture
  length 32, 38–41
  time 40–41
  versus real beam 31–37
Synthetic Aperture Radar
  coherence requirements 46–56
  data collection geometry 57
  early development 2, 5
  modes 4
  optical processing of 6–8
  parametric design 76–78
  SAR sensor 15–18
  See also interferometric SAR
  subsystem error allocation 319
  system overview 13–21
  system performance budget 317
System impulse response
  and peak sidelobes 329
  mainlobe width 321
  measurement 325
  requirements 320
System noise
  See noise

Target
  distributed 330, 338
  point-like 330
  prominent point 281
  vibrating 386–397
Taylor aperture weighting 512
Taylor series expansion 119–125, 460, 466
Three-dimensional imaging 23–24, 367–385
Time-bandwidth product
  azimuth 43–44, 178
  range 178
Tomographic reconstruction 495–499

Ultra-wideband SAR 435, 437–441
Uniform aperture weighting 507–511
Upsampling 158–161

Vector
  data collection 113–116
  motion measurement error 64–65
  slant range 58, 64
  target location 58
Vibrating target 386–397
  data collection model 387–389
  effects on signal history 389
  paired echo focusing 392
  paired echo smearing 217, 390
  simulated examples 217, 396–397
  vibration detection process 394

Waveforms
linear FM 27–30, 61–63
short pulse 27
stepped-frequency 30–31
Wavenumber space 99–105, 409–415, 456–461

ISBN 0-89006-728-7

9 780890 067284 90000

Artech House Publishers BOSTON • LONDON